# Kent Academic Repository

**Gyamfi, Irene Anima (2021)** ***Live cell imaging based study into the role of phosphorylation in regulating the activity and function class I and V myosins.*** **Doctor of Philosophy (PhD) thesis, University of Kent,.**

# LIVE CELL IMAGING BASED STUDY INTO THE ROLE OF PHOSPHORYLATION IN REGULATING THE ACTIVITY AND FUNCTION OF CLASS I AND V MYOSINS

Thesis submitted to
The University of Kent

For the degree of
Doctor of Philosophy
Cell Biology

School of Biosciences
2021

**Irene Anima Gyamfi**

Word count: 60,711

## Declaration

No part of this thesis has been submitted in support of an application for any degree or qualification of the University of Kent or any other University or Institute of learning.

Signed:

Irene Anima Gyamfi

## Acknowledgments

I would like to give many thanks to my supervisor Professor Dan Mulvihill, Professor Mike Geeves and their respective lab groups for their continuous support, patience and the invaluable experience I have gained during my time with the groups. I also wish to thank Dr Martin Thomas, Jeremy Graham and the team at Cairn Research for providing fluorescence imaging and laboratory facilities. Finally, I thank my family and friends for the tremendous motivation throughout the project.

# Abstract

Class I and V myosins are highly-conserved motor proteins that exert force against actin, in order to undertake diverse cellular functions. Myosin I (Myo1) interacts with cellular membranes and actin, with functions in endocytosis and the cell cycle. Myosin V (Myo52) similarly binds to vesicles for transport. The Mulvihill lab has been investigating conserved phosphorylation events in *Schizosaccharomyces pombe* Myo1 and Myo52, which play a role in modulating their activity. Phosphorylation of the phospho-serines is hypothesised to elicit domain-specific changes in conformation and ligand binding to regulate function. The purpose of these phosphorylation sites is yet to be reported in the literature.

This thesis presents the latest findings from fluorescence live cell imaging observing dynamics of myosins and associated proteins in myosin phospho-mutant *S. pombe* strains. It also presents latest models to explain myosin regulation by phosphorylation. Serine-to-alanine substitutions in the phospho-mutants prevent phosphorylation of the sites of interest. TORC2 dependent phosphorylation of these sites modifies myosin conformation and can impact interactions with calmodulin light chains and other associated proteins. The *myo1.S742A* phospho-mutant strain displayed greater monopolar growth in the vegetative cycle. Endocytic actin activity was also significantly different at the ends of the cells during bipolar growth in G2. This indicated Myo1 S742 phosphorylation to have regulatory impact on the switch from monopolar growth to bipolar growth. During the meiotic cycle in these cells, Cam2-GFP foci lifetimes were significantly extended and endocytosis was further minimised, indicating Myo1 S742 phosphorylation is required for Cam2 binding and correct Myo1 function in endocytosis. Myo52 phospho-mutants displayed various changes in polarised cell growth, delocalised actin patches and reduced Myo52 motility. These observations indicate the Myo52 phosphorylation sites have an impact the regulation of cell growth, actin localisation and Myo52 motility. The observations of these myosin phosphorylation sites highlight them as regulators of Myo1 and Myo52 function.

To develop methods of fluorescence imaging, conditions that do not induce phototoxic effects on contractile actin ring constriction were determined and used to study CAR defects in temperature-sensitive tropomoyosin Cdc8 mutant strains, *cdc8.27* and *cdc8.110.* CAR defects revealed *cdc8.27* and *cdc8.110* to impact the actin stabilising function of Cdc8. A novel simultaneous two-channel spinning-disk imaging system, developed by Cairn Research, was also tested with live cells to demonstrate successful imaging of real-time co-movement of fluorescently labelled proteins in the red and green channel, without channel-to-channel bleed. This confirmed the system is able to capture the dynamics of proteins and reduce the time lag in time-lapses acquired by standard confocal imaging systems.

## Table of Contents

## List of Tables and Figures

# Chapter 1: Introduction

The rapid movement and transport of proteins within the living cell are orchestrated by a series of dynamic motor proteins along the cytoskeleton. Intracellular myosin is an abundant motor protein responsible for a plethora of essential cellular processes such as the cell cycle, endocytosis and the transport of vesicles.

In living cells, endocytosis, meiosis, cytokinesis and the rapid molecular transport of organelles are crucial for correct function. The mechanics of these processes follows a dynamic system, orchestrated by a series of myosin motor proteins along the actin filaments of the cytoskeleton in a stepwise fashion. Myosin V is the motor protein responsible for the transport of vesicles and organelles within living cells. It also has a regulatory role in the organisation of the cytoskeletal actin filaments and microtubules. Each 36 nm step, are the broadest steps amongst molecular motors and takes $\approx 10^{-3}$ s (Cappello et al., 2007). During endocytosis, myosin I links actin networks to the plasma membrane. Force generated by myosin I activity in actin nucleation and movement is required for endocytic internalization (Sun et al., 2006). Myosin I is also required for changes in cell polarity and cell growth during the cell cycle (Baker et al., 2019). With fluorescence microscopy, it is observed for as little as ≈7 s and therefore, rapid image capture is imperative for real-time imaging and analysis of myosin motility.

The activity of these myosins is modulated in part by phosphorylation of multiple phosphorylation sites along their structure. During this study, specific phosphorylation sites located in the myosin I neck region IQ (isoleucine-glutamine) motifs and along the whole length of myosin V are of particular interest. In myosin I, calmodulin light chains bind to IQ motifs in a phosphorylation dependent manner, to modulate signalling for its activity. In myosin V, the presence and absence of phosphorylation has unknown results.

*Schizosaccharomyces pombe* (*S. pombe*) have genes for myosins I and V and is often the model used in myosin studies. The unicellular organism has a small genome of which multiple genes are conserved across metazoans e.g. *Homo sapiens* and *Caenorhabditis elegans. S. pombe* are also able to show clear phenotypes that result from genetic mutations. Myosin properties such as localisation, dynamics and interactions with associated proteins have been examined during this project. The simplicity of *S. pombe* and protein analogues make it a suitable model for myosin phospho-regulation studies and phospho-mutant characterisation.

## 1.1 *S. pombe* and the cell cycle

### 1.1.1 *S. pombe,* the model system organism

*S. pombe,* also called fission yeast, is a free-living ascomycete yeast of the kingdom Fungi (Wood et al., 2002). The unicellular organism is a simple model system used to study molecular processes orchestrated by eukaryotic components such as cell cycle regulation, cytoskeletal organisation and organelle biogenesis which are also conserved in humans (Wilson-Grady et al., 2008). This is due to its simple genetic manipulation and conserved mechanisms (Willet et al., 2015). The organism shares more than 172 proteins with human homologues associated with diseases such as cancer and cystic fibrosis. As it is a unicellular eukaryotic organism, it enables the use of thousands of cells for the generation and discovery of mutants and study of biological functions and regulation of molecules (Hoffman et al., 2015).

*S. pombe* exhibits a cylindrical morphology with hemispherical ends. This is shown in Figure 1.1. A single cell measures at approximately 3.5 µm in diameter and 8 - 15 µm in length, depending on the cell cycle stage. At 15 µm, *S. pombe* undergo symmetric closed mitosis (the nuclear envelope does not disintegrate) to produce two daughter cells relatively equal in size. They possess the smallest eukaryotic protein-coding genome of 13.8 Mb. The three chromosomes in *S. pombe* (chromosomes I, II and III) are 5.7 Mb, 4.6 Mb and 3.5 Mb in length (Hoffman et al., 2015). To date, 5064 protein-encoding genes have been recorded. 2430 proteins have published biological functions and over 300 are conserved in vertebrates (Hoffman et al., 2015; Lock et al., 2018)

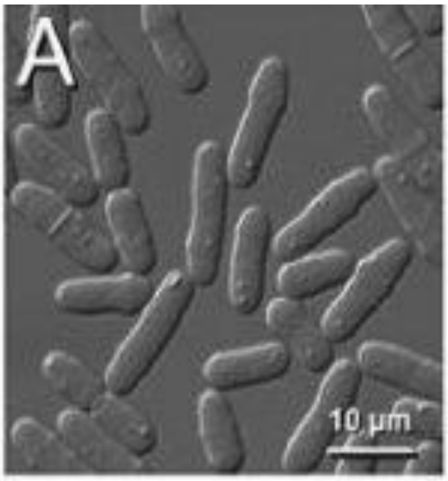

**Figure 1.1.** ***S. pombe*** **have a cylindrical morphology.** A photomicrograph of wild-type *S. pombe* cells in mid-log phase. *S. pombe* have a cylindrical morphology with hemispherical ends. Mitotic (dividing) cells can be seen with a septum in the middle of the cell for cell division. Scale bar - 10 µm. Adapted from Luo et al. (2009).

### 1.1.2 *S. pombe* polarised cell growth and cell cycle

Cell polarity is the asymmetrical ordered distribution of components within the cell. These components include organelles, the cytoskeleton and the plasma membrane. All cells polarise to divide or to define a cell shape and function. Multiple molecules, involved in the regulation of polarisation, are conserved in all eukaryotes. Cell polarity is regulated mainly by Cdc42 (cell division cycle 42). Cdc42 is a small GTPase, which is a molecule that binds to GTP (guanosine triphosphate) and hydrolyses it. When bound to GTP, Cdc42 signals to downstream effectors that maintain cell polarity by regulating cytoskeleton organisation. Cytoskeleton organisation is required for growth processes such as endocytosis, secretion and cell wall synthesis during the cell cycle (Etienne-Manneville, 2004).

Cell polarity is used for directional growth. In *S. pombe,* growth only occurs at the cell ends. Growth polarity changes at three stages of the cell cycle: (i) the restart of growth after cell division; (ii) NETO (new-end-take-off); and (iii) cell division. After cell division, actin moves from the 'new end' (formed from the new cell wall synthesised from the septum, during the cell division) to the 'old end' (the end that existed before cell division). At the old end, actin then facilitates endocytosis and monopolar growth. Upon NETO, actin moves to both ends and the growth polarity changes from monopolar to bipolar. At the start of mitosis, growth halts. Actin leaves both cell ends and localises to the medial region of the cell, where cell division occurs. Actin forms a contractile actin ring for cell division in the medial region (Hirata et al., 2002).

*S. pombe* are routinely used as models for cell growth and cell cycle studies. This is due to its simple rod morphology, elongating growth, medial fission, few chromosomes and rapid growth. Wild-type *S. pombe* cell cycles are 2.5 - 3 hours long in normal growth conditions (Gomez & Forsburg, 2004). Due to elongating growth at the cell tips and the halt in growth during mitosis and cytokinesis, points of mitotic commitment can be estimated based on the length of newly divided cells. Cell lengths can also serve as an indicator for cell cycle stages (Hagan et al., 2016). Figure 1.2 illustrates the cell cycle of *S. pombe.*

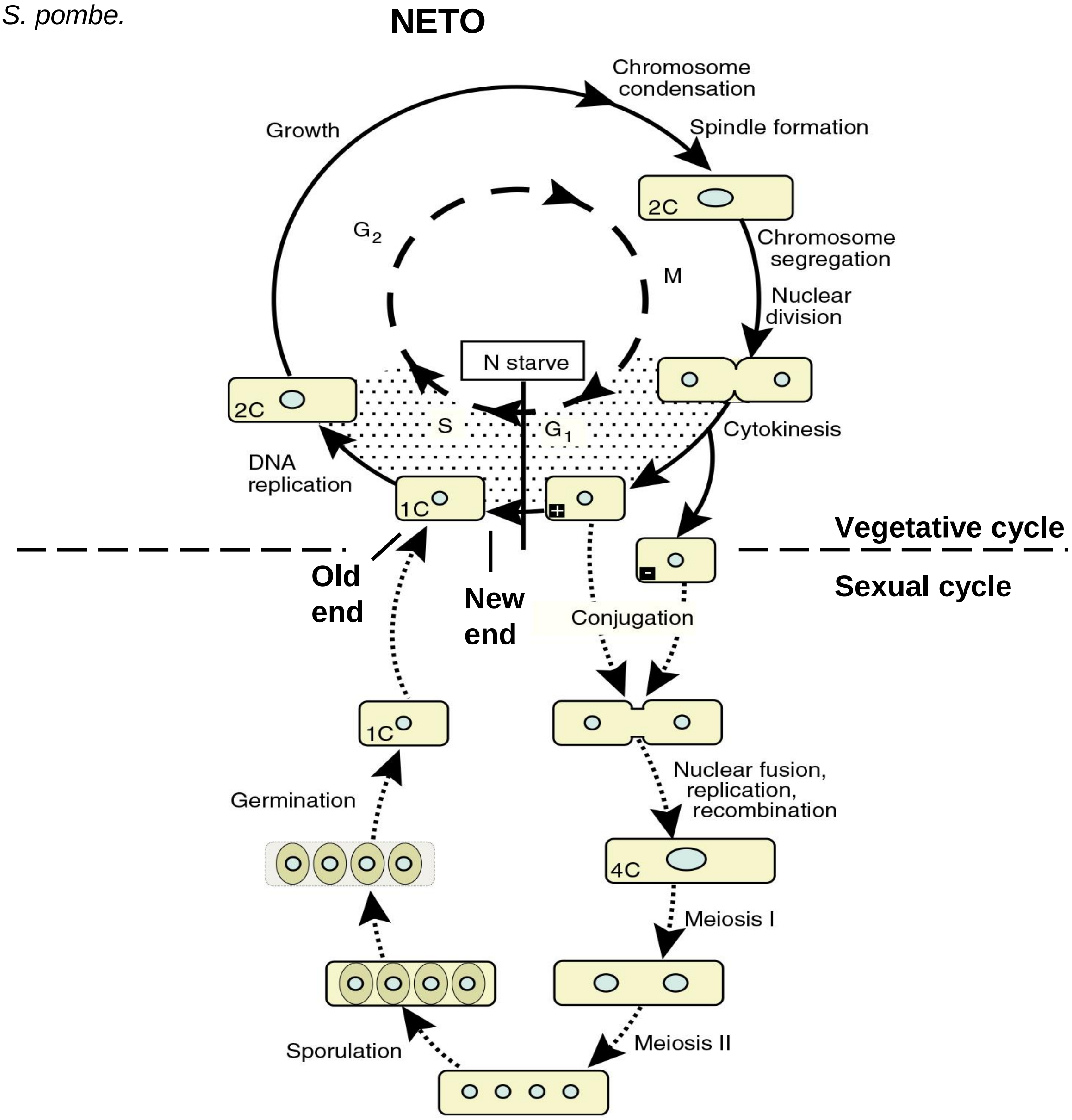

Figure legend on the following page.

**Figure 1.2. The cell cycle of *S. pombe* consists of vegetative and sexual phases.** An illustration of the cell cycle in wild-type *S. pombe.* In rich media, *S. pombe* stay in the vegetative phase of their cell cycle and cell division is mitotic. As cytokinesis (cell division) occurs, cell nuclei begin the G1 phase (gap phase I). In G1, cells have a single copy of the genome (1C DNA). They grow in size and synthesise mRNA and proteins required for DNA replication. The G1 phase is less than 10 % of the whole cell cycle and is quickly followed by S phase (synthesis phase). During S phase, DNA is duplicated within each single nucleus (2C DNA) (Forsburg & Rhind, 2006; Knutsen et al., 2011). This phase also takes 10 % of the cell cycle and is completed before the completion of the previous cytokinesis (Forsburg & Rhind, 2006). The dotted segment of the cycle represents the short G1 and S phases that occur before cytokinesis is complete (Allshire & Ekwall, 2015). The G2 phase (gap phase II) is approximately 70 % of the cell cycle. During this phase, proteins required for mitosis are synthesised. For nuclear division, DNA is condensed into chromosomes. New-end-take-off (NETO) occurs during the late stages of this phase. During NETO, growth changes from monopolar growth at the 'old end' of the cell, to bipolar growth at both the 'old end' and the 'new end' of the cell. Chromosome segregation and nuclear division occur in the M phase (mitosis), which makes up 10 % of the cell cycle. Cytokinesis then occurs and the cycle continues (Forsburg & Rhind, 2006). When starved of nitrogen, *S. pombe* enter the sexual phase and cell division is meiotic. In a pheromone-dependent manner, cells of opposite mating types, Plus (+) and Minus (-), halt their cell cycle in G1 and undergo cytoplasmic fusion during conjugation and nuclear fusion in a process called karyogamy (Krapp et al., 2010). This forms diploid zygotes and DNA replication increases the DNA content from 2N to 4N. DNA in the form of chromosomes undergoes recombination, meiosis I and meiosis II. A cell, termed an ascus, is formed containing four haploid nuclei that are enveloped by synthesised forespore membranes to form forespores (Allshire & Ekwall, 2015). During sporulation, the forespores mature into spores as two layers of spore wall material are deposited in the lumen of the inner and outer prespore membranes (Krapp et al., 2006; Ucisik-Akkaya et al., 2014). The spores are released from the ascus by autolysis of the ascus wall (Allshire & Ekwall, 2015). The spores undergo metabolic and morphological changes during germination in rich media. The newly developed cell is then allowed to continue into the mitotic cell cycle (Plante & Labbé, 2019). Adapted from Allshire & Ekwall (2015).

The cell cycle consist of a vegetative (mitotic) and sexual (meiotic) phase. There are four phases within the vegetative phase: G1 (gap phase I), S (synthesis phase), G2 (gap phase II) and M (mitosis). During G1, protein synthesis occurs, cell size increases and DNA replication is initiated by growth dependent CDK (cyclin-dependent kinase) (Bertoli et al., 2013). The commitment to continue through the cell cycle is also made during this phase, at the G1 checkpoint. This commitment point is termed 'START' in *S. pombe* (Hartwell, 1974; Pardee, 1974). The G1 phase is short in *S. pombe* as it takes up less than 10 % of the cell cycle (Allshire & Ekwall, 2015). In conditions of adequate nitrogen levels, G1 phase is then proceeded by S phase, where genomic duplication occurs (Hagan et al., 2016). During G1-S of the cell cycle, *S. pombe* grow in a monopolar manner from the 'old end' of the cell. The 'old end' refers to the pre-existing end of the cell present in the prior round of cytokinesis that was not formed from the septum (Allshire & Ekwall, 2015).

G2 subsequently is the second growth phase and also involves a checkpoint to commit to mitosis, the G2 checkpoint. G2 makes up 70 % of the cell cycle in *S. pombe.* During late G2, the cell reaches a critical size and initiates a process called new-end-take-off (NETO). This is the start of growth at the cell end formed from the septum in the prior round of cytokinesis (Allshire & Ekwall, 2015). This end is termed the 'new end'. Growth is then bipolar. Chromosome condensation, spindle formation, chromosome segregation and nuclear division then follow NETO, during mitosis. The CAR then constricts and the cell divides into two during cytokinesis (Allshire & Ekwall, 2015).

When starved of nitrogen during G1, cells enter the sexual phase of the cell cycle and undergo meiosis. Haploid *S. pombe* of opposite mating types, P (Plus) and M (Minus), attract one another by the release of P-factor and M-factor pheromones and induce stimulation of mating pheromone receptors (Seike et al., 2019). Once in close proximity to each other, the cells schmoo and conjoin during the conjugation stage. Karyogamy (nuclei fusion), replication and recombination then occur before meiosis I and meiosis II (Allshire & Ekwall, 2015). Four haploid nuclei are produced during the meiotic stages and they are divided and encased in spores within an ascus, during sporulation. The ascus wall undergoes autolysis once the environment is nutrient rich and the spores germinate (Guo & King, 2013). The vegetative cycle then continues (Allshire & Ekwall, 2015). Figure 1.3 shows the morphology of *S. pombe* in the mitotic and meiotic phases of the cell cycle.

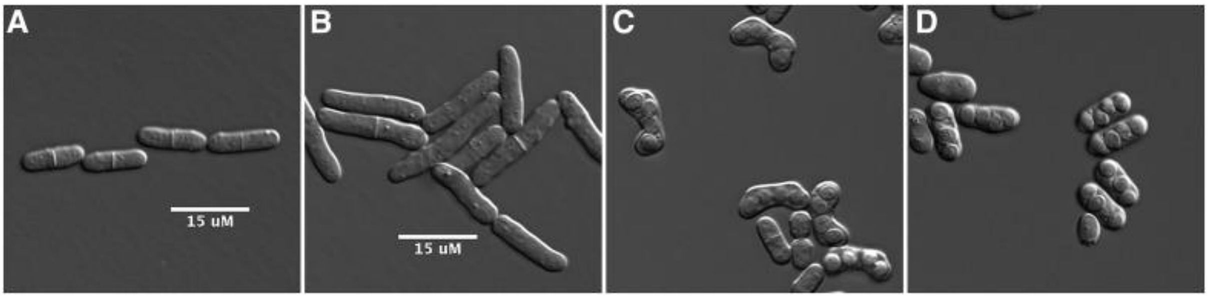

**Figure 1.3. *S. pombe* divide by mitosis and meiosis.** A photomicrograph of meiotic and mitotic *S. pombe* cells. **(A)** Haploid cells forming septa. Haploid cells undergo mitosis when a length of approximately 15 µm is reached. They form a septum in the middle of the cell to cleave individual cells into two cells. **(B)** Diploid cells. Diploid cells undergo mitosis when a length of approximately 24 µm is reached and are approximately 4.4 µm wider than haploid cells. **(C)** Zygotic asci. Zygotic asci are formed when two haploid cells mate, fuse their nuclei together and undergo meiotic nuclear division to form four haploid nuclei. Walls, called spore walls, form around each nucleus. Zygotic asci have a bent morphology due to the angle at which the two cells fuse together to form the zygote. **(D)** Azygotic asci. Azygotic asci are formed when a diploid cell undergoes meiosis. These cells have a short and linear morphology because they are not formed from two mating cells. Scale bar - 15 µm. Adapted from Hoffman et al. (2015).

The *S. pombe* genome possesses homologous genes for myosins and a large majority of actin regulators and actin binding proteins in metazoans (East & Mulvihill, 2011). *S. pombe* only express myosins of class I, II and V; Myo1p of class I, Myo2p and Myp2p of class II and Myo51p and Myo52p of class V (Presti & Martin, 2011). *act1*$^{+}$ is the only actin gene in *S. pombe* and is approximately 90 % homologous to that of budding yeast actin and mammalian skeletal muscle actin and non-muscle β-actin. *S. pombe* actin filaments have been found to be identical to that of actin in muscle cells, however activation of myosin ATPase activity required for muscle contraction is not as robust via *S. pombe* actin filaments (Takaine & Mabuchi, 2007).

## 1.2 Myosin family classification and mutual structure

Myosin I and myosin V are unconventional myosins. Unconventional myosins, first reported in 1973, are actin-dependent motor proteins required for the generation of contractile force. They are multi-functional and are responsible for functions such organelle transport and cell division in eukaryotes (Pollard & Korn, 1973). In order to carry out their functions, the motor proteins associate with actin structures and travel along them. The energy required to move is provided by ATP (adenosine triphosphate) hydrolysis (Foth et al., 2005). In contrast to conventional myosin, such as thick bipolar filament forming myosin II found in muscles, unconventional myosins do not form filaments to execute contractile force. Instead, they act as single actin-associated monomer or dimer molecules.

Myosins have seen been categorized into a super family of 35 different classes, in eukaryotes. Phylogenetic analysis, which led to the genetic based classes, considered a myosin I like gene, of which the myosin V gene was diverged from, making these two genes extremely prevalent. Since myosin genes have diversified, humans have evolved to express myosins from thirteen classes (Pollard et al., 2017).

### 1.2.1 Structural overview of myosins expressed in humans

The thirteen myosins, expressed in humans, have adapted to provide rapid mechanical force for a plethora of processes within the cell such as exocytosis, endocytosis, cytokinesis and locomotion (Batters & Veigel, 2017; Odronitz & Kollmar, 2007). The isoforms share a general structure consisting of an actin binding motor domain, a neck IQ motif domain and a heterogeneous tail domain. Simplified myosin structural domains, expressed in humans, are illustrated in Figure 1.4.

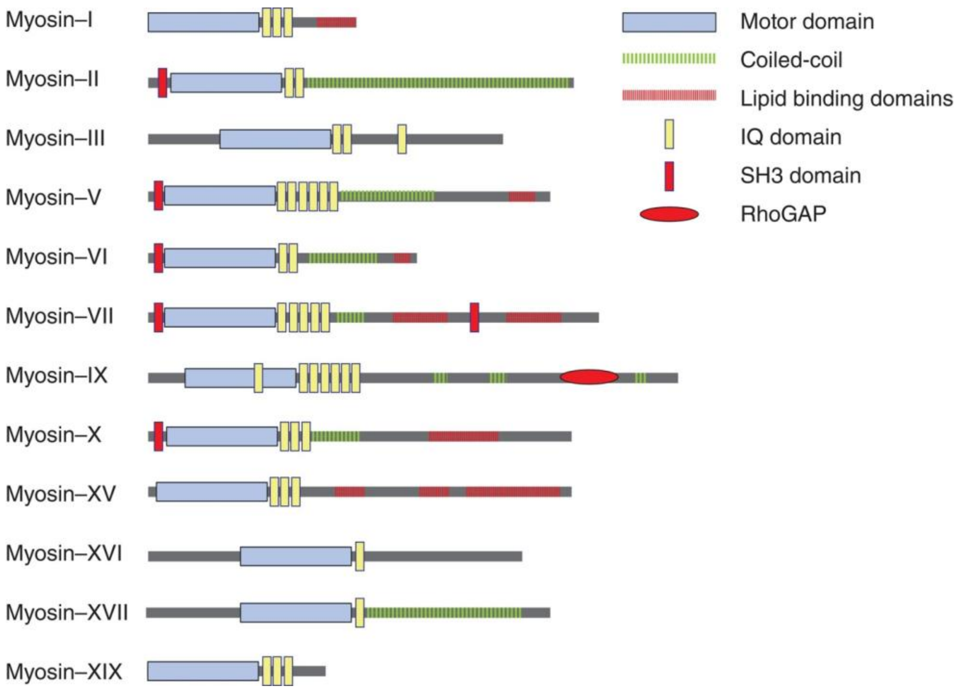

Figure legend on the following page.

**Figure 1.4. Humans express 13 myosin classes.** An illustration of myosin classes and domain structures of human myosins. The myosin classes share conserved motor head domain which binds to actin. In the neck domain, each myosin class possess 1-6 IQ (isoleucine-glutamine) motifs where calmodulin or calmodulin-like light chains bind. This binding induces conformational changes and stiffening of the neck domain, required to execute power stroke in the myosin. Myosins with greater numbers of IQ motif also have larger steps sizes. Myosin dimerisation occurs at the coiled-coil regions. Dimerisation allows processive movement of the myosins. Membrane binding occurs at the lipid binding domains. SH3 (Src homology 3) domains bind to proline-rich sequences and are required in a variety of protein-protein interactions for actin organisation (Anderson et al., 1999). The RhoGAP (Ras homolog GTPase-activating protein) domain found in myosin IX is key for myosin IX function in membrane protrusion and retraction. Adapted from Batters & Veigel (2017).

Although each myosin class is structurally distinct, all myosins consist of three sub-domains; the motor, neck and tail. The sub-domains are decorated with lipid binding domains for membrane binding, IQ motifs for calmodulin binding, SH3 (Src homology 3) domains for the regulation of stability and motility, RhoGAP (Ras homolog GTPase-activating protein) for membrane protrusions and retractions, and coiled-coils for dimerisation or oligomerisation (Hanley et al., 2010; Lowey et al., 2007). Predicted coiled-coil regions have shown not to always infer dimerisation or oligomerisation, an example being coiled-coils predicted in myosin X reported to be a stable SAH (single α-helices) domain instead (Knight et al., 2005).

Therefore these domains interact with a range of proteins to execute cellular functions and in turn, have differing roles to one another (Foth et al., 2005). The structure of a generic myosin heavy chain is illustrated in Figure 1.5. Details of each domain are discussed in Sections 1.2.2., 1.2.3 and 1.2.4.

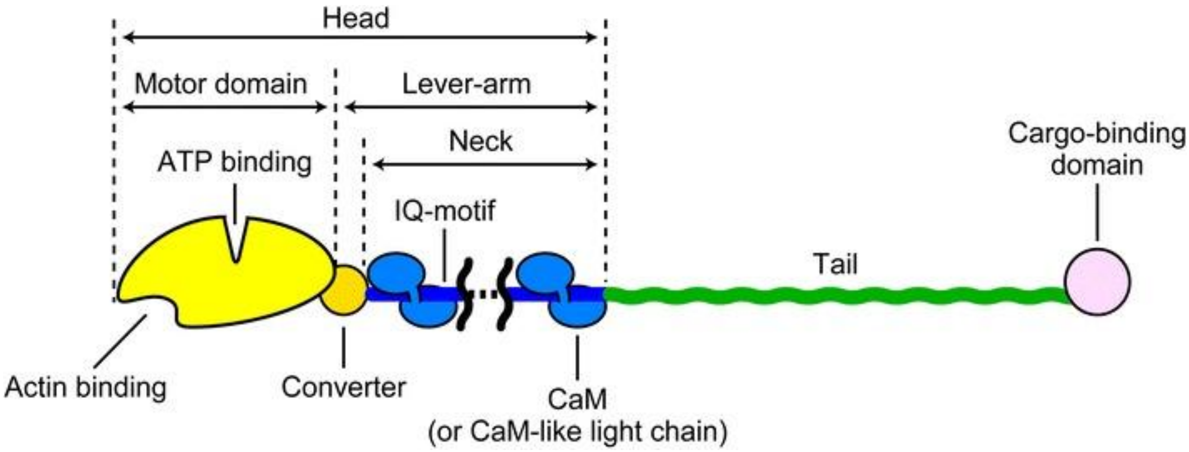

**Figure 1.5. Myosins have motor head, neck and tail domains.** A schematic illustrating the structure of a single headed myosin heavy chain. The N-terminal motor domain contains an actin binding site where actin binds. The motor domain also contains an ATP (adenosine triphosphate) binding site where ATP is hydrolysed. Following the head domain is the lever-arm, which comprises of the converter and neck domains. The flexible converter domain links the motor domain to the neck domain and it rotates as myosins move. The neck domain consists of multiple IQ (isoleucine-glutamine) motifs. The number of IQ motifs in each myosin class varies. Calmodulin or calmodulin-like light chains bind to the IQ motif and induce stiffening of the neck domain required for movement. Following the neck domain, is the tail domain which possess a cargo binding domain in most myosin classes. Tail domains vary in length and amino acid sequences. The variable tail may have an α-helical coiled-coil or a stable SAH (single α-helices) domain. Adapted from Kodera & Ando (2014).

Myosin classes share a common motor head domain. It contains an actin binding domain, where it associates with actin in various structures such as actin filaments and cortical patches. The neck lever arm region is a flexible region along the motor protein, analogous to a pivot point. It has a number of IQ motifs of which myosin light chains bind, to modulate the activity of the myosin. The tail domain is connected to the neck and is the site for specific cargo binding. Genetic diversity between the neck and tail domains has determined a large number of myosin classes and functions.

### 1.2.2 The myosin domains: motor

The myosin globular motor head is an ATPase motor domain that all myosin classes possess. Figure 1.6 displays the crystal structure of the myosin I motor domain.

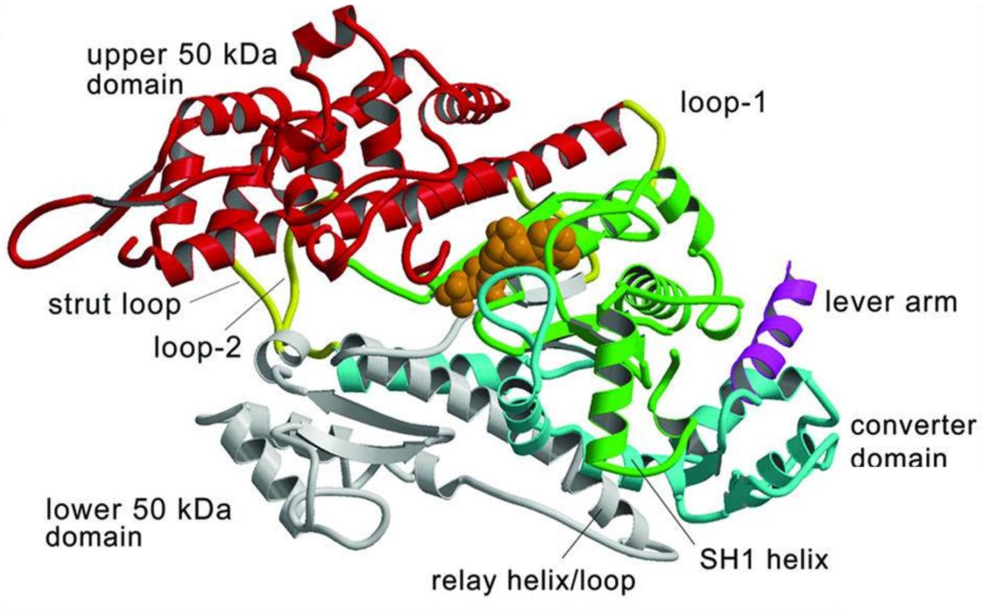

**Figure 1.6. The myosin motor head consists of multiple sub-domains.** Ribbon diagram of the myosin I motor domain of *Dictyostelium discoideum*. The inner cleft of the N-terminus (green) contains the nucleotide-binding site and an ATP analogue (orange) situates within it. Loop-1 (yellow) controls accessibility of the nucleotide-binding site. The motility of the loop correlates with the rate of ADP release. The N-terminus is followed by the upper 50 kDa domain (red) and the lower 50 kDa domain (white). The latter contains actin-binding motifs, which include loop-2 (yellow), and also contains the relay helix. Loop-2 interacts with actin through weak and strong binding interactions. The relay helix relays conformational information across the actin-binding site, the nucleotide-binding site and the converter domain. The C-terminus (cyan) contains the converter domain, the SH1 helix, the start of the lever arm helix (magenta) and an α-helix leading to loop-2 in the actin binding site. The converter domain rotates as the myosin moves. The SH1 helix determines the flexibility and thermal properties of the myosin. Movement of the lever arm helix generates the movement of the myosin (Shibata et al., 2017). The strut loop (yellow) links the upper and lower 50 kDa domains (Kühner & Fischer et al., 2011). Adapted from Kollmar et al. (2002).

A large cleft divides the 50 kDa sub-domain of the head into upper and lower 50 kDa domains of which the outer cleft regions binds to actin through the loops (Kodera & Ando, 2014). The inner cleft regions house the ATP-binding site. The actin and ATP binding sites are located on the conserved catalytic motor head domain and communicate with each other for the generation of contractile force and movement. Movement along the actin filament is regulated by the ATPase cycle (Hartman & Spudich, 2012; Kodera & Ando, 2014)

The duty ratio, the duration of the ATPase cycle myosins spend tightly bound to actin, ranges between myosin classes. Longer durations tightly bound to actin, are often found in myosins that step processively along an individual actin filament. High duty ratio myosin, such as myosin V, can be tightly bound for greater than 50 % of the ATPase cycle (Howard et al., 1997). Low duty ratio myosins, such as myosin II, are tightly bound for less than 10 % of the ATPase cycle (Walklate et al., 2016). Myosin isoforms also have varying maximal actin-activated ATPase activity, differing between approximately 0.13 $s^{-1}$ - 390 $s^{-1}$ (Heissler & Sellers, 2016).

### 1.2.3 The myosin domains: neck

Myosin neck domains consist of 1-6 IQ motifs. Each IQ motif is a sequence of amino acids following a (IQxxxRGxxxR) pattern, where "x" represents any amino acid. The IQ motifs are linked to the rotating converter domain and together form the myosin lever arm (Kodera & Ando, 2014). Greater numbers of IQ motifs in the neck region increases myosin heavy chain length and therefore increases the motor step size. Myosin V can possess three more IQ motifs than myosin I and therefore executes a larger step (Sakamoto et al., 2005).

A ubiquitous $Ca^{2+}$ modulating light chain, called calmodulin, binds to the IQ motifs via non-covalent binding. Calmodulin consists of two pairs of EF-hands linked together by a flexible linker region. $Ca^{2+}$ binds to the EF-hands and induces conformational changes from closed apo-calmodulin ($Ca^{2+}$ free) to open $Ca^{2+}$-calmodulin (Batters & Veigel, 2017). The structures of apo-calmodulin and $Ca^{2+}$-calmodulin are illustrated in Figure 1.7. These conformational changes increase the affinity of calmodulin for myosin. Calmodulin binding to myosin induces stiffening of the myosin neck domain (Heissler & Sellers, 2014). The resultant rigidity of the myosin allows a power stroke to be executed.

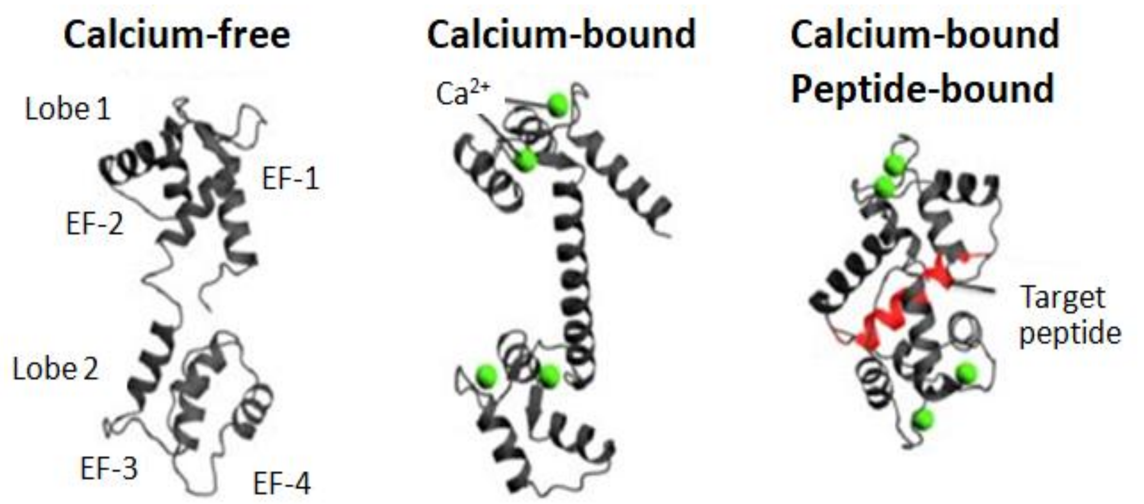

**Figure 1.7. Calmodulin bind to target proteins through a Ca$^{2+}$ dependent conformational change.** An illustration of the structure of calmodulin in the calcium-free, calcium-bound and peptide-bound states. Calmodulin (black) is composed of two lobes that each possess a pair of EF-hands. The two pairs are connected by a flexible linker region. In the calcium-free state, calmodulin holds a closed conformation. Each EF-hand binds to a single Ca$^{2+}$ (green) ion and binding induces a conformational change into an open calcium bound state. Hydrophobic pockets that allow binding to target proteins are exposed in the open state (Lu et al., 2015). Once open, calmodulin binds and wraps around regions of target proteins (red) e.g. the myosin neck domain IQ motifs (Harborne & Kunji, 2018). Calmodulin can also bind to target proteins whilst in the calcium-free state. In this state, C-terminal lobes can hold a semi-open conformation that exposes the hydrophobic pockets (Lu et al., 2015). Adapted from Harborne & Kunji (2018).

*S. pombe,* possess two calmodulins called Cam1 (calmodulin 1) and Cam2 (calmodulin 2). Cam1 and Cam2 bind to myosin IQ motifs. Myosin binding and regulation of myosin function differ with each calmodulin and myosin isoform. Cam1 binding to myosin I is Ca$^{2+}$ dependent and is involved in regulating endocytosis, spore formation and cell division. Cam2 binding is not Ca$^{2+}$ dependent and is not essential for maintaining cell viability. Calmodulin binding to IQ1 is required for binding to IQ2. Calmodulin do not bind to IQ2 alone. Cam1 and Cam2 induce differing conformational changes in the myosin I lever arm and may be a means of directly regulating myosin I activity. Low levels of free Ca$^{2+}$ during vegetative growth is favourable for Cam1 binding. Increases in Ca$^{2+}$ during mating, meiosis and sporulation inhibit Cam1 binding and allows Cam2 to bind to myosin I (Baker et al., 2019).

### 1.2.4 The myosin domains: tail

This variable domain binds to cargo and cell membranes and dictates the specificity of the motor protein. The tail domain is the most diverse domain and it comprises of regions such as coiled-coils for oligomerisation and multiple domains involved in protein binding. These include: PH (pleckstrin homology) domains for binding with PtdIns (phosphoinositides) in cell membranes, SH3 domains for protein-protein interactions in proline rich regions and MyTH/FERM (myosin tail homology, four point-one, ezrin, radixin, moesin) domains required for cargo binding (Heissler & Sellers, 2016; Weck et al., 2016). The multiple functions of myosins are evident in the localisation of the proteins within the cell. Myosins localise to intracellular components where they are used to traffic and anchor cellular components. Myosins bind to specific organelles and molecular complexes via the cargo-binding site of the variable tail domain (Hartman & Spudich, 2012). What anchors specific cargo to myosin tail domains and the governance of this binding is unclear.

### 1.2.5 Phosphorylation sites in myosin I and myosin V domains

Wilson-Grady et al. (2008) reported novel conserved phosphorylation sites in myosin I and myosin V in *S. pombe*. These phosphorylation sites were identified via immobilized metal affinity chromatography (IMAC) or $TiO_2$ phosphopeptide enrichment methods and mass spectrometric analysis (Wilson-Grady et al., 2008). The locations of these phosphorylation sites in myosin I and myosin V are illustrated in Figure 1.8.

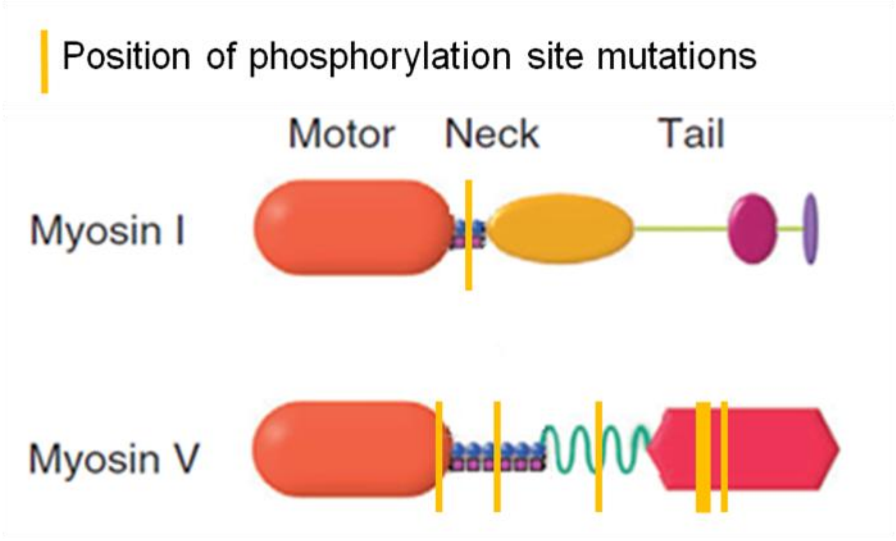

| Phosphorylation site | Domain | Phospho-mutant strain |
|---|---|---|
| Myosin I serine 742 | Head | *myo1.S742A* |
| Myosin V serine 720 | Head | *myo52.S720A* |
| Myosin V serine 798 | Neck | *myo52.S798A* |
| Myosin V serine 985 | Tail | *myo52.S985A* |
| Myosin V serine 1064 | Tail | *myo52.S1064A S1065A* |
| Myosin V serine 1065 | Tail | *myo52.S1064A S1065A* |
| Myosin V serine 1072 | Tail | *myo52.S1072A* |

**Figure 1.8. Serine-to-alanine mutations were generated in conserved phosphorylation sites in the head, neck and tail domains of myosin I and myosin V.** An illustration displaying the locations of the conserved phosphorylation sites of interest in myosin I and myosin V. The conserved phosphorylation sites are located in various domains in the myosins. The orange bars indicate the location of the phosphorylation sites. The myosin I serine 742 phosphorylation site is located in IQ-motifs in the neck domain of myosin I. The myosin V motor head domain contains a phosphorylation site at serine 720. The myosin V neck domain contains a phosphorylation site at serine 798. The tail domain contains phosphorylation sites at serine 985, serine 1064, serine 1065 and serine 1072. During this study, the codons encoding for these phospho-serines in *S. pombe,* were mutated to encode for alanine instead, to study the function of these phosphorylation sites in myosins I and V function. Alanine does not possess a nucleophilic (–OH) group required for phosphorylation. Therefore, phosphorylation does not occur at the mutated phosphorylation sites. Adapted from East & Mulvihill (2011).

The phosphorylation site of interest in myosin I is serine 742. The phosphorylation sites of interest in myosin V are serine 720 in the head domain, serine 798 in a neck domain IQ motif, serine 985 in the coiled-coil region of the tail domain and serine 1064, serine 1065 and serine 1072 in the cargo-binding domain. The phospho-serines at these sites are the targets of unidentified kinases for phosphorylation. However, myosin I serine 742 and myosin V serine 798 have been identified as AGC family kinase consensus phospho-serine sites (Baker et al., 2019).

One focus of this study was to unveil the significance of these conserved phosphorylation sites in myosins I and V function, with the use of phospho-mutant *S. pombe* strains. Phospho-mutant strains in this study express mutant myosin, with changes made to one or two serine residues via SDM (site-directed mutagenesis). The serine residues, modifiable by phosphorylation, are mutated into non-phosphorylatable alanine residues. Alanine is not phosphorylated by kinases as it does not possess a nucleophilic (–OH) group required for phosphorylation. This strategy aimed to highlight possible myosin I and myosin V dysfunction in the absence of phosphorylation at the phosphorylation sites, in turn demonstrating the relevance of these phosphorylation sites in myosin function.

### 1.2.6 Oligomerisation variation within myosin classes

Schematics of myosin I, myosin II and myosin V, used experimentally during this study are shown in Figure 1.9. The schematic illustrates oligomerisation differences in each myosin class. Both myosin II and myosin V form dimers via the coiled-coils in the tail domains of two heavy chains. Dimerisation via the coiled-coil is believed to warrant processive, step-wise translocation in myosin V (Cappello et al., 2007). Immuno-electron microscopy in non-muscle cells, determined the presence of extended coiled-coils in myosin II, which form thick filaments with neighbouring myosin II heavy chains (Langanger et al., 1986). Myosin I, comparatively shorter than myosin II and myosin V, is a monomer and does not possess a coiled-coil in the tail domain.

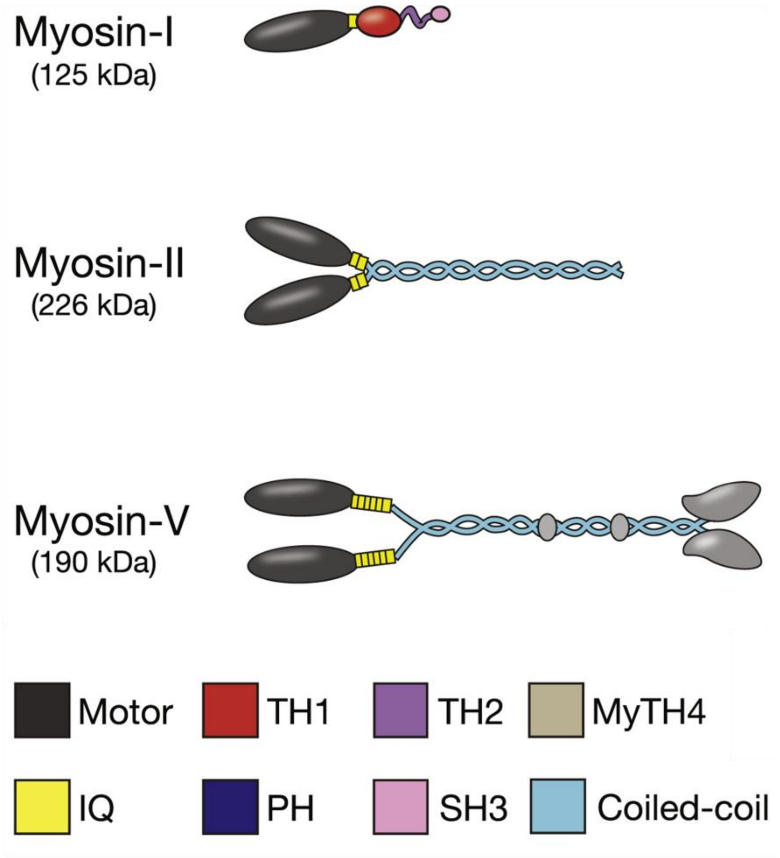

**Figure 1.9. Myosins II and V form dimers.** An illustration of the structure of myosins I, II and V. Myosins motor (black) domains locate at the N-terminus and bind to actin. Motor domains also possess ATP (adenosine triphosphate) binding sites where ATP is hydrolysed and used as mechanical energy. The actin binding motor domain is homologous between myosin classes. The neck domain contains IQ (isoleucine-glutamine) motifs (yellow). Calmodulin light chains bind to the IQ motifs and induce conformational changes in myosin to stiffen the neck domain. Stiffening of the neck domain is required for the movement of myosin. Tail domains bind to myosin cargo or cellular membranes. This domain varies in length and composition in different isoforms and contains; TH1 (Tail Homology 1) (red), TH2 (purple), SH3 (Src Homolog 3) (pink), MyTH4 (Myosin Tail Homology 4) (grey) domains and coiled-coils (blue). Th1 domains bind to cell membrane lipids. TH2 domains are alanine and proline rich and contain an ATP-independent actin-binding site. SH3 domains bind to proline rich regions for protein-protein interactions. MyTH4 domains are part of a structural and functional supramodule needed for cargo binding. The coiled-coil region (light blue) of myosin II and myosin V allow dimers to form. Adapted from Barger et al. (2020).

### 1.2.7 Functional grouping of myosins

Myosins of each class have specific roles and therefore are also categorised into four functional types based on biochemical and mechanical properties: fast movers, slow/efficient force holders, strain sensors or processive transporters (Bloemink & Geeves, 2011). Myosin I monomers are strain sensing myosin. Strain sensing myosin have a low duty ratio meaning they spend a small amount of time bound to actin. This low duty ratio allows strain sensing myosins to link the cell membrane to the cytoskeletal actin structures and function in maintaining cell membrane tension (Heissler & James, 2016). Myosin II thick filaments execute cytoplasmic contractions for the movement of actin filaments and therefore are strain sensors and force holders. Myosin V dimers are grouped as a processive myosin meaning they can translocate, via multiple steps, along actin filaments without detaching from the filaments. This is due to having two motors, extended neck and tail regions and a high duty ratio (Hammer & Sellers, 2012).

## 1.3 Myosin movement and cytoskeletal interactions

### 1.3.1 Actomyosin ATPase cycle

When bound to actin filaments, myosins travel in a step-wise manner. Myosins use ATP to induce conformational changes within the neck domain, required for motility along actin structures (Clayton et al., 2013). Figure 1.10 illustrates how myosin uses ATP for travel during the actomyosin ATPase cycle.

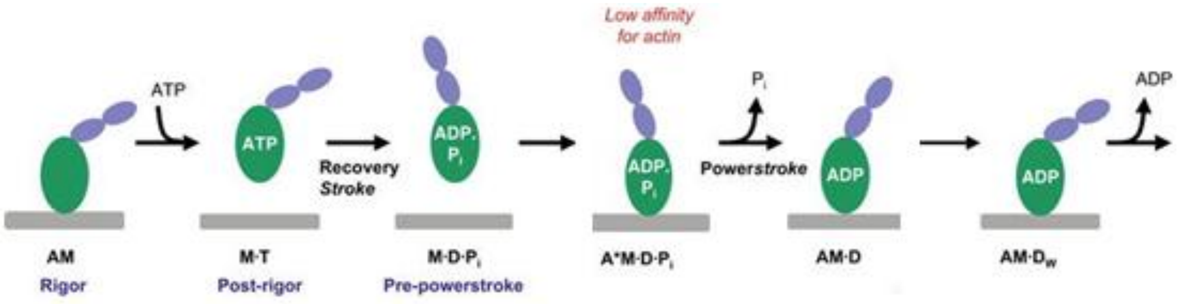

**Figure 1.10. Myosin hydrolyses ATP to move along actin filaments.** An illustration of the actomyosin ATPase cycle. The myosin motor domain is in green, the neck domain is in purple and actin in grey. Changes in the myosin ATP (adenosine triphosphate) bound state and ADP (adenosine diphosphate) bound states trigger conformational changes in myosin. These changes, allow myosin to generate force and move along actin. 1. In a rigor state, the myosin (M) motor head strongly binds to actin (A) forming an actomyosin complex (AM). 2. In the post-rigor state, ATP binds to the myosin motor head, forming ATP-myosin (M·T). The myosin head releases from actin. A recovery stroke occurs and changes the conformation of the myosin neck domain. 3. Pre-powerstroke, the ATP bound to the myosin is hydrolysed into ADP and Pi (inorganic phosphate) and forms myosin-ADP-Pi (M·D·Pi). 4. Myosin binds weakly to actin (A*M.D.Pi), releases Pi and generates force during a powerstroke which changes the position of the lever arm. ADP-myosin remains bound to actin (AM.D). 5. An additional change in the lever position occurs and ADP binding to myosin becomes weak (AM.Dw). ADP is released from myosin and the cycle restarts with the AM state. 'A' specifies 'actin'. 'M' specifies 'myosin'. 'T' specifies 'ATP'. 'D' specifies 'ADP'. Adapted from Altman (2013).

In ATP or ADP-$P_i$-bound states, the motor head's affinity for actin is low (Hartman & Spudich, 2012). The ATPase rate is also low with myosin unbound to actin. Upon ATP hydrolysis and Pi release, the ADP-bound state increases the motor head’s affinity for actin and binds strongly to actin. The chemical energy released from ATP hydrolysis is converted into mechanical work and a conformational change, then induces a power stroke movement along the actin filament (Kodera & Ando, 2014). The assemblies each myosin hold when interacting with actin and membrane phospholipids are illustrated in Figure 1.11.

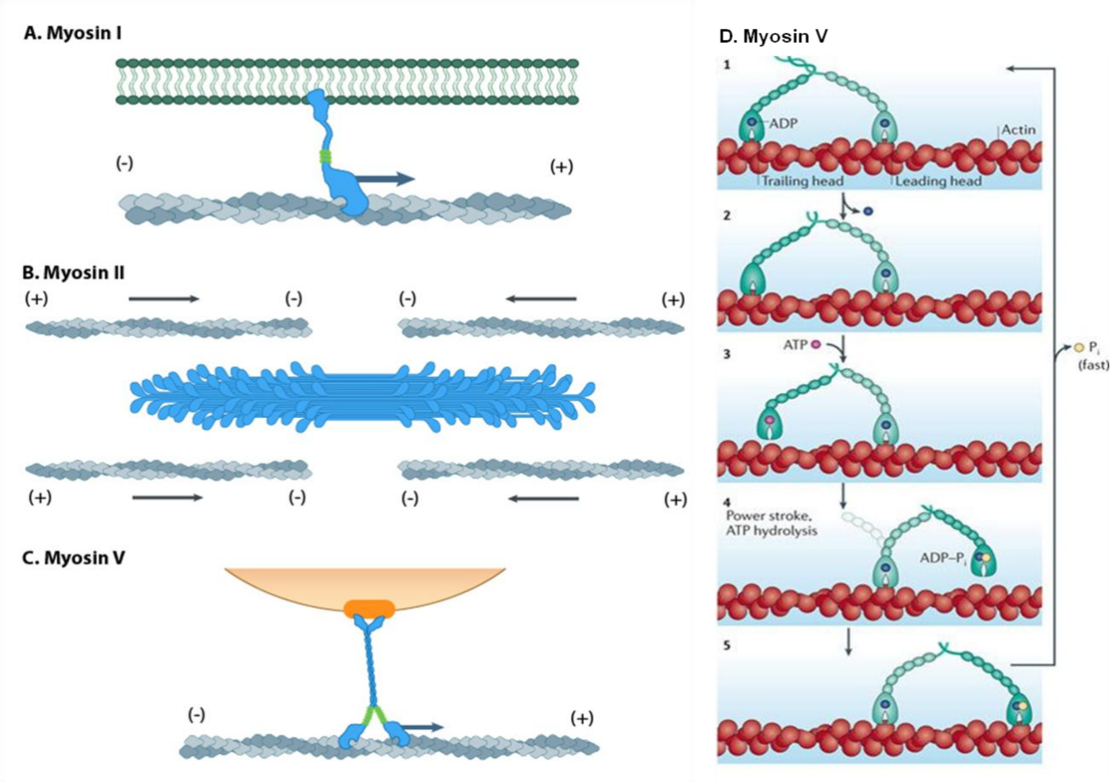

**Figure 1.11. Myosin I, II and V bind and translocate towards the plus end of actin filaments.** An illustration of myosin movement along actin. **(A)** Myosin I monomer tail binds to membrane phospholipids. The myosin I head binds to actin and travels toward the plus end of actin filaments. **(B)** Myosin II bundle together to form thick myosin filaments. Myosin II heads bind to actin and pull actin filaments together for actomyosin contractions. **(C)** Myosin V tails bind to vesicular cargo and carry the cargo along actin filaments in a stepwise, processive manner, towards the plus end of the actin filament. **(D)** Myosin V affinity to actin during the ATPase cycle changes depending on the nucleotide bound state. When in an ATP (adenosine triphosphate)-bound or ADP (adenosine diphosphate) and Pi (inorganic phosphate) (ADP-Pi)-bound state, myosin affinity for actin is low. When in an ADP-bound state or not bound to any nucleotide, myosin affinity for actin is high. Phase 1 - ADP is bound to both actin-bound motor heads. Phase 2 - ADP is released from the trailing head due to intramolecular strain. Phase 3 - the empty trailing head binds to ATP and is released from actin. Phase 4 - the ADP-bound leading head is subject to a power stroke. The movement positions the ADP-Pi-bound trailing head at the front. ATP hydrolysis occurs and this head then becomes the leading head. Phase 5 - the new leading head binds to a new actin binding site, with the release of $P_i$ and increased actin affinity. The process translocates myosin V forward by 36 nm. Adapted from Hammer & Sellers (2012) and MBInfo (n.d.).

Myosin I tails bind to membrane lipids to provide mechanical force and anchorage during endocytosis. Myosin II form polymeric, bipolar thick filaments with one another, via polar interactions at opposite ends. They bind and pull oppositely charged actin filaments, resulting in a movement towards the actin filament plus end and contraction (Cheney et al., 1993; Squire et al., 2017; Vicente-Manzanares et al., 2009). Myosin V tails bind to cargo for organelle transport along actin filaments.

Most myosins travel towards the plus end (growing end) of actin filaments however, myosin VI has been found to travel towards the minus end (Santos et al., 2016). It is known that actin filaments are shared amongst motor proteins however, the governance of myosin trafficking along filaments are unknown. Santos et al. (2016) demonstrated bidirectional movement on a single actin filament by myosin V and VI which leads to questions regarding the possibility of myosin collisions, the consequences of collisions (if any) and the existence of signalling to prevent collisions.

The myosin-actin interaction increases the rate of ATPase activity (Hartman & Spudich, 2012). This movement is amplified by the lever arm of the neck region and is dependent on the lever arm length and flexibility of the converter region. The neck domain extends the stride and largely contributes to the stepping motion of the motor protein (Ovchinnikov et al., 2010). With cargo bound, myosin V can travel up to 1 µm before it dissociates (Ovchinnikov et al., 2010). ATP turnover and the duty ratio of myosin vary between myosin classes (Hartman & Spudich, 2012).

### 1.3.2 Components of the cytoskeleton in *S. pombe*

The filaments that make up the cytoskeleton provide a network to maintain and manipulate cell shape, as well as tracks for motor molecules to carry intracellular cargos within the cell. Myosin I may be involved in the regulation of cell shape (Fletcher & Mullins, 2010). For its maintenance, myosin I and other myosin classes are possibly responsible for the linkage between the plasma membrane and underlying actin filaments (Wenzel et al., 2015).

The main functions of the dynamic cytoskeleton are to organise cell content spatially, connect the cell to the external environment physically and biochemically and to induce cell movement and shape change, with coordination of cytoplasmic regulatory and motor proteins and organelles. It is composed of three principal components which undergo consistent assembly, collapse and reassembly: actin, microtubules and intermediate filaments (IFs). Cytoskeletal structures in *S. pombe* are illustrated in Figure 1.12.

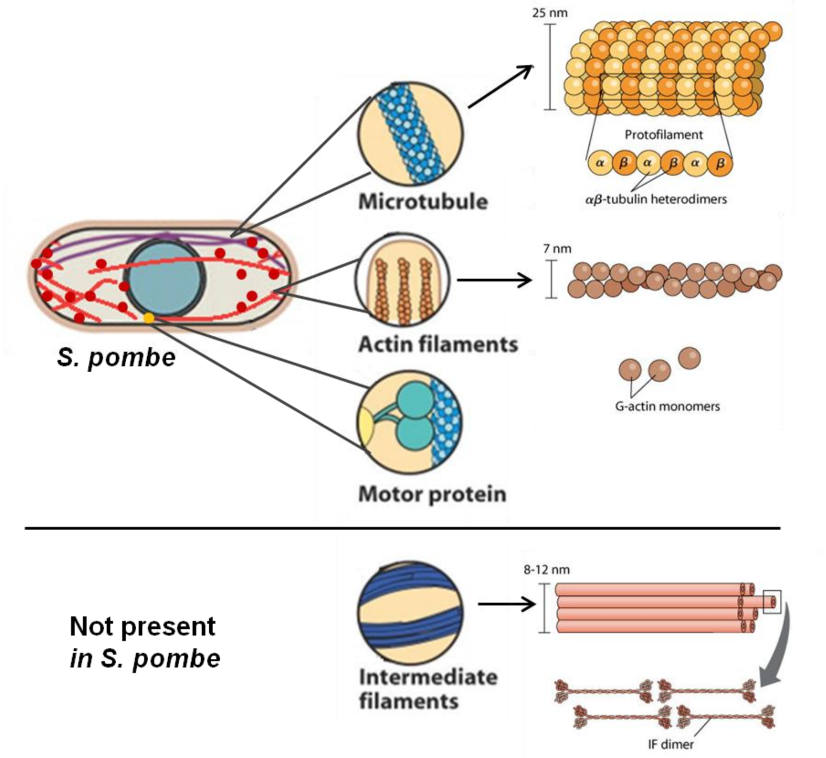

**Figure 1.12. The *S. pombe* cytoskeleton consists of actin structures and microtubules.** Illustration of cytoskeletal actin filaments and microtubule structures in *S. pombe*. Actin filaments comprise of G-actin monomers. The G-actin, orientated in the same direction, polymerise into linear strands. Two strands then wind around each other to form helical filamentous actin (F-actin) microfilaments. Actin filaments are approximately 7 nm wide and have thirteen and a half monomers per turn. A turn occurs every 36 - 37 nm. In *S. pombe*, actin filaments span at different lengths throughout the cell. Filaments are also assembled to form actin patches (red circles) and contractile actin rings (not shown in figure). Contractile actin rings form at the medial region of the cell for cytokinesis. Microtubules are 25 nm wide, hollow tubular structures formed from rows of α-tubulin and β-tubulin heterodimers called protofilaments. Thirteen protofilaments are held together by non-covalent interactions to make up a microtubule. Microtubules maintain cell shape and form mitotic spindles, which separate and distribute chromosomes during cell division. Intermediate filaments (IFs) are eight profilaments (IF tetramers) thick and 10 - 12 nm wide. They are not present in *S. pombe.* Myosin motor proteins bind to actin filaments via their head domains to travel along them, generate force and carry cargo. Motor proteins such as dynein bind to microtubules via their head domains and move along microtubules to transport cargo. Adapted from Hardin et al. (2012) and Karp et al. (2016).

Microtubules, present in eukaryotes, are 25 nm wide, inflexible, furrowed rods which comprise of thirteen globular tubulin protofilaments of dimer forming α-tubulin and β-tubulin molecules. These polar microtubules are constructed for intracellular organelle transportation, maintenance of the integrity of cell shape and cell movement in some cellular anatomy. γ-tubulin molecules also complex to form rings which act as microtubule nucleation sites in the centrosome during mitosis chromosome segregation (Cooper et al., 2000).

IFs are 10-12 nm wide, apolar filaments formed in the cytoplasm and nucleus and consist of a heterogeneous array of proteins including keratin and nestin. They provide structure within the cell as well as form connections in the extracellular matrix at cell junctions via plakin molecular bridge protein attachment (Jefferson et al., 2004). IFs have also been reported to serve as a mediator in the signalling pathway for the control of cell growth, survival and protein targeting (Kim et al., 2007). Contrary to this, IFs are not present in *S. pombe* and therefore have been shown not to be essential for life in unicellular organisms (Erber et al., 1998). IFs also do not serve as motor protein pathways (Karp et al., 2016).

### 1.3.3 Actin structures in *S. pombe*

Actin, discovered in 1942, is a ubiquitous protein and exists as either monomeric globular actin (G-actin) or polymeric filamentous actin (F-actin) (Bugyi & Kellermayer, 2020; Kovar et al., 2011). G-actin is a 42 kDa protein and polymerises to form F-actin. F-actin provides structural support in cells and forms three structures in *S. pombe;* contractile actomyosin rings (CARs), cortical patches and actin filaments. These core structures orchestrate cell division, endocytosis and protein transport respectively, for cell growth (Kovar et al., 2011). Figure 1.13 illustrates the three actin structures formed in *S. pombe*, their associated myosin and actin binding proteins.

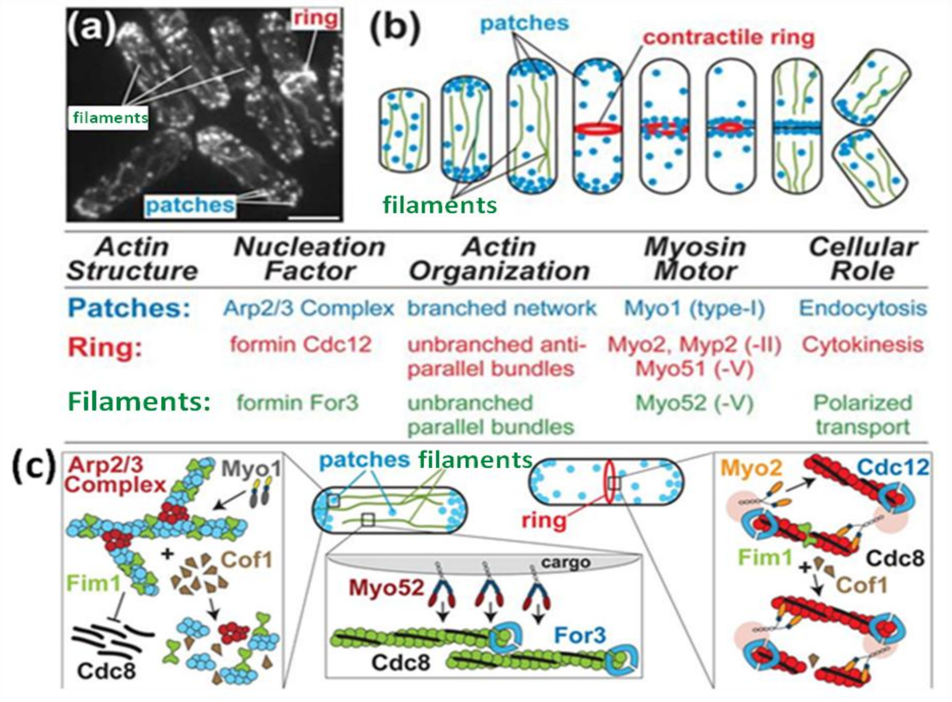

| Actin Structure | Nucleation Factor | Actin Organization | Myosin Motor | Cellular Role |
|---|---|---|---|---|
| Patches: | Arp2/3 Complex | branched network | Myo1 (type-I) | Endocytosis |
| Ring: | formin Cdc12 | unbranched anti-parallel bundles | Myo2, Myp2 (-II)<br>Myo51 (-V) | Cytokinesis |
| Filaments: | formin For3 | unbranched parallel bundles | Myo52 (-V) | Polarized transport |

**Figure 1.13. Actin forms patches, contractile rings and filaments in *S. pombe*.** Summary of actin patch, ring and filament structures formed in *S. pombe.* **(A)** Image of *S. pombe* expressing F-actin fluorescence marker GFP-CHD, highlighting actin filaments, patches and a ring. **(B)** Illustration of actin structures. Actin patches are branched networks of actin filaments and are nucleated by Arp2/3 complex. During interphase, actin patches and Myo1 localises at the cell ends for endocytosis. During cytokinesis, actin patches cluster at the cell equator to deliver proteins for septum formation (Rajagopalan et al., 2003). Contractile actin rings (CARs) are rings of unbranched anti-parallel bundles of actin, nucleated by formin Cdc12. CARs constrict to divide cells. Myo2 and Myo51 are required for ring assembly and Myp2 generates force for ring constriction (Laplante et al., 2015). Actin filaments are unbranched parallel bundles of actin. They are nucleated by formin For3. Myo52 translocates along actin filaments to transport organelles throughout the cell. **(C)** Illustration of fimbrin Fim1 and tropomyosin Cdc8 regulation of actin filament turnover and myosins. In actin patches, Myo1 binds to actin during endocytosis. The short filaments are stabilised by Cdc8 (Palani et al., 2019). Cdc8 binding is hindered by high concentrations of Fim1, which is an F-actin cross-linking protein. It inhibits Cdc8 by displacing Cdc8 from actin (Christensen et al., 2017). When Cdc8 is not bound to actin, cofilin Cof1 severs actin filaments to facilitate filament turnover (Skau et al., 2011). In filaments, Myo52 travels along actin filaments to transport cargo (Breitsprecher & Goode, 2013). In CARs, Myo2 incorporates into nodes. Myo2 pulls on neighbouring actin filaments and compact the nodes together to form the CAR (Pollard et al., 2017). Low concentrations of Fim1 partially inhibit Cdc8 binding. Cdc8 restricts Cof1 severing. Adapted from Kovar et al. (2011).

Formation of actin structures begins with nucleation of actin filaments. ATP-bound monomeric globular actin (ATP G-actin) bind together to form trimeric nucleation seeds (Weston et al., 2012). Trimeric nucleation seeds are unstable and quickly dissociate into monomers, so actin regulators, such as nucleators and nucleation promoting factors, facilitate nucleation. ATP G-actin rapidly polymerise from the nucleation seed to assemble polarised, double stranded, helical polymers. The actin structure therefore becomes polymeric filamentous actin (F-actin). The growing end of the actin filament is termed the 'plus end' or 'barbed end'. Growth at the barbed end is regulated by barbed end cappers. Barbed end cappers bind to the end of the filament and block ATP G-actin from polymerising there. As ATP G-actin is incorporated into the filament, its ATPase activity increases. ATP in ATP G-actin is hydrolysed and a phosphate is released. This leaves ADP G-actin to remain in the filament. The older end of a filament, opposite to the barbed end, is termed the 'minus end' or 'pointed end'. F-actin is cross-linked and bundled to add additional mechanical strength to the actin structure. Cross-linking is carried out by fimbrin Fim1, which binds to two adjacent F-actin.

To be re-organised, F-actin is disassembled at the pointed end because ADP G-actin is more vulnerable to severing by severing proteins such as cofilin Cof1. Cof1 binds to old regions of actin filaments and alters the twisting pattern of the filaments. The deformed twist pattern promotes fragmentation of the filaments (Mikati et al., 2015). The filament then severs due to mechanical discontinuities (Goode et al., 2015). Disassembly cofactors of Cof1, such as Aip1 (actin-interacting protein 1), bind to Cof1 and F-actin and promote actin depolymerisation. CAPs (cyclase-associated proteins) are bifunctional. The CAP N-terminus associates with Cof1-bound F-actin and promotes filament severing. The CAP C-terminus dissociates Cof1 and ADP G-actin from each other so they can be recycled. The Cof1 is freed to continue filament depolymerisation. ADP G-actin is freed to replenish the pool of actin monomers (Bertling et al., 2004). Freed ADP G-actin monomers are converted back into ATP G-actin by nucleotide exchange, which is facilitated by profilin. Profilin binds to ATP G-actin monomers, allows ATP G-actin to be added to the barbed end of another filament, and blocks assembly at the pointed end. The formation and turnover of actin filaments and patches are illustrated in Figure 1. 14.

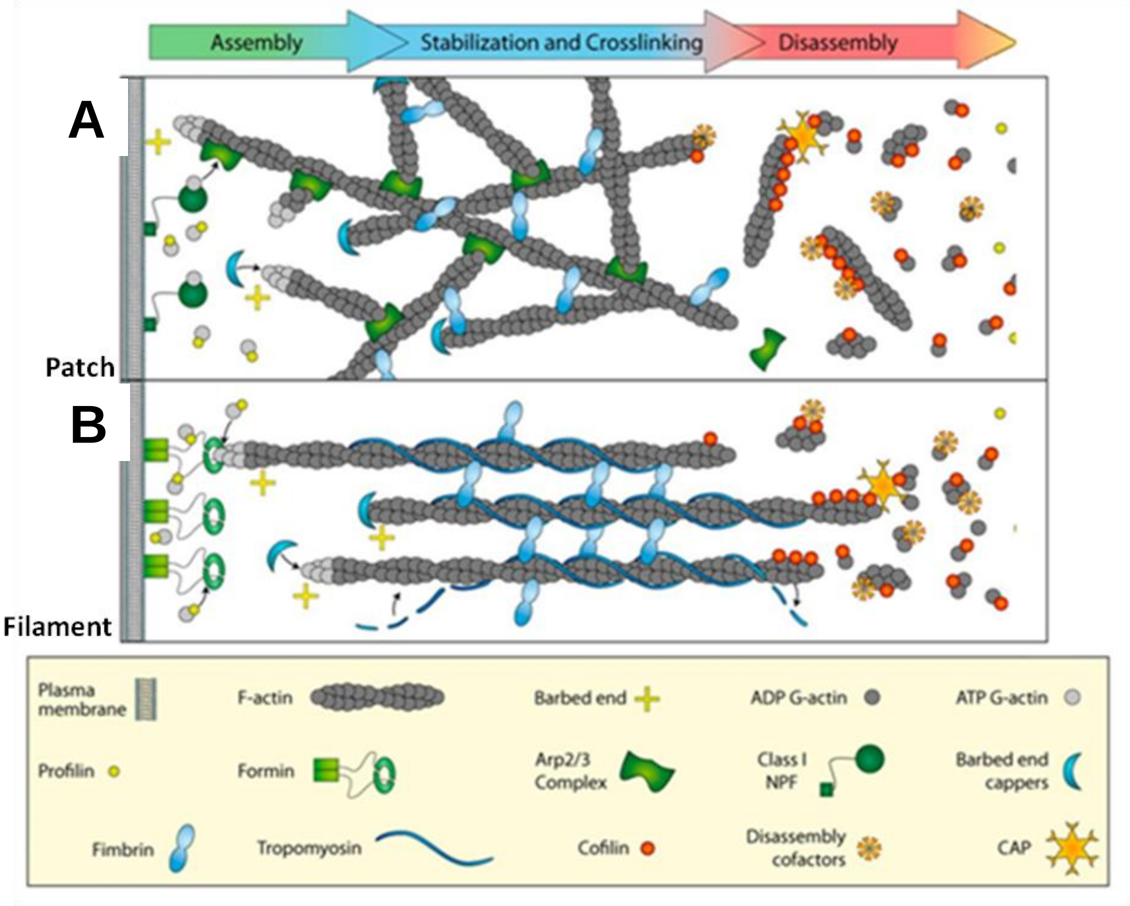

**Figure 1.14. Actin filaments form actin patches.** Illustration of actin filament formation and turnover in actin patches and filaments. Profilin pools ATP G-actin for nucleation. The ATP G-actin polymerise into filaments from the growing barbed end. Barbed end cappers bind to the barbed end to regulate the rate of polymerisation. Filaments are cross-linked by fimbrin for increased stability. ATP G-actin is hydrolysed into ADP G-actin as the filament polymerises. Cofilin then binds and deforms the filament twisting pattern to severe it. Disassembly cofactors bind to cofilin and actin to promote disassembly. CAP promotes severing and dissociates cofilin from ADP G-actin so they can be recycled. **(A)** In actin patches, actin filaments are branched and nucleation is facilitated by class I NPF (nucleation promoting factor) at the plasma membrane and Arp2/3 complex on pre-existing filament. Branched actin filaments are generated at a 70 ° angle (Mullins et al., 1998). **(B)** Actin filaments are unbranched and nucleation is facilitated by formins. Formins bind to barbed ends and deliver ATP G-actin monomers to the filament for polymerisation in a processive manner. The filaments in cables are wrapped by tropomyosin. It forms a continuous polymer around the surface of actin filaments. Tropomyosin stabilises actin filaments and prevents the formation of branched filaments (Skoumpla et al., 2007). Adapted from Goode et al. (2015).

### Actin patches

Actin patches form at sites of endocytosis and cell growth. Formation of cortical actin patches is illustrated in Figure 1.14A. In *S. pombe*, this occurs at the cell tips (East & Mulvihill, 2011). Nucleation of short actin branches is facilitated by class I NPFs (nucleation promoting factors) at the plasma membrane and Arp2/3 complex on previously formed actin filaments (Machesky et al., 1994; Machesky et al., 1999). Arp2/3 complex is a protein complex composed of actin-related proteins Arp2 (actin related protein 2), Arp3 (actin related protein 3), and five other subunit proteins. It is also a downstream effector of cell polarity regulator Cdc42. Arp2/3 complex attaches to the side and pointed ends of pre-existing actin filaments. NPFs interact with Arp2 and Arp3 and cause a conformational change that brings Arp2 and Arp3 in close proximity of each other. NPFs then carry an ATP G-actin monomer to Arp2 and Arp3 and form a trimer of Arp2, Arp3 and actin. The trimer then acts as a nucleation seed for a new actin filament (Weston et al., 2012) Cortical actin patches have been shown to be recruited to the cell tips via transport on actin filaments during interphase, with the barbed end facing the cortical patch (Kamasaki et al., 2005; Pelham & Chang, 2001). The force of actin polymerisation in actin patches drives endocytic invaginations into the cytoplasm and provides lateral force for vesicle scission (Galletta & Cooper, 2010). Myosin I localise at actin patches and bind to membrane phospholipids. Myosin I motor activity also provides force for vesicle scission.

### Actin filaments

Actin filaments are double stranded, helical polymers of G-actin monomers. They span through the cell and serve as pathways for Myosin V to travel along and transport cargo throughout the cell. Actin filament polymerisation is illustrated in Figure 1.14B. Formin For3 is activated by the cell polarity regulator Cdc42. Once activated, it captures actin monomers for nucleation and polymerises unbranched actin filaments (Pruyne et al., 2002; Sagot et al., 2002). As it polymerises actin filaments, it moves processively on the growing end of actin filaments and prevents capping proteins from binding to the growing ends and inhibiting elongation (Breitsprecher & Goode, 2013). Tropomyosin Cdc8 stabilises actin filaments and regulates myosin binding to actin filaments. To regulate myosin binding, tropomyosin blocks myosin binding sites along actin filaments.

### Contractile actin rings (CARs)

The CAR is an actin ring structure that constricts to separate a single cell into two cells during cytokinesis. Its assembly begins during interphase and occurs at the centre of the cell. The cell centre is determined by the position of the nucleus (Wolfe & Gould, 2005). Two mechanisms for CAR formation currently stand: the 'leading cable' and 'search and capture' mechanisms. The 'leading cable' mechanism describes branching of aster-like cables from actin filaments at the centre of the cell, to form a ring composed of two parallel arcs of opposite directions. The 'search and capture' mechanism describes nodes from which actin filaments extend. Myosin II within the node protein complex, captures the extending actin filaments and hauls them together, to pack the actin filaments into cubes. This reoccurring process integrates the nodes and actin filaments to form a contractile ring (East & Mulvihill, 2011). Whilst neither mechanism has been disproved, co-occurrence has been suggested (Hachet & Simanis, 2008; Huang et al., 2008). CAR assembly is illustrated in Figure 1.15.

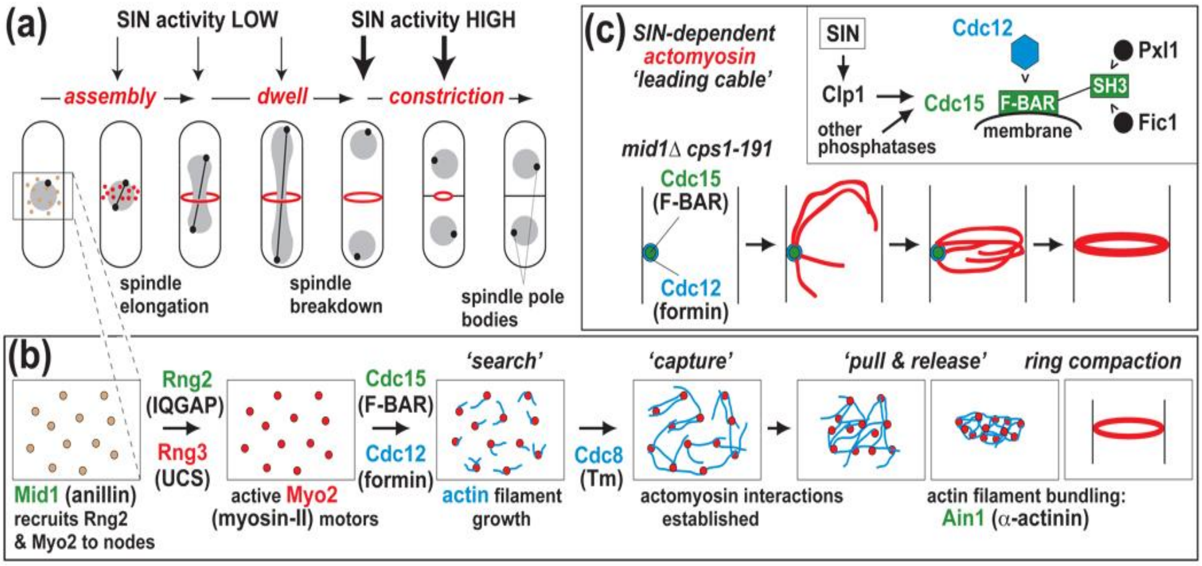

**Figure 1.15. Contractile actin ring assembly and constriction occur by the 'leading cable' and 'search, capture, pull and release' mechanisms in *S. pombe*. (A)** Illustration of CAR (contractile actin ring) formation and constriction relative to SIN (septation initiation network) activity and spindle pole body elongation. The SIN activity induces septation. During assembly and dwelling phases, SIN activity is low. CAR precursor nodes (yellow) form and mature (red) around the nucleus (grey). The spindle pole bodies (black) duplicate and nucleate microtubule spindles. The nodes form a ring. During constriction, SIN activity is high and triggers CAR constriction. **(B)** Illustration of the SCPR (search, capture, pull and release) mechanism. Mid1 nodes (yellow) recruit Rng2 and Myo2. Rng3 activates Myo2 (red). Cdc15 recruits Cdc12 to nucleate actin filaments (blue) from the nodes. Filaments search for neighbouring filaments. Linked filaments are stabilised by Cdc8. Myo2 binds, pulls and releases the filaments and repeat the CPR stages to compact the ring. Ain1 bundles the filaments. **(C)** Illustration of the SIN dependent 'leading cable' mechanism. In *mid1Δ cps1-191* cells, SIN promotes Clp1 and other phosphatases, to dephosphorylate F-BAR protein Cdc15. Cdc15 recruits Cdc12 and deforms septum membranes.Cdc15 recruits Pxl1 and Fic1. Adapted from Kovar et al. (2011).

The SIN (septation initiation network) is a GTPase signalling cascade that comprises of multiple protein kinases. The kinases assemble on a scaffolding complex at spindle pole bodies (the microtubule-organising organelles in *S. pombe* and the equivalent to mammalian centrosomes) by binding to polo-like kinase Plo1 and Cdc2/Cdc13 (cyclin-dependent kinase-cyclin complex), in the spindle pole bodies (Wolfe & Gould, 2005). Plo1 activity is required for mitotic spindle assembly and regulates septation (Mulvihill et al., 1999; Tanaka et al., 2001). Cdc2/Cdc13 controls the G2/M transition of the cell cycle (Decottignies et al., 2001). SIN activity therefore responds to changes in the activity of mitosis regulators (Tebbs & Pollard, 2013; Wolfe & Gould, 2005).

During contractile actin ring assembly and dwelling phases, SIN activity is low. Assembly of the contractile actin ring begins before the onset of mitosis. CAR precursor nodes form around the nucleus. The nodes mature as additional proteins are incorporated into the nodes. The spindle pole bodies duplicate, embed into the nuclear envelope and nucleate microtubule spindles that extend from them (Kovar et al., 2011; Ohta et al., 2012). The microtubule nucleator within the spindle pole bodies is γ-TuC (γ-tubulin complex). In *S. pombe*, a component of spindle pole bodies, called Pcp1, is essential in recruiting γ-TuC to spindle pole bodies during mitosis (Ohta et al., 2012). As microtubule spindles nucleate and elongate from the spindle pole bodies, the nodes begin to compact and form a consistent ring.

During the dwell phase, the diameter of the contractile ring does not change (Wei et al., 2016). The spindles begin to elongate and extend the nucleus towards both ends of the cell, forming a dumbbell shaped nucleus. The spindles then breakdown and the nucleus resolves into two separate nuclei (Yam et al., 2011). During the constriction phase, SIN activity is high and triggers contractile ring constriction and disassembly. It also triggers membrane invagination and the formation of a specialised cell wall called the septum, to divide the cell. The cytoplasm membrane is separated by plasma membrane scission and the septum remodels to form two daughter cells (Pollard & Wu, 2010).

In the SCPR (search, capture, pull and release) ring assembly mechanism, nodes are contractile precursors of the contractile ring. They are protein assemblies that localise at the equator of the cell during interphase and determine the site of division (Pollard & Wu, 2010). Mid1, an anillin-like protein (also known as Dmf1), is a cleavage placement protein and localises at the cell equator and anchors to the cell cortex (Lee & Wu, 2012;

Schwayer et al., 2016). Cell cycle kinases are also recruited to the cell equator with Mid1 and form the nodes. Approximately sixty-five nodes are formed at the equator and anchor to the cell cortex before the onset of mitosis. Nodes that contain approximately twenty-five molecules of Mid1 mature by recruiting approximately: twenty-five molecules of ring assembly protein, Rng2 (IQGAP family member) which in turn recruits twenty-five molecules of Myo2. Once at the node, Myo2 is folded and activated by Rng3 (UCS domain-containing yeast chaperone protein). Myo2 is incorporated into a maturing node (red) (Pollard et al., 2017). Approximately twenty-five molecules of F-BAR (Fes/CIP4 homology-Bin-Amphiphysin-Rvs) domain containing protein Cdc15 and two dimers of formin Cdc12 (actin nucleator) are then recruited to the nodes. Once matured, the nodes are ready for actin assembly (Pollard & Wu, 2010).

In the search phase, one to four actin filaments (blue) orientate in random directions and are nucleated by Cdc12 from each node. Cdc12 is recruited by Cdc15 and binds actin monomers to the filament to elongate it (Kovar et al., 2011). As the filament elongates, Cdc12 moves along it to continue the elongation. The filament can then search the cortex for neighbouring filaments. Neighbouring filaments link together. The coiled-coil homodimer, tropomyosin Cdc8, binds to elongating actin filaments and polymerises around them in a helical fashion. Cdc8 binding stabilises filaments and prevents disassembly of filaments (Pollard & Wu, 2010). In the capture phase, Myo2 within the nodes binds to actin filaments elongating from neighbouring nodes. In the pull and release phase, Myo2 generates motile force along the filament. This draws the nodes together. Interactions between nodes are released by various means such as Myo2 dissociation from captured filaments. Once released, Myo2 repeats the capture, pull and release stages to pull the nodes together and cause ring compaction. To compact the ring further, actin filament cross-linking protein Ain1, binds to actin filaments and bundles them into short anti-parallel bundles (Lee et al., 2012).

The SIN dependent 'leading cable' ring assembly mechanism functions cooperatively with the SCPR mechanism. The mechanism can be observed in the absence of Mid1. A lack of Mid1 node organisation leads to cytokinesis failure. This failure is rescued by delayed septum formation. This rescue and the leading cable mechanism can be observed in *mid1Δ cps1-191* double mutant *S. pombe* cells. These cells lack the spatial organisation of nodes by Mid1 and experience delayed septum formation due to the mutation in β-glucan synthase Bgs1/Cps1. Bgs1/Cps1 is recruited to cell division sites by Cdc42 and it is responsible for the synthesis of the linear β-1,3-glucan component of the septum

(Davidson et al., 2016). The delay in septum formation allows time for the contractile ring to form completely and act as a location for septum deposition by SIN.

SIN promotes the activity of multiple phosphatases, including Clp1 (SIN-dependent Cdc14 family phosphatase). Clp1 dephosphorylates Cdc15. Cdc15 dephosphorylation is required for Cdc15 localisation at the contractile actin ring. There, Cdc15 recruits formin Cdc12. It also assembles into actin filaments that deform septum membranes. The SH3 domain of Cdc15 recruits focal adhesion protein Pxl1 (paxillin-related protein) and Fic1 (C2 domain protein) (Kovar et al., 2011). Pxl1 is required for correct Myo2 organisation in the contractile actin ring, which stabilises the ring and generates force for ring constriction (Pinar et al., 2008). Fic1 localises to the cell division sites and interacts with Cdc15 to re-establish polarised cell growth at the newly formed end of the cell (end formed from the site of division), following cell division (Bohnert & Gould, 2012).

### Actin binding protein of interest: tropomyosin Cdc8

Actin binding proteins (ABP) have been established to have direct effects on the correct function of unconventional myosins. Each ABP forms different actin structures of which specific myosins associate with to function. These associations indicate ABPs play a role in governing myosin molecular mechanisms of function. Tropomyosin was an ABP of interest during this PhD project due to its association to myosin function and polarised cell growth in *S. pombe*.

Tropomyosin is an essential α-helical, coiled-coil, actin binding, homodimer which contributes to the stability of actin filaments. It does this by binding to the side of actin filaments and forms two parallel polymers that wrap around the actin filaments. *S. pombe* possess one tropomyosin isoform, Cdc8. Cdc8 monomers span four actin dimer subunits and form polymers by binding to each other in an end-to-end fashion. They mostly localise at actin filaments and actin contractile rings. Smaller amounts of Cdc8 localise at actin patches.

Cdc8 also plays a role in the actin interactions with other proteins. When Cdc8 is bound to actin, it protects actin from severing by Cof1 and branching by Arp2/3. Cdc8 stabilised actin filaments permit Myo2 activity at actin contractile rings during cytokinesis, and Myo52 activity along actin filaments to regulate cell polarity. It is also a positive regulator of Cdc12 which nucleates and polymerises actin filaments with processive movement along actin filaments. Opposite to this, Cdc8 negatively regulates Myo1 activity at actin patches (Cranz-Mileva et al., 2013).

Cdc8 function is dependent on N-terminal acetylation (Skoumpla et al., 2007). Acetylation is a type of post-translational modification that involves the addition of an acetyl group (-$CH_3CO$) to a target protein or peptide and is mediated by acetyltransferase enzymes (Li et al., 2013). In *S. pombe,* ~80 % of Cdc8 is acetylated and ~20 % is unacetylated. Acetylation is required for Cdc8 to bind to actin with a high affinity and also strengthens Cdc8 end-to-end binding (Coulton et al., 2010). Cdc8 acetylation also modulates myosin binding to actin. Acetylation alters the position Cdc8 polymers lay on actin filaments (Skoumpla et al., 2007). The proposed model explaining the impact of tropomyosin acetylation on Myo2 motility is illustrated in Figure 1.16.

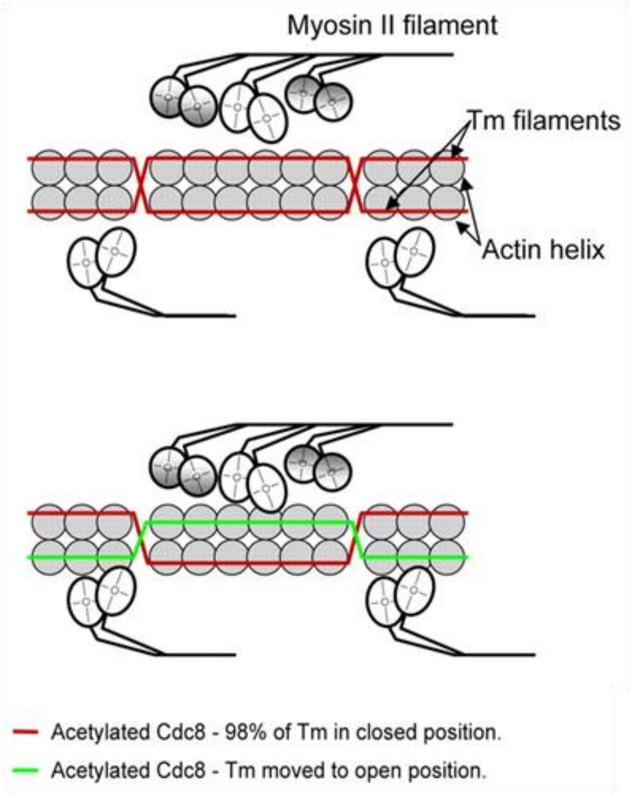

**Figure 1.16. Tropomyosin regulates myosin binding to actin.** Model for tropomyosin acetylation-dependent regulation of myosin II motility. Cdc8 (tropomyosin, Tm) binds to the side of actin to form tropomyosin filaments (red lines) that stabilise helical actin filaments (grey circles). Acetylation of Cdc8 fixes Cdc8 filaments in a rigid closed position with a high affinity for actin. This closed position hinders myosin binding to actin. Myosin II forms thick filaments composed of bundles of myosin II monomers. Myosin II motility is executed by multiple myosin II head domains interacting with actin simultaneously. The force generated by myosin II moves acetylated Cdc8 to an open position. This open position permits myosin II to bind to actin. Adapted from Coulton et al. (2010).

It has been proposed that 98 % of acetylated Cdc8 holds a closed position that only allows myosin to bind weakly to actin. Myo2 thick filaments interact with actin filaments and exert significant force on the actin filaments during cytokinesis. This force is great enough to move acetylated Cdc8 from the closed position to an open position, which allows myosin to bind strongly to actin. Unacetylated Cdc8 is only found in actin filaments that span the cell. It does not bind to actin with a high affinity and therefore does not have a fixed position on the filaments or significantly affect myosin binding to actin (Coulton et al., 2010).

Cdc8 has been suggested to support the correct localisation and motility of Myo52, due to its regulatory role in actin dynamics (Pelham & Chang, 2001; Motegi et al., 2000). Non-functional Cdc8 bring about a 'dumbbell' morphology in *S. pombe,* with a shortage of actin filaments and an inability to divide (Arai & Mabuchi, 2002; Skoumpla et al., 2007). Mutations in Cdc8, and other actomyosin ring proteins, also induce an '*rng*' phenotype which does not form CARs correctly and can develop elongated and branched morphologies (Bathe & Chang, 2010; Karagiannis, 2012). Since there is only one gene that encodes for Cdc8 in *S. pombe*, the organism serves as an ideal model to exemplify consequences of mutant Cdc8 or absences of the ABP (Balasubramanian et al., 1992). During this PhD project, temperature-sensitive Cdc8 mutant *S. pombe* strains were used to study the function of Cdc8 in contractile actin ring placement, assembly and constriction.

## 1.4 Myosin I and myosin V functions in cell growth

### 1.4.1 Myosin I function in endocytosis

Monomeric Myo1 is a single headed protein which consists of a single heavy chain. The heavy chain possesses a highly conserved motor domain of which binds to actin (Bi et al., 2015). The neck domain which possesses the light chain binding region follows the head region. The C-terminal tail domain contains regions of membrane binding and protein interaction. Myo1 plays a fundamental role in the early stages of endocytosis, the cycle cell, gene expression in mammalian cells, the regulation of actin, polarised cell growth and cortical patch formation (Wenzel et al., 2015).

In cells, endocytosis is the internalisation of nutrients and cell surface molecules. This process is required for cell growth. During endocytosis, actin and membrane interactions of individual myosins allow the manipulation of cell shape and vesicle trafficking needed for endocytosis. Endocytosis is dependent on membrane remodelling and the formation of actin filaments, during vesicle internalisation. This is crucial for nutrient sensing and uptake from the external environment (Petrini et al., 2015). Myo1 is involved in actin patch assembly and endocytic internalisation. It serves as an anchor between the cell membrane and actin patches and provides the force required for endocytic internalisation. Myo1 mutations in *S. pombe* induce phenotypes with growth and endocytosis defects, resembling those of *Δmyo1* mutants (Bi et al., 2015).

As well as Myo1, a plethora of other proteins are recruited to sites of endocytosis. The order in which the proteins are recruited in *S. pombe* has been well documented using fluorescence microscopy (Arasada & Pollard, 2011). Endocytosis at *S. pombe* actin patches is illustrated in Figure 1.17.

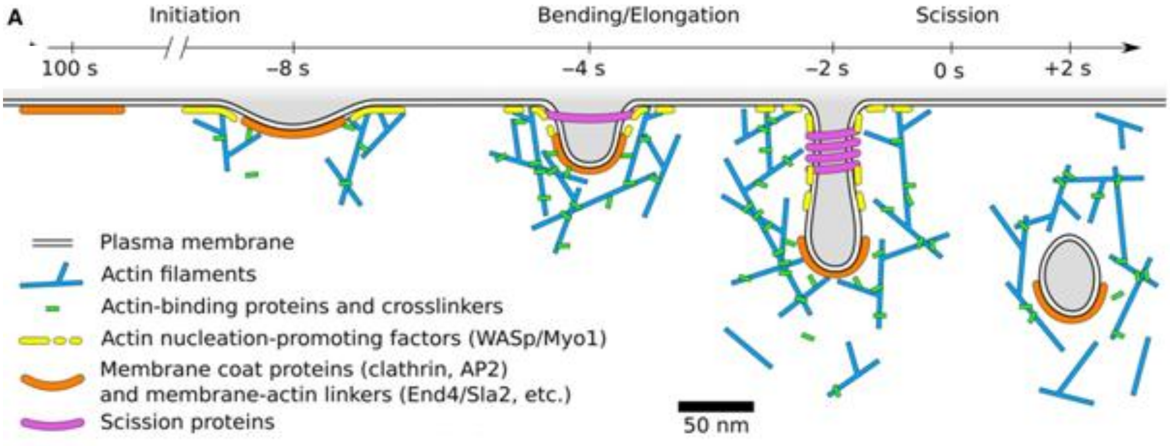

**Figure 1.17. Myo1 anchors the plasma membrane to actin patches during endocytosis.** Illustration of clathrin-mediated endocytosis at actin patches in *S. pombe.* During the initiation phase, clathrin (orange) binds to the cytoplasmic side of the membrane and acts as a mould to form the vesicles. End4/Sla2 (orange) links clathrin to actin filaments (blue). AP-2 (orange) is also recruited to link clathrin to plasma membrane lipids. WASp complexes with Myo1 (yellow) at the plasma membrane. WASp/Myo1 activates actin nucleators. Actin monomers are nucleated and polymerise into short, branched filaments to form actin patches. The actin filaments are nucleated by Arp2/3 complex. Actin cross linkers (green), such as fimbrin, stabilise actin filaments as a network of filaments form. Myo1 anchors the actin filaments to the plasma membrane. During bending/elongation, polymerisation of the actin filaments pulls the invagination further into the cell. Scission proteins (purple), recruited by Myo1, bind to the membrane and polymerise into the invagination, pulling it further within the cell. A narrow tubule forms, scission occurs and the endocytic proteins dissipate. Scale bar - 50 nm. Adapted from Lacy et al. (2018).

Endocytosis in *S. pombe* is clathrin-dependant. Initiation of endocytosis begins with the recruitment of early endocytic proteins, such as clathrin, to promote initial plasma membrane invagination. 100 s before internalisation at time zero, thirty to forty clathrin molecules are recruited to the plasma membrane and form a cap to coat the outside of the invagination (Kovar et al., 2011). The coat stabilises the bilayer curvature. AP-2 (adaptor protein 2 complex) links clathrin to lipids in the plasma membrane (León et al., 2016). Approximately 1 - 2 min after clathrin recruitment, additional adaptor proteins, such clathrin adaptor End4/Sla2 (End4/src-like-adapter 2), accumulate at the plasma membrane to recruit actin and bind early endocytic proteins such as clathrin to actin (Kovar et al., 2011). 8 s before internalisation, WASp (Wiskott–Aldrich Syndrome protein) complexes with Myo1 and cell polarity regulator Cdc42, at the plasma membrane. WASp/Myo1 activates Arp2/3 complex, which rapidly forms dense branched networks of short actin filaments. It also and recruits actin-binding proteins and actin cross linkers, such as fimbrin, to stabilise the networks (Kovar et al., 2011). The actin networks are anchored to the plasma membrane by Myo1.

During the bending/elongation phase, polymerisation of actin filaments and force generated between actin and Myo1 elongate the invagination. Scission proteins, such as F-BAR protein Cdc15, are recruited by Myo1 and sense low curvature in the membrane bilayer and bind to the membrane bilayer. The F-BAR proteins form a base for high curvature sensing F-BAR proteins, such as Bzz1, to bind and polymerise further within the invagination. This deforms the membrane further by pulling the membrane down. A narrow tubule is formed and scission occurs (Shimada et al., 2007). After scission, the endocytic proteins begin to dissipate (Kovar et al., 2011).

*S. pombe* Myo1 possess two IQ motifs in the neck region, which calmodulins Cam1 and Cam2 bind to (Sammons et al., 2011). Cam1 and Cam2 modulate Myo1 activity during endocytosis however, the activity of the two calmodulins differ. Cam1 is recruited with Myo1 during the early stages of endocytosis. Cam2 is recruited later than Cam1 and Myo1 but before vesicle scission. After scission, Cam1 dissociates from Myo1 and leaves the plasma membrane. Cam2 remain associated to endocytic vesicles that internalise into the cell. Myo1 leaves the plasma membrane after Cam1 and Cam2 leave. Cam1 dissociation from Myo1 reduces the rigidity of the Myo1 neck domain. This reduces the tension between Myo1 and actin filaments and results in Myo1 dissociating from the actin filament (Baker et al., 2019).

All aspects of the regulatory pathway that modulates Myo1 function have not been determined. Phosphoproteomics have identified a conserved serine 742 phosphorylation site in the Myo1 neck domain IQ motifs. Phosphorylation of this site has an unknown influence on how calmodulin binding to Myo1 regulates Myo1 function in endocytosis, required for polarised cell growth. During this PhD project, the role of Myo1 serine 742 phosphorylation in Myo1 regulation by calmodulin was investigated. Myo1 function in endocytosis, during the vegetative cycle to the meiotic cycle, was studied in *S. pombe* to assess the significance of Myo1 serine 742 phosphorylation in polarised cell growth.

### 1.4.2 Myosin V function in cargo transport and cytoskeleton organisation

Myosin V functions as a dimer and has a fundamental role in the correct sub-cellular localisation and tethering of organelles e.g. secretory vesicle transport from the centre to the perimeter of the cell (Berg et al., 2001). Myosin V transports cargoes, such as growth vesicles, to the poles of the cells by travelling along helical actin filaments of the cytoskeleton. Myosin V also transports protein vesicles, membranous cargo, lipids and mRNA (Presti & Martin, 2011; Reck-Peterson et al., 2000). Each molecule in a dimer has an N-terminal globular head motor domain attached to a neck domain consisting of six light chain bound IQ motifs, followed by an α-helical coiled-coil dimerisation region and a C-terminal globular cargo-binding site in tail domain (Xie et al., 2006). The motor protein dimer travels towards the barbed end of actin filaments in a hand-over-hand like fashion covering approximately 36 nm each step (Presti & Martin, 2011).

Myosin 51 (Myo51) and myosin 52 (Myo52) are the two class V myosins present in *S. pombe*. Differences between the two myosins lay in their localisation and function. Myo51 appears static in vegetative cells and only localise to sites of cell division during cytokinesis, as a non-essential component of the contractile actin ring. In contrast to this, Myo52 transports cargo throughout the whole length of cells and accumulates at actin-rich regions of growth and vesicle delivery (Motegi et al., 2001; Win et al., 2001). Myo52 is involved in the localisation of α-glucan synthase, Mok1. α-glucans are one of the main structural components of the cell wall in *S. pombe* and is therefore crucial for cell wall synthesis and the maintenance of cell wall integrity, both of which are required for cell growth. In Myo52 deletions, Mok1 does not localise to sites of deposition correctly (Win et al., 2001).

In healthy wild-type cells, Myo52 also localises to the septum of dividing cells. Myo52 deletions exhibit slow forming septa or fail to cleave. This has suggested Myo52 to be responsible for the delivery septum components required for septum maturation and cleavage (Win et al, 2001). Myo52 also transports Bgs1/Cps1 (1,3-β-glucan synthase), an enzyme that synthesises linear 1,3-β-glucan, to regions of cell division because it is a main component of the septum formed during cytokinesis (Davison et al., 2016; Motegi et al., 2001; Mulvihill et al., 2001; Mulvihill et al., 2006; Win et al., 2001).

Myo52 also has a function in vacuole fusion. The *S. pombe* contain approximately eighty vacuoles (Mulvihill et al., 2011). Vacuoles are fundamental organelles, which regulate the storage of water, nutrients and ions (Rains et al., 2017). The acidic environment within vacuoles also allows for the degradation of proteins and ions within the cell. Vacuoles also respond to osmotic stress and other stresses, such a nutrient deprivation (Li & Kane, 2009; Rains et al., 2017) Vacuoles undergo fusion when cells are under osmotic stress (Mulvihill et al., 2011).

Myo52 is also involved in the organisation of actin filaments. In *S. pombe*, Myo52 deletions display short, curled, disorientated actin filaments. Filaments in Myo51 deletions are comparable to wild-type actin filaments. Myo52 has been shown to associate with For3 and possibly transport it to the ends of *S. pombe*, where actin filaments are nucleated and polymerise towards. At the cell ends, For3 can be reused for actin filament assembly. Myo52 may also deliver other actin regulators to the cells ends. Myo52 motor activity along actin filaments also generates a pulling force on the filaments. Myo52 translocation towards the cell ends may drag actin filaments towards the cell interior. Increasing the load of individual Myo52 and the number of Myo52 molecules travelling along actin filaments generates a greater pulling force that promotes actin filament extension. The pulling force generated by Myo52 may cause tension required to extend and assemble actin filaments (Presti et al., 2012). These possible modes of actin organisation by Myo52 are illustrated in Figure 1.18.

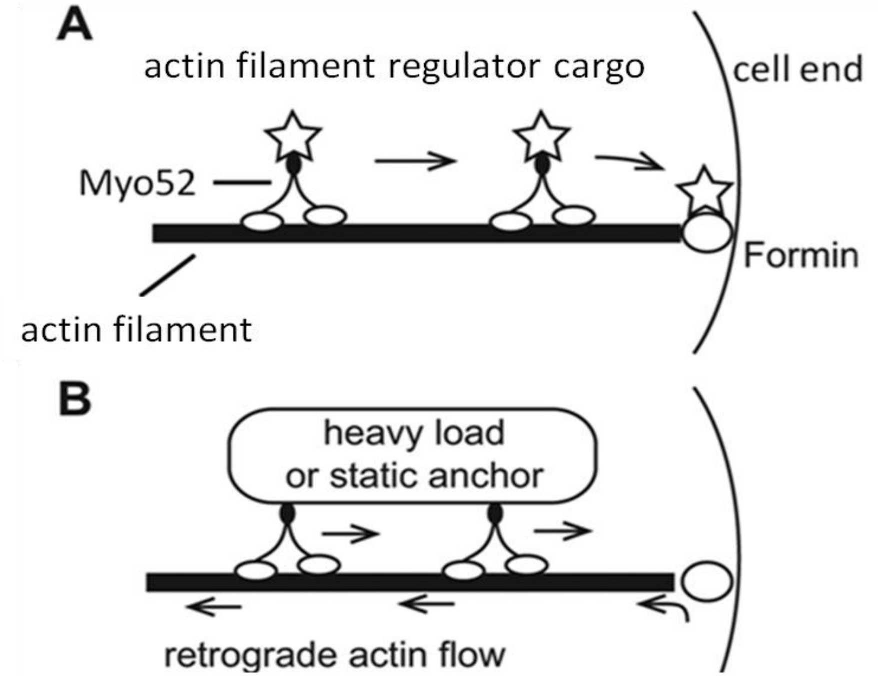

**Figure 1.18. Myo52 may transport actin regulators and generate force to regulate actin filaments.** Model of possible actin filament organisation by Myo52. Actin filaments are nucleated by formin at the cell end. Myo52 binds to filaments via their head domain and translocates along filaments towards the cell end. **(A)** Myo52 binds to actin filament regulators (stars) via its tail domain and transports them as cargo to cell ends to regulate the filaments. **(B)** Translocation of Myo52 and its heavy cargo towards the cell ends may exert force on actin filaments that pull the filaments in the opposite direction and towards the cell interior (retrograde actin flow). This force may promote filament extension. Adapted from Presti et al. (2012).

Alongside actomyosin operations, Myo52 is also involved in governing microtubule dynamics and the turnover of a CLIP170-like protein and microtubule regulator called Tip1 in *S. pombe.* Tip1 binds to the tip of microtubules and is required for microtubules to differentiate between cell ends and cortical regions of the cell. Tip1 also prevents microtubules from undergoing catastrophe (dismantling). This is important for establishing bipolar growth during NETO in *S. pombe* because microtubule activity promotes actin assembly at the growing new end of the cell. Microtubules deposit polarity factors, such as Tea1 and Tea4/Wsh3, to newly growing cell ends. At these cell ends, the polarity factors form complexes with For3. The complexes are called polarisomes and cause the recruitment of For3 to the new cell end. There, For3 allows actin assembly and cell growth to occur at new cell ends. In healthy wild-type cells, microtubules undergo catastrophe when they reach the cell end. In *S. pombe* cells with Myo52 that have a single amino substitution mutation (D55N, aspartic acid 55 to asparagine 55) in the motor domain, microtubules continue to extend and curl along the end of the cell. This is because Tip1 is not removed from the microtubule tip, once the microtubule plus end has reached the cell ends. This suggests Myo52 is involved in the release of Tip1 from the tips of microtubules and promotes microtubule catastrophe at the cell ends. Tip1 ubiquitylation (a protein modification that targets proteins for proteasome-dependent degradation) and proteolysis are also modulated by Myo52. Myo52 associates with ubiquitin receptor Dph1 and targets ubiquitylated Tip1 for proteolysis (Martin-Garcia & Mulvihill, 2009).

Tip1 targets zones of growth in *S. pombe.* These zones of growth have been shown to be positioned and defined in part by a *Drosophila* Furry-like protein called Mor2 (Hirata et al., 2002). In order to position zones of growth, Mor2 functions in cooperation with actin. Mor2 localises to the cell ends and septation site, to position zones of growth, in an actin dependent manner (Hirata et al., 2002; Kinai et al., 2005). Actin localisation to the cell ends is also dependent on Mor2 (Hirata et al., 2002). Mor2 is part of the MOR (morphogenesis Orb6 network) signalling pathway that functions to regulate cell polarity and cell septation. MOR proteins include kinases such as Orb6 and Nak1 (Tay et al., 2019). Mor2 acts as a scaffold that mediates interaction between Orb6 and Nak1 (Gupta, 2013). This interaction is required to activate Orb6 to spatially regulate Cdc42 GTPase. Orb6 spatially restricts Cdc42 activation to the cell ends for polarised growth (Das et al., 2009).

Myo51 deletions have been determined to not impede cell growth however Myo52 deletions result in temperature sensitive and misshapen phenotypes in *S. pombe.* These misshapen cells are shorter, broader and develop multiple septa. Depolarisation of actin structures form in Myo52 deletions but do not in Myo51 deletions. Growth of Myo52 deletions is also slower than Myo51 deletions, which has a growth rate comparable to healthy wild-type cells. Deletion of both Myo51 and Myo52 in a single strain results in cells phenotypically similar to Myo52 deletions. The deletions are therefore is non-additive. The double mutants are viable (Win et al., 2001). Due to these differences in relevance to cell growth, Myo52 was chosen over Myo51 as the isoform of interest in this PhD project.

## 1.5 Regulation of myosin by phosphorylation and cytoplasmic calcium

### 1.5.1 Myosin regulation by phosphorylation

Myosins are regulated by transcriptional regulation, substrate/effector binding and post-translational modification such as glycosylation and phosphorylation. Post-translational modifications can occur at the myosin active sites (orthosteric) or at other locations (allosteric). These modifications can affect multiple aspects of a protein such as ligand and effector binding and auto-inhibition. Post-translational phosphorylation of myosins is a covalent, allosteric process and is a significant regulator of their function. Myosin function is influenced by phosphorylation-induced changes in its ATPase activity and its active and inactive states. Myosin phosphorylation is therefore fundamental in multiple processes in *S. pombe*, including the cell cycle. Phosphorylation sites identified in myosins I, II and V have been found to bring about various processes (Attanapola et al., 2009).

Protein phosphorylation is a post-translational modification which serves to regulate protein function, in response to extracellular signals. During phosphorylation, the negatively charged phosphate group of an ATP molecule is transferred to the hydroxyl group of a serine, threonine or tyrosine protein residue, by a protein kinase enzyme. The negative charges of phosphate groups often induce conformational and functional changes in the phosphorylated protein. Protein phosphatase enzymes catalyse dephosphorylation, which is the removal of phosphate groups, and involves cleavage of the phosphate group via hydrolysis. Phosphorylation of a protein is controlled through signalling cascades which involve chains of phosphorylation events upon upstream kinases and phosphatases. Figure 1.19 illustrates the phosphorylation pathway (Nestler & Greengard, 1999).

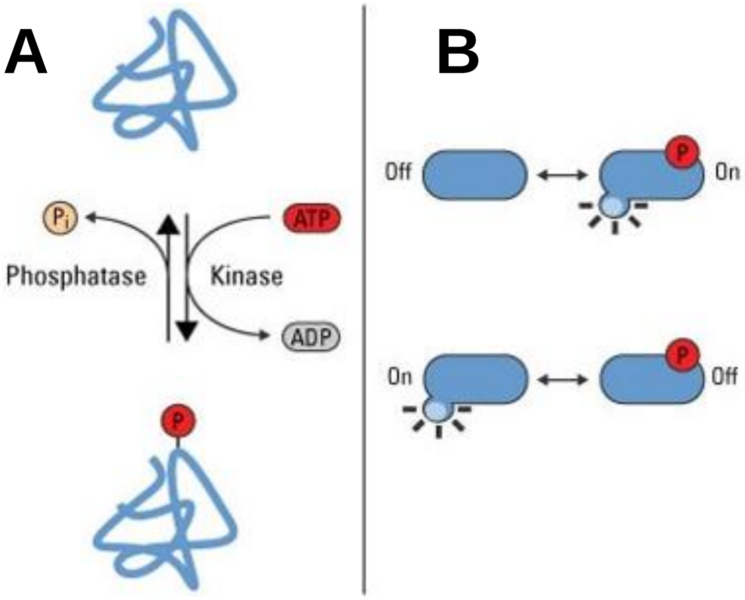

**Figure 1.19. Phosphorylation is a post-translational control for proteins.** Protein phosphorylation and dephosphorylation schematic. **(A)** Protein kinases transfer a phosphate group (Pi) from ATP to the target protein, at a phosphorylation site. Phosphatases catalyse dephosphorylation, the removal of Pi. **(B)** Phosphorylation can induce a conformational change, activation and deactivation, specific to the target protein. Dephosphorylation also induces specific activation and deactivation. Adapted from Thermo Fisher Scientific (n.d.).

The Ste 20 (sterile 20) family of protein kinases are a group of serine/threonine-protein kinases. They phosphorylate Myo1 at conserved phosphorylation sites called TEDS-sites, located in the actin binding site of the myosin motor head domain. At these sites, only threonine (T), glutamate (E), aspartate (D), or serine (S) residues are present. Phosphorylation at these sites regulates motor activity. In *S. pombe,* phosphorylation of TEDS sites has been shown to have a regulatory role in the recruitment and localisation of Myo1 to actin patches for endocytosis. Phosphorylation also increases myosin affinity for actin and promotes actomyosin binding (Attanapola et al., 2009).

Phosphorylation of myosin II and associated light chains have been studied extensively. Myosin II RLC (regulatory light chain) is a light chain that non-covalently binds to myosin II IQ motifs and is structurally similar to calmodulin (Heissler & Sellers, 2014). RLC is phosphorylated by MLCK (myosin light chain kinase) and this occurs in response to upstream signalling in non-muscle cells. It increases actin-activated ATPase activity more than one thousand fold (Scholey et al., 1980; Sellers et al., 1981; Trybus et al., 1989). To generate force, myosin II polymerise into filaments via the coiled-coil domain in their tail domain (Attanapola et al., 2009). In order to polymerise into filaments, RLC phosphorylation is required to induce a conformational change in myosin II, from a compact circular conformation to a linear conformation. The linear conformation enables myosin II to polymerise into filaments. Myosin II coiled-coil phosphorylation is reported to hinder filament assembly and binding to associated proteins (Dulyaninova et al., 2005; Dulyaninova et al., 2013; Even-Faitelson et al., 2006). The RLC phosphorylation-induced conformational change in myosin II is illustrated in Figure 1.20.

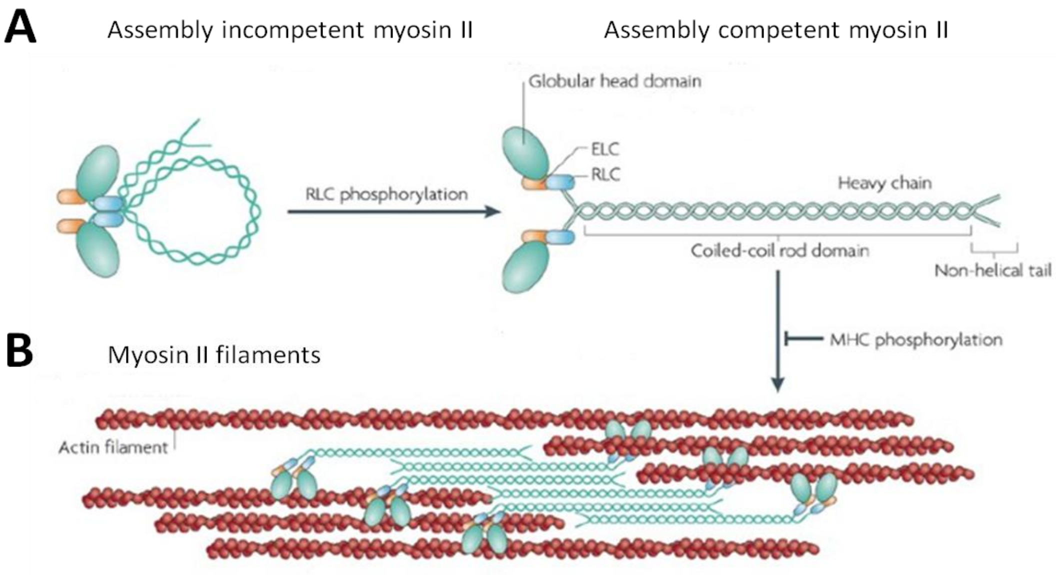

**Figure 1.20. The structure of non-muscle myosin II is dependent on regulatory light chain phosphorylation. (A)** Phosphorylation of myosin II RLC (regulatory light chain) induces a conformational change that enables polymerisation into filaments. Non-muscle myosin II heavy chains contain globular head domains that bind to actin filaments. ELCs (essential light chains) and RLCs bind to the neck domain (below the globular head domains). Myosin II dimers are formed via the coiled-coil domain in the tail domain. In the absence of RLC phosphorylation, myosin II possess a circular conformation, that maintains a head to tail interaction and is unable to assemble into a filament (assembly incompetent). RLC phosphorylation induces a conformational change into a linear conformation (assembly competent). **(B)** Myosin II dimers polymerise into filaments via their tail domains. Myosin II globular head domains bind to actin filaments to bundle actin filaments together and form stress fibres. Polymerisation is inhibited by phosphorylation of the myosin II heavy chain. Adapted from Vicente-Manzanares et al. (2009).

Phosphorylation has also been suggested to modulate cargo binding and release of myosin V. In mitotic *Xenopus* egg extracts, phosphorylation of the myosin V cargo binding domain has shown to result in organelle cargo detachment. CaMKII (calcium/calmodulin–dependent protein kinase II) is responsible for the phosphorylation. Inhibitors of CaMKII reduce release of cargo from myosin V (Karcher et al., 2001). In connection to this, the results of phosphorylation of Myo1 serine 742 and multiple phosphorylation sites along Myo52 are yet to be determined. The impact of phosphorylation on the cell growth functions of Myo1 and Myo52 was a focus of this study.

### 1.5.2 Myosin regulation by calcium

The myosins are exposed to regulation via second messenger divalent cations $Ca^{2+}$. Regulation via $Ca^{2+}$ was of particular interest in this study since it is sensed by calmodulin that bind to myosin IQ motifs in the neck domain. The conserved phosphorylation site myosin I serine 742 is located in the IQ of myosin I. Currently, the impact of myosin I IQ motif phosphorylation on endocytosis for polarised cell growth during the cell cycle is poorly understood (Wilson-Grady et al., 2007). This study explores the impact myosin I serine 742 phosphorylation has on the change from monopolar growth to bipolar growth in the cell cycle, in *S. pombe.* Recent studies within the Mulvihill lab have proposed TORC2-signalling-dependent phosphorylation of conserved myosin I serine 742 as a key regulatory mechanism to myosin I function (Baker et al., 2019).

TOR (Target of Rapamycin) is a conserved, nutrients-responsive serine/threonine-specific protein kinase. It phosphorylates the -OH group of serine and threonine in protein substrates. They phosphorylate protein substrates in response to various stimuli and are part of signalling networks that regulate cell growth (Gonzalez & Rallis, 2017). The stimuli TOR kinases respond to include growth factors, nutrients, energy and stress (Wullschleger et al., 2006). The *S. pombe* genome encodes for two TOR homologues; Tor1 and Tor2 (Otsubo & Yamamato, 2008; Weisman, 2016).

TORC2 (TOR complex 2) is multimeric supercomplex. Tor1 forms the core of TORC2 (Huang & Fingar, 2014; Laplante & Sabatini, 2012; Wullschleger et al., 2006). The function of TORC2 is not fully understood however, it has been reported to co-ordinate actin filament polarity, cell cycle progression, starvation response and survival in response to low glucose levels by phosphorylation of AGC kinase Gad8, at its carboxyl-terminus (Cohen et al., 2018). This includes the G1 arrest and entry into meiosis, when *S. pombe* are starved of nitrogen, mitotic control in response to glucose, cytokinesis, nutrients absorption and responses to osmotic and oxidative stress (Schonbrun et al., 2009; Schonbrun et al., 2013). It is therefore an essential protein for the main responses under starved conditions, sexual development and initiation of stationary phase entry. This has been made evident by observations of Tor1 *S. pombe* mutant cell elongation, osmotic and oxidative stress sensitivity, hampered sexual developmental progression in starved environments and reduced amino acid intake (Ikdea et al., 2008; Kawai et al., 2001; Weisman & Choder, 2001).

TORC2 is regulated by Ryh1 (Rab GTPase) and its guanine nucleotide exchange factor. The GTP-bound, active form of Rhy1 interacts with TORC2 and promotes TORC2 phosphorylation of Gad8 (Hatano et al., 2015). Gad8 is a serine/threonine-specific protein kinase and a homologue of human SGK1/2 kinase. It has been shown to be involved in nuclear functions such as chromosome remodelling, sexual progression, maintenance of cell integrity, bipolar growth initiation and cell cycle progression (Baker et al., 2019; Cohen et al., 2016; Schonbrun et al., 2013). TORC2 binding to Gad8 is required for the transition into mitosis from G2. Cell elongation occurs when this transition is hindered (Ikai et al., 2011; Peterson & Nurse, 2007).

*S. pombe* lacking in TORC2 or Gad8 experience minimal mating and are highly apoptotic beyond log phase (Kawai et al., 2001; Weisman & Choder, 2001). Increased equatorial actin polymerisation, irregular cortical actin patches localisation and actin reconstruction, during NETO, are observed with non-functioning TORC2 (Du et al., 2016; Ikai et al., 2011). Absence of TORC2-Gad8 induces sensitivity to non-permissive conditions such as DNA damage (Ikdea et al., 2008; Schonbrun et al., 2009; Weisman & Choder, 2001). Inhibition of TORC2 also induces cell cycle arrest at G2/M and therefore has role in regulating cell cycle G2/M transition (Gaubitz et al., 2015). The TORC2-Gad8 pathway is shown in Figure 1.21. The pathway features a negative feedback loop in which Gad8 inhibits TORC2 by phosphorylating Tor1 threonine 1972. Phosphorylation of conserved threonine 6 of Gad8 by PKC (protein kinase C), reduces interaction between Gad8 and TORC2. Gad8 threonine 6 phosphorylation therefore aids the prevention of Gad8-mediated inhibition of TORC2 (Du et al., 2016).

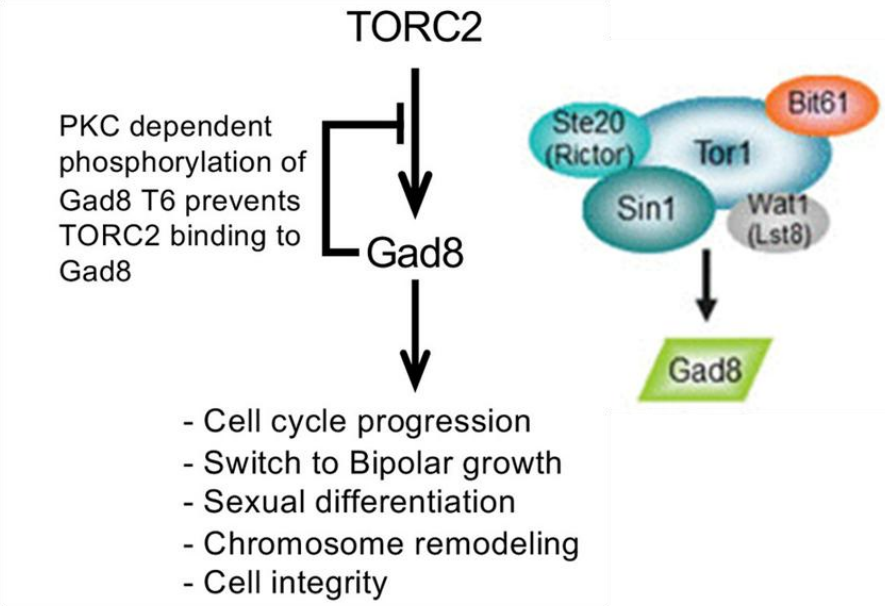

**Figure 1.21. TORC2 and Gad8 regulate cell cycle and progression and polarised cell growth.** Illustration of the TORC2-Gad8 pathway. TORC2 (Target of Rapamycin complex) is a multimeric supercomplex involved in the regulation of cell growth and cell cycle progression during nutrients starvation and stress. In *S. pombe*, TORC2 consists of Tor1, Ste20 (Rictor homologue), Sin1, Bit61 and Wat1 (Lst8 homologue). Tor1 is a serine/threonine-specific protein kinase and is the catalytic subunit of the complex. Ste20 is also a serine/threonine-specific protein kinase that associates with Tor1 (Weisman, 2016). Sin1 binds to Gad8 kinase and recruits it for phosphorylation (Tatebe et al., 2017). Bit61 is a non-essential subunit and its function has not been determined (Cybulski & Hall, 2009). The function of Wat1 has not been determined however, it may have nutrient sensing functions (Loewith et al., 2002). TORC2 phosphorylates Gad8 kinase. (Hatano et al., 2015; Tatebe et al., 2017). Gad8 is an AGC-family kinase. Its phosphorylation promotes Gad8 activity which is essential in cell cycle progression, sexual differentiation, chromosome remodelling, cell integrity and switching from monopolar growth (growth at one end of the cell) to bipolar growth (growth at both ends of the cell) (Hatano et al., 2015). Gad8 activity is inhibited by the phosphorylation of a Gad8 T6 (Gad8 threonine 6) residue by PKC (protein kinase C). Phosphorylation prevents physical interaction between TORC2 and Gad8. It also prevents the Gad8 phosphorylation and inhibition of TORC2. Adapted from Baker et al. (2019) and Weisman (2016).

Myosin function is regulated by $Ca^{2+}$. It can bind to myosin motifs, calmodulin and calmodulin-like light chains and also induce phosphorylation of these light chains. Figure 1.22 illustrates conformational changes observed in myosins I, II and V when exposed to free $Ca^{2+}$. Release of bound calmodulin has been observed in myosin I whilst phosphorylation of RLC proteins has been implied in myosin II. Free $Ca^{2+}$ is said to bring about unfolding of myosin V auto-inhibition (Batters & Veigel, 2017).

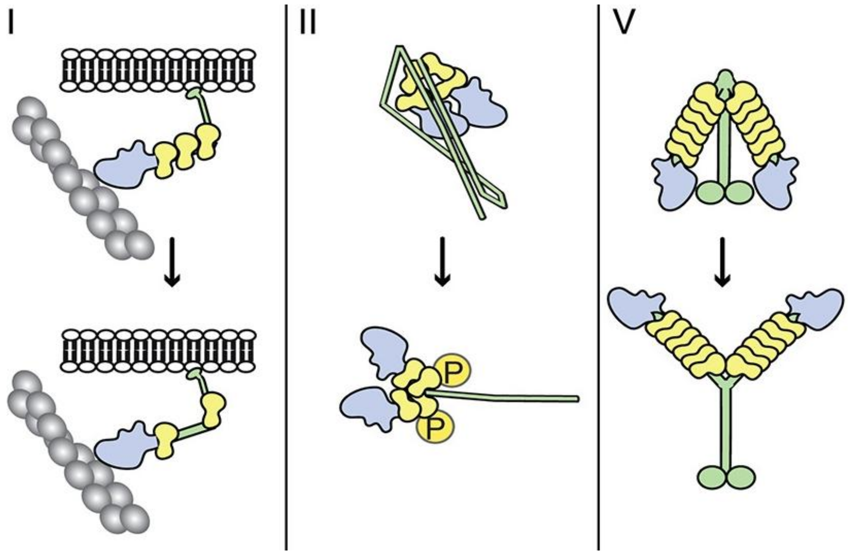

**Figure 1.22. $Ca^{2+}$ induces conformational changes in myosin I, II and V to regulate their function**. Illustration of the conformational changes that occur in myosin I, II and V when exposed to free $Ca^{2+}$. $Ca^{2+}$ can induce conformational changes in myosin (blue) that are specific to each myosin class. Myosin I binds to actin filaments via its head domain and links filaments to plasma membranes by binding to the plasma membrane via its tail domain. Calmodulin (yellow) bind to free $Ca^{2+}$. Mouse myosin Ic has 3 IQ motifs, (IQ1, IQ2 and IQ3). Binding of $Ca^{2+}$ to calmodulin causes calmodulin dissociation from IQ2, since IQ2 has a very weak affinity for $Ca^{2+}$-calmodulin. $Ca^{2+}$ also binds to a domain in myosin Ic called the post-IQ domain. $Ca^{2+}$ binding to this post-IQ domain and $Ca^{2+}$-calmodulin dissociation from myosin IQ motifs, induces conformational changes that increase the flexibility of the myosin tail. Increased flexibility results in the reduction of load and duty and in turn promotes dissociation from actin (Lu et al., 2015). ELC and RLC (Essential and regulatory light chains) (yellow) bind to the neck domain of myosin II. $Ca^{2+}$ binds to ELC and calmodulin. This activates MLCK (myosin light chain kinase) to phosphorylate RLC. 'P' denotes a phosphate group. $Ca^{2+}$ binding to ELC, and RLC phosphorylation cause myosin II to unfold from a closed conformation to an open conformation. The open conformation can interact with actin and regulates myosin II activity. Myosin Va hold an inactive folded conformation in the absence of $Ca^{2+}$. In this conformation, the tail interacts with the head or neck domain. In the presence of $Ca^{2+}$, myosin Va unfolds and $Ca^{2+}$ binding to myosin Va increases rigidity and stability of the myosin Va neck domain so force and movement can be generated. Adapted from Batters & Veigel (2017).

Baker et al. (2019) proposed TORC2–Gad8 dependent regulation of myosin I in *S. pombe,* via Myo1 S742 phosphorylation. TORC2-Gad8-dependent phosphorylation and $Ca^{2+}$ were both incorporated into the regulation of Myo1 function of endocytosis. A significant reduction in Myo1 S742 phosphorylation in *gad8.T6D S. pombe* cells was reported. In these cells, Gad8 threonine 6 (T6) is mutated into an aspartic acid (T6D). Gad8 T6D therefore acts a phospho-mimetic to Gad8 T6 and is recognised by kinases for phosphorylation. *myo1.S742A* cells fail to divide and fail to restrict growth when under nitrogen-starvation-induced G1 arrest. These observations suggested phosphorylation of Myo1 S742 to be dependent on the TORC2–Gad8 signalling pathway (Baker et al., 2019).

Myo1 S742 phosphorylation was found to change the structure of the Myo1 lever arm (Baker et al., 2019). This conformational change was found to regulate Myo1 dynamics and Cam1 dissociation from Myo1 during endocytic events. During endocytosis, Myo1 S742A was observed at the cell membrane for a shorter duration of time than wild-type Myo1, via fluorescence microscopy. After an endocytic event, Cam1 dissociated from Myo1 S742A sooner than it did from wild-type Myo1 (Baker et al., 2019).

Myo1 S742 was shown to be phosphorylated in a cell cycle dependent manner. Approximately 50 % of cellular Myo1 S742 is phosphorylated in G1, before NETO. Phosphorylated Myo1 S742 depletes completely by the end of late G2 (Baker et al., 2019). Data gathered during this PhD project also contributed towards findings reported in the paper.

The development and study of *S. pombe* Myo1 and Myo52 phospho-mutants in this project aimed to determine the role myosin phosphorylation plays in; (i) calmodulin-dependent regulation of Myo1 function in endocytosis required for polarised cell growth during the cell cycle and (ii) regulating Myo52 interactions with associated proteins for cargo transport required for cell growth.

## 1.6 Exploration via live cell fluorescence imaging

Unconventional myosin migrate along actin filament at rapid speeds ranging 0.2 to 60 µm/sec, therefore rapid image capture is imperative for real-time imaging and analysis of myosin motility (Alberts, 2002). During the PhD project, rapid movements of myosins and the dynamic rearrangements of the actin cytoskeleton were studied, via fluorescence microscopy, for greater understanding of the function and regulation of myosins and associated proteins. Fluorescence microscopy of live cells is achieved with the fluorescent labelling of proteins, live cell dyes, as well as other methods to fluorescently label proteins.

### 1.6.1 Fluorescence

Fluorescence was first reported in 1845, when a quinine solution emitted blue light whilst exposed to ultraviolet light (Renz, 2013). Fluorescence is now used to visualise cellular components in live cells. Live cell fluorescence imaging provides a powerful technique to analyse cellular processes in real-time, via time-lapse acquisition. Fluorescent molecules are known as fluorescent probes, fluorochromes or dyes. Fluorochromes conjugated to macromolecules are called fluorophores. To achieve fluorescence, fluorochromes are exposed to defined wavelengths of light, dependent on the fluorochrome (Herman et al., 2015).

Electrons absorb light in discrete amounts called photons. The amount of energy in a photon is expressed by Planck's Law;

$$E = hv = hc/\lambda$$

where $E$ = energy, $h$ = Planck's constant , $v$ = photon frequency, $c$ = the speed of light and $\lambda$ = wavelength. The equation therefore shows shorter wavelengths yield greater amounts of energy. Electrons in the fluorochrome absorb light energy, in the form of photons, and are promoted from a low energy state called the 'ground state', to a higher energy state called the 'excited stated'. This energy is greater than energy gained from heat energy at room temperature. Absorption is very quick and can take only a femtosecond ($10^{-15}$ s). In the excited state, the electrons vibrate and are unstable. The electrons subsequently emit light energy photons, of a longer wavelength than the excitation light, and return to ground state. The light emitted from the fluorochrome is fluorescence. Electrons of each fluorochrome absorb and emit light at specific wavelengths. Fluorochrome fluorescence achieved at these wavelengths form the absorption and emission spectrum, specific to each fluorochrome (Herman et al., 2015). Figure 1.23 illustrates the absorption and emission of light by fluorochrome electrons that result in the changes in fluorochrome electron energy states and fluorochrome fluorescence.

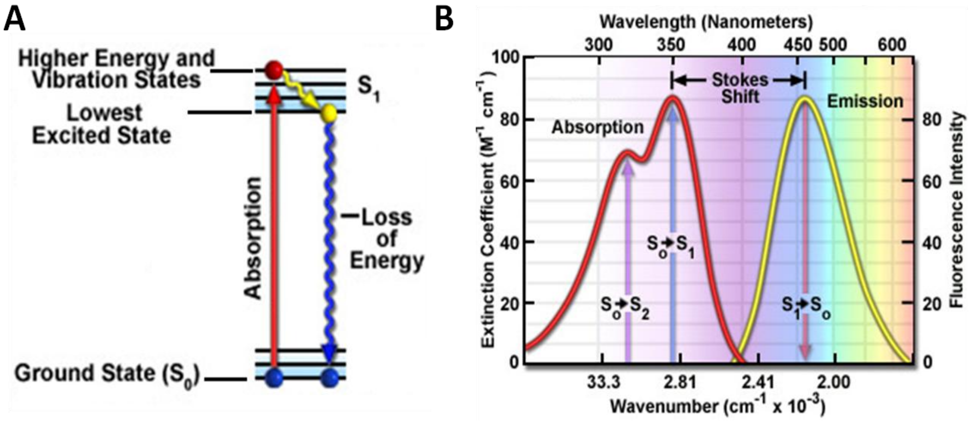

**Figure 1.23. The emission of photons by fluorochromes produces fluorescence.** Illustrations of light energy absorption and emission by electrons in fluorochromes to produce fluorescence. **(A)** Jablonski energy diagram. To fluoresce, electrons in fluorochromes move between different energy states; ground state ($S_0$) and excited state ($S_1$) (parallel lines). $S_0$ is a low energy state. $S_1$ is a high energy, unstable state where the electrons vibrate due to the energy gain. Each energy state has multiple vibration energy states (multiple parallel lines). Before light absorption, electrons are at $S_0$ (blue sphere). When exposed to light, the electrons absorb photons of the excitation light energy (red arrow) and are raised to a high vibration energy state in $S_1$ (red sphere). The electrons then drop to lower $S_1$ vibration energy levels, in a process called vibrational relaxation (yellow arrow, yellow sphere). Once at the lowest $S_1$ vibration state, the electrons emit light energy which is detected as fluorescence (blue arrow). The loss of energy returns the electrons to $S_0$ (blue sphere). **(B)** Absorption and emission spectrum of quinine. All fluorochromes absorb and emit light energy photons of specific wavelengths. Electrons in quinine absorb high energy photons of short wavelengths between 250 - 400 nm (red curve). The wavenumber (number of waves per unit distance) decreases with greater wavelengths. Absorption raises the electrons from $S_0$ to $S_1$ or $S_2$ (a higher excitation vibration level than $S_1$). Shorter wavelengths are required to excite electrons to $S_2$. The electrons then relax to $S_1$. From $S_{1,}$ the unstable, excited electrons emit light energy photons of longer low energy wavelengths between 400 - 600 nm (yellow curve). The emission curve mirrors the $S_0$ to $S_1$ transition peak. Stokes shift is the difference between the maximum excitation and emission wavelengths. Emitted photons contain less light energy than absorbed photons. This difference in wavelength and light energy is due to the energy loss during vibrational relaxation after excitation. The extinction coefficient is a measure of a fluorochrome's ability to absorb light at a specific wavelength. Fluorochromes with higher extinction coefficients have a higher probability of fluorescence. Adapted from Abramowitz et al. (2016) and Herman et al. (2015).

### 1.6.2 Fluorophores

Fluorophores are fluorochromes conjugated to a macromolecule (Herman et al., 2015). They were first identified when green fluorescent protein (GFP) was discovered in *Aequorea victoria* jellyfish in 1962. Since then, different colour variants have been developed (Day & Davidson, n.d.). Fluorophores can be fused to proteins in living cells using recombinant complementary DNA cloning technology. This produces a fluorescent fusion protein which can be visualised in live cells, in real-time using fluorescent microscopy (Piston et al., n.d.). This has allowed for multicolour observation of protein localisation, protein interactions and protein trafficking in living cells (Lippincott-Schwartz et al., n.d.). Figure 1.24 illustrates the structure of *A. victoria* GFP.

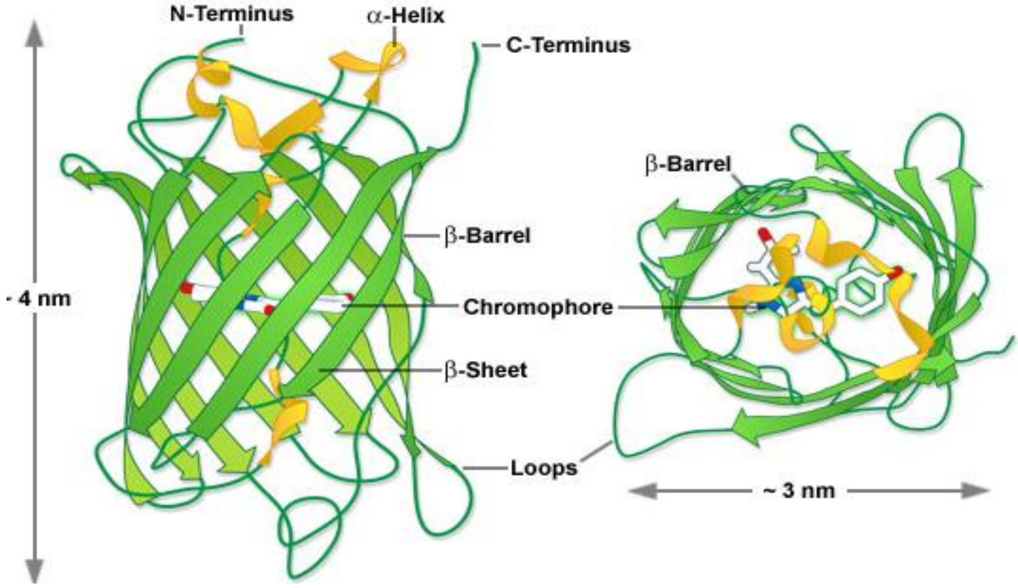

**Figure 1.24. Green Fluorescent Protein is a β-barrel containing a chromophore.** Structure of *A. victoria* Green Fluorescent Protein (GFP). GFP consists of an eleven-stranded β-barrel and a chromophore. The β-barrel is 4 nm in length and 3 nm in width and functions to protect the chromophore. The N-terminus and C-terminus are on the surface of the β-barrel and are used as linkers to fusion proteins. Linking the GFP to a protein does not significantly disrupt its structural integrity. The chromophore is a cyclic tripeptide situated at the centre of the β-barrel. It is responsible for fluorescence upon exposure to the blue range of visible light. Green fluorescence is emitted from the ring system of the fluorochrome. Adapted from Day & Davidson (n.d.).

Photobleaching is the process in which a fluorophore loses its ability to fluoresce due to photon-induced chemical destruction and covalent modification, caused by exposure to excitation light (Song et al., 1995). Excited fluorophores can interact with other molecules, such as oxygen, which results in irreversible covalent modifications. Oxygen interacts with excited fluorophores via two different reactions that cause fluorophore degradation. In the first reaction, energy is transferred from the excited fluorophore to an oxygen molecule. This forms an excited oxygen molecule. In the second reaction, an electron is transferred from the fluorophore to an oxygen molecule and forms a superoxide radical ($O_2^{\bullet-}$). Excited oxygen and superoxide radicals are called ROS (reactive oxygen species) and are involved in downstream reactions that produce other types of ROS. ROS can degrade fluorophores but how they degrade fluorophores is not understood well (Zheng et al., 2014).

Fluorophores can repeat the excitation and emission cycle thousands of times before it become photobleached and unresponsive to excitation light (Herman et al., 2016). Each fluorophore can undergo an average number of excitation and emission cycles specific to its molecular structure and the cellular environment that it is in e.g. pH. To reduce photobleaching, low exposure times and light intensities can be used (Spring & Davidson, n.d.).

### 1.6.3 Wide-field and confocal fluorescence microscopy

Wide-field and confocal microscopy are common types of microscopy used to detect fluorescent single molecules. Both imaging systems were implemented during the project. Figure 1.25 illustrates wide-field and confocal microscopy configurations.

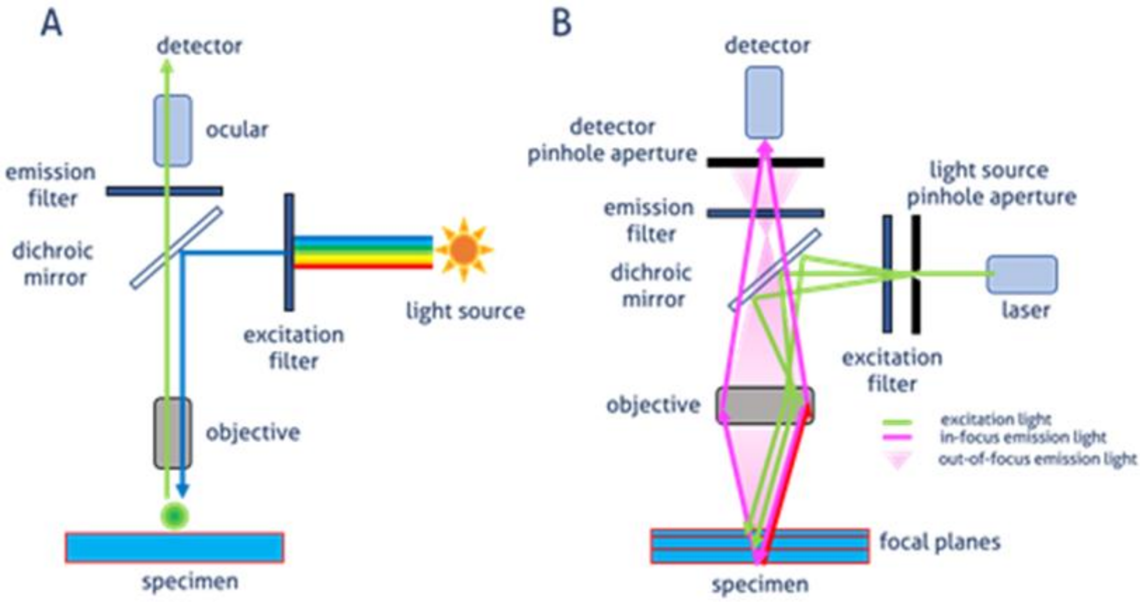

**Figure 1.25. Wide-field and confocal microscopy systems detect fluorescent signals emitted from excited fluorophores.** Illustration of wide-field and confocal microscopy systems. **(A)** Wide-field microscopy configuration. Light from a light source e.g. LEDs (light emitting diodes) passes through an excitation filter to filter the wavelength required to excite the fluorophores used to visualise the sample (blue). The excitation filter rejects all other wavelengths. The dichroic mirror then reflects the filtered excitation light to pass it through the objective lens. The objective lens focuses the light to illuminate the sample. Large areas of the sample are illuminated in this configuration. The excited fluorophores in the sample emit fluorescent light (green) back through the objective lens and towards the dichroic mirror and emission filter. The dichroic mirror and emission filter only allow emission light of the correct wavelength to pass through to the ocular and detector. The microscope user can view the fluorescence with the ocular lens. The emission light is measured by a detector e.g. camera and computer. **(B)** Spinning-disk confocal fluorescence microscopy configuration. Light of a specific wavelength (green) is emitted from a laser. The light is passed through pinholes in the spinning light source pinhole aperture, to focus it to specific focal planes of the sample. Objective lenses with a high numerical aperture (ability to gather light and resolve details) are also used. Fluorescent light emitted from the sample (magenta) is focused into pinholes in the spinning detector pinhole aperture, after being passed through the dichroic mirrors and emission filter. The pinholes allow in-focus emitted light (magenta) through to the detector and reject out-of-focus background fluorescence (light pink). This results in better horizontal and vertical resolution. Adapted from Proteintech (2019).

### Principles of wide-field microscopy

Visualising samples via wide-field microscopy begins with excitation light emission from an LED (light emitting diode) or gas arc-lamp light source. The emitted light is passed through an excitation filter that only allows a specific wavelength of light to pass through it. This wavelength is dependent on the fluorophores being used. If GFP is being used, excitation filters that filter for blue light would be used. This wavelength is ideally the wavelength required for maximum light absorption and excitation of the fluorophore. In fluorescent microscopes, dichroic mirrors are used to direct light towards the sample and detectors. They have different transmission and reflection properties, dependent on the wavelength of the light directed at them. Dichroic mirrors reflect the filtered excitation light to pass it through the objective lens and towards the sample. Whole cells are illuminated in this configuration (Spring & Davidson, n.d.).

Excited fluorophores in the sample emit fluorescent light that is directed towards the dichroic mirror. The dichroic mirror and emission filter allow emitted light of the correct wavelength to pass through to the detector. In the case of GFP, green light emitted from the sample would pass through the dichroic mirror and emission filters. The emitted fluorescent light is then detected by a charge-coupled device (CCD) camera (Spring & Davidson, n.d.).

### Principles of spinning-disk confocal microscopy

Spinning-disk confocal microscopy has multiple benefits over wide-field microscopy. In wide-field microscopy, entire cells are exposed to incoherent light (photons with different frequencies) from LEDs or gas arc-lamps. Out-of-focus light emitted from background fluorescence is detected and reduces the resolution and contrast of images. Spinning-disk confocal microscopes are able to remove out-of-focus light to acquire images with a high contrast and high resolution. Multiple lasers are used as the source of excitation light. They emit coherent light (beams of photons with the same frequency that do not diffuse) (Fellers & Davidson, n.d.).

Only defined focal planes of the cells are exposed to the laser due to spinning-disks perforated with pinholes. The spinning-disks limit the amount of light exposed to the cells. Fluorescence only emitted from the defined focal plane is then focused towards a camera. Background, out-of-focus fluorescence is excluded. This exclusion prevents photodamage of the whole cell and produces images of greater clarity (Wilson, 2017).

Background fluorescence reduces resolution achieved in wide-field microscopy due to illumination of all planes of whole samples and surrounding background. This background fluorescence can cloud fluorophore emissions and therefore reduce the signal-to-noise ratio. Pinholes in confocal spinning-disks reduce the amount of background fluorescence detected. Deconvolution, a computer based process, is often used after image capture to shift photons to points of origin and regain resolution (Wilson, 2017).

In some systems, photomultiplier tubes, are situated beyond the spinning-disks and collect photons from samples once they are exposed. They consist of vacuums which include an electron multiplying component and convert the photons into electrical signals, to be compiled into an image. Each tube collects light of different wavelengths. Confocal microscopy can also acquire images of sample sections for further reduction of background fluorescence (Wilson, 2017).

### 1.6.4 Real-time image capture

To record protein dynamics in real-time, movies called time-lapses are generated from a series of images taken over a set duration of time. Images at a single focal point in the lateral plane (x-y plane) are taken at specific time points. At the same time point, multiple images termed z-slices are also taken along the z-axis. The distance between each z-slice is called the step size. The step sizes can be adjusted. A set of z-slices is called a z-stack. Z-stacks can be flattened to form 2D images called max projections. Max projections display fluorescence from multiple planes of the cell within a 2D image and are generated with image analysis software. Max projections of each time point can be compiled to generate a time-lapse. The duration of a time-lapse and the time points in which z-slices are taken, is varied depending on the velocity of the molecule of interest and the cell area that needs to be captured (Dailey et al., n.d.). Z-slices and max projections are illustrated in Figure 1.26.

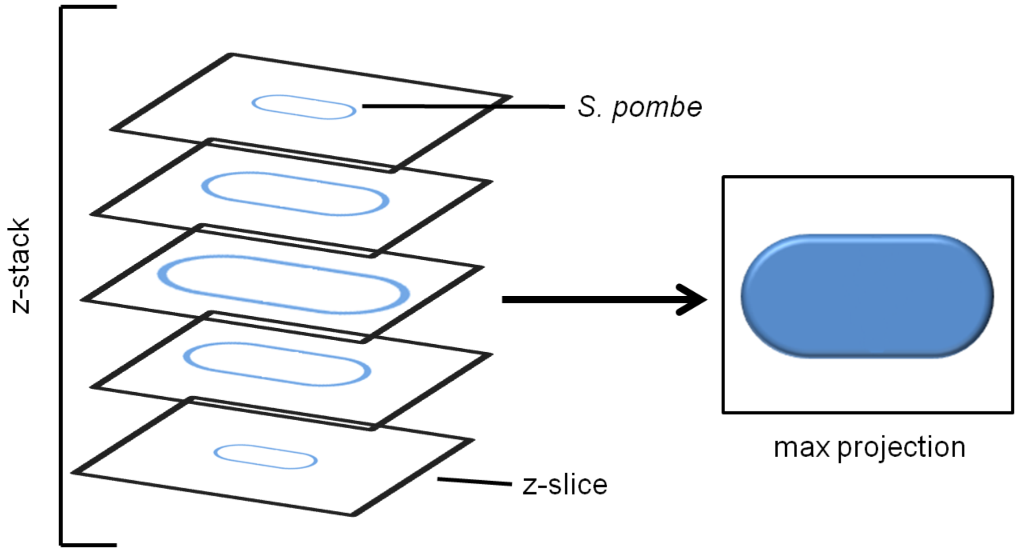

**Figure 1.26. A max projection is a flattened series of images.** Diagram illustrating the formation of max projections when imaging *S. pombe* during fluorescence microscopy. Z-slices are images taken at different focal planes along the z-axis. The number of z-slices and the step size (distance between each z-slice) can be adjusted to cover the whole cell or a specific region of the cell. A set of z-slices forms a z-stack. Z-stacks are flattened into a single image called a max projection which displays fluorescence from the multiple z-slices of the cell. Max projections are generated by imaging analysis software e.g. Metamorph. Image not to scale.

In live cell fluorescence imaging, CCD cameras are often used for image acquisition (Wilson, 2017). CCD cameras detect fluorescent signals and convert them into digital values to generate images. Each CCD camera houses a silicon matrix containing multiple light sensitive elements. These are used as photon detectors. In the silicon matrix, a silicon wafer-photodiode complex defines a single pixel. When exposed to photons from emitted fluorescent light, the silicon wafer releases electrons. The electrons are absorbed by the photodiode. A digital value that corresponds with the electron energy absorbed by the photodiode is generated. The digital values generated for each pixel are used to create an image at each time point (Spring et al., n.d.).

Fluorophores that emit light in different colour channels are used to visualise multiple proteins in a single sample. In order to generate multi-coloured images and time-lapses, images are taken after the excitation/emission filters and LEDs/lasers are changed mechanically. The excitation/emission filters and LEDs/lasers alternate so an image in each colour channel can be taken at each time point. Time elapses between filter and light source changes. Acquisition of z-slices at each time point also increases the amount of time that passes between each time point. Therefore, in multi-channel time-lapses, there is always a time lag between the dynamics of proteins imaged in different colour channels. The millisecond dynamics of proteins are not captured in real-time. Standard spinning-disk confocal microscope systems have an image capture rate of 50 ms (20 Hz).

During this PhD project, a spinning-disk confocal microscope system, capable of simultaneous two-channel imaging, was tested in collaboration with its manufacturer, Cairn Research. In this system, green and red lasers function alternately to illuminate the sample. The excitation/emission filters are on a wheel. The timing of when the lasers turn on is synchronised with the filter wheel. The lasers are on only when the corresponding filters are in place. During this PhD project, the lasers were used with an exposure time of 100 ms. The filter wheel constantly rotates at a speed of 11 Hz to achieve a 10 Hz capture rate (one image captured every 100 ms). This allows images to be simultaneously captured in two different channels. The time lag between the dynamics of proteins imaged in different colour channels is eliminated. To test the system, *S. pombe* strains with proteins labelled with red mCherry and green mNeongreen (mNG) or GFP fluorophores were imaged. This testing aimed to determine correct function of the system and determine suitable imaging conditions to image *S. pombe.*

Live cell imaging considerations

During live cell imaging, the environment in which cells are kept in must be controlled. Parameters such as the cell chamber dimensions, temperature, atmospheric conditions and pH buffering supplied by the culture medium must all be controlled. (Dailey et al., n.d.).

Experimental challenges accompany fluorescent live cell imaging. Major challenges include reducing photobleaching whilst maintaining an ideal signal-to-noise ratio and establishing an ideal environment for the cells to replicate physiological protein dynamics (Ettinger & Wittmann, 2014). Hindrance of normal protein function is also a challenge to overcome when imaging fluorescently labelled proteins. Lifeact, a short peptide which binds to actin filaments, is used as a marker to visualise actin structures (Riedl et al., 2008). The long morphology *lifeact-GFP S. pombe* strains display is an example of potential disruptions in normal actin function.

## 1.7 Aims and Objectives

### 1.7.1 Imaging system optimisation

One focus of the PhD project was development of optimal conditions for fluorescent live cell imaging techniques. Exposure to light during fluorescent live cell imaging can induce damage to the cell. This damage is termed phototoxicity and is induced by heat and reactive oxygen species (ROS). In order to observe cells in conditions close to physiological conditions, phototoxicity must be avoided. One aim of the PhD project was determine whether differences in phototoxic outcomes occur between: (i) frequent exposure to low intensity light exposure and; (ii) infrequent exposure to high intensity light exposure (when the total number of photons exposed to the cell is equal). Phototoxicity has been shown to delay cell cycle progression (Cole, 2014; Laissue et al., 2017). In order to achieve this aim, the rate of contractile actin ring constriction in *rlc1-GFP pcp1-GFP S. pombe* was measured and compared between cells frequently exposed to low intensity light, and cells infrequently exposed to high intensity light. Findings of these experiments were then applied to a study on the molecular basis of temperature sensitivity in temperature sensitive *cdc8.27* and *cdc8.110 S. pombe* and the impact these mutations have in the function of tropomyosin Cdc8, during CAR assembly and constriction. In order to study this temperature sensitivity, CAR constriction in temperature sensitive tropomyosin Cdc8 mutants was observed between 25 $^{o}$C and 36 $^{o}$C.

Another aim of the PhD project was to determine a suitable fluorophore to label Myo52, for experiments to study Myo52 function in live *S. pombe* Myo52 phospho-mutant cells. The discreteness, intensity and photostability of monomeric neongreen (mNG), GFP and 3GFP foci in long-term time-lapses were compared to determine which fluorophore possessed the most suitable properties.

Cairn Research, a collaborator of the Mulvihill lab, is developing a novel simultaneous two-channel spinning-disk acquisition imaging system. It is being developed to enable simultaneous image acquisition of fluorophores in the red and green channel. One aim of the PhD project was to test the imaging system with live cells and determine if the system was capable of detecting signal in the red and green simultaneously, without channel-to-channel bleed through. Time-lapses of *S. pombe* labelled with both mCherry (red fluorophore) and mNG or GFP (green fluorophores) were acquired with the imaging system to determine if red and green signals could be simultaneously recorded without channel-to-channel bleed through.

Conclusions made from this study may be used in future imaging studies to achieve experimental *in vivo* results, as close to physiological conditions as possible.

### 1.7.2 Myosin phospho-regulation

Phosphoproteomic screening has identified a number of phosphorylation sites in myosin I and myosin V of *S. pombe.* These phosphorylation sites have been shown to be conserved in *Homo sapiens*, *Caenorhabditis elegans* and *Saccharomyces cerevisiae.* This suggests biological importance for the correct function of various organisms. The kinases that phosphorylate these sites and the result of phosphorylation are not known.

One aim of this project was to identify roles of these phosphorylation sites in the function and regulation of myosin I and V. *S. pombe* phospho-mutant strains were developed by SDM. With SDM, serine to alanine mutations at the genomic locus were introduced in codons that encode for conserved phosphorylation sites in the myosin. These strains were then used to investigate the role phosphorylation has in the function and regulation of myosin I and myosin V during cell growth in *S. pombe*. Mutations at the genomic locus ensure the phenotypes observed in the *S. pombe* phospho-mutant strains are direct results of the serine to alanine mutations.

In wild-type *S. pombe*, the serine hydroxyl group (-OH) in the phosphorylation sites of interest are phosphorylated. In the *S. pombe* phospho-mutant strains, mutation of the serine residues to alanine will prevent the phosphorylation of the residues because alanine does not possess a hydroxyl group for phosphorylation. The two amino acids have similar properties and therefore any changes in the phenotype will be likely due to the absence of phosphorylation in the phospho-mutants. Serine to aspartic acid, phospho-serine phosphomimetic mutants were also implemented. Aspartic acid mimics phospho-serine because the $COO^-$ is chemically similar to phosphorylated serine. Due to this similarity, serine to aspartic acid mutations can induce levels of activity similar to that of serine phosphorylation.

Changes in *S. pombe* phospho-mutant phenotypes will be observed using fluorescence microscopy. *S. pombe* morphology, size, growth and division will be studied. Myosin deletions have been shown to cause wider and shorter morphologies. This is because myosin I is involved in endocytosis required for polarised cell growth and myosin V transports cell membrane factors in vesicles and also regulates cytoskeleton organisation. In these mutants, a dysfunctional cell cycle and hindered cytokinesis was hypothesised. Changes in the function and regulation of the myosin will also be studied and will then give insight into the function of the myosin phosphorylation sites. Identifying the kinases responsible for the phosphorylation was also planned to shed light on the signalling regulating the myosin.

### Mutation of the myosin I serine 742 phosphorylation site

The Myo1 S742 phosphorylation site is located in the neck domain of Myo1. It has been hypothesised to be involved in the regulation of calmodulin binding as well as the folding of the Myo1 (Baker et al., 2019). An aim of the PhD project was to determine the impact TORC-Gad8-dependent phosphorylation of Myo1 S742 has on the function of Myo1 and the interactions it has with Cam1 and Cam2. Through cell cycle based assays in *myo1.S742A S. pombe,* the significance of TORC-Gad8-dependent phosphorylation of Myo1 S742 on $Ca^{2+}$-dependent calmodulin binding to Myo1 was studied in this thesis to further understand the regulation of Myo1 function during endocytosis, which is required for polarised cell growth. These assays included determining: changes in the monopolar-to-bipolar ratio, rate of growth and actin dynamics during the vegetative cycle. Observations made in the meiotic cycle included determining changes in: Myo1, Cam1 and Cam2 foci lifetimes, the degree of endocytosis, cell polarity and regulation of cell growth in sporulating cells.

### Mutation of the myosin 52 phosphorylation sites

The S720, S798, S985, S1064, S1065 and S1072 phosphorylation sites of Myo52 are of interest as phosphorylation of these sites may contribute to the regulation and function of Myo52. These phosphorylation sites are located in the head, IQ motifs and tail region of Myo52 and the roles of these sites are currently unknown. It is hypothesised serine-to-alanine mutations in the head will affect Myo52 binding to actin. Mutations in the neck region will affect calmodulin or light chain binding, the folding of the protein and cell polarity. Mutations in the tail region may affect cargo binding and myosin motility.

An aim of the PhD project was to determine the impact Myo52 S720, Myo52 S798, Myo52 S985, Myo52 S1064, Myo52 S1065 and Myo52 S1072 phosphorylation has on the function and regulation of Myo52 in cargo transport and cytoskeleton organisation for cell growth in *S. pombe*. During this study, *myo52.S720A*, *myo52.S798A, myo52.S985A, myo52.S1064A S1065A* and *myo52.S1072A* mutations were generated in *S. pombe*. Overall cell growth, cell morphology and the monopolar-to-bipolar ratio of the Myo52 phospho-mutants were measured to determine if phosphorylation of the Myo52 phosphorylation sites of interest impact polarised cell growth. Actin and microtubule localisation and dynamics were observed to identify changes in the Myo52 function in cytoskeletal organisation. Myo52 dynamics were observed to determine the impact Myo52 phosphorylation has on the motility of the motor protein. Finally, Mor2 localisation to regions of cell growth was also observed to determine whether Myo52 phosphorylation impacts Mor2 localisation to the cell ends to determine regions of cell growth.

Wide-field microscopy, spinning-disk confocal microscopy and Metamorph image analysis techniques were utilised for acquisition and analysis of images and time-lapses of fluorescently labelled and stained *S. pombe* strains. For the development of the required strains; cell culture, DNA cloning/site-directed mutagenesis, transformations and genetic crosses were carried out. Further understanding of Myo1 and Myo52 regulation may be used to intervene with the results of phosphorylation mutations or manipulate the phosphorylation status of the phosphorylation sites of interest. These conserved sites may be studied in other models e.g. *S. cerevisiae* and human cells in the future.

# Chapter 2: Materials and methods

## 2.1 Molecular biology methods

0.1 µg DNA was used in all restriction enzyme digests and ligations.

### 2.1.1 General cloning techniques

**Standard restriction digest mixture:**

10 µl 10x buffer (buffer type compatible with enzymes used), 10 µl 0.01 µg/µl plasmid DNA, 2 µl restriction enzyme, $dH_2O$ to a final volume of 100 µl

**Standard ligation mixture:**

2 µl 10x ligation buffer, 1µl 0.1 µg/µl per DNA fragment, 1 µl T4 DNA ligase, $dH_2O$ to a final volume of 100 µl

**Standard PCR mixture:**

41 µl $dH_2O$ , 5 µl high fidelity (HF) buffer, 1 µl 0.01 µg/µl template DNA, 1 µl 1:10 oligonucleotides, 1 µl DNTPs, 1 µl HF enzyme

### 2.1.2 Cloning: site direct mutagenesis (SDM)

**Endogenous DNA labelling PCR mixture:**

41 µl $dH_2O$ , 5 µl HF buffer, 1 µl 0.01 µg/µl v741 template DNA, 1 µl 1:10 oligonucleotides (O648, O649), 1 µl DNTPs, 1 µl HF enzyme

**pGEM ligation mixture:**

6 µl $dH_2O$, 1 µl 0.1 µg/µl PCR product, 1 µl ligase, 1 µl pGEM, 1 µl 10X ligation buffer

**EcoRI digest mixture:**

5 µl $dH_2O$, 2 µl 10X Buffer H, 2 µl 0.05 µg/µl DNA, 1 µl EcoRI.

**SDM PCR mixture:**

41 µl $dH_2O$ , 5 µl HF buffer, 1 µl 0.1 µg/µl v744 template DNA, 1 µl 1:10 oligonucleotides (O481, O482, O634, O635, O636, O637, O638, O639, O650, O651), 1 µl DNTPs, 1 µl HF enzyme

Myo1 tail (v741) was amplified by the endogenous DNA labelling PCR programme using myo1KfII-SpeIF/R primers. PCR product was incubated with 1 µl of DpnI enzyme at 37 °C for 1 hr. The PCR product was subsequently incubated at 65 °C for 10 min, to denature the enzymes. Once cooled to room temperature, the PCR product was ligated into pGEM cloning vector at 4 °C for 2 days.

5 µl of ligate DNA was transformed into *DH10-β E. coli* as described in Section 2.1.6. Mini prepped DNA was digested with EcoRI at 37 °C for 1 hr. Successfully digested DNA was sequenced and the correct constructs were used for SDM (v744). SDM PCR was carried out and PCR products were digested with 1 µl of Dpn1 enzyme at 37 °C for 1 hr or overnight. The SDM PCR products were then digested with restriction enzymes corresponding to the introduced restriction site. Correct digestion was confirmed via gel electrophoresis as described in Section 2.1.5.

### 2.1.3 mNeonGreen (mNG) labelling Myo52

**mNG-Myo52 PCR mixture:**

18 µl GOTaq buffer mixture, 1 µl 0.1 µg/µl template DNA, 1 µl 1:10 oligonucleotides

To label Myo52 with mNG, a mNG-myo52 PCR mix was run through an endogenous DNA labelling PCR programme. 1 µl of PCR product was used to check for product via gel electrophoresis. The PCR product was pooled and phenol chloroform purified as in Section 2.1.2. *mNG-myo52* DNA (932) and *myo52* phospho-mutant *S. pombe* were transformed using 10 µl of DNA as in Section 2.1.7. To select for transformants, the *S. pombe* were replica plated onto YES plates supplemented with 40 µl G418 the following day. Correct clones were cryopreserved in 1 ml of YES supplemented with amino acids and 500 µl of 60 % glycerol.

### 2.1.4 Genomic PCR preparation

$3x10^7$ cells were harvested in YES and re-suspended in 100 µl of 200 mM LiOAc, 1 % SDS. The cells were incbated at 75 °C for 5 min. 300 µl of 100 % EtOH was added and the cells were vortexed. The cells were pelleted at 13, 000 rpm for 3 min. The pellet was gently washed with 70 % EtOH and dried at 65 °C. The cells were re-suspended in 50 µl of $dH_2O$ and pelleted at 13, 200 rpm for 20 sec. Supernatant, containing DNA, was collected into a new microfuge tube. A genomic PCR programme was run. The presence of PCR product was checked via gel electrophoresis as described in Section 2.1.5. DNA was then digested with restriction enzymes corresponding to the introduced restriction site to check for the correct genotype.

### 2.1.5 DNA gel electrophoresis

Agarose powder, heated and dissolved in 0.5 X TAE, was used to make 1 % agarose gel. Ethidium bromide (50 µl diluted into 1 ml of $dH_2O$) was added to the agarose solution and poured. Combs were inserted and the gel was left to set for 30 min. Once set, 5 µl of Hyper Ladder 1 kb (Bioline – BIO-33026) was loaded. DNA was loaded with 5 X DNA Gel Loading Dye (Fisher - BP655-5) and $dH_2O$. The gels were run at 50 V for 1 hr.

### 2.1.6 *E. coli* transformation

**Luria-Bertani (LB) (1 L):**

1 L $H_2O$, 10 g tryptone, 10 g NaCl, 5 g yeast extract

40 µl of competent *E. coli DH10-β* cells were defrosted in ice for 5 min. 1 µl of DNA was added to the *DH10-β* cells and incubated on ice for 30 min. The cells were heat shocked in a water bath at 42 °C for 90 s and subsequently incubated on ice for 2 min. 100 µl of LB was added to the cells and then incubated in a shaking incubator at 36 °C for 30-60 min to recover. The cells and 100 µl of 50 µg/ml ampicillin were plated on a LB late and incubated at 36 °C overnight.

Plates were then stored at 4 °C until the afternoon. Colonies were picked using 20-200 µl pipette tips and inoculated in 5 ml of LB and 5 µl of 50 µg/ml ampicillin. Cells were incubated in a shaking incubator at 36 °C overnight. QIAprep Spin Miniprep Kit (Qiagen - 27106) protocol was followed to extract bacterial DNA. 1 µl of DNA was loaded onto a 1 % agarose gel and run for electrophoresis to confirm DNA presence, as described in Section 2.1.5.

### 2.1.7 *S. pombe* transformation

$2x10^6$ cells/ml in YES were pelleted at 3, 000 rpm for 5 min and re-suspended in 100 µl of LiOAc per transformation. The cells were transferred into a microfuge tube and incubated at 25 °C for 1 hr sideways. ≥1 µg DNA was used for each transformation. 100 µl of 70 % PEG was added to 9-10 µl of DNA, previously purified, and vortexed. The DNA was centrifuged for 1 min at 1, 000 g at 25 °C and incubated at 25 °C for 1 hr. The DNA and cells were flicked every 20 min. 100 µl of cells were added to the DNA, mixed by flicking and incubated for 1 hr. DNA mixed with the cells were flicked every 20 min. The cells were heat shocked at 42 °C for 10 min and rested on ice for 2 min. 1 ml of YES was added and the cells were pelleted at 3.8 rpm for 2 min. The cells were re-suspended in 1 ml YES and transferred to a bijou. The cells were incubated at 25 °C for 1 hr sideways and flicked every 30 min. The cells were pelleted at 3.8 rpm for 2 min and re-suspended in 100 µl of EMMG. They were then plated out on YES or EMMG plates, dependent on the selection. The following day, the cells were replica plated onto the required selection plate.

Plasmids and oligonucleotides used in this study are listed in Table 1.1 and Table 1.2.The molecular biology strategy is illustrated in Figure 2.2.

## 2.2 Cell culture

### 2.2.1 Cell culture: general

**Yeast extract plus supplements (YES) (1 L)**

1 L $dH_2O$, 30 g glucose, 5 g yeast extract

**Edinburgh minimal media (EMMG) (1 L)**

1 L $dH_2O$, 27.3 g Formedium EMM broth without nitrogen, 3.38 g glutamate

*S. pombe* cells were grown according to Moreno et al. (1990). Cells were grown in YES for general growth and transformations. EMMG was used for fluorescence microscopy, mating and selections. Auxotrophic strains were supplemented with the appropriate amino acids at a concentration of 0.23 g/l. *S. pombe* strains used in this study are listed in Table 1.3

### 2.2.2 *S. pombe* growth curves

*S. pombe* strains were cultured in YES media supplemented with the necessary amino acids as in Section 2.2.1, at 20 $^oC$ and 25 $^oC$ over 2 days. The cells were diluted to $0.5x10^6$ cells/ml and 500 µl of cells was pipetted in each well of the 24 well plates. $OD_{600}$ was recorded to measure cell growth over 3 days using a plate reader.

### 2.2.3 Cell culture: mating and meiosis

**MSL (1 L)**

1 L $dH_2O$, 0.1 g NaCl, 1.0 g $KH_2PO_4$, 2.0 g arginine, 10.0 g glucose, 0.2 g $MgSO_4.7H_2O$, 0.1 g $CaSO_4.2H_2O$

**MSL without nitrogen (1 L)**

as above without arginine

Cells were inoculated in 20 ml of MSL with nitrogen media supplemented with 1000 X vitamins, 10,000 X minerals and the required amino acids for 2 days. Cells were washed with MSL without nitrogen 3 times and reconstituted in 20 ml of MSL without nitrogen media supplemented with 1000 X vitamins, 10,000 X minerals and the necessary amino acids for 1 day.

### 2.2.4 *S. pombe* crosses

Two strains with complementing mating types were crossed, as described in Egel et al. (1994). *S. pombe* cells grown on YES agar plates, were streaked and mixed in squares on MSA plates supplemented with the necessary amino acids. $h^+$ x $h^-$ strains were mixed at a ratio of 1:1. $h^{90}$ x $h^{+/-}$ strains were mixed at a ratio of 1:10. The cells were incubated for 2-3 days at 25 °C to be crossed. The cells were scraped and added to 5 µl of β-Glucuronidase (Sigma – G7017) in 1 ml of $dH_2O$. The cells were incubated at 37 °C for 1-2 days, to release spores. 100 µl of cell culture was plated and spores were selected for on plates. Colonies were picked after 2-3 days of growth at 25 °C and streaked onto YES to be cryopreserved.

For cryopreservation, cells were scraped from a YES plate and added to a 2 ml microfuge tube containing 1 ml YES media, supplemented with the required amino acids, and 0.5 ml of 60 % glycerol. The tube was vortexed, frozen in liquid nitrogen and stored at -80 °C.

## 2.3 Fluorescence microscopy

### 2.3.1 Live cells

#### Wide-field fluorescence imaging

10 µl of 1 mg/ml soybean lectin (Sigma- L1395) was spread onto the centre of a 24 mm x 24 mm borosilicate glass cover slip. When dried at room temperature, 20 µl of mid-log cell culture was mounted onto the dried lectin. The cells were left to bind for 8-10 min. The cover slip was tilted to allow excess cells to run onto a tissue. The cover slip was secured onto a 25 mm x 75 mm glass slide with double-sided tape. The cover slip-slide chamber was flooded EMMG or MSL without nitrogen. Wide-field imaging was carried out on cells using an Olympus IX71 wide-field microscope fitted with a Nikon 100 x OTIRFM-SP 1.45 NA oil immersion objective lens and QuantEM Model 512SC Imaging Camera.

All *S. pombe* cells were imaged in the cover slip-slide chamber at 25 $^{o}$C unless otherwise is specified. Cells imaged at temperatures other than 25 $^{o}$C were mounted onto and imaged in a Bioptechs FCS2 Chamber (Bioptechs, Butler, PA). A Bioptechs FCS Controller (Bioptechs, Butler, PA) was used to set the Bioptechs FCS2 Chamber to temperatures of 25 - 36 $^{o}$C.

LEDs were used to excite fluorophores in the *S. pombe* cells at an intensity of 0.2 mA, unless otherwise specified. GFP, 3GFP and mNG were excited at 470 nm. sid2-tomato, mCherry and FM4-64 were excited at 555 nm. Calcofluor was excited at 365 nm. Cells were imaged at 100 x magnification. The imaging conditions used to image each protein are listed in Table 1.4.

### Spinning-disk confocal fluorescence imaging

Spinning-disk confocal imaging was carried out using an Olympus IX73, Crest Crisel X-Light confocal imager spinning-disk confocal system. The microscope was fitted with a Nikon 100 x OTIRFM-SP 1.45 NA oil immersion objective lens and a QuantEM Model 512SC Imaging Camera. *S. pombe* cells were mounted in a Bioptechs FCS2 Chamber. A Bioptechs FCS Controller was used to set the Bioptechs FCS2 Chamber to temperatures of 25 $^{o}$C. Lasers were used to excite fluorophores in the cells. GFP and mNG were excited at 470 nm, 15 - 90 % power. mCherry was excited at 555 nm, 20 % power. 7 z-slices were taken of *myo1-GFP mCherry-lifeact* cells. 13 z-slices were taken of the remaining strains. This was because Myo1 has a greater velocity than Acp1 and Myo52. Cells were imaged at 100 x magnification. The imaging conditions used to image each protein are listed in Table 1.4.

## 2.3.2 Fixed cells

**1 X PBS (1 L)**

150 mM NaCl (8.7 g), 10 mM pH 7.4 phosphate (1.82 g $K_2HPO_4$, 0.23 g $KH_2PO_4$)

Fresh paraformaldehyde (PFA) was prepared for each experiment. 6 ml of PEM was added to 3 g of PFA and incubated at 65 °C for 10 min. The solution was vortexed. 120 µl of 5 M NaOH was added to the solution. The solution was vortexed again and incubated at 65 °C. 120 µl aliquots of 5 M NaOH were added every 2 min until 99 % of the PFA had dissolved. The solution was vortexed between each addition. The total volume was then made up to 9 ml total with PEM. 125 µl of PFA solution was added to 875 µl of cells for 3 min. The cells were washed with 1 X PBS 3 times and re-suspended in 1 ml of 1 X PBS. The cells were mounted as described in Section 2.3.1.

### 2.3.3 Calcofluor staining

Fresh PFA solution was prepared as described in Section 2.3.2. Cells were cultured described in Section 2.1.1. They were then washed in 1 X PBS. In a microfuge tube, 100 µl of PFA solution and 100 µl of 10 mg/ml calcofluor (Fluorescent brightener 28, Sigma - F3543) was added to 900 µl of cells in 1 X PBS and incubated for 10 min at room temperature. The cells were pelleted at 10, 000 rpm for 2 min and re-suspended in 1 ml of 1 X PBS. The cells were then washed twice more and re-suspended in 100 µl of 1 X PBS and mounted as described in Section 2.3.1.

### 2.3.4 FM4-64 staining

Cells were cultured as described in Section 2.2.3 and concentrated to $1x10^7$ cells/ml. In a microfuge tube, 10 µl of 50 µg/ml FM4-64 (Invitrogen - T3166) was added to 100 µl of cells and incubated on ice for 10 min. The cells were washed in MSL without nitrogen, mounted on a cover-slip and imaged as described in Section 2.3.1.

## 2.4 Image analysis

Z-projections, cell length measurements, fluorescence intensity measurements, kymographs and simultaneous two-channel image alignment was carried out using Metamorph image analysis software (Molecular Devices, Sunnyvale, CA). Foci periodicity was determined from the length of time foci were visible to the eye.

### 2.4.1 Kymographs

A kymograph is a single image that displays the movement of fluorescently labelled molecules with respect to the cell and time. They are generated from time-lapses. All kymographs in this thesis show the movement of proteins in relation to the middle of *S. pombe* cells. Figure 2.1 illustrates how kymographs can be interpreted.

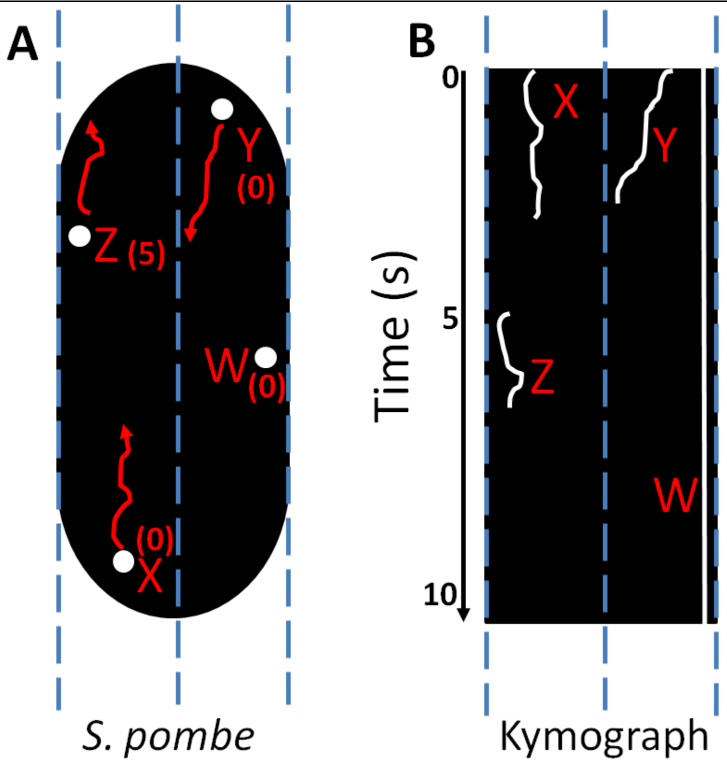

**Figure 2.1. Kymographs are 2D images representing the spatial position of foci over time.** Diagram illustrating how kymographs show protein dynamics in *S. pombe* cells. **(A)** *S. pombe* cell with motile and stationary foci (fluorescently labelled proteins, observed as white dots). Multiple images are taken of the cell in quick succession, using fluorescence microscopy. The images are compiled to make a 10 s time-lapse. The time-lapse displays the cell and foci movement (red arrows). Foci W is stationary throughout the duration of the time-lapse. Foci X, Y and Z move towards or away from the centre of the cell and then leave the plane of focus. The numbers in brackets indicate the time the foci arrive at the plane of focus. The middle and outer edges of the cell are outlined (blue dashed line). **(B)** Kymograph representing foci movement within the cell over time (Y-axis). Movement is shown relative to the middle of the cell and is represented by white lines. The letter and number labels correspond with those in (A). Foci W, X and Y are in the plane of focus at 0 s so their movements are at the top of the kymograph. Foci W is stationary and remains in the plane of focus for the duration of the time-lapse. It is therefore shown as a straight line. Foci Z arrives at the plane of focus at 5 s, therefore its movements are in the middle of kymograph. Diagram not to scale.

## 2.5 Summary tables and figures

**Table 1.1. Plasmids used in this study.** Plasmids made during this study are highlighted in bold.

| Tube | Plasmid |
|---|---|
| 22 | pFA6a-GFP(S65T)kanMX6 |
| **890** | **pGEM-T-easy-myo52-S720A(EagI)-ClaI-SphI** |
| **891** | **pGEM-T-easy-myo52-S798A-ClaI-SphI** |
| **893** | **pGEM-T-easy-myo52-S1072A-ClaI-SphI** |
| **894** | **pBluescriptKS-myo52-S720A-URA4** |
| **895** | **pBluescriptKS-myo52-S720A-URA4** |
| **896** | **pBluescriptKS-myo52-S798A-URA4** |
| **897** | **pBluescriptKS-myo52-S798A-URA4** |
| **898** | **pBluescriptKS-myo52-S985A-URA4** |
| **899** | **pBluescriptKS-myo52-S985A-URA4** |
| **904** | **pBluescriptKS-myo52-S1072A-URA4** |
| **905** | **pBluescriptKS-myo52-S1072A-URA4** |
| **780** | **m120-SphI-pGEM-T-Easy-SphI-myo52-ClaI-S1064AS1065A (v757) -BstBI** |
| **781** | **m120-SphI-pGEM-T-Easy-SphI-myo52-SphI-S1064AS1065A (v757) -BstBI** |
| **757** | **pGEM-T-Easy-SphI-myo52-ClaI-S1064AS1065A** |
| **741** | **pGEM-T-Easy-SphI-myo52-ClaI** |
| 719 | pFA6a kanMX6-mNeongreen |

**Table 1.2. Oligonucleotides used in this study.**

| Tube | Oligonucleotide | Direction | Gene | Concentration | Purpose |
|---|---|---|---|---|---|
| O650 | myo52-S1064AS1065A F | F | myo52 | 1 mg/ml | SDM |
| O651 | myo52-S1064AS1065A R | R | myo52 | 1 mg/ml | SDM |
| O648 | myo52-25bp US Sph1 | F | myo52 | 1 mg/ml | SDM |
| O649 | myo52-25bp DS Cla1 | R | myo52 | 1 mg/ml | SDM |
| O634 | myo52-S720AF | F | myo52 | 1 mg/ml | SDM |
| O635 | myo52-S720AR | R | myo52 | 1 mg/ml | SDM |
| O252 | myo52CtagingF | F | myo52 | 1 µg/µl | Myo52 C-terminus labelling |
| O253 | myo52CtagingR | R | myo52 | 1 µg/µl | Myo52 C-terminus labelling |

**Table 1.3. *S. pombe* strains used in this study.** *S. pombe* strains made during this study are highlighted in bold.

| Strain number | Strain name | Genotype |
|---|---|---|
| 211 | *myo52D* | *myo52D::ura4 ura4.d18 leu1.32 ade6.210* |
| 346 | *myo52-gfp* | *myo52-gfp:kanmx6 leu1-32 ura4-d18 his2-d1* |
| 474 | *atb2-gfp* | *nmt81gfpatb2::kanMX6 leu1.32 his2-* |
| 501 | *myo52Δ leu1+* | *myo52:ura4 ade6-210? ura4? leu1+* |
| 761 | *ura4-d18* | *ura4-d18* |
| 932 | *879Intmyo52:LEU2 (myo52 locus)* | *pku70::his3 leu1.32 his3.d1 ade6.M216 ura4.d18 myo52:LEU2 (myo52 locus)* |
| 1370 | *GFP-mor2* | *kanr:nmt1:GFP:mor2* |
| 1375 | *myo52ΔGFP-mor2* | *myo52::ura4kanr:nmt1:GFP:mor2* |
| 1376 | *myo52-1 GFP-mor2* | *myo52-ts1:ura4kanr:nmt1:GFP:mor2* |
| 1929 | wild type | Prototroph |
| 1980 | *myo52-3gfp* | *myo52-3gfp:kanMX6 prototroph* |
| 2076 | *lifeact-gfp* | *lifeact-gfp:leu+ ade6-m216 ura4-D18* |
| 2435 | *myo1-S742A* | *myo1-S742A:ura4 leu1-32* |
| **2519** | ***myo52-mNG*** | ***myo52-mNG:kanMX6 prototroph*** |
| **2543** | ***pcp1-gfp rlc1-gfp*** | ***pcp1-gfp:kanMX6 rlc1-gfp:kanMX6*** |
| 2544 | *myo1-S742D* | *myo1-S742D:ura4 leu1-32* |
| 2549 | *mCherry-lifeact ura-* | *mCherry-lifeact:leu2 ura4.d18* |
| 2556 | *mCherry-lifeact mNG-myo1* | *mCherry-lifeact:leu2 mNG-myo1:ura4 leu1-32 ura4.d18* |
| 2569 | *mCherry-lifeact myo1-S742A* | *mCherry-lifeact:leu2 myo1-S742A:ura4 ura4.d18 leu1-32* |
| 2571 | *mCherry-lifeact myo1-S742D* | *mCherry-lifeact:leu2 myo1-S742D:ura4 ura4.d18 leu1-32* |
| 2612 | *mNG-myo1-S742A* | *mNG-myo1-S742A:ura4 ura4.d18 leu1-32* |
| **2641** | ***myo52-S1064AS1065A*** | ***pku70::his3 leu1.32 his3.d1 ade6.M216 ura4.d18 myo52 S1064AS1065A:ura4 leu1-32*** |
| ***2681*** | ***mNG-myo1-S742D*** | ***mNG-myo1-S742D:ura4 leu1-32*** |
| **2702** | ***myo52-S1064AS1065A:URA4 nmt81gfp-atb2:kanMX6*** | ***pku70::his3 leu1.32 his3.d1 ade6.M216 ura4.d18 myo52-S1064AS1065A:kanMX6 ura4 leu1-32 nmt81gfpatb2::kanMX6 leu1.32*** |
| **2721** | ***myo52-S1064AS1065A:URA4 mCherry-lifeact*** | ***pku70::his3 leu1.32 his3.d1 ade6.M216 ura4.d18 myo52-S1064AS1065A:URA4 mCherry-lifeact:LEU2 leu1-32 ura4-d18*** |
| **2725** | ***myo52-S1064AS1065A mor2-gfp*** | ***pku70::his3 leu1.32 his3.d1 ade6.M216 ura4.d18 myo52-S1064AS1065A:kanMX6 ura4 leu1-32 kanr:nmt1:GFP:mor2 ura4-d18*** |
| **2734** | ***h90 mNG-myo1*** | ***mNG-myo1:URA4 ura4.d18*** |
| **2755** | ***myo52 S1064AS1065A-mNG*** | ***pku70::his3 leu1.32 his3.d1 ade6.M216 ura4.d18 myo52 S1064AS1065A-mNG:kanMX6 ura4 leu1-32*** |
| **2758** | ***myo1-S742D cam2-gfp*** | ***myo1-S742D:URA4 cam2-gfp:kanMX6 leu1-32*** |
| 2772 | *cdc8-27 rlc1-gfp* | *rlc1-gfp:kanMX6 cdc8-27* |
| 2773 | *cdc8-110 rlc1-gfp* | *rlc1-gfp:kanMX6 cdc8-110* |
| ***2801*** | ***cam2-gfp*** | ***cam2-gfp:kanMX6ura4.d18*** |
| ***2802*** | ***cam1-gfp*** | ***cam1-gfp:kanMX6ura4.d18*** |
| ***2808*** | ***myo1-S742A cam2-gfp*** | ***myo1-S742A:URA4 cam2-gfp:kanMX6 ura.d18*** |

| | | |
|---|---|---|
| | | leu1-32 |
| 2815 | myo1-S742A cam1-gfp | myo1-S742A:URA4 cam1-gfp:kanMX6 ura.d18 leu1-32 |
| 2820 | myo1-S742D:URA4 cam1.gfp:kanMX6 | myo1-S742D:URA4 cam1-gfp:kanMX6 ura.d18 leu1-32 |
| 2855 | myo52-S720A | myo52-S720A:ura4 leu1-32 |
| 2859 | myo52-S798A | myo52-S798A:ura4 leu1-32 |
| 2864 | myo52-S985A | myo52-S985A:ura4 leu1-32 |
| 2868 | myo52-S1072A | myo52-S1072A:ura4 leu1-32 |
| 2901 | myo52-mNG mCherry-lifeact | myo52-mNG:kanMX6 mCherry-lifeact:LEU2 prototroph |
| 2908 | acp1-gfp mCherry-lifeact | acp1-gfp:kanMX6 mCherry-lifeact:LEU2 leu1-32 |
| 2935 | myo52-S720A lifeact-gfp | myo52-S720A:ura4 lifeact-gfp:leu+ pku70::his3 ade6-m216 ura4-D18 |
| 2938 | myo52-S798A lifeact-gfp | myo52-S798A:ura4 lifeact-gfp:leu+ pku70::his3 ade6-m216 ura4-D18 |
| 2941 | myo52-S985A lifeact-gfp | myo52-S985A:ura4 lifeact-gfp:leu+ pku70::his3 ade6-m216 ura4-D18 |
| 2945 | myo52-S1072A lifeact-gfp | myo52-S1072A:ura4 lifeact-gfp:leu+ pku70::his3 ade6-m216 ura4-D18 |
| - | myo52-S720A atb2-gfp | pku70::his3 leu1.32 his3.d1 ade6.M216 ura4.d18 myo52-S720A:kanMX6 ura4 nmt81gfpatb2::kanMX6 |
| - | myo52-S798A atb2-gfp | pku70::his3 leu1.32 his3.d1 ade6.M216 ura4.d18 myo52-S798A:kanMX6 ura4 nmt81gfpatb2::kanMX6 |
| - | myo52-S985A atb2-gfp | pku70::his3 leu1.32 his3.d1 ade6.M216 ura4.d18 myo52-S985A:kanMX6 ura4 nmt81gfpatb2::kanMX6 |
| - | myo52-S1072A atb2-gfp | pku70::his3 leu1.32 his3.d1 ade6.M216 ura4.d18 myo52-S1072A::kanMX6 ura4 nmt81gfpatb2::kanMX6 |

**Table 1.4. Imaging conditions used to image *S. pombe* cells in this study.** * - Rlc1-GFP Pcp1-GFP was imaged during cytokinesis to generate CAR time-lapses. To capture CAR constriction, mitotic cells displaying Rlc1-GFP foci at the periphery of the equatorial plane (plane of division) and Pcp1-GFP foci perpendicular and in close proximity to the equatorial plane were imaged. ** - mCherry-Lifeact time-lapses were generated from imaging Myo1 phospho-mutant strains. Cells of a long morphology exhibit bipolar growth and were deemed cell in G2. *** - cells were fixed before calcofluor staining.

| **GFP, 3GFP, mNG (470 nm)** | | | | | | |
|---|---|---|---|---|---|---|
| **Molecule** | **Exposure time (ms)** | **Light source** | **Z-slices** | **Temperature (°C)** | **Mounting apparatus** | **Specific cell cycle stage** |
| **Acp1** | 100 | Laser 15 mW | 13 | 25 | FCS2 chamber | None |
| **Atb2** | 100 | LED 0.2 mA | 11 | 25 | Glass slide | None |
| **Cam1** | 100 | LED 0.2 mA | 11 | 25 | Glass slide | Sporulating, non-sporulating |
| **Cam2** | 100 | LED 0.2 mA | 11 | 25 | Glass slide | Sporulating, non-sporulating |
| **Mor2** | 100 | LED 0.2 mA | 13 | 25 | Glass slide | None |
| **Myo1** | 100<br>100 | LED 0.2 mA<br>Laser 90 mW | 11<br>7 | 25 | Glass slide<br>FCS2 chamber | Sporulating, non-sporulating |
| **Myo52** | 50<br>100 | LED 0.2 mA<br>Laser 90 mW | 11<br>13 | 25 | Glass slide<br>FCS2 chamber | None |
| **Pcp1 and Rlc1** | 50 | LED 0.2 mA, | 21 | 25-36 | FCS2 chamber | Cytokinesis* |
| **sid2-tomato, mCherry, FM4-64 (555 nm)** | | | | | | |
| **Molecule** | **Exposure time (ms)** | **Light source** | **Z-slices** | **Temperature (°C)** | **Mounting apparatus** | **Specific cell cycle** |

| | | | | | | **stage** |
|---|---|---|---|---|---|---|
| **Lifeact** | 100 | LED 0.2 mA<br>Laser 20 mW | 11<br>7, 13 | 25 | Glass slide<br>FCS2 chamber | Bipolar (G2)**<br>None |
| **Vesicle lipids** | 100 | LED 0.2 mA, | 11 | 25 | Glass slide | Sporulating, non-sporulating |

**Calcofluor (365 nm)**

| **Molecule** | **Exposure time (ms)** | **Light source** | **Z-slices** | **Temperature (°C)** | **Mounting apparatus** | **Specific cell cycle stage** |
|---|---|---|---|---|---|---|
| **Glucans (cell wall)*** ** | 100 | LED 0.2 mA | None | 25 | Glass slide | None |

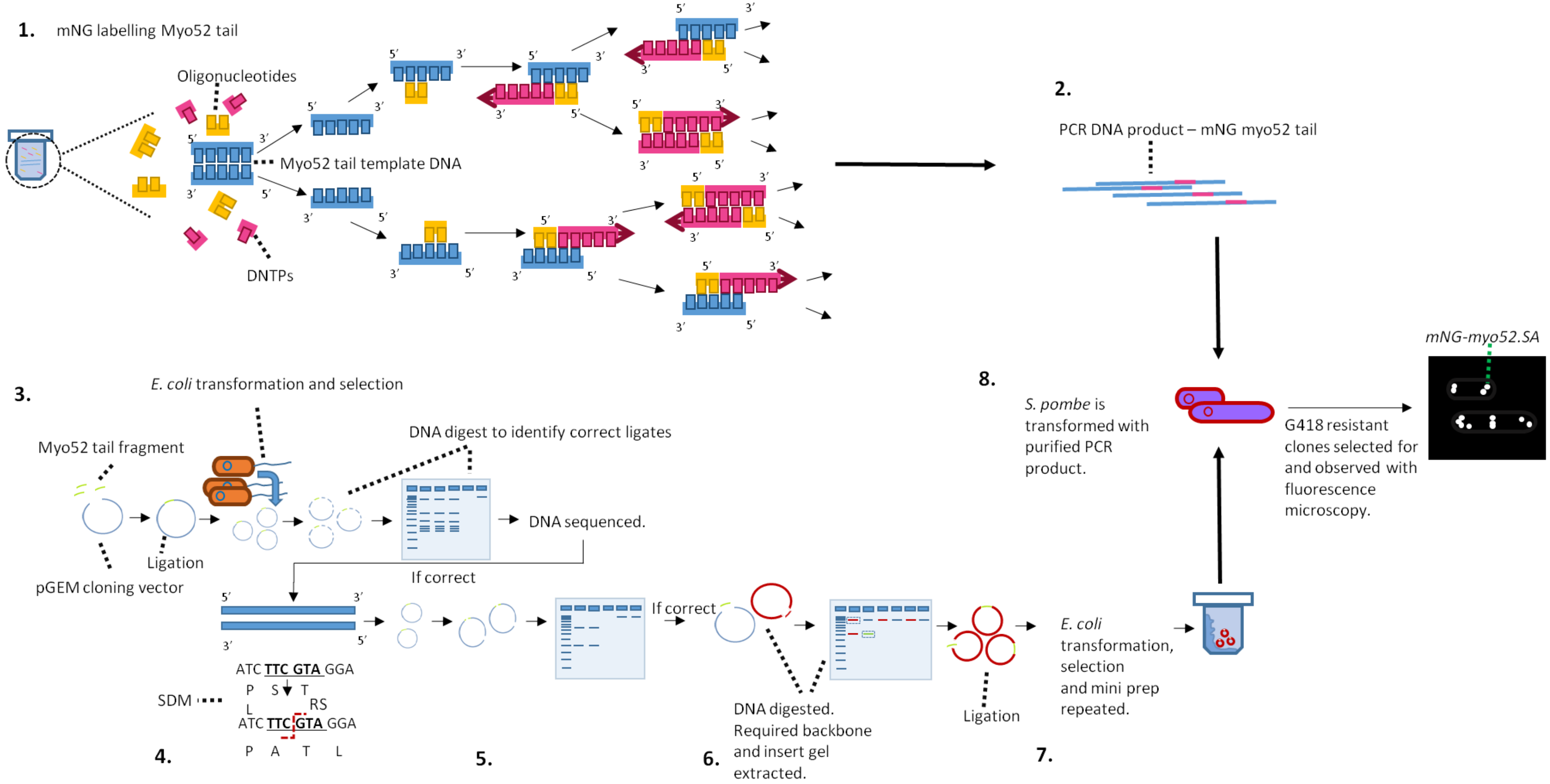
1.
mNG labelling Myo52 tail
Oligonucleotides
Myo52 tail template DNA
DNTPs
5′
3′
2.
PCR DNA product – mNG myo52 tail
3.
E. coli transformation and selection
Myo52 tail fragment
Ligation
pGEM cloning vector
DNA digest to identify correct ligates
DNA sequenced.
If correct
4.
SDM
ATC TTC GTA GGA
P S T
L RS
ATC TTC GTA GGA
P A T L
5.
If correct
6.
DNA digested.
Required backbone
and insert gel
extracted.
Ligation
7.
E. coli
transformation,
selection
and mini prep
repeated.
8.
S. pombe is
transformed with
purified PCR
product.
G418 resistant
clones selected for
and observed with
fluorescence
microscopy.
mNG-myo52.SA

**Figure 2.2. The Myo52 phospho-mutants were generated by site-directed mutagenesis.** Myo52 serine-to-alanine site-directed mutagenesis and mNG labelling strategy schematic. **(1 - 2)** mNG labelling of the *myo52* tail and amplification, via PCR. **(3)** *myo52* tail ligation into pGEM cloning vector and transformation into *E.coli.* Mini prepped DNA extracted and correct ligates identified via restriction enzyme digests and electrophoresis. DNA is sequenced. **(4)** Serine-to-alanine point mutations were introduced into Myo52 serine 742 via SDM via PCR, rendering it unable to be phosphorylated. **(5)** Correct PCR product identified via restriction (RS) enzyme digests and electrophoresis. Amino acid sequence does not reflect sequences used. **(6)** *myo52.S1064A S1065A* tail fragment extracted from pGEM and *myo52* plasmid backbone extracted via restriction enzyme digests and electrophoresis and ligated. **(7)** Ligates transformed into *E.coli* and mini-prepped. **(8)** *myo52-mNG* and *myo52. S1064A S1065A-mNG* transformed into *S. pombe* and observed via fluorescence microscopy. Diagram not to scale.

# Chapter 3: Wide-field and confocal fluorescence imaging optimisation

## 3.1. Defining optimal imaging conditions to minimise phototoxicity and bleaching

As fluorescence microscopy is the main readout of this study, it was essential to determine optimal imaging conditions for the observation of fluorescently labelled proteins in live cells, in real-time. Whether differences in phototoxic outcomes occur between; (i) frequent low intensity light exposure and; (ii) infrequent high intensity light exposure, was to be elucidated and in turn give an indication on conditions needed for minimum photodamage throughout the remainder of the study. Therefore, finding suitable and definitive conditions for a compromise between the need to see fine details and reduce toxicity was an initial focus of this study.

Fluorescence microscopy is a widely used means to visualise and study live organisms and the proteins within them. To image fluorescently labelled proteins *in vivo*, cells are exposed to surges of high intensity light photons to achieve excitation and emission in fluorescent labels. During excitation, fluorescent labels release heat and ROS (reactive oxygen species). These are unstable compounds which can damage chemical structures and biomolecules (Laiusse et al., 2017). ROS, such as hydrogen peroxide and superoxide radicals, are formed from organic molecules within cells, such as flavins, that absorb light energy photons, react with oxygen and degrade (Gorgidze et al., 1998; Rosner et al., 2016; Schneckenburger et al., 2012). ROS can cause damage to DNA, proteins and lipids via oxidation. During oxidation, ROS 'steal' electrons from molecules. ROS can damage DNA by oxidising nucleoside bases (Srinivas et al., 2019). The DNA base guanine is the DNA base most susceptible to oxidation. This is because guanine has a low redox potential, meaning it has a tendency to lose an electron (Aguiar et al., 2013). Guanine oxidation can result in the formation of 7,8-dihydro-8-oxoguanine (8-oxoG). This can result in guanine-to-thymine or guanine-to-adenine substitutions and double-strand breaks in DNA (Aguiar et al., 2013; Srinivas et al., 2019). ROS can induce redox-dependant protein modifications that promote damage by inactivating protein function e.g. enzyme activity, conformational changes. An example of this is thiol oxidation of α-tubulin by hydrogen peroxide, which results in impaired microtubule polymerisation (O'Flaherty and Matsushita-Fournier, 2017). Polyunsaturated fatty acids in cell membranes and organelle membranes are susceptible to ROS oxidation. Lipid oxidation causes loss of lipid symmetry in phospholipid bilayers and acts as a cell death signal that can trigger programmed cell death (Itri et al., 2014; Su et al., 2019). This photodamage in live cells can lead to disorder in normal cell growth and function. The damaging effect caused by light is therefore termed 'phototoxicity' (Icha et al., 2017).

Phototoxicity has been reported to induce events such as: intracellular $Ca^{2+}$ transients, perturbation of cell division, bone abnormalities during developmental stages of growth, expression of stress related-proteins and reduced metabolic activity (Carlton et al., 2010; Jemielita et al., 2012; McDonald et al., 2012; Roehlecke et al., 2009). As well as causing damage in live cells, light released during fluorophore excitation can cause fluorophores to also react with oxygen and degrade. This degradation is termed photobleaching and is therefore linked to phototoxicity (Carlton et al., 2010).

ROS are also produced in natural cell metabolism. They can be produced intentionally to regulate signalling pathways via oxidation, or produced as a waste product of mitochondrial metabolism. In excess, ROS cause damage to the cellular structures (Zhang et al., 2016). Oxidative stress is the excess of ROS caused by an imbalance of ROS production and ROS destruction. In normal physiological conditions, cells of all organisms are kept under mild oxidative stress (Poljsak et al., 2013). Live organisms have natural defences against ROS to prevent an excess of ROS. Antioxidants such as glutathione are utilised by live organisms to detoxify ROS. The small molecule antioxidants couple with enzymatic antioxidants such as glutathione peroxidase for detoxification (Icha et al., 2017). Under mild oxidative stress, the balance between ROS production and antioxidant activity is kept slightly in favour of ROS production. This slight imbalance is required for optimal cell signalling. Any increase in ROS production, caused by endogenous or exogenous factors, disrupts the slight imbalance between ROS production and antioxidant activity and leads to damage of cellular structures (Poljsak et al., 2013). Therefore antioxidant defence against ROS is limited to maintaining mild oxidative stress (Icha et al., 2017).

Exposure to intense light does not often occur in natural environments but is a common compromise made for the use of fluorescence microscopy. There is a considerable lack of definitive imaging protocols to achieve minimal photodamage. Taken together with the fact that phototoxicity thresholds are organism-specific and varies within the same organism, measuring and categorising levels of phototoxicity can be difficult (Laiusse et al., 2017).

In this chapter, fluorescence microscopy conditions that will induce minimal phototoxicity in *S. pombe* throughout the PhD project were determined. A series of light intensities and time-lapse durations were used to monitor the progression of contractile actin ring constriction in the cells. Rlc1-GFP and Pcp1-GFP were used as markers for the contractile actin ring. Suitable fluorescence microscopy conditions were selected by comparing contractile actin ring constriction in cells exposed to; (i) frequent low intensity light exposure and (ii) and infrequent high intensity light exposure.

To apply the determined imaging conditions to a working example study, the imaging conditions were used to study contractile actin ring formation and constriction in temperature-sensitive Cdc8 *S. pombe* mutants, *cdc8.27* and *cdc8.110*. Rlc1-GFP was used as a marker for the contractile actin ring. Contractile actin ring constriction was recorded at various restrictive temperatures to assess the significance of the *cdc8.27* and *cdc8.110* alleles in the actin stabilising function of Cdc8, in contractile actin ring formation and constriction. Published data from that study has been included in this chapter (Johnson et al., 2018).

Fluorescence microscope components used in this PhD project were provided by Cairn Research. A simultaneous, two-channel, spinning-disk confocal imaging system, newly developed by Cairn Research, was tested during this PhD project. Cairn Research had previously tested the system with dry samples i.e. highlighter ink. *myo52-mNG mCherry-lifeact*, *acp1-GFP mCherry-lifeact* and *mNG-myo1 mCherry-lifeact S. pombe* strains were used as biological samples to test if the system could successfully record green and red fluorescence simultaneously. Exposure times and laser powers that achieve sufficient fluorescent signal in the green and red channels were determined through the testing.

### 3.1.1 Exposure to high light intensities at infrequent time points does not induce accelerated contractile actomyosin ring constriction in *S. pombe*

Cell cycle progression appears to slow down when cells are under phototoxic conditions (Cole, 2014; Laissue et al., 2017). Identification and visualisation of possible prolonging, stoppage or collapse of cell cycle stages can be achieved with extended time-lapse recordings. CAR constriction in *S. pombe* is often used as an indicator of normal cell function and health and is now a well-characterised process which has provided insight into the assembly and regulation of actin structures in eukaryotes (Karagiannis, 2012). The constriction of the CAR can be conveniently followed as there are numerous stable, labelled proteins associated to the CAR which can be used to monitor/visualise the CAR. Myosin II (Myo2) is associated to the CAR during constriction and provides mechanical energy during the process. Therefore, it was of particular interest to investigate changes in CAR constriction rates in *S. pombe,* exposed to different levels of light energy.

In order to do so, Rlc1 (regulatory light chain 1) and spindle pole body protein, Pcp1 were chosen as markers for the CAR and were imaged during CAR constriction in *S. pombe.* Rlc1 is a Myo2 binding regulatory light chain. It is not essential for viability however, it is important in Myo2 filament formation. Myo2 is a major component of the contractile actin ring. When phosphorylated, Rlc1 induces a conformational change in Myo2 that allows Myo2 to form filaments. Rlc1 was used as a marker for Myo2 and CAR constriction because it is bound to Myo2 in the CAR. Fluorescent labelling of Rlc1 with GFP does not affect cell viability as it is non-essential. (Le Goff et al., 2000; Motegi et al., 2000). Rlc1-GFP also has no impact on CAR function (Le Goff et al., 2000; Naqvi et al., 2000). Pcp1 is contained within the inner plaque of the spindle pole body, which is the *S. pombe* equivalent of the centrosome. Therefore Pcp1 was also used as a marker for cell cycle progression.

To explore phototoxic differences between infrequent high energy light exposure and frequent low energy light exposure, live *rlc1-GFP pcp1-GFP S. pombe*, developed in the Mulvihill lab via genetic crosses, were exposed to light currents of 0.2 mA, 1.0 mA and 2.1 mA during CAR constriction. CAR constriction was recorded with time-lapses beginning with ring assembly and ending once CAR constriction was complete. The time-lapses were compiled from images taken once every 1 min with 0.2 mA current, every 3 min with 1.0 mA current and every 6 min with 2.1 mA current. This was to ensure each sample was exposed to the same amount of photons for the duration of the experiment. Recordings began during ring assembly and ended once ring constriction was complete. GFP foci intensity and diameter of the CARs were manually measured at each time point, using Metamorph software.

Images acquired from the time-lapses are shown in Figure 3.1.1. Figure 3.1.1 is a series of z-projection images taken from time-lapses, showing the progression of CAR assembly and constriction in *rlc1-GFP pcp1-GFP S. pombe* cells. The cells were exposed to 0.2 mA every 1 min, 1.0 mA every 3 min and 2.1 mA every 6 min. An exposure time of 50 ms was used and the cells were recorded for 60 min. One cell from each condition is shown. At 0 min, CAR assembly had already begun. The cells were not captured at equal stages of CAR assembly. During CAR assembly, Rlc1-GFP localised at the periphery of the equatorial plane (middle of the cell) and gradually populated the centre to form a ring.

Arrows highlight Pcp1-GFP. A pair of Pcp1-GFP foci, localised at the spindle pole bodies embedded in the nuclear envelope (not seen), were perpendicular to the CAR. By 12 min, the CAR formed and is shown by the consistent line of Rlc1-GFP along the equatorial plane. The nucleus (not shown) divided into two nuclei. The nuclei and Pcp1-GFP migrated to the poles of the cell. By 24 min, CAR constriction had begun. During constriction, Rlc1-GFP foci pooled together and increased GFP intensity at the centre of the equatorial plane. The CAR continued to constrict and reduced in size during the 36 min and 48 min time points. By 60 min, CAR constriction was complete and its components dissipated. Increasing light exposure at infrequent intervals did not induce visible structural disruptions to CAR assembly and constriction.

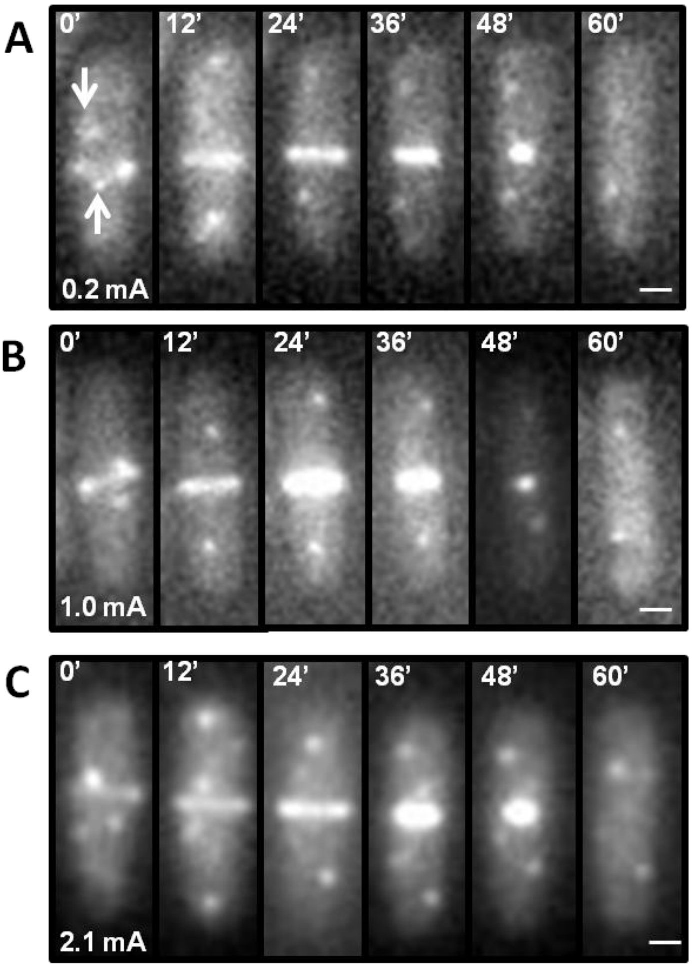

**Figure 3.1.1. Exposure to increasing light intensities, at less frequent intervals does not induce structural defects in the CAR during assembly and constriction, in *rlc1-GFP pcp1-GFP S. pombe*.** Max projections from time-lapses of CAR assembly and constriction in *rlc1-GFP pcp1-GFP S. pombe*. CAR assembly and constriction was recorded in *rlc1-GFP pcp1-GFP* cells over 60 min. Images were taken periodically when exposed to varying light currents, with a 50 ms exposure time. **(A)** 0.2 mA light every 1 min. **(B)** 1.0 mA light every 3 min. **(C)** 2.1 mA every 6 min. One cell from each condition is shown. 21 z-slices were taken. The time-lapse began at 0 min. At 0 min, CAR assembly was occurring. Rlc1-GFP gradually populated the equatorial plane, situated in the middle of the cell to form a ring. This ring was the CAR. Arrows highlight Pcp1-GFP. A pair of Pcp1-GFP foci, in spindle pole bodies embedded in the nuclear envelope (not shown), were perpendicular to the CAR. The cells were not captured at equal stages of CAR assembly. By 12 min, the CAR had formed. It is a consistent line of Rlc1-GFP along the equatorial plane. The nucleus divided (not shown). Pcp1-GFP migrated to the poles of the cell with newly divided nuclei. By 24 min, CAR constriction began. The band of Rlc1-GFP narrowed. Constriction continued through the 36 min and 48 min time points. By 60 min, CAR constriction was complete and its components dissipated. Scale bar - 1 μm.

To determine if the three different imaging conditions induced an increase or reduction in CAR constriction rate in the cells, CAR circumference and GFP intensity were measured along the equatorial plane at each time point of the time-lapses using Metamorph image analysis software. Measurements are displayed in Figure 3.1.2. A line was drawn along the equatorial plane using the line tool function. GFP intensity was measured in pixels along the line using the line scan function. This is shown in Figure 3.1.2A. The equatorial plane is marked with the red dotted line. The total GFP intensity along the CAR was calculated. Total GFP intensity along the equatorial plane was calculated at every time point. To ensure Rlc1-GFP fluorescence from the CAR was measured and background fluorescence was excluded, only GFP intensities above 6,200 a.u., 9,700 a.u. and 20,000 a.u. were used to calculate the total GFP intensity of the CAR in cells exposed to 0.2 mA, 1.0 mA and 2.0 mA light respectively. Intensities below these thresholds were considered background fluorescence and not used to calculate total GFP intensity. These thresholds were determined from GFP intensities measured at the periphery of the equatorial plane. In these regions, GFP intensity consistently fell below the intensity threshold values as CAR constriction progressed. The diameter of the CAR was also measured.

GFP intensities of the CAR were added together to make the total GFP intensity of the CAR. Total GFP intensities were calculated for each time point. The total GFP intensity at each time point was made relative to the highest total GFP intensity recorded in the time lapse. This was to calculate relative GFP intensity. Relative GFP intensities were calculated in a single cell, in each condition. The circumference of the CAR at each time point was also calculated. Figures 3.1.2B, Figures 3.1.2C, Figures 3.1.2D show the change in relative CAR GFP intensity and circumference during CAR assembly and constriction in cells exposed to 0.2 mA light every 1 min (Figure 3.1.2B); 1.0 mA light every 3 min (Figure 3.1.2C); 2.1 mA every 6 min (Figure 3.1.2D). These measurements are shown in Figure 3.1.2.

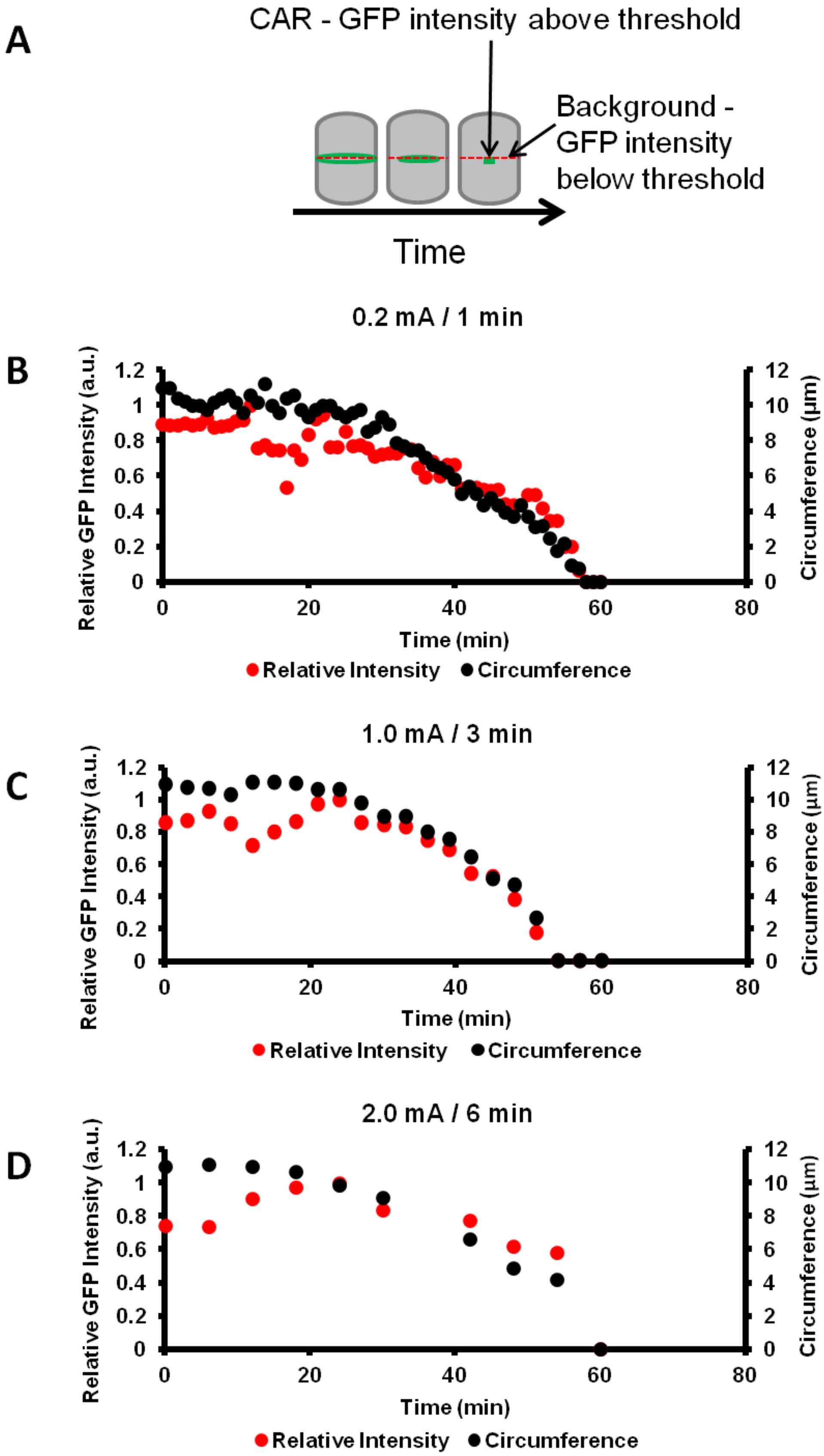

Figure legend on the following page.

**Figure 3.1.2. Exposure to increasing light intensities, at less frequent intervals, does not impact the rate of CAR constriction in *rlc1-GFP pcp1-GFP S. pombe*.** Rlc1-GFP intensity and CAR diameter were measured from time-lapses of CAR assembly and constriction to generate dot plots, which illustrate changes in relative total CAR GFP intensity and circumference during CAR assembly and constriction in *rlc1-GFP pcp1-GFP* under phototoxic stress. **(A)** Illustration displaying how GFP intensity was measured along the CAR in *S. pombe*. The green CAR constricts at the equatorial plane. The red dotted line indicates where GFP intensity was measured in pixels, as the green CAR constricts over time using the Metamorph line tool function. GFP intensities were measured at every time point using the Metamorph line scan function. As the CAR constricts, Rlc1-GFP foci condense to the centre of the equatorial plane. Rlc1-GFP foci leave the periphery of the equatorial plane and therefore GFP intensity at the periphery of the plane reduces. GFP intensities greater than 6,200 a.u., 9,700 a.u. and 20,000 a.u. were used to calculate the total GFP intensity of the CAR in cells exposed to 0.2 mA, 1.0 mA and 2.0 mA light respectively. GFP intensities below the thresholds were considered background fluorescence and discounted. CAR diameter was used to calculate the circumference. **(B)** Dot plot displaying reduction in GFP intensity and circumference during CAR. Total GFP intensities of the CAR were made relative to the highest total GFP intensity measured during the time-lapse. CAR assembly occurred at time points between 0 - 24 min. CAR constriction occurred from 24 min. Changes in CAR circumference were used to determine CAR constriction rates. 0.2 mA every 1 min. Constriction occurred at a rate of 0.20 μm/min. **(C)** 1.0 mA every 3 min. Constriction occurred at a rate of 0.35 μm/min **(D)** 2.1 mA every 6 min. Constriction occurred at a rate of 0.27 μm/min . *n*=1.

CAR assembly occurred between 0 - 24 min in all three conditions. During assembly, a complete ring was not yet formed. The total GFP intensity fluctuated as the Rlc1-GFP foci moved. Assembly rates of the samples were not comparable because the cells were not recorded at equal stages of CAR assembly. CAR constriction begun at approximately 24 min in each cell. Circumference and total GFP intensity decreased as CAR constriction occurred. Ring constriction rates were calculated from the change in CAR circumference over time. CAR circumference decreased at a rate of 0.20 μm/min, 0.35 μm/min and 0.27 μm/min in the 0.2 mA/1 min, 1.0 mA/3 min and 2.1 mA/6 min light exposure conditions respectively. These results suggest exposing cells to light of increasing intensities, at less frequent time points, does not change CAR constriction rate. Delivering photons from low intensity light at frequent time points, as opposed to delivery of photons from high intensity light at infrequent time points, was shown not to be a means of reducing phototoxicity that impact CAR constriction.

Although observing CAR assembly and constriction did not highlight phototoxic effects of exposing cells to high intensity light, subsequent experiments observing CAR constriction (described in the following chapters) had cells exposed to 0.2 mA light for 50 ms, every 3 min. These imaging conditions produces images with sufficient GFP signal intensity for CAR analysis with minimal chance of photodamage. 3 min time points would allow gradual CAR constriction to be observed.

## 3.2 Contractile actomyosin rings collapse at restrictive temperatures in temperature-sensitive *cdc8.27* and *cdc8.110 S. pombe* backgrounds

An ideal working example of when to consider the impact of phototoxicity on cellular processes and fluorophore signal detection, is when CAR constriction is monitored in *S. pombe* mutants of proteins essential for CAR assembly and constriction via fluorescence microscopy. Knowledge on the mechanisms that ensure the completion of CAR constriction is currently lacking (Karagiannis, 2012).  Mutant CAR proteins, such as proteins with genetic point mutations, can be assessed in *S. pombe* via fluorescence microscopy to determine the function of CAR proteins in CAR assembly and constriction.

Imaging conditions determined in Section 3.1 were therefore used to monitor CAR constriction in Johnson et al. (2018). This study assessed the molecular basis of temperature sensitivity in TS (temperature-sensitive) *S. pombe* tropomyosin Cdc8 mutants, *cdc8.27* and *cdc8.110* (Johnson et al., 2018). Cdc8 is an essential actin binding protein that wraps around and stabilises actin filaments in the CAR.  *cdc8.27* has a single E129K (glutamic acid-to-lysine) amino acid substitution by the C-terminus and *cdc8.110* has two amino acid substitutions, A18T (alanine-to-threonine) and E31K (glutamic acid-to-lysine), by the N-terminus (Johnson et al., 2018). Proteins in TS *S. pombe* mutants function normally in the permissive temperature for normal growth, 25 $^{o}$C. Temperatures higher than 25 $^{o}$C are restrictive and disrupt function of the mutant protein and cell growth. Simply shifting TS *S. pombe* mutants from 25 $^{o}$C to a higher restrictive temperature can highlight the role the protein has in cell growth. The molecular basis of temperature-sensitivity in TS mutants is yet to be determined (Johnson et al., 2018).

Protein function in TS mutants is dependent on temperature and at restrictive temperatures above 25 °C, the cells become more sensitive to protein defects. To determine defects induced by mutations in Cdc8, the *cdc8.27 rlc1-GFP* and *cdc8.110 rlc1-GFP* mutant strains were incubated and acclimatised to the permissive temperature for normal growth in *S. pombe* (25 °C) and restrictive temperatures (28 °C, 30 °C, 32 °C, 34 °C, 36 °C) over 48 hr. The cells were then imaged within a Bioptechs FCS2 chamber. To minimise phototoxic damage, cells were exposed to 50 ms light and imaged at 3 min intervals. Exposure to 0.2 mA light for 50 ms every 1 min was shown to not affect CAR assembly and constriction in *rlc1-GFP pcp1-GFP* cells in Section 3.1. Therefore defects observed in *cdc8.27 rlc1-GFP* and *cdc8.110 rlc1-GFP* cells were due to the *cdc8.27* and *cdc8.110* mutations and the resultant Cdc8 dysfunction, not phototoxicity. Failure in CAR constriction due to reduced actin stability provided by Cdc8 was hypothesised, with more severe abnormalities at higher temperatures. Phototoxicity was not the focus of these experiments.

Figure 3.2.1 shows *cdc8.110* induces disrupted CAR assembly and constriction in *cdc8.110 rlc1-GFP* cells at 25 °C. *cdc8.27* did not induce disruptions in CAR assembly and constriction in *cdc8.27 rlc1-GFP* cells at 25 °C. The series of max projections from time-lapses, display the progression of CAR assembly and constriction in *cdc8*$^+$ *rlc1-GFP, cdc8.27 rlc1-GFP* and *cdc8.110 rlc1-GFP* cells, in 9 min intervals. GFP images show Rlc1-GFP. Transmitted images show the morphology and septum of the each cell. Only one transmitted image was taken of *cdc8.110 rlc1-GFP* cells.

At 25 °C, no abnormalities were observed in the wild-type *cdc8*$^+$ *rlc1-GFP* and *cdc8.27 rlc1-GFP* cells. The cells possessed healthy cell morphologies, CAR formation and constriction (Figure 3.2.1A, Figure 3.2.1B). 25 °C is a restrictive temperature for *cdc8.110 rlc1-GFP S. pombe*. At this temperature, Rlc1-GFP in *cdc8.110 rlc1-GFP* cells did not localise to the equatorial plane correctly. Formation of the CAR was prolonged. Between 27 - 36 min, the CAR appeared to collapse and reform. An aberrant ring was formed and constricted after the delay (Figure 3.2.1C). In wild-type *cdc8*$^+$ cells, the contractile ring is kept anchored to the cell cortex by Mid1 (Lee & Wu, 2012; Schwayer et al., 2016). The CAR in *cdc8.110 rlc1-GFP* cells appeared displaced and slid along the cell cortex, prior to constriction. This observation suggests the CAR may not be sufficiently attached to the cell cortex.

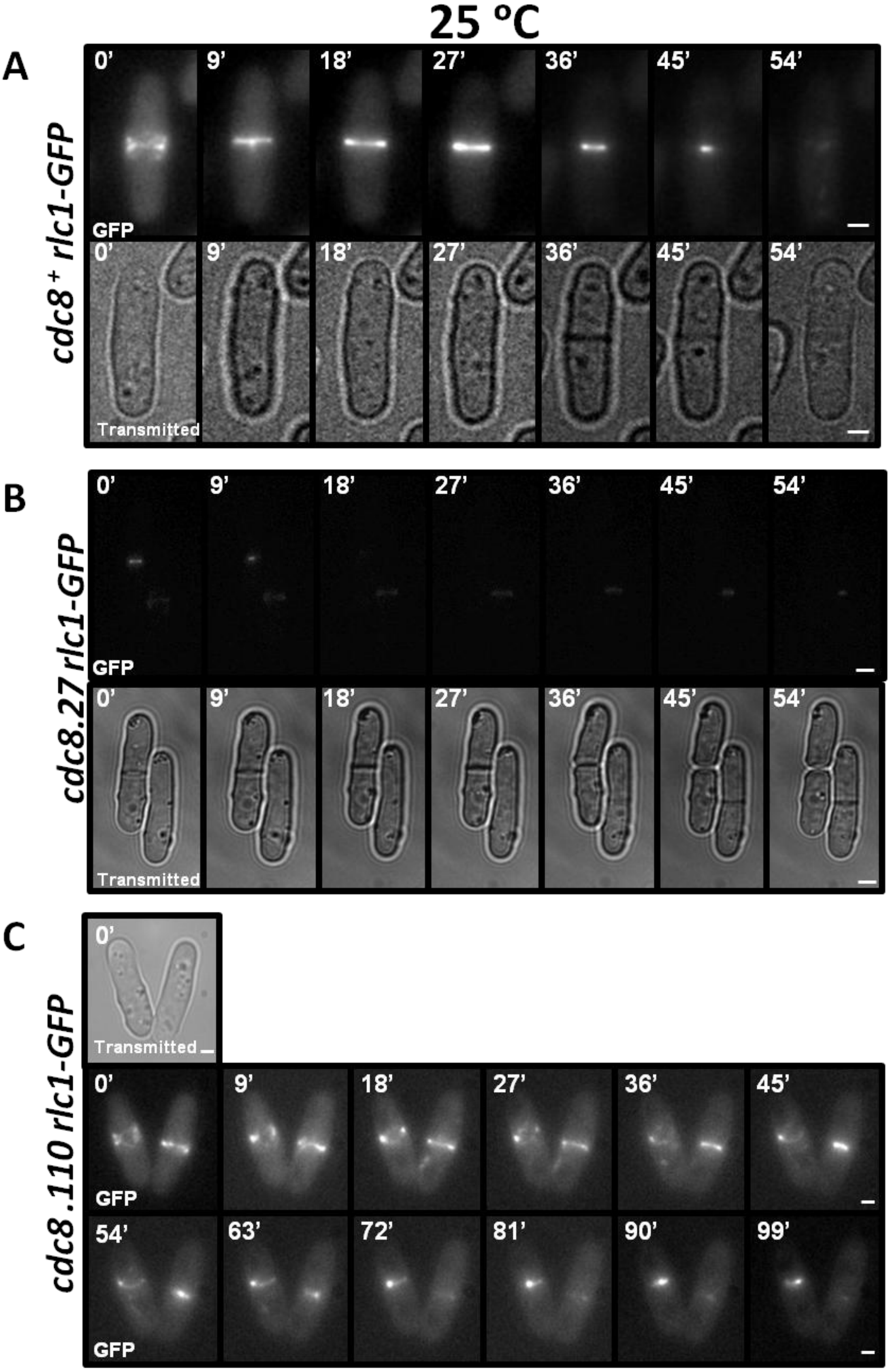

Figure legend on the following page.

**Figure 3.2.1. At 25 °C, CAR constriction is disrupted in temperature-sensitive *cdc8.110 rlc1-GFP* cells but not in temperature-sensitive *cdc8.27 rlc1-GFP* cells.** Max projections from time-lapses of CAR assembly and constriction in wild-type *cdc8*$^+$ *rlc1-GFP, cdc8.27 rlc1-GFP* and *cdc8.110 rlc1-GFP S. pombe* held at 25 °C for 48 hr. CAR assembly and constriction were recorded in the cells over 60 - 110 min. Images were taken periodically with 0.2 mA light for 50 ms, every 3 min. Images were taken in the GFP channel to visualise the CAR, and the transmitted light channel to visualise the septum (black line along the equatorial plane) formed during the later stages of ring constriction. 21 z-slices were taken. The time-lapse began at 0 min. The cells were not captured at equal stages of CAR assembly or constriction. **(A)** CAR assembly and constriction in wild-type *cdc8*$^+$ *rlc1-GFP* cells*.* One cell is shown. At 0 min, CAR assembly was occurring. Rlc1-GFP gradually populated the equatorial plane situated in the middle of the cell to form a ring. This ring is the CAR. By 18 min, a uniform CAR was formed. It is a consistent line of Rlc1-GFP along the equatorial plane. By 36 min, CAR constriction began. The band of Rlc1-GFP narrowed and a septum formed. By 54 min, CAR constriction was complete and its components began to dissipate. **(B)** CAR constriction in *cdc8.27 rlc1-GFP* cells*.* Normal CAR constriction occurred in the two cells shown. At 0 min, the CAR and septum had already formed in the cell on the left-hand side (LHS). The CAR was assembling in the cell on the right-hand side (RHS). Both CAR constricted as time passed. By 36 min, septum constriction in the LHS cell began to separate the cell into two daughter cells. The septum formed in the RHS cell by 45 min. By 54 min, CAR constriction in the LHS cell was complete. **(C)** CAR assembly and constriction in *cdc8.110 rlc1-GFP* cells*.* Delayed constriction in aberrant CAR occurred in the two cells shown. At 0 min, the CAR was assembling in the cell on the LHS. An aberrant CAR formed in the cell on the RHS. By 36 min, the CAR had not formed and was displaced in the cell on the LHS. CAR constriction began in the cell on the RHS. At 72 min, CAR began in the cell on the LHS. The CAR slowly dissipated in the cell on the RHS. At 99 min, the CAR in the cell on the RHS remained in constriction. Multiple transmitted light images were not part of the dataset. Scale bar - 1 µm.

Healthy, wild-type *S. pombe* have a straight morphology. Actin maintains correct cell shape and polarity in the cell. A bent morphology in *S. pombe* can result from disruptions in actin function to maintain cell shape and polarity. Images in the GFP and transmitted light channels were taken of wild-type *cdc8*$^+$ *rlc1-GFP, cdc8.27 rlc1-GFP* and *cdc8.110 rlc1-GFP* cells to identify morphological defects. Bent morphologies were observed in *cdc8.110 rlc1-GFP* cells*.* The degree of the bends was measured to highlight actin defects induced by *cdc8.110*. At 25 °C, 5 ° bends were consistently observed only in *cdc8.110 rlc1-GFP* cells at 25 °C. 5 ° bends were therefore deemed a result of disrupted actin function caused by *cdc8.110*. Double septa and a longer morphology were also observed in *cdc8.110 rlc1-GFP* cells at 25 °C. This is shown in Figure 3.2.2, which shows a field of cells in the GFP channel showing Rlc1-GFP, and the transmitted light channel showing the cell morphology. Cells in this figure were treated in the same condition as cells shown in Figure 3.2.1.

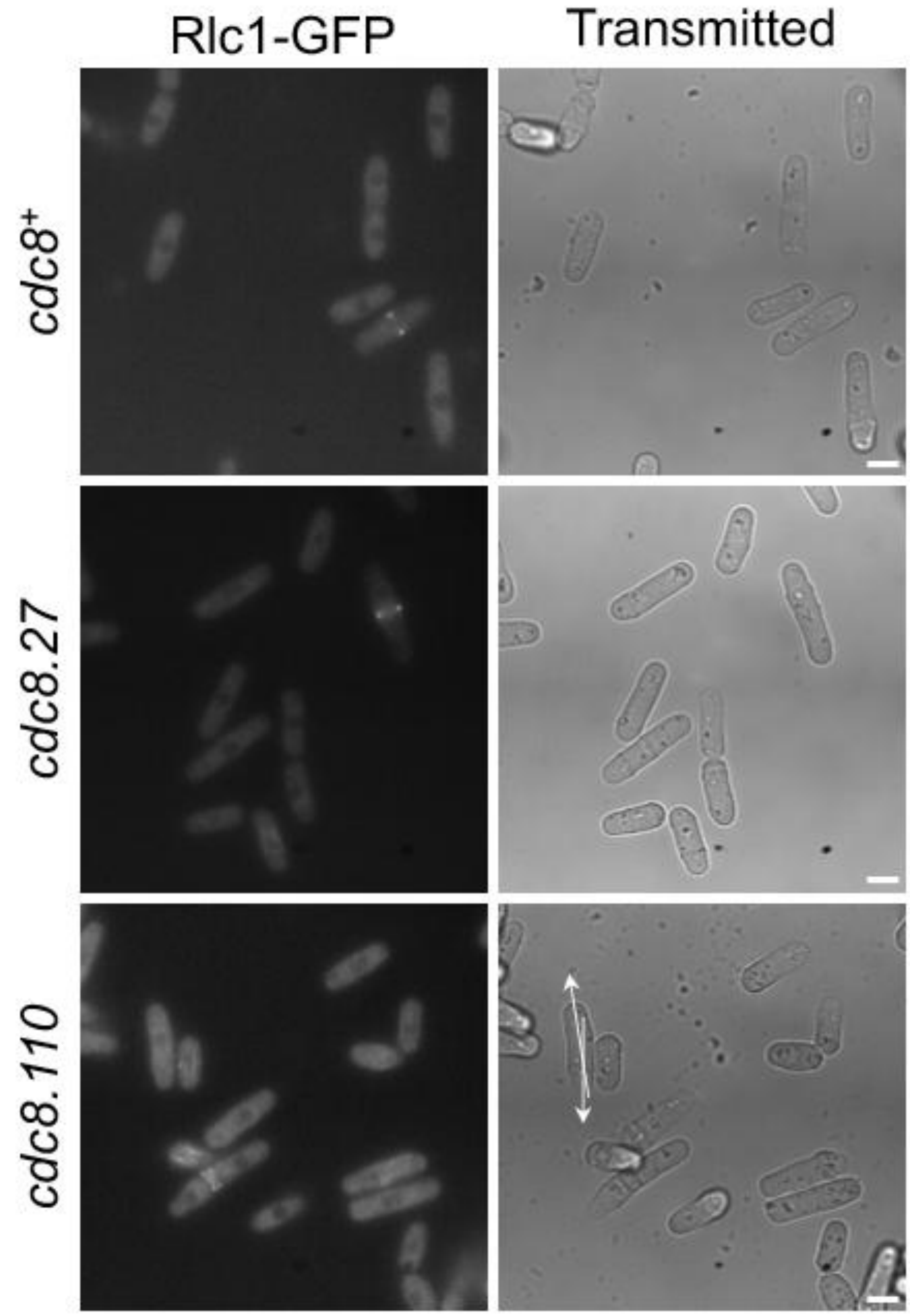

Figure legend on the following page.

**Figure 3.2.2. *cdc8.110* induces double septa and a bent morphology in temperature-sensitive *cdc8.110 rlc1-gfp S. pombe*.** GFP and transmitted light max projections of wild-type *cdc8*$^+$ *rlc1-GFP, cdc8.27 rlc1-GFP* and *cdc8.110 rlc1-GFP S. pombe*, incubated at 25 °C for 48 hr. The cells were exposed to 50 ms light, every 3 min for 60 min. 21 z-slices were taken. Double septa and a bent morphology were observed only in *cdc8.110 rlc1-gfp* cells*.* 5 ° bends were consistently observed and were deemed a result of disruptions in actin function in maintaining cell shape and polarity. Arrows indicate a 5 ° bend in the morphology of *cdc8.110* cells. 5 ° bends were not observed in wild-type *cdc8*$^+$ *rlc1-GFP* cells and temperature sensitive *cdc8.27 rlc1-GFP* cells*.* Scale bar – 5 µm.

CAR assembly and constriction were then imaged in *cdc8.27 rlc1-GFP* and *cdc8.110 rlc1-GFP* cells at 30 °C, 32 °C, 34 °C and 36 °C. Progression of CAR assembly and constriction at 30 °C and 34 °C are shown in Figure 3.2.3 and Figure 3.2.4 respectively. Wild-type *cdc8*$^+$ *rlc1-GFP* cells were not imaged at these temperatures.

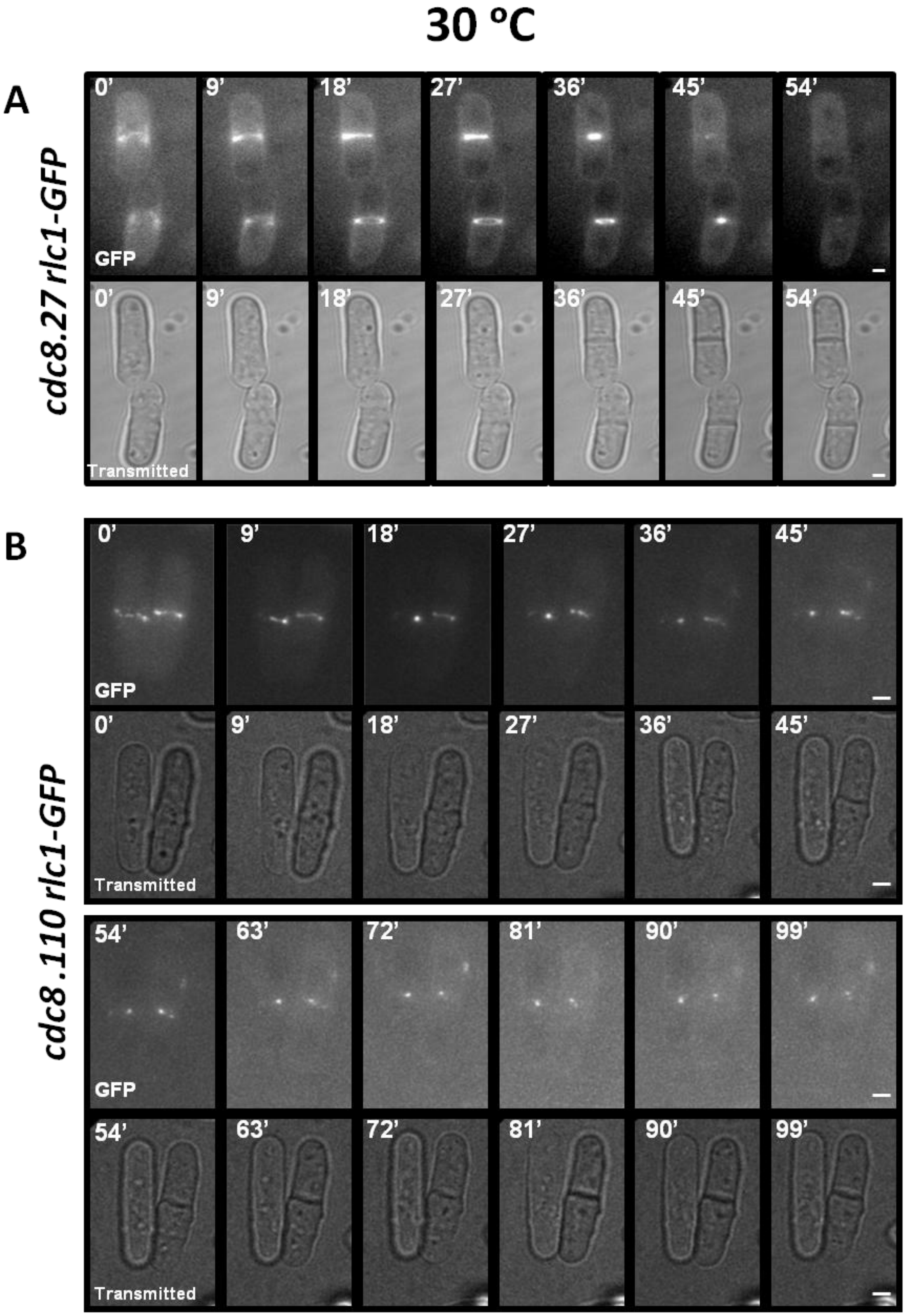

Figure legend on the following page.

**Figure 3.2.3. At 30 °C, CAR constriction is disrupted in *cdc8.110 rlc1-GFP* but not in *cdc8.27 rlc1-GFP S. pombe.*** Max projections from time-lapses of CAR assembly and constriction in temperature-sensitive*, cdc8.27 rlc1-GFP* and *cdc8.110 rlc1-GFP S. pombe*, held at 30 °C for 48 hr. CAR assembly and constriction were recorded in the cells over 60 - 110 min. Images were taken periodically with 0.2 mA light for 50 ms, every 3 min. Images were taken in the GFP channel to visualise the CAR, and the transmitted light channel to visualise the septum (black line along the equatorial plane) formed during the later stages of ring constriction. 21 z-slices were taken. The time-lapse began at 0 min. The cells were not captured at equal stages of CAR assembly or constriction. **(A)** CAR assembly and constriction in *cdc8.27 rlc1-GFP* cells. Normal CAR constriction occurred in the two cells shown. At 0 min, CAR assembly was occurring. Rlc1-GFP gradually populated the equatorial plane situated in the middle of the cell to form a ring. This ring is the CAR. By 18 min, a uniform CAR was formed. It is a consistent line of Rlc1-GFP along the equatorial plane. By 36 min, CAR constriction began. The band of Rlc1-GFP narrowed and a septum formed. By 54 min, CAR constriction was complete and its components dissipated. **(B)** CAR constriction in *cdc8.110 rlc1-GFP* cells*.* Delayed constriction in aberrant CAR occurred in the two cells shown. At 0 min, inconsistent CAR had already formed in the cells. Both CAR slowly constricted over the 99 min. By 18 min, a septum formed in the cell on the right hand side (RHS). The cell on the left hand side (LHS) did not form a septum within the 99 min. Scale bar - 1 µm.

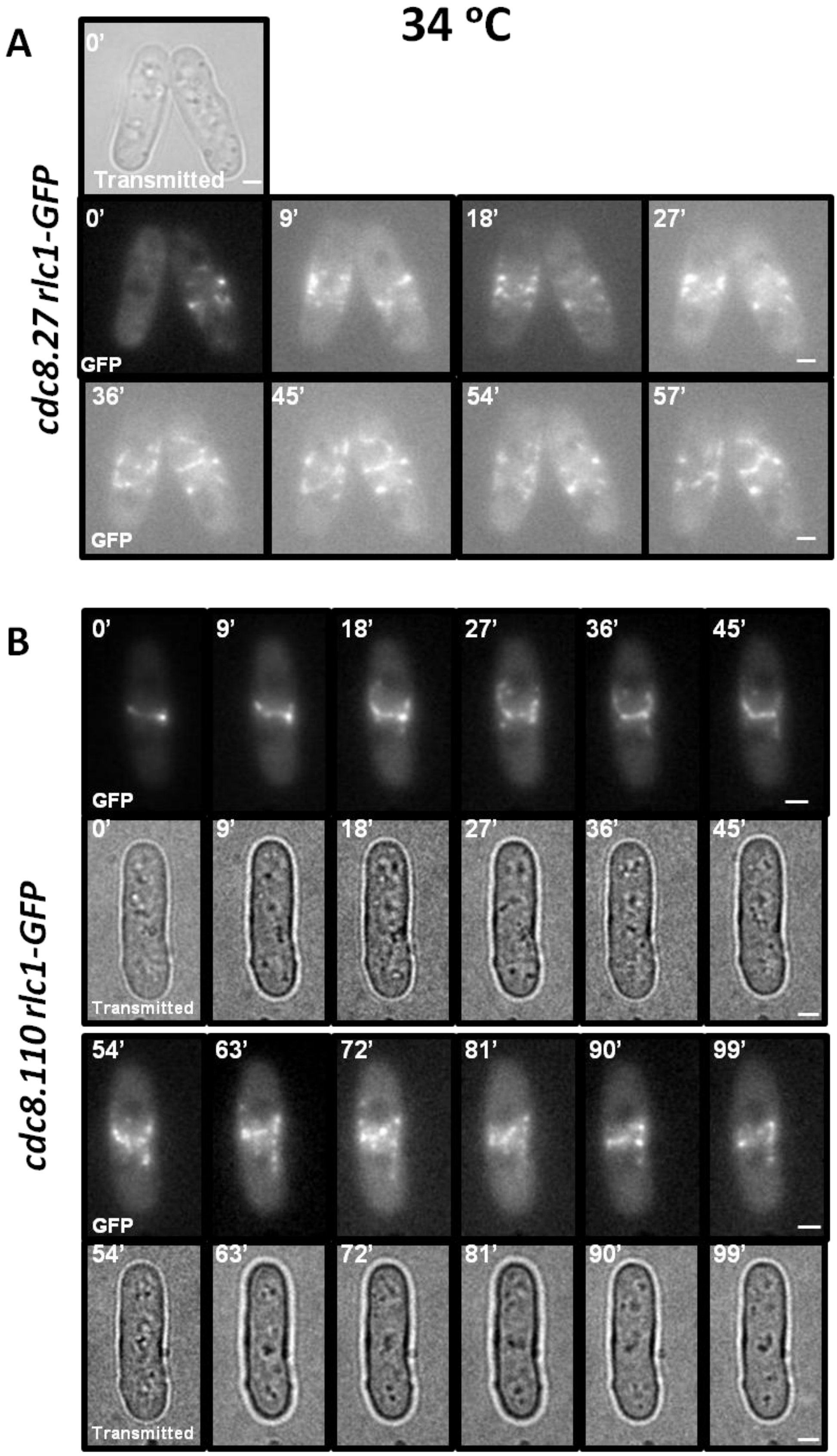

Figure legend on the following page.

**Figure 3.2.4. At 34 °C, CAR fails to form and constrict in *cdc8.27 rlc1-GFP* and *cdc8.110 rlc1-GFP S. pombe.*** Max projections from time-lapses of CAR maturation and constriction in temperature-sensitive *cdc8.27 rlc1-GFP* and *cdc8.110 rlc1-GFP S. pombe*, held at 34 °C for 48 hr. CAR maturation and constriction were recorded in the cells over 60 - 110 min. Images were taken periodically with 0.2 mA light for 50 ms, every 3 min. Images were taken in the GFP channel to visualise the CAR, and the transmitted light channel to visualise the septum (black line along the equatorial plane) formed during the later stages of ring constriction. 21 z-slices were taken. The time-lapse began at 0 min. The cells were not captured at equal stages of CAR maturation or constriction. **(A)** Failed CAR formation and constriction in *cdc8.27 rlc1-GFP* cells*.* Rlc1-GFP failed to localise at the equatorial plane in the two cells shown. The CAR did not form or constrict. Multiple transmitted light images were not part of the dataset. **(B)** Failed CAR formation and constriction in *cdc8.110 rlc1-GFP* cells*.* At 0 min, an aberrant CAR was forming. By 18 min, the CAR began to collapse upon constriction. A septum did not form. Scale bar - 1 μm.

The severity of defects in CAR structure and constriction increased with increasing temperature. The deformed structures ranged from aberrant CAR that eventually constricted, aberrant CAR that failed to constrict and non-contractile CAR. *cdc8.27 rlc1-GFP* cells displayed normal CAR constriction at 30 °C (Figure 3.2.3). Incubation at 32 °C and 34 °C, produced irregular Rlc1-GFP localisation in *cdc8.27 rlc1-GFP* cells*.* The CAR were often displaced, suggesting the deformed actin structures were formed with a lack of attachment to the cell cortex. Constriction of the CAR was delayed or did not occur at all (Figure 3.2.4, Figure 3.2.5). CAR in *cdc8.110 rlc1-GFP* cells at 30 °C appeared to be non-uniform and displaced but constriction was observed (Figure 3.2.3). At 34 °C, CAR assembly was followed by complete collapse of the ring. Constriction was not observed (Figure 3.2.4, Figure.3.2.5). At 36 °C, ring assembly did not occur in either Cdc8 mutant strains. This is summarised in Figure 3.2.5.

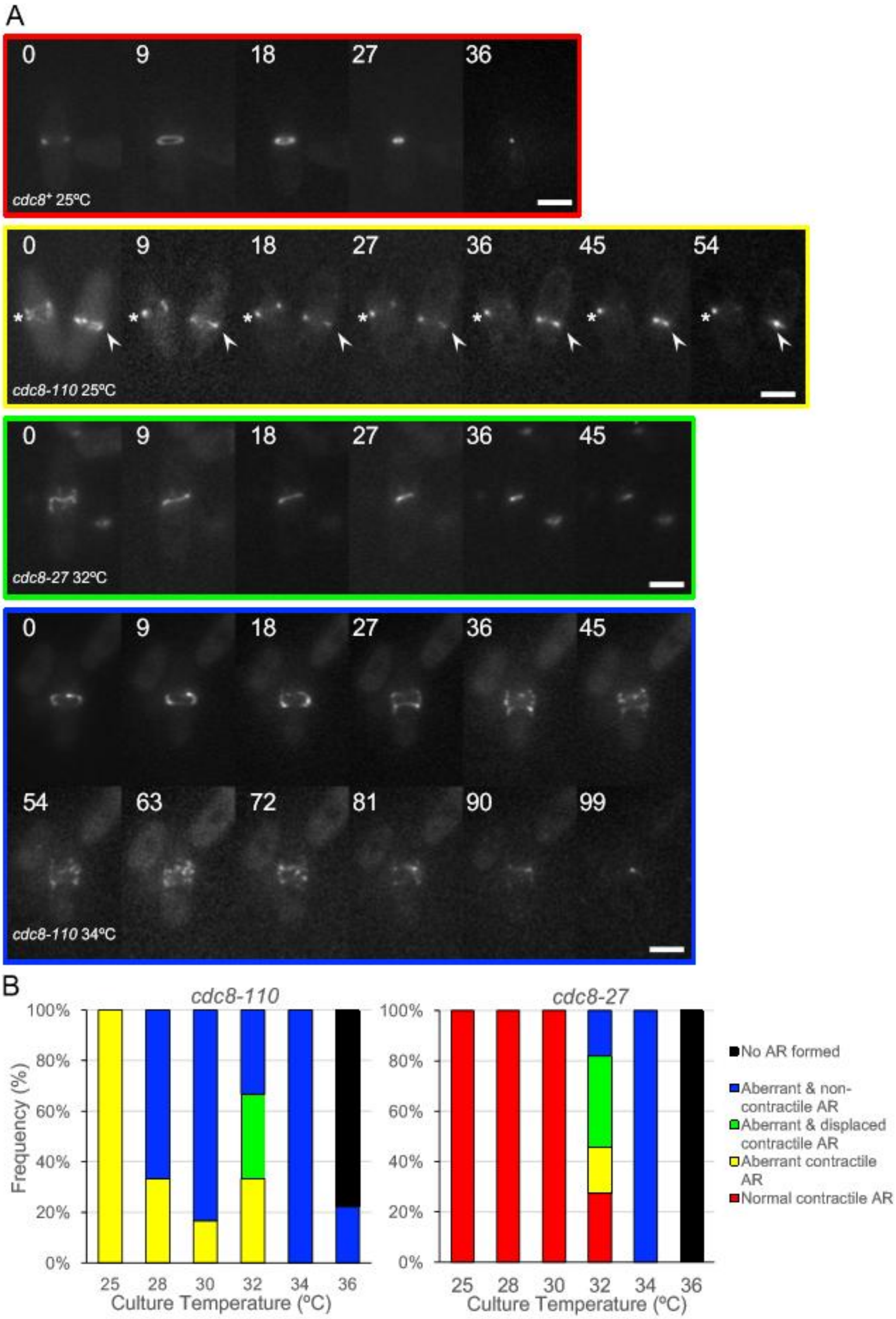

Figure legend on the following page.

**Figure 3.2.5. At higher restrictive temperatures, structural defects in CAR are exacerbated and CAR does not constrict in *cdc8.27 rlc1-GFP* and *cdc8.110 rlc1-GFP S. pombe.*** **(A)** Summary of max projections from time-lapses of CAR maturation and constriction in wild-type *cdc8*$^+$ *rlc1-GFP* (25 ºC), and temperature sensitive *cdc8.27 rlc1-GFP* (32 ºC) and *cdc8.110 rlc1-GFP* (25 ºC, 34 ºC) *S. pombe*, held at the corresponding temperatures for 48 hr. CAR maturation and constriction were recorded in the cells over 60 - 110 min. Images were taken periodically with 0.2 mA light for 50 ms, every 3 min. Images were taken in the GFP channel to visualise the CAR. 21 z-slices were taken. The time-lapse began at 0 min. The cells were not captured at equal stages of CAR maturation or constriction. The cells formed: normal contractile actin rings (red boarder); aberrant contractile rings with delayed constriction (arrow) and aberrant CAR (asterisk) (yellow boarder); aberrant and displaced contractile rings that were not attached to the cell cortex (green boarder); aberrant and non-contractile actin rings that collapsed and did not constrict (blue boarder). Scale bar – 5 µm. **(B)** Quantification of > 45 cells that displayed CAR defects in *cdc8.27 rlc1-GFP* and *cdc8.110 rlc1-GFP* cells, per temperature. Bar colours correlate with the boarder colours in (A). Adapted from Johnson et al. (2018).

The experiments described above assessed the impact the *cdc8.27* and *cdc8.110* alleles have on the actin stabilising function of Cdc8. CAR constriction was monitored in temperature sensitive *cdc8.27 rlc1-GFP* and *cdc8.110 rlc1-GFP* cells. The structural CAR defects and non-contractile rings observed in these cells are consistent with the actin stabilising role Cdc8 plays. The displaced CAR confirmed the *cdc8.27* and *cdc8.110* alleles hinder the attachment of the CAR actin to the cell cortex and the overall placement of the CAR. The two point mutations in the *cdc8.110* allele appeared to have an additive effect on Cdc8 function as the defects observed in *cdc8.110 rlc1-GFP* cells were more severe than in *cdc8.27 rlc1-GFP* cells. Bent morphologies observed in *cdc8.110 rlc1-GFP* cells shows correct Cdc8 function is required to maintain the correct cell polarity in *S. pombe*.

## 3.3 Monomeric neongreen fluorophore photostability is superior to GFP and 3GFP fluorophores

As studying myosin dynamics within live cells was an aim during this PhD, it was required to determine a suitable fluorophore for myosin fluorescent labelling. The fluorescent protein mNG (mNeongreen) possesses superior optical properties over commonly used fluorescent proteins such as GFP and it is reported to be the brightest monomeric green-yellow fluorescent protein to date (Shaner et al., 2013). It has also been shown to be 1.5 - 3 times brighter than GFPs and YFPs (Dean & Palmer, 2014). To determine if mNG would be a suitable fluorophore for the study of myosin dynamics, a *myo52-mNG S. pombe* strain was developed in the lab. Myo52 was the motor of choice as it is a fast moving myosin and is often faint under fluorescent conditions, therefore making it challenging to visualise without a bright fluorophore.

To also determine if mNG has more suitable properties for fluorescent observation of Myo52 than fluorophores with similar excitation and emission spectral profiles, Myo52-mNG properties were compared to Myo52-GFP and Myo52-3GFP in live *S. pombe.* GFP is a monomer. 3GFP is a GFP trimer (Mossner et al., 2020). *myo52-GFP sid2-tdtomato* and *myo52-3GFP sid2-tdtomato* cells were used to differentiate between the *myo52-GFP, myo52-3GFP* and *myo52-mNG* cells during imagining. *myo52-mNG* cells were cultured mixed with either *myo52-GFP sid2-tdtomato* or *myo52-3GFP sid2-tdtomato.* Time-lapses of Myo52 dynamics within the cells were recorded. Figure 3.3.1 shows a comparison of max projections from time-lapses of each mixed culture.

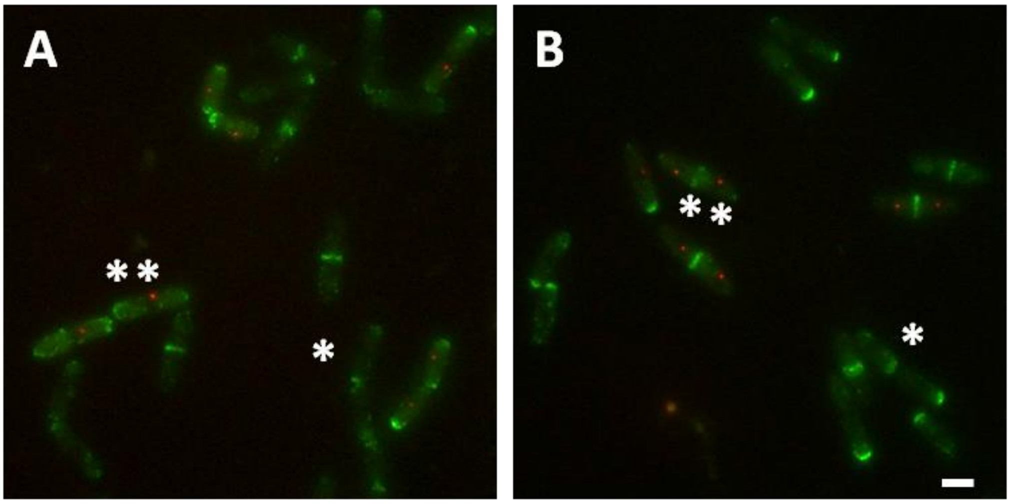

**Figure 3.3.1. Myo52-mNG produces more discrete foci with less background fluorescence than Myo52-GFP and Myo52-3GFP in *S. pombe.*** Comparison of max projections displaying Myo52-mNG, Myo52-GFP and Myo52-3GFP in *S. pombe. myo52-mNG* cells were imaged with *myo52-GFP sid2-tdtomato* or *myo52-3GFP sid2-tdtomato* cells for foci intensity and resolution comparison. *myo52-mNG* cells are marked with '*'. *myo52-3GFP sid2-tdtomato* and *myo52-3GFP* cells are marked with '**'. The cells were exposed to 50 ms light at 25 $^{o}$C. 13 z-slices were taken. Scale bar - 3.5 μm. **(A)** *myo52-mNG* and *myo52-3GFP sid2-tdtomato* cells. **(B)** *myo52-mNG* cells and *myo52-GFP sid2-tdtomato* cells.

Clearest foci were observed in *myo52-mNG* cells. Myo52-3GFP foci were larger than Myo52-mNG and Myo52-GFP. Foci close to one another would be difficult to differentiate. Foci may also appear aggregated especially at the cell ends. The background fluorescence was noticeably the lowest in *myo52-mNG* cells. Myo52-mNG, Myo52-GFP and Myo52-3GFP foci intensities were measured, using Metamorph software, to compare the average intensity and photostability over time. Figure 3.3.2 shows the average foci intensity of Myo52-mNG, Myo52-GFP and Myo52-3GFP. It also shows the decrease in foci intensity over time, when exposed to 50 ms 0.2 mA light over 399 min. For each strain, foci intensity values were made relative to the highest foci intensity measured in the specific strain.

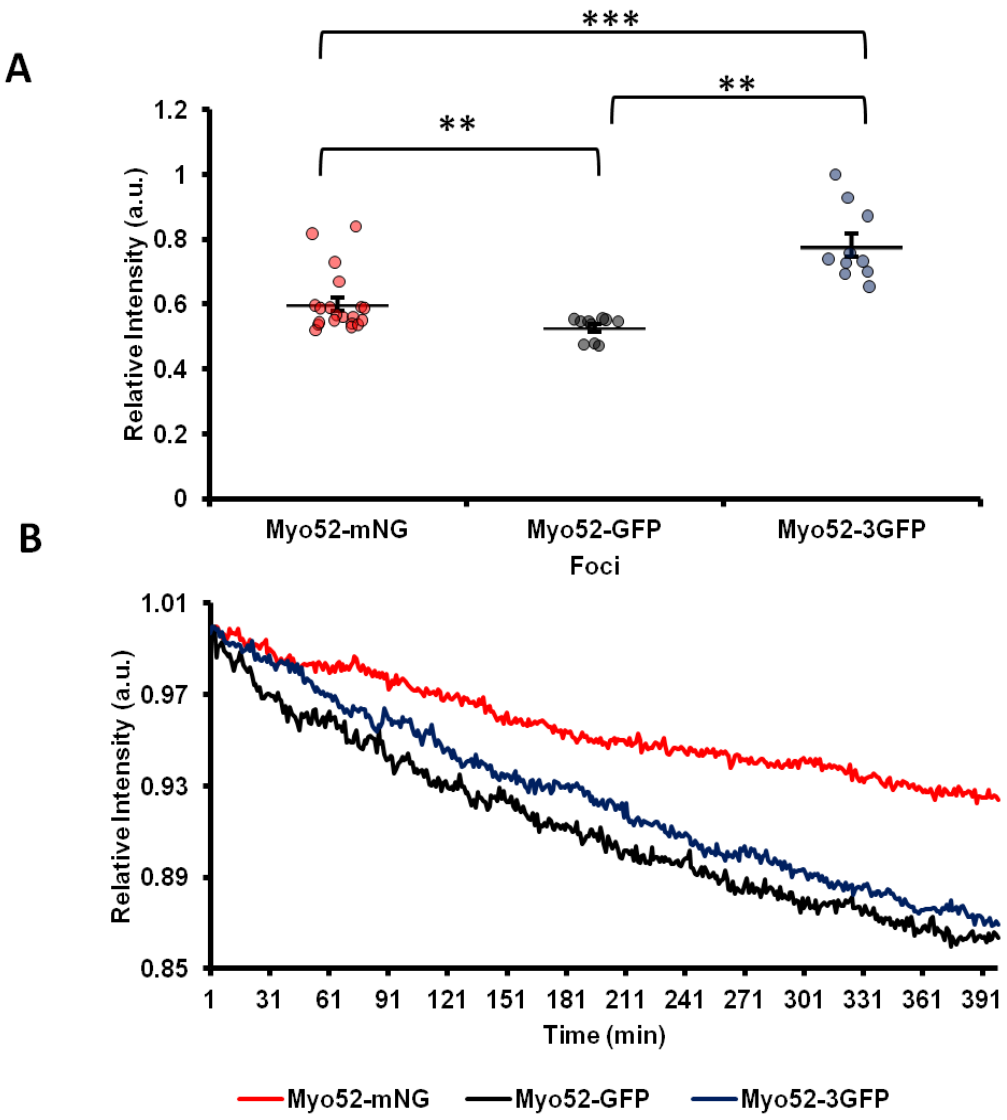

Figure legend on the following page.

**Figure 3.3.2. mNG is brighter than GFP and more photostable than GFP and 3GFP.** Comparison of Myo52-mNG, Myo52-GFP and Myo52-3GFP foci intensity and photostability. *myo52-mNG* cells were imaged with *myo52-GFP sid2-tdtomato* and *myo52-3GFP sid2-tdtomato S. pombe.* **(A)** Average foci intensity of each fluorophore, relative to the highest foci intensity measured in the brightest fluorophore, 3GFP. Error bars represent standard error of the mean (SEM). Myo52-3GFP intensity (0.78 ± 0.11 a.u.) was greater than Myo52-GFP (0.53 ± 0.04 a.u.) and Myo52-mNG intensities (0.60 ± 0.09 a.u.) (mean ± SEM). Significant differences were measured between all fluorophore intensity using a Student's *t*-test. ** $p \leq 0.01$. *** $p \leq 0.001$. **(B)** Average relative foci intensity over time was measured to determine fluorophore photostability. Average relative foci intensity decreased by 0.07 a.u., 0.13 a.u. and 0.14 a.u., over 399 min, in Myo52-mNG, Myo52-3GFP and Myo52-GFP respectively. Therefore, mNG was the most photostable fluorophore during long-term exposure to light. Approximate SEM of the average relative intensity at each time point: Myo52-mNG - 0.004 a.u.; Myo52-GFP - 0.011 a.u.; Myo52-3GFP - 0.012 a.u.. The cells were exposed to 50 ms, 0.2 mA light for 399 min at 25 $^{o}$C. 13 z-slices were taken. $n \geq 10$. '*n*' indicates the number of foci measured.

Average relative intensities of 0.60 ± 0.09 a.u., 0.53 ± 0.04 a.u. and 0.78 ± 0.11 a.u. (mean ± SEM) and were measured for Myo52-mNG, Myo52-GFP and Myo52-3GFP respectively. (Figure 3.3.2A). A student's *t*-test was used to determine significant difference between the intensities. A significant difference in intensity was determined between all three fluorophores ($p \leq 0.01$). Myo52-mNG showed the most consistent average relative intensity during long-term exposure to 50 ms light. Over 399 min, the average relative intensity of the foci decreased by 0.07 a.u., 0.13 a.u. and 0.14 a.u. for Myo52-mNG, Myo52-3GFP and Myo52-GFP respectively. Therefore, mNG was the most photostable fluorophore (Figure 3.3.2B). Although the brightest, Myo52-3GFP produced the greatest background fluorescence and the largest foci. Background fluorescence and large foci would make it difficult to differentiate individual foci. For this reason, 3GFP was not used in further experiments. mNG was the most photostable fluorophore, produced the most discrete foci and was significantly brighter than GFP. For these reasons, mNG was chosen as the fluorophore of use for Myo52 labelling in the Myo52 phospho-mutant strains in subsequent experiments described in Chapter 4.

## 3.4 The Cairn Research simultaneous two-channel spinning-disk confocal imaging system is capable of simultaneously detecting red and green fluorophores without channel-to-channel bleed-through

A novel simultaneous two-channel spinning-disk acquisition imaging system is currently being developed by Cairn Research. The system enables real-time protein co-movement acquisition of proteins fluorescently labelled with fluorophores in two different fluorescence channels. Standard wide-field fluorescent imaging systems have limitations when imaging two proteins at the same time. These limitations include channel-to-channel bleed-through (fluorophores with overlapping spectral profiles), filter set availability and illumination of whole sample volumes, which causes blurring from out of focus planes above and below the plane of focus. The simultaneous two-channel system was applied to a spinning-disk confocal imaging system to circumvent these limitations with reduced channel-to-channel bleed-through, detection limited to the plane of focus to reject background and the use of rapidly switching lasers for excitation and emission flexibility (St. Crorix et al., 2005).

Standard spinning confocal microscope systems have an image capture rate of 50 ms (20 Hz). An image can be captured every 200 ms. They image in two different channels by alternating between two sets of excitation/emission filters and LEDs/lasers so an image can be taken in each channel at each time point. At each time point, z-slices in the first channel are taken once the correct filters are in place and the correct LED/laser is on. Then the excitation/emission filters and LEDs/lasers change to take z-slices in the second channel. It takes time to acquire z-slices, change between excitation/emission filters and LEDs/lasers. The millisecond dynamics of the proteins that occur during the change of excitation/emission filters and LEDs/lasers are not captured. Therefore, there is always a time lag between the dynamics of proteins captured in multi-channel time-lapses. The millisecond dynamics of proteins are not captured in real-time.

In the simultaneous two-channel spinning-disk confocal microscope system being developed by Cairn Research, blue and green excitation lasers function alternately to illuminate the sample. The sample emits green and red light respectively. The excitation/emission filters are on a wheel that constantly rotates at a speed of 11 Hz. The lasers are synchronised with the filter wheel and are timed to turn on when the corresponding filters are in place. During this PhD project, the lasers were used with an exposure time of 100 ms. The filter wheel spins at 11 Hz so it is in place before the laser turns on. This allows for a 10 Hz capture rate i.e. one image captured every 100 ms. This is two times faster than standard confocal microscopes. The time lag between the dynamics of proteins imaged in two different channels is therefore halved.

The simultaneous two-channel spinning-disk confocal microscope system is therefore a suitable system to use for protein-protein interaction and co-localisation studies. Myosins co-localise with light chains such as calmodulin and cytoskeletal components such as actin. The proteins fluidly move both dependent and independently of each other. The simultaneous two-channel spinning-disk confocal microscope system would therefore be useful in acquiring time-lapses with accurate real-time dynamics of myosin and a second protein.

The system was assembled by Cairn Research. Work conducted during this PhD project did not include the production or assembly of the system hardware or software. The system had not been previously tested with biological samples. This section describes experiments that were carried out to test if the system could: (i) simultaneously detect fluorophores in the red and green channels; (ii) simultaneously detect red and green fluorophores without bleed-through between the two channels (without detection of fluorescence in the wrong channel); (iii) simultaneously record co-movement of two proteins labelled with green and red fluorophores. Laser power and exposure times were initially set for single channel acquisition to test if the system could detect fluorophores in the red and green channel without channel-to-channel bleed through. *myo52-mNG mCherry-lifeact* cells were used. Lifeact, a short peptide which binds to actin microfilaments, was used as a marker to visualise actin structures (Riedl et al., 2008). *myo52-mNG mCherry-lifeact* were imaged in either the green or the red channel to detect and capture time-lapses of Myo52-mNG and mCherry-lifeact separately. The cells were exposed to 470 nm light (green excitation) at 20 mW power for 100 ms or 555 nm light (red excitation) at 20 mW power for 100 ms, at 25 °C. 13 z-slices were taken.

Figure 3.4.1 shows max projection images from time-lapses of *myo52-mNG mCherry-lifeact* cells. Metamorph image analysis software was used to view the live display of the field of view on a computer. The field of view in the green and red channels are displayed adjacent to each other, at the same time. The green dotted lines outline the region where the green channel is displayed. Myo52-mNG foci fluorescence is shown in this region. The red dotted lines outline the region the red channel is displayed. mCherry fluorescence is shown in this region. mCherry-Lifeact filaments are shown in this region (Figure 3.4.1B). Fluorescence from Myo52-mNG was only detected in the green channel when *myo52-*

*mNG mCherry-lifeact* cells were exposed to 470 nm light only (Figure 3.4.1A). Fluorescence from mCherry-Lifeact was only detected in the red channel when *myo52-mNG mCherry-lifeact* cells were exposed to 555 nm light only (Figure 3.4.1B). Therefore, the system detected fluorophores in the red and green channels without channel-to-channel bleed through.

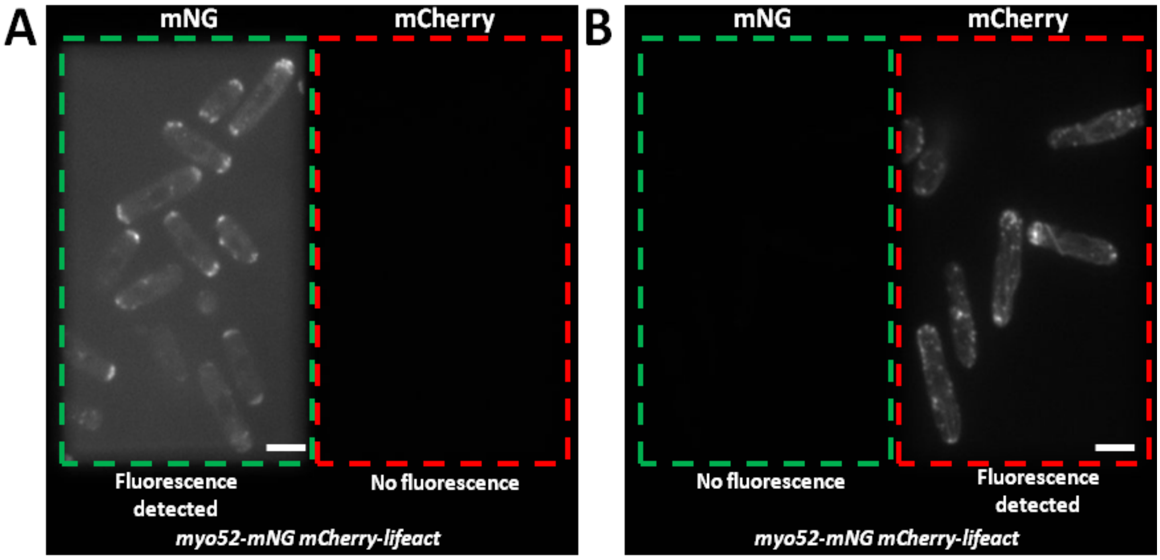

**Figure 3.4.1. mNG and mCherry were detected and captured without channel-to-channel bleed through in single channel time-lapses by the simultaneous two-channel spinning disk confocal microscope.** Max projection images from time-lapses of *myo52-mNG mCherry-lifeact S. pombe*. The imaging system is configured so fluorescence in the green and red channels is displayed beside each other during imaging. The green boarder outlines the region green fluorescence (mNG-Myo52 foci) is displayed. The red boarder outlines the region red fluorescence (mCherry-Lifeact filaments) is displayed. **(A)** Cells were exposed to 470 nm light to excite mNG. Myo52-mNG was only detected in the green channel. No mNG fluorescence was detected in the red channel. **(B)** Cells were exposed to 555 nm light to excite mCherry. mCherry-Lifeact was only detected in the red channel. No mCherry fluorescence was detected in the green channel. The cells were exposed to 470 nm light at 20 mW power to image in the green channel, or exposed to 555 nm light at 20 mW power to image in the red channel. Imaging was carried out at 25 $^{o}$C. 13 z-slices were taken. Scale bar - 3.5 µm.

Simultaneous two-channel time-lapses were then acquired to determine if the system could simultaneously record co-movement of two proteins labelled with green and red fluorophores. *myo52-mNG mCherry-lifeact*, *acp1-GFP mCherry-lifeact* and *mNG-myo1 mCherry-lifeact* cells were imaged simultaneously in the red and green channels. The cells were exposed to 470 nm and 555 nm light within 100 ms of each other. The power of the 470 nm light was adjusted in each strain to achieve optimal fluorophore signal (mNG-Myo52 and Myo1-mNG - 90 mW; Acp1-GFP- 15 mW). Myo1 moves faster than Myo52, Acp1 and Lifeact. Myo1-mNG foci are visible for approximately 11 s. Therefore 7 z-slices of Myo1-mNG were taken instead of 13 z-slices, to reduce the amount of time spent acquiring images. mNG/GFP and mCherry fluorescence were successfully recorded simultaneously.

After image acquisition, Metamorph was used to manually generate a composite image using the overlay images function (combination of images in the red and green channels). To generate a composite image, one channel region on the image is manually selected and overlaid over the other channel region. The two regions are then aligned by eye. Background fluorescence in the composite images was reduced using Metamorph. Figure 3.4.2 shows max projection images of the *myo52-mNG mCherry-lifeact*, *acp1-GFP mCherry-lifeact* and *mNG-myo1 mCherry-lifeact* cells, taken from time-lapses. The green and red channel regions are outlined by the green and red dotted lines. The composite image shows an overlay of the two channel regions. mNG-Myo52 is shown in green and mCherry-Lifeact is shown in magenta.

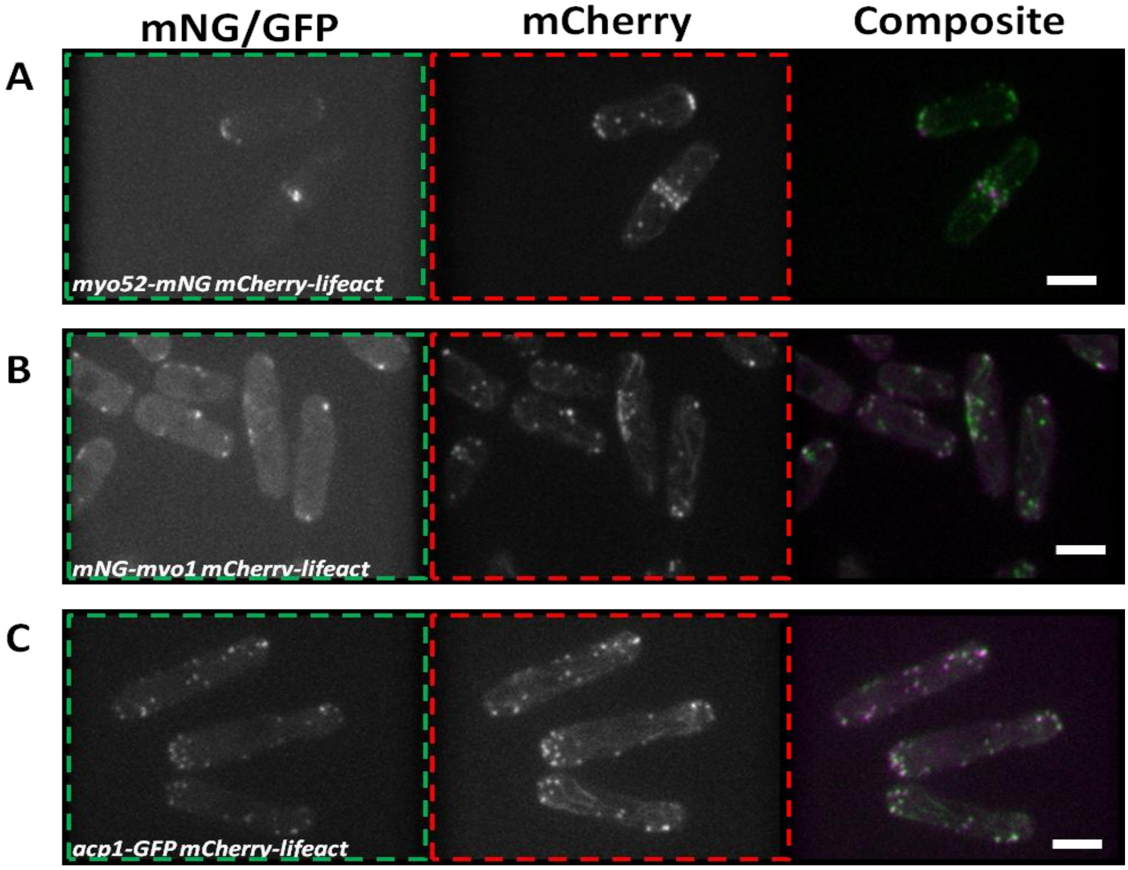

Figure legend on the following page.

**Figure 3.4.2 mNG and mCherry fluorescence, in *S. pombe* strains co-expressing proteins labelled with mNG/GFP and mCherry, were captured simultaneously by the simultaneous two-channel spinning-disk confocal microscope.** Max projection images from two-channel time-lapses of *myo52-mNG mCherry-lifeact*, *mNG-myo1 mCherry-lifeact,* and *acp1-GFP mCherry-lifeact S. pombe.* Images show from left to right: mNG or GFP labelled proteins in the green channel (470 nm); mCherry-Lifeact in the red channel (555 nm); a composite overlay of the images in the green and red channels. mNG and GFP labelled proteins are displayed in green. mCherry-Lifeact is displayed in magenta. The time-lapses were overlaid and aligned manually using Metamorph software to generate composite time-lapses and max projection images.  No channel-to-channel bleed through was observed. **(A)** *myo52-mNG mCherry-lifeact* cells. The cells were exposed to 470 nm at 90 mW power and 555 nm at 20 mW power. 13 z-slices were taken. **(B)** *mNG-myo1 mCherry-lifeact* cells. The cells were exposed to the same light conditions as *myo52-mNG mCherry-lifeact* cells but 7 z-slices were taken. **(C)** *acp1-GFP mCherry-lifeact* cells. The cells were exposed to 470 nm at 15 mW power and 555 nm at 20 mW power. 13 z-slices were taken. All strains were imaged at 25 $^{o}$C. Scale bar - 3.5 µm.

No channel-to-channel bleed-through or significant compromise in image quality was observed during simultaneous acquisition. Signal-to-noise ratios were greater than that observed during wide-field microscopy in all strains however, variation in signal-to-noise ratio between Acp1-GFP, mNG-Myo1 and Myo52-mNG remained unchanged. mNG-Myo52 remained to the emit the weakest signal in this system. mCherry-Lifeact was observed to have the highest signal-to-noise ratio. Background fluorescence was reduced in the composite time-lapses, using the Metamorph background and shading statistical correction function. With this function, a region of a background area was selected with the rectangle tool. Average background intensity was then subtracted from the image. This background removal also reduced mCherry-Lifeact signal, resulting in weak filament signals. The background values subtracted from the image may have been too high. Further work is required to reduce background fluorescence and improve alignment of composite images.

Imaging of *myo52-mNG mCherry-lifeact*, *mNG-myo1 mCherry-lifeact* and *acp1-GFP mCherry-lifeact S. pombe* showed the simultaneous two-channel spinning-disk confocal microscope was capable of simultaneously recording proteins labelled with red and green fluorophores, without channel-to-channel bleed through. Composite time-lapses showing co-movement of mCherry-Lifeact and the GFP and mNG labelled proteins were generated and initial background reduction and alignment was explored. This preliminary testing of the simultaneous two-channel spinning-disk confocal microscope and image processing has provided data to contribute to the development of the system. The system was not used in experiments described in the remainder of thesis because it is still in development but it could enable capture of real-time co-localisation and co-movement of myosins and various proteins they interact with e.g. calmodulin.

## 3.5 Chapter 3 summary

Initial experiments were conducted to determine fluorescence imaging conditions that induce minimal phototoxicity. These conditions were to be applied to subsequent fluorescence microscopy experiments assessing the dynamics of Myo1 and Myo52 in phospho-mutant *S. pombe* during the PhD project.

In this chapter, differences between the phototoxic damaged induced by frequent low intensity light exposure and infrequent high intensity light exposure was investigated in *rlc1-GFP pcp1-GFP S. pombe* ((i) 0.2 mA light every 1 min; (ii) 1.0 mA light every 3 min; (iii) 2.1 mA light every 6 min). Imaging conditions were adjusted to keep the amount of photons the cells were exposed to equal. CAR assembly and constriction were monitored via fluorescence microscopy for 60 min. The GFP intensity along the equatorial plane was measured to follow the constriction of the CAR. The circumference of the CAR was also measured. Disruptions in CAR assembly and constriction were used as indicators of phototoxicity.

Infrequent high intensity light exposure was hypothesised to induce phototoxicity that results in the disruption of CAR assembly and constriction. No correlation between light exposure frequency, intensity and CAR constriction rate was observed (0.20 µm/min, 0.35 µm/min and 0.27 µm/min constriction in the 0.2 mA/1 min, 1.0 mA/3 min and 2.1 mA/6 min light exposure conditions respectively). No structural defects in the CAR were observed with infrequent high intensity light exposure (Figure 3.1.1). Based on these results, exposure to infrequent doses of high intensity light does not induce more phototoxicity that affects CAR assembly or constriction than exposure to frequent doses of low intensity light (Figure 3.1.1, Figure 3.1.2). Phototoxicity was not evident through the assessment of CAR, however it may have been detected through other observations e.g. increasing intracellular $Ca^{2+}$ (Laiusse et al., 2017).

The experiment described above is limited by the number of cells observed as $n = 1$, per imaging condition. A larger sample size would allow for means to be calculated and Student's *t*-test analysis to be conducted to determine significant differences between CAR contraction rates. In future experiments based on CAR, a phototoxicity threshold may be determined. A phototoxicity threshold will determine the imaging range in which phototoxicity is not detected. A dose-response curve can determine the phototoxicity threshold. A dose-response curve can be developed from initially imaging cells with the minimum light exposure and intensity required to visualise the CAR and maintain cell viability. Light exposure and intensity is then increased until phototoxicity in the form of CAR defects is observed (Laiusse et al., 2017). Observations of phototoxicity can be made using imaging conditions above the phototoxicity threshold.

Alongside monitoring of CAR constriction, the degree of phototoxicity in the cells could also be measured by the amount of ROS produced within the cells during exposure to light. Phototoxicity induces the production of ROS. ROS production could be detected during fluorescence microscopy with a ROS-reactive dye called CM-$H_2$DCFDA (5-(and-6)-chloromethyl-2',7'-dichlorodihydrofluorescein diacetate). CM-$H_2$DCFDA is not fluorescent until its acetate group ($C_2H_3O_2^-$) is cleaved by esterases and oxidised by various ROS including $H_2O_2$. This forms fluorescent CM-DCF (chloromethyl-2',7'-dichlorofluorescin). When stained with CM-$H_2$DCFDA, CM-DCF fluorescence would be used as a measure of ROS production during the time-lapses (Oparka et al., 2016; Wojtala et al., 2014). Total CM-DCF intensity may highlight differences in the degree of phototoxicity induced by frequent low intensity light exposure and infrequent high intensity light exposure, which are not apparent in CAR constriction rate.

Phototoxicity is frequently assessed using cell growth rate. Light-induced damage reduces the growth rate of cells. Cell growth can be recorded with time-lapses longer than the 4 hr doubling time of *S. pombe*. The cells can be imaged in a microfludics device, which is a device that provides a constant supply of fresh media to cells (Frey et al., 2015). The cells will be kept viable during the long-term time-lapse. The fresh supply of media would provide the cells with oxygen and reduce the occurrence of ROS production, in response to a lack of oxygen, which would occur in the sealed Bioptechs FCS2 Chamber used in the experiments conducted in this PhD project (Guzy et al., 2007). The cell number is quantified in images from the first and last time point. To quantify cell number, individual cells can be segmented (outlined) in the images and quantified using image analysis software such as PombeX or CellX (Peng et al., 2013), Growth rates can then be determined by the difference in cell number in the first and last time point (Schmidt et al., 2020) and growth rates can be calculated as follows:

$$Growth\ rate = \frac{log_2 \frac{cells_{T_f}}{cells_{T_i}}}{time}$$

$Cells_{Tf}$ is the number of cells at the final time point. $Cells_{Ti}$ is the number of cells at the initial time point. This assessment of cell growth would demonstrate the overall affect of phototoxicity on the cell.

Imaging conditions used to monitor CAR were shown not to impact CAR assembly and constriction. There were then applied to experiments exploring the molecular basis of temperature-sensitivity in TS *cdc8.27* and *cdc8.110 S. pombe* and the impact these mutations have in the actin stabilising function of Cdc8, during CAR assembly and constriction. *cdc8.27* possess C-terminal E129K amino acid substitution and *cdc8.110* possess two N-terminal amino acid substitutions, A18T and E31K. CAR assembly and constriction was monitored in temperature-sensitive *cdc8.27 rlc1-GFP* and *cdc8.110 rlc1-GFP S. pombe* exposed to 0.2 mA light every 1 min. The cells were imaged at a range of permissive and restrictive temperatures (25 °C, 28 °C, 30 °C, 32 °C, 34 °C and 36 °C) to bring about CAR defects induced by the Cdc8 mutations. Structural defects of increasing severity were observed in the CAR with increasing temperature. Defects included aberrant non-contractile rings, CAR displacement, delayed constriction, CAR collapse and the inability to form (Figure 3.2.1, Figure 3.2.3, Figure 3.2.4, Figure 3.2.5). Double septa and bent morphologies were also observed in the cells (Figure 3.2.2). An addictive effect was observed in the *cdc8.110 rlc1-GFP* double mutant since CAR defects were more severe than in *cdc8.27 rlc1-GFP* cells. These defects show Cdc8 E129, Cdc8 A18 and Cdc8 E31 are required for attachment to the cell cortex, correct placement, formation and constriction of the CAR.

In experiments described in this section of the thesis, *cdc8*$^{+}$ *rlc1-GFP* CAR assembly and constriction took approximately 50 min. Similar to experiments in this chapter, published studies monitoring CAR assembly and constriction, with Rlc1-GFP as a marker, have shown CAR assembly and constriction to take ~50 min in healthy wild-type *S. pombe* (Gu et al., 2015; Pollard & Wu, 2010). In future experiments, visualising Pcp1, as in Section

3.1, would help define the stage of CAR assembly and constriction in each cell upon recording. Pcp1 moves between the equatorial plane and the cell ends during CAR assembly. A profile of Rlc1-GFP and Pcp1-GFP dynamics could be made, to define the start of CAR assembly and constriction, by repeating time-lapses of CAR assembly and constriction in *rlc1-GFP pcp1-GFP* cells. In Section 3.1, only one *rlc1-GFP pcp1-GFP* cell was captured during CAR assembly per condition (Figure 3.1.1, Figure 3.1.2). Therefore a profile could not be defined. Transmitted light images were not taken throughout the whole duration of CAR at all temperatures. Transmitted light images would have shown if septa were formed in the cells and if it was positioned correctly. Future experiments should include these images.

Further fluorescence microscopy-based experiments to assess *cdc8.27* and *cdc8.110* could include observations of Mid1-mCherry during CAR constriction in *cdc8.27* and *cdc8.110* cells. Rlc1-GFP in *cdc8.27 rlc1-GFP* and *cdc8.110 rlc1-GFP* cells failed to localise at the equatorial plane and were displaced at restrictive temperatures. Time-lapses of Rlc1-GFP and Mid1-mCherry localisation and interactions during CAR may highlight if displacement of the CARs in *cdc8.27* and *cdc8.110* cells are due to failure to interact with Mid1.

Intensity and photostability of mNG, GFP and 3GFP fluorophores were compared to determine the most suitable fluorophore to label Myo52, and observe Myo52 dynamics in Myo52 phospho-mutant strains. The intensities of Myo52-mNG, Myo52-GFP and Myo52-3GFP foci in *S. pombe* were measured during time-lapses to determine their average intensity and photostability (Figure 3.3.1). The time-lapses showed Myo52-3GFP foci were the brightest with an intensity of 0.78 ± 0.11 a.u. (mean ± SEM). This was greater than Myo52-GFP (0.53 ± 0.04 a.u.) and Myo52-mNG intensities (0.60 ± 0.09 a.u.). The fluorophores were exposed to 50 ms, 0.2 mA light over 399 min in a long-term time-lapse to assess the photostability of the fluorophores. 0.07 a.u., 0.13 a.u. and 0.14 a.u. decreases were observed in Myo52-mNG, Myo52-3GFP and Myo52-GFP average relative intensities respectively. mNG was the most photostable fluorophore and therefore chosen as the fluorophore to label Myo52 in subsequent experiments. Although it is not brighter than 3GFP, mNG exhibited clearer foci than 3GFP. As the dynamics of individual foci were to be assessed in the Myo52 phospho-mutants, mNG would be the preferred fluorophore to visually assess foci over 3GFP.

A simultaneous two-channel spinning-disk confocal microscope, developed by Cairn Research for real-time acquisition of protein co-movement of proteins labelled with fluorophores in the red and green channels, was tested to confirm if the system could acquire red and signal simultaneously without channel-to-channel bleed through. To determine if the red and green fluorophores were detected without channel-to-channel bleed through, time-lapses of Myo52-mNG and mCherry-Lifeact in *myo52-mNG mCherry-lifeact* cells were taken individually. The cells were exposed to either 470 nm light to excite mNG/GFP or 555 nm light to excite mCherry. Fluorescence was only detected in one channel each time. This showed no channel-to-channel bleed through occurred (Figure 3.4.1). *myo52-mNG mCherry-lifeact, acp1-GFP mCherry-lifeact* and *mNG-myo1 mCherry-lifeact* cells were then simultaneously imaged in the red and green channels. The simultaneous two-channel spinning-disk confocal microscope detected and recorded mCherry and mNG or GFP simultaneously. Images in the red and green channels were aligned using Metamorph to develop composite time-lapses displaying co-movement of Myo52-mNG*,* Acp1-GFP and mNG-Myo1 with mCherry-Lifeact (Figure 3.4.2).

Improvements must be made to the image processing needed to produce aligned images with minimal background noise. As there was a great amount of mNG and GFP background fluorescence, background was removed using Metamorph. Average background intensity values were used for background removal. This background removal also reduced mCherry-Lifeact signal. The images were aligned based on the cell shape however, background fluorescence causes difficulties in differentiating between the cell and the background. To reduce background fluorescence in future experiments, minimum background intensity could be subtracted from the images rather than average background intensity. An image of a blank area with no cells may also be used as a separate background image to subtract from the images. Background fluorescence values, in and around the cell, may have been too high and resulted in too much background being removed. Alternatively, a constant intensity value may be subtracted from the images. Transmitted light images could be included in the composite overlay to define an outline of the cell. Transmitted light images cannot be acquired during simultaneous two-channel spinning-disk confocal imaging however they may be acquired before the imaging in the fluorescent channels. Eventual photobleaching was also observed after prolonged imaging of an individual sample. For simultaneous imaging, the exposure time must be set the 100 ms therefore the exposure time cannot be reduced. Light power may be reduced in future experiments which require long-term time-lapses, to reduce the rate of photobleaching.

Future experiments to test the imaging system could compare the dynamics of two co-localising proteins in time-lapses acquired by the simultaneous two-channel spinning-disk microscope system and a standard spinning-disk confocal microscope. Comparison of the time-lapses would reveal a time lag in the dynamics of proteins imaged by the standard spinning-disk confocal and the simultaneous two-channel spinning-disk microscope system. Proteins that co-localise in time-lapses acquired by the simultaneous two-channel spinning confocal system may not co-localise to the same degree in time-lapses acquired by a standard spinning-disk confocal microscope, thus revealing a time lag in image acquisition in thus system.

Once imaging processing is optimised, the simultaneous two-channel confocal microscope system would enable capture of real-time co-localisation and co-movement of proteins labelled with red and green fluorophore. It can be applied to co-localisation experiments of myosin and proteins it interacts with, such as calmodulin. Differences between co-localisation at different stages of the *S. pombe* life cycle could also be studied.

Imaging conditions used in this chapter to minimise phototoxicity were applied to the experiments described in the following chapters. Chapter 4 describes wide-field fluorescence microscopy-based experiments used to assess the dynamics of Myo52 and proteins it interacts with, in Myo52 phospho-mutant *S. pombe* strains. In wild-type *S. pombe*, a serine residue is phosphorylated at Myo52 S720, Myo52 S798, Myo52 S985, Myo52 S1064, Myo52 S1065 and Myo52 S1072 phosphorylation sites. A point mutation in the phospho-mutant strains converts the serine to an alanine. This prevents phosphorylation of the phosphorylation sites. Due to the photostability of mNG described in this chapter, mNG was used to label Myo52 for assessment via fluorescence microscopy.

# Chapter 4: Phospho-regulation of fission yeast myosin V, Myo52

Myo52 is a motor protein present in eukaryotes, which transports cargo, such as secretory vesicles, to the poles of the cells. It transports cargo by travelling along actin filaments in a processive manner. The domains of Myo52 serve different functions when transporting cargo throughout the cell. The N-terminal head domain of Myo52 interacts with actin filaments as the protein travels processively along actin filaments. The neck domain is the location where light chains called calmodulin, bind to Myo52 and regulate the protein by a conformational change in Myo52. The C-terminal tail domain of Myo52 contains the cargo binding domain which bind to the cargo.

Myo52 is involved in the transportation of molecules required for cell growth, actin filament formation and the maintenance and extension of microtubules. For cell growth, Myo52 transports Mok1 and Bgs1/Cps1 which produce glucans that are structural components of the cell wall and the septum formed during cytokinesis (Davison et al., 2016; Motegi et al., 2001; Mulvihill et al., 2001; Mulvihill et al., 2006; Win et al., 2001). Regions of cell growth are determined by proteins of the MOR signalling pathway, which include Orb6, Nak1 and Mor2 (Hirata et al., 2002; Kinai et al., 2005; Tay et al., 2019). Mor2 acts a scaffolding protein that mediates interactions between Orb6 and Nak1. These interactions are required for Orb6 to spatially restrict Cdc42 activation to the cell ends for polarised growth (Gupta, 2013; Das et al., 2009; Tay et al., 2019). For actin filament formation, Myo52 transports actin regulators such as For3. It associates with For3 and delivers it to the cell ends of *S. pombe*, where For3 then nucleates actin filaments. Myo52 translocation along actin filaments may also exert forces which promote the extension of actin filaments (Presti et al., 2012). For the maintenance and extension of microtubules, Myo52 is involved in the release of Tip1 from the end of microtubules and Tip1 ubiquitylation. Tip1 allows microtubules to differentiate between cortical regions of the cell and the cell ends. Microtubules do not undergo catastrophe unless Tip1 is removed. Myo52 associates with Dph1 which targets Tip1 for ubiquitylation (Martin-Garcia & Mulvihill, 2009).

Myo52 S720, Myo52 S798, Myo52 S985, Myo52 S1064, Myo52 S1065 and Myo52 S1072 phospho-serines have been identified as conserved phosphorylation sites along Myo52, via proteomic screening (Tay et al., 2019; Wilson-Grady et al., 2008). To identify the phosphorylation sites, immobilized metal affinity chromatography (IMAC) and titanium dioxide chromatography (TiO2) were used to isolate Myo52 phosphopeptides from proteins of lysed *S. pombe*. The phosphopeptides were analysed by liquid chromatography with tandem mass spectrometry (LC-MS/MS) (Tay et al., 2019; Wilson-Grady et al., 2008). The role the Myo52 phosphorylation sites play, the kinases that phosphorylate them and the regulatory system are unknown. The level of phosphorylation of these sites and whether the phosphorylation is cell cycle dependent is also unknown.

There is a high level of certainty that phosphorylation at the Myo52 phosphorylation sites impact Myo52 function within the cell (Peterson, personal communication, 2017; Wilson-Grady et al., 2008). It has been hypothesised phosphorylation of Myo52 S720, Myo52 S798, Myo52 S985, Myo52 S1064, Myo52 S1065 and Myo52 S1072 affects the function of Myo52. In order to elucidate the function of these specific sites, phospho-mutant *S. pombe* strains were developed via SDM (site-directed mutagenesis). SDM cloning was performed to introduce mutations in the codon for the translation of the phospho-serine using an established marker switching approach and is illustrated in Chapter 2, Figure 2.2 (Baker et al., 2019; MacIver et al., 2003; Martin-Garcia & Mulvihill, 2009). Serine to alanine amino acid substitutions were introduced at the phosphorylation site. Myo52 S720 (TCT) was converted to Myo52 S720A (GCC). Myo52 S798 (AGC) was converted to Myo52 S798A (GCG). Myo52 S985 (TCT) was converted to Myo52 S985A (GCT). As Myo52 serine 1064 and serine 1065 are in close proximity to each other, a *myo52.S1064A S1065A* double mutant strain was generated to determine if an additive effect would occur in the absence of phosphorylation at two phosphorylation sites. Myo52 S1064 and Myo52 S1065 (TCTAGT) were converted to Myo52 S1064A and Myo52 S1065A (GCTGCA). The *myo52.S1072A* plasmid was generated by another member of the Mulvihill lab. The mutations result in the transcription of an alanine instead of a serine. Alanine is an amino acid that cannot be phosphorylated because it does not possess a nucleophilic (–OH) group required for phosphorylation. Therefore the serine to alanine mutation prevents phosphorylation at the site.

The effects of the mutations at the Myo52 phosphorylation sites were studied through observations of the Myo52 phospho-mutants' growth and possible temperature-sensitivity from $OD_{600}$ plate reader readings and fluorescent microscopy observations of the cell morphology, cell polarity, actin filament dynamics, Myo52 dynamics, microtubule dynamics and Mor2 localisation. *mNG-myo52* and *myo52.S1064A S1065A-mNG* were the only clones successfully derived for the observation of Myo52 in the mNG background. Attempts to generate *myo52.S720A-mNG*, *myo52.S798-mNG*, *myo52.S985-mNG* and *myo52.S1072-mNG* cells were unsuccessful.

## 4.1 The absence of Myosin 52 phosphorylation induces growth defects in *S. pombe*

### 4.1.1 Myosin 52 phospho-mutations disrupt growth at log-phase

Myo52 transport organelles within the cell and function in CAR constriction (Mulvihill et al., 2001; Mulvihill et al., 2006). The phospho-mutants were examined to determine whether phosphorylation of serines within Myo52 impact growth. Growth curves were generated via $OD_{600}$ absorbance readings of the phospho-mutants, from early log-phase to late log-phase. The $OD_{600}$ readings were taken as a measure of overall cell growth which is a combination of cell number and cell size. Growth was examined at 20 °C and 25 °C to identify possible temperature-sensitivity (Win et al., 2001). Figure 4.1.1 displays the growth curves generated over 32 - 40 hr.

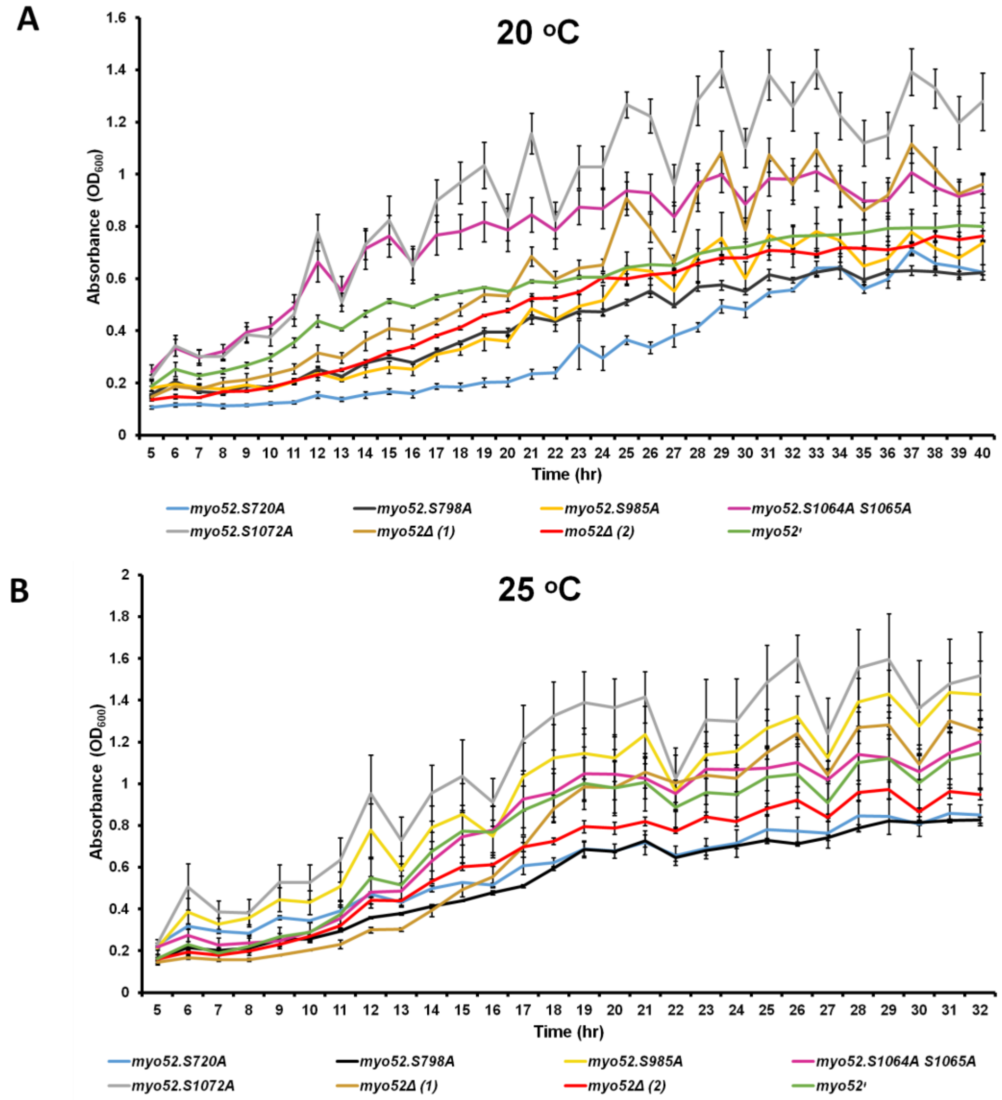

Figure legend on the following page.

**Figure 4.1.1. The lack of Myo52 S720, Myo52 S798 and Myo52 S1072 phosphorylation induces cold-sensitivity at 20 ᵒC in *S. pombe.*** Growth curves of *myo52.S720A, myo52.S798A, myo52.S985A, myo52.S1064A S1065A, myo52.S1072A, myo52Δ* and *myo52$^+$* cells at 20 ᵒC and 25 ᵒC, over 32 hr and 40 hr respectively. $OD_{600}$ readings were used as an indication of overall cell growth (cell size and cell number). **(A)** Growth of the Myo52 phospho-mutant *S. pombe* at 20 ᵒC. Cells displayed slower growth at 20 ᵒC than at 25 ᵒC*. myo52.S720A* and *myo52.S798A* produced an $OD_{600}$ of 0.62 ± 0.03 and 0.62 ± 0.01 (mean ± SEM) respectively, at 40 hr. These $OD_{600}$ were significantly less than wild-type *myo52$^+$* $OD_{600}$ of 0.80 ± 0.05 ($p \leq 0.05$) (Student's *t*-test). *myo52.S985A* and *myo52.S1064A S1065A,* produced $OD_{600}$ of 0.74 ± 0.08 and 0.94 ± 0.07 respectively, at 40 hr. These $OD_{600}$ had no significant difference to wild-type *myo52$^+$* cells. *myo52.S1072A* cells, produced an $OD_{600}$ of 1.28 ± 0.11 and which was significantly greater than the wild-type *myo52$^+$* $OD_{600}$ ($p \leq 0.01$)*.* This indicates the *myo52.S1072A* cells were larger than wild-type *myo52$^+$* cells due to an arrest in the cell cycle*.* **(B)** Growth of the Myo52 phospho-mutant *S. pombe* at 25 ᵒC. At 32 hr, the strains produced the following $OD_{600}$: *myo52.S720A* - 0.85 ± 0.05; *myo52.S798A* - 0.83 ± 0.01; *myo52.S985A* - 1.43 ± 0.16; *myo52.S1064A S1065A* - 1.20 ± 0.15; *myo52.S1072A* - 1.52 ± 0.21; *myo52Δ* (1) - 1.25 ± 0.02; *myo52Δ* (2) - 0.95 ± 0.02; *myo52$^+$* - 1.15 ± 0.17. No significant difference was observed between the $OD_{600}$ of the wild-type *myo52$^+$* strain and the mutant strains. When compared to growth at 20 ᵒC, the data suggests *myo52.S720A, myo52.S798A* and *myo52.S1072A* cells are cold-sensitive at 20 ᵒC. Comparison of $OD_{600}$ readings of the remaining strains at 20 ᵒC and 25 ᵒC suggests the strains are not cold-sensitive. The cells were cultured at 20 ᵒC and 25 ᵒC for 2 days. $OD_{600}$ readings were taken of the cells at the respective temperatures, using a plate reader. Each curve is an average of three independent cultures. The error bars show standard error of the mean (SEM).

In all strains, growth at 20 ᵒC was expected to be slower than at 25 ᵒC. Healthy *S. pombe* typically have a generation time of 4 hr at 25 ᵒC (Peterson & Russell, 2016). Doubling times of approximately 6.5 hr and 4 hr were observed in *myo52$^+$* cells at 20 ᵒC and 25 ᵒC respectively. In comparison to $OD_{600}$ readings at the permissive temperature of 25 ᵒC, *myo52$^+$* $OD_{600}$ readings at the restrictive temperature of 20 ᵒC were lower. At 40 hr and 32 hr, $OD_{600}$ readings of 0.80 ± 0.05 and 1.15 ± 0.17 were recorded in *myo52$^+$* cells at 20 ᵒC and 25 ᵒC respectively. $OD_{600}$ peaks were lessened at 20 ᵒC in all strains. Growth rates were also more linear at 20 ᵒC. These two observations suggest reduced cell growth at 20 ᵒC in *myo52$^+$* cells.

At 20 °C, the $OD_{600}$ of *myo52.S720A* and *myo52.S798A* cells were 0.62 ± 0.03 and 0.62 ± 0.01 (mean ± SEM) respectively, at 40 hr. These were significantly less than the wild-type *myo52*$^+$ $OD_{600}$ ($p \leq 0.05$). The 40 hr $OD_{600}$ of *myo52.S985A* and *myo52.S1064A S1065A* were 0.74 ± 0.08 and 0.94 ± 0.07 respectively and were not significantly different to wild-type *myo52*$^+$. *myo52.S1072A* cells produced an $OD_{600}$ of 1.28 ± 0.11 which was significantly greater than wild-type *myo52*$^+$ ($p \leq 0.01$). These data suggest the *myo52.S1072A* cells were larger than *myo52*$^+$ due to an arrest in the cell cycle. At 25 °C, no significant difference was observed between the $OD_{600}$ of the wild-type *myo52*$^+$ strain and all the mutant strains. Comparisons of growth at 20 °C and 25 °C, suggest *myo52.S720A, myo52.S798A* and *myo52.S1072A* cells are cold-sensitive at 20 °C. The colder temperature may affect the folding of Myo52 or its interactions with actin, calmodulins and cargo.

Through repeated cell counts during culturing of the mutant strains at 25 °C, slower growth was observed in the Myo52 phospho-mutants in comparison to healthy *myo52*$^+$ cells. Therefore, the observed $OD_{600}$ in *myo52.S1072A* cells may be due to increased cell size rather than cell number. Lack of phosphorylation at this phosphorylation site may therefore perturb the maintenance of correct cell shape. An alternative method of quantifying cell growth is required to measure cell growth in future experiments. A Coulter Counter may be used to quantify cell number.

### 4.1.2 Myosin 52 phospho-mutations reduce cell length and alter cell polarity

Myo52 is involved in the transport of alpha-glucan synthase, Mok1, and (1,3) beta-D-glucan synthase catalytic subunit, Bgs1, for cell wall synthesis (Motegi et al., 2001; Mulvihill et al., 2001; Mulvihill et al., 2006; Win et al., 2001). To determine the morphology and changes in the cell wall of the Myo52 phospho-mutants, cell wall glucans were stained with calcofluor and the cells were visualised using fluorescence microscopy (Hamer et al., 2006). Typical cell morphologies for each strain are shown in Figure 4.1.2.

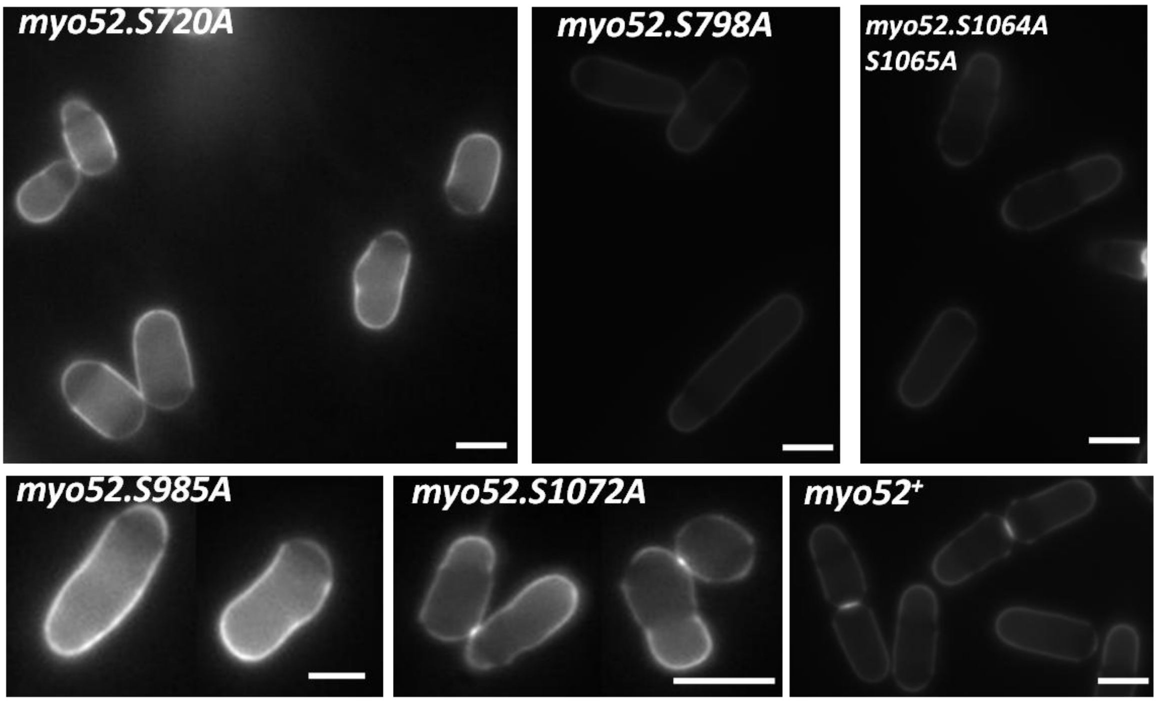

**Figure 4.1.2. Bent morphologies and variations in the cell length of the *S. pombe* Myo52 phospho-mutants show phosphorylation of Myo52 S720, Myo52 S798, Myo52 S985, Myo52 S1064, Myo52 S1065 and Myo52 S1072 is required to maintain correct cell shape, length and polarity in *S. pombe*.** Single z-slice images displaying *myo52.S720A, myo52.S798A, myo52.S985A, myo52.S1064A S1065A, myo52.S1072A* and *myo52*$^+$ *S. pombe* cells stained with calcofluor, to visualise (1, 3) β-D-glucan and cellulose in the septum and cell wall. The lack of phosphorylation at Myo52 S720, Myo52 S798, Myo52 S985, Myo52 S1064, Myo52 S1065 and Myo52 S1072 results in bent morphologies and varied cell length. *myo52.S720A, myo52.S985A,* and *myo52.S1072A* cells displayed shorter morphologies than wild-type *myo52*$^+$ cells. Cells longer than wild-type *myo52*$^+$ were observed in the *myo52.S798A* and *myo52.S1064A S1065A* strains. Bent morphologies were observed in all Myo52 phospho-mutant strains. These morphologies suggest a loss of polarity within the cells. Cells were cultured in YES media supplemented with amino acids for 2 days, at 25 $^{o}$C. They were then fixed with paraformaldehyde and stained with calcofluor on ice. The cells were imaged at 25 $^{o}$C, with an exposure time of 100 ms. A single z-slice was taken. Scale bar - 3.5 μm.

Bent morphologies, not exhibited in healthy *myo52*$^+$ *S. pombe*, were observed in all the phospho-mutant strains. *S. pombe* remain in monopolar growth during interphase and switch to bipolar growth during NETO. The ratio of monopolar and bipolar growth during interphase in calcofluor stained cells was then determined (Cortés et al., 2007). Calcofluor stains cellulose and linear (1, 3) β-D-glucan. Differences between the monopolar-to-bipolar ratio of wild-type *myo52*$^{+}$ cells and the Myo52 phospho-mutants were use used to identify if phosphorylation of Myo52 S720, Myo52 S798, Myo52 S985, Myo52 S1064, Myo52 S1065 and Myo52 S1072 plays a role in maintaining polarity within *S. pombe*.

Calcofluor staining allows for the visualisation of points of growth termed birth scars. They appear as dark bands across calcofluor stained cells. Birth scars form where septa from previous cell divisions were located. Mature septa are composed of three layers. The layers consist of an inner primary septum layer with secondary septa layers either side of it. The structure of the septum is displayed in Figure 4.1.3A. The secondary septa, that become part of the cell wall and the new ends after cell separation, bind to less calcofluor than the primary septum, and regions of the cell wall synthesised during interphase. This is because cellulose and linear (1,3) β-D-glucan are predominantly in the primary septum and the cell wall. Therefore, the cell wall formed from a secondary septum appears as a dark cap at the new end of a calcofluor stained cell (Sipiczki, 2007). The dark cap remains at the new end until the cell begins NETO. Newly synthesised cell wall pushes the birth scar back within the cells as growth occurs laterally at the new end (Mitchison & Nurse, 1985). The position of birth scars can indicate where cell division has previously occurred, the cell end where growth has occurred and the direction of the growth. Therefore, observations of birth scars can determine the polarity of a cell.

A dark cap in a calcofluor stained cell shows the new end of the cell. A cell with a dark cap at one end and no other birth scars is monopolar because growth has only occurred at the old of the cell. A cell with a birth scar in the central region of the cell is bipolar because cell growth has occurred at both ends of the cell and the birth scar to been pushed to the middle of the cell by the newly synthesised cell wall. The number of monopolar cells and bipolar cells was manually quantified in a sample of each Myo52 phospho-mutant strain. Monopolar-to-bipolar ratios of each strain was calculated and are shown in Figure 4.1.3

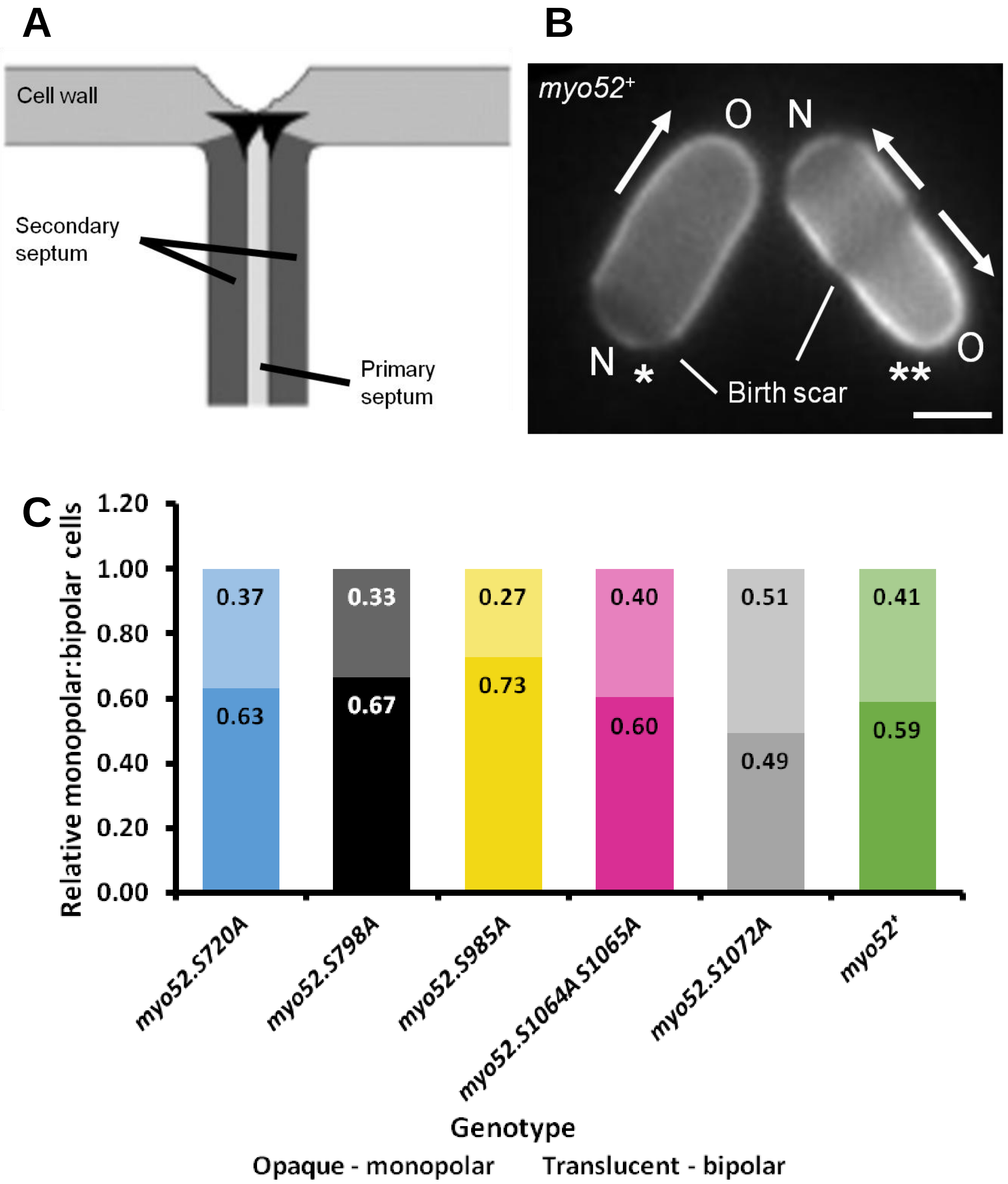

Figure legend on the following page.

**Figure 4.1.3. Variation in the relative monopolar-to-bipolar cell ratio of the Myo52 phospho-mutant *S. pombe* cells suggests phosphorylation of Myo52 S720, Myo52 S798, Myo52 S985 and Myo52 S1072 is involved in maintaining correct cell polarity in *S. pombe.*** **(A)** Illustration of the septum of a dividing cell. The septum is made up of a single primary septum and two secondary septa. Calcofluor stains secondary septum less than primary septum. Adapted from Sipiczki (2007). **(B)** Image of wild-type *myo52*$^+$ *S. pombe* stained with calcofluor*.* Dark bands in the calcofluor staining are termed birth scars. Birth scars mark regions where the secondary septum, from the previous cell division, was formed. Cells with a birth scar at the 'new end' of the cell, and have the appearance of a dark cap, were considered monopolar (*). Cells with at least one birth scar in between the cell ends were considered bipolar (**). 'O' indicates the old end. 'N' indicates the new end. The arrows illustrate the direction of growth. Cells were cultured in YES media supplemented with amino acids for 2 days, at 25 °C. They were then fixed with paraformaldehyde and stained with calcofluor on ice. The cells were imaged at 25 °C, with an exposure time of 100 ms. A single z-slice was taken. Scale bar - 3.5 μm. **(C)** Bar chart displaying the relative monopolar-to-bipolar cell ratio of *myo52.S720A, myo52.S798A, myo52.S985A, myo52.S1064A S1065A, myo52.S1072A* and wild-type *myo52*$^+$ calcofluor stained *S. pombe* cells. The number of the monopolar cells and bipolar cells were manually quantified and made relative to the total number of cells. The monopolar-to-bipolar ratio was calculated from the relative number of monopolar and bipolar cells. The opaque portions at the bottom of the bars represent the relative number of monopolar cells. The translucent portions at top of the bars represent the relative number of bipolar cells. The number in each bar is the relative number of cells for the corresponding category. These numbers make up the terms of the ratio. The monopolar-to-bipolar ratio of the wild-type *myo52*$^+$ cells was 0.59:0.41. The monopolar-to-bipolar ratios of *myo52.S720A, myo52.S798A* and *myo52.S985A* were 0.63:0.37, 0.67:0.33 and 0.73:0.27 respectively. These ratios have 4 %, 8 % and 14 % differences to the wild-type *myo52*$^+$ monopolar-to-bipolar ratio*.* A larger proportion of cells in these strains were monopolar than wild-type *myo52*$^+$*. myo52.S1064A S1065A* displayed a monopolar-to-bipolar ratio of 0.60:0.40 which was similar to wild-type *myo52*$^+$ cells*. myo52.S1072A* displayed a monopolar-to-bipolar ratio of 0.49:0.51 and a 10 % difference to the *myo52*$^+$ monopolar-to-bipolar ratio. Therefore a smaller proportion of *myo52.S1072A* cells were monopolar than *myo52*$^+$. *n* ≥ 67. '*n'* indicates the number of cells measured from each strain.

As this experiment was not repeated, further work is required to determine the significance in the differences between the monopolar-to-bipolar ratios, however the variation can provide an indication in the differences. *myo52*$^+$ cells had an approximate relative monopolar-to-bipolar ratio of 0.59:0.41. A larger portion of *myo52.S720A, myo52.S798A, myo52.S985A* cells were under monopolar growth with respective relative monopolar-to-bipolar ratios of 0.63:0.37, 0.67:0.33 and 0.73:0.27 which have a 4 %, 8 % and 14 % difference to the *myo52*$^+$ monopolar-to-bipolar ratio*. myo52.S1072A* cells displayed a monopolar-to-bipolar ratio of 0.49:0:0.51 and a 10 % decrease in the monopolar cells. The *myo52.S1064A S1065A* monopolar-to-bipolar ratio was 0.60:0.40 and was comparable to *myo52*$^+$ (1 *%* difference) Collectively, the data suggest the switching between monopolar and bipolar growth is altered uniquely within each Myo52 phospho-mutant background. Myo52 S720, Myo52 S798 and Myo52 S985 phosphorylation may play a regulatory role in the initiation of bipolar growth at NETO. Myo52 S1072 phosphorylation may play an inhibitory role to in the regulation of bipolar growth at NETO. Myo52 S1064 S1065 phosphorylation may have minimal or no impact on the regulation of bipolar growth at NETO.

Cell lengths were also measured from the calcofluor stained images. Cells both longer and shorter than *myo52*$^+$ cells were observed in the phospho-mutant strains (Figure 4.1.2). Cell lengths were measured, using Metamorph imaging analysis software, to identify possible consistent differences in cell length between the mutant strains. Figure 4.1.4 displays the measured cell lengths.

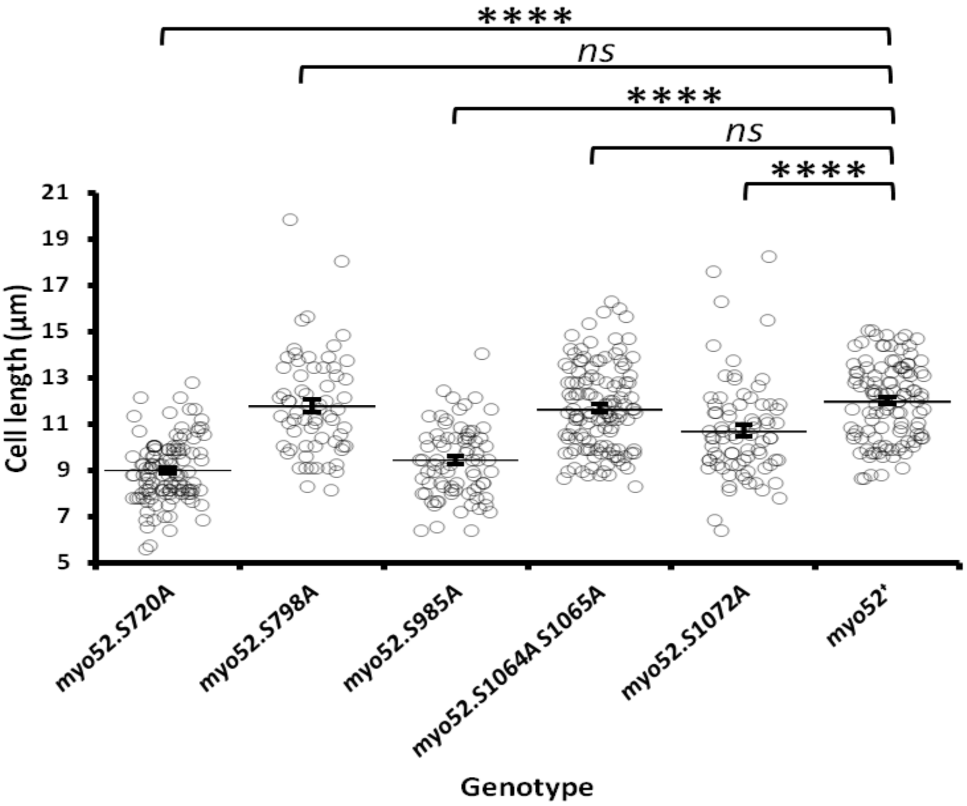

**Figure 4.1.4. Variation in the length of the Myo52 phospho-mutant *S. pombe* cells show phosphorylation of Myo52 S720, Myo52 S985 and Myo52 S1072 is involved in determining cell length in *S. pombe.*** Dot plot displaying Myo52 phospho-mutant mean cell length. Error bars represent standard error of the mean (SEM). Student's *t*-tests were used to determine significant differences between the length of the Myo52 phospho-mutants and *myo52*$^{+}$ cells*.* The average length of *myo52.S720A* (8.99 ± 0.13 µm), *myo52.S985A* (9.44 ± 0.18 µm) and *myo52.S1072A* cells (10.72 ± 0.24 µm) were significantly shorter than the average length of wild-type *myo52*$^{+}$ cells (12.00 ± 0.16 µm) (mean ± SEM) ($p \leq 0.0001$). The average length of *myo52.S798A* (11.80 ± 0.27 µm) and *myo52.S1064A S1065A* cells (11.68 ± 0.16 µm) were not significantly greater than the average length of *myo52*$^{+}$ cells*.* ****$p \leq 0.0001$. '*ns*' denotes the difference is not statistically significant (Student's *t*-test). Cell lengths were measured from images of calcofluor stained cells. Cells were cultured in YES media supplemented with amino acids for 2 days, at 25 °C. They were then fixed with paraformaldehyde and stained with calcofluor on ice. To be imaged, the calcofluor stained cells were exposed to 100 ms at 25 °C. A single z-slice was taken. The line tool in the Metamorph image analysis software was used to measure the cell lengths. $n \geq 67$. '*n*' indicates the number of cells measured from each strain.

*myo52*$^+$ cells measured at 12.00 ± 0.16 μm (mean ± SEM) long. *myo52.S720A, myo52.S985A* and *myo52.S1072A* cells were observed to be significantly shorter than *myo52*$^+$ cells with average lengths of 8.99 ± 0.13 μm, 9.44 ± 0.18 μm and 10.72 ± 0.24 μm respectively ($p \leq 0.0001$). *myo52.S798A* and *myo52.S1064A S1065A* cells measured to be 11.80 ± 0.27 μm and 11.68 ± 0.16 μm in length respectively, and similar to that of *myo52*$^+$ cells. Therefore, these data suggest *myo52.S720A, myo52.S985A* and *myo52.S1072A* cells to exhibit reduced longitudinal cell growth due to the lack of phosphorylation at the corresponding phosphorylation sites. The movement of Myo52 along actin filaments, which induces force required for actin polymerisation towards the cell ends, may be hindered by the lack of phosphorylation at Myo52 phosphorylation sites. This could subsequently hinder the localisation Mor2 to the cell ends. MOR signalling network components will not be complexed by Mor2. Therefore, Cdc42 activation and the positioning of growth zones may also be reduced.

## 4.2 Myosin 52 phosphorylation is required for correct localisation and motility of actin structures but not microtubules in *S. pombe*

### 4.2.1 Correct actin localisation and dynamics are disrupted in the Myo52 phospho-mutants

Myo52 function is notably dependent on the assembly of the cytoskeleton. Correct formation of actin filaments allows Myo52 to translocate throughout the cell and carry various cargoes to their intended location. Lifeact-GFP dynamics in the phospho-mutant backgrounds was recorded to determine if Myo52 phosphorylation, which has been shown to impact the maintenance of cell shape, had knock-on effects on actin structures. Lifeact, a short peptide which binds to actin microfilaments, was used as a marker to visualise actin structures (Riedl et al., 2008). Figure 4.2.1 displays Lifeact-GFP localisation and dynamics within the Myo52 phospho-mutants.

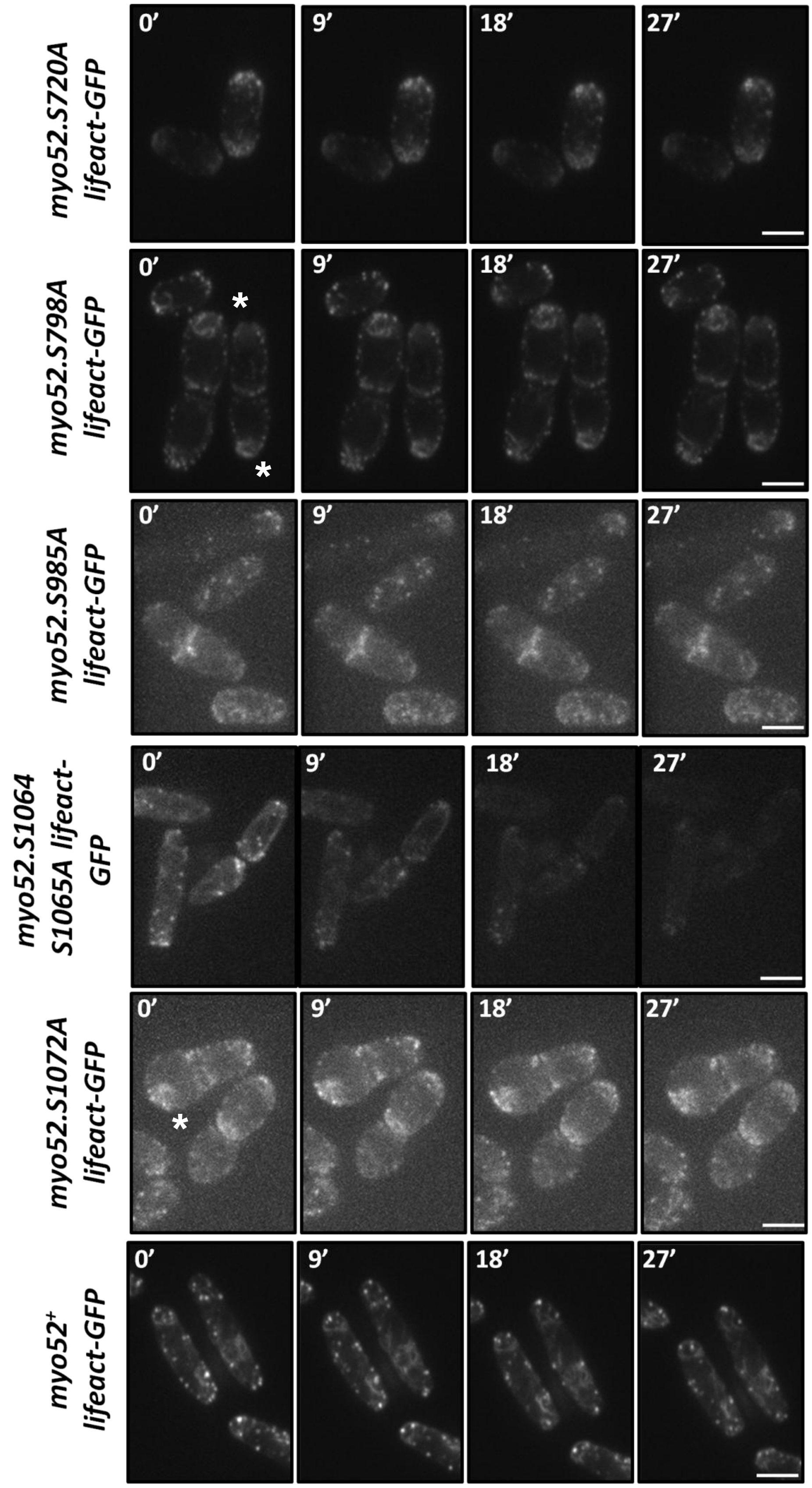

Figure legend on the following page.

**Figure 4.2.1. A lack of Myo52 S720, Myo52 S798, Myo52 S985 and Myo52 S1072 phosphorylation causes actin patches to delocalise and disrupts actin filament polymerisation in *S. pombe.*** Max projections from time-lapses of Lifeact-GFP dynamics in *myo52.S720A lifeact-GFP, myo52.S798A lifeact-GFP*, *myo52.S985A lifeact-GFP*, *myo52.S1064A S1065A lifeact-GFP*, *myo52.S1072A lifeact-GFP* and *myo52$^+$ lifeact-GFP S. pombe*. In all Myo52 phospho-mutants except *myo52.S1064A S1065A*, Lifeact-GFP foci were smaller and greater in quantity than in wild-type *myo52$^+$ lifeact-GFP,* suggesting delocalisation of actin patches in those strains. Less actin filaments were also observed in the mentioned Myo52 phospho-mutant strains. The filaments that were observed appeared curled at the end of the cells and do not extend into the cell. '*' indicates curled actin filaments. These observations suggest actin filament polymerisation is disrupted in the mentioned Myo52 phospho-mutant strains. Cells were cultured in EMMG media supplemented with amino acids for 2 days, at 25 °C. The cells were imaged over 55 s. 11 z-slices were taken of cells incubated at 25 °C, with an exposure time of 50 ms. Scale bar - 3.5 µm.

An elongated morphology was observed in wild-type *myo52$^+$* cells. The Lifeact-GFP labelled Myo52 phospho-mutant cells exhibited a plump and rounded morphology, not observed in the calcofluor stained cells. This morphology is likely to be due to the Lifeact labelling which impacts actin function (Courtemanche et al., 2016; Flores et al., 2019). Actin patches in all Myo52 phospho-mutants, except *myo52. S1064A S1065A lifeact-GFP,* were smaller and greater in quantity in comparison to wild-type *myo52$^+$* cells. This observation suggests delocalisation of actin patches in the *myo52.S720A lifeact-GFP, myo52.S798A lifeact-GFP*, *myo52.S985A lifeact-GFP* and *myo52.S1072A lifeact-GFP* strains. Less actin filaments were observed in the mentioned Myo52 phospho-mutant strains. The filaments that were observed were curled and situated only at the end of the cell, suggesting actin filament polymerisation is disrupted in the mentioned Myo52 phospho-mutant strains. Therefore the phosphorylation of Myo52 S720, Myo52 S798, Myo52 S985 and Myo52 S1072 is suggested to be required for correct localisation of actin patches and polymerisation of actin filaments. Significant photobleaching was only observed in *myo52.S1064A S1065A* cells and was likely to be an indication of poor viability. Actin patch localisation in this strain was comparable to wild-type *myo52$^+$* and filaments were also observed in this strain. These observations suggest Myo52 S1064 S1065 phosphorylation does not impact the ability of actin to localise into actin patches or polymerise into filaments.

By eye, Lifeact-GFP foci movement appeared less mobile in the phospho-mutants than the continuous movement in *myo52*$^{+}$ cells. To confirm the lack of Lifeact-GFP movement in the phospho-mutants, kymographs were generated. Lifeact-GFP speeds were calculated by measuring foci movement in the x direction (distance) and in the y direction (time), using the segmented line tool in the Metamorph image analysis software. The kymographs and dot plots displaying the speed of Lifeact-GFP in the Myo52 phospho-mutants are shown in Figure 4.2.2.

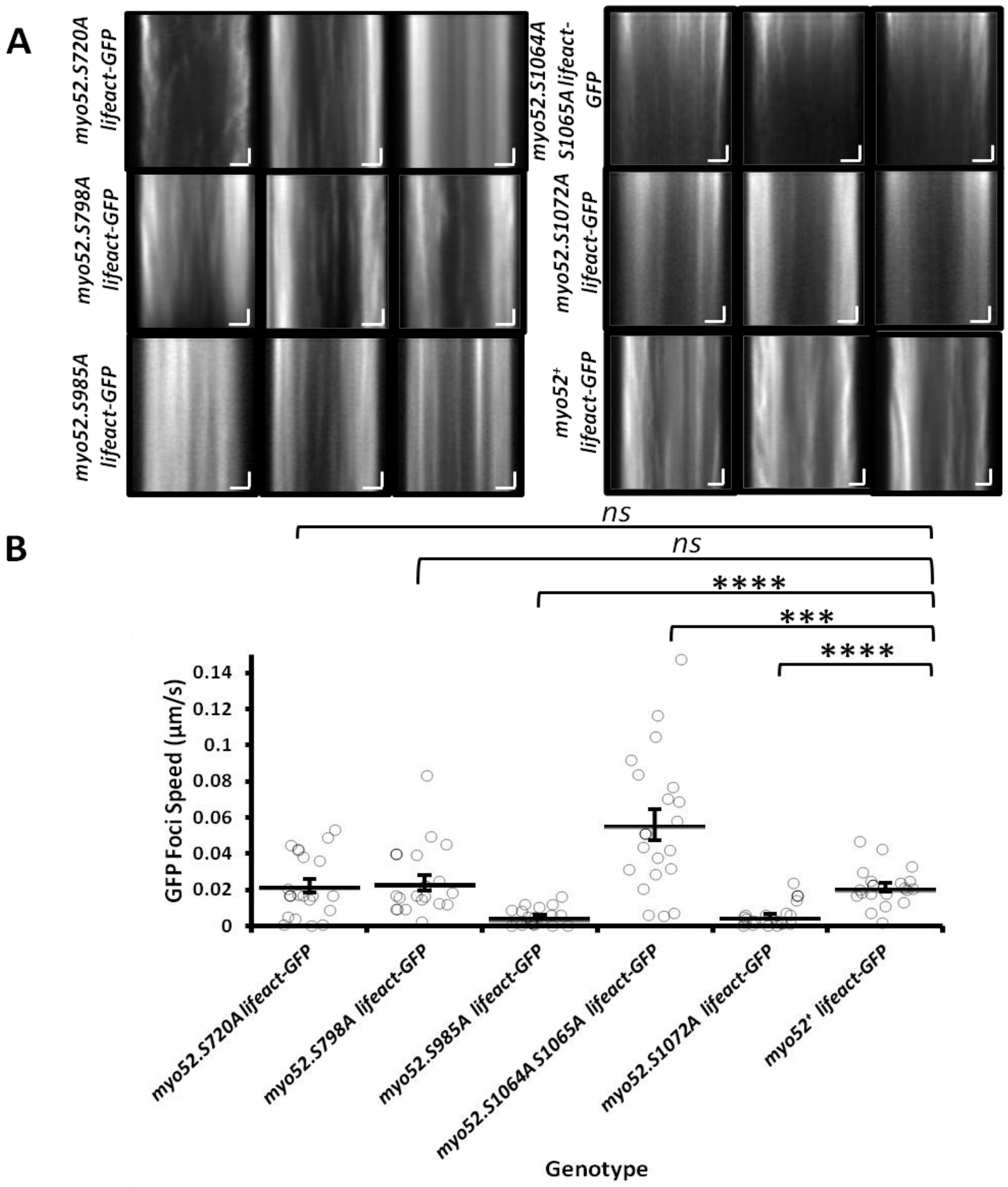

Figure legend on the following page.

**Figure 4.2.2. Altered Lifeact-GFP motility in the Myo52 phospho-mutant *S. pombe* shows phosphorylation of Myo52 S985 and Myo52 S1064, Myo52 S1065 and Myo52 S1072 is involved in regulating actin motility in *S. pombe.* (A)** Kymographs displaying dynamics of Lifeact-GFP in Myo52 phospho-mutants and *myo52*$^+$ cells over 55 s. Lateral movements of Lifeact-GFP foci are shown by the horizontal direction in the signal lines. No lateral movement is shown by straight Lifeact-GFP signal lines. A lack of Lifeact-GFP movement was observed more frequently in the Myo52 phospho-mutant cells than in wild-type *myo52*$^+$ cells. GFP signal reduced with time in *myo52.S1064A S1065A* cells due to bleaching of GFP. The kymographs were generated using Metamorph. Horizontal scale bar (distance) - 2 µm. Vertical scale bar (time) - 5.5 s. **(B)** Dot plot displaying the speed of Lifeact-GFP lateral movement in the Myo52 phospho-mutants. Error bars represent standard error of the mean (SEM). Student's *t*-tests were used to determine significant differences between the speeds of Lifeact-GFP in the Myo52 phospho-mutants and wild-type *myo52*$^+$ cells*.* The average speed of Lifeact-GFP in *myo52.S985A* (0.005 ± 0.001 µm/s) and *myo52.S1072A* (0.005 ± 0.001 µm/s) (mean ± SEM) respectively, were significantly slower than the speed of Lifeact-GFP in wild-type *myo52*$^+$ cells (0.021 ± 0.002 µm/s). Lifeact-GFP in *myo52.S1064A S1065A* (0.561 ± 0.008 µm/s) was measured to be significantly faster than in wild-type *myo52*$^+$ cells*.* The average speed of Lifeact-GFP in *myo52.S720A* (0.022 ± 0.003 µm/s) and *myo52.S798A* (0.024 ± 0.004 µm/s) were not significantly different to Lifeact-GFP in *myo52*$^+$*.* *** $p \leq 0.001$, **** $p \leq 0.0001$. '*ns*' denotes the difference is not statistically significant (Student's *t*-test). Cells were cultured in EMMG media supplemented with amino acids for 2 days, at 25 $^o$C. To be imaged, the cells were exposed to 50 ms at 25 $^o$C. 11 z-slices were taken to capture the images. To measure the Lifeact-GFP speed from the kymographs in (A), the segmented line tool in the Metamorph image analysis software was used to outline the foci movement. The lengths of the signal lines, measured in the x direction (distance) and y direction (time), were used to calculate the speed of the foci. $n \geq 20$. '*n'* indicates the number of Lifeact-GFP foci measured from each strain.

Actin patches move at 0.32 µm/s and have lifetimes of approximately 2 min (Pelham & Chang, 2001). In these experiments, the average speed of Lifeact-GFP lateral movement in *myo52*$^+$ cells was measured to be 0.021 ± 0.002 µm/s (mean ± SEM), based on kymographs of Lifeact-GFP motility. Lifeact-GFP in *myo52.S985A* and *myo52.S1072A* was 0.005 ± 0.001 µm/s and 0.005 ± 0.001 µm/s respectively and were significantly slower than Lifeact-GFP in wild-type *myo52*$^+$cells ($p \leq 0.0001$). The average speed of Lifeact-GFP lateral movement in *myo52.S1064A S1065A* was 0.561 ± 0.008 µm/s was therefore significantly faster than in *myo52*$^{+}$ ($p \leq 0.001$). The average speed of Lifeact-GFP lateral movement in *myo52.S720A* and *myo52.S798A* were measured to be 0.022 ± 0.003 μm/s and 0.024 ± 0.004 μm/s respectively, and therefore were not significantly different to Lifeact-GFP in wild-type *myo52*$^{+}$ cells. Long Lifeact-GFP foci lifetimes of more than 5 min in all the phospho-mutant kymographs suggest a lack of Lifeact-GFP lateral movement and activity. Lifeact-GFP foci distribution in the strains was not altered in the phospho-mutant cells, as foci were seen to localise along the CAR, cell periphery and cell ends. Therefore, the data suggests the absence of Myo52 phosphorylation at Myo52 S985 and Myo52 S1072 results in the disruption of actin motility. As a greater range of Lifeact-GFP speeds were observed in *myo52.S1064A S1065A,* the absence of phosphorylation at Myo52 S1064 and Myo52 S1065 may result in a loss of actin motility regulation.

### 4.2.2 Microtubules in the Myo52 phospho-mutants have no morphological defects

Myo52 is involved in the governance of microtubule dynamics by regulating catastrophe at cell ends and turnover of the microtubule regulator, tip elongation protein, Tip1 (Martin-Garcia & Mulvihill, 2009). To determine if Myo52 phosphorylation at the sites of interest impact microtubules dynamics, α-tubulin, *GFP-atb2* strains were generated in the Myo52 phospho-mutant backgrounds. Figure 4.2.3 displays GFP-Atb2 dynamics within the Myo52 phospho-mutants.

All strains, including wild-type *myo52*$^{+}$ cells, were of a shorter morphology. Cells were also circular and segmented. Wild-type *myo52*$^{+}$ cells did not possess healthy wild-type morphology and were not used as a healthy positive control. Despite this, the microtubules observed in *myo52.S720A, myo52.S798A, myo52.S985A, myo52.S1064A S1065A, myo52.S1072A* and wild-type *myo52*$^{+}$ *S. pombe* did not display morphological defects (Sato et al., 2009). These observations suggest phosphorylation of Myo52 S720, Myo52 S798, Myo52 S985, Myo52 S1064, Myo52 S1065 and Myo52 S1072 play no regulatory role in the function of Myo52 in the release of Tip1 from the ends of microtubules and its proteolysis.

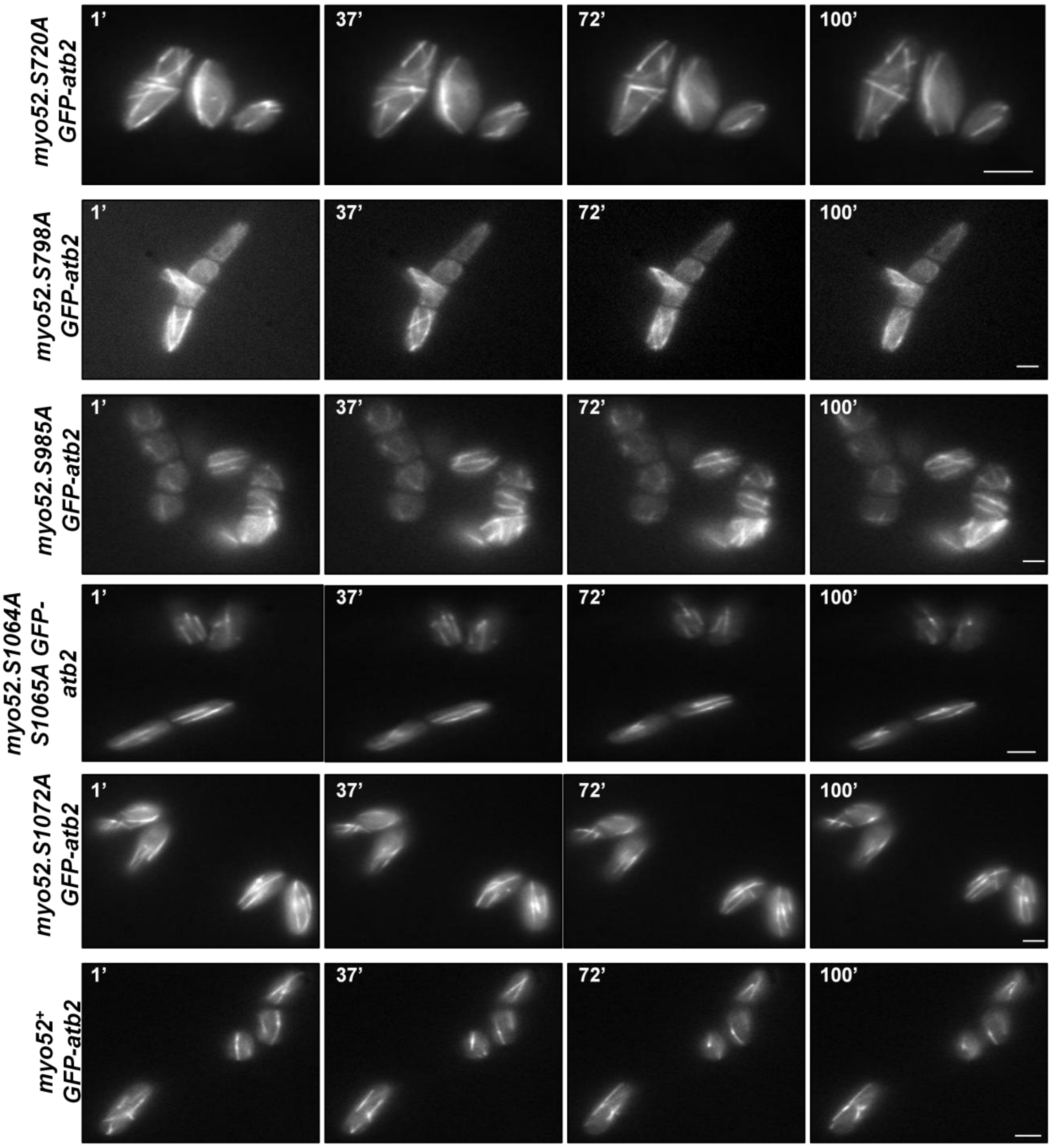

**Figure 4.2.3. Microtubules in the *S. pombe* Myo52 phospho-mutants do not display defects in structure or dynamics.** A montage of max projections from time-lapses of GFP-Atb2 dynamics in *myo52.S720A GFP-atb2, myo52.S798A GFP-atb2, myo52.S985A GFP-atb2, myo52.S1064A S1065A GFP-atb2, myo52.S1072A GFP-atb2* and *myo52*$^{+}$ *GFP-atb2 S. pombe* cells over 100 s. The microtubules in the Myo52 phospho-mutants were dynamic and elongated towards the cell edges. Despite no microtubule defects being observed, the cells displayed segmented and circular morphologies. Cells were cultured in EMMG media supplemented with amino acids for 2 days, at 25 $^{o}$C. The cells were imaged over 100 s. 11 z-slices were taken of cells incubated at 25 $^{o}$C, with an exposure time of 100 ms. Scale bar - 2 μm.

## 4.3 Myosin 52 dynamics is reduced in the absence of Myo52 S1064 and Myo52 S1065 phosphorylation

To examine how phosphorylation impacts Myo52 motility, Myo52 was labelled with the bright fluorescent protein, mNeongreen (mNG). Myo52 was successfully labelled with mNG in wild-type *myo52*$^+$ and *myo52.S1064A S1065A* cells to make *Myo52-mNG* and *myo52.S1064A S1065A-mNG* cells. The cells were cultured in EMMG at 25 °C and Myo52 localisation and movements were examined. Dynamics were recorded and Figure 4.3 displays example images, kymographs and a dot plot displaying the speed of Myo52-mNG foci.

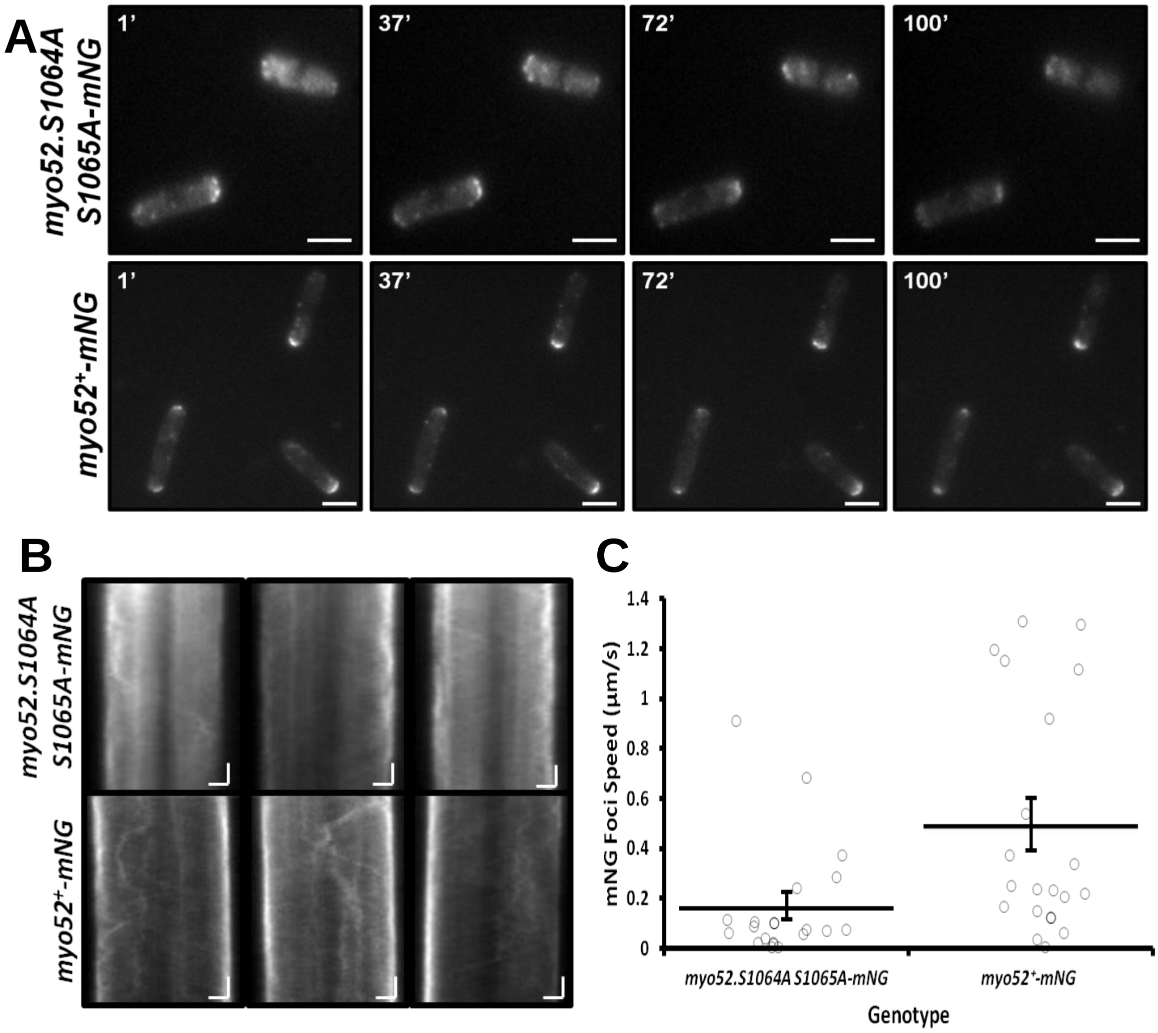

Figure legend on the following page.

**Figure 4.3. Reduced Myo52-mNG motility in *myo52.S1064A S1065A-mNG S. pombe* shows phosphorylation of Myo52 S1064 and Myo52 S1065 is involved in regulating Myo52 motility in *S. pombe.*** **(A)** Max projections taken from time-lapses displaying Myo52-mNG in *myo52.S1064A S1065A-mNG* and wild-type *myo52$^+$-mNG S. pombe*. Cells were cultured in EMMG media supplemented with amino acids for 2 days, at 25 °C. 13 z-slices were taken of cells incubated at 25 °C, with an exposure time of 50 ms, over 65 s. Scale bar - 3.5 µm. **(B)** Kymographs displaying dynamics of Myo52-mNG in *myo52.S1064A S1065A-mNG* and *myo52$^+$-mNG* cells over 65 s. Immotile Myo52-mNG foci in *myo52.S1064A S1065A-mNG* cells are shown by straight Myo52-mNG signal lines. Motile Myo52-mNG foci are shown by the horizontal direction in the signal lines. Immotile Myo52-mNG foci were observed more frequently in *myo52.S1064A S1065A-mNG* cells than in *myo52$^+$-mNG* cells. Horizontal scale bar (distance) - 2 µm. Vertical scale bar (time) - 6.5 s. The kymographs were generated using Metamorph image analysis software. **(C)** Dot plot displaying the speed of Myo52-mNG in the *myo52.S1064A S1065A-mNG* and *myo52$^+$-mNG S. pombe.* Error bars represent standard error of the mean (SEM). Student's *t*-tests were used to determine significant differences between the speed of Myo52-mNG in *myo52.S1064A S1065A-mNG* and *myo52$^+$-mNG.* The average speed of Myo52-mNG in *myo52.S1064A S1065A-mNG* (0.17 ± 0.05 µm/s) was significantly slower than the average speed of Myo52-mNG in *myo52$^+$-mNG* (0.50 ± 0.11 µm/s) (mean ± SEM) ($p \leq 0.01$). To measure the Myo52-mNG speed from the kymographs in (B), the segmented line tool in the Metamorph image analysis software was used to outline the foci movement. The lengths of the signal lines measured in the x direction (distance) and y direction (time) were used to calculate the speed of the foci. $n \geq 20$. '*n*' indicates the number of Myo52-mNG foci measured from each strain.

Myo52 moves at 0.5 – 2 µm/s in *S. pombe* (Li et al., 2018). In these experiments, the average speed of Myo52-mNG in *myo52$^+$-mNG* cells was measured to be 0.50 ± 0.11 µm/s (mean ± SEM), based on kymographs of Myo52-mNG motility. Myo52-mNG in *myo52.S1064A S1065A-mNG* was 0.17 ± 0.05 µm/s and was significantly slower than Myo52-mNG in *myo52$^+$-mNG* cells ($p \leq 0.01$). Myo52-mNG foci distribution in *myo52.S1064A S1065A-mNG* was not altered, as foci were seen to localise along the CAR, throughout the length of the cells and cell ends. Therefore, these data suggest the absence of Myo52 phosphorylation at Myo52 S1064 and Myo52 S1065 results in reduced Myo52 motility.

## 4.4 The absence of phosphorylation at Myo52 S1064 and Myo52 S1065 does not impact Mor2 localisation

Mor2, a *S. pombe* Furry-like protein, is needed for polarised cell growth. It is associated to actin and localises at the cell ends and where septation occurs. Localisation of Mor2 and microtubules at these sites are dependent on one other. There is interplay between Mor2 and microtubules through a microtubule end factor, Tip1 (Hirata et al., 2002). CLIP170-like protein, Tip1, localises at the distal tips of the microtubules which polymerise towards the ends of *S. pombe* cells. Tip1 is required for microtubules to distinguish between the cell ends and cortical regions and also prevents microtubule catastrophe at the cell ends until it dissociates from the microtubules (Brunner & Nurse, 2000). Tip1 targets growth zones to guide microtubules to the cell ends. Microtubule targeting regions diffuse from the cell ends in *mor2-282* mutants at 36 °C however in such conditions, Tip1 remains associated with microtubules. Such observations suggest Mor2 is involved in the positioning of growth zones, targeted by Tip1 (Hirata et al., 2002).

For normal microtubule depolymerisation to occur in *S. pombe,* Myo52 modulates Tip1 localisation and facilitates its ubiquitin-dependent proteolysis, causing the latter by increasing Tip1 removal from microtubule ends and interacting with ubiquitin receptor Dph1 to claim Tip1 for degradation (Martín-García & Mulvihill, 2009). To determine if Myo52 phosphorylation bears importance in the localisation and in turn function of Mor2, *GFP-mor2* strains were generated in the *myo52.S1064A S1065A* phospho-mutant background to produce *myo52.S1064A S1065A GFP-mor2 S. pombe.* At the same time, Mor2 localisation was compared to *myo52-1 GFP-mor2* and *myo52Δ GFP-mor2* mutant strains. Myo52-1 has a mutation within the N-terminus of the motor domain and was used to compare the absence of Myo52 S1064 and Myo52 S1064 phosphorylation with the absence of a functioning Myo52 motor head domain (Martín-García & Mulvihill, 2009). Figure 4.4 displays GFP-Mor2 in *myo52.S1064A S1065A GFP-mor2, myo52-1 GFP-mor2, myo52Δ GFP-mor2* and *myo52*$^+$ *GFP-mor2* cells, visualised via fluorescence microscopy.

In *myo52.S1064A S1065A GFP-mor2* cells, GFP-Mor2 localised at both cell ends and was comparable to that of GFP-Mor2 in *myo52*$^+$ *GFP-mor2* cells*.* Large GFP-Mor2 foci, assumed to be GFP-Mor2 aggregates, were also observed throught the cells of the Myo52 phospho-mutant strain. In *myo52-1 GFP-mor2* cells, GFP-Mor2 was dispersed throughout the cells and along the CAR. It was not observed at the cells ends to the extent GFP-Mor2 in *myo52⁺ GFP-mor2* cells and *myo52.S1064A S1065A* cells did. Therefore the data collectively suggest Myo52 is not the lone protein required for the localisation of Mor2 to the cell ends and phosphorylation of Myo52 S1064 and Myo52 S1065 is also not required. Motor domain activity is required for the Mor2 localisation however localisation is not severely impacted by Myo52 S1064 and Myo52 S1065 phosphorylation. The Myo52 phospho-mutant data indicates Myo52 S1064 and Myo52 S1065 have a regulatory role rather than are dependent for localisation.

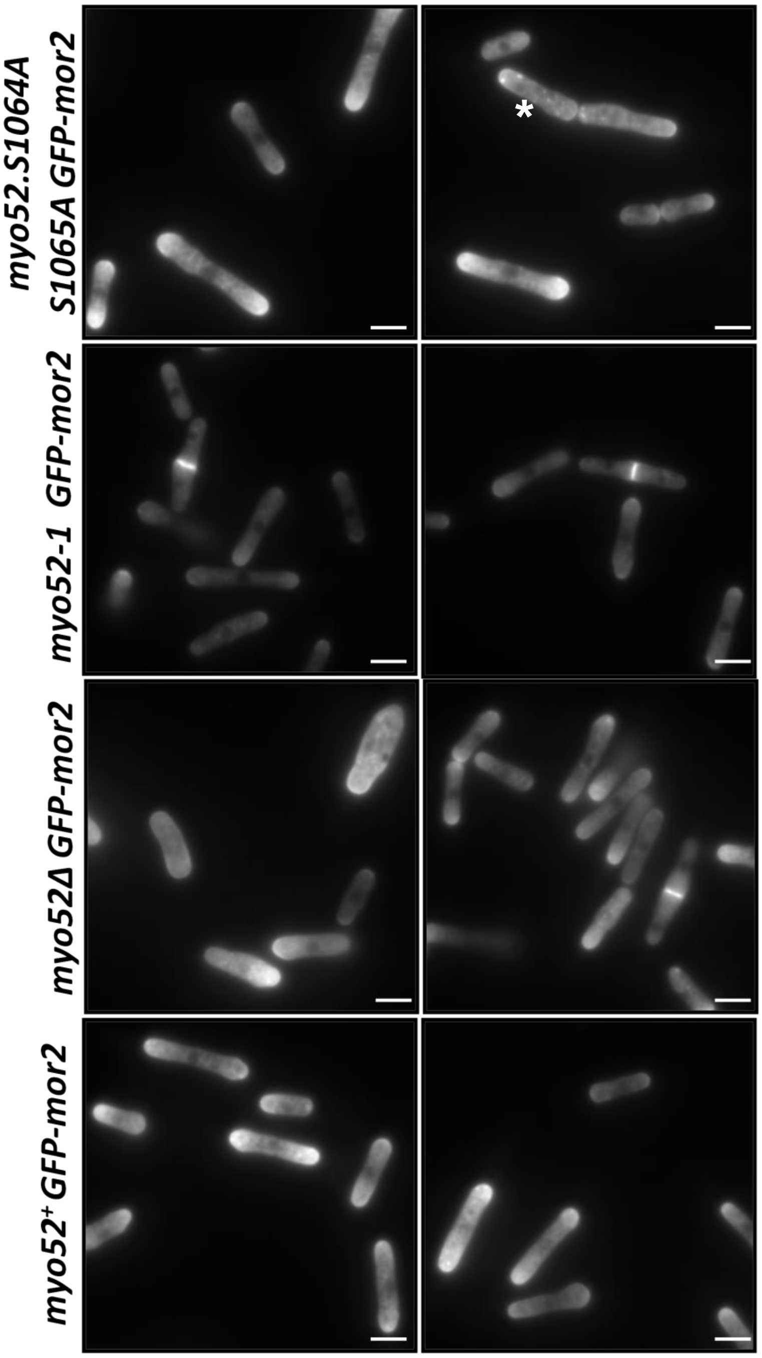

Figure legend on the following page.

**Figure 4.4. Myo52 S1064 and Myo52 S1065 phosphorylation is not required for the localisation of Mor2 to the cell ends of *S. pombe*.** Max projections of GFP-Mor2 localisation in *myo52.S1064A S1065A GFP-mor2*, *myo52-1 GFP-mor2*, *myo52Δ GFP-mor2* and *myo52*$^+$ *GFP-mor2 S. pombe.* GFP-Mor2 in *myo52.S1064A S1065A GFP-mor2* localised at the cell ends, as it does in *myo52*$^+$ *GFP-mor2* also formed aggregates displayed as large GFP-Mor2 foci (highlighted with '*'). *myo52-1 GFP-mor2* and *myo52Δ GFP-mor2* displayed delocalised GFP-Mor2, dispersed throughout the cell. Myo52 motor head function is therefore required for Mor2 localisation by Myo52; however, localisation is not dependent of Myo52 function alone. Myo52 S1064 and Myo52 S1065 phosphorylation are not required for Mor2 localisation to the cell ends however, it may play a regulatory role in Mor2 distribution once at the cell end. Cells were cultured in EMMG media supplemented with amino acids for two days, at 25 °C. 11 z-slices were taken of cells incubated at 25 °C, with an exposure time of 100 ms to develop the max projection. Scale bar - 3.5 μm

## 4.5 Chapter 4 summary

In this chapter, growth rate, tempreture-sensitivity, cell polarity, cell length, actin dynamics, Myo52 dynamics and Mor2 localisation were studied in the Myo52 phospho-mutants. These were studied to determine if phosphorylation of Myo52 S720, Myo52 S798, Myo52 S985, Myo52 S1064, Myo52 S1065 and Myo52 S1072 have an impact on the function of Myo52 in regulating cell growth, cell length, correct cell polarity, actin dynamics, Myo52 dynamics and Mor2 localisation.

To determine if the Myo52 phosphorylation sites of interest play a role in cell growth, $OD_{600}$ readings were taken from a 32 hr and 40 hr incubation of *myo52.S720A, myo52.S798A, myo52.S985A, myo52.S1064A S1065A* and *myo52.S1072A* cells at 20 °C and 25 °C. *myo52.S720A* and *myo52.S798A* cells produced $OD_{600}$ readings significant less than wild-type *myo52*$^+$ cells at 20 °C. The $OD_{600}$ of *myo52.S985A* and *myo52.S1064A S1065A* cells had no significant difference to wild-type *myo52*$^+$ cells at 20 °C. The $OD_{600}$ of *myo52.S1072A* cells was greater than wild-type *myo52*$^+$ cells at 20 °C. These results indicate *myo52.S720A, myo52.S798A* and *myo52.S1072A* cells are cold-sensitive at 20 °C. The results also indicate the *myo52.S1072A* cells were larger than wild-type *myo52*$^+$ cells due to an arrest in the cell cycle. At 25 °C, no difference was observed between the $OD_{600}$ of wild-type *myo52*$^+$ strain and the Myo52 phospho-mutant strains (Figure 4.1.1). Culturing and cell counts at 20 °C and 25 °C did not reflect the results from $OD_{600}$

readings since the Myo52 phospho-mutants consistantly displayed growth slower than wild-type *myo52*$^+$ cells*.* The Myo52 phospho-mutants have misshapen phenotypes and can grow to be longer and wider than wild-type *myo52*$^+$ cells. With this in consideration, the $OD_{600}$ readings may also be reflective of the cell size rather than cell growth. Measuring cell growth using a Coulter Counter would be more accurate. With a Coulter Counter, cell number and size can be determined and accurate growth curves can be generated.

To observe the morphology of the Myo52 phospho-mutants and determine if the Myo52 phosorylation sites of interest play a role in maintaining correct cell shape, the cells were stained with calcofluor and observed using fluorescence microscopy. Bent morphologies and varied cell lengths were observed (Figure 4.1.2). These observations suggested a loss of cell polarity. To compare the polarity of the Myo52 phospho-mutants to wild-type *myo52*$^+$ cells, the monopolar-to-bipolar ratio for each strain was quantified from images of the calcofluor stained cells. The monopolar-to-bipolar ratio of the wild-type *myo52*$^+$ cells was 0.59:0.41. The monopolar-to-bipolar ratio of *myo52.S720A, myo52.S798A, myo52.S985A* cells were 0.63:0.37 0.67:0.33 and 0.73:0.27 respectively. These data suggest a larger proportion of cells in these strains were undergoing monopolar growth than in the wild-type *myo52*$^+$ cells. NETO may be delayed in the cell cycle of these cells. *myo52.S1064A S1065A* cells had a monopolar-bipolar ratio of 0.60:0.40 which was comparable to wild-type *myo52*$^+$ cells and suggests Myo52 S1064 and Myo52 S1065 phosphorylation does not impact cell polarity. The monopolar-to-bipolar ratio of *myo52.S1072A* cells was 0.49:0.51, which suggests a larger portion of cells in this strain were undergoing bipolar growth. NETO may be earlier in the cell cycle than in the wild-type *myo52*$^+$ cells (Figure 4.1.3). Phosphorylation of Myo52 S720, Myo52 S798, Myo52 S985 and Myo52 S1072 may play a role in the regulation of cell polarity.

Possible connections between Myo52 S720, Myo52 S798, Myo52 S985 and Myo52 S1072 phosphorylation and NETO factors may be explored in future experiments. NETO factors include: (i) protein kinases such as p21-activated kinase (PAK) Orb2, (ii) actin binding proteins such as End4/Sla2 and (iii) proteins that may act as scaffold proteins in protein complexes, such as Tea1 and Tea4/Wsh3 (Martin & Chang, 2005). Deletion of the C-terminal talin-like domain of End4/Sla2 disrupts the switch from monopolar growth to bipolar growth and the localisation of actin patches at the new cell end, during NETO (Castagnetti et al., 2005). Tea1, Tea4/Wsh3 and For3 form complexes that are part of polarisomes. The polarisomes localise to the new cell ends and promote NETO

(Castagnetti et al., 2005). Orb2 has been shown to phosphorylate Tea1 *in vitro*. *S. pombe* carrying the hypomorphic allele *orb2-34* only display monopolar growth similar to that of *tea1Δ,* which suggests Orb2 is also involved in the regulation of polarised cell growth (Kim et al., 2003). Future experiments may be carried out to explore possible links between Myo52 S720, Myo52 S798, Myo52 S985 and Myo52 S1072 phosphorylation and the function of these NETO factors. The localisation of the NETO factors in the Myo52 phospho-mutants may be observed via fluorescence microscopy. Co-immunoprecipitation may also be carried out to determine possible interactions between Myo52 and the NETO factors and if Myo52 phosphorylation is required for such interactions.

The length of the Myo52 phospho-mutant cells were measured using images of the calcofluor stained cells, to determine if phosphorylation of the phosphorylation sites of interest impact cell growth with respect to cell length. Lengths statistically different to the length wild-type *myo52*$^+$ cells were only observed in *myo52.S720A, myo52.S985A* and *myo52.S1072A* cells. These cells were significantly shorter than wild-type *myo52*$^+$ cells with average lengths of 8.99 ± 0.13 µm, 9.44 ± 0.18 µm and 10.72 ± 0.24 µm (mean ± SEM) respectively. *myo52*$^+$ cells were 12.00 ± 0.16 µm long (Figure 4.1.4). These data suggest phosphorylation of Myo52 S720, Myo52 S985 and Myo52 S1072 impact the regulation of longitudinal cell growth. As longitudinal movement of Myo52 induces force that promotes actin polymerisation, phosphorylation of Myo52 S720, Myo52 S985 and Myo52 S1072 may hinder the translocation of Myo52 and hinder actin polymerisation. This may also hinder actin dependent localisation of Mor2 to the cell ends and the positioning of zone of growth by Orb6 and Cdc42. To determine defects in Myo52 motility, *myo52.S720A-mNG, myo52.S985A-mNG* and *myo52.S1072A-mNG S. pombe* strains can be made to observe Myo52-mNG motility via fluorescence microscopy. No correlation between changes in the cell polarity and cell length was observed in the Myo52 phospho-mutants.

To determine if the Myo52 phosphorylation sites of interest play a role in regulating actin dynamics, Lifeact dynamics were observed in the Myo52 phospho-mutants expressing Lifeact-GFP. Lifeact-GFP distribution in all Myo52 phospho-mutants, except the *myo52.S1064A S1065A* strain, showed that actin fails to localise into actin patches correctly and produces few filaments, of which are curled and are only situated at the end cells, as a result of absent Myo52 phosphorylation (Figure 4.2.1). Kymographs of Lifeact-GFP foci dynamics showed Lifeact-GFP moved laterally at speeds of 0.005 ± 0.001 µm/s, 0.561 ± 0.008 µm/s and 0.005 ± 0.001 µm/s (mean ± SEM) in *myo52.S985A,* *myo52.S1064A S1065A* and *myo52.S1072A* cells respectively, therefore suggesting Myo52 S985, Myo52 S1064, Myo52 S1065 and Myo52 S1072 phosphorylation to be involved in regulating actin speed in *S. pombe* (Figure 4.2.2). The defects in actin patch localisation, motility and filament polymerisation may be the cause of the growth defects observed in the Myo52 phospho-mutants (Figure 4.1.1, Figure 4.1.2, Figure 4.1.3, Figure 4.1.4). Many foci were captured in each kymograph. This made it difficult to differentiate between individual foci in the kymographs. Total internal reflection fluorescence (TIRF) microscopy would allow only single Lifeact-GFP foci and filaments, close to the cell surface, to be imaged. Fewer Lifeact- GFP foci would be detected in a single frame so individual foci can be differentiated in kymographs. Imaris for Tracking Imaging Analysis software can be used to observe Lifeact-GFP dynamics in all directions in future experiments.

To determine if the Myo52 phosphorylation sites of interest play a role in regulating microtubule dynamics and polymerisation to the ends of the cell, Abt2 dynamics were observed in the Myo52 phospho-mutants expressing GFP-Atb2. The microtubules did not display any morphological defects and extended to the ends of the cells in Myo52 phospho-mutant strains (Figure 4.2.3). These data suggest phosphorylation of Myo52 S720, Myo52 S798, Myo52 S985, Myo52 S1064, Myo52 S1065 and Myo52 S1072 does not impact the regulation of microtubule dynamics and polymerisation to the cell ends. The cells used in this experiment, including wild-type *myo52*$^{+}$ *GFP-atb2* displayed a short and circular morphology and were segmented. This morphology may be due to the labelling of Atb2 with GFP. Immunofluorescence may be used in future experiments to visualise the structure of microtubules in the Myo52 phospho-mutants. Fluorescently labelled antibodies could be used to stain and visualise Atb2 in fixed cells via fluorescent microscopy.

Myo52 in *myo52.S1064A S1065A* was labelled with mNG to observe its dynamics and determine if Myo52 S1064 and Myo52 S1065 phosphorylation plays a role in regulating Myo52 dynamics. The average speed of Myo52-mNG in *myo52.S1064A S1065A-mNG* and wild-type *myo52*$^{+}$*-mNG* cells were 0.50 ± 0.11 μm/s and 0.17 ± 0.05 μm/s (mean ± SEM) respectively (Figure 4.3). The significant difference between the speeds of Myo52 in the two strains suggests Myo52 S1064 and Myo52 S1065 phosphorylation plays a role in the regulation of Myo52 motility in *S. pombe.* This experiment is to be applied to *myo52.S720A, myo52.S798A, myo52.S985A,* and *myo52.S1072A* to determine if phosphorylation of the corresponding phosphorylation sites also impacts Myo52 motility.

Mor2 in *myo52.S1064A S1065A* cells was labelled with GFP to observe the localisation of Mor2 and determine if Myo52 S1064 and Myo52 S1065 phosphorylation plays a role in regulating the localisation of Mor2 to the cell ends, for it to act as a scoffolding protein required for the activation of Orb6. Orb6 then acts to define zones of growth (Figure 4.4). GFP-Mor2 localised to the cell ends in *myo52.S1064A S1065A GFP-mor2* cells and therefore it was concluded that Myo52 S1064 and Myo52 S1065 phosphorylation was not required for Mor2 localisation to the cell ends in *S. pombe.* It may have a role in regulating Mor2 localisation once at the cell ends because Mor2 aggregates, observed as large GFP-Mor2 foci, were formed in *myo52.S1064A S1065A GFP-mor2* cells. In the future, this experiment is to be applied to *myo52.S720A, myo52.S798A, myo52.S985A,* and *myo52.S1072A* to determine if phosphorylation of the corresponding phosphorylation sites has a function in the localisation of Mor2 in *S. pombe*. Delocalisation of Mor2 in the Myo52 phospho-mutants could be investigated further by assessing possible interactions between Myo52 and Mor2 via co-immunoprecipitation.

The absence of phosphorylation at these phosphorylation site results in morphological and temperature-sensitive growth defects. Myo52 also impacts normal polarised cell growth as changes between monopolar and bipolar growth in the Myo52 phospho-mutants were not comparable to that of wild-type *myo52*$^{+}$ cells*.* Reduced actin motility in the Myo52 phospho-mutants may be the cause of the observed defects and therefore indicates a regulatory function of Myo52 in the motility of actin. The absence of phosphorylation at Myo52 S1064 and Myo52 S1065 reduces Myo52 motility and is likely to impact interactions and conformations involved in Myo52 motility. Finally, Myo52 motor domain activity has been shown to be required for Mor2 localisation however, tail domain phosphorylation is not.

In future experiments, serine-to-aspartic acid mutations may be used to mimic constant phosphorylation at the Myo52 phosphorylation sites of interest. Aspartic acid mimics a phosphorylated serine because they are similar in sturucture and charge. Generating serine to aspartic acid mutants would allow for comparisons to be made between Myo52 function in the absence of phosphorylation, constant phosphorylation, and in wild-type conditions.

The following chapter describes experiments carried out to determine the function of Myo1 S742 phosphorylation in the regulation of endocytosis for polarised cell growth and during vegetative and meiotic life cycles in *S. pombe.* Myo1 S742A is a Myo1 phospho-mutant of which Myo1 serine 742 is mutated to an alanine. As in the Myo52 phospho-mutants, the Myo1 phospho-mutant cannot be phosphorylated. The phenotypes displayed by *myo1.S742A* highlighted the regulatory impact Myo1 S742 phosphorylation has on light chain binding to Myo1. Binding of the light chains Calmodulin 1 and Calmodulin 2 were shown to affect endocytic activity of Myo1, actin activity, cell polarity and spore formation.

# Chapter 5: Phospho-regulation of fission yeast myosin I serine 742

Myo1 and calmodulin light chain binding has been found to be involved in the regulation of the vegetative and meiotic stages of the cell cycle. Myo1 function is regulated in part by calmodulin binding in the IQ region of the Myo1 neck domain. Calmodulin binding causes a conformational change in Myo1 and induces stiffness in the neck domain which is required for Myo1 motility. Myo1 S742 (Myo1 serine S742) is phosphorylated from the end of G1. Myo1 S742 phosphorylation has been proposed to induce a conformational change in the Myo1 neck domain (Baker et al., 2019). The impact Myo1 S742 phosphorylation has on the functions of Myo1, Cam1 (calmodulin 1) and Cam2 (calmodulin 2), and interactions between them, was explored via fluorescence imaging observing cell growth. The localisation and foci lifetime of Myo1, Cam1, Cam2 and Lifeact during varying stages of the cell cycle were also studied. In this chapter, results from an investigation into the role of Myo1 S742 phosphorylation in Myo1 function are presented. Recently published data has been included in this chapter (Baker et al., 2019).

## 5.1 Myo1 S742 phosphorylation impacts the monopolar-to-bipolar ratio in *S. pombe* resulting in a more monopolar population

In *S. pombe*, growth only occurs at the cell ends and switches from monopolar (growth at one end of the cell) to bipolar (growth at both ends of the cell), during NETO in G2 of the cell cycle (Mitchison & Nurse, 1985). Correct timing of the switch between monopolar and bipolar growth is crucial for maintaining a normal growth cycle. Incorrect growth patterns can impact cell division, cell structure and integrity. Myo1 is a fundamental protein during the cell cycle as it has roles in cell growth and endocytosis.

To determine the possible role Myo1 S742 phosphorylation has in the regulation of polarised cell growth, cell cycle and growth patterns were examined in *myo1.S742A* and *myo1.S742D* mutant *S. pombe* strains. SDM (site-directed mutagenesis) was used for the generation of *myo1.S742A* cells in which Myo1 S742 was converted into an alanine, resulting in the prevention of Myo1 S742A phosphorylation. *myo1.S742D* cells, generated via the same method, is a phospho-serine-to-aspartic acid mutant which was used as a phospho-mimetic of constant phosphorylation.

Differences in the monopolar-to-bipolar ratio may provide an indication on the function of Myo1 S742 phosphorylation in the cell cycle and cell growth. Monopolar and bipolar cell growth were examined in *myo1.S742A*, *myo1.S742D* and wild-type *myo1*$^+$ *S. pombe* cells using calcofluor staining, as explained in Section 4.1.2. Examples of monopolar and bipolar growth in *myo1.S742A*, *myo1.S742D* and wild-type *myo1*$^+$ strains are shown in Figure 5.1A. The monopolar-to-bipolar ratio was then quantified manually. Quantification results are summarised in Figure 5.1B

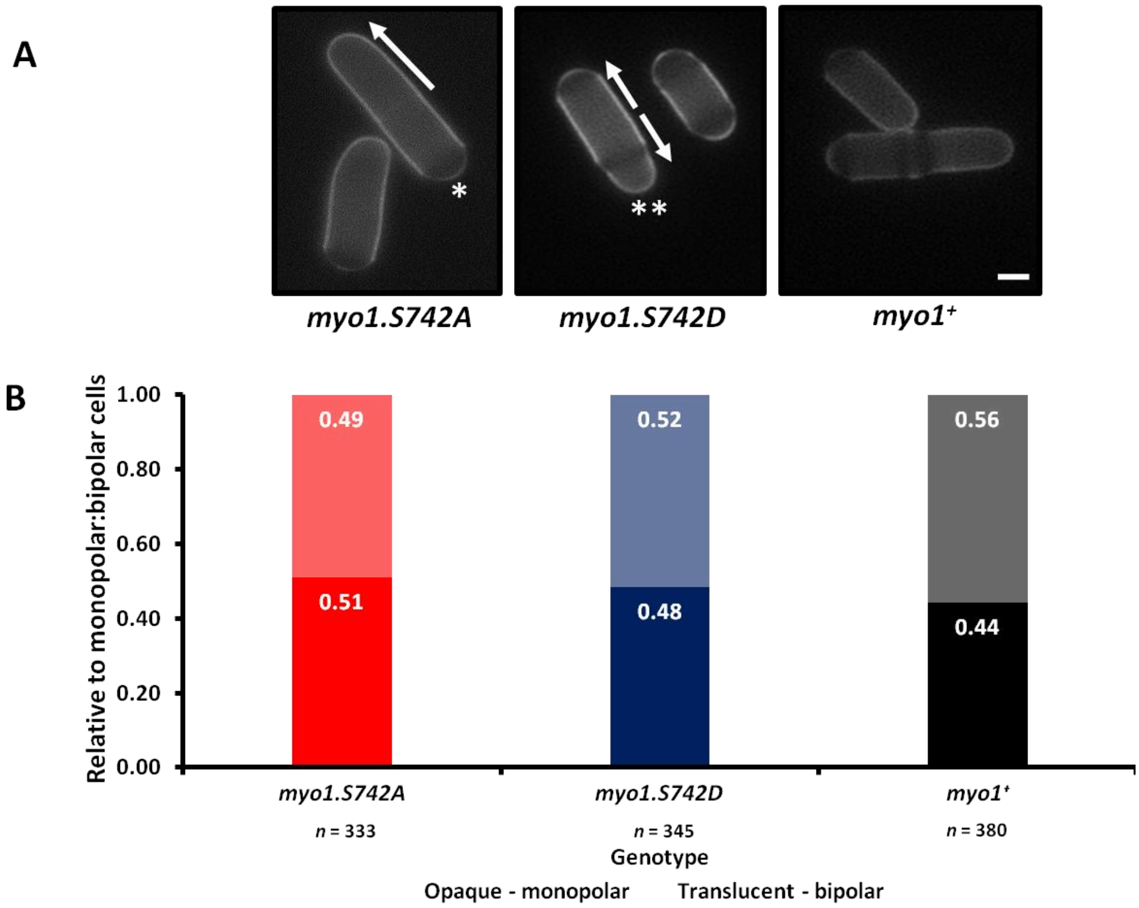

Figure legend on the following page.

**Figure 5.1. Phosphorylation of Myo1 S742 impacts the monopolar-to-bipolar cell ratio in *S. pombe.*** **(A)** Single z-slice images displaying *myo1.S742A, myo1.S742D* and wild-type *myo1*$^+$ *S. pombe* cells stained with calcofluor. The cells were stained to visualise (1,3) β-D-glucan and cellulose in the septum and cell wall. Birth scars (dark bands in the staining) were observed to determine monopolar or bipolar growth in the cells. Cells were cultured in YES media supplemented with amino acids for 2 days, at 25 °C. They were then fixed with paraformaldehyde and stained with calcofluor on ice. The cells were imaged at 25 °C, with an exposure time of 100 ms. A single z-slice was taken. Scale bar - 3.5 μm. **(B)** Bar chart displaying the relative monopolar-to-bipolar cell ratio of *myo1.S742A, myo1.S742D* and wild-type *myo1*$^+$ *S. pombe* strains. For each strain, the number of monopolar cells and bipolar cells were manually quantified and made relative to the total number of cells. The monopolar-to-bipolar cell ratio was calculated from the relative number of monopolar and bipolar cells. The opaque portions at the bottom of the bars represent the relative number of monopolar cells. The translucent portions at top of the bars represent the relative number of bipolar cells. The number in each bar is the relative number of cells for the corresponding category. These numbers make up the terms of the ratio. The monopolar-to-bipolar ratio of the wild-type *myo1*$^+$ cells was 0.44:0.56. The monopolar-to-bipolar ratio of *myo1.S742A* and *myo1.S742D* cells were 0.51:0:49 and 0.48:0:52 respectively. There was a 7 % and 4 % increase in monopolar cells in the *myo1.S742A* and *myo1.S742D* strains respectively, when compared to wild-type *myo1*$^+$ cells. $n \geq 333$. '*n*' indicates the number of cells measured from each strain.

Monopolar-to-bipolar ratios of 0.51:0:49, 0.48:0:52 and 0.44:0.56 were determined for the *myo1.S742A, myo1.S742D* and wild-type *myo1*$^+$ strains respectively. The *myo1.S742A* strain was 7 % more monopolar than the wild-type *myo1*$^+$ strain. The mean lengths of the *myo1.S742A, myo1.S742D* and wild-type *myo1*$^+$ *S. pombe* cells were 12.04 ± 0.12 μm, 11.39 ± 0.10 μm and 10.66 ± 0.09 μm respectively (mean ± SEM) ($n \geq 333$). *myo1.S742A* and *myo1.S742D* cells were significantly longer than wild-type *myo1*$^+$ cells ($p < 0.05$). This may be due to a delay in NETO. These data suggest Myo1 S742 phosphorylation impacts the regulation of monopolar and bipolar growth in *S. pombe*.

## 5.2 Myo1 S742 phosphorylation modulates Cam1, Cam2 and Myo1 function and is required for Cam2 binding to Myo1 IQ motif during the meiotic life cycle

Myo1 activity is regulated by calmodulin light chain binding. Cam1 and Cam2 bind to IQ motifs, located in the Myo1 neck region. Cam1 binding and affinity to myosin is dependent on changing $Ca^{2+}$ levels during the cell cycle, while Cam2 binding is not. Cam1 binds to Myo1 when intracellular $Ca^{2+}$ levels are low and this includes during the later phases of G1 of the vegetative cycle. Cam1 is initially bound to the Myo1 IQ motifs as the low $Ca^{2+}$ levels at this point in the cell cycle favour Cam1 binding to Myo1 (Baker et al., 2019; Moser et al., 1995; Moser et al., 1997; Toya et al., 2008). Cam1 co-immunoprecipitates with Myo1 IQ in the absence of $Ca^{2+}$. Co-immunoprecipitation is disrupted with the addition of $Ca^{2+}$ and Cam1 does not co-immunoprecipitate with Myo1 that lacks IQ1 (Toya et al., 2008). Cam1 has also been shown to bind to both Myo1 IQ1 and IQ2 only in low cellular $Ca^{2+}$ concentrations. Cam1 binding caused a drop in FRET in recombinant FRET constructs, composed of CyPet and YPet separated by the two Myo1 IQ motifs, at low $Ca^{2+}$ concentrations (Baker et al., 2019). *cdc10-v50* cell arrest in-house experiments have also shown Myo1 S742 to be phosphorylated at the end of G1. Myo1 S742 was also confirmed to be in the phosphorylated state in mating and sporulating cells (Baker et al., 2019).

At the end of the vegetative cycle, an intracellular influx of $Ca^{2+}$ occurs (Baker et al., 2019). Cam1 is less likely to bind to Myo1 in higher concentrations of $Ca^{2+}$ so Cam2 is able to bind to the vacant IQ motif binding sites. Cam2 abundance also increases upon mating and meiosis which also increases the likelihood of Cam2 binding to Myo1 (Baker et al., 2019). Cam2 binding has been associated with Myo1 function during the meiotic cycle, however definitive roles of these calmodulins during the meiotic life cycle have not been clearly defined (Baker et al., 2019),

To decipher the roles Cam1 and Cam2 play in the vegetative and meiotic cycles, the transition between the two cycles, and their dependence on Myo1 S742 phosphorylation, Cam1-GFP and Cam2-GFP dynamics were observed in vegetative and sporulating cells. mNG-Myo1 was also observed to study the distribution of Myo1 during the vegetative and meiotic cycle. Time-lapses were recorded of Cam1-GFP, Cam2-GFP and mNG-Myo1 in the *myo1.S742A* and *myo1.S742D* mutants in vegetative and sporulating states, to also determine if Myo1 S742 phosphorylation plays a role in foci lifetime (length of time foci is visible by eye), localisation and provide an indication on the interactions between Myo1 and the calmodulin.

Max projections showing the localisation of Cam1-GFP, Cam2-GFP and mNG-Myo1 in the *myo1.S742A* mutant background are displayed in Figure 5.2.1A. Images of the *myo1.S742D* and wild-type *myo1*$^{+}$ backgrounds are not shown. Fluorescence imaging revealed an abundance of Cam1-GFP and Cam2-GFP foci inside spores of the sporulating cells, with the majority of foci situated around the spore periphery and few foci outside the spores of sporulating cells. Less mNG-Myo1 foci were observed inside the spores of sporulating cells however, most Myo1 foci localised to a single large focus within the individual spores. The foci inside the spores of sporulating cells in all strains displayed reduced dynamics and extended lifetimes in comparison to vegetative cells. Cam2-GFP displayed the most extended foci lifetimes in the sporulating cells.  In vegetative cells, Cam1-GFP and Cam2-GFP were distributed throughout the cell. mNG-Myo1 foci were located at the cell ends for endocytosis. Foci dynamics and lifetimes of Cam2-GFP in vegetative and sporulating (inside spores and ascus cytoplasm) cells are displayed in kymographs shown in Figure 5.2.1B. Extended foci lifetimes are displayed in the sporulating *myo1.S742A cam2-GFP* cells and are shown by long straight Cam2-GFP signal lines.

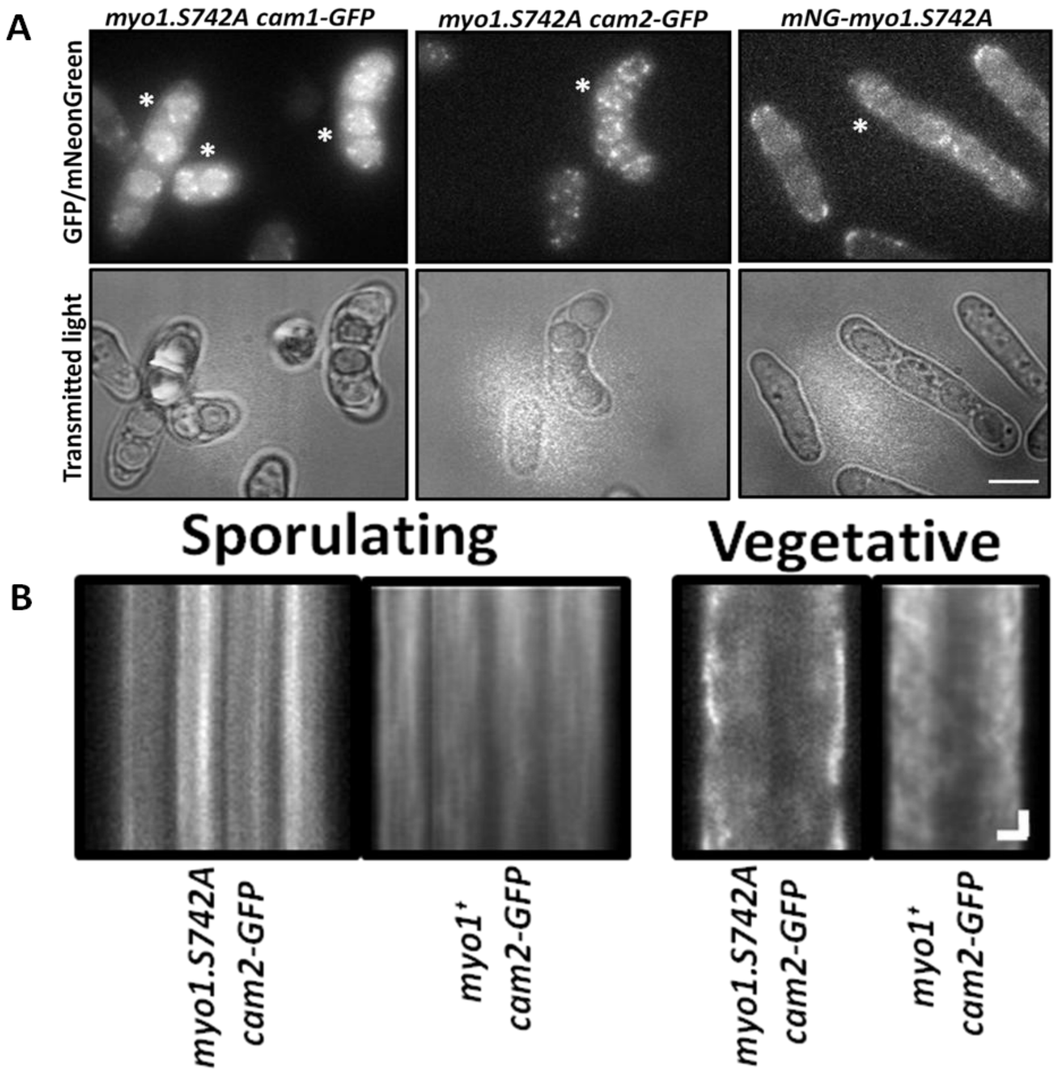

Figure legend on the following page.

**Figure 5.2.1. Cam1, Cam2 and Myo1 localise to the periphery of spores and display reduced dynamics and extended foci lifetimes in sporulating *S. pombe* cells. (A)** Max projections and transmitted images from time-lapses of Cam1-GFP, Cam2-GFP and mNG-Myo1 dynamics in sporulating and vegetative *myo1.S742A cam1-GFP, myo1.S742A cam2-GFP* and *mNG-myo1.S742A S. pombe* cells. '*' indicates a sporulating cell in the meiotic cell cycle. Unmarked cells are in the vegetative state. In all strains, foci in the sporulating cells show an accumulation of Cam1-GFP, Cam2-GFP and mNG-Myo1 inside the four spherical spores. These foci displayed reduced dynamics and extended lifetimes (length of time foci is visible by eye). Cam2-GFP foci appeared to have the most extended lifetime. Foci in vegetative cells were dynamic and did not display extended lifetimes. The same localisation patterns were observed in the wild-type *myo1*$^+$ background (not shown). Cells were cultured at 25 °C in MSL media supplemented with amino acids, vitamins and minerals for 2 days. The cells were then washed with MSL without nitrogen three times and reconstituted and cultured in MSL without nitrogen, supplemented with amino acids, vitamins and minerals for 1 day. 11 z-slices were taken for each max projection over 110 s at 25 °C, with an exposure time of 100 ms. Scale bar - 3.5 µm. **(B)** Kymographs displaying dynamics of Cam2-GFP in sporulating and vegetative *myo1.S742A* and wild-type *myo1*$^+$ cells over 110 s. Less dynamic Cam2-GFP foci with extended lifetimes in the sporulating cells are shown by long straight Cam2-GFP signal lines. More dynamic Cam2-GFP foci are shown by short signal lines. Less dynamic Cam2-GFP foci were observed most frequently in the sporulating *myo1.S742A* cells. Cam2-GFP foci were more dynamic in vegetative *myo1.S742A* cells and did not have extended lifetimes. The kymographs were generated using Metamorph. Horizontal scale bar (distance) - 1.75 µm. Vertical scale bar (time) - 11 s.

To determine differences in the activity of Myo1, Cam1 and Cam2, induced by a lack of Myo1 S742 phosphorylation, the foci lifetimes of Cam1-GFP, Cam2-GFP and mNG-Myo1 in the *myo1.S742A, myo1.S742D* and wild-type *myo1*$^+$ backgrounds were quantified by eye and are shown in Figure 5.2.2.

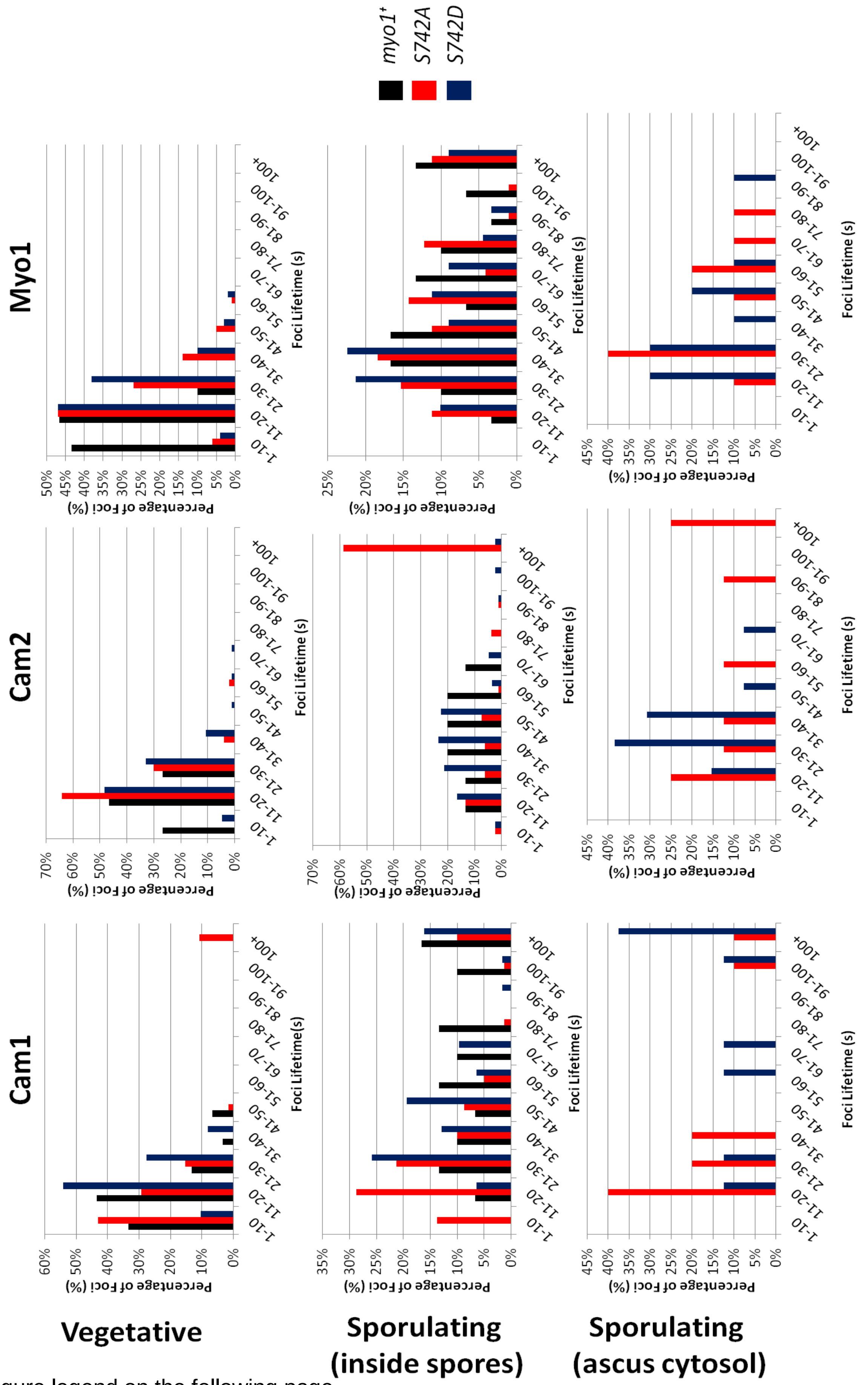

Figure legend on the following page.

**Figure 5.2.2. A lack of Myo1 S742 phosphorylation prevents Cam2 binding to Myo1 and reduces Myo1 activity during the meiotic phase of the cell cycle in *S. pombe.*** Bar charts displaying Cam1-GFP*,* Cam2-GFP and mNG-Myo1 foci lifetimes in the spores and ascus cytosol in the *myo1.S742A, myo1.S742D* and wild-type *myo1*$^+$ backgrounds. Foci lifetimes were quantified by eye from time-lapses of *myo1.S742A cam1-GFP, myo1.S742A cam2-GFP* and *mNG-myo1.S742A* phospho-mutants and wild-types *myo1*$^+$ *cam1-GFP, myo1*$^+$ *cam2-GFP* and *mNG-myo1*$^+$*.* Cam1-GFP: in vegetative cells, the foci lifetime of Cam1-GFP in the *myo1.S742A cam1-GFP*, *myo1.S742D cam1-GFP* and *mNG-myo1*$^+$ *cam1-GFP* strains was ~11 s (foci lifetime ≤ 20 s: *myo1.S742A* - 72 %; *myo1.S742D* - 64 %; *mNG-myo1*$^+$ - 77 %). Inside the spores of sporulating cells, Cam1-GFP foci lifetime ranged between 1 s and > 100 s. Cam1-GFP foci lifetimes in *myo1.S742A cam1-GFP* were shorter than in *myo1.S742D cam1-GFP* and wild-type *myo1*$^+$ *cam1-GFP* cells (foci lifetime ≤ 20 s: *myo1.S742A* - 43 %; *myo1.S742D* - 7 %; *myo1*$^+$ - 7 %). Cam2-GFP: in vegetative cells, Cam2-GFP foci lifetimes were ~11 s in all strains (foci lifetime ≤ 20 s: *myo1.S742A* - 64 %; *myo1.S742D* - 53 %; *myo1*$^+$ - 76 %). In sporulating cells, Cam2-GFP foci lifetimes in *myo1.S742A cam2-GFP* were considerably longer than in the *myo1.S742D cam2-GFP* and wild-type *myo1*$^+$ *cam2-GFP* backgrounds (foci lifetime ≥ 100 s: *myo1.S742A* - 59 %; *myo1.S742D* - 2 %; *myo1*$^+$ - 0 %). The extended foci lifetime of Cam2-GFP in *myo1.S742A cam2-GFP* suggests Myo1 S742 phosphorylation prevents Cam2 binding to Myo1. mNG-Myo1: in vegetative cells, the mNG-Myo1 foci lifetime in wild-type *mNG-myo1*$^+$ was ~11 s and marginally shorter than foci lifetimes in *myo1.S742A mNG-myo1*$^+$ and *myo1.S742D mNG-myo1*$^+$ cells (foci lifetime ≤ 20 s: *myo1.S742A* - 53 %; *myo1.S742D* - 51 %; *myo1*$^+$ - 90 %). In sporulating cells of all strains, mNG-Myo1 foci lifetimes ranged between 11 s and > 100 s and had a similar distribution to Cam1-GFP foci lifetimes. This similarity in *myo1.S742A* cells suggests Myo1 S742 phosphorylation impacts Myo1 and Cam1 function in sporulating cells. Sporulating (ascus cytosol): Cam1-GFP, Cam2-GFP and mNG-Myo1 foci were only observed outside of the spores in the *myo1.S742A* and *myo1.S742D* backgrounds. Foci lifetimes ranged between 11 s and > 100 s. *n* ≥ 30. '*n*' indicates the number of foci lifetimes quantified per strain.

Quantification revealed Cam1-GFP foci in all backgrounds to have a foci lifetime of ~11 s in the vegetative cycle (foci lifetime ≤ 20 s: *myo1.S742A* - 72 %; *myo1.S742D* - 64 %; *mNG-myo1*$^+$ - 77 %) (Baker et al., 2019). Inside the spores of sporulating cells, Cam1-GFP foci lifetimes ranged from 1 s to > 100 s. Foci lifetimes were frequently shorter in *myo1.S742A* and *myo1.S742D* cells, when compared to wild-type *myo1*$^+$ cells (foci lifetime

≤ 20 s: *myo1.S742A* - 43 %; *myo1.S742D* - 7 %; *myo1*$^+$ - 7 %). In the ascus cytosol (sporulating cells), no Cam1-GFP foci were observed in the wild-type *myo1*$^+$ cells. *myo1.S742A* and *myo1.S742D* cells displayed Cam1-GFP foci lifetimes ranging between 11 s and >100 s, however the majority of foci seen in *myo1.S742A* cells had lifetimes between 11 s and 40 s.

In the vegetative cycle, Cam2-GFP foci lifetimes between strains reflected distributions of Cam1-GFP. Foci lifetimes of ~11 s were recorded in all strains (foci lifetime ≤ 20 s: *myo1.S742A* - 64 %; *myo1.S742D* - 53 %; *myo1*$^+$ - 76 %) (Baker et al., 2019). Inside spores (sporulating cells), Cam2-GFP foci lifetimes were greater than vegetative foci lifetimes in all strains. There was a clear discrepancy observed between the Cam2-GFP lifetimes in *myo1.S742A* and wild-type *myo1*$^+$ cells. The average foci lifetime in *myo1.S742A* cells was approximately >100 s and 35 s in wild-type *myo1*$^+$ cells. Foci in *myo1.S742D* cells followed approximately the same foci lifetime range as wild-type *myo1*$^+$ cells (foci lifetime ≥ 100 s: *myo1.S742A* - 59 %; *myo1.S742D* - 2 %; *myo1*$^+$ - 0 %). In wild-type *myo1*$^+$ cells, levels of intracellular $Ca^{2+}$ increase during sporulation. Cam2 levels also increase during meiosis. The increase in $Ca^{2+}$ and Cam2 levels favour Cam2 binding to Myo1 over Cam1 binding (Baker et al., 2019). Cam2 and Myo1 function at the edge of the forespore membrane for the formation of the forespore membrane. At the membrane, Myo1 assists the assembly of F-actin which is also required for the deposition of materials for formation of the forespore membrane (Itadani et al., 2006; Toya et al., 2008) Therefore, these data suggest the lack of phosphorylation in *myo1.S742A* cells hinders Cam2 interactions with Myo1 for forespore formation during the meiotic phase of the cell cycle. In the ascus cytosol (sporulating cells), Cam2-GFP foci lifetimes in *myo1.S742A* ranged from 11 s to >100 s. Cam2-GFP foci lifetimes in *myo1.S742D* cells were no greater than 70 s. No Cam2-GFP foci were observed in wild-type *myo1*$^+$ ascus cytosol.

In vegetative cells, mNG-Myo1 foci lifetimes between all strains also followed Cam1-GFP and Cam2-GFP distributions. Foci lifetimes in the *myo1.S742A* and *myo1.S742D* backgrounds were greater than in wild-type *myo1*$^+$ cells however (foci lifetime ≤ 20 s: *myo1.S742A* - 53 %; *myo1.S742D* - 51 %; *myo1*$^+$ - 90 %). Inside spores, foci lifetime was widely spread between 11 s and >100 s and followed a similar distribution to that of Cam1-GFP, in all strains. Myo1 and Cam1 foci were shorter in *myo1.S742A* cells in comparison to wild-type *myo1*$^+$ cells. Myo1 and Cam1 foci lifetimes are also shorter in *cam2Δ* (Baker et al., 2019). These data suggest Myo1 and Cam1 function during the meiotic phase of the cell cycle is disrupted in *myo1.S742A* cells and Myo1 S742 phosphorylation is required for Cam2 to bind to Myo1 for its function in forespore membrane formation. In the ascus cytosol, mNG-Myo1 foci lifetimes in *mNG-myo1.S742A* and *mNG-Myo1.S742D* cells ranged between 11 s and 80 s, and 11 s and 90 s respectively.

## 5.3 Endocytosis and Myo1 levels are reduced in the absence of Myo1 S742 phosphorylation in sporulating *S. pombe* cells, due to a lack of Cam2 binding to the Myo1 IQ motif

Spores formed within *S. pombe* are quiescent cells which are resistant to environmental stress (Fukunishi et al., 2014). Spores maintain a quiescent state with reduced metabolic activity, transcription and translation (Kumar & Srivastava, 2016). The thick spore wall of spores provides resistance to environmental stress. Spore walls are thicker and have a different composition to vegetative cell walls. Vegetative cell walls are mainly composed of α-glucans, β-glucans and galactomannan, whereas spore walls also contain chitosan and a proteinaceous layer, mainly made up of a protein called Isp3. Isp3 forms an insoluble layer around the spore which provides protection against stresses (Fukunishi et al., 2014; Tahara et al., 2021).

During endocytosis at the plasma membrane of sporulating cells, vesicles traffic molecules from the plasma membrane of the cell to the membrane of the spores, for the formation of the of the spore wall (Morishita & Engebrecht, 2005). Myo1 is involved in the formation of F-actin which is required for the deposition of materials for formation of the forespore membrane (Itadani et al., 2006; Toya et al., 2008). Endocytosis within the spores is not expected, as they are quiescent (Kumar & Srivastava, 2016). Endocytosis has been shown to not occur in the spores of *S. cerevisiae* and *S. pombe* with the use of the FM4-64 dye (Kashiwazaki et al., 2011; Morishita & Engebrecht, 2005). FM4-64 is a fluorescent dye composed of amphiphilic molecules that reversibly separate in lipid membranes. The molecules cannot diffuse through plasma membranes due to their positively charged heads. The quantum yield of the molecules is also high in lipid environments and low aqueous solution (Li et al., 2009). When applied to live *S. pombe*, FM4-64 is internalised through endocytosis within vesicles which provide lipid rich environments for FM4-64 to be visualised. Therefore, FM4-64 makes an excellent marker for endocytosis. FM4-64 would be internalised into spores if endocytosis occurs at the spore wall. *S. cerevisiae* and *S. pombe* stained with FM4-64 display internalised FM4-64 which collects at the spore peripheries but not within the spore, indicating that molecules are deposited to the spore wall but not endocytosed within the spore (Kashiwazaki et al., 2011; Morishita & Engebrecht, 2005).

In sporulating cells, Cam1, Cam2 and Myo1 localised to the spores within the cells. Cam1, Cam2 and Myo1 foci lifetimes were longer in the spores of sporulating cells than in vegetative cells (Figure 5.2.2). This observation suggested reduced activity of Cam1, Cam2 and Myo1 and this is consistent with minimised endocytosis within spores. The extended foci lifetime of Cam2 in sporulating *myo1.S742A* cells suggested Myo1 S742 phosphorylation impacts the Cam2 association to Myo1 during sporulation. Sporulating *mNG-myo1.S742A, mNG-myo1.S742D* and *mNG-myo1*$^+$ cells were stained with FM4-64 to provide an indication of the level of endocytosis in sporulating cells and determine if the extended foci lifetimes observed in Cam1, Cam2 and Myo1 are a result of reduced endocytic activity during meiosis. A difference in the localisation of Myo1 in sporulating *myo1.S742A* cells was also to be determined. Z-projections of FM4-64 stained *mNG-myo1.S742A, mNG-myo1.S742D* and *mNG-myo1*$^+$ cells are displayed in Figure 5.3.

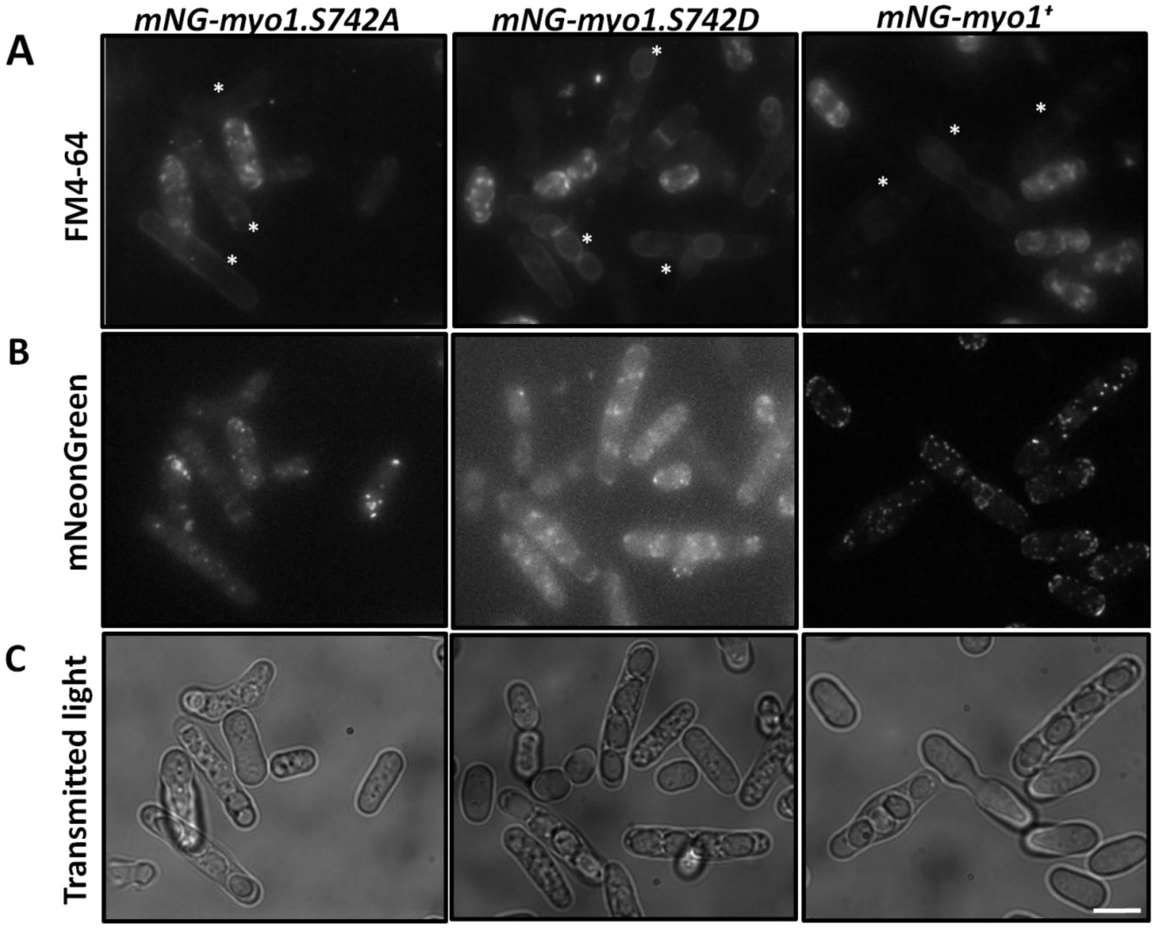

Figure legend on the following page.

**Figure 5.3. Endocytosis and the abundance of Myo1 are diminished in sporulating *S. pombe* cells.** Max projections of FM4-64 stained meiotic *mNG-myo1.S742A, mNG-myo1.S742D* and wild-type *mNG-myo1*$^{+}$ cells. **(A)** FM4-64 signal in the red channel. '*' indicates sporulating cells of which endocytosis of FM4-64 was reduced in comparison to non-sporulating cells. A greater amount of FM4-64 was endocytosed by non-sporulating cells in all strains and is shown by greater FM4-64 staining within those cells. Endocytosis into the quiescent spores does not occur. *mNG-myo1.S742D* and wild-type *mNG-myo1*$^{+}$ cells internalised FM4-64 which was observed to concentrate at the periphery of the spores within the cells. FM4-64 was internalised less by *mNG-myo1.S742A* cells and was observed to concentrate outside of some *mNG-myo1.S742A* cells, showing FM4-64 was not internalised in all cells. **(B)** mNG-Myo1 signal in the green channel. A reduced number of mNG-Myo1 was observed in *mNG-myo1.S742A* cells in comparison to *myo1.S742D* and wild-type *mNG-myo1*$^{+}$ cells. **(C)** Transmitted light. The morphology of the cells and the spores are displayed in these images. Scale bar - 3.5 μm. Cells were cultured at 25 $^{o}$C in MSL media supplemented with amino acids, vitamins and minerals for 2 days. The cells were then washed with MSL without nitrogen three times and reconstituted and cultured in MSL without nitrogen, supplemented with amino acids, vitamins and minerals for 1 day. The cells were incubated with FM4-64 on ice for 10 min. The cells were then washed in MSL without nitrogen and imaged. 11 z-slice images were taken at 25 $^{o}$C, with exposure times of 50 ms (mNG) and 100 ms (FM4-64).

Figure 5.3 shows an abundance of FM4-64 was endocytosed by non-sporulating cells and can be seen by the greater FM4-64 signal in those cells. FM4-64 endocytosis was diminished in sporulating *mNG-myo1.S742A, mNG-myo1.S742D* and *mNG-myo1*$^{+}$ cells, in comparison to non-sporulating cells. FM4-64 was not internalised by the quiescent spores. In sporulating *myo1.S742D* and *mNG-myo1*$^{+}$ cells, FM4-64 concentrated to the periphery of the spores. Sporulating *mNG-myo1.S742A* cells internalised the least amount of FM4-64. FM4-64 was also observed on the outside of the cell wall of sporulating *mNG-myo1.S742A* cells showing endocytosis did not occur in all cells. mNG-Myo1 was less abundant in *mNG-myo1.S742A* cells*.* This confirms endocytosis is minimised in sporulating cells and Myo1 S742 phosphorylation impacts Myo1 activity for endocytosis during sporulation in the meiotic cycle. The reduced endocytosis is due to the increase in intracellular $Ca^{2+}$ levels during the meiotic cycle, which induces Cam2 binding to Myo1 to modulate the endocytic activity of Myo1 (Baker et al., 2019). This is consistent with the increased Cam2-GFP lifetimes observed in *myo1.S742A* cells which suggested a lack of

Cam2 binding to the Myo1 IQ motif in the absence of Myo1 S742 phosphorylation (Figure 5.2.2). The lack of mNG-Myo1 in *mNG-myo1.S742A* cells is also consistent with reduced levels of Myo1 at actin patches in *cam2Δ* cells (Sammons et al., 2011).

## 5.4 A lack of Myo1 S742 phosphorylation results in reduced cell growth in vegetative *S. pombe*

Growth curves were generated to determine possible aberrant cell growth induced by Myo1 S742A in the *mNG-myo1.S742A*, *myo1.S742A cam1-GFP* and *myo1.S742A cam2-GFP* strains that were to be used to assess Cam1, Cam2 and Myo1 dynamics in sporulating and vegetative cells. As in Section 4.1.1, $OD_{600}$ readings were taken as a measure of overall cell growth (combination of cell number and cell size). The growth curves are shown in Figure 5.4.

Slower growth was observed in each *myo1.S742A* strain, when compared to wild-types *myo1*$^{+}$ cells*. mNG-myo1.S742A cam1-GFP* cell growth was slower than wild-type mNG-*myo1*$^{+}$ from 6 hr. GFP labelling of Cam1 may have caused reduced growth in these strains due to steric hindrance, which may interfere with Cam1 binding to the plethora of proteins it usually binds to for multiple processes (Sharma & Parameswaran, 2018). Slower growth at the end of the log phase of growth was observed in *myo1.S742A cam2-GFP* and *mNG-myo1.S742A* cells (from 15 hr and 15.5 hr respectively). These data suggest Myo1 S742 phosphorylation is involved in cell growth regulation in vegetative *S. pombe* cells.

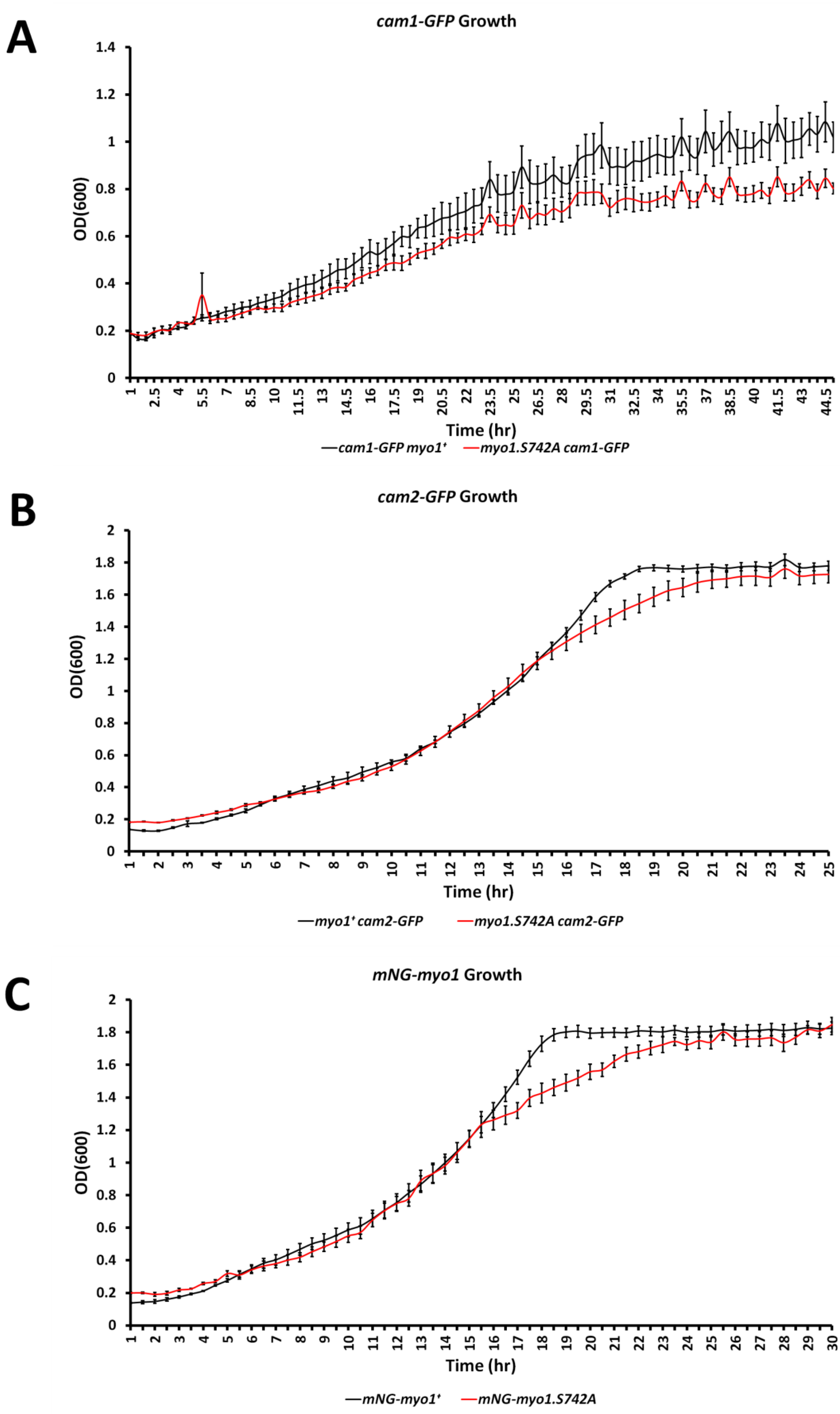

Figure legend on the following page.

**Figure 5.4. The absence of Myo1 S742 phosphorylation results in slower growth in vegetative *S. pombe* cells.** Growth curves of *cam1-GFP, cam2-GFP* and *mNG-myo1* cells in *myo1.S742A* and *myo1*$^+$ backgrounds, over 25 - 45.5 hr at 25 $^o$C. OD$_{600}$ readings were used as an indication of overall cell growth (cell size and cell number). Log phase is shown by the region of exponential increase in OD$_{600}$. Stationary phase is shown by the plateau on OD$_{600}$. *myo1.S742A cam1-GFP, myo1.S742A cam2-GFP* and *mNG-myo1.S742A* cells displayed slower growth than the wild-types *myo1*$^+$ *cam1-GFP, myo1*$^+$ *cam2-GFP* and *mNG-myo1*$^+$ cells. **(A)** Growth of *myo1.S742A cam1-GFP* and wild-type *myo1*$^+$ *cam1-GFP* cells*. myo1.S742A cam1-GFP* cells displayed slower growth from 6 hr. Noise in both growth curves was assumed to be due to variation in the operation of the plate reader. **(B)** Growth of *myo1.S742A cam2-GFP* and wild-type *myo1*$^+$ *cam2-GFP* cells*. myo1.S742A cam2-GFP* cells displayed slower growth at the end of the log growth phase, from 15 hr. **(C)** Growth of *mNG-myo1.S742A* and wild-type *mNG-myo1*$^+$ cells*. mNG-myo1.S742A* cells displayed slower growth at the end of the log growth phase, from 15.5 hr. The cells were cultured in YES media at 25 $^o$C for 2 days. OD$_{600}$ readings were taken of the cells using a plate reader. Each curve is an average of three independent cultures. The error bars show standard error of the mean (SEM).

## 5.5 A lack of Myo1 S742 phosphorylation induces uneven actin activity at the ends of cells in G2

During G1-S of the cell cycle, *S. pombe* growth is monopolar and growth only occurs from the 'old end' of the cell. The 'old end' refers to the cell end present prior to the previous cytokinesis. NETO which is the start of growth from the 'new end' (the end created from the previous cytokinesis), occurs during G2 of the cell cycle. The growth is then bipolar. The bidirectional growth continues through to M phase of the cell cycle.

Endocytosis for cell growth occurs at the ends of *S. pombe* cells. Myo1 and actin are concomitantly recruited to the cell ends for endocytosis. There, actin-membrane linkers, such as End4/Sla2, link actin to the clathrin in the membrane coat. Branched filaments of actin form actin patches and bind to Myo1 (Kovar et al., 2011). Myo1 anchors the actin to the membrane and promotes actin polymerisation for actin patch formation. Elongation of the actin filaments and force generated between actin and Myo1 elongates the endocytic invaginations that eventually undergo scission and form endocytic vesicles (Kovar et al., 2011; Manenschijn et al., 2019).

To determine whether Myo1 S742 phosphorylation contributes to the regulation of actin patch formation and localisation during endocytosis, actin patches were examined in *myo1.S742A mCherry-lifeact, myo1.S742D mCherry-lifeact* and wild-type *myo1$^{+}$ mCherry-lifeact* cells, using fluorescence microscopy. Time-lapses of mCherry-Lifeact in these cells were generated to observe the localisation and dynamics of actin. Images of mCherry-Lifeact in *myo1.S742A mCherry-lifeact, myo1.S742D mCherry-lifeact* and wild-type *myo1$^{+}$ mCherry-lifeact* cells are shown in Figure 5.5.1.

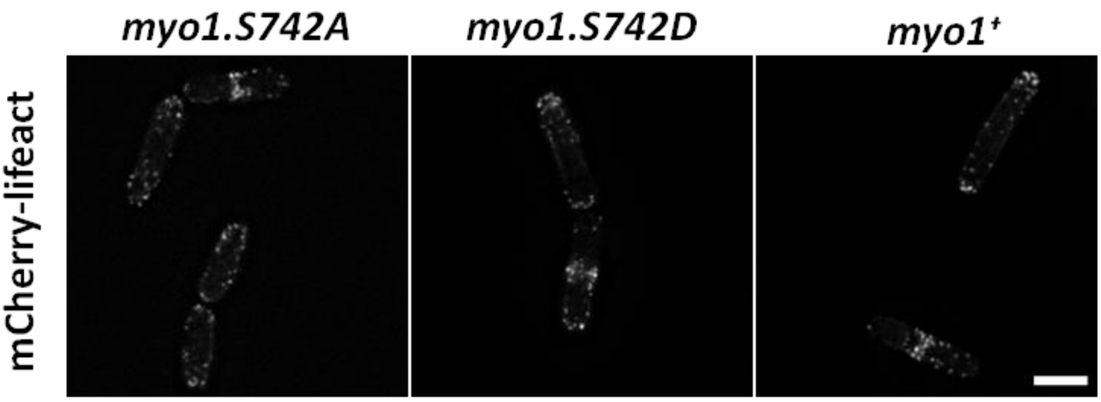

**Figure 5.5.1. Myo1 S742 phosphorylation is not required for actin patch formation and localisation to the cell ends for endocytosis in *S. pombe.*** Max projections from time-lapses of mCherry-Lifeact in *myo1.S742A mCherry-lifeact, myo1.S742D mCherry-lifeact* and *myo1$^{+}$ mCherry-lifeact S. pombe* cells. Dynamic mCherry-Lifeact foci were present at the cell ends in all strains. This observation suggests Myo1 S742 phosphorylation is not required for actin patch formation or localisation to the cell ends. Cells were cultured in EMMG media supplemented with amino acids for 2 days, at 25 °C. 11 z-slices were taken of cells incubated at 25 °C, with an exposure time of 100 ms to develop the max projection. Scale bar - 3.5 µm.

To determine if Myo1 S742 phosphorylation plays a role in actin patch activity during endocytosis, mCherry-Lifeact foci lifetimes at the ends of cells in G2 were quantified. It was hypothesised mCherry-Lifeact foci lifetimes would be not be a significantly different between the two ends of bipolar cells in G2. Should Myo1 S742 phosphorylation play a role in actin patch activity during endocytosis, a significant difference between the mCherry-Lifeact lifetimes at the two ends would be observed in *myo1.S742A* cells during G2. Cells separated from other cells and with a long morphology were considered in G2. mCherry-Lifeact foci lifetimes in *myo1.S742A mCherry-lifeact, myo1.S742D mCherry-lifeact* and *myo1$^{+}$ mCherry-lifeact* cells were quantified as in Section 5.2. Kymographs and dot plots displaying the mCherry-Lifeact foci lifetimes during G2 are displayed in Figure 5.5.2.

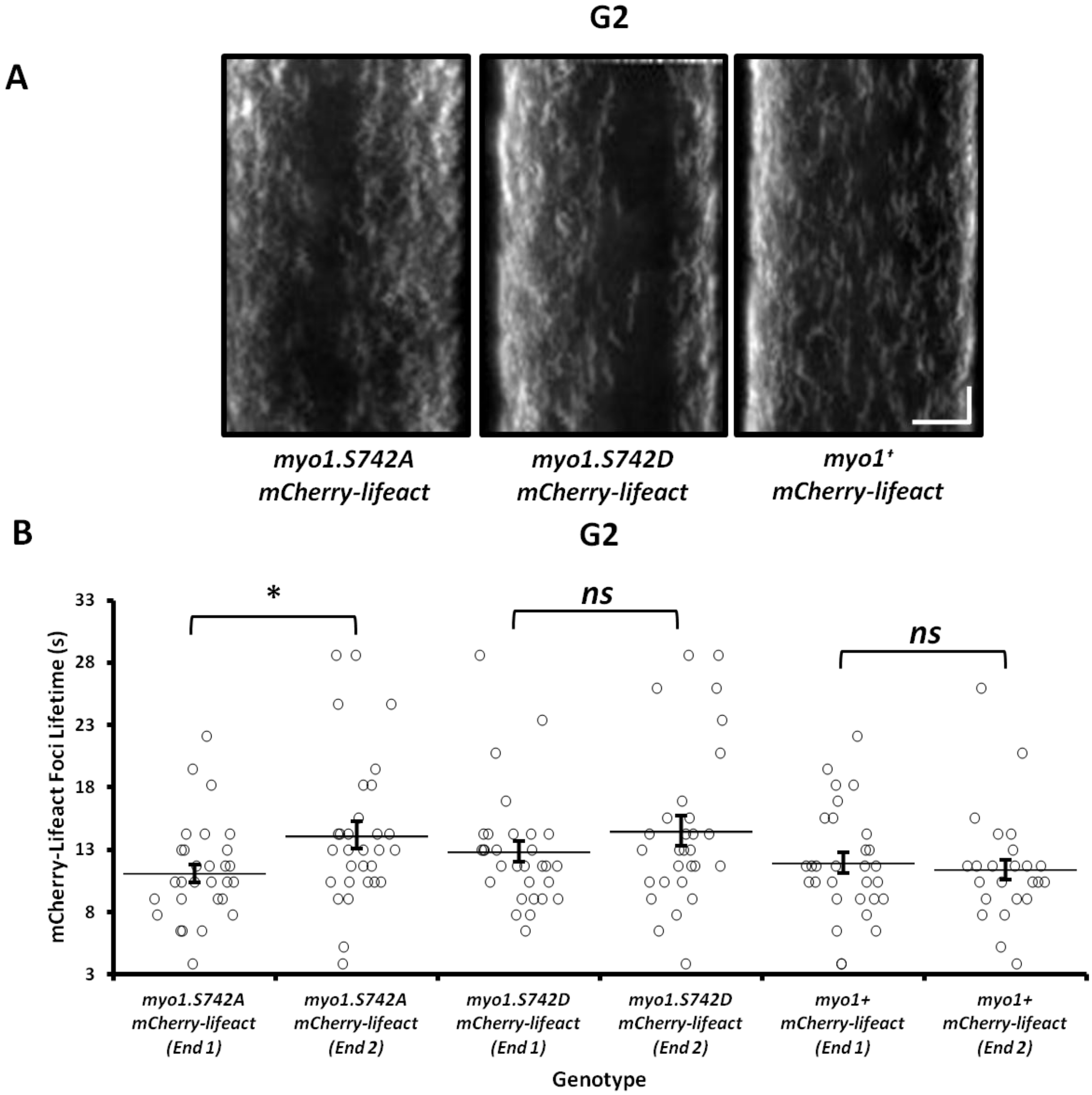

Figure legend on the following page.

**Figure 5.5.2. Difference in mCherry-Lifeact foci lifetimes at the ends of *myo1.S742A mCherry-lifeact* cells during G2 show phosphorylation of Myo1 S742 plays a regulatory role in actin patch activity and growth at the ends of *S. pombe* cells. (A)** Kymographs displaying dynamics of mCherry-Lifeact during G2 in *myo1.S742A mCherry-lifeact, myo1.S742D mCherry-lifeact* and wild-type *myo1*$^+$ *mCherry-lifeact* cells over 130 s. Motility is shown by horizontal direction in the signal lines. The kymographs were generated using Metamorph. Horizontal scale bar (distance) - 1.25 μm. Vertical scale bar (time) - 13 s. **(B)** Dot plot displaying the foci lifetime of mCherry-Lifeact in *myo1.S742A mCherry-lifeact, myo1.S742D mCherry-lifeact* and wild-type *myo1*$^+$ *mCherry-lifeact S. pombe.* Error bars represent standard error of the mean (SEM). Student's *t*-tests were used to determine significant differences between the foci lifetimes of mCherry-Lifeact at the old and new ends of the cells ($p \leq 0.05$). No significant difference between the average mCherry-Lifeact foci lifetimes was observed between the two cell ends of the wild-type *myo1*$^+$ *mCherry-lifeact* cells, which is consistent with bipolar growth expected during G2 (end 1 - 11.96 ± 0.83 s; end 2 - 11.40 ± 0.78 s) (mean ± SEM). The average mCherry-Lifeact foci lifetime was significantly shorter at one end of *myo1.S742A mCherry-lifeact* cells (end 1 - 11.09 ± 0.72 s; end 2 - 14.17 ± 1.08 s) ($p \leq 0.05$). These data suggest actin activity for endocytosis is greater at one end of *myo1.S742A mCherry-lifeact* cells during G2 and Myo1 S742 phosphorylation therefore impacts the regulation bipolar growth patterns during G2. $n \geq 30$. '*n*' indicates the number of mCherry-Lifeact foci measured from each strain. * $p \leq 0.05$. '*ns*' denotes the difference is not statistically significant.

During G2, the average mCherry-Lifeact foci lifetime was not significantly different between the old and new cell ends of wild-type *myo1*$^+$ *mCherry-lifeact* cells (end 1 - 11.96 ± 0.83 s; end 2 - 11.40 ± 0.78 s) (mean ± SEM). This data suggests actin activity for endocytosis at the ends of the wild-type *myo1*$^+$ *mCherry-lifeact* cells was even and is consistent with bipolar growth expected during G2. A significant difference in average mCherry-Lifeact foci lifetime was observed between the ends of *myo1.S742A mCherry-lifeact* (end 1 - 11.31 ± 0.86 s; end 2 - 13.95 ± 1.24 s) ($p \leq 0.05$), suggesting actin activity for endocytosis was different between the old and new end of *myo1.S742A mCherry-lifeact* cells. No significant difference in average mCherry-Lifeact foci lifetime was observed in *myo1.S742D mCherry-lifeact* cells. Collectively, these data suggest Myo1 S742 phosphorylation plays a regulatory role in actin activities for endocytosis and bipolar growth during G2. The difference in actin lifetimes at the ends of *myo1.S742A* cells is consistent with the greater proportion of monopolar cells in the *myo1.S742A* strain (Figure

5.1), suggesting there is a delay in NETO caused by the lack of Myo1 S742 phosphorylation. It is also consistent with the increased cell length of *myo1.S742A* cells.

## 5.6 Myo1 S742 phosphorylation is required for correct spore formation, cell polarity regulation and cell growth regulation in sporulating *S. pombe.*

Protein function in cells is dependent on temperature. Enzyme reactions double every 10 $^{o}$C and *S. pombe* growth rates double at 34 $^{o}$C, compared to at 25 $^{o}$C. However at higher temperatures, cells are more sensitive to minor defects in proteins. To determine whether Myo1 S742 phosphorylation is required to regulate polarised cell growth during meiosis, *mNG-myo1.S742A, myo1.S742A cam1-GFP, myo1.S742A cam2-GFP* and wild-type *mNG-myo1*$^{+}$ cells were grown on solid MSL media (to induce meiosis and sporulation) at the restrictive temperature of 34 $^{o}$C. The cells were grown at 34 $^{o}$C to exacerbate the impact of Myo1 S742A on the cell. Images of the cells were taken with transmitted light to observe the morphology of the cells and are displayed in Figure 5.6.

Figure 5.6 shows transmitted light images of sporulating cells with various abnormal morphologies observed in all the *myo1.S742A* strains. Morphologies ranged from long and short, wide and angular, club-like, bent and globular, suggesting complete loss of polarity within the cells. Schmooing cells (undergoing conjugation) with bent or elongated schmooing ends, and sporulating cells with less or more than four spores were also observed. The number of cells with abnormal morphologies was quantified manually. Defects were observed in 56.7 % of *myo1.S742A cam1-GFP* cells, 7.3 % of *myo1.S742A cam2*-GFP cells, 16.7 % of *mNG-myo1.S742A* cells and 1.4 % of wild-type *mNG-myo1*$^{+}$ cells. The higher percentage of morphological abnormalities in *myo1.S742A cam1-GFP* cells is consistent with the slower growth of *myo1.S742A cam1-GFP* cells (Figure 5.4) and temperature sensitivity observed in *myo1Δ* (Toya et al., 2008). The greater percentage of morphological defects in all the *myo1.S742A* strains suggests Myo1 S742 phosphorylation is required to maintain correct cell growth regulation, cell polarity and spore formation, in sporulating *S. pombe* cells.

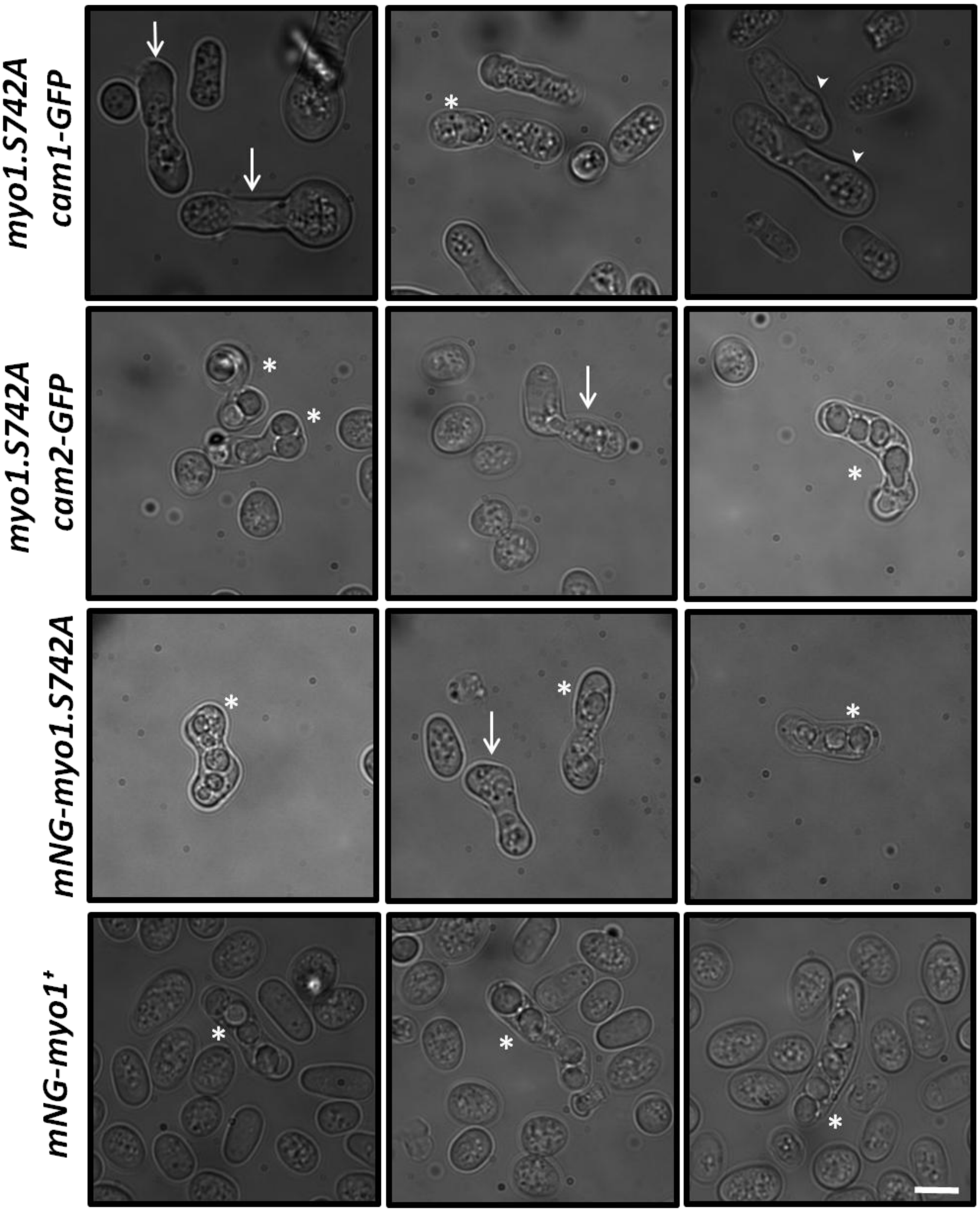

Figure legend on the following page.

**Figure 5.6. A lack of Myo1 S742 phosphorylation results incorrect spore formation and a loss in cell polarity and growth regulation in sporulating *S. pombe* cells.** Transmitted light images of abnormal cell shape and spore formation in *myo1.S742A cam1-GFP, myo1.S742A cam2-GFP, mNG-myo1.S742A* and wild-type *mNG-myo1*$^+$ cells at 34 °C. In all *myo1.S742A* strains, multiple defects were observed: sporulating cells with an incorrect number of spores and deformed spores; schmooing cells (cells undergoing conjugation) with bent or elongated schmooing ends; loss of cell polarity and regulation of growth. Defected cells made up 56.7 % of *myo1.S742A cam1-GFP* cells, 7.3 % of *myo1.S742A cam2*-GFP cells, 16.7 % of *mNG-myo1.S742A* cells and 1.4 % of wild-type *mNG-myo1*$^+$ cells. These data suggest Myo1 S742 phosphorylation is required for the regulation of cell growth, cell polarity and correct sporulation *S. pombe* cells. '*' indicates sporulating cells. Arrows indicates cells with bent or extended schmooing tips. Arrowheads indicate cells that have lost polarity and the regulation of cell growth. Cells were cultured at 34 °C on solid MSL media without nitrogen and supplemented with amino acids, vitamins and minerals for 3 days. The cells were then scraped from the plate and imaged in MSL liquid media without nitrogen at 34 °C. The images were taken with transmitted light with an exposure time of 50 ms. $n \geq 65$. '*n*' indicates the number of cells quantified in each strain. Scale bar - 3.5 µm.

## 5.7 Chapter 5 summary

In this chapter, Myo1 S742 phosphorylation has been shown to play a role in the regulation and maintenance of polarised cell growth. The absence of phosphorylation of Myo1 S742 caused, slower growth rates and morphology defects, indicating loss of normal polarity in *myo1.S742A* cells. Impact on cell polarity was also shown through an increase in monopolar cells in vegetative *S. pombe,* and actin dynamics in G2 cells suggesting different rates of endocytosis at the old and new cell ends. In sporulating cells, Myo1 S742 phosphorylation was shown to regulate Cam2 activity, and may not be required for Myo1 co-localisation with Cam1.

To determine if Myo1 S742 phosphorylation plays a role in the regulation of monopolar and bipolar growth in *S. pombe*, the monopolar-to-bipolar ratio was quantified in calcofluor stained *myo1.S742A*, *myo1.S742D* and wild-type *myo1*$^+$ cells. A larger proportion of *myo1.S742* and *myo1.S742D* cells showed monopolar growth. There was a 7 % and 4 % difference between the *myo1*$^+$ monopolar-to-bipolar ratio and *myo1.S742A* and *myo1.S742D* monopolar-to-bipolar ratios respectively (Figure 5.1B). *myo1.S742A* and *myo1.S742D* cells were also significantly longer than wild-type *myo1*$^+$ cells. These data suggest a delay in NETO in *myo1.S742A* cells and Myo1 S742 phosphorylation is therefore involved in the switch from monopolar growth to bipolar growth in *S. pombe.*

Cam1, Cam2 and Myo1 dynamics were then studied during the vegetative and meiotic cycles to determine the impact of Myo1 S742 phosphorylation on the interaction of the calmodulins with Myo1 and their activity for endocytosis during these cycles. Time-lapses of Cam1-GFP, Cam2-GFP and mNG-Myo1 localisation and dynamics were recorded in the *myo1.S742A*, *myo1.S742D* and wild-type *myo1*$^+$ cells. In vegetative cells in all strains, Cam1-GFP and Cam2-GFP were distributed throughout the cells and mNG-Myo1 localised to the ends of the cells, where endocytosis occurs (Figure 5.2.1A). The foci lifetimes of Cam1-GFP, Cam2-GFP and mNG-Myo1 in the vegetative cells were ~11 s in all strains, suggesting Myo1 S742 phosphorylation does not impact Cam1, Cam2 and Myo1 activity in vegetative cells (Figure 5.2.2).

In sporulating cells, the three proteins localised to the peripheries of the spores and the foci lifetimes were longer than in vegetative cells, indicating reduced activity of the proteins in sporulating cells. In sporulating cells, Cam1-GFP and mNG-Myo1 displayed foci lifetimes ranging from 1 s to >100 s in all strains. The variations of Cam1-GFP and mNG-Myo1 foci lifetimes were similar to each other suggesting co-localisation and interactions between the two proteins. The absence of Myo1 S742 phosphorylation reduced the foci lifetime of mNG-Myo1 and Cam1-GFP foci in *myo1.S742A* cells (Figure 5.2.2). These data suggest Myo1 S742 phosphorylation impacts Myo1 and Cam1 function in sporulating cells. Cam2-GFP displayed extended lifetimes of >100 s in the *myo1.S742A* background. This data suggests binding of Cam2 to Myo1 was hindered in the absence of Myo1 S742 phosphorylation. This would therefore hinder Myo1 and Cam2 function in forespore formation in sporulating cells (Figure 5.2.2). In future experiments, co-immunoprecipitation could be used to determine if Cam1 and Cam2 binding to Myo1 is hindered in *myo1.S742A* cells.

FM4-64 stained sporulating cells confirmed minimised endocytosis in sporulating *myo1.S742A*, *myo1.S742D* and wild-type *myo1*$^{+}$ cells (Figure 5.3). This is consistent with the longer foci lifetimes of Cam1, Cam2 and Myo1 in sporulating cells (Figure 5.2.2). The absence of Myo1 S742 phosphorylation reduced the degree of endocytosis in *myo1.S742A* cells even further as FM4-64 was observed to concentrate outside of the cell wall of some cells. The abundance of Myo1 in *myo1.S742A* cells was less than wild-type *myo1*$^{+}$ cells. Low $Ca^{2+}$ levels during the meiotic cycle favour Cam2 binding to Myo1 (Baker et al., 2019) and *myo1.S742A* results in increased Cam2 foci lifetimes and hinders Cam2 binding to Myo1 (Figure 5.2.2). Taken together with these facts, the low level of Myo1 suggests Myo1 S742 phosphorylation is required for Cam2 to bind to Myo1 in order to modulate endocytic activity of Myo1. This is consistent with reduced levels of Myo1 in actin patches in *cam2Δ* cells (Sammons et al., 2011).

Growth curves of *cam1-GFP, cam2-GFP* and *mNG-myo1* cells in the *myo1.S742A, myo1.S742D* and wild-type *myo1*$^{+}$ backgrounds were generated to determine if a lack of Myo1 S742 phosphorylation disrupts growth. The growth curves showed the lack of Myo1 S742 phosphorylation caused slower overall growth (cell size and number) towards the end of the log phase of growth in all strains, suggesting Myo1 phosphorylation is involved in the regulation of cell growth in vegetative cells (Figure 5.4). The mean cell length of *myo1.S742A* cells was 12.04 ± 0.12 µm and the mean length of wild-type *myo1*$^{+}$ cells was 10.66 ± 0.09 µm (mean ± SEM). As *myo1.S742A* cells are significantly longer than wild-type *myo1*$^{+}$ cells, the increase in cell number may be hindered in the *myo1.S742A* cells by a delay in NETO (Figure 5.1). In future experiments, a Coulter counter may be used to determine if the reduction in overall cell growth in *myo1.S742A* cells is due to a slower increase in cell number.

Actin patch dynamics were observed in time-lapses of G2 *mCherry-lifeact* cells in the *myo1.S742A, myo1.S742D* and wild-type *myo1*$^+$ backgrounds, to determine if Myo1 S742 phosphorylation had an impact on actin patch formation and localisation during endocytosis. mCherry-Lifeact foci were motile at both ends of the cells, suggesting Myo1 S742 phosphorylation is not required for the formation and localisation of actin patches at the cell ends (Figure 5.5.1). To determine if Myo1 S742 phosphorylation had an impact on actin activity for endocytosis in vegetative cells in G2, mCherry-Lifeact foci lifetimes were recorded. There was a significant difference between lifetimes of foci at the two cell ends of *myo1.S742A mCherry-lifeact* cells (Figure 5.5.2). A significant difference was not observed between the ends of wild-type *myo1*$^+$ *mCherry-lifeact* cells and this is consistent with bipolar growth expected during G2. These data suggest actin activity for endocytosis was different between the old and new end of the *myo1.S742A mCherry-lifeact* cells due to the lack of phosphorylation of Myo1 S742. This is consistent with the suggested delay in NETO in the *myo1.S742A* background (Figure 5.1). Therefore, Myo1 S742 phosphorylation plays a regulatory role in actin activities for endocytosis and bipolar growth during G2 of the vegetative cycle.

To determine if Myo1 S742 phosphorylation impacts the regulation of polarised cell growth in sporulating cells, the morphology of nitrogen starved *myo1.S742A cam1-GFP, myo1.S742A cam2-GFP, mNG-myo1.S742A* and wild-type *myo1*$^+$ cells were observed. Cells in the *myo1.S742A* background displayed a number of morphological defects such as bent and elongated schmooing ends, an incorrect number of spores and appeared enlarged and club-like, which indicated a loss of polarity (Figure 5.6). A greater percentage of *myo1.S742A cam1-GFP* cells had morphological defects (56.7 %) and this is consistent with the slower growth of the strain (Figure 5.4A). The abnormal morphologies in sporulating cells in the *myo1.S742A* background may be related to the lack of Cam2 binding to Myo1 for Myo1 to function in forespore membrane formation (Figure 5.2.2). These data suggest Myo1 S742 phosphorylation is required to maintain correct cell growth, cell polarity and spore formation, in sporulating *S. pombe* cells.

# Chapter 6: Discussion

Unconventional myosin motors are actin associated proteins which function in an array of intercellular processes, within non-muscle cells. Myo1 is involved in endocytosis and cell cycle regulation and the main function of Myo52 is to transport cargo such as vesicles throughout the cell. Myosin function is managed by a variety of means including phosphorylation. Phosphorylation is a post-translational modification, executed by kinase enzymes, in which a phosphate group is attached to a protein at specific phosphorylation sites and induces various changes in state and function, specific to each protein. It is essential for the regulation of protein function and therefore many cellular processes. Broadening what is understood of its relevance in myosin function therefore is of great significance.

## 6.1 Fluorescence imaging optimisation

One focus of the PhD study concentrated on phototoxicity, which is light induced damage to live cells. ROS scavenging antioxidants, within living organisms, insufficiently preserve cells from photodamage during fluorescence microscopy. CAR constriction was monitored with long term time-lapses of CAR constriction in *rlc1-GFP pcp1-GFP S. pombe* cells, to determine whether differences in phototoxic outcomes occur between (i) frequent low intensity light exposure and; (ii) infrequent high intensity light exposure. Without altering the total amount of light energy delivered to samples, delivering light at higher exposure times and over a longer period of time, has previously been said to allow live cells to utilise protective ROS mechanisms more efficiently than if light was delivered at higher intensities over a shorter period of time. This would involve the combination of increasing time intervals between exposure time points, reducing light intensity and lengthening the exposure time (Carpenter et al., 2009; Dixit & Cyr, 2003; Koester et al., 1999; Tenevez et al., 2012).

In this study, without changing the total light exposure to cells, no difference in CAR constriction rates was observed when cells were frequently exposed to low intensity light or infrequently exposed to high intensity light (Figure 3.1.2). The different exposures did not induce structural defects in the CAR either (Figure 3.1.1). Since phototoxicity was not evident through the assessment of CAR constriction, other aspects of the cell may be studied for phototoxic damage to the cell in future experiments. Phototoxicity may have been detected by through other observations e.g. increasing intracellular $Ca^{2+}$ (Laiusse et al., 2017).

Exposure to higher powers of light during widefield and confocal microscopy have been shown to increase intracellular $Ca^{2+}$ transients in live guinea pig smooth muscle cells and bovine articular chondrocytes (specialised cells in cartilage), stained with fluorescent calcium indicators called Fluo 3-AM and Fluo 4-AM (Archer & Francis-West, 2003; Knight et al., 2003; McDonald et al., 2012). When bound to $Ca^{2+}$, the fluorescence intensity of Fluo 3-AM and Fluo 4-AM increases more than one hundred-fold. Antioxidant ascorbate was also applied to the chondrocytes which significantly reduced the occurrence of $Ca^{2+}$ transients. This showed the increase in $Ca^{2+}$ was mediated by free radicals (Knight et al., 2003). This methodology may be applied to *S. pombe* to monitor phototoxicity. A dose-response-curve could also be produced to determine a phototoxicity threshold (the highest light power which does not produce a significant increase in intracellular $Ca^{2+}$ transients. ROS production can also be measured with ROS-reactive dye, CM-$H_2$DCFDA. CM-DCF fluorescence from CM-$H_2$DCFDA can be used as an indication of ROS production induced by light exposure (Section 3.5).

A common means of measuring photodamage in *S. pombe* is to measure cell proliferation during light exposure using a microfluidic device (Frey at al., 2015; Schmidt et al., 2020). Cell number could be quantified in transmitted light images of cells before and after exposure to light, whilst kept in a microfluidic device. Cells can be segmented and quantified using imaging analysis software such as PombeX or CellX. The growth rate of cells exposed to different imaging conditions can then be calculated (Section 3.5).

Other means of reducing phototoxicity may be pulse illumination and the use of longer wavelengths (e.g. red light) for fluorescent excitation, due to their lower energy and lower absorbance into biomolecules (Dixit & Cyr, 2003; Gordidze et al., 1998; Khodjakov & Rieder, 2006). Red fluorescent markers are dimmer than green markers however and may require greater light intensity for detection. Therefore, compromises must be taken to maintain the viability of the live cells. Readouts for studies related to the function of Myo1 and Myo52, such as cell cycle timings and cytoplasmic $Ca^{2+}$ levels, may become inaccurate due to subtle phototoxicity within the cell (Icha et al., 2017). Therefore, further work on reducing phototoxic effects in the cell must be conducted if data, as close to physiological conditions, is to be obtained.

Monitoring CAR constriction showed 0.2 mA light exposure for 50 ms, every 3 min had no effect on CAR constriction (Figure 3.1.1). These imaging conditions were used to assess the significance of the *cdc8.27* and *cdc8.110* alleles in the Cdc8 function of stabilising actin during contractile actin ring formation and constriction. Increasing temperatures (25 °C, 30 °C, 34 °C) induced CAR formation and construction defects of increasing severity. The CAR defects included aberrant contractile rings, delayed constriction, displaced CAR detached from the cell cortex, the inability to constrict and collapse (Figure 3.2.1, Figure 3.2.3, Figure 3.2.4). These defects showed Cdc8 E129, Cdc8 A18 and Cdc8 E31 are required for correct CAR formation, attachment to the cell cortex and constriction. *cdc8.110* induced CAR defects were more severe and were induced from lower temperatures, in comparison to *cdc8.27.* Bent morphologies were also observed in this strain (Figure 3.2.2). These observations suggest the Cdc8 A18T and Cdc8 E31K substitution mutations had an addictive effect on CAR function and Cdc8 function in actin stabilising is needed to maintain correct cell shape.

The impact of *cdc8.27* and *cdc8.110* on the structure and thermostability of Cdc8 was further shown by Johnson et al. (2018). Circular dichroism (CD) analysis showed unfolding of the α-helices that run along the entire length of the Cdc8.27 and Cdc8.110 mutants, at 50 °C (Johnson et al., 2018). Cdc8 exists in acetylated and non-acetylated forms. N-terminal acetylation of Cdc8 allows Cdc8 to bind to actin with a high affinity and strengthens Cdc8 end-to-end binding (Coulton et al., 2010). The unfolding occurred with two thermal transitions in the acetylated form and one thermal transition in the non-acetylated form. Subsequent cooling at 10 °C caused complete reversal of the unfolding. Decreased thermostability was observed in non-acetylated Cdc8.27 and Cdc8.110 in comparison to wild-type non-acetylated Cdc8, whilst acetylation caused an increase in Cdc8.27 and Cdc8.110 thermostability in comparison to wild-type acetylated Cdc8. Co-sedimentation experiments on Cdc8.27 at 20 °C also showed acetylated and non-acetylated Cdc8.27 had lower affinity to actin (Johnson et al., 2018). These observations are consistent with the CAR and cell growth defects observed in *cdc8.27* and *cdc8.110 S. pombe.* It is currently unknown why N-terminal acetylation would bring about stabilisation of Cdc8.27 and Cdc8.110 and not wild-type Cdc8. Cdc8 A18T, Cdc8 E31K and Cdc8 E129K are located at opposite ends of Cdc8 and acetylation and amino-acid modifications have been shown to have long distance effects on tropomyosin structure, in previous studies (Johnson et al., 2018). The exact mechanisms that are induced in temperature-sensitive mutants, to bring about disorder and disruption to biological processes, are yet to be fully understood.

As the CAR in *cdc8.27 rlc1-GFP* and *cdc8.110 rlc1-GFP* cells appeared to be displaced and slide along the cell cortex, future experiments could include observations of Mid1-mCherry during CAR constriction in *cdc8.27* and *cdc8.110* mutants. Mid1 is a cleavage placement protein which anchors to the cell cortex and determines the site of cell division (Pollard & Wu, 2010). *mid1Δ* cells fail to undergo cytokinesis which is consistent with the cytokinetic failure observed in *cdc8.27 rlc1-GFP* and *cdc8.110 rlc1-GFP* cells (Figure 3.2.5). *mid1-mCherry rlc1-GFP* cells could be developed, in the mutant and wild-type backgrounds, to observe where the CAR forms in relation to Mid1-mCherry and can indicate if the CAR fails to attach to Mid1. Cytokinesis failure is rescued by a delay in septum formation induced by *cps1-191,* which is a D277N (aspartic acid to asparagine) substitution in Bgs1/Cps1 (Dundon & Pollard, 2020). As the delay in septum formation allows time for CAR to form properly in *mid1Δ cps1-191* cells, *cdc8.27 cps1-191 rlc1-GFP* and *cdc8.110 cps1-191 rlc1-GFP* strains may be observed to determine if CAR constriction is also rescued (Davidson et al., 2016). This would indicate the CAR displacement in *cdc8.27* and *cdc8.110* cells is related to failure to attach to Mid1.

Spinning-disk confocal imaging was optimised to simultaneously image labels in the green and red fluorescent channels, without channel-to-channel bleed-through, and is ideal for co-movement and co-localisation studies (Figure 3.4.1, Figure 3.4.2). Although this was largely successful, further optimisation is required to improve the methods to align the overlaid images in the different channels to view composite images, using the Metamorph software. Misalignment could display localisation incorrectly or falsely suggest co-localisation, therefore correct alignment is crucial for use of the simultaneous imaging system. The images were aligned based on the cell shape however this is difficult to outline in the fluorescent channels due to background fluorescence mainly in the green channel. Average background intensity values were used to remove background fluorescence however, this background removal also reduced mCherry-Lifeact signal.

In order to improve the alignment of overlaid images in future experiments, background fluorescence intensity values from a blank field of view with no cells can be used as a separate background image to subtract background fluorescence intensity values from images instead of using the average background intensity value. The average background intensity value, from images which include cells, may have been too high and subtraction of this value may have resulted in the removal of too much mCherry-Lifeact signal. A constant intensity value may then be set to subtract from all images in the experiment. A reduction in the signal-to-noise ratios, largely in the green channel would be beneficial, as it would allow clearer visualisation of cell morphologies, foci, filaments and other intracellular structures. An outline of the cell morphology from transmitted light images, acquired before or after the simultaneous two-channel spinning-disk image acquisition, can also be included in the composite overlay to improve the alignment of the images.

The simultaneous two-channel spinning-disk confocal imaging system would provide a means of simultaneously observing two proteins labelled with red and green fluorophores, in real-time. The system acquires images in the red and green channel simultaneously and therefore reduces the time delay that occurs when alternating between channels. The imaging system would be a useful tool to observe the motility and co-localisation of myosins and proteins they associate with, e.g. calmodulin light chains and could be applied to experiments described in this thesis and future experiments.

## 6.2 Phospho-regulation of myosin V

The conserved phosphorylation sites: Myo52 S720, Myo52 S798, Myo52 S985, Myo52 S1064, Myo52 S1065 and Myo52 S1072, have been identified in the head, neck and tail domains of Myo52 via proteomic screens (Peterson, personal communication, 2017; Tay et al., 2019; Wilson-Grady et al., 2008). To identify the significance of phosphorylation at these sites, *myo52.S720A, myo52.S798A, myo52.S985A, myo52.S1064A S1065A* and *myo52.S1072A* Myo52 phospho-mutant *S. pombe* strains with redundant phosphorylation sites were developed. In these strains, substitution mutations converted the serines, which are usually phosphorylated, into alanines. The alanines cannot be phosphorylated, therefore the strains demonstrate phenotypes that result in the lack of phosphorylation at those phosphorylation sites. Myo52, actin, Atb2 and Mor2 were studied in these strains, via fluorescence imaging, to determine the impact phosphorylation of the Myo52 phosphorylation sites has on the function of Myo52, correct cell growth and regulation of cytoskeletal components.

Examination of the phospho-mutants suggested the Myo52 phosphorylation sites of interest do impact Myo52 function in maintaining correct cell growth (Figure 4.1.1) cell length (Figure 4.1.4) and cell polarity regulation (Figure 4.1.2, Figure 4.1.3). Myo52 phosphorylation was shown to be imperative in enabling actin motility within the cell (Figure 4.2.1, Figure 4.2.2) and Myo52 S1064 S1065 phosphorylation is required for correct Myo52 motility (Figure 4.3). A summary of the observations made of the Myo52 phospho-mutants is shown in Table 2.

**Table 2. The lack of Myo52 S720, Myo52 798 and Myo52 1072 phosphorylation results in growth defects correlated to changes in polarity.** The table summarises observations made of the Myo52 phospho-mutant strains in comparison to the wild-type *myo52*$^{+}$ background. There is a correlation between the decreased overall growth at 20 $^{o}$C and larger proportion of monopolar growth observed in *myo52.S720A* and *myo52.S798A* cells*.* There is also a correlation between the increased growth and larger proportion of bipolar cells observed in *myo52.S1072A* cells*.* No other correlations were observed in the remaining strains. All strains displayed a defect in actin localisation or actin speed. 'NS' indicates no significant difference to the wild-type *myo52*$^{+}$ background. Slower Myo52 speed and Mor2 aggregates were observed in *myo52.S1064A S1065A* cells (not included in the table).

| **Strain** | **Overall growth - $OD_{600}$ at 20 $^{o}$C** | **Overall growth - $OD_{600}$ at 25 $^{o}$C** | **Polarity** | **Cell length** | **Actin localisation** | **Actin speed** |
|---|---|---|---|---|---|---|
| ***myo52.S720A*** | Decreased | NS | More monopolar | Shorter | Delocalised | NS |
| ***myo52.S798A*** | Decreased | NS | More monopolar | NS | Delocalised | NS |
| ***myo52.S985A*** | NS | NS | More monopolar | Shorter | Delocalised | Slower |
| ***myo52.S1064A S1065A*** | NS | NS | Comparable to wild-type | NS | Comparable to wild-type | Faster |
| ***myo52.S1072A*** | Increased | NS | More bipolar | Shorter | Delocalised | Slower |

At 20 $^{o}$C, *myo52.S720A* cells displayed reduced overall growth in comparison to wild-type *myo52*$^{+}$ cells. This was not observed at 25 $^{o}$C which suggests *myo52.S720A,* is cold-sensitive at 20 $^{o}$C (Figure 4.1.1). A larger proportion of *myo52.S720A* cells were monopolar (Figure 4.1.3) and were shorter (Figure 4.1.4) than wild-type *myo52*$^{+}$ cells*.* As Myo52 S720 is located in the head of Myo52, it may be possible that phosphorylation at this site is required for actin binding and/or motility along the actin filaments. Actin was delocalised in this strain and the strain did not display actin filaments (Figure 4.2.1). These defects may be the result of lacking Myo52 motility. Myo52 motility generates force that promotes actin filament polymerisation. The delivery of For3, which enables actin filaments to polymerise, may also be hindered in this strain (Presti et al., 2012). The actin defects may also have contributed to the bent and short morphology of *myo52.S720A* cells (Figure 4.1.2) as well as the change in polarity (Figure 4.1.3). Myo52 motility is required for Myo52 to transport the α-glucan synthase, Mok1, and β-1,3-glucan synthase, Bgs1, to areas of cell growth and cytokinesis for the development of the cell wall (Davison et al., 2016; Motegi et al., 2001; Mulvihill et al., 2001; Mulvihill et al., 2006; Win et al., 2001). The localisation of Bgs1 is cytoplasmic in *myo52Δ* cells (Mulvihill et al., 2006). Mok1 is delocalised and up regulated in *myo52Δ* cells. A lack of Mok1 and Bgs1 transport by Myo52 may be the cause of the reduced cell growth and morphological defects observed in *myo52.S720A* cells.

Multiple mutations in the Myo52 motor head domain have been shown to induce reduced Myo52 motility or abolish movement. Mutations in the myosin motor head relay helix, changes the affinity of the motor head for actin. Y509G (tyrosine 509 to glycine 509) and G689A (glycine 689 to alanine 689) substitutions in the Myo52 relay helix cause a reduction in Myo52 velocity, whereas F490A (phenylalanine 490 to alanine 490) and G689V (glycine 689 to valine 689) substitutions abolish Myo52 movements (Grallert et al., 2007). Myo52 with mutations in the ATP binding domain within the motor head domain has been shown to not co-localise with actin. These mutated Myo52 form large immotile foci instead (Mulvihill et al., 2006). Fluorescence microscopy may be used in future experiments to determine if Myo52 S720A is motile and is able to co-localise with actin.

At 20 °C, *myo52.S798A* cells also displayed reduced overall growth not observed at 25 °C which suggests *myo52.S798A* cells are cold-sensitive at 20 °C (Figure 4.1.1). A larger proportion of *myo52.S798A* cells were also monopolar when compared to wild-type *myo52*$^{+}$ cells (Figure 4.1.3). Myo52 S798 is located in the neck domain which is composed of IQ motifs. Grallert et al. (2007) have shown deletion of all Myo52 IQ motifs does not affect the *in vivo* mean velocity of Myo52. This was shown by measuring the velocity of GFP-Myo52ΔIQ in *S. pombe*. Without the neck domain, it was suggested that multiple Myo52 dimers may associate into arrays. In these arrays, the coiled-coil regions act as lever arms for non-processive movement of Myo52 (Grallert et al., 2007). As the neck domain of Myo52 is not needed for Myo52 movement, reduced overall growth observed in *myo52.S798A* cells may be due to a possible impact on calmodulin binding to the IQ motifs or the regulation of auto-inhibition (globular tail domain binding to the motor domain) (Grallert et al., 2007). Increased Myo52 auto-inhibition could subsequently lead to reduced motility along the actin filaments and disrupt actin polymerisation observed in this strain (Figure 4.2.1). Increased auto-inhibition may be observed using cryo-electron microscopy.

*myo52.S985A* cells were observed to have a larger proportion of monopolar cells (Figure 4.1.3) and were shorter than wild-type *myo52*$^+$ cells (Figure 4.1.4). Actin foci were delocalised and slower than in wild-type *myo52*$^+$ cells (Figure 4.2.1, Figure 4.2.2). Mulvihill et al. (2006) showed Myo52 lacking the coiled-coiled domain does not localise into discreet foci or co-localise with actin. Without a coiled-coil domain, Myo52 cannot form dimers. The observation therefore showed Myo52 monomers are not motile or localise with actin (Mulvihill et al., 2006). If the lack of Myo52 S985 phosphorylation has an impact on Myo52 dimerisation, the larger proportion of monopolar cells and shorter length of *myo52.S985A* cells may be due to the failure to form dimers and move along actin. In future experiments, an immunoblot could be carried out to determine if Myo52 S985 exists as monomer.

*myo52.S1064A S1065A* cells did not display defects in overall growth, polarity, cell length or actin localisation (Figure 4.1.1, Figure 4.1.3, Figure 4.1.4, Figure 4.2.1). These observations suggest Myo52 S1064 and Myo52 S1065 phosphorylation does not impact overall growth, polarity, cell length and actin localisation. A lack of Myo52 S1064 and Myo52 S1065 phosphorylation has been shown to induce faster actin foci dynamics, slower Myo52 foci dynamics and aggregates of Mor2 (Figure 4.2.2, Figure 4.3, Figure 4.4). Mor2 localisation is actin dependent (Hirata et al., 2002). The altered actin and Myo52 motility may have contributed to the formation of Mor2 aggregates in the *myo52.S1064A S1065A* cells. *mor2-282,* which is a substitution of a conserved glycine 1709 with aspartic acid in Mor2, has been shown to cause Mor2 to form discrete foci with the appearance of aggregates. The mutant Mor2-282 is therefore defective in Mor2 localisation (Hirata et al., 2002). Mor2 aggregates were also observed in *myo52.S1064A S1065A* cells but to a much lesser degree. The formation of Mor2 aggregates in *mor2-282* cells supports the fact that Myo52 S1064 and Myo52 S1065 phosphorylation may have a regulatory function in Mor2 localisation.

In contrast to *myo52.S1064A S1065A* cells, *myo52.S1072A* cells displayed greater overall growth at 20 °C than wild-type *myo52*$^+$ cells, which was not observed at 25 °C (Figure 4.1.1). This observation therefore suggested cold-sensitivity in *myo52.S1072A* cells. The strain was also shorter than wild-type *myo52*$^+$ cells and displayed actin defects (Figure 4.2.1, Figure 4.2.1). The difference in the phenotypes displayed by *myo52.S1072A* cells suggests Myo52 S1072 phosphorylation plays a role in the regulation of actin, cell polarity and cell growth. As *myo52.S1072A* cells have a short morphology, the increased overall cell growth may be a result of increased cell number and/or increased cell mass. The use of a Coulter counter would provide a measure of changes in cell concentration to determine the growth of *myo52.S1072A* cells. A lack of Myo52 S1072 phosphorylation may hinder Myo52 binding to For3 and therefore the delivery of For3 to the cell ends, for actin polymerisation (Presti et al., 2012).

A number of future experiments could be applied to all the Myo52 phospho-mutants to further explore the impact of Myo52 phosphorylation on the function of Myo52 for correct cell growth, polarity and cytoskeleton regulation. Win et al. (2000) reported reduced cell growth in *myo52Δ* cells at 29 °C. In future experiments, the growth rate of Myo52 phospho-mutants at various temperatures could be determined with the use of a Coulter counter rather than measuring $OD_{600}$ with a plate reader. Whether a lack of Myo52 phosphorylation causes a greater reduction in growth rate than *myo52Δ* could be determined.

In *S. pombe,* bent morphologies arise when the direction of growth diverges from axially straight. Deletions in proteins with roles in cell polarity and cytoskeleton regulation such as tip elongation aberrant 1, Tea1 (cell polarity maintenance), Tea2 (kinesin), Tea4 (cell polarity maintenance) and Pom1 (cell morphogenesis) have been shown to bring about bent morphologies (Abenza et al., 2014). Bent morphologies were also observed in all the Myo52 phospho-mutant strains. These observations suggest Myo52 phosphorylation is involved in the regulation of cell polarity or interactions with polarity regulating proteins (Figure 4.1.2). The lack of actin motility observed in Myo52 phospho-mutants may also have induced bends in the cell shape (Figure 4.2.1, Figure 4.2.2, Figure 4.2.3). Genetic crosses of the Myo52 phospho-mutant strains and a cell polarity factor deletion can generate double deletion mutants e.g. *myo52.S720A Δpom1.* The double mutation may cause an additive negative effect on cell polarity and result in morphology defects of increased severity. These defects could be observed via calcofluor staining. An increase in the severity of polarity defects would indicate phosphorylation of the Myo52 sites of interests plays a role in the regulation of cell polarity. Fluorescently labelled phospho-mutant Myo52 and polarity factors may provide insight into possible links between the proteins e.g. changes in localisation.

Myo52 has also been shown to redirect cell wall synthesising machinery between cell poles and the cell equator (Gachet & Hyams, 2005; Mulvihill et al., 2006). As the cell wall provides structural integrity, Myo52 phosphorylation may also be implemented in the structural maintenance of the cell. Cell wall synthesis may also be disrupted in the Myo52 phospho-mutant strains. Myo52 delivers Mok1 and Bgs1, to regions of cell wall deposition at the cell ends during interphase and the septum during cell division, for the production of α-glucan and β-D-glucan needed in the cell wall (Cortes et al., 2005). To characterise bent morphologies within each of the Myo52 phospho-mutant strains, a fixed degree of angular deviation must be defined and applied to quantification of bent cells. Fluorescence microscopy of wild-type *myo52*$^+$ cells has shown Myo52 co-localises with Bgs1 and Mok1 at the cell ends during interphase and the septum during cell division (Mulvihill et al., 2006, Win et al., 2001). Fluorescence microscopy could be used to determine changes in Myo52 co-localisation with Mok1 and Bgs1 in the Myo52 phospho-mutant cells. Co-immunoprecipitation may be used to determine if the phospho-mutant Myo52 bind to Mok1 and Bgs1.

Changes in growth polarity, as well as the bent morphologies and differences in cell length, may be resultant of the non-motile actin observed in the phospho-mutants (Figure 4.2.2). Myo52 transports For3 to cell ends to contribute to actin filament organisation. Myo52 translocation also provides tension on actin filaments which is required for filament assembly and extension by pulling on the actin filaments (Presti et al., 2012). Myo52 may fail to execute these processes correctly due to the lack of phosphorylation along Myo52. Kymographs showed the actin foci in all strains, including the wild-type *myo52*$^+$, were slower than the reported actin speed report in the literature (Figure 4.2.2). This may be due to the fact that the kymographs are restricted to capturing lateral movement. In future experiments, Lifeact-GFP could be observed in all dimensions using Imaris for Tracking imaging analysis software.

Mor2, involved in growth polarity establishment, successfully localised at the cell ends of *myo52.S1064A 1065A* cells suggesting Myo52 S1064 and Myo52 S1065 phosphorylation is not essential for Mor2 function (Figure 4.4). Mor2 localisation in the remaining four Myo52 phospho-mutant backgrounds should be studied in further work to determine if Mor2 localisation may be dependent on phosphorylation at a particular site. Any binding interactions between Myo52 and Mor2 could be identified via co-immunoprecipitation. Binding defects in the Myo52 phospho-mutants would also be highlighted by co-immunoprecipitation.

The lack of Myo52 S1064 and Myo52 S1065 phosphorylation reduced Myo52 dynamics (Figure 4.3). As these phosphorylation sites are located in the tail domain which is involved in cargo binding and not actin binding, it is possible the absence of phosphorylation at sites located in the motor head or neck domains may cause disruptions of greater severity to Myo52 actin binding and therefore dynamics. Difficulty was faced developing strains to fluorescently visualise Myo52 in the Myo52 phospho-mutant backgrounds. Future work may benefit from implementing electroporation to encourage DNA uptake during *S. pombe* transformations, monitoring associated proteins such as calmodulins as markers for Myo52 or the use of different fluorescent labels.

The future experiments described above can include Latrunculin A (LatA) treated wild-type *myo52*$^+$ cells*.* LatA is an actin polymerisation inhibitor. It binds to the nucleotide binding site of G-actin which to prevents actin polymerisation (Yarmola et al., 2000). The defects in the Myo52 phospho-mutants could be compared to defects in LatA treated cells. This would provide an indication into which defects were due to incorrect function of actin in the Myo52 phospho-mutants. *for3Δ* cells may also be applied to the future experiments to compare defect in this strain to defects in the Myo52 phospho-mutant strains. This would provide an indication into if failure of the Myo52 phospho-mutants to deliver For3 to the cell ends, results in the multiple defects observed in the mutant strains. Grallert et al. (2007) has shown Myo52 only moves at the cell equator in *for3Δ* cells. The strain only has CAR associated actin filaments. The actin filaments observed in the Myo52 phospho-mutants were either CAR associated or curled and located at the cell ends. These observations therefore suggest delivery of For3 to the cell ends is not completely interrupted in all the Myo52 phospho-mutant strains. In future experiments, Mor2 localisation in all the Myo52 phospho-mutants would be studied, since it localises to the cell ends in an actin dependent manner (Hirata et al., 2002; Kinai et al., 2005).

SDM can be used to make a phospho-serine-to-aspartic acid substitutions in Myo52 to generate *myo52.S720D, myo52.S798D, myo52.S985D, myo52.S1064D S1065D, myo52.S1072D* mutant strains. These phospho-mutants strains can be applied to all future experiments as a phospho-mimetic of constant phosphorylation.

## 6.3 Phospho-regulation of myosin I

Myo1 phospho-serine S742, located in an IQ-motif in the neck domain and its phosphorylation has been proposed to induce a conformational change in the neck domain. The Myo1 S742 phosphorylation was studied for further understanding of its role in Myo1 and calmodulin function, during endocytosis in the vegetative and meiotic life cycles, as well as the initiation of bipolar growth during NETO. A greater understanding of these routine changes in growth patterns can add to what is currently known about the intricacies of the cell cycle. A *myo1.S742A* strain, unable to be phosphorylated at the Myo1 phospho-serine S742, was developed within the lab via SDM. Live cell fluorescent imaging assays were utilised to monitor polarised cell growth patterns in the vegetative and meiotic life cycle. The data gathered indicated calmodulin activity and the initiation of bipolar growth during the vegetative life cycle to be dependent on Myo1 S742 phosphorylation. The absence of phosphorylation at Myo1 S742 also resulted in a temperature-sensitive phenotype with cell shape and spore formation defects.

Various observations of *myo1.S742A* cells indicated Myo1 S742 phosphorylation has an impact on the switch from monopolar growth to bipolar growth, during NETO in the vegetative life cycle. These observations include: slower rates of overall growth towards the end of the log-phase (Figure 5.4), an increased proportion of monopolar vegetative cells (Figure 5.1), asymmetrical endocytic actin patch activity at the ends of cells during G2 (Figure 5.5.2) and significantly greater cell length. These observations collectively suggest a delay in NETO occurs and the redistribution of actin patches for bipolar growth during G2 is disrupted in *myo1.S742A* cells, due to the lack of Myo1 phosphorylation (Hirata et al., 2016; Marks & Hyams, 1985).

During NETO endocytic actin patches are redistributed equally to both ends of the cell for endocytosis to occur at both ends and bipolar cell growth (Marks & Hyams, 1985). In *myo1.S742A* cells, actin patch activity was asymmetrical at the two ends of the cell. This is consistent with the fact that Sla2/End4 actin patch markers in *myo1.S742A* cells do not redistribute to the new end of newly divided cells. This was shown by less Sla2-mCherry fluorescence measured at the new end of newly divided *sla2-mCherry myo1.S742A* cells compared to wild-type *sla2-mCherry myo1*$^+$ (Baker et al., 2019). Prior to this in early interphase, (G1 pre-NETO), Myo1 S742 is phosphorylated. Approximately half of all Myo1 in the cell is a phosphorylated at S742. This level of phosphorylation then decreases as cells progress into G2. This was shown by the detection of phosphorylated Myo1 S742 in wild-type *myo1*$^+$ G1 arrested cells, by western blot using phospho-specific anti-Myo1 S742 antibodies. In extracts from cells released from G1 arrest, the amount of phosphorylated Myo1 S742 decreased to undetectable levels as the cell progressed through to the end of late G2. Myo1 S742 phosphorylation is therefore cycle cell dependent. Taken together, these findings indicate the peak of Myo1 S742 phosphorylation at G1 has regulatory significance in the redistribution of actin needed for endocytosis and bipolar growth, during NETO (Baker et al., 2019). *myo1.S742A* cells were significantly longer than wild-type *myo1*$^+$ cells suggesting a delay in cell division. This is consistent with the need for Myo1 S742 phosphorylation for the initiation of bipolar growth. Myo1 S742 phosphorylation and Cam1 binding to Myo1 is thought to cause a conformational change in the motor protein. The conformational change stiffness the Myo1 lever arm and enables Myo1 to generate force for motility. Myo1 S742 phosphorylation and Cam1 binding therefore moderates Myo1 activity in endocytosis and the initiation of bipolar growth in the vegetative cycle (Baker et al., 2019).

The polarity factor Tea4 is also distributed to the new cell ends during NETO, where it binds to For3 and forms part of the polarisome and also promotes the recruitment of For3. For3 then nucleates actin (Martin-Garcia & Mulvihill, 2009). *tea4*Δ *myo1.S742A* cells showed *myo1.S742A* does not have an additive effect on polarity defects observed in *tea4*Δ e.g. bent morphology. *cam2*Δ *tea4*Δ does cause an additive effect in polarity defects, which suggests Myo1 and Cam2 also have independent functions in the regulation of polarised cell growth during the vegetative cycle (Baker et al., 2019).

Observations of Cam1, Cam2 and Myo1 dynamics using fluorescent microscopy provided great insight in the differences between their activity during the vegetative cycle and the meiotic cycle, as well as the impact Myo1 S742 phosphorylation has on this activity (Figure 5.2.1, Figure 5.2.2). During the vegetative cycle, the $Ca^{2+}$ level within *S. pombe* cells is low (100 - 200 nM) which favours Cam1 binding to Myo1 (Ma et al., 2011; Miseta et al., 1999). Quantitative proteomic analysis determined the relative abundance of Myo1: Cam1: Cam2 to be 0.45: 1.56: 1 (Marguerat et al., 2012). This favours Cam1 binding to Myo1 over Cam2 during the vegetative cycle. TIRF microscopy of vegetative *mNG-myo1* and *cam1-GFP* cells has shown the peak intensity of Cam1-GFP during endocytic events is two times greater than the mNG-Myo1 peak intensity. This is consistent with the Cam1 binding to both Myo1 IQ motifs during the vegetative cycle. Endocytic events in *myo1.S742A* showed no difference in Cam1-GFP and mNG-Myo1 peak intensities, indicating *myo1.S742A* does not disrupt Cam1 binding to both Myo1 IQ motifs during the vegetative cycle (Baker et al., 2019). This is consistent with the unchanged foci lifetimes of Cam1-GFP in vegetative *myo1.S742A* cells (Figure 5.2.2).

*S. pombe* enter the meiotic cycle upon starvation and TORC2 and Gad8 signalling up-regulation. Myo1 S742 phosphorylation increases in mating and meiotic sporulating cells.

This was shown by the detection of phosphorylated Myo1 S742 in *myo1*$^+$ *fus1Δ* cells (cells arrested between the cell contact and cell fusion stages of mating) and wild-type *myo1*$^+$ spores, by western blot using phospho-specific anti-Myo1 S742 antibodies (Peterson et al., 1995). Calmodulin binding to myosin is calcium dependant. Calcium influxes that take place during mating pheromone release, meiosis and sporulation, provide favourable conditions for Cam2 binding (Carbó et al., 2017; Iida et al., 1990). $Ca^{2+}$ levels become approximately ten times greater than in vegetative cycle (Suizu et al., 1995). The abundance of Cam2 also increases. These conditions favour Cam2 binding to Myo1 (Baker et al., 2019).

Increased Cam1-GFP, Cam2-GFP and mNG-Myo1 lifetimes were observed within wild-type *myo1*$^+$ sporulating cells in comparison to vegetative cells (Figure 5.2.1, Figure 5.2.2). mCherry-Lifeact foci also had extended foci lifetimes in sporulating cells in comparison to in vegetative cells (Baker et al., 2019). These observations indicate reduced endocytic activity in the sporulating cells. Consistent with Myo1 and Cam2 involvement in prespore membrane formation, increased Myo1 and Cam2 lifetimes may indicate a halt in Myo1 endocytic activities (Itadani et al., 2006; Toya et al., 2001). The absence of Myo1 S742 phosphorylation further exacerbated the reduction in Cam2 dynamics within sporulating cells, suggesting Myo1 S742 phosphorylation is usually utilised for the promotion of Myo1 endocytic activity (Figure 5.2.1, Figure 5.2.2).The extended Cam2-GFP foci lifetime in *myo1.S742A* suggests a lack of Cam2 binding to Myo1, which is required to modulate the rate of endocytosis in sporulating cells. The rate of endocytosis in sporulating cells is reduced when compared to vegetative cells. A single Cam2 molecule has been shown to bind to IQ1 of Myo1 in the presence of $Ca^{2+}$ and Myo1 S742 phosphorylation. Cam2 binding to Myo1 IQ1 brings about conformational change in the first half of the Myo1 lever arm, making it more rigid. The second half of the Myo1 neck, where the vacant IQ2 is situated, is left flexible. In this state, Myo1 is tension insensitive. The flexible region causes slowed interactions between actin and Myo1 and results in the extended foci lifetimes observed in sporulating cells (Baker et al., 2019). Myo1 foci were only observed outside of spores, in the acus cytosol, in *myo1.S742A* and *myo1.S742D.*

The non-occurrence of endocytosis in spores complies with previous studies regarding endocytosis during meiosis (Figure 5.3) (Kashiwazaki et al., 2011). During spore formation, spore wall material deposition and spore wall formation occurs at later stages, once prespores are formed (Kashiwazaki et al., 2011). Once the materials within the spores have been encapsulated by the spore wall, no external factors may be required for spore maintenance. This is supported by the fact that spores are insusceptible to environmental factors and endocytosis as the cell membrane is highly selective during meiosis (Krapp et al., 2010; Kashiwazaki et al., 2011). In sporulating cells, the lack of Myo1 S742 phosphorylation impacts Cam2 binding to Myo1. This prevents the regulation of Myo1 activity in endocytosis at the cell membrane and results in almost a complete absence of endocytosis in the *myo1.S742* background (Figure 5.3).

A number of future experiments could be applied to the *myo1.S742A* strain to further explore the impact of Myo1 S742 phosphorylation on the function of Myo1 for endocytosis and correct polarised cell growth, in the vegetative and meiotic cell cycles. A reduced rate of overall growth (cell number and size) was observed at the end of the log phase of *myo1.S742A* cell growth (Figure 5.4). To confirm this reduced growth was due to a reduced rate in cell proliferation, a Coulter counter may be used to quantify changes in cell density with time.

The simultaneous two-channel spinning-disk confocal imaging system may be used to generate time-lapses of co-localisation and motility of two of the proteins of interest during the vegetative and meiotic life cycles e.g. Cam1, Cam2, Myo1 or actin. A time-lapse displaying the co-localisation of Cam1 and Cam2 at the membrane of *cam1-mCherry cam2-GFP* cells has been published by Baker et al. (2019) and was acquired using TIRF microscopy. Use of the simultaneous two-channel spinning-disk confocal imaging system would provide a more accurate acquisition of the protein dynamics.

Co-immunoprecipitation may be used to confirm binding of the calmodulins to Myo1 at different stages of the vegetative and meiotic life cycles and make comparisons between *myo1.S742A* and wild-type *myo1*$^+$ cells*.* Binding of two Cam1 molecules to Myo1 S742A may be confirmed during the vegetative life cycle. *cdc10.v50 myo1.S742A* and *cdc25.22 myo1.S742A* cells arrest at G1 and G2 respectively, when incubated at 36 °C. These strains could be used to confirm Cam1 remains bound to Myo1 at these stages of vegetative life cycle. A lack of Cam2 binding to Myo1 S742A during the meiotic life cycle may also be confirmed. Mating *fus1Δ myo1.S742A* cells may be used to confirm a lack of Cam2 binding in *myo1.S742A* cells during meiotic life cycle.

Proteins associated with meiosis and the mating process may be studied in a similar fashion to that of Myo1 and the calmodulins, for further understanding of roles Myo1 S742 phosphorylation plays in the cell cycle. Another protein of interest may be Fus1, a protein essential for resolution of the cell wall in cell fusion during mating. Fus1 interacts with profilin, Cdc3. Profilin is an actin binding protein also needed for cell fusion. Artificial destabilisation of filamentous actin has been proven to induce cell fusion disruptions (Kurahashi et al., 2002). Taken together with the fact that Myo1 has interwoven dependence on and governance of actin function, investigating Fus1 activity in the absence of Myo1 S742 phosphorylation may provide insight into its significance in downstream processes in the life cycle.

Myo1 S742 phosphorylation has been shown to be Gad8 dependent (Baker et al., 2019). The kinase responsible for the phosphorylation of Myo1 S742 phosphorylation may be identified by determining Myo1 S742 phosphorylation via western blots, using Myo1 S742 phospho-specific antibodies on the cell extracts of protein kinase-deletions. Cam1, Cam2, Myo1 and actin dynamics during the vegetative and meiotic cycle, and proportion of monopolar and bipolar cells may also be compared to *myo1.S742A* cells (Bimbó et al., 2005).

During this PhD, phosphorylation of conserved phosphorylation sites in the head, neck and domains of Myo52 has been shown to impact overall cell growth, cell polarity, cell length, actin localisation and motor dynamics. Phosphorylation of phospho-serine S742, located the IQ motif of Myo1, has been shown to enable correct endocytic activity of Myo1, for the switch of monopolar to bipolar cell growth during NETO in the vegetative life cycle in *S. pombe*. Myo1 S742 phosphorylation has also been shown to reduce endocytic activity of Myo1 to maintain the quiescent state of sporulating cells during the meiotic cycle. The findings gathered on the phospho-regulation of Myo1 and Myo52 function and the interplay between the motor proteins, the cytoskeleton and associated proteins for normal cell function within *S. pombe*, holds value as these data may be translated into other model systems. *S. pombe* share genes encoding for myosins with higher eukaryotes including humans.

Myo52 and Myo1 are linked to kidney diseases in humans. Autosomal dominant polycystic kidney disease is hereditary kidney disease. Abnormal differentiation and proliferation of kidney tubular epithelial cells cause fluid-filled cysts in the kidneys. This leads to chronic kidney failure. A mutated PKD2 (polycystin-2) gene results in the disease state. The PKD2 gene is conserved in all organisms and encodes for Pkd2. In *S. pombe*, PKD2 encodes for Pkd2 which is a mechanosensitive ion channel in vesicles that contributes to cell wall synthesis and membrane trafficking. Myo52 has been linked to the transport of vesicles containing Pkd2 to the cell ends during G2, where entry of $Ca^{2+}$ into the vesicle through Pkd2 results in the activation of Bsg1 for cell wall deposition (Aydar & Palmer, 2009).

Mutations in Myo1 have been linked to FSGS (focal segmental glomerulosclerosis). FSGS is a kidney disease in which proteinuria (protein excretion into the urine) occurs due to disruption of the protein filtration barrier in the kidney. This disruption is caused by defects in specialised epithelial cells called podocytes. Myo1e expressed in the podocytes plays a role in the integrity of cell-cell junctions of podocytes. Two missense mutations in Myo1 conserved residues have been identified in individuals with FSGS. T119I (threonine 119 to isoleucine 119) and A159P (alanine 159 to proline 159) are both located in regions of the motor head domain involved in ATP binding and hydrolysis. Equivalent mutations, T140I (threonine 140 to isoleucine 140) and A181P (alanine 181 to proline 181), have been studied in *S. pombe* Myo1 and were shown to disrupt Myo1 binding to actin, localisation, functional activity in endocytic actin patches, stability and folding. From these observations, the mutant Myo1e were concluded to fail to link the plasma membrane of podocytes to the actin cytoskeleton or fail to recruit actin filaments to the plasma membrane. Failure to link the membrane to the actin cytoskeleton can therefore cause incorrect in podocyte adhesion, endocytosis and cell shape regulation (Bi et al., 2015).

Therefore the preliminary findings on Myo1 and Myo52 phospho-regulation described in this thesis can contribute to current knowledge of myosin function and can be applied to further studies of possible disease states linked to the function of Myo1 and Myo52.

## Reference List:

Abenza, J. F., Chessel, A., Raynaud, W. G., & Carazo-Salas, R. (2014). Dynamics of cell shape inheritance in fission yeast. *PloS One, 9*(9), Article e106959. doi:10.1371/journal.pone.0106959

Abramowitz, M., Flynn, B. O., Parry-Hill, M. J., & Davidson, M. W. (2016). *Interactive tutorials - Jablonski energy diagram.* Molecular Expressions. https://micro.magnet.fsu.edu/primer/java/jablonski/lightandcolor/

Aguiar, P. H. N., Furtado, C., Repolês, B.,M., Ribeiro, G. A., Mendes, I. C., Peloso, E. F., Gadelha, F. R., Macedo, A. M., Franco, G. R., Pena, S. D. J., Teixeira, S. M. R., Vieira, L. Q., Guarneri, A. A., Andrade, L. O., & Machado, C. R. (2013). Oxidative stress and DNA lesions: The role of 8-oxoguanine lesions in *Trypanosoma cruzi* cell viability. *PLoS Neglected Tropical Diseases, 7*(6), Article e2279. doi:10.1371/journal.pntd.0002279

Ahuja, R., Pinyol, R., Reichenbach, N., Custer, L., Klingensmith, J., Kessels, M. M., & Qualmann, B. (2007). Cordon-bleu is an actin nucleation factor and controls neuronal morphology. *Cell, 131*(2), 337-350. doi:10.1016/j.cell.2007.08.030

Alberts, B., Johnson, A., & Lewis, J. (2002). Molecular motors. In B. Alberts, D. Bray, J. Lewis, M. Raff, K. Roberts, & P. Walter (Eds.), *Molecular biology of the cell (4th edition)*. Garland Science. https://www.ncbi.nlm.nih.gov/books/NBK26888/

Allshire, R. C., & Ekwall, K. (2015). Epigenetic regulation of chromatin states in *Schizosaccharomyces pombe*. *Cold Spring Harbor Perspectives in Biology, 7*(7), Article a018770. doi:10.1101/cshperspect.a018770

Altman, D. (2013). Myosin work and motility: Mechanism. In G. C. K. Roberts (Ed.), *Encyclopedia of Biophysics* (pp. 1671-1679). Springer Berlin Heidelberg. doi:10.1007/978-3-642-16712-6_754

Anderson, B. L., Boldogh, I., Evangelista, M., Boone, C., Greene, L. A., & Pon, L. A. (1998). The Src homology domain 3 (SH3) of a yeast type I myosin, Myo5p, binds to verprolin and is required for targeting to sites of actin polarization. *Journal of Cell Biology, 141*(6), 1357-1370. doi:10.1083/jcb.141.6.1357

---

Arai, R., & Mabuchi, I. (2002). F-actin ring formation and the role of F-actin cables in the fission yeast *Schizosaccharomyces pombe*. *Journal of Cell Science, 115*(5), 887-898. doi:10.1242/jcs.115.5.887

Arasada, R., & Pollard, T. D. (2011). Distinct roles for F-BAR proteins Cdc15p and Bzz1p in actin polymerization at sites of endocytosis in fission yeast. *Current Biology, 21*(17), 1450-1459. doi:10.1016/j.cub.2011.07.046

Archer, C. W., & Francis-West, P. (2003). The chondrocyte. *The International Journal of Biochemistry & Cell Biology, 35*(4), 401-404. doi:S1357272502003011

Asakawa, K., Kume, K., Kanai, M., Goshima, T., Miyahara, K., Dhut, S., Tee, W. W., Hirata, D., & Toda, T. (2006). The V260I mutation in fission yeast alpha-tubulin Atb2 affects microtubule dynamics and EB1-Mal3 localization and activates the Bub1 branch of the spindle checkpoint. *Molecular Biology of the Cell, 17*(3), 1421-1435. doi:10.1091/mbc.e05-08-0802

Attanapola, S. L., Alexander, C. J., & Mulvihill, D. P. (2009). Ste20-kinase-dependent TEDS-site phosphorylation modulates the dynamic localisation and endocytic function of the fission yeast class I myosin, Myo1. *Journal of Cell Science, 122*(21), 3856-3861. doi:10.1242/jcs.053959

Aydar, E., & Palmer, C. P. (2009). Polycystic kidney disease channel and synaptotagmin homologues play roles in *Schizosaccharomyces pombe* cell wall Synthesis/Repair and membrane protein trafficking. *Journal of Membrane Biology, 229*(3), 141-152. doi:10.1007/s00232-009-9180-6

Baker, K., Gyamfi, I. A., Mashanov, G. I., Molloy, J. E., Geeves, M. A., & Mulvihill, D. P. (2019). TORC2-Gad8-dependent myosin phosphorylation modulates regulation by calcium. *Elife, 8*, Article e51150. doi:10.7554/eLife.51150

Balasubramanian, M. K., Helfman, D. M., & Hemmingsen, S. M. (1992). A new tropomyosin essential for cytokinesis in the fission yeast *S. pombe*. *Nature, 360*(6399), 84-87. doi:10.1038/360084a0

Barger, S. R., Gauthier, N. C., & Krendel, M. (2020). Squeezing in a meal: Myosin functions in phagocytosis. *Trends in Cell Biology, 30*(2), 157-167. doi:10.1016/j.tcb.2019.11.002

Bathe, M., & Chang, F. (2010). Cytokinesis and the contractile ring in fission yeast: Towards a systems-level understanding. *Trends in Microbiology, 18*(1), 38-45. doi:10.1016/j.tim.2009.10.002

Batters, C., & Veigel, C. (2016). Mechanics and activation of unconventional myosins. *Traffic, 17*(8), 860-871. doi:10.1111/tra.12400

Berepiki, A., Lichius, A., & Read, N. D. (2011). Actin organization and dynamics in filamentous fungi. *Nature Reviews Microbiology, 9*(12), 876-887. doi:10.1038/nrmicro2666

Berg, J. S., Powell, B. C., & Cheney, R. E. (2001). A millennial myosin census. *Molecular Biology of the Cell, 12*(4), 780-794. doi:10.1091/mbc.12.4.780

Bertling, E., Hotulainen, P., Mattila, P. K., Matilainen, T., Salminen, M., & Lappalainen, P. (2004). Cyclase-associated protein 1 (CAP1) promotes cofilin-induced actin dynamics in mammalian nonmuscle cells. *Molecular Biology of the Cell, 15*(5), 2324-2334. doi:10.1091/mbc.e04-01-0048

Bertoli, C., Skotheim, J. M., & de Bruin, R. A. M. (2013). Control of cell cycle transcription during G1 and S phases. *Nature Reviews Molecular Cell Biology, 14*(8), 518-528. doi:10.1038/nrm3629

Bi, J., Carroll, R. T., James, M. L., Ouderkirk, J. L., Krendel, M., & Sirotkin, V. (2015). Effects of FSGS-associated mutations on the stability and function of myosin-1 in fission yeast. *Disease Models & Mechanisms, 8*(8), 891-902. doi:10.1242/dmm.020214

Bimbó, A., Jia, Y., Poh, S. L., Karuturi, R. K., den Elzen, N., Peng, X., Zheng, L., O'Connell, M., Liu, E. T., Balasubramanian, M. K., & Liu, J. (2005). Systematic deletion analysis of fission yeast protein kinases. *Eukaryotic Cell, 4*(4), 799-813. doi:10.1128/EC.4.4.799-813.2005

Bloemink, M. J., & Geeves, M. A. (2011). Shaking the myosin family tree: Biochemical kinetics defines four types of myosin motor. *Seminars in Cell & Developmental Biology, 22*(9), 961-967. doi:10.1016/j.semcdb.2011.09.015

Bohnert, K. A., & Gould, K. L. (2012). Cytokinesis-based constraints on polarized cell growth in fission yeast. *PLoS Genetics, 8*(10), Article e1003004. doi:10.1371/journal.pgen.1003004

Breitsprecher, D., & Goode, B. L. (2013). Formins at a glance. *Journal of Cell Science, 126*(1), 1-7. doi:10.1242/jcs.107250

Bugyi, B., & Kellermayer, M. (2020). The discovery of actin: “to see what everyone else has seen, and to think what nobody has thought”. *Journal of Muscle Research and Cell Motility, 41*(1), 3-9. doi:10.1007/s10974-019-09515-z

Cappello, G., Pierobon, P., Symonds, C., Busoni, L., Christof, J., Gebhardt, M., Rief, M., & Prost, J. (2007). Myosin V stepping mechanism. *Proceedings of the National Academy of Sciences, 104*(39), 15328-15333. doi:10.1073/pnas.0706653104

Carbó, N., Tarkowski, N., Ipiña, E. P., Dawson, S. P., & Aguilar, P. S. (2017). Sexual pheromone modulates the frequency of cytosolic $Ca^{2+}$ bursts in *Saccharomyces cerevisiae*. *Molecular Biology of the Cell, 28*(4), 501-510. doi:10.1091/mbc.e16-07-0481

Carlton, P. M., Boulanger, J., Kervrann, C., Sibarita, J., Salamero, J., Gordon-Messer, S., Bressan, D., Haber, J. E., Haase, S., Shao, L., Winoto, L., Matsuda, A., Kner, P., Uzawa, S., Gustafsson, M., Kam, Z., Agard, D. A., & Sedat, J. W. (2010). Fast live simultaneous multiwavelength four-dimensional optical microscopy. *Proceedings of the National Academy of Sciences of the United States of America, 107*(37), 16016-16022. doi:10.1073/pnas.1004037107

Carpentier, P., Violot, S., Blanchoin, L., & Bourgeois, D. (2009). Structural basis for the phototoxicity of the fluorescent protein KillerRed. *FEBS Letters, 583*(17), 2839-2842. doi:10.1016/j.febslet.2009.07.041

Castagnetti, S., Behrens, R., & Nurse, P. (2005). End4/Sla2 is involved in establishment of a new growth zone in *Schizosaccharomyces pombe. Journal of Cell Science, 118*(9), 1843-1850. doi:10.1242/jcs.02311

Chen, R., Wu, R., Zhang, G., Gao, Y., Xiao, L., & Jia, S. (2014). Electron transfer-based single molecule fluorescence as a probe for nano-environment dynamics. *Sensors (Basel, Switzerland), 14*(2), 2449-67. doi:10.3390/s140202449

Cheney, R. E., Riley, M. A., & Mooseker, M. S. (1993). Phylogenetic analysis of the myosin superfamily. *Cell Motility and the Cytoskeleton, 24*(4), 215-223. doi:10.1002/cm.970240402

Christensen, J. R., Hocky, G. M., Homa, K. E., Morganthaler, A. N., Hitchcock-DeGregori, S., Voth, G. A., & Kovar, D. R. (2017). Competition between tropomyosin, fimbrin, and ADF/cofilin drives their sorting to distinct actin filament networks. *Elife, 6*, Article e23152. doi:10.7554/eLife.23152

Clayton, J. E., Pollard, L. W., Sckolnick, M., Bookwalter, C. S., Hodges, A. R., Trybus, K. M., & Lord, M. (2014). Fission yeast tropomyosin specifies directed transport of myosin-V along actin cables. *Molecular Biology of the Cell, 25*(1), 66-75. doi:10.1091/mbc.e13-04-0200

Coffman, V. C., Sees, J. A., Kovar, D. R., & Wu, J. (2013). The formins Cdc12 and For3 cooperate during contractile ring assembly in cytokinesis. *Journal of Cell Biology, 203*(1), 101-114. doi:10.1083/jcb.201305022

Cohen, A., Habib, A., Laor, D., Yadav, S., Kupiec, M., & Weisman, R. (2018). TOR complex 2 in fission yeast is required for chromatin-mediated gene silencing and assembly of heterochromatic domains at subtelomeres. *Journal of Biological Chemistry, 293*(21), 8138–8150. doi:10.1074/jbc.RA118.002270

Cohen, A., Kupiec, M., & Weisman, R. (2016). Gad8 protein is found in the nucleus where it interacts with the MluI cell cycle box-binding factor (MBF) transcriptional complex to regulate the response to DNA replication stress. *Journal of Biological Chemistry, 291*(17), 9371-9381. doi:10.1074/jbc.M115.705251

Cole, R. (2014). Live-cell imaging. *Cell Adhesion & Migration*, *8*(5), 452-459. doi:10.4161/cam.28348

Cooper, G. (2000). *The cell: a molecular approach.* (2nd ed.). Sinauer Associates. https://www.ncbi.nlm.nih.gov/books/NBK9839/

Cortés, J. C. G., Carnero, E., Ishiguro, J., Sánchez, Y., Durán, A., & Ribas, J. C. (2005). The novel fission yeast (1,3) β-D-glucan synthase catalytic subunit Bgs4p is essential during both cytokinesis and polarized growth. *Journal of Cell Science, 118*(1), 157-174. doi:10.1242/jcs.01585

---

Cortés, J. C. G., Konomi, M., Martins, I. M., Muñoz, J., Moreno, M. B., Osumi, M., Durán A., & Ribas, J. C. (2007). The (1,3)β-d-glucan synthase subunit Bgs1p is responsible for the fission yeast primary septum formation. *Molecular Microbiology, 65*(1), 201-217. doi:10.1111/j.1365-2958.2007.05784.x

Coulton, A. T., East, D. A., Galinska-Rakoczy, A., Lehman, W., & Mulvihill, D. P. (2010). The recruitment of acetylated and unacetylated tropomyosin to distinct actin polymers permits the discrete regulation of specific myosins in fission yeast. *Journal of Cell Science, 123*(19), 3235-3243. doi:10.1242/jcs.069971

Courtemanche, N., Pollard, T. D., & Chen, Q. (2016). Avoiding artefacts when counting polymerized actin in live cells with LifeAct fused to fluorescent proteins. *Nature Cell Biology, 18*(6), 676-683. doi:10.1038/ncb3351

Cranz-Mileva, S., Pamula, M. C., Barua, B., Desai, B., Hong, Y. H., Russell, J., Walworth N. C., & Hitchcock-DeGregori, S. (2013). A molecular evolution approach to study the roles of tropomyosin in fission yeast. *Plos One, 8*(10), Article e76726. doi:10.1371/journal.pone.0076726

Cybulski, N., & Hall, M. N. (2009). TOR complex 2: A signaling pathway of its own. *Trends in Biochemical Sciences, 34*(12), 620-627. doi:10.1016/j.tibs.2009.09.004

Dailey, M. E., Focht, D. C., Khodjakov, A., Rieder, C. L., Claxton, N. S., Olenych, S. G., Griffin, J. D., & Davidson, M. W. (n.d.). *Maintaining live cells on the microscope stage*. Nikon Instruments. https://www.microscopyu.com/applications/live-cell-imaging/maintaining-live-cells-on-the-microscope-stage

Das, M., Wiley, D. J., Chen, X., Shah, K., & Verde, F. (2009). The conserved NDR kinase Orb6 controls polarized cell growth by spatial regulation of the small GTPase Cdc42. *Current Biology, 19*(15), 1314-1319. doi:10.1016/j.cub.2009.06.057

Davidson, R., Pontasch, J. A., & Wu, J. (2016). Sbg1 is a novel regulator for the localization of the β-glucan synthase Bgs1 in fission yeast. *Plos One, 11*(11), Article e0167043. doi:10.1371/journal.pone.0167043

Day, R. N., & Davidson, M. W. (n.d.). *Education in microscopy and digital imaging.* Zeiss. http://zeiss-campus.magnet.fsu.edu/articles/probes/jellyfishfps.html de León, N., Hoya, M., Curto, M., Moro, S., Yanguas, F., Doncel, C., & Valdivieso, M. (2016). The AP-2 complex is required for proper temporal and spatial dynamics of endocytic patches in fission yeast. *Molecular Microbiology, 100*(3), 409-424. doi:10.1111/mmi.13327

De Virgilio, C., & Loewith, R. (2006). The TOR signalling network from yeast to man. *The International Journal of Biochemistry & Cell Biology, 38*(9), 1476-1481. doi:10.1016/j.biocel.2006.02.013

Dixit, R., & Cyr, R. (2003). Cell damage and reactive oxygen species production induced by fluorescence microscopy: Effect on mitosis and guidelines for non-invasive fluorescence microscopy. *The Plant Journal, 36*(2), 280-290. doi:10.1046/j.1365-313X.2003.01868.x

Du, W., Forte, G. M., Smith, D., & Petersen, J. (2016). Phosphorylation of the amino-terminus of the AGC kinase Gad8 prevents its interaction with TORC2. *Open Biology, 6*(3), Article 150189. doi:10.1098/rsob.150189

Dulyaninova, N. G., & Bresnick, A. R. (2013). The heavy chain has its day: Regulation of myosin-II assembly. *Bioarchitecture, 3*(4), 77-85. doi:10.4161/bioa.26133

Dulyaninova, N. G., Malashkevich, V. N., Almo, S. C., & Bresnick, A. R. (2005). Regulation of myosin-IIA assembly and Mts1 binding by heavy chain phosphorylation. *Biochemistry, 44*(18), 6867-6876. doi:10.1021/bi0500776

Dundon, S. E. R., & Pollard, T. D. (2020). Microtubule nucleation promoters Mto1 and Mto2 regulate cytokinesis in fission yeast. *Molecular Biology of the Cell*, *31*(17), 1846-1856. doi:10.1091/mbc.E19-12-0686

East, D. A., & Mulvihill, D. P. (2011). Regulation and function of the fission yeast myosins. *Journal of Cell Science, 124*(9), 1383-1390. doi:10.1242/jcs.078527

Edamatsu, M., & Toyoshima, Y. Y. (2003). Fission yeast synaptobrevin is involved in cytokinesis and cell elongation. *Biochemical and Biophysical Research Communications, 301*(3), 641-645. doi:10.1016/S0006-291X(03)00017-2

Egel, R., Willer, M., Kjaerulff, S., Davey, J., & Nielsen, O. (1994). Assessment of pheromone production and response in fission yeast by a halo test of induced sporulation. *Yeast, 10*(10), 1347-1354. doi:10.1002/yea.320101012

Erber, A., Riemer, D., & Bovenschulte, M. (1998). Molecular phylogeny of metazoan intermediate filament proteins. *Journal of Molecular Evolution, 47*(6), 751-762. doi:10.1007/PL00006434

Etienne-Manneville, S. (2004). Cdc42 - the centre of polarity. *Journal of Cell Science, 117*(8), 1291-1300. doi:10.1242/jcs.01115

Ettinger, A., & Wittmann, T. (2014). Chapter 5 - fluorescence live cell imaging. *Methods in Cell Biology, 123*, 77-94. doi:10.1016/B978-0-12-420138-5.00005-7

Even-Faitelson, L., & Ravid, S. (2006). PAK1 and aPKCzeta regulate myosin II-B phosphorylation: A novel signaling pathway regulating filament assembly. *Molecular Biology of the Cell, 17*(7), 2869-2881. doi:10.1091/mbc.e05-11-1001

Fellers, T. J., & Davidson, M. W. (n.d.). *Theory of confocal microscopy - Introduction to confocal microscopy*. Olympus. http://www.olympusconfocal.com/theory/confocalintro.html

Feng, Z., Okada, S., Cai, G., Zhou, B., & Bi, E. (2015). Myosin-II heavy chain and formin mediate the targeting of myosin essential light chain to the division site before and during cytokinesis. *Molecular Biology of the Cell, 26*(7), 1211-1224. doi:10.1091/mbc.E14-09-1363

Fletcher, D. A., & Mullins, R. D. (2010). Cell mechanics and the cytoskeleton. *Nature, 463*(7280), 485-492. doi:10.1038/nature08908

Flores, L. R., Keeling, M. C., Zhang, X., Sliogeryte, K., & Gavara, N. (2019). Lifeact-TagGFP2 alters F-actin organization, cellular morphology and biophysical behaviour. *Scientific Reports, 9*(1), Article 3241. doi:10.1038/s41598-019-40092-w

Forsburg, S. L., & Rhind, N. (2006). Basic methods for fission yeast. *Yeast, 23*(3), 173-183. doi:10.1002/yea.1347

Foth, B. J., Goedecke, M. C., & Soldati, D. (2006). New insights into myosin evolution and classification. *Proceedings of the National Academy of Sciences of the United States of America, 103*(10), 3681-3686. doi:10.1073/pnas.0506307103

Frey, O., Rudolf, F., Schmidt, G. W., & Hierlemann, A. (2015). Versatile, simple-to-use microfluidic cell-culturing chip for long-term, high-resolution, time-lapse imaging. *Analytical Chemistry, 87*(8), 4144-4151. doi:10.1021/ac504611t

Fukunishi, K., Miyakubi, K., Hatanaka, M., Otsuru, N., Hirata, A., Shimoda, C., & Nakamura, T. (2014). The fission yeast spore is coated by a proteinaceous surface layer comprising mainly Isp3. *Molecular Biology of the Cell, 25*(10), 1549-1559. doi:10.1091/mbc.E13-12-0731

Gachet, Y., & Hyams, J. S. (2005). Endocytosis in fission yeast is spatially associated with the actin cytoskeleton during polarised cell growth and cytokinesis. *Journal of Cell Science, 118*(18), 4231-4242. doi:10.1242/jcs.02530

Galletta, B. J., & Cooper, J. A. (2009). Actin and endocytosis: Mechanisms and phylogeny. *Current Opinion in Cell Biology, 21*(1), 20-27. doi:10.1016/j.ceb.2009.01.006

Gaubitz, C., Oliveira, T. M., Prouteau, M., Leitner, A., Karuppasamy, M., Konstantinidou, G., Rispal, D., Eltschinger, S., Robinson, G. C., Thore, S., Aebersold, R., Schaffitzel, C., & Loewith, R. (2015). Molecular basis of the rapamycin insensitivity of target of rapamycin complex 2. *Molecular Cell, 58*(6), 977-988. doi:10.1016/j.molcel.2015.04.031

Gillespie, P. G., & Cyr, J. L. (2002). Calmodulin binding to recombinant myosin-1c and myosin-1c IQ peptides. *BMC Biochemistry, 3*(1), Article 31. doi:10.1186/1471-2091-3-31

Gómez, E. B., & Forsburg, S. L. (2004). Analysis of the fission yeast *Schizosaccharomyces pombe* cell cycle. In H. B. Lieberman (Ed.), *Cell cycle checkpoint control protocols* (pp. 93-111). Humana Press. doi:10.1385/1-59259-646-0:93

Gonzalez, S., & Rallis, C. (2017). The TOR signaling pathway in spatial and temporal control of cell size and growth. *Frontiers in Cell and Developmental Biology, 5*, Article 61. doi:10.3389/fcell.2017.00061

Goode, B. L., Eskin, J. A., & Wendland, B. (2015). Actin and endocytosis in budding yeast. *Genetics, 199*(2), 315-358. doi:10.1534/genetics.112.145540

---

Gorgidze, L. A., Oshemkova, S. A., & Vorobjev, I. A. (1998). Blue light inhibits mitosis in tissue culture cells. *Bioscience Reports, 18*(4), 215-224. doi:10.1023/A:1020104914726

Grallert, A., Martín-García, R., Bagley, S., & Mulvihill, D. P. (2007). In vivo movement of the type V myosin Myo52 requires dimerisation but is independent of the neck domain. *Journal of Cell Science, 120*(23), 4093-4098. doi:10.1242/jcs.012468

Gu, Y., Yam, C., & Oliferenko, S. (2015). Rewiring of cellular division site selection in evolution of fission yeasts. *Current Biology, 25*(9), 1187-1194. doi:10.1016/j.cub.2015.02.056

Guo, H., & King, M. (2013). A quality control mechanism linking meiotic success to release of ascospores. *PloS One, 8*(12), Article e82758. doi:10.1371/journal.pone.0082758

Gupta, S. (2013). *Understanding regulation of the cytoskeleton during cell cycle transitions through examination of crosstalk between homologous fission yeast pathways, septation initiation network and morphogenesis ORB6 network: A dissertation.* [Doctoral dissertation, *University of Massachusetts Medical School*] GSBS Dissertations and Theses. https://escholarship.umassmed.edu/gsbs_diss/693

Guzy, R. D., Mack, M. M., & Schumacker, P. T. (2007). Mitochondrial complex III is required for hypoxia-induced ROS production and gene transcription in yeast. *Antioxidants & Redox Signaling, 9*(9), 1317-1328. doi:10.1089/ars.2007.1708

Hachet, O., & Simanis, V. (2008). Mid1p/anillin and the septation initiation network orchestrate contractile ring assembly for cytokinesis. *Genes & Development, 22*(22), 3205-3216. doi:10.1101/gad.1697208

Hagan, I. M., Grallert, A., & Simanis, V. (2016). Analysis of the *Schizosaccharomyces pombe* cell cycle. *Cold Spring Harbor Protocols, 2016*(9), 735-747. doi:10.1101/pdb.top082800

Hamer, E. C., Moore, C. B., & Denning, D. W. (2006). Comparison of two fluorescent whiteners, calcofluor and blankophor, for the detection of fungal elements in clinical specimens in the diagnostic laboratory. *Clinical Microbiology and Infection, 12*(2), 181-184. doi:10.1111/j.1469-0691.2005.01321.x

Hammer, J. A., & Sellers, J. R. (2012). Walking to work: Roles for class V myosins as cargo transporters. *Nature Reviews Molecular Cell Biology, 13*(1), 13-26. doi:10.1038/nrm3248

Hanley, P. J., Xu, Y., Kronlage, M., Grobe, K., Schön, P., Song, J., Sorokin L., Schwab A., & Bähler, M. (2010). Motorized RhoGAP myosin IXb (Myo9b) controls cell shape and motility. *Proceedings of the National Academy of Sciences of the United States of America, 107*(27), 12145-12150. doi:10.1073/pnas.0911986107

Hardin, J., Bertoni, G., Kleinsmith, L. J., & Becker, W. M. (2012). *Becker's world of the cell (8th edition).* Benjamin Cummings.

Hartman, M. A., & Spudich, J. A. (2012). The myosin superfamily at a glance. *Journal of Cell Science, 125*(7), 1627-1632. doi:10.1242/jcs.094300

Hartwell, L. H. (1974). *Saccharomyces cerevisiae* cell cycle. *Bacteriological Reviews, 38*(2), 164-198. https://pubmed.ncbi.nlm.nih.gov/4599449/

Hatano, T., Morigasaki, S., Tatebe, H., Ikeda, K., & Shiozaki, K. (2015). Fission yeast Ryh1 GTPase activates TOR complex 2 in response to glucose. *Cell Cycle, 14*(6), 848-856. doi:10.1080/15384101.2014.1000215

Heissler, S. M., & Sellers, J. R. (2014). Myosin light chains: Teaching old dogs new tricks. *Bioarchitecture, 4*(6), 169-188. doi:10.1080/19490992.2015.1054092

Heissler, S. M., & Sellers, J. R. (2016). Various themes of myosin regulation. *Journal of Molecular Biology, 428*(9), 1927-1946. doi:10.1016/j.jmb.2016.01.022

Hercyk, B. S., Rich-Robinson, J., Mitoubsi, A. S., Harrell, M. A., & Das, M. E. (2019). A novel interplay between GEFs orchestrates Cdc42 activity during cell polarity and cytokinesis in fission yeast. *Journal of Cell Science, 132*(23), Article jcs236018. doi:10.1242/jcs.236018

Herman, B., Centonze Frohlich, V. E., Lakowicz, J. R., Murphy, D. B., Spring, K. R., & Davidson, M. W. (2015). *Fluorescence microscopy basic concepts in fluorescence.* Molecular Expression. https://micro.magnet.fsu.edu/primer/techniques/fluorescence/fluorescenceintro.html

Herman, B., Parry-Hill, M. J., Johnson, I. D., & Davidson, M. W. (2016). *Fluorescence microscopy interactive tutorials - photobleaching*. Molecular Expression. https://micro.magnet.fsu.edu/primer/java/fluorescence/photobleaching/

Hirata, D., Kishimoto, N., Suda, M., Sogabe, Y., Nakagawa, S., Yoshida, Y., Mizunuma M., Miyakawa T., Ishiguro J., & Toda, T. (2002). Fission yeast Mor2/Cps12, a protein similar to *Drosophila Furry,* is essential for cell morphogenesis and its mutation induces Wee1-dependent G2 delay. *The EMBO Journal, 21*(18), 4863-4874. doi:10.1093/emboj/cdf495

Hoffman, C. S., Wood, V., & Fantes, P. A. (2015). An ancient yeast for young geneticists: A primer on the *Schizosaccharomyces pombe* model system. *Genetics, 201*(2), 403-423. doi:10.1534/genetics.115.181503

Howard, J. (1997). Molecular motors: Structural adaptations to cellular functions. *Nature, 389*(3), 561-567. doi:10.1007/s12551-014-0141-7

Huang, Y., Yan, H., & Balasubramanian, M. K. (2008). Assembly of normal actomyosin rings in the absence of Mid1p and cortical nodes in fission yeast. *Journal of Cell Biology, 183*(6), 979-988. doi:10.1083/jcb.200806151

Huang, K., & Fingar, D. C. (2014). Growing knowledge of the mTOR signaling network. *Seminars in Cell & Developmental Biology, 36*, 79-90. doi:10.1016/j.semcdb.2014.09.011

Icha, J., Weber, M., Waters, J. C., & Norden, C. (2017). Phototoxicity in live fluorescence microscopy, and how to avoid it. *Bioessays, 39*(8), Article 1700003. doi:10.1002/bies.201700003

Iida, H., Yagawa, Y., & Anraku, Y. (1990). Essential role for induced $Ca^{2+}$ influx followed by [Ca2+]i rise in maintaining viability of yeast cells late in the mating pheromone response pathway. A study of [Ca2+]i in single *Saccharomyces cerevisiae* cells with imaging of fura-2. *The Journal of Biological Chemistry, 265*(22), 13391-13399. doi:10.1016/S0021-9258(19)38311-5

Ikai, N., Nakazawa, N., Hayashi, T., & Yanagida, M. (2011). The reverse, but coordinated, roles of Tor2 (TORC1) and Tor1 (TORC2) kinases for growth, cell cycle and separase-mediated mitosis in *Schizosaccharomyces pombe*. *Open Biology, 1*(3), Article 110007. doi:10.1098/rsob.110007

Ikeda, K., Morigasaki, S., Tatebe, H., Tamanoi, F., & Shiozaki, K. (2008). Fission yeast TOR complex 2 activates the AGC-family Gad8 kinase essential for stress resistance and cell cycle control. *Cell Cycle, 7*(3), 358-364. doi:10.4161/cc.7.3.5245

Itadani, A., Nakamura, T., & Shimoda, C. (2006). Localization of type I myosin and F-actin to the leading edge region of the forespore membrane in *Schizosaccharomyces pombe*. *Cell Structure and Function, 31*(2), 181-195. doi:10.1247/csf.06027

Itri, R., Junqueira, H. C., Mertins, O., & Baptista, M. S. (2014). Membrane changes under oxidative stress: The impact of oxidized lipids. *Biophysical Reviews, 6*(1), 47-61. doi:10.1007/s12551-013-0128-9

Jefferson, J. J., Leung, C. L., & Liem, R. K. H. (2004). Plakins: Goliaths that link cell junctions and the cytoskeleton. *Nature Reviews Molecular Cell Biology, 5*(7), 542-553. doi:10.1038/nrm1425

Johnson, C. A., Brooker, H. R., Gyamfi, I., O'Brien, J., Ashley, B., Brazier, J. E., Dean A., Embling J., Grimsey, E., Tomlinson, A. C., Wilson, E.G., Geeves, M., & Mulvihill, D. P. (2018). Temperature sensitive point mutations in fission yeast tropomyosin have long range effects on the stability and function of the actin-tropomyosin copolymer. *Biochemical and Biophysical Research Communications, 506*(2), 339-346. doi:10.1016/j.bbrc.2017.10.109

Kamasaki, T., Arai, R., Osumi, M., & Mabuchi, I. (2005). Directionality of F-actin cables changes during the fission yeast cell cycle. *Nature Cell Biology, 7*(9), 916-917. doi:10.1038/ncb1295

Kanai, M., Kume, K., Miyahara, K., Sakai, K., Nakamura, K., Leonhard, K., Wiley, D. J., Verde, F., Toda, T., & Hirata, D. (2005). Fission yeast MO25 protein is localized at SPB and septum and is essential for cell morphogenesis. *The EMBO Journal, 24*(17), 3012-3025. doi:10.1038/sj.emboj.7600782

Karagiannis, J. (2012). Ensuring the faithful execution of cytokinesis in *Schizosaccharomyces pombe*. *Communicative & Integrative Biology, 5*(3), 265-271. doi:10.4161/cib.19860

Karcher, R. L., Roland, J. T., Zappacosta, F., Huddleston, M. J., Annan, R. S., Carr, S. A., & Gelfand, V. I. (2001). Cell cycle regulation of myosin-V by calcium/calmodulin-dependent protein kinase II. *Science, 293*(5533), 1317-1320. doi:10.1126/science.1061086

Karp, G., Iwasa, J., & Marshall, W. (2016). *Karp's cell and molecular biology: Concepts and experiments (8th edition).* John Wiley.

Kashiwazaki, J., Yamasaki, Y., Itadani, A., Teraguchi, E., Maeda, Y., Shimoda, C., & Nakamura, T. (2011). Endocytosis is essential for dynamic translocation of a syntaxin 1 orthologue during fission yeast meiosis. *Molecular Biology of the Cell, 22*(19), 3658-3670. doi:10.1091/mbc.E11-03-0255

Kawai, M., Nakashima, A., Ueno, M., Ushimaru, T., Aiba, K., Doi, H., & Uritani, M. (2001). Fission yeast Tor1 functions in response to various stresses including nitrogen starvation, high osmolarity, and high temperature. *Current Genetics, 39*(3), 166-174. doi:10.1007/s002940100198

Khodjakov, A., & Rieder, C. L. (2006). Imaging the division process in living tissue culture cells. *Methods, 38*(1), 2-16. doi:10.1016/j.ymeth.2005.07.007

Kim, A. H. J., Suleiman, H., & Shaw, A. S. (2016). New approaches in renal microscopy: Volumetric imaging and superresolution microscopy. *Current Opinion in Nephrology and Hypertension, 25*(3), 159-167. doi:10.1097/MNH.0000000000000220

Kim, H., Yang, P., Catanuto, P., Verde, F., Lai, H., Du, H., Chang F., & Marcus, S. (2003). The kelch repeat protein, Tea1, is a potential substrate target of the p21-activated kinase, Shk1, in the fission yeast, *Schizosaccharomyces pombe*. *Journal of Biological Chemistry, 278*(32), 30074-30082. doi:10.1074/jbc.M302609200

Knight, M. M., Roberts, S. R., Lee, D. A., & Bader, D. L. (2003). Live cell imaging using confocal microscopy induces intracellular calcium transients and cell death. *American Journal of Physiology-Cell Physiology, 284*(4), C1083-C1089. doi:10.1152/ajpcell.00276.2002

Knight, P. J., Thirumurugan, K., Xu, Y., Wang, F., Kalverda, A. P., Stafford, W. F., Sellers J. R., & Peckham, M. (2005). The predicted coiled-coil domain of myosin 10 forms a novel elongated domain that lengthens the head. *Journal of Biological Chemistry, 280*(41), 34702-34708. doi:10.1074/jbc.M504887200

Knutsen, J. H. J., Rein, I. D., Rothe, C., Stokke, T., Grallert, B., & Boye, E. (2011). Cell-cycle analysis of fission yeast cells by flow cytometry. *PloS One, 6*(2), Article e17175. doi:10.1371/journal.pone.0017175

Kodera, N., & Ando, T. (2014). The path to visualization of walking myosin V by high-speed atomic force microscopy. *Biophysics Reviews, 6*(3), 237-260. doi:10.1007/s12551-014-0141-7

Koester, H. J., Baur, D., Uhl, R., & Hell, S. W. (1999). $Ca^{2+}$ fluorescence imaging with pico- and femtosecond two-photon excitation: Signal and photodamage. *Biophysical Journal, 77*(4), 2226-2236. doi:10.1016/S0006-3495(99)77063-3

Koide, H., Kinoshita, T., Tanaka, Y., Tanaka, S., Nagura, N., zu Hörste G., M., Miyagi A., & Ando, T. (2006). Identification of the single specific IQ motif of myosin V from which calmodulin dissociates in the presence of $Ca^{2+}$. *Biochemistry, 45*(38), 11598-11604. doi:10.1021/bi0613877

Kollmar, M., Dürrwang, U., Kliche, W., Manstein, D. J., & Kull, F. J. (2002). Crystal structure of the motor domain of a class-I myosin. *The EMBO Journal, 21*(11), 2517-2525. doi:10.1093/emboj/21.11.2517

Kovar, D. R., Sirotkin, V., & Lord, M. (2011). Three's company: The fission yeast actin cytoskeleton. *Trends in Cell Biology, 21*(3), 177-187. doi:10.1016/j.tcb.2010.11.001

Kozak, M., & Kaksonen, M. (2019). Phase separation of Ede1 promotes the initiation of endocytic events. *Biorxiv,* Article 861203. doi:10.1101/861203

Krapp, A., Collin, P., Cokoja, A., Dischinger, S., Cano, E., & Simanis, V. (2006). The *Schizosaccharomyces pombe* septation initiation network (SIN) is required for spore formation in meiosis. *Journal of Cell Science, 119*(14), 2882-2891. doi:10.1242/jcs.03025

Krapp, A., del Rosario, E. C., & Simanis, V. (2010). The role of *Schizosaccharomyces pombe dma1* in spore formation during meiosis. *Journal of Cell Science, 123*(19), 3284-3293. doi:10.1242/jcs.069112

Kühner, S., & Fischer, S. (2011). Structural mechanism of the ATP-induced dissociation of rigor myosin from actin. *Proceedings of the National Academy of Sciences of the United States of America, 108*(19), 7793-7798. doi:10.1073/pnas.1018420108

Kumar, R., & Srivastava, S. (2016). Quantitative proteomic comparison of stationary/G0 phase cells and tetrads in budding yeast. *Scientific Reports, 6*(1), Article 32031. doi:10.1038/srep32031

Kurahashi, H., Imai, Y., & Yamamoto, M. (2002). Tropomyosin is required for the cell fusion process during conjugation in fission yeast. *Genes to Cells, 7*(4), 375-384. doi:10.1046/j.1365-2443.2002.00526.x

Laissue, P. P., Alghamdi, R. A., Tomancak, P., Reynaud, E. G., & Shroff, H. (2017). Assessing phototoxicity in live fluorescence imaging. *Nature Methods, 14*(7), 657-661. doi:10.1038/nmeth.4344

Langanger, G., Moeremans, M., Daneels, G., Sobieszek, A., De Brabander, M., & De Mey, J. (1986). The molecular organization of myosin in stress fibers of cultured cells. *The Journal of Cell Biology, 102*(1), 200-209. doi:10.1083/jcb.102.1.200

Laplante, C., Berro, J., Karatekin, E., Hernandez-Leyva, A., Lee, R., & Pollard, T. D. (2015). Three myosins contribute uniquely to the assembly and constriction of the fission yeast cytokinetic contractile ring. *Current Biology, 25*(15), 1955-1965. doi:S0960-9822(15)00683-1

Laplante, M., & Sabatini, D. (2012). mTOR signaling in growth control and disease. *Cell, 149*(2), 274-293. doi:10.1016/j.cell.2012.03.017

Le Goff, X., Motegi, F., Salimova, E., Mabuchi, I., & Simanis, V. (2000). The *S. pombe rlc1* gene encodes a putative myosin regulatory light chain that binds the type II myosins Myo3p and Myo2p. *Journal of Cell Science, 113*(23), 4157-4163. doi:10.1242/jcs.113.23.4157

Lee, I., & Wu, J. (2012). Characterization of Mid1 domains for targeting and scaffolding in fission yeast cytokinesis. *Journal of Cell Science, 125*, 2973-2985. doi:10.1242/jcs.102574

Lee, I., Coffman, V. C., & Wu, J. (2012). Contractile-ring assembly in fission yeast cytokinesis: Recent advances and new perspectives. *Cytoskeleton, 69*(10), 751-763. doi:10.1002/cm.21052

---

Lee, W. L., Bezanilla, M., & Pollard, T. D. (2000). Fission yeast myosin-I, Myo1p, stimulates actin assembly by Arp2/3 complex and shares functions with WASp. *The Journal of Cell Biology, 151*(4), 789-800. doi:10.1083/jcb.151.4.789

Li, D., Hérault, K., Oheim, M., & Ropert, N. (2009). FM dyes enter via a store-operated calcium channel and modify calcium signaling of cultured astrocytes. *Proceedings of the National Academy of Sciences of the United States of America, 106*(51), 21960-21965. doi:10.1073/pnas.0909109106

Li, H., Ye, F., Ren, J., Wang, P., Du, L., & Liu, J. (2018). Active transport of cytoophidia in *Schizosaccharomyces pombe. The FASEB Journal, 32*(11), 5891-5898. doi:10.1096/fj.201800045RR

Li, Q., Clarke, I. J., & Smith, A. I. (2013). Chapter 234 - acetylation. In A. J. Kastin (Ed.), *Handbook of biologically active peptides (2nd edition)* (pp. 1711-1714). Academic Press. doi:10.1016/B978-0-12-385095-9.00234-7

Lippincott-Schwartz, J., Herman, B., & Davidson, M. W. (n.d.). *Theory of confocal microscopy - fluorophores for confocal microscopy.* Olympus. http://www.olympusconfocal.com/theory/fluorophoresintro.html

Lock, A., Rutherford, K., Harris, M. A., Hayles, J., Oliver, S. G., Bähler, J., & Wood, V. (2018). PomBase 2018: user-driven reimplementation of the fission yeast database provides rapid and intuitive access to diverse, interconnected information. *Nucleic Acids Research, 47*(D1), D821-D827*.* doi:10.1093/nar/gky961

Loewith, R., Jacinto, E., Wullschleger, S., Lorberg, A., Crespo, J. L., Bonenfant, D., Oppliger, W., Jenoe P., & Hall, M. N. (2002). Two TOR complexes, only one of which is rapamycin sensitive, have distinct roles in cell growth control. *Molecular Cell, 10*(3), 457-468. doi:10.1016/S1097-2765(02)00636-6

Lowey, S., Saraswat, L. D., Liu, H., Volkmann, N., & Hanein, D. (2007). Evidence for an interaction between the SH3 domain and the N-terminal extension of the essential light chain in class II myosins. *Journal of Molecular Biology, 371*(4), 902-913. doi:10.1016/j.jmb.2007.05.080

Lu, Q., Li, J., Ye, F., & Zhang, M. (2015). Structure of myosin-1c tail bound to calmodulin provides insights into calcium-mediated conformational coupling. *Nature Structural & Molecular Biology, 22*(1), 81-88. doi:10.1038/nsmb.2923

Luo, J., Matsuo, Y., Gulis, G., Hinz, H., Patton-Vogt, J., & Marcus, S. (2009). Phosphatidylethanolamine is required for normal cell morphology and cytokinesis in the fission yeast *Schizosaccharomyces pombe. Eukaryotic Cell, 8*(5), 790-799. doi:10.1128/EC.00029-09

Ma, Y., Sugiura, R., Koike, A., Ebina, H., Sio, S. O., & Kuno, T. (2011). Transient receptor potential (TRP) and Cch1-Yam8 channels play key roles in the regulation of cytoplasmic $Ca^{2+}$ in fission yeast. *PloS One, 6*(7), Article e22421. doi:10.1371/journal.pone.0022421

Machesky, L. M., Atkinson, S. J., Ampe, C., Vandekerckhove, J., & Pollard, T. D. (1994). Purification of a cortical complex containing two unconventional actins from *Acanthamoeba* by affinity chromatography on profilin-agarose. *Journal of Cell Biology, 127*(1), 107-115. doi:10.1083/jcb.127.1.107

Machesky, L. M., Mullins, R. D., Higgs, H. N., Kaiser, D. A., Blanchoin, L., May, R. C., Hall, M. E., & Pollard, T. D. (1999). Scar, a WASp-related protein, activates nucleation of actin filaments by the Arp2/3 complex. *Proceedings of the National Academy of Sciences of the United States of America, 96*(7), 3739-3744. doi:10.1073/pnas.96.7.3739

MacIver, F. H., Glover, D. M., & Hagan, I. M. (2003). A 'marker switch' approach for targeted mutagenesis of genes in *Schizosaccharomyces pombe*. *Yeast, 20*(7), 587-594. doi:10.1002/yea.983

Martin, S. G., & Chang, F. (2005). New end take off: Regulating cell polarity during the fission yeast cell cycle. *Cell Cycle, 4*(8), 1046-1049. doi:10.4161/cc.4.8.1853

Martín-García, R., & Mulvihill, D. P. (2009). Myosin V spatially regulates microtubule dynamics and promotes the ubiquitin-dependent degradation of the fission yeast CLIP-170 homologue, Tip1. *Journal of Cell Science, 122*(21), 3862-3872. doi:10.1242/jcs.054460

MBInfo. (n.d.). *What is myosin?* https://www.mechanobio.info/cytoskeleton-dynamics/what-are-motor-proteins/what-is-myosin/

---

McDonald, A., Harris, J., MacMillan, D., Dempster, J., & McConnell, G. (2012). Light-induced $Ca^{2+}$ transients observed in widefield epi-fluorescence microscopy of excitable cells. *Biomedical Optics Express, 3*(6), 1266-1273. doi:10.1364/BOE.3.001266

Mikati, M. A., Breitsprecher, D., Jansen, S., Reisler, E., & Goode, B. L. (2015). Coronin enhances actin filament severing by recruiting cofilin to filament sides and altering F-actin conformation. *Journal of Molecular Biology, 427*(19), 3137-3147. doi:10.1016/j.jmb.2015.08.011

Miseta, A., Fu, L., Kellermayer, R., Buckley, J., & Bedwell, D. M. (1999). The golgi apparatus plays a significant role in the maintenance of $Ca^{2+}$ homeostasis in the *vps33Δ* vacuolar biogenesis mutant of *Saccharomyces cerevisiae*. *The Journal of Biological Chemistry, 274*(9), 5939-5947. doi:S0021-9258(19)87742-6

Mitchison, J. M., & Nurse, P. (1985). Growth in cell length in the fission yeast *Schizosaccharomyces pombe*. *Journal of Cell Science, 75*(1), 357-376. doi:10.1242/jcs.75.1.357

Moreno, S., Sanchez, Y., & Rodriguez, L. (1990). Purification and characterization of the invertase from *Schizosaccharomyces pombe*. A comparative analysis with the invertase from *Saccharomyces cerevisiae*. *The Biochemical Journal, 267*(3), 697-702. doi:10.1042/bj2670697

Morishita, M., & Engebrecht, J. (2005). End3p-mediated endocytosis is required for spore wall formation in *Saccharomyces cerevisiae*. *Genetics, 170*(4), 1561-1574. doi:10.1534/genetics.105.041459

Moser, M. J., Flory, M. R., & Davis, T. N. (1997). Calmodulin localizes to the spindle pole body of *Schizosaccharomyces pombe* and performs an essential function in chromosome segregation. *Journal of Cell Science, 110*(15), 1805-1812. doi:10.1242/jcs.110.15.1805

Moser, M. J., Lee, S. Y., Klevit, R. E., & Davis, T. N. (1995). $Ca^{2+}$ binding to calmodulin and its role in *Schizosaccharomyces pombe* as revealed by mutagenesis and NMR spectroscopy. *Journal of Biological Chemistry, 270*(35), 20643-20652. doi:10.1074/jbc.270.35.20643

Mossner, S., Phan, H. T., Triller, S., Moll, J. M., Conrad, U., & Scheller, J. (2020). Multimerization strategies for efficient production and purification of highly active synthetic cytokine receptor ligands. *PloS One, 15*(4), Article e0230804. doi:10.1371/journal.pone.0230804

Motegi, F., Arai, R., & Mabuchi, I. (2001). Identification of two type V myosins in fission yeast, one of which functions in polarized cell growth and moves rapidly in the cell. *Molecular Biology of the Cell, 12*(5), 1367-1380. doi:10.1091/mbc.12.5.1367

Motegi, F., Nakano, K., & Mabuchi, I. (2000). Molecular mechanism of myosin-II assembly at the division site in *Schizosaccharomyces pombe*. *Journal of Cell Science, 113*(10), 1813-1825. doi:10.1242/jcs.113.10.1813

Mullins, R. D., Heuser, J. A., & Pollard, T. D. (1998). The interaction of Arp2/3 complex with actin: Nucleation, high affinity pointed end capping, and formation of branching networks of filaments. *Proceedings of the National Academy of Sciences of the United States of America, 95*(11), 6181-6186. doi:10.1073/pnas.95.11.6181

Mulvihill, D. P., Edwards, S. R., & Hyams, J. S. (2006). A critical role for the type V myosin, Myo52, in septum deposition and cell fission during cytokinesis in *Schizosaccharomyces pombe*. *Cell Motility and the Cytoskeleton, 63*(3), 149-161. doi:10.1002/cm.20113

Mulvihill, D. P., Petersen, J., Ohkura, H., Glover, D. M., & Hagan, I. M. (1999). Plo1 kinase recruitment to the spindle pole body and its role in cell division in *Schizosaccharomyces pombe. Molecular Biology of the Cell, 10*(8), 2771-2785. doi:10.1091/mbc.10.8.2771

Mulvihill, D. P., Pollard, P. J., Win, T. Z., & Hyams, J. S. (2001). Myosin V-mediated vacuole distribution and fusion in fission yeast. *Current Biology, 11*(14), 1124-1127. doi:10.1016/S0960-9822(01)00322-0

Nakano, K., Satoh, K., Morimatsu, A., Ohnuma, M., & Mabuchi, I. (2001). Interactions among a fimbrin, a capping protein, and an actin-depolymerizing factor in organization of the fission yeast actin cytoskeleton. *Molecular Biology of the Cell, 12*(11), 3515-3526. doi:10.1091/mbc.12.11.3515

Naqvi, N. I., Wong, K. C. Y., Tang, X., & Balasubramanian, M. K. (2000). Type II myosin regulatory light chain relieves auto-inhibition of myosin-heavy-chain function. *Nature Cell Biology, 2*(11), 855-858. doi:10.1038/35041107

Nestler, E. J., & Greengard, P. (1999). Protein phosphorylation is of fundamental importance in biological regulation. In G. J. Siegel, B. W. Agranoff, & R. W. Albers (Eds.), *Basic neurochemistry: Molecular, cellular and medical aspects*. Lippincott-Raven. https://www.ncbi.nlm.nih.gov/books/NBK28063/

Nurnberg, A., Kitzing, T., & Grosse, R. (2011). Nucleating actin for invasion. *Nature Reviews Cancer, 11*(3), 177-187. doi:10.1038/nrc3003

O'Flaherty, C., & Matsushita-Fournier, D. (2017). Reactive oxygen species and protein modifications in spermatozoa. *Biology of Reproduction, 97*(4), 577-585. doi:10.1093/biolre/iox104

Odronitz, F., & Kollmar, M. (2007). Drawing the tree of eukaryotic life based on the analysis of 2,269 manually annotated myosins from 328 species. *Genome Biology, 8*(9), Article R196. doi:10.1186/gb-2007-8-9-r196

Ohta, M., Sato, M., & Yamamoto, M. (2012). Spindle pole body components are reorganized during fission yeast meiosis. *Molecular Biology of the Cell, 23*(10), 1799-1811. doi:10.1091/mbc.E11-11-0951

Oparka, M., Walczak, J., Malinska, D., van Oppen, L. M. P. E., Szczepanowska, J., Koopman, W. J. H., & Wieckowski, M. R. (2016). Quantifying ROS levels using CM-H2DCFDA and HyPer. *Methods; Current Methods to Unravel Reactive Oxygen Species (ROS) Biology, 109*, 3-11. doi:10.1016/j.ymeth.2016.06.008

Otsubo, Y., & Yamamato, M. (2008). TOR signaling in fission yeast. *Critical Reviews in Biochemistry and Molecular Biology, 43*(4), 277-283. doi:10.1080/10409230802254911

Palani, S., Köster, D. V., Hatano, T., Kamnev, A., Kanamaru, T., Brooker, H. R., Hernandez-Fernaud, J. R., Jones, A. M. E., Millar, J. B. A., Mulvihill, D. P., & Balasubramanian, M. K. (2019). Phosphoregulation of tropomyosin is crucial for actin cable turnover and division site placement. *The Journal of Cell Biology, 218*(11), 3548-3559. doi:10.1083/jcb.201809089

Pardee, A. B. (1974). A restriction point for control of normal animal cell proliferation. *Proceedings of the National Academy of Sciences of the United States of America, 71*(4), 1286-1290. doi:10.1073/pnas.71.4.1286

Pelham, R. J., & Chang, F. (2001). Role of actin polymerization and actin cables in actin-patch movement in *Schizosaccharomyces pombe*. *Nature Cell Biology, 3*(3), 235-244. doi:10.1038/35060020

Peng, J., Chen, Y., Green, M. D., Sabatinos, S. A., Forsburg, S. L., & Hsu, C. (2013). PombeX: Robust cell segmentation for fission yeast transillumination images. *PloS One, 8*(12), Article e81434. doi:10.1371/journal.pone.0081434

Petersen, J., & Nurse, P. (2007). TOR signalling regulates mitotic commitment through the stress MAP kinase pathway and the polo and Cdc2 kinases. *Nature Cell Biology, 9*(11), 1263-1272. doi:10.1038/ncb1646

Petersen, J., & Russell, P. (2016). Growth and the environment of *Schizosaccharomyces pombe*. *Cold Spring Harbor Protocols, 2016*(3), Article pdb.top079764. doi:10.1101/pdb.top079764

Petersen, J., Weilguny, D., Egel, R., & Nielsen, O. (1995). Characterization of *fus1* of *Schizosaccharomyces pombe*: A developmentally controlled function needed for conjugation. *Molecular and Cellular Biology, 15*(7), 3697-3707. doi:10.1128/MCB.15.7.3697

Petrini, E., Baillet, V., Cridge, J., Hogan, C. J., Guillaume, C., Ke, H., Brandetti, E., Walker, S., Koohy, H., Spivakov, M., & Varga-Weisz, P. (2015). A new phosphate-starvation response in fission yeast requires the endocytic function of myosin I. *Journal of Cell Science, 128*(20), 3707-3713. doi:10.1242/jcs.171314

Pinar, M., Coll, P. M., Rincón, S. A., & Pérez, P. (2008). *Schizosaccharomyces pombe* Pxl1 is a paxillin homologue that modulates Rho1 activity and participates in cytokinesis. *Molecular biology of the Cell, 19*(4), 1727-1738. doi:10.1091/mbc.e07-07-0718

Piston, D. W., Patterson, G. H., Lippincott-Schwartz, J., Claxton, N. S. & Davidson, M. W. (n.d.). *Introduction to fluorescent proteins*. Nikon Instruments. https://www.microscopyu.com/techniques/fluorescence/introduction-to-fluorescent-proteins

Plante, S., & Labbé, S. (2019). Spore germination requires ferrichrome biosynthesis and the siderophore transporter Str1 in *Schizosaccharomyces pombe*. *Genetics, 211*(3), 893. doi:10.1534/genetics.118.301843

---

Poljsak, B., Šuput, D., & Milisav, I. (2013). Achieving the balance between ROS and antioxidants: When to use the synthetic antioxidants. *Oxidative Medicine and Cellular Longevity, 2013*, Article 956792. doi:10.1155/2013/956792

Pollard, L. W. (2017). *Myo2 motor function in the contractile ring and the regulation of fission yeast cytokinesis.* [Doctoral dissertation, Vermont University] Graduate College Dissertations and Theses. https://scholarworks.uvm.edu/graddis/701

Pollard, L. W., Bookwalter, C. S., Tang, Q., Krementsova, E. B., Trybus, K. M., & Lowey, S. (2017). Fission yeast myosin Myo2 is down-regulated in actin affinity by light chain phosphorylation. *Proceedings of the National Academy of Sciences of the United States of America, 114*(35), E7236-E7244. doi:10.1073/pnas.1703161114

Pollard, T. D., & Earnshaw, W. C. (2017). Chapter 36 - motor proteins. In T. D. Pollard, W. C. Earnshaw, J. Lippincott-Schwartz, & G. T. Johnson (Eds.), *Cell biology (3rd edition)* (pp. 623-638). Elsevier. doi:10.1016/B978-0-323-34126-4.00036-0

Pollard, T. D., & Korn, E. D. (1973). *Acanthamoeba* myosin. I. isolation from *Acanthamoeba castellanii* of an enzyme similar to muscle myosin. *Journal of Biological Chemistry, 248*(13), 4682-4690.doi:10.1016/S0021-9258(19)43718-6

Pollard, T. D., & Wu, J. (2010). Understanding cytokinesis: Lessons from fission yeast. *Nature Reviews Molecular Cell Biology, 11*(2), 149-155. doi:10.1038/nrm2834

Presti, L. L., Chang, F., & Martin, S. G. (2012). Myosin Vs organize actin cables in fission yeast. *Molecular Biology of the Cell, 23*(23), 4579-4591. doi:10.1091/mbc.e12-07-0499

Presti, L. L., & Martin, S. (2011). Shaping fission yeast cells by rerouting actin-based transport on microtubules. *Current Biology, 21*(24), 2064-2069. doi:10.1016/j.cub.2011.10.033

Proteintech. (2019). *If imaging: Widefield versus confocal microscopy*. https://www.ptglab.com/news/blog/if-imaging-widefield-versus-confocal-microscopy/

Pruyne, D., Evangelista, M., Yang, C., Bi, E., Zigmond, S., Bretscher, A., & Boone, C. (2002). Role of formins in actin assembly: Nucleation and barbed-end association. *Science, 297*(5581), 612-615. doi:10.1126/science.1072309

Quinlan, M. E., Heuser, J. E., Kerkhoff, E., & Dyche Mullins, R. (2005). *Drosophila* spire is an actin nucleation factor. *Nature, 433*(7024), 382-388. doi:10.1038/nature03241

Rajagopalan, S., Wachtler, V., & Balasubramanian, M. (2003). Cytokinesis in fission yeast: A story of rings, rafts and walls. *Trends in Genetics, 19*(7), 403-408. doi:10.1016/S0168-9525(03)00149-5

Reck-Peterson, S. L., Provance, D. W., Mooseker, M. S., & Mercer, J. A. (2000). Class V myosins. Biochimica et Biophysica Acta*, 1496*(1), 36-51. doi:10.1016/S0167-4889(00)00007-0

Renz, M. (2013). Fluorescence microscopy - A historical and technical perspective. *Cytometry, 83*(9), 767-779. doi:10.1002/cyto.a.22295

Ridley, A. J. (2006). Rho GTPases and actin dynamics in membrane protrusions and vesicle trafficking. *Trends in Cell Biology, 16*(10), 522-529. doi:10.1016/j.tcb.2006.08.006

Roehlecke, C., Schaller, A., Knels, L., & Funk, R. H. W. (2009). The influence of sublethal blue light exposure on human RPE cells. *Molecular Vision, 15*, 1929-1938. https://www.ncbi.nlm.nih.gov/pmc/articles/PMC2751800/

Rösner J., Liotta A., Angamo E. A., Spies C., Heinemann U., & Kovács, R. (2016). Minimizing photodecomposition of flavin adenine dinucleotide fluorescence by the use of pulsed LEDs. *Journal of Microscopy, 264*(2), 215-223. doi:10.1111/jmi.12436

Safer, D., Golla, R., & Nachmias, V. T. (1990). Isolation of a 5-kilodalton actin-sequestering peptide from human blood platelets. *Proceedings of the National Academy of Sciences of the United States of America, 87*(7), 2536-2540. https://www.ncbi.nlm.nih.gov/pmc/articles/PMC53724/

Sagot, I., Rodal, A. A., Moseley, J., Goode, B. L., & Pellman, D. (2002). An actin nucleation mechanism mediated by Bni1 and profilin. *Nature Cell Biology, 4*(8), 626-631. doi:10.1038/ncb834

Sakamoto, T., Yildiz, A., Selvin, P. R., & Sellers, J. R. (2005). Step-size is determined by neck length in myosin V. *Biochemistry, 44*(49), 16203-16210. doi:10.1021/bi0512086

Sammons, M. R., James, M. L., Clayton, J. E., Sladewski, T. E., Sirotkin, V., & Lord, M. (2011). A calmodulin-related light chain from fission yeast that functions with myosin-I and PI 4-kinase. *Journal of Cell Science, 124*(14), 2466-2477. doi:10.1242/jcs.067850

Santos, A., Kalita, J., & Rock, R. S. (2016). Slow and steady wins the race: Encounters of myosin-5 and myosin-6 on shared actin filaments. *Biorxiv,* Article 087940. doi:10.1101/087940

Sato, M., Toya, M., & Toda, T. (2009). Visualization of fluorescence-tagged proteins in fission yeast: The analysis of mitotic spindle dynamics using GFP-tubulin under the native promoter. *Methods in Molecular Biology, 545*, 185-203. doi:10.1007/978-1-60327-993-2_11

Schluter, K., Jockusch, B. M., & Rothkegel, M. (1997). Profilins as regulators of actin dynamics. *Biochimica et Biophysica Acta,* 1359, 97-109. doi:10.1016/S0167-4889(97)00100-6

Schmidt, G. W., Cuny, A. P., & Rudolf, F. (2020). Preventing photomorbidity in long-term multi-color fluorescence imaging of *Saccharomyces cerevisiae* and *S. pombe*. *G3, 10*(12), 4373-4385. doi:10.1534/g3.120.401465

Schneckenburger H., Weber P., Wagner M., Schickinger, S., Richter, V., Bruns, T., Strauss, W. S. L., & Wittig, R. (2012). Light exposure and cell viability in fluorescence microscopy. *Journal of Microscopy, 245*(3), 311-318. doi:10.1111/j.1365-2818.2011.03576.x

Scholey, J. M., Taylor, K. A., & Kendrick-Jones, J. (1980). Regulation of non-muscle myosin assembly by calmodulin-dependent light chain kinase. *Nature, 287*(5779), 233-235. doi:10.1038/287233a0

Schonbrun, M., Kolesnikov, M., Kupiec, M., & Weisman, R. (2013). TORC2 is required to maintain genome stability during S phase in fission yeast. *Journal of Biological Chemistry, 288*(27), 19649-19660. doi:10.1074/jbc.M113.464974

Schonbrun, M., Laor, D., López-Maury, L., Bähler, J., Kupiec, M., & Weisman, R. (2009). TOR complex 2 controls gene silencing, telomere length maintenance, and survival under DNA-damaging conditions. *Molecular and Cellular Biology, 29*(16), 4584-4594. doi:10.1128/MCB.01879-08

Schwayer, C., Sikora, M., Slováková, J., Kardos, R., & Heisenberg, C. (2016). Actin rings of power. *Developmental Cell, 37*(6), 493-506. doi:10.1016/j.devcel.2016.05.024

Seike, T., Shimoda, C., & Niki, H. (2019). Asymmetric diversification of mating pheromones in fission yeast. *PLOS Biology, 17*(1), Article e3000101. doi:10.1371/journal.pbio.3000101

Sellers, J. R., Pato, M. D., & Adelstein, R. S. (1981). Reversible phosphorylation of smooth muscle myosin, heavy meromyosin, and platelet myosin. *Journal of Biological Chemistry, 256*(24), 13137-13142. doi:10.1016/S0021-9258(18)43018-9

Shaner, N. C., Lambert, G. G., Chammas, A., Ni, Y., Cranfill, P. J., Baird, M. A., Baird M. A., Sell, B. R., Allen, J. R., Day, R. N., Israelsson, M., Davidson, M. W., & Wang, J. (2013). A bright monomeric green fluorescent protein derived from *Branchiostoma lanceolatum*. *Nature Methods, 10*(5), 407-409. doi:10.1038/nmeth.2413

Sharma, R. K., & Parameswaran, S. (2018). Calmodulin-binding proteins: A journey of 40 years. *Cell Calcium, 75*, 89-100. doi:10.1016/j.ceca.2018.09.002

Shen, M., Zhang, N., Zheng, S., Zhang, W., Zhang, H., Lu, Z., Su, Q. P., Sun, Y., Ye, K., & Li, X. (2016). Calmodulin in complex with the first IQ motif of myosin-5a functions as an intact calcium sensor. *Proceedings of the National Academy of Sciences of the United States of America, 113*(40), E5812-E5820. doi:10.1073/pnas.1607702113

Shibata, K., Koyama, T., Inde, S., Iwai, S., & Chaen, S. (2017). Mutations in the SH1 helix alter the thermal properties of myosin II. *Biophysics and Physicobiology, 14*, 67-73. doi:10.2142/biophysico.14.0_67

Shimada, A., Niwa, H., Tsujita, K., Suetsugu, S., Nitta, K., Hanawa-Suetsugu, K., Akasaka, R., Nishino, Y., Toyama, M., Chen, L., Liu, Z., J., Wang, B., C., Yamamoto, M., Terada, T., Miyazawa, A., Tanaka, A., Sugano, S., Shirouzu, M., Nagayama, K., Takenawa, T., & Yokoyama, S. (2007). Curved EFC/F-BAR-domain dimers are joined end to end into a filament for membrane invagination in endocytosis. *Cell, 129*(4), 761-772. doi:10.1016/j.cell.2007.03.040

Sipiczki, M. (2007). Splitting of the fission yeast septum. *FEMS Yeast Research, 7*(6), 761-770. doi:10.1111/j.1567-1364.2007.00266.x

Skau, C. T., Courson, D. S., Bestul, A. J., Winkelman, J. D., Rock, R. S., Sirotkin, V., & Kovar, D. R. (2011). Actin filament bundling by fimbrin is important for endocytosis, cytokinesis, and polarization in fission yeast. *The Journal of Biological Chemistry, 286*(30), 26964-26977. doi:10.1074/jbc.M111.239004

Skoumpla, K., Coulton, A. T., Lehman, W., Geeves, M. A., & Mulvihill, D. P. (2007). Acetylation regulates tropomyosin function in the fission yeast *Schizosaccharomyces pombe*. *Journal of Cell Science, 120*(9), 1635-1645. doi:10.1242/jcs.001115

Song, L., Hennink, E. J., Young, I. T., & Tanke, H. J. (1995). Photobleaching kinetics of fluorescein in quantitative fluorescence microscopy. *Biophysical Journal, 68*(6), 2588-2600. doi:10.1016/S0006-3495(95)80442-X

Spring, K. R., & Davidson, M. W. (n.d.). *Introduction to fluorescence microscopy*. Nikon Instruments. https://www.microscopyu.com/references/fluorophore-photobleaching

Spring, K. R., Fellers, T. J., & Davidson, M. W. (n.d.). *Introduction to charge-coupled devices (CCDs).* Nikon Instruments. https://www.microscopyu.com/digital-imaging/introduction-to-charge-coupled-devices-ccds

Squire, J. M., Paul, D. M., & Morris, E. P. (2017). Myosin and actin filaments in muscle: Structures and interactions. In D. A. D. Parry, & J. M. Squire (Eds.), *Fibrous proteins: Structures and mechanisms* (pp. 319-371). Springer International Publishing. doi:10.1007/978-3-319-49674-0_11

Srinivas, U. S., Tan, B. W. Q., Vellayappan, B. A., & Jeyasekharan, A. D. (2019). ROS and the DNA damage response in cancer. *Redox Biology; Redox Regulation of Cell State and Fate, 25*, Article 101084. doi:10.1016/j.redox.2018.101084

St. Croix, C. M., Shand, S. H., & Watkins, S. C. (2005). Confocal microscopy: Comparisons, applications, and problems. *Biotechniques, 39*(6), S2-S5. doi:10.2144/000112089

Su, L., Zhang, J., Gomez, H., Murugan, R., Hong, X., Xu, D., Jiang, F., Peng, Z. (2019). Reactive oxygen species-induced lipid peroxidation in apoptosis, autophagy, and ferroptosis. *Oxidative Medicine and Cellular Longevity, 2019*, Article 5080843. doi:10.1155/2019/5080843

Suizu, T., Tsutsumi, H., Kawado, A., Suginami, K., Imayasu, S., & Murata, K. (1995). Calcium ion influx during sporulation in the yeast *Saccharomyces cerevisiae*. *Canadian Journal of Microbiology, 41*(11), 1035-1037. doi:10.1139/m95-143

Sun, Y., Martin, A. C., & Drubin, D. G. (2006). Endocytic internalization in budding yeast requires coordinated actin nucleation and myosin motor activity. *Developmental Cell, 11*(1), 33-46. doi:10.1016/j.devcel.2006.05.008

Tahara, Y. O., Miyata, M., & Nakamura, T. (2021). Quick-freeze, deep-etch electron microscopy reveals the characteristic architecture of the fission yeast spore. *Journal of Fungi, 7*(1), Article 7. doi:10.3390/jof7010007

Takaine, M., & Mabuchi, I. (2007). Properties of actin from the fission yeast *Schizosaccharomyces pombe* and interaction with fission yeast profilin. *The Journal of Biological Chemistry, 282*, 21683-21694. doi:10.1074/jbc.M611371200

Tanaka, K., Petersen, J., MacIver, F., Mulvihill, D. P., Glover, D. M., & Hagan, I. M. (2001). The role of Plo1 kinase in mitotic commitment and septation in *Schizosaccharomyces pombe. The EMBO Journal, 20*(6), 1259-1270. doi:10.1093/emboj/20.6.1259

Tatebe, H., Murayama, S., Yonekura, T., Hatano, T., Richter, D., Furuya, T., Kataoka S., Furuita, K., Kojima, C., Shiozaki, K. (2017). Substrate specificity of TOR complex 2 is determined by a ubiquitin-fold domain of the Sin1 subunit. *Elife, 6*, Article e19594. doi:10.7554/eLife.19594

Tay, Y. D., Leda, M., Spanos, C., Rappsilber, J., Goryachev, A. B., & Sawin, K. E. (2019). Fission yeast NDR/LATS kinase Orb6 regulates exocytosis via phosphorylation of the exocyst complex. *Cell Reports, 26*(6), 1654-1667. doi:10.1016/j.celrep.2019.01.027

Tebbs, I. R., & Pollard, T. D. (2013). Separate roles of IQGAP Rng2p in forming and constricting the *Schizosaccharomyces pombe* cytokinetic contractile ring. *Molecular Biology of the Cell, 24*(12), 1904-1917. doi:10.1091/mbc.E12-10-0775

Thermo Fisher Scientific. (n.d.). *Phosphorylation.* https://www.thermofisher.com/uk/en/home/life-science/protein-biology/protein-biology-learning-center/protein-biology-resource-library/pierce-protein-methods/phosphorylation.html#1

Tinevez, J., Dragavon, J., Baba-Aissa, L., Roux, P., Perret, E., Canivet, A., Galy, V., & Shorte, S. (2012). Chapter fifteen - A quantitative method for measuring phototoxicity of a live cell imaging microscope. In P. M. Conn (Ed.), *Methods in enzymology* (pp. 291-309) Academic Press. doi:10.1016/B978-0-12-391856-7.00039-1

Toya, M., Motegi, F., Nakano, K., Mabuchi, I., & Yamamoto, M. (2001). Identification and functional analysis of the gene for type I myosin in fission yeast. *Genes to Cells, 6*(3), 187-199. doi:10.1046/j.1365-2443.2001.00414.x

Trybus, K. M. (1989). Filamentous smooth muscle myosin is regulated by phosphorylation. *The Journal of Cell Biology, 109*(6), 2887-2894. doi:10.1083/jcb.109.6.2887

Trybus, K. M. (2008). Myosin V from head to tail. *Cellular and Molecular Life Sciences: CMLS, 65*(9), 1378-1389. doi:10.1007/s00018-008-7507-6

Trybus, K. M., Gushchin, M. I., Lui, H., Hazelwood, L., Krementsova, E. B., Volkmann, N., & Hanein, D. (2007). *Effect of calcium on calmodulin bound to the IQ motifs of myosin V.* doi:10.1074/jbc.M701636200

Ucisik-Akkaya, E., Leatherwood, J. K., & Neiman, A. M. (2014). A genome-wide screen for sporulation-defective mutants in *Schizosaccharomyces pombe. G3, 4*(6), 1173-1182. doi:10.1534/g3.114.011049

Vicente-Manzanares, M., Ma, X., Adelstein, R. S., & Horwitz, A. R. (2009). Non-muscle myosin II takes centre stage in cell adhesion and migration. *Nature Reviews Molecular Cell Biology, 10*(11), 778-790. doi:10.1038/nrm2786

Walklate, J., Ujfalusi, Z., & Geeves, M. A. (2016). Myosin isoforms and the mechanochemical cross-bridge cycle. *The Journal of Experimental Biology, 219*(2), 168-174. doi:10.1242/jeb.124594

Weck, M. L., Grega-Larson, N. E., & Tyska, M. J. MyTH4-FERM myosins in the assembly and maintenance of actin-based protrusions. *Current Opinion in Cell Biology,* 44, 68-78. doi:10.1016/j.ceb.2016.10.002

Wei, B., Hercyk, B. S., Mattson, N., Mohammadi, A., Rich, J., DeBruyne, E., Clark, M. M., & Das, M. (2016). Unique spatiotemporal activation pattern of Cdc42 by Gef1 and Scd1 promotes different events during cytokinesis. *Molecular Biology of the Cell, 27*(8), 1235-1245. doi:10.1091/mbc.E15-10-0700

Weisman, R. (2016). Target of rapamycin (TOR) regulates growth in response to nutritional signals. *Microbiology Spectrum, 4*(5). doi:10.1128/microbiolspec.FUNK-0006-2016

Weisman, R., & Choder, M. (2001). The fission yeast TOR homolog*, tor1* $^{+}$, is required for the response to starvation and other stresses via a conserved serine. *Journal of Biological Chemistry, 276*(10), 7027-7032. doi:10.1074/jbc.M010446200

Wenzel, J., Ouderkirk, J. L., Krendel, M., & Lang, R. (2015). Class I myosin Myo1e regulates TLR4-triggered macrophage spreading, chemokine release, and antigen presentation via MHC class II. *European Journal of Immunology, 45*(1), 225-237. doi:10.1002/eji.201444698

Weston, L., Coutts, A. S., & La Thangue, N. B. (2012). Actin nucleators in the nucleus: An emerging theme. *Journal of Cell Science, 125*, 3519-3527. doi:10.1242/jcs.099523

Willet, A. H., McDonald, N. A., & Gould, K. L. (2015). Regulation of contractile ring formation and septation in *Schizosaccharomyces pombe*. *Current Opinion in Microbiology, 28*, 46-52. doi:10.1016/j.mib.2015.08.001

Wilson, M. (2017). *Introduction to widefield microscopy.* Leica Microsystems. https://www.leica-microsystems.com/science-lab/introduction-to-widefield-microscopy/

Wilson-Grady, J., Villen, J., & Gygi, S. P. (2008). Phosphoproteome analysis of fission yeast. *Journal of Proteome Research, 7*(3), 1088-1097. doi:10.1021/pr7006335

Win, T. Z., Gachet, Y., Mulvihill, D. P., May, K. M., & Hyams, J. S. (2001). Two type V myosins with non-overlapping functions in the fission yeast *Schizosaccharomyces pombe*: Myo52 is concerned with growth polarity and cytokinesis, Myo51 is a component of the cytokinetic actin ring. *Journal of Cell Science, 114*(1), 69-79. doi:10.1242/jcs.114.1.69

Wojtala, A., Bonora, M., Malinska, D., Pinton, P., Duszynski, J., & Wieckowski, M. R. (2014). Chapter thirteen - methods to monitor ROS production by fluorescence microscopy and fluorometry. In L. Galluzzi, & G. Kroemer (Eds.), *Methods in enzymology* (pp. 243-262) Academic Press. doi:10.1016/B978-0-12-416618-9.00013-3

Wolfe, B. A., & Gould, K. L. (2005). Split decisions: Coordinating cytokinesis in yeast. *Trends in Cell Biology, 15*(1), 10-18. doi:10.1016/j.tcb.2004.11.006

Wood, V., Gwilliam, R., Rajandream, M., Lyne, M., Lyne, R., Stewart, A., Sgouros, J., Peat, N., Hayles, J., Baker, S., Basham, D., Bowman, S., Brooks, K., Brown, D., Chillingworth, T., Churcher, C., Collins, M., Cronin, A., Davis, P., Feltwell, T., Fraser, A., Gentles, S., Goble, A., Hamlin, N., Harris, D., Hidalgo, J., Hodgson, G., Holroyd, S., Hornsby, T., Howarth, S., Huckle, E. J., Hunt, S., Jagels, K., James, K., Jones, L., Jones, M., Leather, S., McDonald, S., McLean, J., Mooney, P., Moule, S., Mungall, K., Murphy, L., Niblett, D., Odell, C., Oliver, K., O'Neil, S., Pearson, D., Quail, M. A., Rabbinowitsch, E., Rutherford, K., Rutter, S., Saunders, D., Seeger, K., Sharp, S., Skelton, J., Simmonds, M., Squares, R., Squares, S., Stevens, K., Taylor, K., Taylor, R. G., Tivey, A., Walsh, S., Warren, T., Whitehead, S., Woodward, J., Volckaert, G., Aert, R., Robben, J., Grymonprez, B., Weltjens, I., Vanstreels, E., Rieger, M., Schäfer, M., Müller-Auer, S., Gabel, C., Fuchs, M., Fritzc, C., Holzer, E., Moestl, D., Hilbert, H., Borzym, K., Langer, I., Beck, A., Lehrach, H., Reinhardt, R., Pohl, T. M., Eger, P., Zimmermann, W., Wedler, H., Wambutt, R., Purnelle, B., Goffeau, A., Cadieu, E., Dréano, S., Gloux, S., Lelaure, V., Mottier, S., Galibert, F., Aves, S. J., Xiang, Z., Hunt, C., Moore, K., Hurst, S. M., Lucas, M., Rochet, M., Gaillardin, C., Tallada, V. A., Garzon, A., Thode, G., Daga, R. R., Cruzado, L., Jimenez, J., Sánchez, M., del Rey, F., Benito, J., Domínguez, A., Revuelta, J. L., Moreno, S., Armstrong, J., Forsburg, S. L., Cerrutti, L., Lowe, T., McCombie, W. R., Paulsen, I., Potashkin, J., Shpakovski, G. V., Ussery, D., Barrell, B. G., & Nurse, P. (2002). The genome sequence of *Schizosaccharomyces pombe*. *Nature, 415*(6874), 871-880. doi:10.1038/nature724

Wullschleger, S., Loewith, R., & Hall, M. N. (2006). TOR signaling in growth and metabolism. *Cell, 124*(3), 471-484. doi:10.1016/j.cell.2006.01.016

Xie, P., Dou, S., & Wang, P. (2006). Model for kinetics of myosin-V molecular motors. *Biophysical Chemistry, 120*(3), 225-236. doi:10.1016/j.bpc.2005.11.008

Yam, C., He, Y., Zhang, D., Chiam, K., & Oliferenko, S. (2011). Divergent strategies for controlling the nuclear membrane satisfy geometric constraints during nuclear division. *Current Biology, 21*(15), 1314-1319. doi:10.1016/j.cub.2011.06.052

Yarmola, E. G., Somasundaram, T., Boring, T. A., Spector, I., & Bubb, M. R. (2000). Actin-latrunculin A structure and function. Differential modulation of actin-binding protein function by latrunculin A. *Journal of Biological Chemistry, 275*(36), 28120-28127. doi:10.1074/jbc.M004253200

Zhang, J., Wang, X., Vikash, V., Ye, Q., Wu, D., Liu, Y., & Dong, W. (2016). ROS and ROS-mediated cellular signaling. *Oxidative Medicine and Cellular Longevity, 2016*, Article 4350965. doi:10.1155/2016/4350965

Zheng, Q., Jockusch, S., Zhou, Z., & Blanchard, S. C. (2014). The contribution of reactive oxygen species to the photobleaching of organic fluorophores. *Photochemistry and Photobiology, 90*(2), 448-454. doi:10.1111/php.12204

# Appendices

During this PhD project, the following contributions were made to the listed papers.

## Appendix 1:

Baker, K., Gyamfi, I. A., Mashanov, G. I., Molloy, J. E., Geeves, M. A., & Mulvihill, D. P. (2019). TORC2-Gad8-dependent myosin phosphorylation modulates regulation by calcium. *Elife, 8*, Article e51150. doi:10.7554/eLife.51150

mNG-Myo1, Cam1-GFP and Cam2-GFP dynamics were recorded in time-lapses of wild-type *myo1*$^+$ meiotic sporulating cells to determine their activity during meiotic cycle (Video 5, Video 6, Video 7). mNG-Myo1, Cam1-GFP and Cam2-GFP foci were observed in a fixed position and less dynamic than foci in wild-type *myo1*$^+$ vegetative cells. The foci lifetimes were also greater than in wild-type *myo1*$^+$ vegetative cells. Meiotic sporulating wild-type *mNG-myo1* cells were stained with FM4-64 to show diminished endocytosis in fusing and meiotic cells (Figure 8E). This indicated the reduction of mNG-Myo1, Cam1-GFP and Cam2-GFP foci dynamics is due to minimised endocytosis in meiotic cells (Baker et al., 2019). This data is described in this thesis (Figure 5.2.2, Figure 5.3). mNG-Myo1, Cam1-GFP and Cam2-GFP dynamics in the meiotic sporulating cells *myo1.S742A* mutant cells were also recorded (no figure). Cam2-GFP foci lifetimes in meiotic sporulating *myo1.S742A* cells were longer than 2 min, suggesting Myo1 S742 phosphorylation is required for Cam2 to bind to Myo1 in sporulating cells. This data is described in this thesis (Figure 5.2.2),

Sporulating *myo1.S742A* cells grown on solid MSL displayed various morphological defects e.g. long and short, wide and angular, club-like, bent and globular. Schmooing cells displayed bent or elongated schmooing ends and some sporulating cells had less or more than four spores. These morphologies suggested unregulated cell growth and loss of polarity in sporulating *myo1.S742A* cells (Baker et al., 2019). This data is described in this thesis (Figure 5.6).

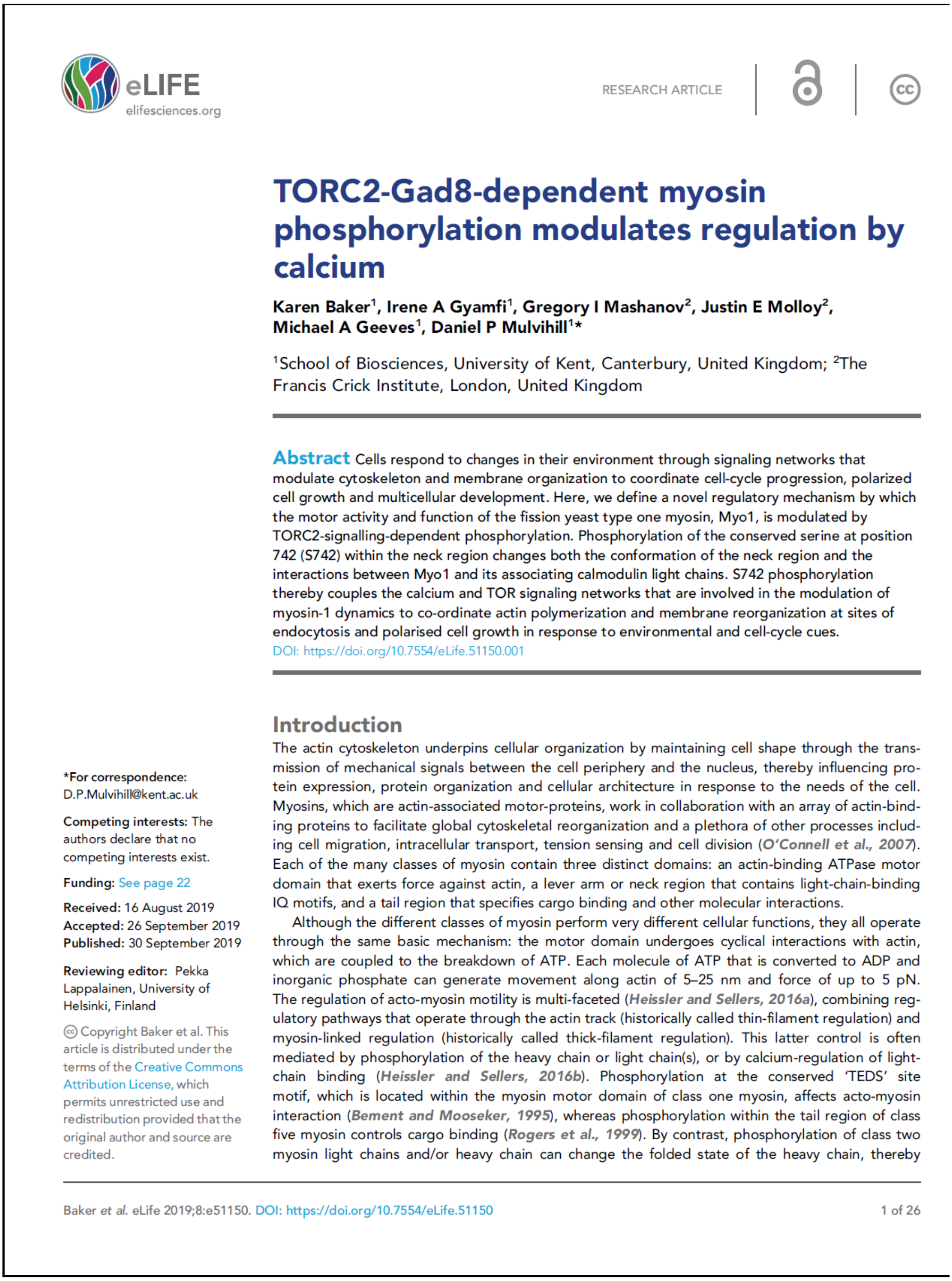

eLIFE
elifesciences.org

RESEARCH ARTICLE

# TORC2-Gad8-dependent myosin phosphorylation modulates regulation by calcium

**Karen Baker[1], Irene A Gyamfi[1], Gregory I Mashanov[2], Justin E Molloy[2], Michael A Geeves[1], Daniel P Mulvihill[1]***

[1]School of Biosciences, University of Kent, Canterbury, United Kingdom; [2]The Francis Crick Institute, London, United Kingdom

**Abstract** Cells respond to changes in their environment through signaling networks that modulate cytoskeleton and membrane organization to coordinate cell-cycle progression, polarized cell growth and multicellular development. Here, we define a novel regulatory mechanism by which the motor activity and function of the fission yeast type one myosin, Myo1, is modulated by TORC2-signalling-dependent phosphorylation. Phosphorylation of the conserved serine at position 742 (S742) within the neck region changes both the conformation of the neck region and the interactions between Myo1 and its associating calmodulin light chains. S742 phosphorylation thereby couples the calcium and TOR signaling networks that are involved in the modulation of myosin-1 dynamics to co-ordinate actin polymerization and membrane reorganization at sites of endocytosis and polarised cell growth in response to environmental and cell-cycle cues.

DOI: https://doi.org/10.7554/eLife.51150.001

***For correspondence:** D.P.Mulvihill@kent.ac.uk

**Competing interests:** The authors declare that no competing interests exist.

**Funding:** See page 22

**Received:** 16 August 2019
**Accepted:** 26 September 2019
**Published:** 30 September 2019

**Reviewing editor:** Pekka Lappalainen, University of Helsinki, Finland

## Introduction

The actin cytoskeleton underpins cellular organization by maintaining cell shape through the transmission of mechanical signals between the cell periphery and the nucleus, thereby influencing protein expression, protein organization and cellular architecture in response to the needs of the cell. Myosins, which are actin-associated motor-proteins, work in collaboration with an array of actin-binding proteins to facilitate global cytoskeletal reorganization and a plethora of other processes including cell migration, intracellular transport, tension sensing and cell division (*O'Connell et al., 2007*). Each of the many classes of myosin contain three distinct domains: an actin-binding ATPase motor domain that exerts force against actin, a lever arm or neck region that contains light-chain-binding IQ motifs, and a tail region that specifies cargo binding and other molecular interactions.

Although the different classes of myosin perform very different cellular functions, they all operate through the same basic mechanism: the motor domain undergoes cyclical interactions with actin, which are coupled to the breakdown of ATP. Each molecule of ATP that is converted to ADP and inorganic phosphate can generate movement along actin of 5–25 nm and force of up to 5 pN. The regulation of acto-myosin motility is multi-faceted (*Heissler and Sellers, 2016a*), combining regulatory pathways that operate through the actin track (historically called thin-filament regulation) and myosin-linked regulation (historically called thick-filament regulation). This latter control is often mediated by phosphorylation of the heavy chain or light chain(s), or by calcium-regulation of light-chain binding (*Heissler and Sellers, 2016b*). Phosphorylation at the conserved 'TEDS' site motif, which is located within the myosin motor domain of class one myosin, affects acto-myosin interaction (*Bement and Mooseker, 1995*), whereas phosphorylation within the tail region of class five myosin controls cargo binding (*Rogers et al., 1999*). By contrast, phosphorylation of class two myosin light chains and/or heavy chain can change the folded state of the heavy chain, thereby

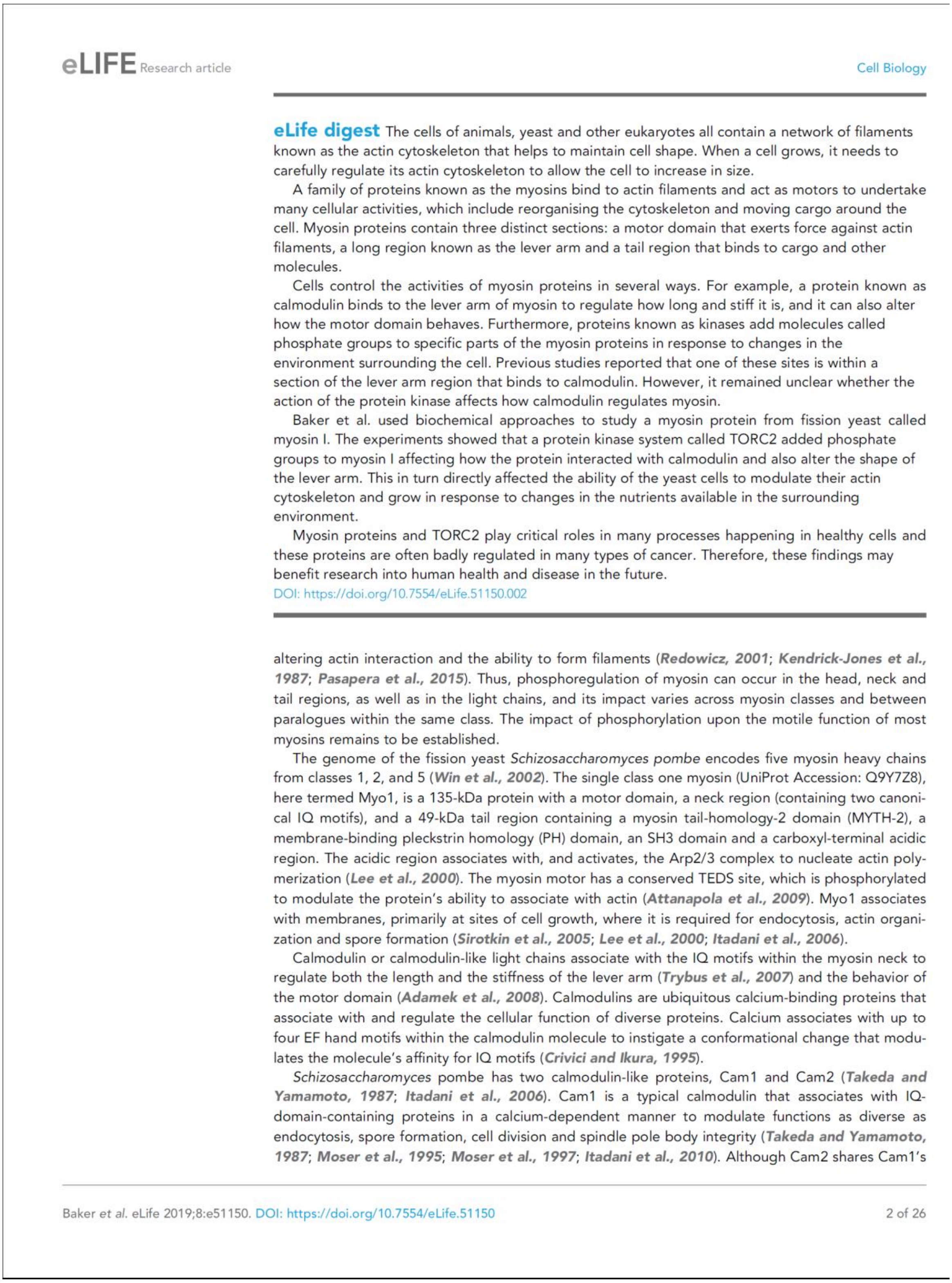

**eLife digest** The cells of animals, yeast and other eukaryotes all contain a network of filaments known as the actin cytoskeleton that helps to maintain cell shape. When a cell grows, it needs to carefully regulate its actin cytoskeleton to allow the cell to increase in size.

A family of proteins known as the myosins bind to actin filaments and act as motors to undertake many cellular activities, which include reorganising the cytoskeleton and moving cargo around the cell. Myosin proteins contain three distinct sections: a motor domain that exerts force against actin filaments, a long region known as the lever arm and a tail region that binds to cargo and other molecules.

Cells control the activities of myosin proteins in several ways. For example, a protein known as calmodulin binds to the lever arm of myosin to regulate how long and stiff it is, and it can also alter how the motor domain behaves. Furthermore, proteins known as kinases add molecules called phosphate groups to specific parts of the myosin proteins in response to changes in the environment surrounding the cell. Previous studies reported that one of these sites is within a section of the lever arm region that binds to calmodulin. However, it remained unclear whether the action of the protein kinase affects how calmodulin regulates myosin.

Baker et al. used biochemical approaches to study a myosin protein from fission yeast called myosin I. The experiments showed that a protein kinase system called TORC2 added phosphate groups to myosin I affecting how the protein interacted with calmodulin and also alter the shape of the lever arm. This in turn directly affected the ability of the yeast cells to modulate their actin cytoskeleton and grow in response to changes in the nutrients available in the surrounding environment.

Myosin proteins and TORC2 play critical roles in many processes happening in healthy cells and these proteins are often badly regulated in many types of cancer. Therefore, these findings may benefit research into human health and disease in the future.

DOI: https://doi.org/10.7554/eLife.51150.002

altering actin interaction and the ability to form filaments (***Redowicz, 2001***; ***Kendrick-Jones et al., 1987***; ***Pasapera et al., 2015***). Thus, phosphoregulation of myosin can occur in the head, neck and tail regions, as well as in the light chains, and its impact varies across myosin classes and between paralogues within the same class. The impact of phosphorylation upon the motile function of most myosins remains to be established.

The genome of the fission yeast *Schizosaccharomyces pombe* encodes five myosin heavy chains from classes 1, 2, and 5 (***Win et al., 2002***). The single class one myosin (UniProt Accession: Q9Y7Z8), here termed Myo1, is a 135-kDa protein with a motor domain, a neck region (containing two canonical IQ motifs), and a 49-kDa tail region containing a myosin tail-homology-2 domain (MYTH-2), a membrane-binding pleckstrin homology (PH) domain, an SH3 domain and a carboxyl-terminal acidic region. The acidic region associates with, and activates, the Arp2/3 complex to nucleate actin polymerization (***Lee et al., 2000***). The myosin motor has a conserved TEDS site, which is phosphorylated to modulate the protein's ability to associate with actin (***Attanapola et al., 2009***). Myo1 associates with membranes, primarily at sites of cell growth, where it is required for endocytosis, actin organization and spore formation (***Sirotkin et al., 2005***; ***Lee et al., 2000***; ***Itadani et al., 2006***).

Calmodulin or calmodulin-like light chains associate with the IQ motifs within the myosin neck to regulate both the length and the stiffness of the lever arm (***Trybus et al., 2007***) and the behavior of the motor domain (***Adamek et al., 2008***). Calmodulins are ubiquitous calcium-binding proteins that associate with and regulate the cellular function of diverse proteins. Calcium associates with up to four EF hand motifs within the calmodulin molecule to instigate a conformational change that modulates the molecule's affinity for IQ motifs (***Crivici and Ikura, 1995***).

*Schizosaccharomyces* pombe has two calmodulin-like proteins, Cam1 and Cam2 (***Takeda and Yamamoto, 1987***; ***Itadani et al., 2006***). Cam1 is a typical calmodulin that associates with IQ-domain-containing proteins in a calcium-dependent manner to modulate functions as diverse as endocytosis, spore formation, cell division and spindle pole body integrity (***Takeda and Yamamoto, 1987***; ***Moser et al., 1995***; ***Moser et al., 1997***; ***Itadani et al., 2010***). Although Cam2 shares Cam1's

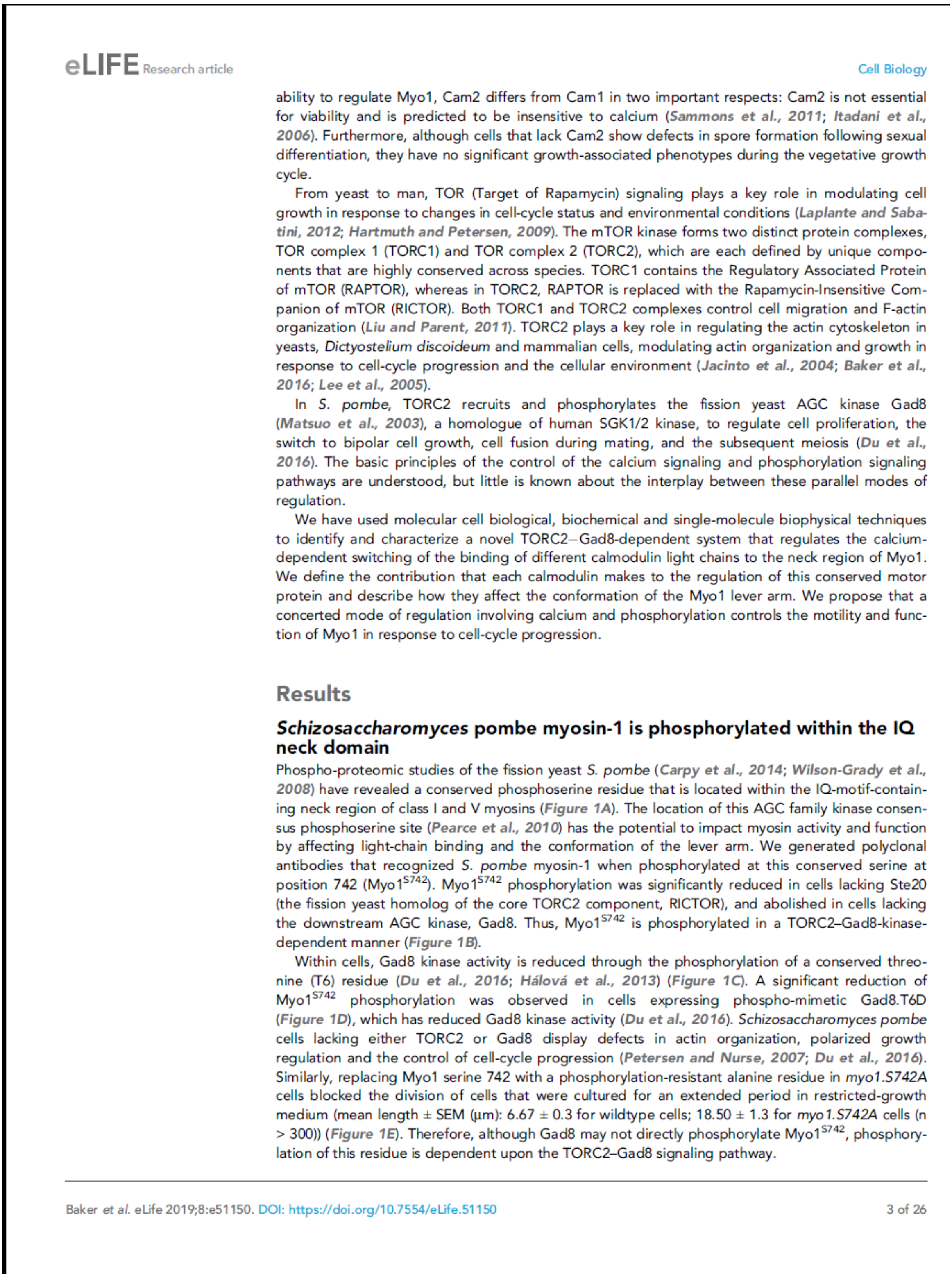

ability to regulate Myo1, Cam2 differs from Cam1 in two important respects: Cam2 is not essential for viability and is predicted to be insensitive to calcium (**Sammons et al., 2011**; **Itadani et al., 2006**). Furthermore, although cells that lack Cam2 show defects in spore formation following sexual differentiation, they have no significant growth-associated phenotypes during the vegetative growth cycle.

From yeast to man, TOR (Target of Rapamycin) signaling plays a key role in modulating cell growth in response to changes in cell-cycle status and environmental conditions (**Laplante and Sabatini, 2012**; **Hartmuth and Petersen, 2009**). The mTOR kinase forms two distinct protein complexes, TOR complex 1 (TORC1) and TOR complex 2 (TORC2), which are each defined by unique components that are highly conserved across species. TORC1 contains the Regulatory Associated Protein of mTOR (RAPTOR), whereas in TORC2, RAPTOR is replaced with the Rapamycin-Insensitive Companion of mTOR (RICTOR). Both TORC1 and TORC2 complexes control cell migration and F-actin organization (**Liu and Parent, 2011**). TORC2 plays a key role in regulating the actin cytoskeleton in yeasts, *Dictyostelium discoideum* and mammalian cells, modulating actin organization and growth in response to cell-cycle progression and the cellular environment (**Jacinto et al., 2004**; **Baker et al., 2016**; **Lee et al., 2005**).

In *S. pombe*, TORC2 recruits and phosphorylates the fission yeast AGC kinase Gad8 (**Matsuo et al., 2003**), a homologue of human SGK1/2 kinase, to regulate cell proliferation, the switch to bipolar cell growth, cell fusion during mating, and the subsequent meiosis (**Du et al., 2016**). The basic principles of the control of the calcium signaling and phosphorylation signaling pathways are understood, but little is known about the interplay between these parallel modes of regulation.

We have used molecular cell biological, biochemical and single-molecule biophysical techniques to identify and characterize a novel TORC2–Gad8-dependent system that regulates the calcium-dependent switching of the binding of different calmodulin light chains to the neck region of Myo1. We define the contribution that each calmodulin makes to the regulation of this conserved motor protein and describe how they affect the conformation of the Myo1 lever arm. We propose that a concerted mode of regulation involving calcium and phosphorylation controls the motility and function of Myo1 in response to cell-cycle progression.

## Results

### *Schizosaccharomyces* pombe myosin-1 is phosphorylated within the IQ neck domain

Phospho-proteomic studies of the fission yeast *S. pombe* (**Carpy et al., 2014**; **Wilson-Grady et al., 2008**) have revealed a conserved phosphoserine residue that is located within the IQ-motif-containing neck region of class I and V myosins (**Figure 1A**). The location of this AGC family kinase consensus phosphoserine site (**Pearce et al., 2010**) has the potential to impact myosin activity and function by affecting light-chain binding and the conformation of the lever arm. We generated polyclonal antibodies that recognized *S. pombe* myosin-1 when phosphorylated at this conserved serine at position 742 (Myo1$^{S742}$). Myo1$^{S742}$ phosphorylation was significantly reduced in cells lacking Ste20 (the fission yeast homolog of the core TORC2 component, RICTOR), and abolished in cells lacking the downstream AGC kinase, Gad8. Thus, Myo1$^{S742}$ is phosphorylated in a TORC2–Gad8-kinase-dependent manner (**Figure 1B**).

Within cells, Gad8 kinase activity is reduced through the phosphorylation of a conserved threonine (T6) residue (**Du et al., 2016**; **Hálová et al., 2013**) (**Figure 1C**). A significant reduction of Myo1$^{S742}$ phosphorylation was observed in cells expressing phospho-mimetic Gad8.T6D (**Figure 1D**), which has reduced Gad8 kinase activity (**Du et al., 2016**). *Schizosaccharomyces pombe* cells lacking either TORC2 or Gad8 display defects in actin organization, polarized growth regulation and the control of cell-cycle progression (**Petersen and Nurse, 2007**; **Du et al., 2016**). Similarly, replacing Myo1 serine 742 with a phosphorylation-resistant alanine residue in *myo1.S742A* cells blocked the division of cells that were cultured for an extended period in restricted-growth medium (mean length ± SEM (µm): 6.67 ± 0.3 for wildtype cells; 18.50 ± 1.3 for *myo1.S742A* cells (n > 300)) (**Figure 1E**). Therefore, although Gad8 may not directly phosphorylate Myo1$^{S742}$, phosphorylation of this residue is dependent upon the TORC2–Gad8 signaling pathway.

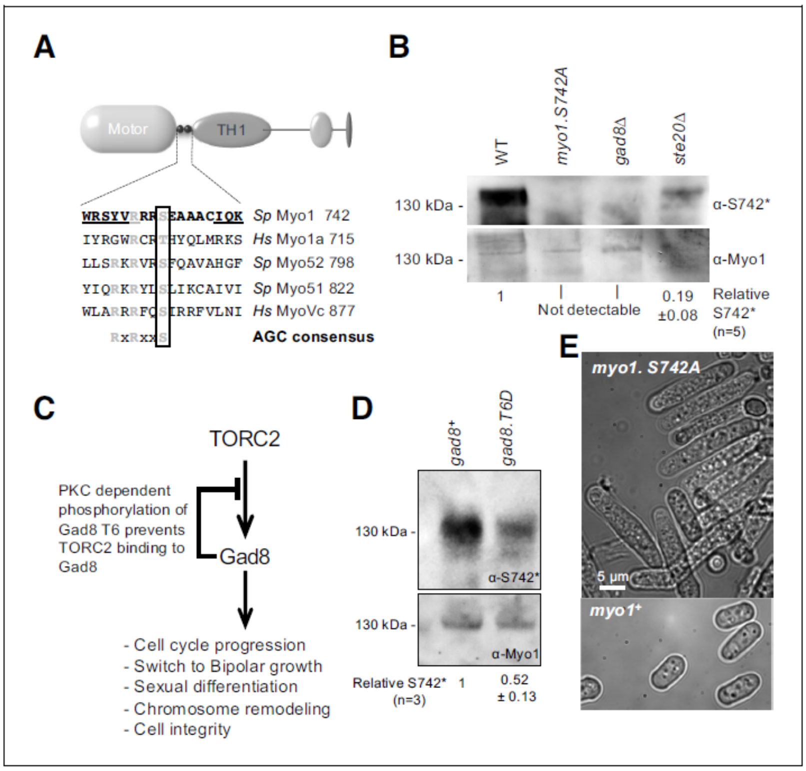

**Figure 1.** Myo1 serine 742 phosphorylation is TORC2 dependent. (A) The sequence alignment of myosin IQ regions highlights an AGC kinase consensus sequence that is conserved in class I and V myosins. Underlined residues are those within IQ motifs. (B) Western blots of extracts from *myo1*$^{+}$, *myo1-S742A*, *gad8Δ* and *ste20Δ* cells probed with phospho-specific anti-Myo1$^{S742}$ (upper panel) and anti-Myo1 (lower panel) antibodies demonstrate antigen specificity and a Myo1$^{S742}$ phosphorylation-state dependence upon the TORC2–Gad8 pathway. Ponceau staining was used to monitor equal loading. Relative Myo1$^{S742}$ phosphorylation levels were calculated from five independent equivalent experiments (mean ± sd). (C) A schematic of the TORC2–Gad8 signaling pathway. (D) Myo1$^{S742}$ phosphorylation is reduced in *gad8.T6D* cells, which have reduced Gad8 kinase activity. Relative Myo1$^{S742}$ phosphorylation levels were calculated from three independent equivalent experiments (mean ± sd). (E) Nitrogen-starved wildtype (WT) and *myo1.S742A* cells. In contrast to WT cells, in which growth arrests, *myo1.S742A* cells continue to grow upon nitrogen-starvation-induced G$_1$ arrest. Scale bar: 5 µm.

DOI: https://doi.org/10.7554/eLife.51150.003

We conclude that TORC2-directed Gad8-dependent phosphorylation at S742 regulates Myo1 activity.

## Phosphorylation affects the structure of the lever arm of Myo1

As serine 742 lies within the IQ motif of the Myo1 neck region, we asked whether Myo1$^{S742}$ phosphorylation alters calmodulin binding and the conformation of the neck region. Isoforms of the Ca$^{2+}$-sensitive fission yeast calmodulin (wild type Cam1 and a Cam1.T6C cysteine mutant, allowing conjugation to a fluorescent probe) were purified from bacteria co-expressing the fission yeast NatA amino-α-acetyl-transferase complex in their native amino-terminally (Nt) acetylated forms (**Eastwood et al., 2017**). Two methods were used to measure Ca$^{2+}$-dependent changes in Cam1 conformation. First, a Förster resonance energy transfer (FRET)-based sensor was generated

consisting of N-terminal CyPet donor and C-terminal YPet acceptor fluorophores fused in-frame with Cam1 (***Nguyen and Daugherty, 2005***) (***Figure 2A***). Second, Nt-acetylated Cam1.T6C was conjugated to a cysteine-reactive synthetic fluorophore 2-(4'-(iodoacetamido) anilino naphthalene-6-sulfonic acid (IAANS)). IAANS fluorescence changes in response to changes in its local environment, so the fluorescence emission of this fusion will change in response to calcium-induced changes in Cam1 conformation. The Ca-binding affinity reported by the Cam1-FRET sensor (***Figure 2C***, $pCa_{50}$: 6.12) reflects the global change in Cam1 conformation, whereas the $Ca^{2+}$-dependent change in IAANS' fluorescence signal (***Figure 2C***-inset, $pCa_{50}$: 6.54) reflects changes in the local environment of the amino lobe of Cam1.

Together these probes demonstrated that $Ca^{2+}$ binding induced a change in Cam1 conformation. The rate of $Ca^{2+}$ ion release from Cam1 was independently measured by monitoring changes in the fluorescence of the $Ca^{2+}$ indicator Quin-2 (***Tsien, 1980***). The time-course of $Ca^{2+}$ ion release exhibited three phases, fast, medium and slow, of approximately equal amplitude (rate constants 137, 12.9 and 2.0 $s^{-1}$, respectively), indicating that the cation has different affinities for each $Ca^{2+}$ binding lobe of Cam1 (***Figure 2D***).

To characterize Cam1 binding to the IQ neck region of Myo1, recombinant FRET constructs were produced in which CyPet and YPet were separated by one of the two Myo1 IQ motifs or by both of these motifs ($Myo1^{IQ1}$-FRET, $Myo1^{IQ2}$-FRET or $Myo1^{IQ12}$-FRET) (***Figure 2B*** and ***Figure 2—figure supplement 1***). Cam1 binding to the IQ motif(s) stabilizes the $\alpha$-helix and results in a drop in FRET signal in the absence of calcium (***Figure 2E–G***). This drop in signal correlates with a Cam1-bound IQ12 neck region length of 4.6 nm (***Wu and Brand, 1994***), close to the 4.7 nm length predicted from the modeled structure (based upon PDB structure 4R8G). Analysis of interactions between Cam1 and $Myo1^{IQ12}$–FRET revealed two distinct phases to the association of Cam1 molecules with the combined $Myo1^{IQ12}$ motifs. Each phase contributed 50% of the overall change in signal (***Figure 2F***). The first Cam1–$Myo1^{IQ12}$-binding event corresponded to an affinity of less than 0.1 µM (binding was too tight to calculate affinity with higher precision), whereas the second event correlated with an approximately 10-fold weaker binding affinity (0.68 µM). This association was sensitive to calcium (pCa of 5.87) (***Figure 2C***), indicating that Cam1 can only associate with both Myo1 IQ motifs at low cellular $Ca^{2+}$ concentrations. Interestingly, while Cam1 bound tightly to a single, isolated, $Myo1^{IQ1}$ alone ($K_d$ <0.1 µM), no detectable association was observed for the equivalent single $Myo1^{IQ2}$ motif (***Figure 2E***). Together these data are consistent with a sequential cooperative binding mechanism in which the stable residency of Cam1 in the first IQ position is required before calmodulin can bind to $Myo1^{IQ2}$.

Replacing serine 742 within the IQ neck region with a phosphomimetic aspartic acid residue had no significant impact upon the affinity, calcium sensitivity or cooperative nature of the interaction between Myo1 and Cam1 (***Figure 2F***). However, the S742D replacement resulted in a change in maximum FRET signal upon Cam1 binding ($F_{max}$ 46.05 vs 31.64) (***Figure 2F***), indicating that $Myo1^{S742}$ phosphorylation changes the conformation of the lever arm upon Cam1 binding, rather than modulating the affinity of the neck region for Cam1.

## Phosphorylation regulates Myo1 dynamics and endocytosis

Immunofluorescence using $Myo1^{S742}$ phospho-specific antibodies confirmed the presence of serine-742 phosphorylated Myo1 at cortical foci (***Figure 3A***). To explore how this phosphorylation affected Myo1 and calmodulin dynamics in vivo, we generated prototroph *S. pombe* strains in which endogenous *myo1*, *cam1*, or *cam2* genes were fused to cDNA encoding monomeric fluorescent proteins (***Figure 3—figure supplement 1***). Using high-speed (20 fps) single-molecule total internal reflection fluorescence (TIRF) imaging, we explored how $Myo1^{S742}$ phosphorylation impacts Myo1 and Cam1 dynamics and function in vivo. Myo1 and Cam1 associated with the cell membrane in two distinct ways: we observed both (i) rapid, transient, binding of single Myo1 molecules to the cell membrane, characterized by low-intensity, single, stepwise, changes in intensity (***Video 1***), alongside (ii) longer endocytic events that were much brighter and took much longer (***Video 2***).

The rapid, single-molecule, interactions of Myo1 and Cam1 with the membrane had low mobility (0.03 $\mu m^2.s^{-1}$), ~10 times slower than the diffusion of integral membrane proteins (***Mashanov et al., 2010***). The individual, diffraction-limited fluorescent spots appeared and disappeared at the cell membrane in a single step. The durations of these short single-molecule events (defined as the period over which individual objects were observed and their paths tracked) were exponentially

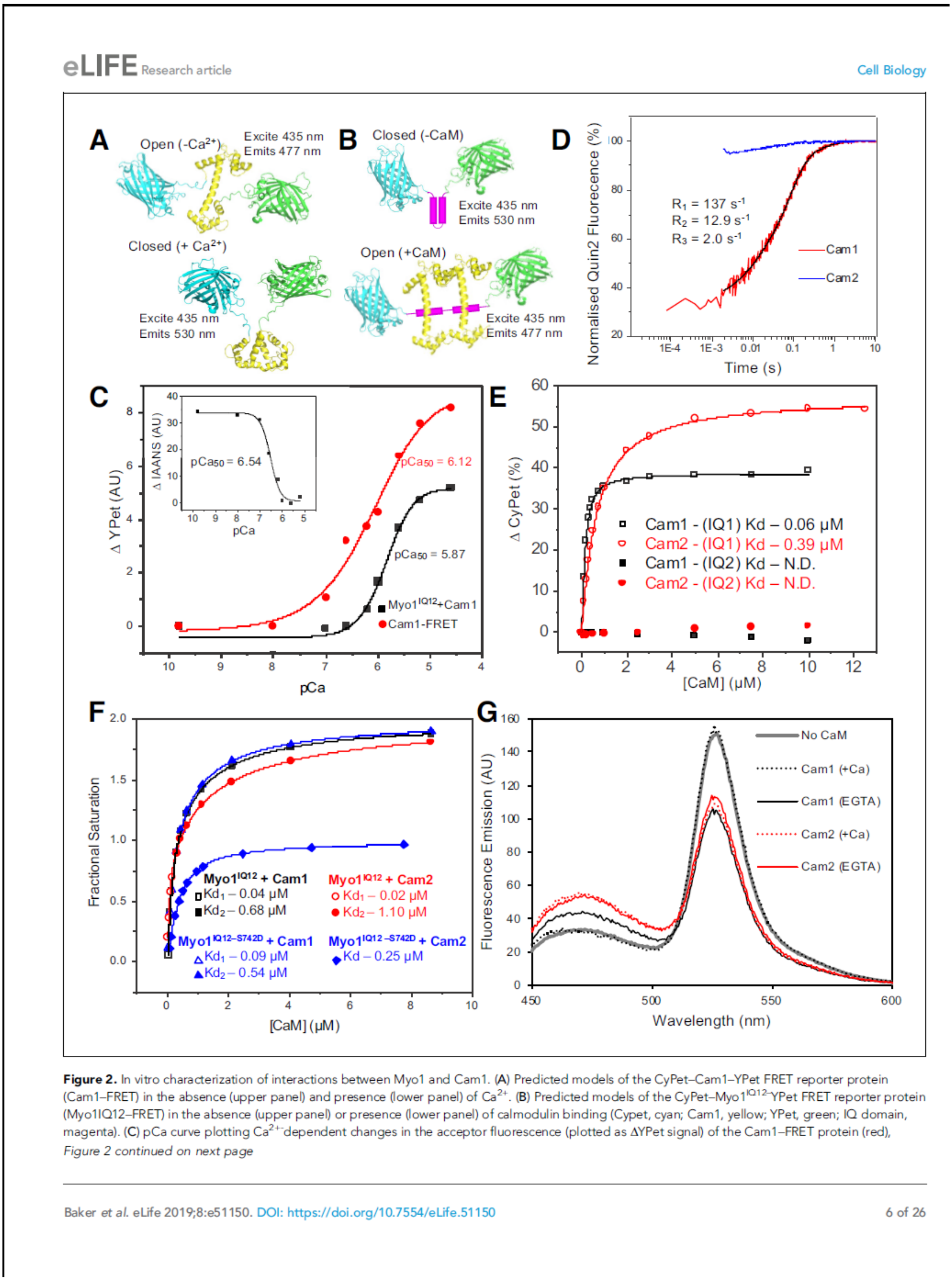

eLIFE Research article

Cell Biology

**Figure 2.** In vitro characterization of interactions between Myo1 and Cam1. **(A)** Predicted models of the CyPet–Cam1–YPet FRET reporter protein (Cam1–FRET) in the absence (upper panel) and presence (lower panel) of Ca$^{2+}$. **(B)** Predicted models of the CyPet–Myo1$^{IQ12}$–YPet FRET reporter protein (Myo1IQ12–FRET) in the absence (upper panel) or presence (lower panel) of calmodulin binding (Cypet, cyan; Cam1, yellow; YPet, green; IQ domain, magenta). **(C)** pCa curve plotting Ca$^{2+}$-dependent changes in the acceptor fluorescence (plotted as ΔYPet signal) of the Cam1–FRET protein (red),

*Figure 2 continued on next page*

Baker et al. eLife 2019;8:e51150. DOI: https://doi.org/10.7554/eLife.51150

6 of 26

eLIFE Research article

Cell Biology

*Figure 2 continued*

Cam1 association with Myo1$^{IQ12}$-FRET (black) and change in the fluorescence of IAANS-labelled Cam1–T6C (inset). (**D**) Transient curves of changes in Quin2 fluorescence induced by $Ca^{2+}$ release from Cam1 (red) (with three exponential fit best fit (black)) and from Cam2 (blue) illustrate that only Cam1 associates with $Ca^{2+}$. (**E**) Curves plotting Cam1- (black) and Cam2-dependent (red) changes of the FRET donor signal of Myo1–FRET proteins containing single IQ domains (IQ1, empty shapes; IQ2, filled shapes) each show that CaM associates with IQ1 but not with an equivalent single IQ2 motif region. (**F**) Curves plotting Cam1- (squares and triangles) and Cam2-dependent (circles and diamonds) changes in the FRET donor signal of either 0.5 µM wild type (black and red) or S742D phosphomimetic (blue) Myo1$^{IQ12-}$FRET proteins show that although phosphorylation does not significantly impact Cam1 binding, it results in a drop of about 50% in Cam2 interaction. (**G**) Spectra of 0.5 µM Myo1$^{IQ12-}$FRET reporter alone (grey line) or of 0.5 µM Myo1$^{IQ12-}$FRET reporter mixed with 10 µM saturating concentrations of: Cam1 + $Ca^{2+}$ (black dotted line), Cam1 – $Ca^{2+}$ (black solid line), Cam2 + $Ca^{2+}$ (red dotted line), or Cam1 – $Ca^{2+}$ (red solid line).
DOI: https://doi.org/10.7554/eLife.51150.004

The following figure supplements are available for figure 2:

**Figure supplement 1.** Purified proteins used during in vitro studies.
DOI: https://doi.org/10.7554/eLife.51150.005

**Figure supplement 2.** Cam1 and Cam2 do not interact directly.
DOI: https://doi.org/10.7554/eLife.51150.006

distributed with mean lifetime of ~8 $s^{-1}$ (n = 152) (***Video 1***). The distribution of the durations of individual Myo1 events is shown in ***Figure 3—figure supplement 1***. By contrast, during endocytic events, the fluorescence signal increased gradually (at a rate corresponding to ~13 molecules.$s^{-1}$) to a peak amplitude corresponding to ~45 molecules of mNeongreen.Myo1, which persisted for ~6 s (plateau phase), before decaying back to baseline level (at a rate of ~14 molecules.$s^{-1}$) (***Figure 3B***, ***Video 2***). The duration ($T_{dur}$) of endocytic events (measured as described in the Materials and methods) was 13.84 s ± 0.39 (mean ± SEM, n = 50) (***Figure 3C***). Although there was significant variation in the maximum mNeongreen.Myo1 intensity (2373 ± 155 AU), there was no correlation between maximum intensity (measured during the plateau phase) and event duration (not shown).

The fluorescence intensity dynamics of Cam1.GFP during endocytic events were similar to those of mNeongreen.Myo1, but $T_{dur}$ was significantly shorter for Cam1.GFP ($p<0.0001$), 10.99 s +/– 0.21 (n = 52) while the peak (plateau) intensity for Cam1.GFP was roughly double that measured for mNeongreen.Myo1 and equivalent to ~90 GFP molecules (***Figure 3C***), consistent with the occupation of both IQ sites within the Myo1 neck region by Cam1. The briefer event duration observed for Cam1 is best explained by the dissociation of Cam1 from Myo1 before Myo1 leaves the endocytic patch. This process was confirmed by two-color imaging of *mNeongreen.myo1 cam1.mCherry* cells, which revealed how Myo1 and Cam1 arrived simultaneously at the endocytic patch, before Cam1.mCherry disassociated ~3 s before mNeongreen.Myo1 (***Figure 3D***, ***Figure 3—figure supplement 1***).

Myo1 and Cam1 dynamics in *myo1.S742A* cells during endocytosis revealed how Myo1$^{S742A}$ had average assembly and disassembly rates and peak intensity measurements that were identical to those of wild-type Myo1, yet the duration of the signal ($T_{dur}$) was 1.5 s shorter for Myo1$^{S742A}$ (12.3 s + /- 0.31 n = 67) (***Figure 3E*** and ***Figure 3—figure supplement 1***). Consistent with the in vitro data, the *myo1.S742A* mutation did not impact on the ability of Cam1 molecules to bind both IQ motifs, as the average assembly and disassembly rates and the plateau intensity for Cam1 were the same in both wild-type and *myo1.S742A* cells. However, Myo1$^{S742A}$ and Cam1 proteins disassociated simultaneously and somewhat earlier during the endocytic event than in otherwise isogenic wild-type cells.

## Myo1 S742 is phosphorylated in a cell-cycle-dependent manner to regulate polarized cell growth

Upon cell division, fission yeast cells grow exclusively from the old cell end that existed in the parental cell. At a point during interphase (called New End Take Off (NETO)), there is a transition to bipolar growth (***Mitchison and Nurse, 1985***). This cell-cycle switch in growth pattern correlates precisely with a parallel redistribution of endocytic actin patches (***Marks and Hyams, 1985***).

The TIRF imaging data were consistent with widefield, 3D, time-lapse imaging that showed that the lifetimes of Myo1 and Cam1 foci were shorter in *myo1.S742A* cells than in *myo1$^+$* cells

Baker *et al.* eLife 2019;8:e51150. DOI: https://doi.org/10.7554/eLife.51150

7 of 26

eLIFE Research article Cell Biology

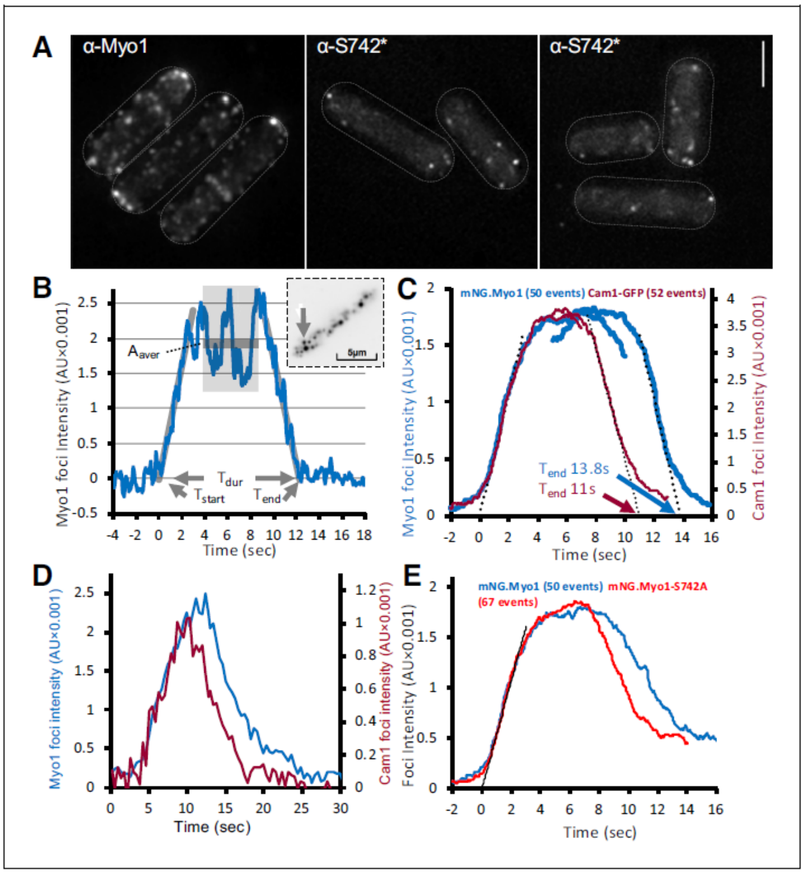

**Figure 3.** Myo1 and Cam1 dynamics in wild-type and *myo1.S742A* cells. (A) Maximum projections from 31-z stack widefield immunofluorescence images of wild-type cells, probed with anti-Myo1 (left panel) or anti-Myo1$^{S742*}$ phosphospecific (right panels) antibodies, illustrate that S742 phosphorylated Myo1 localizes to cortical foci (scale bar, 5 μm). (B) An example relative-intensity trace of a single mNeongreen.Myo1 endocytic event. Linear fitting (grey lines, 60 points) was used to find the maximum gradient for both the rising and the falling slope. The intercept with zero intensity level was used to calculate $T_{start}$, $T_{end}$, and subsequently, the duration of the event $T_{dur}$. See detailed description in the Materials and methods section. Insert: an arrow highlights the analyzed endocytotic event (5 × 5 pixels area). (C) Averaged profile for individual Myo1 (blue) and Cam1 (red) membrane-association events, synchronized relative to $T_{start}$ and $T_{end}$. Dotted lines show fitted rising (Myo1, 537 AU/sec; Cam1, 1073 AU/sec) and falling (Myo1, 567 AU/sec; Cam1, 1028 AU/sec) gradients. (D) An example fluorescence trace from simultaneous two-color imaging of a Myo1 (blue line) and Cam1 (red line) membrane-association event observed in *mNeongreen.myo1 cam1.mCherry* cells is consistent with the relative intensities and timings observed using single-fluorophore strains. (E) Averaged intensity trajectories of individual Myo1 (blue line) and Myo1.S742A (red line) endocytosis events from TIRFM imaging of *mNeongreen.myo1* and *mNeongreen.myo1.S742A* cells, respectively.

DOI: https://doi.org/10.7554/eLife.51150.007

The following figure supplement is available for figure 3:

**Figure supplement 1.** Relative TIRF profiles.

DOI: https://doi.org/10.7554/eLife.51150.008

Baker et al. eLife 2019;8:e51150. DOI: https://doi.org/10.7554/eLife.51150 8 of 26

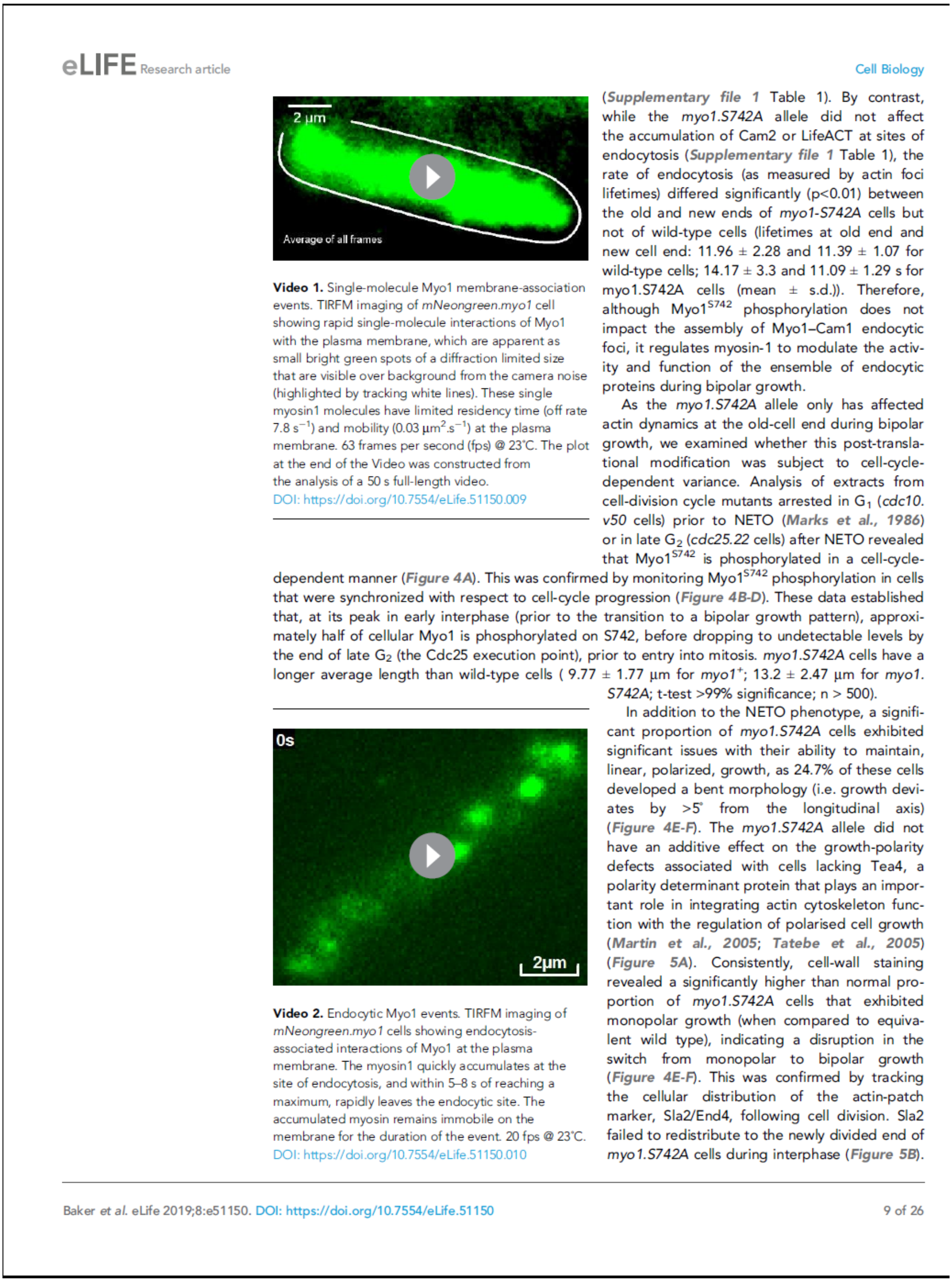

**Video 1.** Single-molecule Myo1 membrane-association events. TIRFM imaging of *mNeongreen.myo1* cell showing rapid single-molecule interactions of Myo1 with the plasma membrane, which are apparent as small bright green spots of a diffraction limited size that are visible over background from the camera noise (highlighted by tracking white lines). These single myosin1 molecules have limited residency time (off rate 7.8 $s^{-1}$) and mobility (0.03 $\mu m^2.s^{-1}$) at the plasma membrane. 63 frames per second (fps) @ 23˚C. The plot at the end of the Video was constructed from the analysis of a 50 s full-length video.
DOI: https://doi.org/10.7554/eLife.51150.009

(*Supplementary file 1* Table 1). By contrast, while the *myo1.S742A* allele did not affect the accumulation of Cam2 or LifeACT at sites of endocytosis (*Supplementary file 1* Table 1), the rate of endocytosis (as measured by actin foci lifetimes) differed significantly ($p<0.01$) between the old and new ends of *myo1-S742A* cells but not of wild-type cells (lifetimes at old end and new cell end: 11.96 ± 2.28 and 11.39 ± 1.07 for wild-type cells; 14.17 ± 3.3 and 11.09 ± 1.29 s for myo1.S742A cells (mean ± s.d.)). Therefore, although Myo1$^{S742}$ phosphorylation does not impact the assembly of Myo1–Cam1 endocytic foci, it regulates myosin-1 to modulate the activity and function of the ensemble of endocytic proteins during bipolar growth.

As the *myo1.S742A* allele only has affected actin dynamics at the old-cell end during bipolar growth, we examined whether this post-translational modification was subject to cell-cycle-dependent variance. Analysis of extracts from cell-division cycle mutants arrested in $G_1$ (*cdc10.v50* cells) prior to NETO (*Marks et al., 1986*) or in late $G_2$ (*cdc25.22* cells) after NETO revealed that Myo1$^{S742}$ is phosphorylated in a cell-cycle-dependent manner (*Figure 4A*). This was confirmed by monitoring Myo1$^{S742}$ phosphorylation in cells that were synchronized with respect to cell-cycle progression (*Figure 4B-D*). These data established that, at its peak in early interphase (prior to the transition to a bipolar growth pattern), approximately half of cellular Myo1 is phosphorylated on S742, before dropping to undetectable levels by the end of late $G_2$ (the Cdc25 execution point), prior to entry into mitosis. *myo1.S742A* cells have a longer average length than wild-type cells ( 9.77 ± 1.77 µm for *myo1*$^+$; 13.2 ± 2.47 µm for *myo1.S742A*; t-test >99% significance; n > 500).

In addition to the NETO phenotype, a significant proportion of *myo1.S742A* cells exhibited significant issues with their ability to maintain, linear, polarized, growth, as 24.7% of these cells developed a bent morphology (i.e. growth deviates by >5˚ from the longitudinal axis) (*Figure 4E-F*). The *myo1.S742A* allele did not have an additive effect on the growth-polarity defects associated with cells lacking Tea4, a polarity determinant protein that plays an important role in integrating actin cytoskeleton function with the regulation of polarised cell growth (*Martin et al., 2005*; *Tatebe et al., 2005*) (*Figure 5A*). Consistently, cell-wall staining revealed a significantly higher than normal proportion of *myo1.S742A* cells that exhibited monopolar growth (when compared to equivalent wild type), indicating a disruption in the switch from monopolar to bipolar growth (*Figure 4E-F*). This was confirmed by tracking the cellular distribution of the actin-patch marker, Sla2/End4, following cell division. Sla2 failed to redistribute to the newly divided end of *myo1.S742A* cells during interphase (*Figure 5B*).

**Video 2.** Endocytic Myo1 events. TIRFM imaging of *mNeongreen.myo1* cells showing endocytosis-associated interactions of Myo1 at the plasma membrane. The myosin1 quickly accumulates at the site of endocytosis, and within 5–8 s of reaching a maximum, rapidly leaves the endocytic site. The accumulated myosin remains immobile on the membrane for the duration of the event. 20 fps @ 23˚C.
DOI: https://doi.org/10.7554/eLife.51150.010

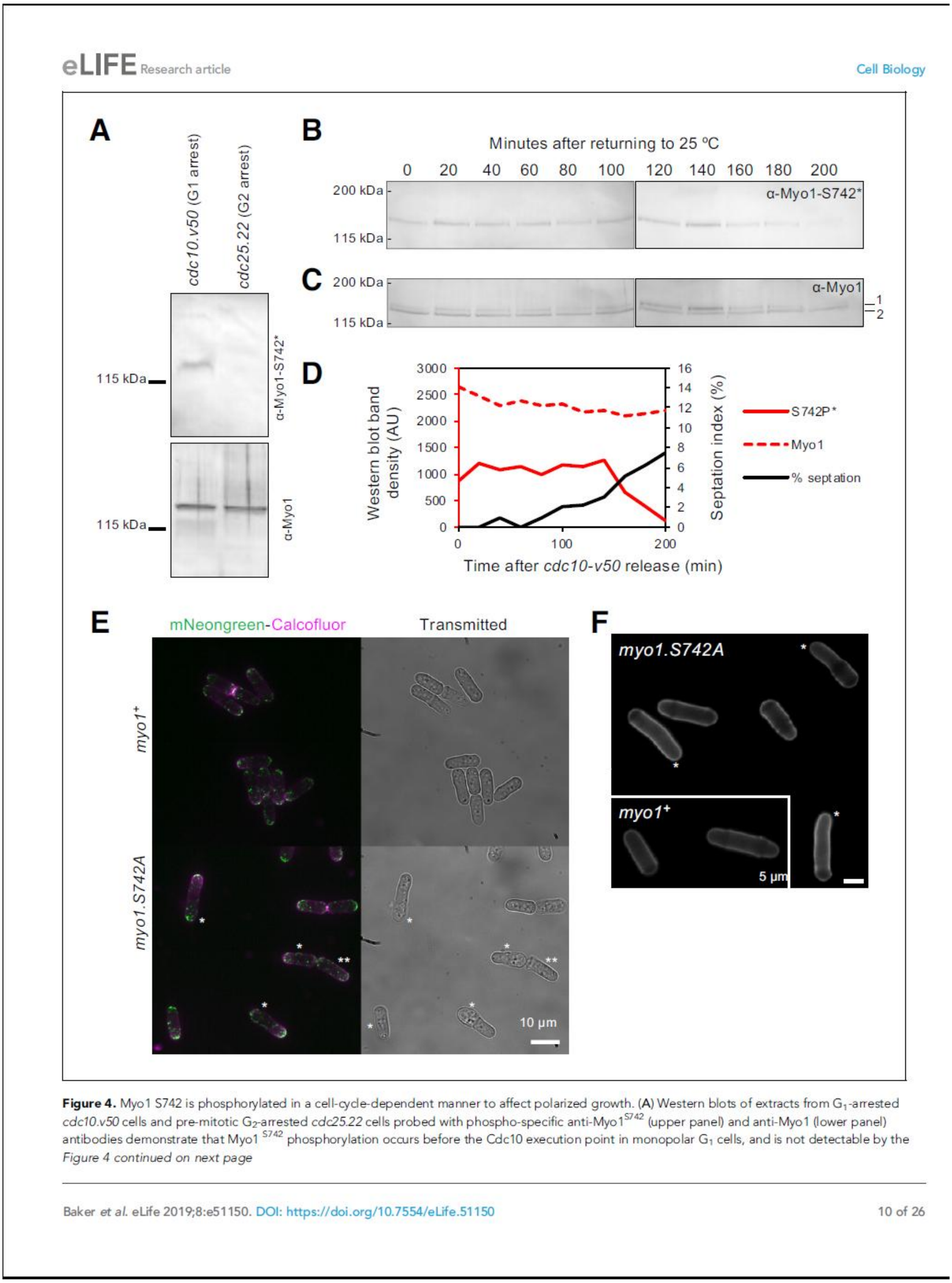

**Figure 4.** Myo1 S742 is phosphorylated in a cell-cycle-dependent manner to affect polarized growth. (A) Western blots of extracts from G$_1$-arrested *cdc10.v50* cells and pre-mitotic G$_2$-arrested *cdc25.22* cells probed with phospho-specific anti-Myo1$^{S742}$ (upper panel) and anti-Myo1 (lower panel) antibodies demonstrate that Myo1 $^{S742}$ phosphorylation occurs before the Cdc10 execution point in monopolar G$_1$ cells, and is not detectable by the

*Figure 4 continued on next page*

*Figure 4 continued*

Cdc25 execution point at the end of G$_2$ (n = 3). (**B–D**) A *cdc10.v50* culture was synchronized in G$_1$ by shifting to 36˚C for 240 min before returning to 25˚C at time 0. Samples of cells were taken every 20 min from the release and processed for western blotting to monitor Myo1$^{S742}$ phosphorylation. The membrane was first probed with phosphospecific anti-Myo1$^{S742*}$ antibodies (**B**), and subsequently probed with anti-Myo1 antibodies to monitor total Myo1 (**C**). Both phosphorylated (1) and non-phosphorylated (2) Myo1 bands can be observed in panel (**C**). Equal loading was monitored by Ponceau staining of the membrane. (**D**) Densitometry measurements of phosphorylated Myo1$^{S742}$ (from panel (**B**)) and total Myo1 (both bands from panel (**C**)) are plotted along with the % of cells in the culture with septa. (**E**) Myosin-1 distribution (green), calcofluor-stained regions of cell growth (magenta), and cell outline (transmitted image) of prototroph *mNeongreen.myo1*$^{+}$ and *mNeongreen.myo1.S742A* cells cultured in EMMG medium at 34˚C. Asterisks highlight cells that have morphology defects. Scale bar, 10 µm. (**F**) Calcofluor-stained WT and *myo1.S742A* cells. Asterisks highlight long bent cells displaying monopolar growth. Scale bar, 5 µm.

DOI: https://doi.org/10.7554/eLife.51150.011

This failure of *myo1.S742A* cells to switch to bipolar growth, a and restrict growth upon nutrient depletion (***Figure 1E***) is consistent with the reduced growth rate at the end of the log phase and with growth to an overall higher density upon reaching the stationary phase (***Figure 5C***).

We conclude that cell-cycle-dependent changes in Myo1$^{S742}$ phosphorylation modulate the ability of the myosin lever arm region to regulate endocytosis and polarized growth.

## Cam2 associates with internalized endosomes and not with Myo1 during vegetative growth

Myo1 has been reported to associate with a second calmodulin-like protein, Cam2, via its second IQ motif (***Sammons et al., 2011***). However, our data indicate that Cam1 occupies both Myo1 IQ motifs during endocytosis. Widefield microscopy revealed that Myo1 and Cam1 dynamics (***Figure 6A***) at endocytic foci differ significantly from Cam2 dynamics at these foci. Cam2 is recruited to sites of endocytosis later than Myo1 and Cam1, but prior to vesicle scission/budding, whereupon, like CAP-ZA$^{Acp1}$, Sla2 and actin, Cam2 remains associated with laterally oscillating, internalized, endosomes (***Figure 6B–C***). Similarly, simultaneous imaging of Cam1 and Cam2 in *cam1.mCherry cam2.gfp* cells revealed how each protein localizes to a significant proportion of foci lacking the other calmodulin, thereby highlighting the different timings of the engagement of each molecule with the endocytic machinery (***Figure 6D***). Finally, although Cam1 recruitment to endocytic foci is abolished when Myo1 is absent (***Figure 6E***), the intensity, volume and number of Cam2 foci actually increases in the absence of Myo1 (***Figure 6F Supplementary file 1*** Table 1), even though the internalization and lateral 'oscillating' dynamics of Cam2 and actin were dependent on Myo1 (***Figure 6F & G***). We assume that this arises from the requirement for prior action of Cam1 for vesicle budding.

TIRF imaging revealed that, on average, a total of ~30 Cam2 molecules were recruited to each endocytic focus (compared to 45 and 90 molecules observed for Myo1 and Cam1, respectively), and that the kinetics of Cam2 recruitment to foci differed significantly to those observed for both Myo1 and Cam1. The Cam2 signal often increased steadily, before an abrupt decline (***Figure 7A***), which contrasts with the more gradual (sigmoidal) rise and decay in intensity observed for Myo1 and Cam1 (***Figure 3C, E***). TIRF microscopy (TIRFM) confirmed that Cam2 continued to be associated with the endocytic vesicles after they were internalized and their connection with the cell membrane was broken (***Video 3***). Background-corrected intensity traces of Cam2 dynamics at the membrane patch before, during, and after the end of endocytosis showed that the signal rapidly dropped to baseline (<1 s) (***Figure 7A***), with the Cam2-labelled vesicles remaining visible close to the membrane but moved inwardly, away from the location of the endocytic event. A large number of these mobile, internalized Cam2-labelled vesicles were seen moving within the cytoplasm with relatively low cytosolic background signal (***Video 3***), indicating that much of the Cam2 was associated with endocytic vesicles and remained bound to mature endosomes. We conclude that endocytosis was inhibited, with Cam2 persisting on the endosome while Myo1 remained at the plasma membrane during and after endosome abscission, as previously reported (***Figure 6A***, ***Video 2***) (***Sirotkin et al., 2010***; ***Berro and Pollard, 2014***; ***Picco et al., 2015***). Thus, although Cam1 and Cam2 both localize to sites of endocytosis, they appear to do so at different times, and each have different Myo1 dependencies.

To correlate Myo1-Cam1 dynamics at sites of endocytosis with the internalization of the mature endosome into the cytoplasm, we followed Cam1 and Cam2 dynamics simultaneously in *cam1.*

**A**

| | wt | *myo1.S742A* | *tea4Δ* | *cam2Δ* | *tea4Δ*<br>*myo1.S742A* | *tea4Δ*<br>*cam2Δ* |
|---|---|---|---|---|---|---|
| Average cell length (μm) | 9.77 | 13.2 | 12.5 | 13.2 | 12.5 | 12.7 |
| % Bent >5º off long axis | 0.4 | 24.7 | 51.7 | 18.3 | 49.4 | 66.7 |
| % multiple growth zones | 0.0 | 0.0 | 5.7 | 0.0 | 4.6 | 18.9 |
| n | >500 | >500 | 88 | 83 | 88 | 91 |

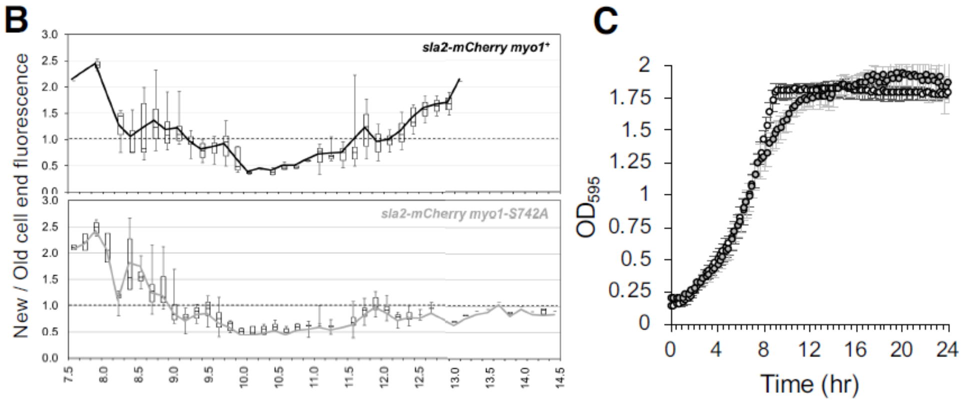

**Figure 5.** Myo1$^{S742}$ phosphorylation impacts polarized cell growth. (**A**) Average length and frequency of growth defects in WT, *myo1.S742A*, *tea4Δ*, *cam2Δ*, *tea4Δ myo1.S742A*, and *tea4Δ cam2Δ* cells. (**B**) Ratio of Sla2-mCherry fluorescence at 'new':'old' cell ends, averaged from >30 growing mid-log *sla2-mCherry myo1⁺* (upper panel) and *sla2-mCherry myo1.S742A* (lower panel) cells. Boxes plots show the median and quartile for each length measured, whereas the lines are plots of the mean values at each length measured. (**C**) Averaged growth curves from three independent experiments of prototroph wild-type (empty circles) and *myo1.S742A* (gray-filled circles) cells cultured in EMMG medium at 34˚C. Slower growth is apparent at the end of log phase in *myo1.S742A* cells, which grow more until reaching the stationary phase. Error bars denote the s.d. of the mean.

DOI: https://doi.org/10.7554/eLife.51150.012

*mCherry cam2.gfp* cells (***Video 4***). An average curve (***Figure 7B***), generated from profiles of 65 two-color individual endocytic events, synchronized relative to the $T_{start}$ of Cam1 (see ***Figure 3B, C***), shows that Cam2 moves away from the cell surface shortly after Cam1 leaves but before Myo1 leaves, with the time of abscission ($T_{scis}$) occurring on average 11.4 s after the event starts ($T_{start}$). Therefore endosome scission takes place immediately prior to the Myo1 disassembly phase (***Figure 3B***), and around the time when Cam1 dissociates from Myo1 (***Figure 3C***). Intriguingly, although the overall distribution of Myo1 and Cam1 appeared to be unaffected in *cam2Δ* cells, the number, volume and intensity of foci were significantly reduced (***Figure 7C, D***; ***Supplementary file 1*** Table 1).

## Serine 742 phosphorylation increases the affinity of a single Cam2 molecule for Myo1

In vitro analysis revealed how two Cam2 molecules can associate with the unphosphorylated Myo1$^{IQ12}$ region (***Figure 2F***) in a process that has two distinct phases. In contrast to Cam1, in which the two Myo1$^{IQ12}$ binding events contributed equally to the change in FRET signal, for Cam2, 70% of the signal change was brought about by a single binding event, associated with an affinity of 1.10 μM. The smaller amplitude and tighter binding signal is not accurately measurable, but the combined change in signal is consistent with two binding events.

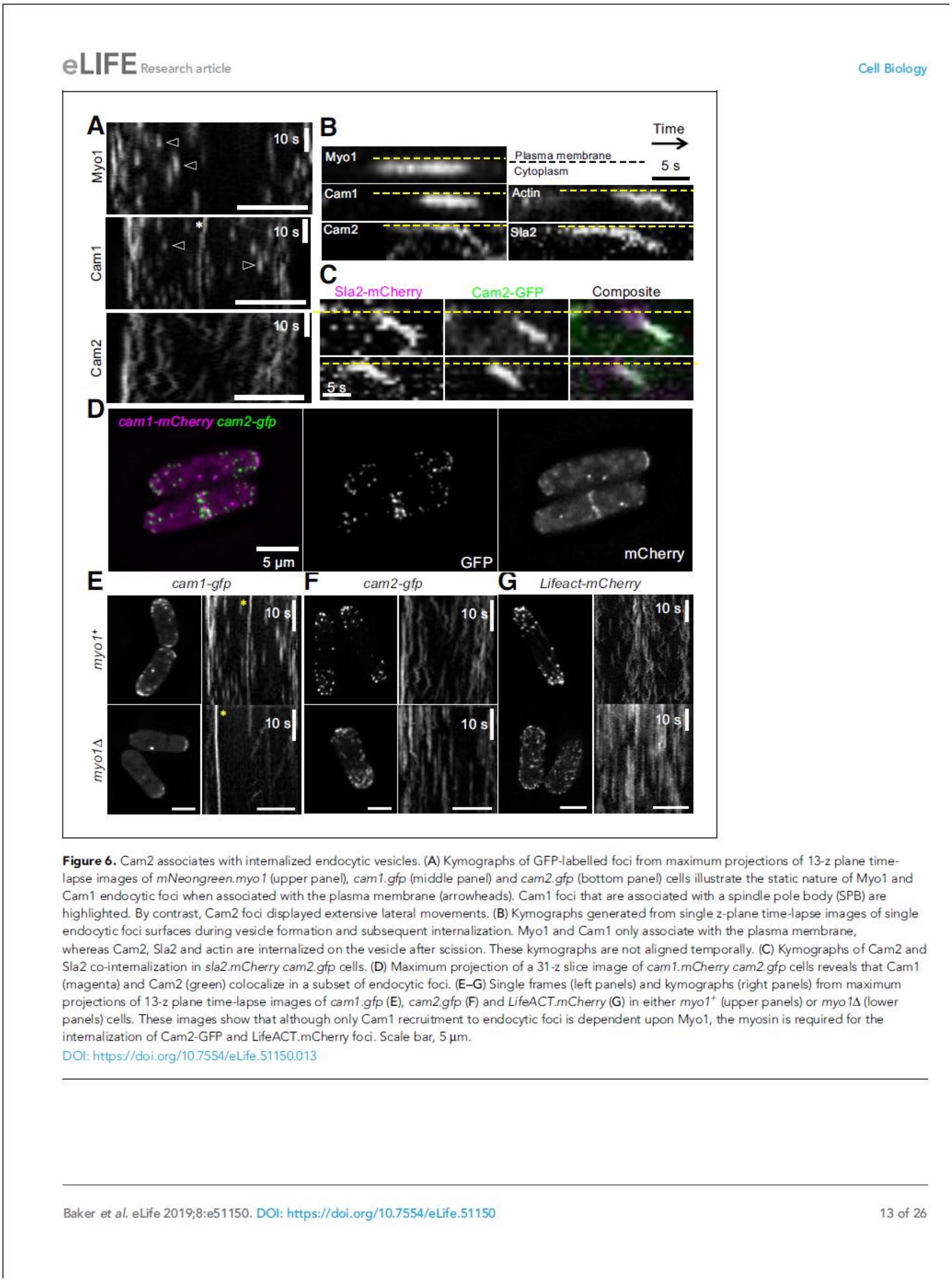

eLIFE Research article

Cell Biology

**Figure 6.** Cam2 associates with internalized endocytic vesicles. **(A)** Kymographs of GFP-labelled foci from maximum projections of 13-z plane time-lapse images of *mNeongreen.myo1* (upper panel), *cam1.gfp* (middle panel) and *cam2.gfp* (bottom panel) cells illustrate the static nature of Myo1 and Cam1 endocytic foci when associated with the plasma membrane (arrowheads). Cam1 foci that are associated with a spindle pole body (SPB) are highlighted. By contrast, Cam2 foci displayed extensive lateral movements. **(B)** Kymographs generated from single z-plane time-lapse images of single endocytic foci surfaces during vesicle formation and subsequent internalization. Myo1 and Cam1 only associate with the plasma membrane, whereas Cam2, Sla2 and actin are internalized on the vesicle after scission. These kymographs are not aligned temporally. **(C)** Kymographs of Cam2 and Sla2 co-internalization in *sla2.mCherry cam2.gfp* cells. **(D)** Maximum projection of a 31-z slice image of *cam1.mCherry cam2.gfp* cells reveals that Cam1 (magenta) and Cam2 (green) colocalize in a subset of endocytic foci. **(E–G)** Single frames (left panels) and kymographs (right panels) from maximum projections of 13-z plane time-lapse images of *cam1.gfp* **(E)**, *cam2.gfp* **(F)** and *LifeACT.mCherry* **(G)** in either *myo1*$^{+}$ (upper panels) or *myo1Δ* (lower panels) cells. These images show that although only Cam1 recruitment to endocytic foci is dependent upon Myo1, the myosin is required for the internalization of Cam2-GFP and LifeACT.mCherry foci. Scale bar, 5 µm.

DOI: https://doi.org/10.7554/eLife.51150.013

Baker *et al.* eLife 2019;8:e51150. DOI: https://doi.org/10.7554/eLife.51150 13 of 26

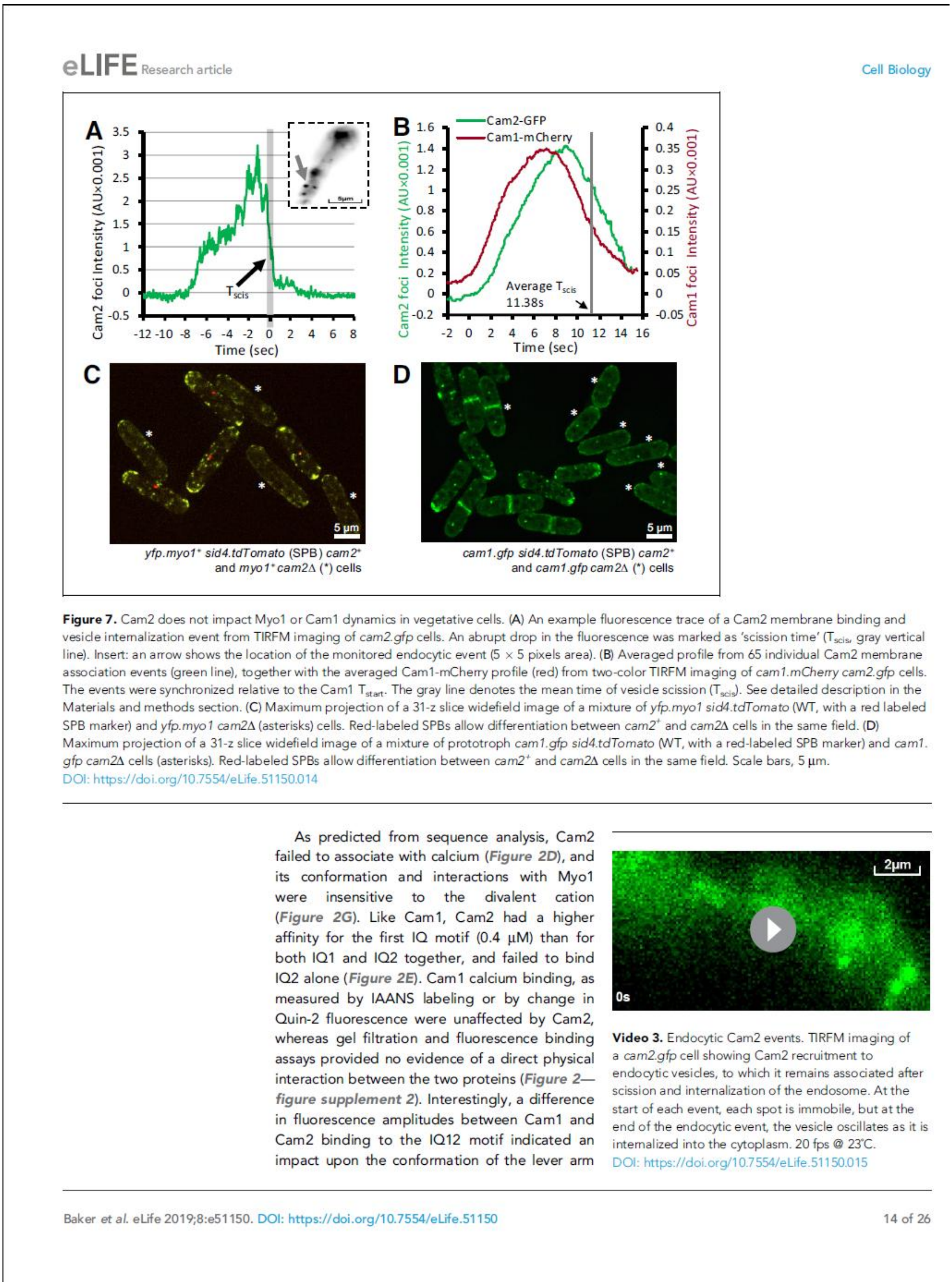

*yfp.myo1⁺ sid4.tdTomato* (SPB) *cam2⁺* and *myo1⁺ cam2Δ* (*) cells

*cam1.gfp sid4.tdTomato* (SPB) *cam2⁺* and *cam1.gfp cam2Δ* (*) cells

**Figure 7.** Cam2 does not impact Myo1 or Cam1 dynamics in vegetative cells. (**A**) An example fluorescence trace of a Cam2 membrane binding and vesicle internalization event from TIRFM imaging of *cam2.gfp* cells. An abrupt drop in the fluorescence was marked as 'scission time' ($T_{scis}$, gray vertical line). Insert: an arrow shows the location of the monitored endocytic event (5 × 5 pixels area). (**B**) Averaged profile from 65 individual Cam2 membrane association events (green line), together with the averaged Cam1-mCherry profile (red) from two-color TIRFM imaging of *cam1.mCherry cam2.gfp* cells. The events were synchronized relative to the Cam1 $T_{start}$. The gray line denotes the mean time of vesicle scission ($T_{scis}$). See detailed description in the Materials and methods section. (**C**) Maximum projection of a 31-z slice widefield image of a mixture of *yfp.myo1 sid4.tdTomato* (WT, with a red labeled SPB marker) and *yfp.myo1 cam2Δ* (asterisks) cells. Red-labeled SPBs allow differentiation between *cam2⁺* and *cam2Δ* cells in the same field. (**D**) Maximum projection of a 31-z slice widefield image of a mixture of prototroph *cam1.gfp sid4.tdTomato* (WT, with a red-labeled SPB marker) and *cam1.gfp cam2Δ* cells (asterisks). Red-labeled SPBs allow differentiation between *cam2⁺* and *cam2Δ* cells in the same field. Scale bars, 5 μm.

DOI: https://doi.org/10.7554/eLife.51150.014

As predicted from sequence analysis, Cam2 failed to associate with calcium (*Figure 2D*), and its conformation and interactions with Myo1 were insensitive to the divalent cation (*Figure 2G*). Like Cam1, Cam2 had a higher affinity for the first IQ motif (0.4 μM) than for both IQ1 and IQ2 together, and failed to bind IQ2 alone (*Figure 2E*). Cam1 calcium binding, as measured by IAANS labeling or by change in Quin-2 fluorescence were unaffected by Cam2, whereas gel filtration and fluorescence binding assays provided no evidence of a direct physical interaction between the two proteins (*Figure 2—figure supplement 2*). Interestingly, a difference in fluorescence amplitudes between Cam1 and Cam2 binding to the IQ12 motif indicated an impact upon the conformation of the lever arm

**Video 3.** Endocytic Cam2 events. TIRFM imaging of a *cam2.gfp* cell showing Cam2 recruitment to endocytic vesicles, to which it remains associated after scission and internalization of the endosome. At the start of each event, each spot is immobile, but at the end of the endocytic event, the vesicle oscillates as it is internalized into the cytoplasm. 20 fps @ 23°C.

DOI: https://doi.org/10.7554/eLife.51150.015

(*Figure 2G*), providing a potential mechanism to control Myo1 motor activity directly. However, Myo1$^{S742}$ phosphorylation had no measurable impact upon the dynamics and distribution of Cam2 within *S. pombe* cells undergoing normal vegetative growth (*Figure 8A; Supplementary file 1* Table 1).

## Cam1 and Cam2 associate with Myo1 during meiosis

Calcium levels within log phase yeast cells are relatively low (100–200 nM) (*Ma et al., 2011*; *Miseta et al., 1999*), and so provide conditions that favor the association of Cam1 with Myo1 (pCa, 5.87). Analysis of cell fluorescence indicated the relative abundance of Myo1: Cam1: Cam2 within the *S. pombe* cell to be 0.25: 1.56: 1 (*Supplementary file 1* Table 1), which is similar to the ratio defined by quantitative proteomic analysis of 0.45: 1.56: 1 (*Marguerat et al., 2012*). Similarly, image analysis of Cam1–GFP fluorescence showed how 1.7% of Cam1 associated with discrete foci within cells (*Supplementary file 1* Table 1), 40% of which was dependent upon Myo1, with the majority associating with the SPB (*Figure 6E*). This indicates that ~0.68% of cellular Cam1 associates with Myo1 at dynamic endocytic foci. These relative protein levels, binding affinities and low Ca$^{2+}$ concentrations favor Cam1 binding to Myo1, over Cam2 at both IQ sites (*Figure 8B*), consistent with in vivo observations.

Although Ca$^{2+}$ levels are low during vegetative growth, sporadic prolonged calcium bursts occur upon pheromone release during mating (*Carbó et al., 2017*; *Iida et al., 1990*), and levels elevate significantly (~10 fold) during the subsequent meiosis and sporulation (*Suizu et al., 1995*). Cam1 would be less likely to bind to Myo1 in these conditions (pCa, 5.87). We observed that Myo1$^{S742}$ is phosphorylated in mating and meiotic cells (*Figure 8C*). Cam2 abundance simultaneously increases significantly in relation to Cam1 upon starvation, mating and entry into meiosis (*Mata and Bähler, 2006*; *Mata et al., 2002*). These conditions favor interactions between Myo1 and Cam2 over an association of Cam1 with Myo1 (*Figure 8B*), which is consistent with important roles for both Myo1 and Cam2 at the leading edge of forespore membrane formation during meiosis (*Toya et al., 2001*; *Itadani et al., 2006*). Consistent with this prediction, the lifetimes and dynamics of Myo1, Cam1 and Cam2 foci differ significantly from those observed in vegetative cells ($p<0.0001$), with foci lasting significantly longer (>1 min) in meiotic and sporulating cells (*Supplementary file 1* Table 1). In contrast to vegetative cells, in cells undergoing meiosis and subsequent spore formation, cortical foci containing accumulations of Cam2 and actin (like those containing like Myo1 and Cam1) were less dynamic, lacking any oscillation and remaining in a fixed position, and had a significantly longer lifetime than foci within actively growing cells (*Figure 8D*, *Supplementary file 1* Table 1, *Videos 5–8*). Consistent with this, endocytosis is significantly diminished in fusing and meiotic cells (*Figure 8E*) containing the stable Myo1, Cam1, Cam2 or actin foci, indicating that the reduction in foci dynamics minimizes endocytosis in meiotic cells.

Finally, we used the *myo1.S742A* allele to monitor the impact of Myo1$^{S742}$ phosphorylation on Myo1, Cam1 and Cam2 dynamics during meiosis. In contrast to wild-type cells, the lifetime of Myo1 and Cam1 foci were not significantly different to each other in *myo1.S742A* cells. In addition, the lifetime of the Myo1 and Cam1 foci in *myo1.S742A* cells were significantly reduced when compared to those in the wild type. Cam2 dynamics did not correlate with Myo1 in *myo1.S742A* cells, which is in contrast to those in the wild type (*Supplementary file 1* Table 1). Myo1 and Cam1 foci were also seen to be shorter in *cam2Δ* cells during meiosis, when compared to those in wild type cells (*Supplementary file 1* Table 1). These data indicate that Myo1$^{S742}$ phosphorylation is required for Cam2 to interact with the Myo1 IQ motif and thereby reduce Myo1 foci dynamics.

The majority of Cam2 foci in meiotic cells lacking Myo1$^{S742}$ phosphorylation remained present in the cell for longer than two mins. Such timing differs significantly from the dynamics of non-phosphorylatable Myo1$^{S742A}$, indicating that normal Cam1 and Cam2 interactions with Myo1 were abolished in Myo1$^{S742A}$ cells. Consistent with observations of *myo1.S742A* cells grown to stationary phase (*Figure 1E*), heterothallic (h$^{90}$) nitrogen-starved G$_1$-arrested *myo1.S742A* cells failed to inhibit polar growth (*Figure 8F*). 27.9% of mating *myo1.S742A* cells continued to grow at their mating (schmooing) tips (vs of *myo1$^+$* 1.8% cells; n > 100), and meioses frequently produced asci with an abnormal number of unequally sized spores (*Figure 8F* , arrowheads) ( 0.9% of *myo1$^+$* asci, 13.1% of *myo1.S742A* asci; n > 100). This spore defect phenotype is reminiscent of the meiotic phenotype of *cam2Δ* cells (*Itadani et al., 2006*), which supports the view that increases in cellular Ca$^{2+}$ and Myo1$^{S742}$ phosphorylation are both key for Cam2 association with and regulation of Myo1.

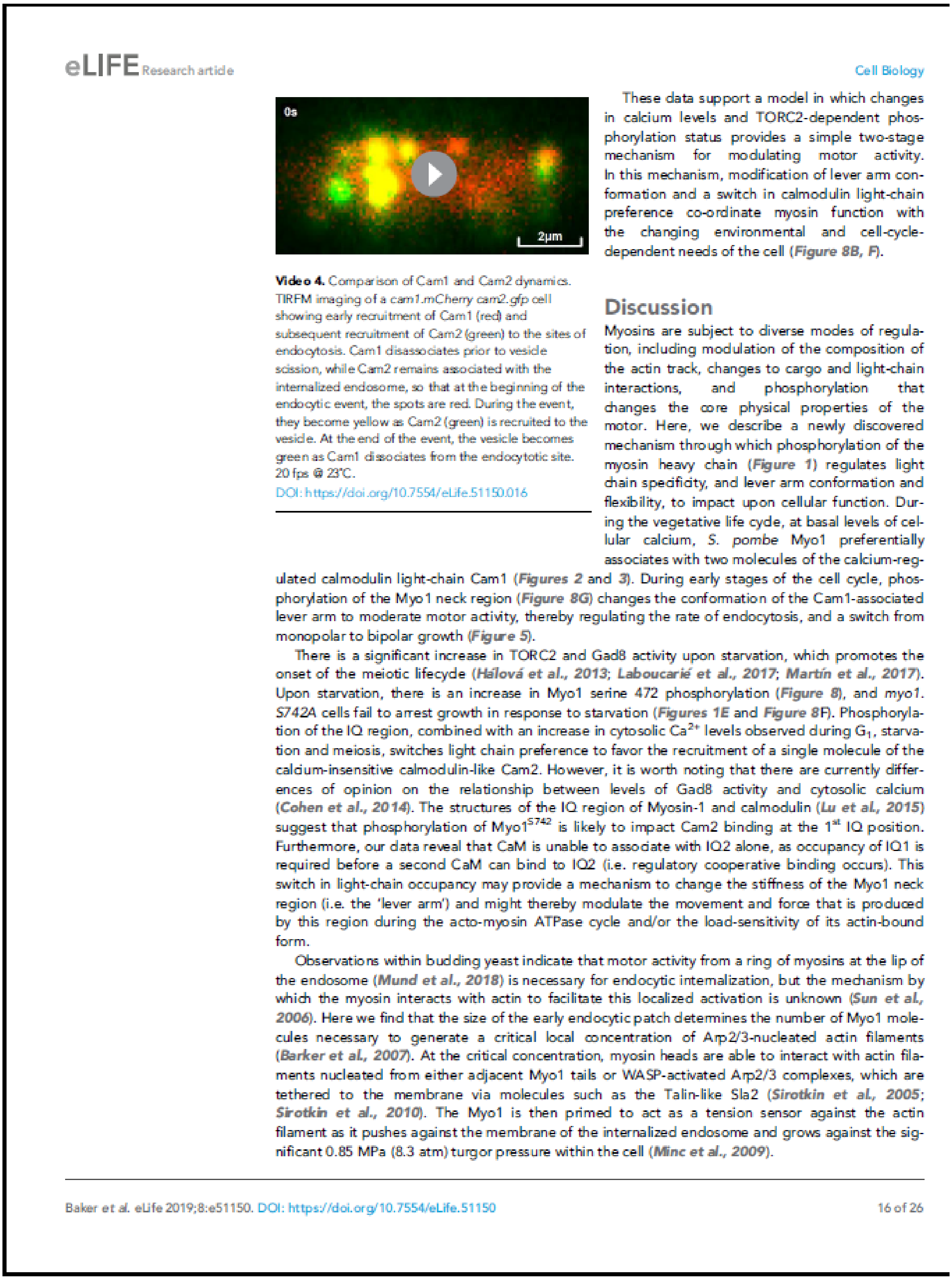

**Video 4.** Comparison of Cam1 and Cam2 dynamics. TIRFM imaging of a *cam1.mCherry cam2.gfp* cell showing early recruitment of Cam1 (red) and subsequent recruitment of Cam2 (green) to the sites of endocytosis. Cam1 disassociates prior to vesicle scission, while Cam2 remains associated with the internalized endosome, so that at the beginning of the endocytic event, the spots are red. During the event, they become yellow as Cam2 (green) is recruited to the vesicle. At the end of the event, the vesicle becomes green as Cam1 dissociates from the endocytotic site. 20 fps @ 23˚C.

DOI: https://doi.org/10.7554/eLife.51150.016

These data support a model in which changes in calcium levels and TORC2-dependent phosphorylation status provides a simple two-stage mechanism for modulating motor activity. In this mechanism, modification of lever arm conformation and a switch in calmodulin light-chain preference co-ordinate myosin function with the changing environmental and cell-cycle-dependent needs of the cell (***Figure 8B, F***).

## Discussion

Myosins are subject to diverse modes of regulation, including modulation of the composition of the actin track, changes to cargo and light-chain interactions, and phosphorylation that changes the core physical properties of the motor. Here, we describe a newly discovered mechanism through which phosphorylation of the myosin heavy chain (***Figure 1***) regulates light chain specificity, and lever arm conformation and flexibility, to impact upon cellular function. During the vegetative life cycle, at basal levels of cellular calcium, *S. pombe* Myo1 preferentially associates with two molecules of the calcium-regulated calmodulin light-chain Cam1 (***Figures 2*** and ***3***). During early stages of the cell cycle, phosphorylation of the Myo1 neck region (***Figure 8G***) changes the conformation of the Cam1-associated lever arm to moderate motor activity, thereby regulating the rate of endocytosis, and a switch from monopolar to bipolar growth (***Figure 5***).

There is a significant increase in TORC2 and Gad8 activity upon starvation, which promotes the onset of the meiotic lifecycle (***Hálová et al., 2013***; ***Laboucarié et al., 2017***; ***Martín et al., 2017***). Upon starvation, there is an increase in Myo1 serine 472 phosphorylation (***Figure 8***), and *myo1.S742A* cells fail to arrest growth in response to starvation (***Figures 1E*** and ***Figure 8***F). Phosphorylation of the IQ region, combined with an increase in cytosolic $Ca^{2+}$ levels observed during $G_1$, starvation and meiosis, switches light chain preference to favor the recruitment of a single molecule of the calcium-insensitive calmodulin-like Cam2. However, it is worth noting that there are currently differences of opinion on the relationship between levels of Gad8 activity and cytosolic calcium (***Cohen et al., 2014***). The structures of the IQ region of Myosin-1 and calmodulin (***Lu et al., 2015***) suggest that phosphorylation of $Myo1^{S742}$ is likely to impact Cam2 binding at the $1^{st}$ IQ position. Furthermore, our data reveal that CaM is unable to associate with IQ2 alone, as occupancy of IQ1 is required before a second CaM can bind to IQ2 (i.e. regulatory cooperative binding occurs). This switch in light-chain occupancy may provide a mechanism to change the stiffness of the Myo1 neck region (i.e. the 'lever arm') and might thereby modulate the movement and force that is produced by this region during the acto-myosin ATPase cycle and/or the load-sensitivity of its actin-bound form.

Observations within budding yeast indicate that motor activity from a ring of myosins at the lip of the endosome (***Mund et al., 2018***) is necessary for endocytic internalization, but the mechanism by which the myosin interacts with actin to facilitate this localized activation is unknown (***Sun et al., 2006***). Here we find that the size of the early endocytic patch determines the number of Myo1 molecules necessary to generate a critical local concentration of Arp2/3-nucleated actin filaments (***Barker et al., 2007***). At the critical concentration, myosin heads are able to interact with actin filaments nucleated from either adjacent Myo1 tails or WASP-activated Arp2/3 complexes, which are tethered to the membrane via molecules such as the Talin-like Sla2 (***Sirotkin et al., 2005***; ***Sirotkin et al., 2010***). The Myo1 is then primed to act as a tension sensor against the actin filament as it pushes against the membrane of the internalized endosome and grows against the significant 0.85 MPa (8.3 atm) turgor pressure within the cell (***Minc et al., 2009***).

eLIFE Research article Cell Biology

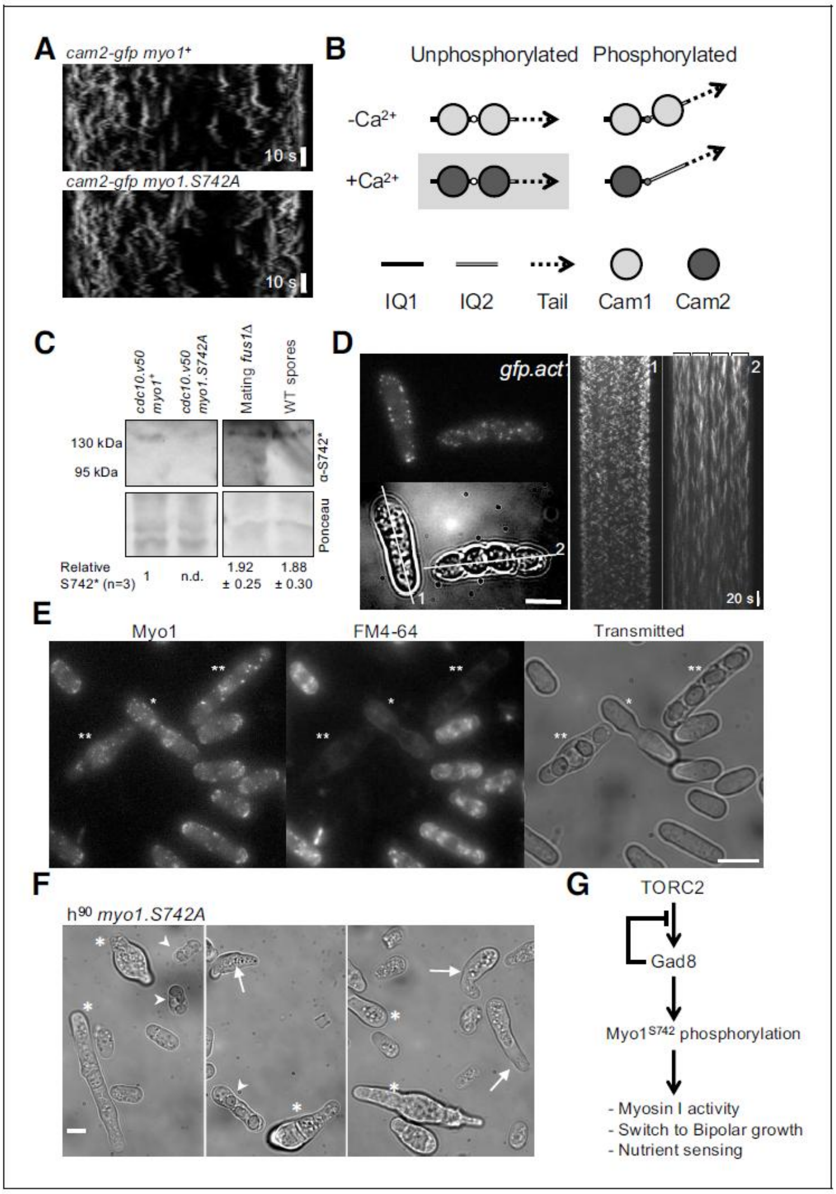

**Figure 8.** Myo1 S742 phosphorylation regulated Cam1 and Cam2 dynamics during meiosis. (**A**) Kymographs of Cam2.GFP foci dynamics in *myo1⁺* (upper panel) and *myo1.S742A* (lower panel) cells. (**B**) Scheme of the consequences of phosphorylation of Myo1$^{Ser742}$ (small empty circle) and Ca$^{2+}$ levels upon the binding of Cam1 (light gray filled circle) and Cam2 (dark gray filled circle) to the IQ1 (solid thick black line) and IQ2 (double line) motifs of Myo1, and the impact on the relative orientation of the myosin lever arm (dashed arrow). The highlighted combination of unphosphorylated

*Figure 8 continued on next page*

Baker *et al.* eLife 2019;8:e51150. DOI: https://doi.org/10.7554/eLife.51150 17 of 26

*Figure 8 continued*

Myo1$^{S742}$ and Ca$^{2+}$ does not normally occur in cells. (**C**) Western blots of extracts from G$_1$-arrested *cdc10.v50 myo1$^+$*, *cdc10.v50 myo1-S742A*, and conjugation arrested (starved, premeiotic cells) *fus1Δ* cells, and from meiotic spores, probed with phospho-specific anti-Myo1$^{S742}$ antibodies (upper panel). Ponceau staining (lower panel) confirms that Myo1S742 remains phosphorylated from the end of G$_1$, through conjugation until the end of meiosis (n = 5). Relative Myo1$^{S742}$ phosphorylation levels were calculated from three independent equivalent experiments (mean ± sd). (**D**) Left panel: maximum projection of a 13-z slice GFP fluorescence image (top) and a transmitted light image (bottom) from a time-lapse of vegetative (cell 1) and meiotic (cell 2) *gfp-act1* cells. Image from a GFP-act signal. The kymographs in the right panels were generated along the two dotted axes. (**E**) Maximum projection of mNeongreen-Myo1 fluorescence (left), FM4-64 fluoresence (middle) and transmitted light images of a mixed population of vegetative, fusing (*) and sporulating (**) *mNG-myo1$^+$* cells, illustrating that endocytosis is reduced in meiotic cells. Scale bar, 10 µm. (**F**) Micrographs illustrating *myo1.S742A* cell morphology on solid starvation medium. Asterisks highlight cells with unregulated growth and polarity defects; arrows highlight cells with elongated or abnormally bent shmooing (conjugation) tips; arrow heads highlight meiotic cells with defective spore formation. Scale bar, 5 µm. (**G**) A schematic of the TORC2–Gad8–Myo1$^{S742}$ signaling pathway.

DOI: https://doi.org/10.7554/eLife.51150.017

The number of Myo1 molecules at the plasma membrane focus remains constant as the membrane is internalized until 2 s after Cam1 disassociates from Myo1. The trigger for Cam1 release is unknown, but the speed at which the event takes place indicates that it is likely to be initiated by a rapid localized spike in calcium. This could perhaps be driven by a critical level of membrane deformation coupled to calcium influx, similar to processes proposed for mechano-transduction and the role of mammalian myosin-1 within the stereocilia of the inner ear (***Adamek et al., 2008***; ***Batters et al., 2004***).

Once Cam1 detaches from the Myo1 molecule, the neck loses rigidity, reducing tension between the myosin motor and the actin filament, to promote detachment from F-actin (***Lewis et al., 2012***; ***Mentes et al., 2018***). Single molecules of Myo1 do not reside for long at the plasma membrane (off rate is ~8 sec$^{-1}$, ***Video 1***), so without an interaction with actin, Myo1 would leave the endocytic patch a second or so after losing its Cam1 light chain. Therefore, after Cam1 release, there is a 2 s delay in the disappearance of Myo1 signal as it disassociates from the endocytic machinery (***Figure 3C, D***).

The conformation and rigidity of the Myo1 lever arm therefore play a key role in modulating the tension-sensing properties of the motor domain. This is consistent with our data showing that wild-type phosphorylation-competent Myo1 resides at the membrane ~1.8 s longer than does Myo1 mutant protein that cannot be phosphorylated at serine 742 (Myo1$^{S742A}$) (***Figure 3—figure supplement 1***). Phosphorylation-dependent changes in the conformation of the myosin neck provide a simple mechanism to modulate the rate of endocytosis according to the size and needs of the cell. Similarly, in the presence of Ca$^{2+}$ and Myo1$^{S742}$ phosphorylation, a single Cam2 resides at the IQ1 motif of the neck (***Figure 8B***). While bringing about a change in the conformation of the first half of the myosin lever arm (adjacent to the motor domain), the vacant IQ2 motif allows flexibility within the carboxyl half of the neck region. This would provide a relatively tension-insensitive motor that stalls against the actin polymer, which would therefore persist significantly longer at the endocytic foci, as observed to occur here in meiotic cells (***Figure 8D***, ***Supplementary file 1*** Table 1). These changes in lever-arm properties change the overall rate of endocytosis, as observed in differences in the time taken for endosomes to internalize within the cytoplasm (***Supplementary file 1*** Tables 1 and 2).

**Video 5.** Myo1 dynamics in interphase and meiotic cells. Time-lapse of maximum projections from 13-z slice widefield images of *mNeongreen.myo1* cells showing typical examples of Myo1 dynamics in vegetative and meiotic (highlighted with arrow) cells. Frame rate: 650 msec/frame.

DOI: https://doi.org/10.7554/eLife.51150.018

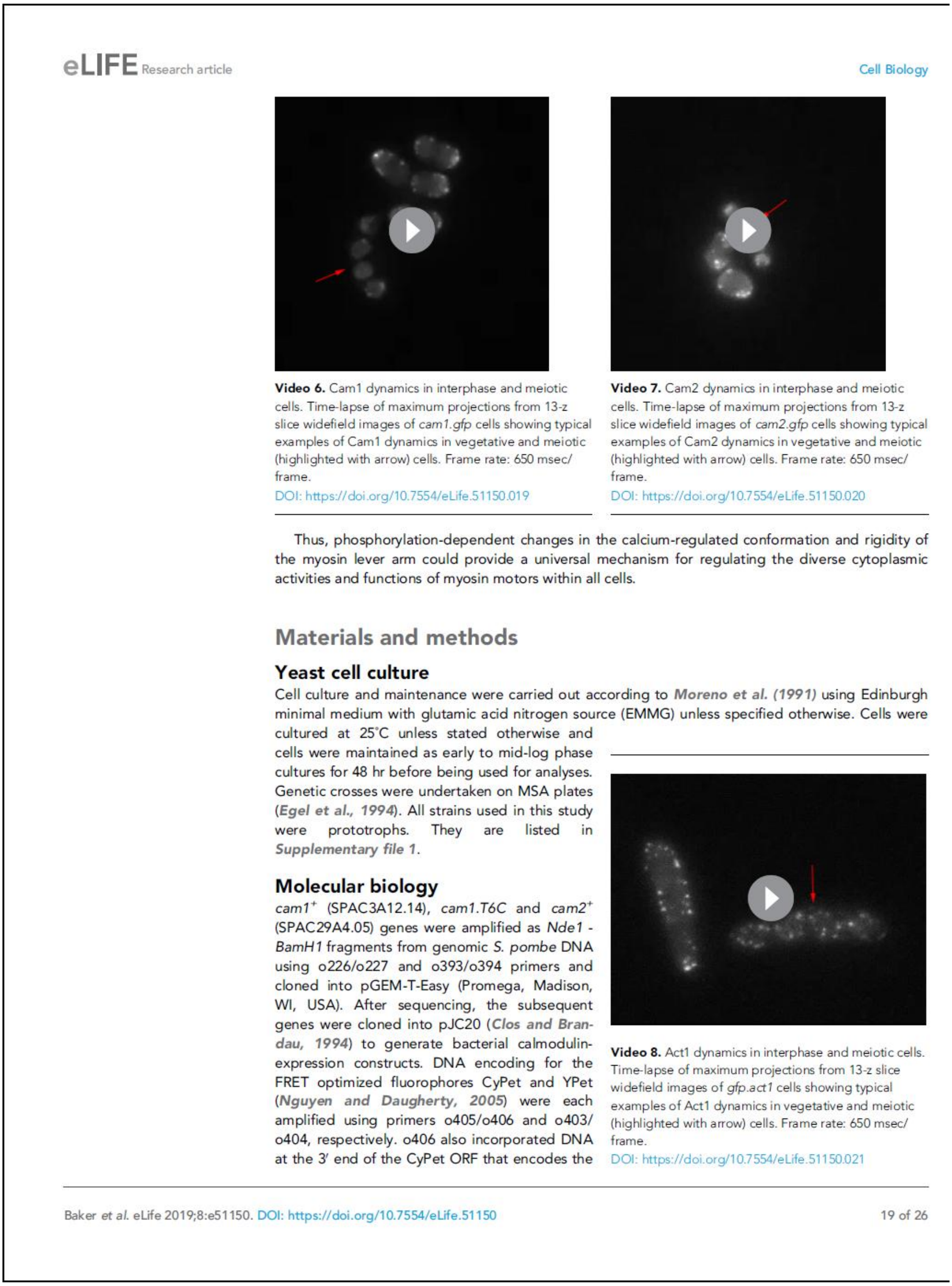

eLIFE Research article

Cell Biology

**Video 6.** Cam1 dynamics in interphase and meiotic cells. Time-lapse of maximum projections from 13-z slice widefield images of *cam1.gfp* cells showing typical examples of Cam1 dynamics in vegetative and meiotic (highlighted with arrow) cells. Frame rate: 650 msec/frame.

DOI: https://doi.org/10.7554/eLife.51150.019

**Video 7.** Cam2 dynamics in interphase and meiotic cells. Time-lapse of maximum projections from 13-z slice widefield images of *cam2.gfp* cells showing typical examples of Cam2 dynamics in vegetative and meiotic (highlighted with arrow) cells. Frame rate: 650 msec/frame.

DOI: https://doi.org/10.7554/eLife.51150.020

Thus, phosphorylation-dependent changes in the calcium-regulated conformation and rigidity of the myosin lever arm could provide a universal mechanism for regulating the diverse cytoplasmic activities and functions of myosin motors within all cells.

## Materials and methods

### Yeast cell culture

Cell culture and maintenance were carried out according to **Moreno et al. (1991)** using Edinburgh minimal medium with glutamic acid nitrogen source (EMMG) unless specified otherwise. Cells were cultured at 25˚C unless stated otherwise and cells were maintained as early to mid-log phase cultures for 48 hr before being used for analyses. Genetic crosses were undertaken on MSA plates (**Egel et al., 1994**). All strains used in this study were prototrophs. They are listed in ***Supplementary file 1***.

### Molecular biology

*cam1*$^{+}$ (SPAC3A12.14), *cam1.T6C* and *cam2*$^{+}$ (SPAC29A4.05) genes were amplified as *Nde1* - *BamH1* fragments from genomic *S. pombe* DNA using o226/o227 and o393/o394 primers and cloned into pGEM-T-Easy (Promega, Madison, WI, USA). After sequencing, the subsequent genes were cloned into pJC20 (**Clos and Brandau, 1994**) to generate bacterial calmodulin-expression constructs. DNA encoding for the FRET optimized fluorophores CyPet and YPet (**Nguyen and Daugherty, 2005**) were each amplified using primers o405/o406 and o403/o404, respectively. o406 also incorporated DNA at the 3′ end of the CyPet ORF that encodes the

**Video 8.** Act1 dynamics in interphase and meiotic cells. Time-lapse of maximum projections from 13-z slice widefield images of *gfp.act1* cells showing typical examples of Act1 dynamics in vegetative and meiotic (highlighted with arrow) cells. Frame rate: 650 msec/frame.

DOI: https://doi.org/10.7554/eLife.51150.021

Baker *et al.* eLife 2019;8:e51150. DOI: https://doi.org/10.7554/eLife.51150 19 of 26

first IQ motif of the Myo1 neck region, whereas o404 included DNA encoding a Gly3His6 tag at the 3′ of the YPet ORF. The two DNA fragments were cloned into pGEM-T-Easy in a three-way ligation reaction to generate pGEM-CyPet–Myo1IQ1–YPet. The CyPet–Myo1$^{IQ1}$–YPet DNA was subsequently sequenced and cloned as a Nde1 - BamH1 fragment into pJC20 (**Clos and Brandau, 1994**) to generate pJC20CyPet–Myo1$^{IQ1}$–YPet. Complementary oligonucleotides o425 and o426 were annealed together and ligated into BglII – Xho1 cut pJC20CyPet–Myo1$^{IQ1}$–YPet to generate pJC20CyPet–Myo1$^{IQ12}$–YPet. Similarly, the complementary oligonucleotides o429 and o430 were annealed together and subsequently ligated into Sal1-BglII cut pJC20CyPet–Myo1$^{IQ1}$–YPet and the subsequent Xho1 fragment was excised to generate pJC20CyPet–Myo1$^{IQ2}$–YPet. Site-directed mutagenesis was carried out using the pJC20CyPet–Myo1$^{IQ12}$–YPet template and o427 and o428 primers to generate pJC20CyPet–Myo1$^{IQ12}$S742D–YPet. Complementary oligonucleotides o449 and o450 were annealed together and ligated into Nru1 – Xho1 digested pJC20CyPet–Myo1$^{IQ12}$S742D–YPet to generate pJC20CyPet–Myo1$^{IQ12}$S742A–YPet. All plasmids were sequenced upon construction. Strains with fluorophore-tagged alleles of *cam1*$^+$ and *cam2*$^+$ were generated as described previously using appropriate templates and primers (**Bähler et al., 1998**). Strains in which the *myo1.S742A*, *myo1.S742D*, *mNeongreen-myo1*, *mNeongreen-myo1.S742A*, or *mNeongreen-myo1.S742D* alleles replaced the endogenous *myo1*$^+$ gene (SPBC146.13c) were generated using a marker switching method (**MacIver et al., 2003**). Oligonucleotides are described in **Supplementary file 2**.

## Protein expression and purification

All recombinant proteins were expressed and purified from BL21 DE3 *Escherichia coli* cells, except Cam1 proteins for which BL21 DE3 pNatA cells (**Eastwood et al., 2017**) were used to allow amino-terminal acetylation (**Figure 2—figure supplement 1**). For calmodulin purification, cell lysates were resuspended in Buffer A (50 mM Tris, 2 mM EDTA, 1 mM DTT, 0.1 mM PMSF (pH 7.5)) and pre-cleared by high-speed centrifugation (48,500 RCF; 30 min; 4˚C), before ammonium sulphate was added to the supernatant at 35% saturation, and the mixture incubated for 30 min at 4˚C. Precipitated proteins were removed by centrifugation (48,500 RCF; 30 min; 4˚C). For Cam1 purifications, the precipitation-cleared supernatant was added to a pre-equilibrated 10 ml phenyl sepharose (CL-4B) column (Buffer B: 50 mM Tris, 1 mM DTT, 1 mM $NaN_3$, 5 mM $CaCl_2$ (pH 8.0)), then washed in four volumes of Buffer B before being eluted as fractions in Buffer C (50 mM Tris, 1 mM DTT, 1 mM $NaN_3$, 5 mM EGTA (pH 8.0)). For Cam2 purification, the precipitation-cleared supernatant underwent a second round of ammonium sulphate precipitation and clearing, and the subsequent supernatant was subjected to isoelectric precipitation (pH 4.3) and centrifugation (48,500 RCF: 30 min; 4˚C). The resultant pellet was resuspended in Buffer A and heated to 80˚C for 5 min, before denatured proteins were removed by centrifugation (16,000 RCF; 5 min). *His-tagged* proteins were purified in native conditions using prepacked, pre-equilibrated 5 ml $Ni^{2+}$ columns.

## Immunological techniques

Standard immunological methods were used as described (**Harlow and Lane, 1988**). Serine 742 phosphorylation-state specific anti-Myo1 antibodies were raised against phosphate-conjugated peptide encompassing Myo1 serine 742 in SPF rabbits (Eurogentec, Seraing, Belgium). These antibodies were subsequently affinity-purified.

## Analysis of yeast extracts

Protein extracts were prepared and analyzed as described elsewhere (**Baker et al., 2016**). For western blot analysis, anti-Myo1 sera was diluted 1:1000, whereas Myo1 serine 742 phosphorylation state specific antibodies were used at a dilution of 1:50. Gel densitometry was undertaken using ImageJ software.

## Fast reaction kinetics

All transient kinetics were carried out using a HiTech Scientific DF-61 DX2 Stopped Flow apparatus (TgK Scientific, Bradford-upon-Avon, UK) at 20˚C. All data were acquired as the average of 3–5 consecutive shots and analyzed using the KineticStudio software supplied with the equipment. Quin-2 fluorescence was excited at 333 nm and a Schott GG445 cut off filter was used to monitor fluorescence above 445 nm. IAANS (2-(4′-(iodoacetamido)anilino)-naphthalene-6-sulfonic acid) was excited

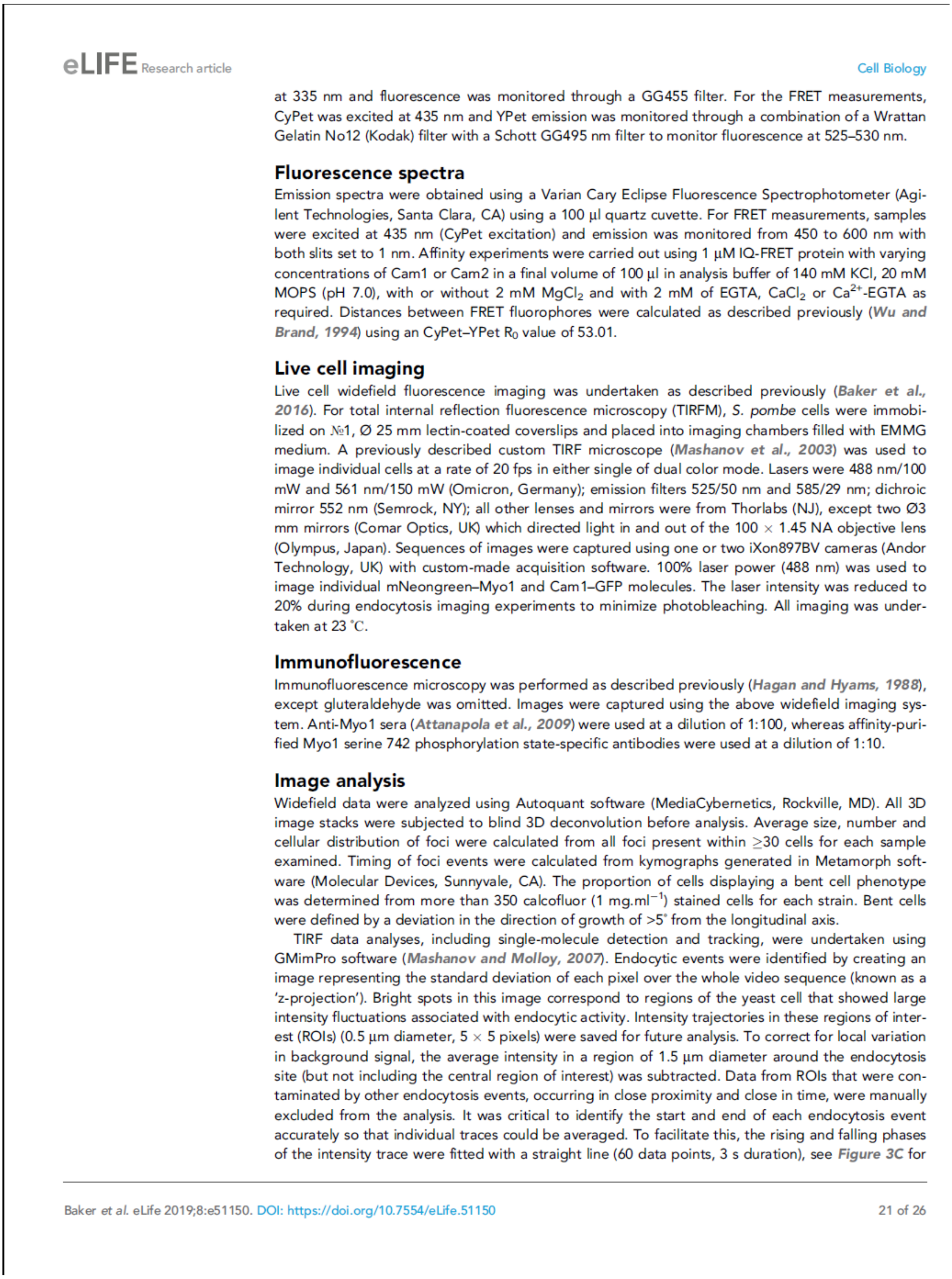

at 335 nm and fluorescence was monitored through a GG455 filter. For the FRET measurements, CyPet was excited at 435 nm and YPet emission was monitored through a combination of a Wrattan Gelatin No12 (Kodak) filter with a Schott GG495 nm filter to monitor fluorescence at 525–530 nm.

## Fluorescence spectra

Emission spectra were obtained using a Varian Cary Eclipse Fluorescence Spectrophotometer (Agilent Technologies, Santa Clara, CA) using a 100 µl quartz cuvette. For FRET measurements, samples were excited at 435 nm (CyPet excitation) and emission was monitored from 450 to 600 nm with both slits set to 1 nm. Affinity experiments were carried out using 1 µM IQ-FRET protein with varying concentrations of Cam1 or Cam2 in a final volume of 100 µl in analysis buffer of 140 mM KCl, 20 mM MOPS (pH 7.0), with or without 2 mM $MgCl_2$ and with 2 mM of EGTA, $CaCl_2$ or $Ca^{2+}$-EGTA as required. Distances between FRET fluorophores were calculated as described previously (**Wu and Brand, 1994**) using an CyPet–YPet $R_0$ value of 53.01.

## Live cell imaging

Live cell widefield fluorescence imaging was undertaken as described previously (**Baker et al., 2016**). For total internal reflection fluorescence microscopy (TIRFM), *S. pombe* cells were immobilized on №1, Ø 25 mm lectin-coated coverslips and placed into imaging chambers filled with EMMG medium. A previously described custom TIRF microscope (**Mashanov et al., 2003**) was used to image individual cells at a rate of 20 fps in either single of dual color mode. Lasers were 488 nm/100 mW and 561 nm/150 mW (Omicron, Germany); emission filters 525/50 nm and 585/29 nm; dichroic mirror 552 nm (Semrock, NY); all other lenses and mirrors were from Thorlabs (NJ), except two Ø3 mm mirrors (Comar Optics, UK) which directed light in and out of the 100 × 1.45 NA objective lens (Olympus, Japan). Sequences of images were captured using one or two iXon897BV cameras (Andor Technology, UK) with custom-made acquisition software. 100% laser power (488 nm) was used to image individual mNeongreen–Myo1 and Cam1–GFP molecules. The laser intensity was reduced to 20% during endocytosis imaging experiments to minimize photobleaching. All imaging was undertaken at 23 ˚C.

## Immunofluorescence

Immunofluorescence microscopy was performed as described previously (**Hagan and Hyams, 1988**), except gluteraldehyde was omitted. Images were captured using the above widefield imaging system. Anti-Myo1 sera (**Attanapola et al., 2009**) were used at a dilution of 1:100, whereas affinity-purified Myo1 serine 742 phosphorylation state-specific antibodies were used at a dilution of 1:10.

## Image analysis

Widefield data were analyzed using Autoquant software (MediaCybernetics, Rockville, MD). All 3D image stacks were subjected to blind 3D deconvolution before analysis. Average size, number and cellular distribution of foci were calculated from all foci present within ≥30 cells for each sample examined. Timing of foci events were calculated from kymographs generated in Metamorph software (Molecular Devices, Sunnyvale, CA). The proportion of cells displaying a bent cell phenotype was determined from more than 350 calcofluor (1 $mg.ml^{-1}$) stained cells for each strain. Bent cells were defined by a deviation in the direction of growth of >5˚ from the longitudinal axis.

TIRF data analyses, including single-molecule detection and tracking, were undertaken using GMimPro software (**Mashanov and Molloy, 2007**). Endocytic events were identified by creating an image representing the standard deviation of each pixel over the whole video sequence (known as a 'z-projection'). Bright spots in this image correspond to regions of the yeast cell that showed large intensity fluctuations associated with endocytic activity. Intensity trajectories in these regions of interest (ROIs) (0.5 µm diameter, 5 × 5 pixels) were saved for future analysis. To correct for local variation in background signal, the average intensity in a region of 1.5 µm diameter around the endocytosis site (but not including the central region of interest) was subtracted. Data from ROIs that were contaminated by other endocytosis events, occurring in close proximity and close in time, were manually excluded from the analysis. It was critical to identify the start and end of each endocytosis event accurately so that individual traces could be averaged. To facilitate this, the rising and falling phases of the intensity trace were fitted with a straight line (60 data points, 3 s duration), see **Figure 3C** for

example. The intercept of this line with the baseline intensity gave the $t_{start}$ and $t_{end}$ values and event duration ($T_{dur}$ = $T_{end}$ $Tst_{art}$) (see *Figure 7A*). The amplitude (intensity) of the event $A_{av}$ was measured at the middle of the event by averaging 60 data points from 5th to 8th second from the $T_{start}$ (gray bar on *Figure 3B*). Intensity traces for each given condition were synchronized to the starting point ($T_{start}$) and averaged. (Except Cam2-GFP traces, which were synchronized using $t_{start}$ measured from simultaneously acquired Cam1-mCherry signal.) Similarly, traces were synchronized to their end point ($T_{end}$) and averaged. The mean duration of the events ($T_{dur}$) for each condition was then used to reconstruct the mean intensity changes with calculated errors for event amplitude and timing (*Supplementary file 1* Table 2). We used the results of single-molecule imaging experiments to calculate the number of single fluorescent molecules contributing to the spot intensity at a given time. As the falling and rising phases of most events fitted well to a simple linear equation, the slope of the fitted lines was used to estimate the rate of accumulation and dissociation of the fluorescent molecules (*Figure 3C*). As Cam2-GFP remained bound to the endocytic vesicle, when vesicle scission occurred, intensity fell rapidly to zero as the vesicle diffused from the TIRF evanescent field; the time of scission was defined as $T_{scis}$ (*Figure 7A*). Single-particle tracking was performed using GMimPro (*Mashanov and Molloy, 2007*) (ASPT module) so that the paths (or trajectories) of individual Myo1 molecules bound to cell membrane could be traced. Trajectories were analyzed to yield mean intensities for individual mNeonGreen- and eGFP-labeled proteins, which could be used to estimate the number of fluorescently tagged molecules associated with each endocytotic event. Intensity-versus-time plots were generated from averages of >30 foci for each protein in each genetic background examined.

## Acknowledgements

We thank M Balasubramanian, I Hagan, P Nurse, C Shimoda and T Pollard for strains; and Ben Goult, Iain Hagan and Janni Petersen for stimulating discussions and comments on the manuscript. This work was supported by the University of Kent and by funding from the Biotechnology and Biological Sciences Research Council (BB/J012793/1 and BB/M015130/1), by a Royal Society Industry Fellowship to DPM; by a CASE industrial bursary from Cairn Research Ltd to KB and by the Francis Crick Institute, which receives core funding from Cancer Research UK (FC001119), the UK Medical Research Council (FC001119) and the Wellcome Trust (FC001119 to GIM and JEM).

## Additional information

### Funding

| Funder | Grant reference number | Author |
|---|---|---|
| Biotechnology and Biological Sciences Research Council | BB/J012793/1 | Michael A Geeves<br>Daniel P Mulvihill |
| Biotechnology and Biological Sciences Research Council | BB/M015130/1 | Daniel P Mulvihill |
| Royal Society | Industry Fellowship | Daniel P Mulvihill |
| Cancer Research UK | FC001119 | Gregory I Mashanov<br>Justin E Molloy |
| Medical Research Council | FC001119 | Gregory I Mashanov<br>Justin E Molloy |
| Wellcome | FC001119 | Gregory I Mashanov<br>Justin E Molloy |
| Cairn Research Ltd, Faversham, UK | iCASE industrial bursary | Karen Baker |

The funders had no role in study design, data collection and interpretation, or the decision to submit the work for publication.

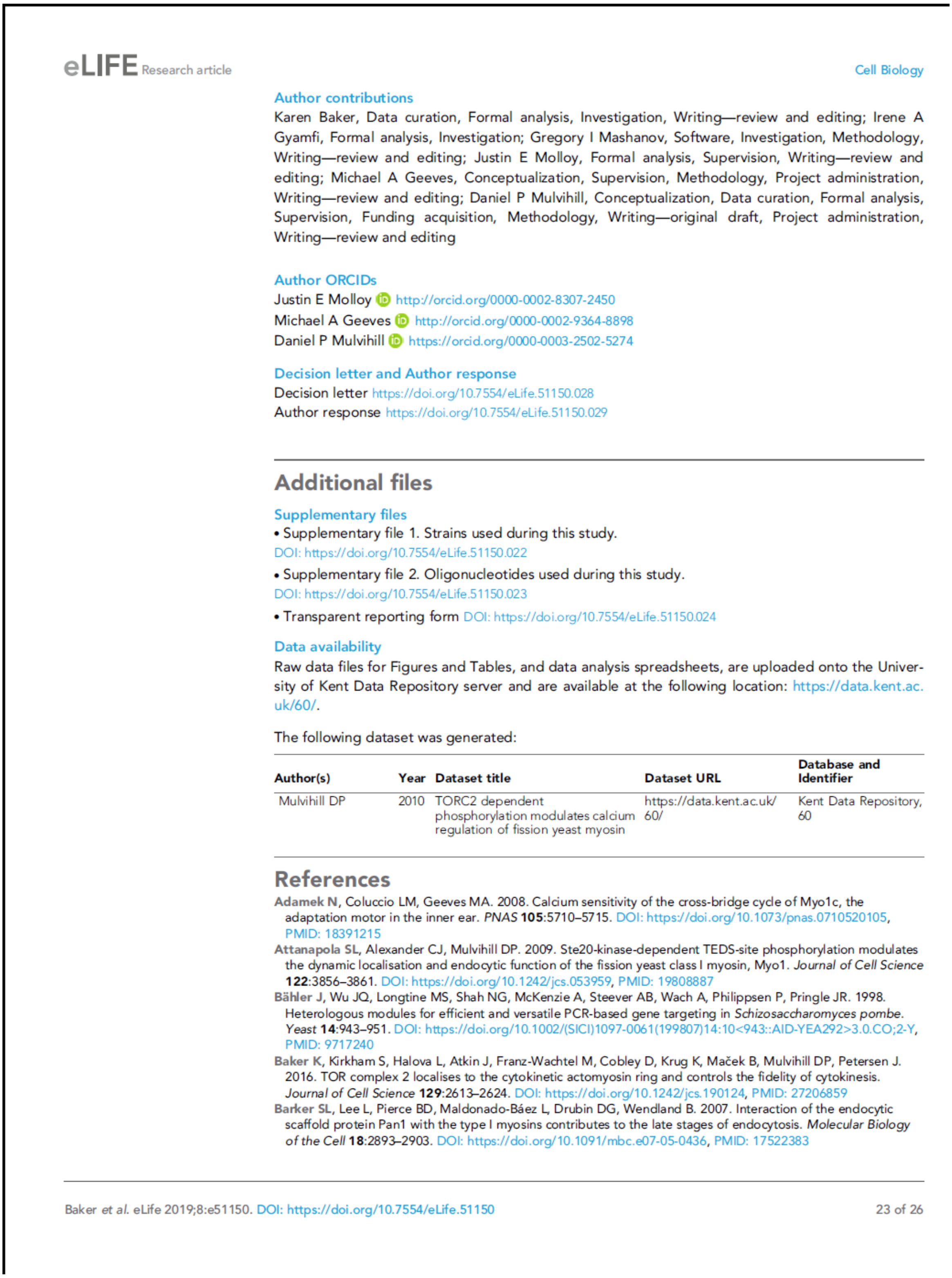

### Author contributions

Karen Baker, Data curation, Formal analysis, Investigation, Writing—review and editing; Irene A Gyamfi, Formal analysis, Investigation; Gregory I Mashanov, Software, Investigation, Methodology, Writing—review and editing; Justin E Molloy, Formal analysis, Supervision, Writing—review and editing; Michael A Geeves, Conceptualization, Supervision, Methodology, Project administration, Writing—review and editing; Daniel P Mulvihill, Conceptualization, Data curation, Formal analysis, Supervision, Funding acquisition, Methodology, Writing—original draft, Project administration, Writing—review and editing

### Author ORCIDs

Justin E Molloy http://orcid.org/0000-0002-8307-2450
Michael A Geeves http://orcid.org/0000-0002-9364-8898
Daniel P Mulvihill https://orcid.org/0000-0003-2502-5274

### Decision letter and Author response

Decision letter https://doi.org/10.7554/eLife.51150.028
Author response https://doi.org/10.7554/eLife.51150.029

## Additional files

### Supplementary files

- Supplementary file 1. Strains used during this study.
DOI: https://doi.org/10.7554/eLife.51150.022
- Supplementary file 2. Oligonucleotides used during this study.
DOI: https://doi.org/10.7554/eLife.51150.023
- Transparent reporting form DOI: https://doi.org/10.7554/eLife.51150.024

### Data availability

Raw data files for Figures and Tables, and data analysis spreadsheets, are uploaded onto the University of Kent Data Repository server and are available at the following location: https://data.kent.ac.uk/60/.

The following dataset was generated:

| Author(s) | Year | Dataset title | Dataset URL | Database and Identifier |
|---|---|---|---|---|
| Mulvihill DP | 2010 | TORC2 dependent phosphorylation modulates calcium regulation of fission yeast myosin | https://data.kent.ac.uk/60/ | Kent Data Repository, 60 |

## References

**Adamek N**, Coluccio LM, Geeves MA. 2008. Calcium sensitivity of the cross-bridge cycle of Myo1c, the adaptation motor in the inner ear. *PNAS* **105**:5710–5715. DOI: https://doi.org/10.1073/pnas.0710520105, PMID: 18391215

**Attanapola SL**, Alexander CJ, Mulvihill DP. 2009. Ste20-kinase-dependent TEDS-site phosphorylation modulates the dynamic localisation and endocytic function of the fission yeast class I myosin, Myo1. *Journal of Cell Science* **122**:3856–3861. DOI: https://doi.org/10.1242/jcs.053959, PMID: 19808887

**Bähler J**, Wu JQ, Longtine MS, Shah NG, McKenzie A, Steever AB, Wach A, Philippsen P, Pringle JR. 1998. Heterologous modules for efficient and versatile PCR-based gene targeting in *Schizosaccharomyces pombe*. *Yeast* **14**:943–951. DOI: https://doi.org/10.1002/(SICI)1097-0061(199807)14:10<943::AID-YEA292>3.0.CO;2-Y, PMID: 9717240

**Baker K**, Kirkham S, Halova L, Atkin J, Franz-Wachtel M, Cobley D, Krug K, Maček B, Mulvihill DP, Petersen J. 2016. TOR complex 2 localises to the cytokinetic actomyosin ring and controls the fidelity of cytokinesis. *Journal of Cell Science* **129**:2613–2624. DOI: https://doi.org/10.1242/jcs.190124, PMID: 27206859

**Barker SL**, Lee L, Pierce BD, Maldonado-Báez L, Drubin DG, Wendland B. 2007. Interaction of the endocytic scaffold protein Pan1 with the type I myosins contributes to the late stages of endocytosis. *Molecular Biology of the Cell* **18**:2893–2903. DOI: https://doi.org/10.1091/mbc.e07-05-0436, PMID: 17522383

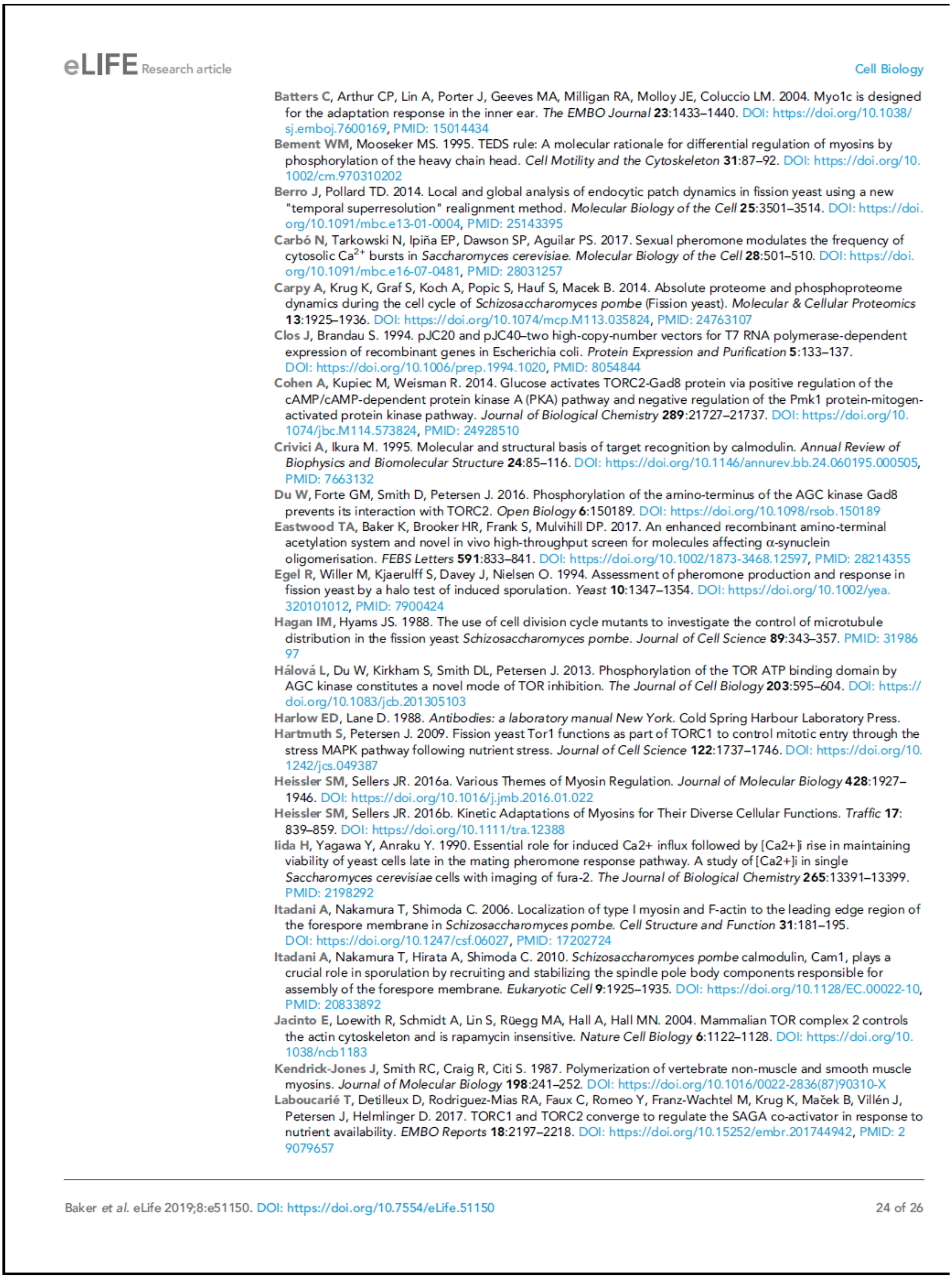

**Batters C**, Arthur CP, Lin A, Porter J, Geeves MA, Milligan RA, Molloy JE, Coluccio LM. 2004. Myo1c is designed for the adaptation response in the inner ear. *The EMBO Journal* **23**:1433–1440. DOI: https://doi.org/10.1038/sj.emboj.7600169, PMID: 15014434

**Bement WM**, Mooseker MS. 1995. TEDS rule: A molecular rationale for differential regulation of myosins by phosphorylation of the heavy chain head. *Cell Motility and the Cytoskeleton* **31**:87–92. DOI: https://doi.org/10.1002/cm.970310202

**Berro J**, Pollard TD. 2014. Local and global analysis of endocytic patch dynamics in fission yeast using a new "temporal superresolution" realignment method. *Molecular Biology of the Cell* **25**:3501–3514. DOI: https://doi.org/10.1091/mbc.e13-01-0004, PMID: 25143395

**Carbó N**, Tarkowski N, Ipiña EP, Dawson SP, Aguilar PS. 2017. Sexual pheromone modulates the frequency of cytosolic $Ca^{2+}$ bursts in *Saccharomyces cerevisiae*. *Molecular Biology of the Cell* **28**:501–510. DOI: https://doi.org/10.1091/mbc.e16-07-0481, PMID: 28031257

**Carpy A**, Krug K, Graf S, Koch A, Popic S, Hauf S, Macek B. 2014. Absolute proteome and phosphoproteome dynamics during the cell cycle of *Schizosaccharomyces pombe* (Fission yeast). *Molecular & Cellular Proteomics* **13**:1925–1936. DOI: https://doi.org/10.1074/mcp.M113.035824, PMID: 24763107

**Clos J**, Brandau S. 1994. pJC20 and pJC40–two high-copy-number vectors for T7 RNA polymerase-dependent expression of recombinant genes in Escherichia coli. *Protein Expression and Purification* **5**:133–137. DOI: https://doi.org/10.1006/prep.1994.1020, PMID: 8054844

**Cohen A**, Kupiec M, Weisman R. 2014. Glucose activates TORC2-Gad8 protein via positive regulation of the cAMP/cAMP-dependent protein kinase A (PKA) pathway and negative regulation of the Pmk1 protein-mitogen-activated protein kinase pathway. *Journal of Biological Chemistry* **289**:21727–21737. DOI: https://doi.org/10.1074/jbc.M114.573824, PMID: 24928510

**Crivici A**, Ikura M. 1995. Molecular and structural basis of target recognition by calmodulin. *Annual Review of Biophysics and Biomolecular Structure* **24**:85–116. DOI: https://doi.org/10.1146/annurev.bb.24.060195.000505, PMID: 7663132

**Du W**, Forte GM, Smith D, Petersen J. 2016. Phosphorylation of the amino-terminus of the AGC kinase Gad8 prevents its interaction with TORC2. *Open Biology* **6**:150189. DOI: https://doi.org/10.1098/rsob.150189

**Eastwood TA**, Baker K, Brooker HR, Frank S, Mulvihill DP. 2017. An enhanced recombinant amino-terminal acetylation system and novel in vivo high-throughput screen for molecules affecting α-synuclein oligomerisation. *FEBS Letters* **591**:833–841. DOI: https://doi.org/10.1002/1873-3468.12597, PMID: 28214355

**Egel R**, Willer M, Kjaerulff S, Davey J, Nielsen O. 1994. Assessment of pheromone production and response in fission yeast by a halo test of induced sporulation. *Yeast* **10**:1347–1354. DOI: https://doi.org/10.1002/yea.320101012, PMID: 7900424

**Hagan IM**, Hyams JS. 1988. The use of cell division cycle mutants to investigate the control of microtubule distribution in the fission yeast *Schizosaccharomyces pombe*. *Journal of Cell Science* **89**:343–357. PMID: 3198697

**Hálová L**, Du W, Kirkham S, Smith DL, Petersen J. 2013. Phosphorylation of the TOR ATP binding domain by AGC kinase constitutes a novel mode of TOR inhibition. *The Journal of Cell Biology* **203**:595–604. DOI: https://doi.org/10.1083/jcb.201305103

**Harlow ED**, Lane D. 1988. *Antibodies: a laboratory manual New York*. Cold Spring Harbour Laboratory Press.

**Hartmuth S**, Petersen J. 2009. Fission yeast Tor1 functions as part of TORC1 to control mitotic entry through the stress MAPK pathway following nutrient stress. *Journal of Cell Science* **122**:1737–1746. DOI: https://doi.org/10.1242/jcs.049387

**Heissler SM**, Sellers JR. 2016a. Various Themes of Myosin Regulation. *Journal of Molecular Biology* **428**:1927–1946. DOI: https://doi.org/10.1016/j.jmb.2016.01.022

**Heissler SM**, Sellers JR. 2016b. Kinetic Adaptations of Myosins for Their Diverse Cellular Functions. *Traffic* **17**:839–859. DOI: https://doi.org/10.1111/tra.12388

**Iida H**, Yagawa Y, Anraku Y. 1990. Essential role for induced Ca2+ influx followed by [Ca2+]i rise in maintaining viability of yeast cells late in the mating pheromone response pathway. A study of [Ca2+]i in single *Saccharomyces cerevisiae* cells with imaging of fura-2. *The Journal of Biological Chemistry* **265**:13391–13399. PMID: 2198292

**Itadani A**, Nakamura T, Shimoda C. 2006. Localization of type I myosin and F-actin to the leading edge region of the forespore membrane in *Schizosaccharomyces pombe*. *Cell Structure and Function* **31**:181–195. DOI: https://doi.org/10.1247/csf.06027, PMID: 17202724

**Itadani A**, Nakamura T, Hirata A, Shimoda C. 2010. *Schizosaccharomyces pombe* calmodulin, Cam1, plays a crucial role in sporulation by recruiting and stabilizing the spindle pole body components responsible for assembly of the forespore membrane. *Eukaryotic Cell* **9**:1925–1935. DOI: https://doi.org/10.1128/EC.00022-10, PMID: 20833892

**Jacinto E**, Loewith R, Schmidt A, Lin S, Rüegg MA, Hall A, Hall MN. 2004. Mammalian TOR complex 2 controls the actin cytoskeleton and is rapamycin insensitive. *Nature Cell Biology* **6**:1122–1128. DOI: https://doi.org/10.1038/ncb1183

**Kendrick-Jones J**, Smith RC, Craig R, Citi S. 1987. Polymerization of vertebrate non-muscle and smooth muscle myosins. *Journal of Molecular Biology* **198**:241–252. DOI: https://doi.org/10.1016/0022-2836(87)90310-X

**Laboucarié T**, Detilleux D, Rodriguez-Mias RA, Faux C, Romeo Y, Franz-Wachtel M, Krug K, Maček B, Villén J, Petersen J, Helmlinger D. 2017. TORC1 and TORC2 converge to regulate the SAGA co-activator in response to nutrient availability. *EMBO Reports* **18**:2197–2218. DOI: https://doi.org/10.15252/embr.201744942, PMID: 29079657

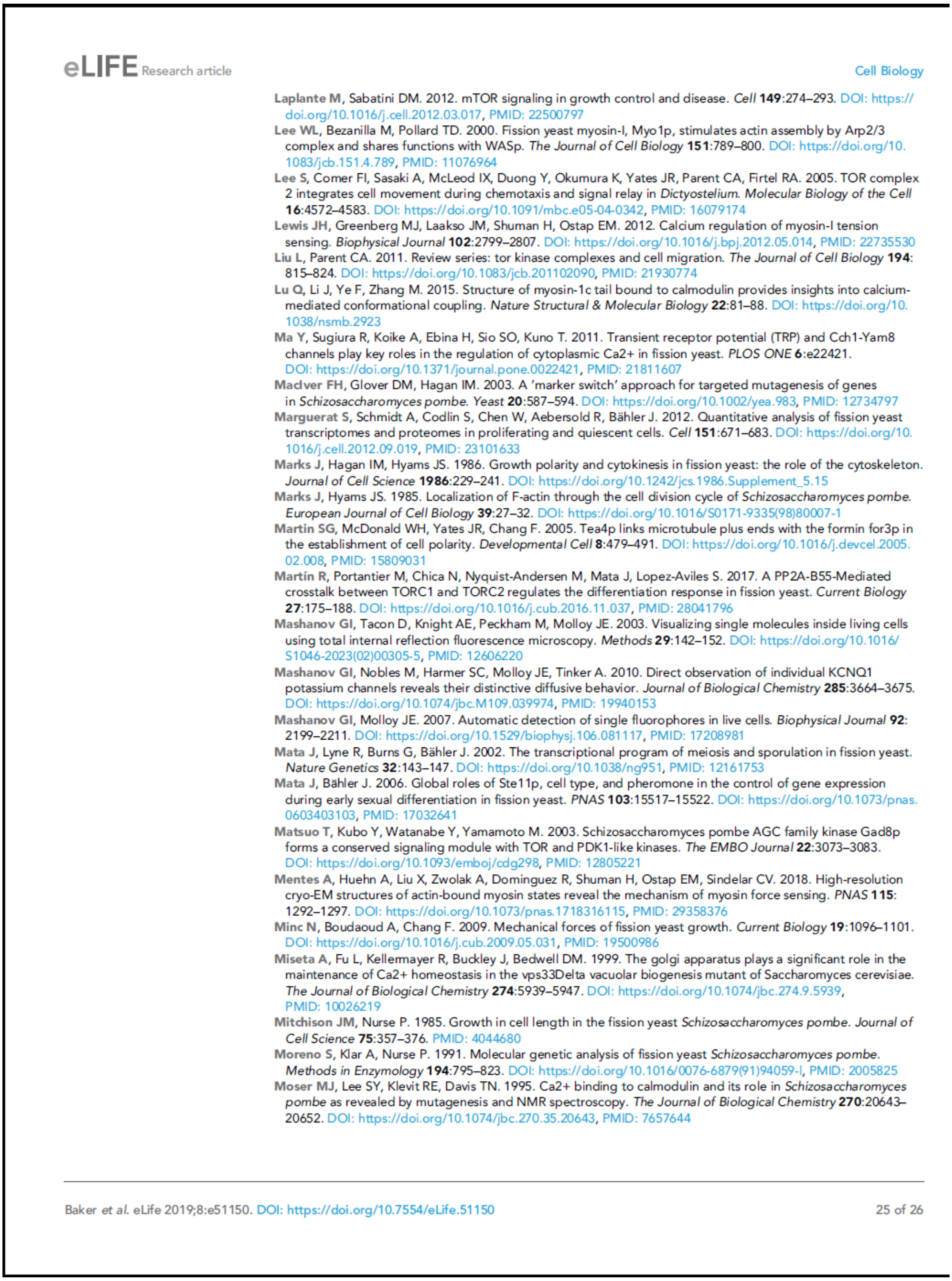

**Laplante M**, Sabatini DM. 2012. mTOR signaling in growth control and disease. *Cell* **149**:274–293. DOI: https://doi.org/10.1016/j.cell.2012.03.017, PMID: 22500797

**Lee WL**, Bezanilla M, Pollard TD. 2000. Fission yeast myosin-I, Myo1p, stimulates actin assembly by Arp2/3 complex and shares functions with WASp. *The Journal of Cell Biology* **151**:789–800. DOI: https://doi.org/10.1083/jcb.151.4.789, PMID: 11076964

**Lee S**, Comer FI, Sasaki A, McLeod IX, Duong Y, Okumura K, Yates JR, Parent CA, Firtel RA. 2005. TOR complex 2 integrates cell movement during chemotaxis and signal relay in *Dictyostelium*. *Molecular Biology of the Cell* **16**:4572–4583. DOI: https://doi.org/10.1091/mbc.e05-04-0342, PMID: 16079174

**Lewis JH**, Greenberg MJ, Laakso JM, Shuman H, Ostap EM. 2012. Calcium regulation of myosin-I tension sensing. *Biophysical Journal* **102**:2799–2807. DOI: https://doi.org/10.1016/j.bpj.2012.05.014, PMID: 22735530

**Liu L**, Parent CA. 2011. Review series: tor kinase complexes and cell migration. *The Journal of Cell Biology* **194**:815–824. DOI: https://doi.org/10.1083/jcb.201102090, PMID: 21930774

**Lu Q**, Li J, Ye F, Zhang M. 2015. Structure of myosin-1c tail bound to calmodulin provides insights into calcium-mediated conformational coupling. *Nature Structural & Molecular Biology* **22**:81–88. DOI: https://doi.org/10.1038/nsmb.2923

**Ma Y**, Sugiura R, Koike A, Ebina H, Sio SO, Kuno T. 2011. Transient receptor potential (TRP) and Cch1-Yam8 channels play key roles in the regulation of cytoplasmic Ca2+ in fission yeast. *PLOS ONE* **6**:e22421. DOI: https://doi.org/10.1371/journal.pone.0022421, PMID: 21811607

**MacIver FH**, Glover DM, Hagan IM. 2003. A 'marker switch' approach for targeted mutagenesis of genes in *Schizosaccharomyces pombe*. *Yeast* **20**:587–594. DOI: https://doi.org/10.1002/yea.983, PMID: 12734797

**Marguerat S**, Schmidt A, Codlin S, Chen W, Aebersold R, Bähler J. 2012. Quantitative analysis of fission yeast transcriptomes and proteomes in proliferating and quiescent cells. *Cell* **151**:671–683. DOI: https://doi.org/10.1016/j.cell.2012.09.019, PMID: 23101633

**Marks J**, Hagan IM, Hyams JS. 1986. Growth polarity and cytokinesis in fission yeast: the role of the cytoskeleton. *Journal of Cell Science* **1986**:229–241. DOI: https://doi.org/10.1242/jcs.1986.Supplement_5.15

**Marks J**, Hyams JS. 1985. Localization of F-actin through the cell division cycle of *Schizosaccharomyces pombe*. *European Journal of Cell Biology* **39**:27–32. DOI: https://doi.org/10.1016/S0171-9335(98)80007-1

**Martin SG**, McDonald WH, Yates JR, Chang F. 2005. Tea4p links microtubule plus ends with the formin for3p in the establishment of cell polarity. *Developmental Cell* **8**:479–491. DOI: https://doi.org/10.1016/j.devcel.2005.02.008, PMID: 15809031

**Martín R**, Portantier M, Chica N, Nyquist-Andersen M, Mata J, Lopez-Aviles S. 2017. A PP2A-B55-Mediated crosstalk between TORC1 and TORC2 regulates the differentiation response in fission yeast. *Current Biology* **27**:175–188. DOI: https://doi.org/10.1016/j.cub.2016.11.037, PMID: 28041796

**Mashanov GI**, Tacon D, Knight AE, Peckham M, Molloy JE. 2003. Visualizing single molecules inside living cells using total internal reflection fluorescence microscopy. *Methods* **29**:142–152. DOI: https://doi.org/10.1016/S1046-2023(02)00305-5, PMID: 12606220

**Mashanov GI**, Nobles M, Harmer SC, Molloy JE, Tinker A. 2010. Direct observation of individual KCNQ1 potassium channels reveals their distinctive diffusive behavior. *Journal of Biological Chemistry* **285**:3664–3675. DOI: https://doi.org/10.1074/jbc.M109.039974, PMID: 19940153

**Mashanov GI**, Molloy JE. 2007. Automatic detection of single fluorophores in live cells. *Biophysical Journal* **92**:2199–2211. DOI: https://doi.org/10.1529/biophysj.106.081117, PMID: 17208981

**Mata J**, Lyne R, Burns G, Bähler J. 2002. The transcriptional program of meiosis and sporulation in fission yeast. *Nature Genetics* **32**:143–147. DOI: https://doi.org/10.1038/ng951, PMID: 12161753

**Mata J**, Bähler J. 2006. Global roles of Ste11p, cell type, and pheromone in the control of gene expression during early sexual differentiation in fission yeast. *PNAS* **103**:15517–15522. DOI: https://doi.org/10.1073/pnas.0603403103, PMID: 17032641

**Matsuo T**, Kubo Y, Watanabe Y, Yamamoto M. 2003. Schizosaccharomyces pombe AGC family kinase Gad8p forms a conserved signaling module with TOR and PDK1-like kinases. *The EMBO Journal* **22**:3073–3083. DOI: https://doi.org/10.1093/emboj/cdg298, PMID: 12805221

**Mentes A**, Huehn A, Liu X, Zwolak A, Dominguez R, Shuman H, Ostap EM, Sindelar CV. 2018. High-resolution cryo-EM structures of actin-bound myosin states reveal the mechanism of myosin force sensing. *PNAS* **115**:1292–1297. DOI: https://doi.org/10.1073/pnas.1718316115, PMID: 29358376

**Minc N**, Boudaoud A, Chang F. 2009. Mechanical forces of fission yeast growth. *Current Biology* **19**:1096–1101. DOI: https://doi.org/10.1016/j.cub.2009.05.031, PMID: 19500986

**Miseta A**, Fu L, Kellermayer R, Buckley J, Bedwell DM. 1999. The golgi apparatus plays a significant role in the maintenance of Ca2+ homeostasis in the vps33Delta vacuolar biogenesis mutant of Saccharomyces cerevisiae. *The Journal of Biological Chemistry* **274**:5939–5947. DOI: https://doi.org/10.1074/jbc.274.9.5939, PMID: 10026219

**Mitchison JM**, Nurse P. 1985. Growth in cell length in the fission yeast *Schizosaccharomyces pombe*. *Journal of Cell Science* **75**:357–376. PMID: 4044680

**Moreno S**, Klar A, Nurse P. 1991. Molecular genetic analysis of fission yeast *Schizosaccharomyces pombe*. *Methods in Enzymology* **194**:795–823. DOI: https://doi.org/10.1016/0076-6879(91)94059-I, PMID: 2005825

**Moser MJ**, Lee SY, Klevit RE, Davis TN. 1995. Ca2+ binding to calmodulin and its role in *Schizosaccharomyces pombe* as revealed by mutagenesis and NMR spectroscopy. *The Journal of Biological Chemistry* **270**:20643–20652. DOI: https://doi.org/10.1074/jbc.270.35.20643, PMID: 7657644

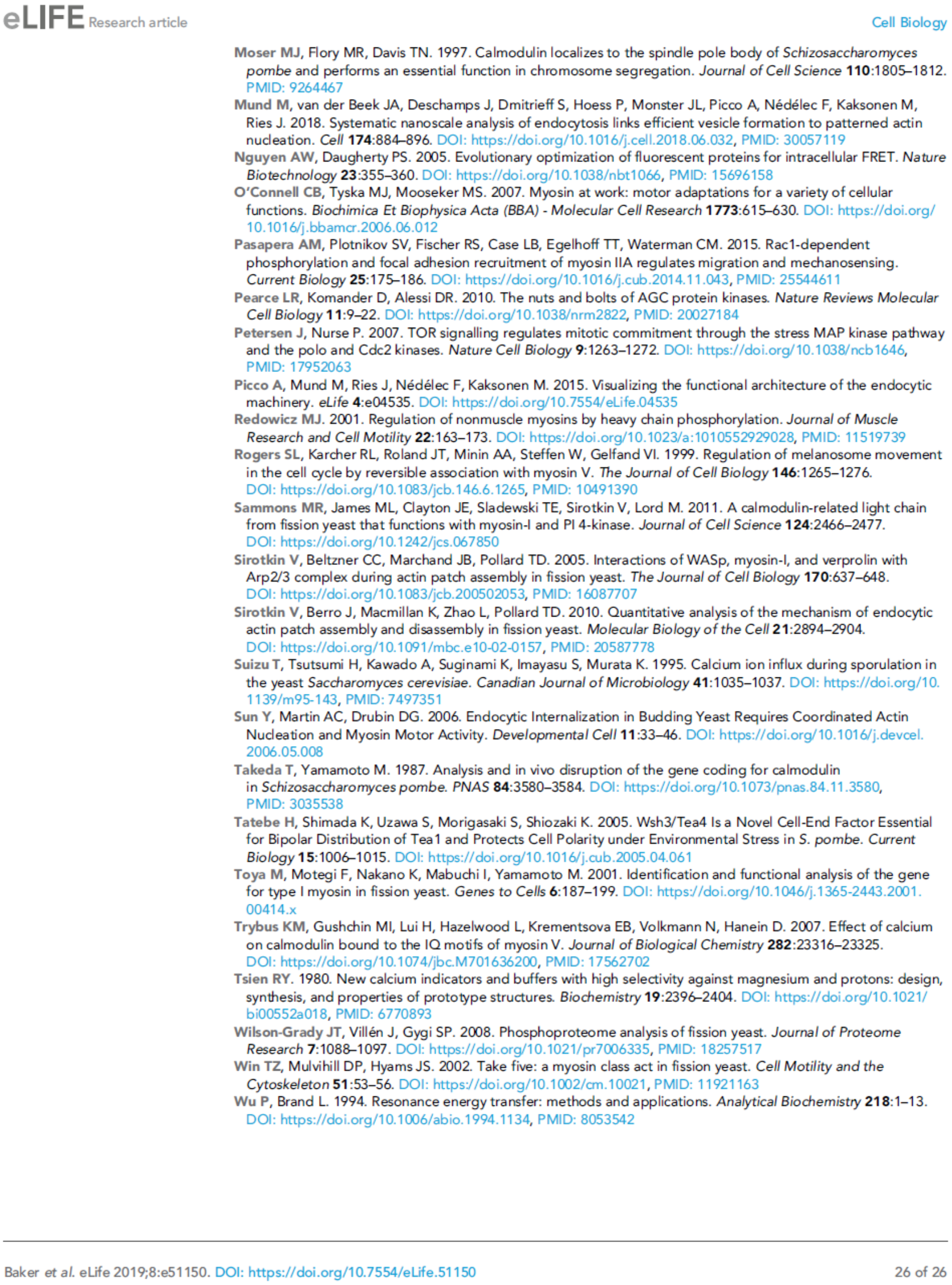

**Moser MJ**, Flory MR, Davis TN. 1997. Calmodulin localizes to the spindle pole body of *Schizosaccharomyces pombe* and performs an essential function in chromosome segregation. *Journal of Cell Science* **110**:1805–1812. PMID: 9264467

**Mund M**, van der Beek JA, Deschamps J, Dmitrieff S, Hoess P, Monster JL, Picco A, Nédélec F, Kaksonen M, Ries J. 2018. Systematic nanoscale analysis of endocytosis links efficient vesicle formation to patterned actin nucleation. *Cell* **174**:884–896. DOI: https://doi.org/10.1016/j.cell.2018.06.032, PMID: 30057119

**Nguyen AW**, Daugherty PS. 2005. Evolutionary optimization of fluorescent proteins for intracellular FRET. *Nature Biotechnology* **23**:355–360. DOI: https://doi.org/10.1038/nbt1066, PMID: 15696158

**O'Connell CB**, Tyska MJ, Mooseker MS. 2007. Myosin at work: motor adaptations for a variety of cellular functions. *Biochimica Et Biophysica Acta (BBA) - Molecular Cell Research* **1773**:615–630. DOI: https://doi.org/10.1016/j.bbamcr.2006.06.012

**Pasapera AM**, Plotnikov SV, Fischer RS, Case LB, Egelhoff TT, Waterman CM. 2015. Rac1-dependent phosphorylation and focal adhesion recruitment of myosin IIA regulates migration and mechanosensing. *Current Biology* **25**:175–186. DOI: https://doi.org/10.1016/j.cub.2014.11.043, PMID: 25544611

**Pearce LR**, Komander D, Alessi DR. 2010. The nuts and bolts of AGC protein kinases. *Nature Reviews Molecular Cell Biology* **11**:9–22. DOI: https://doi.org/10.1038/nrm2822, PMID: 20027184

**Petersen J**, Nurse P. 2007. TOR signalling regulates mitotic commitment through the stress MAP kinase pathway and the polo and Cdc2 kinases. *Nature Cell Biology* **9**:1263–1272. DOI: https://doi.org/10.1038/ncb1646, PMID: 17952063

**Picco A**, Mund M, Ries J, Nédélec F, Kaksonen M. 2015. Visualizing the functional architecture of the endocytic machinery. *eLife* **4**:e04535. DOI: https://doi.org/10.7554/eLife.04535

**Redowicz MJ**. 2001. Regulation of nonmuscle myosins by heavy chain phosphorylation. *Journal of Muscle Research and Cell Motility* **22**:163–173. DOI: https://doi.org/10.1023/a:1010552929028, PMID: 11519739

**Rogers SL**, Karcher RL, Roland JT, Minin AA, Steffen W, Gelfand VI. 1999. Regulation of melanosome movement in the cell cycle by reversible association with myosin V. *The Journal of Cell Biology* **146**:1265–1276. DOI: https://doi.org/10.1083/jcb.146.6.1265, PMID: 10491390

**Sammons MR**, James ML, Clayton JE, Sladewski TE, Sirotkin V, Lord M. 2011. A calmodulin-related light chain from fission yeast that functions with myosin-I and PI 4-kinase. *Journal of Cell Science* **124**:2466–2477. DOI: https://doi.org/10.1242/jcs.067850

**Sirotkin V**, Beltzner CC, Marchand JB, Pollard TD. 2005. Interactions of WASp, myosin-I, and verprolin with Arp2/3 complex during actin patch assembly in fission yeast. *The Journal of Cell Biology* **170**:637–648. DOI: https://doi.org/10.1083/jcb.200502053, PMID: 16087707

**Sirotkin V**, Berro J, Macmillan K, Zhao L, Pollard TD. 2010. Quantitative analysis of the mechanism of endocytic actin patch assembly and disassembly in fission yeast. *Molecular Biology of the Cell* **21**:2894–2904. DOI: https://doi.org/10.1091/mbc.e10-02-0157, PMID: 20587778

**Suizu T**, Tsutsumi H, Kawado A, Suginami K, Imayasu S, Murata K. 1995. Calcium ion influx during sporulation in the yeast *Saccharomyces cerevisiae*. *Canadian Journal of Microbiology* **41**:1035–1037. DOI: https://doi.org/10.1139/m95-143, PMID: 7497351

**Sun Y**, Martin AC, Drubin DG. 2006. Endocytic Internalization in Budding Yeast Requires Coordinated Actin Nucleation and Myosin Motor Activity. *Developmental Cell* **11**:33–46. DOI: https://doi.org/10.1016/j.devcel.2006.05.008

**Takeda T**, Yamamoto M. 1987. Analysis and in vivo disruption of the gene coding for calmodulin in *Schizosaccharomyces pombe*. *PNAS* **84**:3580–3584. DOI: https://doi.org/10.1073/pnas.84.11.3580, PMID: 3035538

**Tatebe H**, Shimada K, Uzawa S, Morigasaki S, Shiozaki K. 2005. Wsh3/Tea4 Is a Novel Cell-End Factor Essential for Bipolar Distribution of Tea1 and Protects Cell Polarity under Environmental Stress in *S. pombe*. *Current Biology* **15**:1006–1015. DOI: https://doi.org/10.1016/j.cub.2005.04.061

**Toya M**, Motegi F, Nakano K, Mabuchi I, Yamamoto M. 2001. Identification and functional analysis of the gene for type I myosin in fission yeast. *Genes to Cells* **6**:187–199. DOI: https://doi.org/10.1046/j.1365-2443.2001.00414.x

**Trybus KM**, Gushchin MI, Lui H, Hazelwood L, Krementsova EB, Volkmann N, Hanein D. 2007. Effect of calcium on calmodulin bound to the IQ motifs of myosin V. *Journal of Biological Chemistry* **282**:23316–23325. DOI: https://doi.org/10.1074/jbc.M701636200, PMID: 17562702

**Tsien RY**. 1980. New calcium indicators and buffers with high selectivity against magnesium and protons: design, synthesis, and properties of prototype structures. *Biochemistry* **19**:2396–2404. DOI: https://doi.org/10.1021/bi00552a018, PMID: 6770893

**Wilson-Grady JT**, Villén J, Gygi SP. 2008. Phosphoproteome analysis of fission yeast. *Journal of Proteome Research* **7**:1088–1097. DOI: https://doi.org/10.1021/pr7006335, PMID: 18257517

**Win TZ**, Mulvihill DP, Hyams JS. 2002. Take five: a myosin class act in fission yeast. *Cell Motility and the Cytoskeleton* **51**:53–56. DOI: https://doi.org/10.1002/cm.10021, PMID: 11921163

**Wu P**, Brand L. 1994. Resonance energy transfer: methods and applications. *Analytical Biochemistry* **218**:1–13. DOI: https://doi.org/10.1006/abio.1994.1134, PMID: 8053542

## Appendix 2:

Brooker, H. R., Gyamfi, I. A., Wieckowska, A., Brooks, N. J., Mulvihill, D. P., & Geeves, M. A. (2018). A novel live-cell imaging system reveals a reversible hydrostatic pressure impact on cell-cycle progression. *Journal of Cell Science, 131*(15), Article jcs212167. doi: 10.1242/jcs.212167.

Cell cycle delay induced by hydrostatic pressure was studied in strains with deletions in cell cycle checkpoint pathway proteins, to determine if the pressure-induced cell cycle delay was due to inhibition in cell cycle control. The cycle checkpoint pathway proteins included Sty1 (MAP kinase), Wis1 (MAP kinase kinase), Mad2 (spindle assembly checkpoint protein) and Wee1 (negative regulator of mitosis). *sty1Δ*, *wis1Δ*, *mad2Δ* and *wee1Δ* cells were applied to 100 bar pressure in a fluorescence microscopy pressure chamber for 20 hr (no figure). Previously in the study, exposure to 100 bar pressure was shown to cause delays in cytokinetic actomyosin ring constriction and increased length in wild-type cells. Deletion of Sty1, Wis1, Mad2 and Wee1 did not significantly change the delay in cell cycle progression (Student's *t*-test < 50 % level of significance). This was determined by the relative increase in cell length after exposure to 100 bar pressure. The ratios of pressure-induced difference in average cell length were; wild type: 1.15; *sty1Δ*: 1.14; *wis1Δ*: 1.18; *mad2Δ*: 1.21; *wee1Δ*: 1.19 (*n* > 200 cells per strain) (Brooker et al., 2018). This data is not described in this thesis.

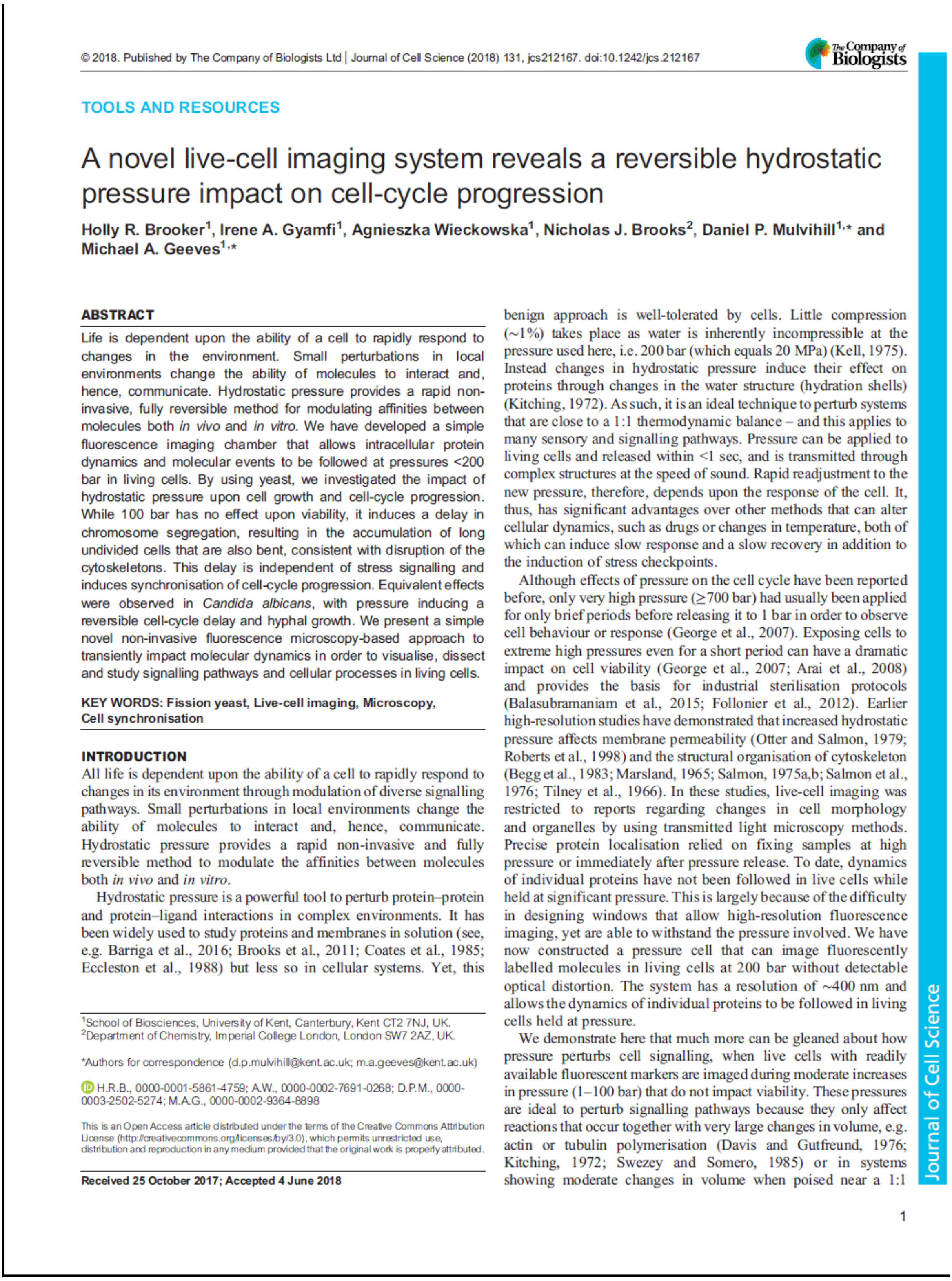

© 2018. Published by The Company of Biologists Ltd | Journal of Cell Science (2018) 131, jcs212167. doi:10.1242/jcs.212167

TOOLS AND RESOURCES

# A novel live-cell imaging system reveals a reversible hydrostatic pressure impact on cell-cycle progression

**Holly R. Brooker[1], Irene A. Gyamfi[1], Agnieszka Wieckowska[1], Nicholas J. Brooks[2], Daniel P. Mulvihill[1],* and Michael A. Geeves[1],***

## ABSTRACT

Life is dependent upon the ability of a cell to rapidly respond to changes in the environment. Small perturbations in local environments change the ability of molecules to interact and, hence, communicate. Hydrostatic pressure provides a rapid non-invasive, fully reversible method for modulating affinities between molecules both *in vivo* and *in vitro*. We have developed a simple fluorescence imaging chamber that allows intracellular protein dynamics and molecular events to be followed at pressures <200 bar in living cells. By using yeast, we investigated the impact of hydrostatic pressure upon cell growth and cell-cycle progression. While 100 bar has no effect upon viability, it induces a delay in chromosome segregation, resulting in the accumulation of long undivided cells that are also bent, consistent with disruption of the cytoskeletons. This delay is independent of stress signalling and induces synchronisation of cell-cycle progression. Equivalent effects were observed in *Candida albicans*, with pressure inducing a reversible cell-cycle delay and hyphal growth. We present a simple novel non-invasive fluorescence microscopy-based approach to transiently impact molecular dynamics in order to visualise, dissect and study signalling pathways and cellular processes in living cells.

**KEY WORDS: Fission yeast, Live-cell imaging, Microscopy, Cell synchronisation**

## INTRODUCTION

All life is dependent upon the ability of a cell to rapidly respond to changes in its environment through modulation of diverse signalling pathways. Small perturbations in local environments change the ability of molecules to interact and, hence, communicate. Hydrostatic pressure provides a rapid non-invasive and fully reversible method to modulate the affinities between molecules both *in vivo* and *in vitro*.

Hydrostatic pressure is a powerful tool to perturb protein–protein and protein–ligand interactions in complex environments. It has been widely used to study proteins and membranes in solution (see, e.g. Barriga et al., 2016; Brooks et al., 2011; Coates et al., 1985; Eccleston et al., 1988) but less so in cellular systems. Yet, this benign approach is well-tolerated by cells. Little compression (~1%) takes place as water is inherently incompressible at the pressure used here, i.e. 200 bar (which equals 20 MPa) (Kell, 1975). Instead changes in hydrostatic pressure induce their effect on proteins through changes in the water structure (hydration shells) (Kitching, 1972). As such, it is an ideal technique to perturb systems that are close to a 1:1 thermodynamic balance – and this applies to many sensory and signalling pathways. Pressure can be applied to living cells and released within <1 sec, and is transmitted through complex structures at the speed of sound. Rapid readjustment to the new pressure, therefore, depends upon the response of the cell. It, thus, has significant advantages over other methods that can alter cellular dynamics, such as drugs or changes in temperature, both of which can induce slow response and a slow recovery in addition to the induction of stress checkpoints.

Although effects of pressure on the cell cycle have been reported before, only very high pressure (≥700 bar) had usually been applied for only brief periods before releasing it to 1 bar in order to observe cell behaviour or response (George et al., 2007). Exposing cells to extreme high pressures even for a short period can have a dramatic impact on cell viability (George et al., 2007; Arai et al., 2008) and provides the basis for industrial sterilisation protocols (Balasubramaniam et al., 2015; Follonier et al., 2012). Earlier high-resolution studies have demonstrated that increased hydrostatic pressure affects membrane permeability (Otter and Salmon, 1979; Roberts et al., 1998) and the structural organisation of cytoskeleton (Begg et al., 1983; Marsland, 1965; Salmon, 1975a,b; Salmon et al., 1976; Tilney et al., 1966). In these studies, live-cell imaging was restricted to reports regarding changes in cell morphology and organelles by using transmitted light microscopy methods. Precise protein localisation relied on fixing samples at high pressure or immediately after pressure release. To date, dynamics of individual proteins have not been followed in live cells while held at significant pressure. This is largely because of the difficulty in designing windows that allow high-resolution fluorescence imaging, yet are able to withstand the pressure involved. We have now constructed a pressure cell that can image fluorescently labelled molecules in living cells at 200 bar without detectable optical distortion. The system has a resolution of ~400 nm and allows the dynamics of individual proteins to be followed in living cells held at pressure.

We demonstrate here that much more can be gleaned about how pressure perturbs cell signalling, when live cells with readily available fluorescent markers are imaged during moderate increases in pressure (1–100 bar) that do not impact viability. These pressures are ideal to perturb signalling pathways because they only affect reactions that occur together with very large changes in volume, e.g. actin or tubulin polymerisation (Davis and Gutfreund, 1976; Kitching, 1972; Swezey and Somero, 1985) or in systems showing moderate changes in volume when poised near a 1:1

---

[1]School of Biosciences, University of Kent, Canterbury, Kent CT2 7NJ, UK.
[2]Department of Chemistry, Imperial College London, London SW7 2AZ, UK.

*Authors for correspondence (d.p.mulvihill@kent.ac.uk; m.a.geeves@kent.ac.uk)

H.R.B., 0000-0001-5861-4759; A.W., 0000-0002-7691-0268; D.P.M., 0000-0003-2502-5274; M.A.G., 0000-0002-9364-8898

**Received 25 October 2017; Accepted 4 June 2018**

equilibrium or steady-state position (Geeves and Pearson, 2013). These latter reactions include $Ca^{2+}$- and nucleotide-binding reactions, as well as conformational changes of proteins (Geeves and Gutfreund, 1982; Pearson et al., 2008). High pressure (>200 bar) is lethal to most prokaryotic and eukaryotic cells.

We used the genetically tractable fission yeast model system and this simple pressure chamber to study the impact pressure has upon cellular functions. The simple rod-like shape and size of fission yeast allows live-cell imaging studies of diverse cellular processes. Upon pressure application of 100 bar, mid-log fission yeast cells became elongated and underwent a cell-cycle delay. While actin patch dynamics and endocytosis are unaffected, fluorescent protein labelling revealed a significant delay in chromosome segregation and subsequent cytokinesis. Intriguingly, the growth of the yeast culture became synchronised with respect to cell-cycle progression at 100 bar. We were able to reversibly arrest cell division and induce synchronisation of cell-cycle progression. The pressure failed to induce a mitogen-activated stress response within the yeast cells. For example, while the stress activation pathway kinase, p38, was seen to import into the nucleus in response to a 10°C change in temperature, this signalling protein remained cytoplasmic upon exposure to 100 bar hydrostatic pressure. We also examined the impact pressure has upon the cell-cycle progression of the pathological yeast *Candida albicans*. Like fission yeast cells, *C. albicans* underwent cell-cycle arrest when pressure was applied at 100 bar, and hyphal growth was also induced. Normal vegetative growth was rapidly restored upon returning to atmospheric pressure. Thus, we describe here a novel mechanism to rapidly and reversibly disrupt molecular interactions without impacting on cell viability, and provide an exciting opportunity to dissect cell growth and signalling pathways in living cells.

## RESULTS

The effects of pressure on growth of bacteria, yeast cells and animals has been well documented (Demazeau and Rivalain, 2011; Larson et al., 1918), and pressures of above 200 bar result in cell death. Here, we were interested in the effects of moderate elevated pressure that perturbs cell growth and signalling but does not result in cell death. Initial control studies used a static pressure chamber that could maintain high pressure for several hours but the cells could not be observed directly while held at high pressure. Fission yeast cells, in mid-log phase at 25°C, were placed in the pressure chamber and exposed to elevated pressure for times between 1 and 24 h before pressure was returned to 1 bar, and samples were collected for viewing using standard microscopy or were plated out to assess viability.

Exposure to 100 bar for up to 24 h had no discernible effect on cell viability once returned to 1 bar (Fig. 1C). In contrast, 24 h exposure to high pressure (200 bar) reduced cell viability to zero. Shorter exposure time reduced viability almost linearly over the first 4 h only (~20% per hour; Fig. 1C). This was consistent with previous observations that short bursts of very high pressure (≥700 bar) have a dramatic impact upon cell viability (George et al., 2007; Arai et al., 2008). Observations of the fixed cells after exposure to pressure indicated that relative cell length increased 1.4 fold (to 15 µm) after 4 h at 100 bar (Fig. 1A) and then remained fairly constant. Exposure to 200 bar resulted in an increased variation in cell length. Exposure to 100 bar resulted in only a small (~25%) increase in the estimated doubling time of the cells (hereafter referred to as generation time), whereas exposure to 200 bar caused a dramatic increase in generation time (Fig. 1B). Cells that had been kept at 200 bar for 14 h (peak of increased length and generation time) followed by immediate aldehyde fixation are shown in Fig. 1D. They have a bent rod shape with lengths often more than twice that of the normal cell.

The changes reported here are intriguing, but to understand what happens to the cell at pressure is difficult without direct observation of cells that grow under pressure. This is why we designed a high-pressure chamber with windows that allow direct observation of the yeast cells at elevated pressure. The key aim was to design a window able to withstand the high pressure force on the window and, at the same time, keep the working distance between lens and sample

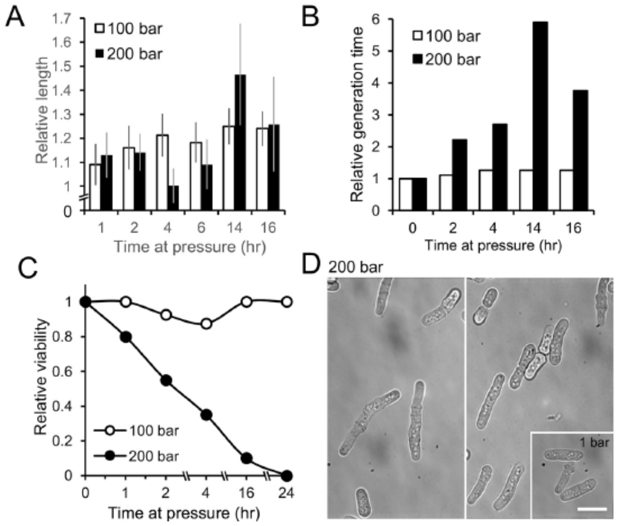

**Fig. 1. Impact of high pressure on fission yeast.** (A-C) Fission yeast cells were cultured at 25°C under pressures of 1, 100 or 200 bar for different times. Calculated were the cell length (A), generation time (B) and cell viability (C) relative to control cells that were kept at 1 bar. Data represent averages of >100 cells for each condition and time point. Each experiment was repeated three times. Error bars represent ±s.e.m. Student's *t*-test were applied to indicate significant differences (99% level of confidence) in cell length (A), generation time (B) and viability of cells when incubated at either 100 or 200 bar pressure for >2 h. (D) Different fields of view of cells treated the same way. Micrographs illustrating bent and long cell physiology of cells immediately fixed after they had been incubated at 200 bar for 14 h. Inset show equivalent for cells cultured for same period at 1 bar pressure. Scale bar:10 µm (all three micrographs).

to a minimum (<2 mm) in order to allow high-resolution imaging. Our design is shown in Fig. 2 (and Fig. S1) and described in the Materials and Methods. Using this system in conjunction with a computer-controlled high-pressure pump to add medium allows to apply rapid changes in the hydrostatic pressure (i.e. increases from 1–200 bar within 2 s), followed by maintaining stable pressure for >20 h before rapid release of pressure.

We explored several different distance lenses to image fission yeast cells (illustrated in Fig. 3A). Images were captured by using a 0.5 mm-thick quartz coverslip (window) in combination with a 40×0.6NA air lens, 60×0.7 NA air lens or a 1.0 NA water lens. A thinner 0.15 mm glass coverslip was used with a 60×1.4 NA oil lens. Using fluorescently labelled calmodulin (Cam1), an established marker of enodcytosis and polarised cell growth (Fig. 3A), fluorescence images of *cam1-YFP* fission yeast all showed the contractile ring just before cell division and an accumulation of Cam1-YFP foci at the growing tips of the cell during interphase. All images were collected at a pressure of 1 bar and demonstrate the intrinsic imaging performance of the system.

Exposure of the thin windows to high pressure was expected to distort the window shape and, indeed, the microscope required refocussing after the chamber had been pressurised; however, thereafter the image remained stable and no further refocussing was required beyond the usual. It was important to evaluate the image for distortion at elevated pressure. Fig. 3B shows images of a rabbit skeletal muscle (100 µm in diameter) with a regular and repeated striation pattern. This pattern, due to the overlapping thick and thin filaments of the sarcomere is repeated along the length of the muscle fibre with a repeat length of 2.2 µm for a muscle at natural rest length, and provided a useful calibration system for any distortion of the windows. It also illustrated the absence of any significant compression of the muscle. The sarcomere was imaged under a pressure of 1 and 130 bar, the merged image is also shown. The two images are superimposable, indicating no change in the muscle structure and no distortion of the image due to optical artefacts. In fact, studies of muscle fibres, in which small-angle X-ray diffraction was used (Knight et al., 1993) show no change in the spacing of the filaments within the muscle fibre beyond that expected from the

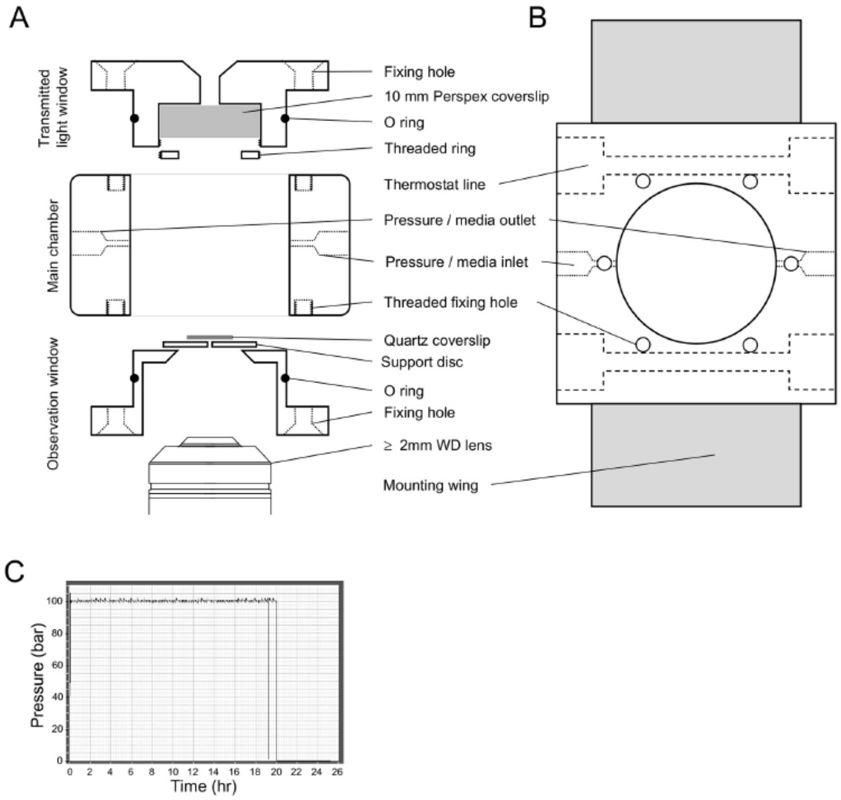

**Fig. 2. Fluorescence microscopy pressure chamber.** (A,B) Schematic diagram showing a cross section (A) and overhead (B) view of the high-pressure imaging chamber. (C) A typical overnight pressure trace demonstrating long-term maintenance and stability of 100 bar pressure within the imaging chamber system.

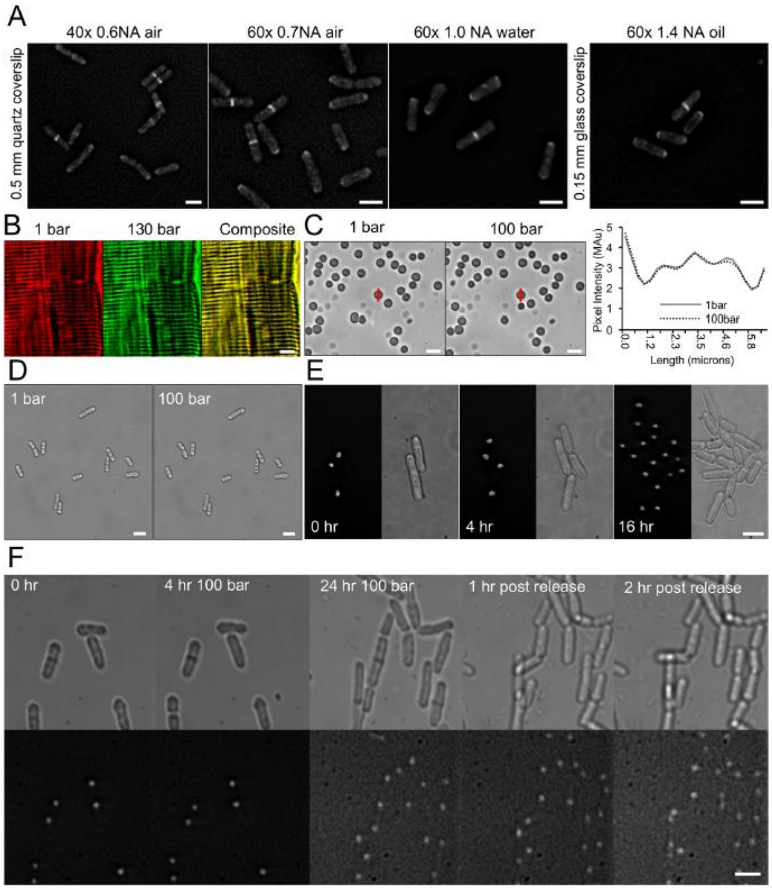

**Fig. 3. Image quality and live-cell imaging.** (A) Micrographs of live *cam1-YFP* fission yeast cells in the pressure chamber mounted onto 0.5 mm quartz or 0.15 mm glass coverslips. Lenses with differing working distance and numerical aperture values were used as indicated. (B) Images of a rabbit muscle sarcomere mounted within the pressure chamber. Images were taken at a pressure of 1 bar (red) or 130 bar (green), using 1 mm borosilicate glass windows. The merged image (composite; yellow) shows no distortion of image across the field of view, the precise sarcomere pattern is maintained. (C) Images of porcine red blood corpuscles (left) mounted in the pressure chamber. Images were taken at pressures of 1 and 100 bar, using the same windows as in B. The line profile (red vertical line) of the same cell is shown in the graph (right), indicating that hydrostatic pressure does not compress or distort membrane structures. (D) Images of *S. pombe* cells at 1 and 100 bar pressure show unaltered cells. (E,F) Time-lapse images of *S. pombe hht-gfp* cells cultured in the pressure chamber showing GFP fluorescence (images on the left in E, bottom images in F) and transmitted light (images on the right in E, top images in F) under pressure of 1 bar (E) or 100 bar (F) for 0, 4 and 24 h before release to 1 bar for 2 h. Scale bars: 10 µm.

compression of water [isothermal compressibility =$4.57\times10^{10}$ m$^2$ N$^{-1}$ at 25°C, or ~0.46% per 100 bar (Weast et al., 1984)].

Imaging porcine red blood cells (Fig. 3C) produced a similar result. The cells appear identical under pressure of 1 and 100 bar. A line profile through the same cell at the two pressures also appears identical, indicating no compression or deformity of the ~4.5-µm cell and no discernible image distortion at the resolution limit. Consistent with this, when cells from a log-phase culture of fission yeast were mounted within the chamber, the application of 100 bar pressure had no instantaneous effect upon the size, shape or integrity of the living yeast cell when compared with cells imaged at normal atmospheric pressure (Fig. 3D). As cells are maintained in medium within the chamber, we tested the ability to follow nuclear division and growth of *S. pombe* cells expressing GFP-labelled histone Hht1 (hht-GFP:kanMX6, hereafter referred to as *hht-gfp*) (Fig. 3E). By using the chamber it was possible to follow growth and nuclear organisation through multiple rounds of the cell cycle, with generation times almost equivalent to those published for equivalent cells in liquid culture (Fantes and Nurse, 1977).

We next used the same strain to examine the precise impact pressure has upon the growth and cell cycle. Cells were mounted within the chamber on the imaging system, before increasing

Journal of Cell Science (2018) 131, jcs212167. doi:10.1242/jcs.212167

hydrostatic pressure of the medium to 100 bar. This pressure was maintained for 24 h, while cell growth and nuclear organisation were monitored (Fig. 3F). Although the overall cell-cycle time was equivalent during atmospheric and 100 bar pressure, a delay in commitment to mitosis was observed in cells kept at 100 bar compared to cells at normal pressure. Consistent with the above data, we observed an accumulation of long cells, which contained either a single nucleus (Fig. 3F) indicating a delay in mitotic progression, or two nuclei and a non-cleaved septum (Fig. 3F arrowhead). To ensure cells remained viable for the duration of this and subsequent experiments, cell growth was monitored upon return to a pressure of 1 bar at the end of the incubation (after 24 h). Consistent with a delay in M-phase progression, these longer cells went through a rapid round of cell division upon returning to atmospheric pressure (Fig. 3F, 1h and 2h post release). At 100 bar pressure there is no direct perturbation of protein structure, and this effect is most likely due to biochemical responses (e.g. changes in equilibria) within the cell.

To characterise the nature of the pressure that induced delay in cell division, the experiment was repeated, images were captured at multiple locations on the window every 30 min, and the average cell length and average number of nuclei per cell were calculated by measuring >300 cells at each time point (Fig. 4A). The mean cell length was consistently seen to increase for 10 hr when cells were subjected to 100 bar, but rapidly returned to normal length on pressure release (Fig. 4A, red line). Surprisingly, monitoring of the ratio between mono- and bi-nucleated cells revealed pressure-induced multiple rounds of synchronised nuclear division throughout the pressure chamber (Fig. 4A, blue line). To further examine this delay in cell-cycle progression, we used a strain expressing the Cam1, homologue of calmodulin fused to YFP (*cam1-YFP* cells) to allow simultaneous monitoring of spindle pole dynamics and actin-associated growth machinery. In contrast to *cam1-YFP* cells cultured within the chamber at 1 bar, which displayed a normal dynamic distribution of Cam1 (Fig. 4B, Movie 1), *cam1-YFP* cells at 100 bar pressure showed cytokinetic actomyosin rings that failed to constrict at the same rate as cells cultured at 1 bar pressure (Fig. 4C, arrowheads). In addition spindle poles failed to elongate and mitotic cells failed to progress beyond anaphase (Movie 2).

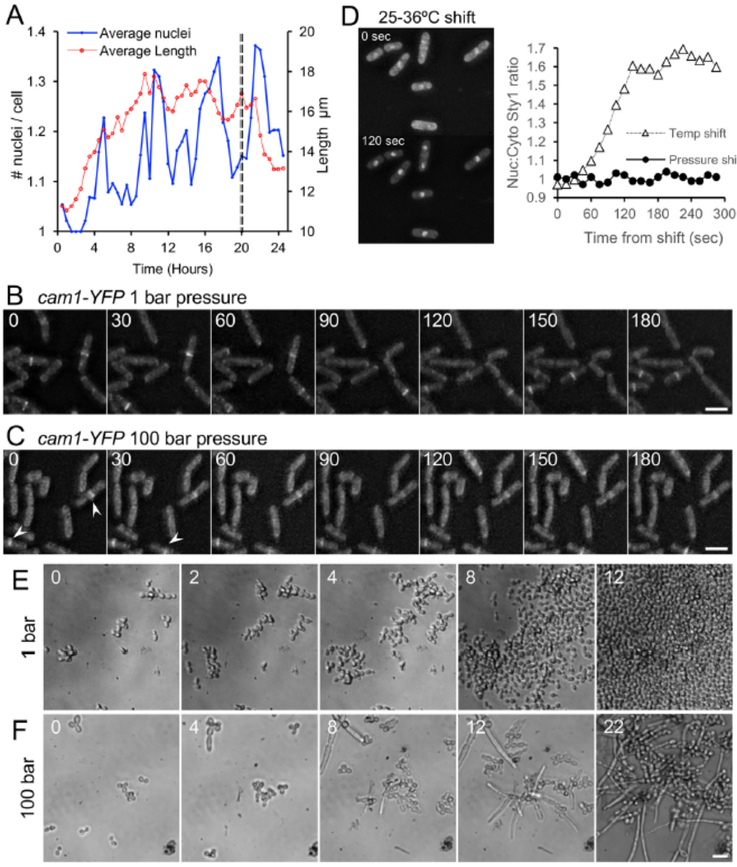

**Fig. 4. Pressure of 100 bar reversibly alters cell-cycle progression in *S. pombe* and *C. albicans*.** (A) Graph showing the average change in cell length (red) and the average change in the number of nuclei per cell (blue) in *S. pombe hht-gfp* cells when cultured at 100 bar for 20 h, indicating that pressure induces synchronisation of cell cycle progression. The dashed vertical line indicates the time at which the pressure was reduced to 1 bar. For this representative experiment >300 cells were measured and analysed at each time point indicated. (B,C) Time-lapse images of *cam1-YFP* fission yeast cells mounted in the pressure chamber at 1 bar (B) or 100 bar (C). Images show pressure-induced accumulation of long cells with Cam1 foci accumulation (indicating polarised cell growth) at the cell equator (arrowheads). Numbers within images indicate the time (in min) exposed to pressure. (D) Nuclear import of the GFP-labelled MAP kinase Sty1 in response to temperature and pressure. While the ratio of nuclear: cytoplasmic Sty1-GFP signal (Nuc:Cyto) rapidly increased upon increasing temperature from 25 to 36°C (images and triangles in graph), increasing hydrostatic pressure from 1 to 100 bar had no discernable effect upon Sty1 distribution (filled circles) over the same time scale. (E,F) Time-lapse images showing the growth pattern of *C. albicans* cells cultured for up to 22 h in the pressure chamber at 1 bar – resulting in normal growth (E) – or 100 bar – resulting in decreased and switch to pseudohyphal growth (F). Scale bars: 10 µm.

It has previously been reported that short 10 min bursts of significantly higher pressures (~1000 bar) induce a MAP kinase stress response that can impact survival (George et al., 2007). To explore whether the non-toxic 100-bar-induced delays observed here were brought about by a similar activation of the stress response, we monitored nuclear shuttling of the MAP kinase Sty1. In the absence of stress Sty1 is normally cytoplasmic; however, within minutes of detecting stress, it accumulates within the nucleus to phosphorylate transcription factors in order to trigger a stress response (Gaits et al., 1998). Using an *S. pombe sty1-gfp* strain that expresses a Sty1-GFP fusion protein (Zuin et al., 2005), we followed Sty1 dynamics following either rapid increase in temperature or pressure within the chamber. While rapid increase in temperature from 25–36°C induced redistribution of Sty1 into the nucleus of cells, increasing pressure to 100 bar had no impact upon Sty1 localisation over the same time period, as it remained cytoplasmic (Fig. 4D).

To explore these findings further, we examined the pressure-induced retardation of *S. pombe* cell-cycle progression in strains that carried deletions in genes encoding the checkpoint pathway protein Sty1 (MAP kinase; *sty1*Δ), Wis1 (MAP kinase kinase; *wis1*Δ), Mad2 (spindle assembly checkpoint protein; *mad2*Δ) or Wee1 (negative regulator of mitosis; *wee1*Δ) (He et al., 1997; Russell and Nurse, 1987; Shiozaki and Russell, 1995; Warbrick and Fantes, 1991). Intriguingly, deletion of any one of these checkpoint and regulatory proteins had no significant effect (Student's *t*-test <50% level of significance) on the pressure-induced delay in cell-cycle progression, as measured by the relative increase in cell length after culturing cells at 100 bar for 20 h [ratio of pressure-induced difference in average cell length ($n$>200 cells per sample); wild type: 1.15; *sty1*Δ: 1.14; *wis1*Δ: 1.18; *mad2*Δ: 1.21; *wee1*Δ: 1.19] (data not shown). Together these data indicate the observed delays in cell-cycle progression are brought about by disruption in the integrity of normal cytoskeletal dynamics rather than inhibition in cell-cycle control.

In a final investigation into the effect of hydrostatic pressure on yeast growth dynamics, we investigated the impact pressure has upon the growth of a different yeast cell, the pathogenic budding yeast *Candida albicans*. Under standard growth conditions, *C. albicans* laboratory strains displayed a normal, vegetative budding-yeast-like, rapid growth pattern (Fig. 4E). However, when these cells were cultured at a pressure of 100 bar, we observed not only dramatic delay in growth but also a switch to pseudohyphal growth (i.e. cells became elongated, showed unipolar budding pattern, stayed physically attached to each other, invaded the growth substrate) (Fig. 4F), which was reversed on release of pressure (not shown).

## DISCUSSION

Here, we have described a simple to use moderately high-pressure fluorescence-imaging system that allows non-invasive and non-toxic monitoring of protein and organelle dynamics in living yeast cells. The system has the potential to find wide use at the interface between molecular and cell biology in living organisms as diverse as bacteria and mammalian cells, as well as in observing development in small metazoan organisms.

Applying changes in hydrostatic pressure has been widely used to study protein–protein, protein–ligand and protein–membrane interactions by using either purified proteins or the same proteins in intact cells (Demazeau and Rivalain, 2011). The ability to study the same molecular process using the same perturbation method with both isolated proteins and in cells provides an attractive and invaluable method to define the role of specific molecular events within cell physiology. However, while the ability to use fluorescent proteins and dyes to label molecules has enabled their location, colocalisation and redistribution to be examined in a living cell, the lack of a high-pressure live-cell imaging system has limited the use of pressure as a perturbation tool. The effects of pressure on cellular architecture have been studied by using fixed cells as, until recently, fluorescent imaging systems have not been used on live cells at high pressure. Here, we have described the analysis of individual proteins and organelles of cells at high pressure. We have shown that moderate changes in pressure have a benign effect on cells, report minimal effects a pressure of 100 bar has upon cell viability and on activation of their stress pathways. However, the same pressure perturbs the cell in several striking ways, slowing growth, inhibiting cell division and altering cell morphology. Dissecting which signalling pathways, cellular components and molecules are involved will now be possible.

There are clear advantages of using pressure to modulate the cell. The speed of application and release of the pressure (potentially within <1 ms) allows a sequence of events to be followed in real time. Crucially the easy reversibility of the effects of pressure allows us to define whether the same pathways operate during both inhibition and recovery of the pressure effect. A stable cell population can be repeatedly exposed to pressure changes without impacting cell viability.

By their nature, perturbation methods tend to make small changes to the system, such that only delicately poised equilibria or steady-states are affected. For example, it is well known that protein unfolding can be induced by exposure to high pressure; however, the protein needs to be poised near the transition between folded and unfolded state (by high temperature or the addition of organic solvent), i.e. before the modest pressures used here will induce any unfolding of most proteins. Similarly, the equilibrium between 'on' and 'off' states of a signalling system (calmodulin and/or troponin C, channel opening, G-proteins; see Conti et al., 1984; Eccleston et al., 1988; Pearson et al., 2008; Petrov et al., 2011) will only be perturbed when the system is poised between 'on' and 'off' states. For example, exposure to high pressure will activate muscle contraction when free $Ca^{2+}$ is near the reaction equilibrium of the troponin C-binding reaction but not at high or low $Ca^{2+}$ levels (Fortune et al., 1994). Thus, perturbation of a cell will depend upon which signalling pathways are operative at time of perturbation; i.e. the effects of pressure may be expected to be different in interphase versus cell division, during log-growth versus stress conditions or in stimulated versus non-stimulated cells.

There are many potential applications for this technology to not only further our understanding of mechanisms and molecular equilibria within a living cell, but also in the development of novel drug therapies. Moderate pressure allows the inducible disruption of the cytoskeleton and to have discrete effects on structures of different dynamic stability (e.g. at the cell surface versus within cytosol, stress fibres versus cortical actin, microtubule filaments versus spindle fibres).

It has long been established that the application of pressure can stall cell division in a wide variety of cells (Marsland, 1938; Salmon, 1975a,b; Salmon et al., 1976). Here, we have shown that this process is not only fully reversible but that it does not activate the stress response pathway. In addition, we also reported a reversible pressure-induced synchronisation of cell growth and division and that, interestingly, upon release to normal pressure, the whole cell population underwent a rapid round of cell division. This allowed us to examine bulk signalling within an entire population of cells.

Finally, the observation that modest increases in pressure (100–200 bar) can induce pseudohyphal growth in the pathogenic yeast *C. albicans* is consistent with previous studies describing that this growth state can be induced by disruption of actin cytoskeleton dynamics (Sudbery, 2011), and provides an attractive mechanism to screen for hyphal inhibitors to identify drug therapies that might prevent transition to the pathogenic invasive growth state.

## MATERIALS AND METHODS

### Cell culture

The fission yeast used in the study were prototrophic *cam1-YFP:kanMX6*, *hht*-GFP:kanMX6 (hht-GFP); sty1-GFP:kanMX6 (sty1-gfp); *sty1::URA4, mad2::URA4, wee1::URA4 wis1::URA4* and wild-type strains. *cam1-YFP* cells were generated as described previously (Bähler et al., 1998) using appropriate primers and template. All strains were backcrossed and validated prior to use. Cell culture and maintenance were carried out according to Moreno et al., 1991, using filter-sterilised Edinburgh minimal medium (EMM) containing glutamic acid as a nitrogen source (EMMG). The *Candida albicans* strain used is a derivative of the strain BWP17 (Wilson et al., 1999) *ura3*::imm434/*ura3*::imm434 *iro1*/*iro1*::imm434 *his1*::hisG/*his1*::hisG *arg4*/*arg4*, which was cultured in synthetic complete (SC) medium (Formedium, Hunstanton, UK). All cells were maintained in early to mid-log phase for 48 h before analysis. Early-log phase pre-conditioned minimal medium was used in all time-lapse experiments.

### Preparation of cell samples

Small-bundle muscle fibres were dissected from rabbit psoas muscle and membranes removed by treatment with detergent for 2 h (0.5% Brij-58; Sigma Aldrich) under relaxing conditions (70 mM propionic acid, 8 mM $MgCl_2$, 5 mM EGTA, 7 mM ATP-$Na_2$, 6 mM imidazole pH 6.8), and were then stored in 50% glycerol at −20°C until required as described by Knight et al. (1993). Porcine red blood cells were isolated from freshly drawn blood (sourced from a local abattoir) by centrifugation and washed three times with Tris-buffered isotonic saline (0.12 M KCl, 10 mM Tris, pH 7.4).

### Microscopy

Imaging was undertaken on an Olympus IX73 microscope with either LUCPLFLN 40×0.6NA, LUCPLFLN 60×0.7NA long-working-distance air lenses, LUMPLFLN 60× W 1.0NA water-immersion lenses or PLANAPO 60×1.4 NA oil-immersion lenses. Samples were illuminated using LED light sources (Cairn Research Ltd, Faversham, UK) with appropriate long-pass filters (Chroma, Bellows Falls, VT). Images were captured by using an Evolve EMCCD camera (Photometrics, Tucson, AZ), and the imaging system was controlled using Metamorph software (Molecular Devices, Sunnyvale, CA). Each 3D-maximum projection of volume data were calculated from *z*-plane images, spaced 0.5 µm apart, using Metamorph software.

### Standard pressure chamber

The effects of pressure on cell viability, length and generation time used a pressure chamber originally designed for collection of small-angle X-ray scattering data of muscle fibres (Knight et al., 1993). Hydrostatic pressure was applied to this chamber by using a Kontron Instruments 422 HPLC pump (Watford, UK) and controlled using Labview software (National Instruments, Austin, TX). While this chamber was maintaining stable pressures of >500 bar for several hours, its windows were unsuitable for optical imaging.

### High-pressure imaging chamber design

The cell design is shown in Fig. 2 and based on the design of a pressure chamber used for studying the effects of pressure on contracting muscle fibres (Fortune et al., 1991; Knight et al., 1993). Components of the imaging cell were built at Cairn Research Ltd (Faversham, Kent, UK) and in the University of Kent Engineering Workshop. It was milled from a single 6×6×3 cm block of 316-stainless steel (sourced from Orion Alloys Ltd, Harlow, Essex, UK) with a 3.5-cm diameter cylinder through the middle. The window mounts were inserted from opposite sides of this hole and each held in position by six stainless steel screws (M4). The upper window mount held a 10-mm-thick perspex window, which provided a pathway for transmitted light. The lower mount was designed specifically to match the shape of the objective lenses used for fluorescence observation and allowed the lens to approach a stainless-steel disc used to support the observation window. O-rings on the surface of the window mounts provided the pressure seal with the wall of the cylinder block. Ports allowed connection via standard high-pressure liquid chromatography (HPLC) tubing to the pressure line, and a manual HPLC valve (SSI 02-0120) allowed chamber flushing and pressure release. The chamber was flushed and hydrostatic pressure applied and maintained as above. Pressure was applied and maintained using a Kontron 422 HPLC pump.

The design of the window was a balance between the working distance, the pressure range used and the size of the window. In order to allow rapid assembly and disassembly of the chamber, and to optimise assembly for specific conditions, the window consisted of three parts. The window mount (described above), a 1-cm diameter glass disc forming the window and a 2-cm diameter supporting stainless steel disc used to set the diameter of the observation window. The window mount and the stainless steel disc had highly polished surfaces to facilitate a seal between each pair of surfaces, the disc and glass window were held in place by glue. To test window performance an acetone/cellulose glue (a mixture of acetone-disolved cellulose that had been allowed to evaporate to required viscosity) was used that allowed rapid replacement of window and disc. For longer term use the window components were fixed in place using Araldite epoxy-adhesive (Huntsman Advanced Materials, Switzerland). The shortest working distance at a pressure of 100 bar was achieved by using a 1-mm-thick stainless steel disc with 1-mm-diameter window apertures and a standard 8-mm-diameter circular quartz coverslip that was 0.5 mm thick. Higher pressures and larger diameters of observation window were possible by using thicker glass and/or stainless steel discs but only together with increased working distance and, hence, poorer optical resolution. Use of specialist materials for the windows (diamond or sapphire) may allow higher pressures and lower working distances but at a much higher cost.

### Mounting cells for observation within the chamber

Before use, the chamber was sterilised with alcohol, assembled and flushed through with sterile water and sterile pre-conditioned medium. Cells were then mounted (without centrifugation) directly onto lectin-coated (Sigma L2380; 1 mg/ml) prepared quartz discs. The chamber was reassembled with the quartz disc and mounted cells in place (Fig. 2), and pre-conditioned medium was pumped through the system until all air bubbles had been excluded from the chamber. The chamber was then fitted onto the imaging system described above.

#### Acknowledgements

The authors thank Cairn Research Ltd, University of Kent School of Engineering and its Digital Arts workshop for machining components of the chamber.

#### Competing interests

The authors declare no competing or financial interests.

#### Author contributions

Conceptualization: M.A.G., D.P.M.; Methodology: H.R.B., N.J.B., M.A.G., D.P.M.; Software: M.A.G.; Validation: M.A.G., D.P.M.; Formal analysis: H.R.B., M.A.G., D.P.M.; Investigation: H.R.B., I.A.G., A.W., M.A.G., D.P.M.; Resources: M.A.G., D.P.M.; Data curation: I.A.G., D.P.M.; Writing - original draft: M.A.G., D.P.M.; Writing - review & editing: M.A.G., D.P.M.; Visualization: D.P.M.; Supervision: M.A.G., D.P.M.; Project administration: M.A.G., D.P.M.; Funding acquisition: M.A.G., D.P.M.

#### Funding

This work was supported by the University of Kent, funding from the Biotechnology and Biological Sciences Research Council (BB/K012045/1) and Royal Society Industry Fellowship to D.P.M., a CASE bursary to H.R.B., and Wellcome Trust programme grant (085309) to M.A.G. Deposited in PMC for immediate release.

**Supplementary information**

Supplementary information available online at
http://jcs.biologists.org/lookup/doi/10.1242/jcs.212167.supplemental

**References**

**Arai, S., Kawarai, T., Arai, R., Yoshida, M., Furukawa, S., Ogihara, H. and Yamasaki, M.** (2008). Cessation of cytokinesis in Schizosaccharomyces pombe during growth after release from high hydrostatic pressure treatment. *Biosci. Biotechnol. Biochem.* **72**, 88-93.

**Bähler, J., Wu, J.-Q., Longtine, M. S., Shah, N. G., McKenzie, A., III, Steever, A. B., Wach, A., Philippsen, P. and Pringle, J. R.** (1998). Heterologous modules for efficient and versatile PCR-based gene targeting in Schizosaccharomyces pombe. *Yeast* **14**, 943-951.

**Balasubramaniam, V. M. B., Martínez-Monteagudo, S. I. and Gupta, R.** (2015). Principles and application of high pressure-based technologies in the food industry. *Annu. Rev. Food Sci. Technol.* **6**, 435-462.

**Barriga, H. M. G., Law, R. V., Seddon, J. M., Ces, O. and Brooks, N. J.** (2016). The effect of hydrostatic pressure on model membrane domain composition and lateral compressibility. *Phys. Chem. Chem. Phys.* **18**, 149-155.

**Begg, D. A., Salmon, E. D. and Hyatt, H. A.** (1983). The changes in structural organization of actin in the sea urchin egg cortex in response to hydrostatic pressure. *J. Cell Biol.* **97**, 1795-1805.

**Brooks, N. J., Ces, O., Templer, R. H. and Seddon, J. M.** (2011). Pressure effects on lipid membrane structure and dynamics. *Chem. Phys. Lipids* **164**, 89-98.

**Coates, J. H., Criddle, A. H. and Geeves, M. A.** (1985). Pressure-relaxation studies of pyrene-labelled actin and myosin subfragment 1 from rabbit skeletal muscle. Evidence for two states of acto-subfragment 1. *Biochem. J.* **232**, 351-356.

**Conti, F., Inoue, I., Kukita, F. and Stühmer, W.** (1984). Pressure dependence of sodium gating currents in the squid giant axon. *Eur. Biophys. J.* **11**, 137-147.

**Davis, J. S. and Gutfreund, H.** (1976). The scope of moderate pressure changes for kinetic and equilibrium studies of biochemical systems. *FEBS Lett.* **72**, 199-207.

**Demazeau, G. and Rivalain, N.** (2011). High hydrostatic pressure and biology: a brief history. *Appl. Microbiol. Biotechnol.* **89**, 1305-1314.

**Eccleston, J. F., Kanagasabai, T. F. and Geeves, M. A.** (1988). The kinetic mechanism of the release of nucleotide from elongation factor Tu promoted by elongation factor Ts determined by pressure relaxation studies. *J. Biol. Chem.* **263**, 4668-4672.

**Fantes, P. and Nurse, P.** (1977). Control of cell size at division in fission yeast by a growth-modulated size control over nuclear division. *Exp. Cell Res.* **107**, 377-386.

**Follonier, S., Panke, S. and Zinn, M.** (2012). Pressure to kill or pressure to boost: a review on the various effects and applications of hydrostatic pressure in bacterial biotechnology. *Appl. Microbiol. Biotechnol.* **93**, 1805-1815.

**Fortune, N. S., Geeves, M. A. and Ranatunga, K. W.** (1991). Tension responses to rapid pressure release in glycerinated rabbit muscle fibers. *Proc. Natl. Acad. Sci. USA* **88**, 7323-7327.

**Fortune, N. S., Geeves, M. A. and Ranatunga, K. W.** (1994). Contractile activation and force generation in skinned rabbit muscle fibres: effects of hydrostatic pressure. *J. Physiol.* **474**, 283-290.

**Gaits, F., Degols, G., Shiozaki, K. and Russell, P.** (1998). Phosphorylation and association with the transcription factor Atf1 regulate localization of Spc1/Sty1 stress-activated kinase in fission yeast. *Genes Dev.* **12**, 1464-1473.

**Geeves, M. A. and Gutfreund, H.** (1982). The use of pressure perturbations to investigate the interaction of rabbit muscle myosin subfragment 1 with actin in the presence of MgADP. *FEBS Lett.* **140**, 11-15.

**Geeves, M. A. and Pearson, D. S.** (2013). Kinetics: relaxation methods. In *Encyclopedia of Biophysics* (ed. G.C. Roberts), pp. 1207-1212. Berlin, Heidelberg: Springer Berlin Heidelberg.

**George, V. T., Brooks, G. and Humphrey, T. C.** (2007). Regulation of cell cycle and stress responses to hydrostatic pressure in fission yeast. *Mol. Biol. Cell* **18**, 4168-4179.

**He, X. W., Patterson, T. E. and Sazer, S.** (1997). The Schizosaccharomyces pombe spindle checkpoint protein mad2p blocks anaphase and genetically interacts with the anaphase-promoting complex. *Proc. Natl. Acad. Sci. USA* **94**, 7965-7970.

**Kell, G. S.** (1975). Density, thermal expansivity, and compressibility of liquid water from 0° to 150°C: correlations and tables for atmospheric pressure and saturation reviewed and expressed on 1968 temperature scale. *J. Chem. Eng. Data* **20**, 97-105.

**Kitching, J. A.** (1972). The effects of pressure on organisms: a summary of progress. *Symp. Soc. Exp. Biol.* **26**, 473-482.

**Knight, P. J., Fortune, N. S. and Geeves, M. A.** (1993). Effects of pressure on equatorial x-ray fiber diffraction from skeletal muscle fibers. *Biophys. J.* **65**, 814-822.

**Larson, W. P., Hartzell, T. B. and Diehl, H. S.** (1918). The effect of high pressures on bacteria. *J. Infect. Dis.* **22**, 271-279.

**Marsland, D. A.** (1938). The effects of high hydrostatic pressure upon cell division in Arbacia eggs. *J. Cell. Comp. Physiol.* **12**, 57-70.

**Marsland, D.** (1965). Partial reversal of the anti-mitotic effects of heavy water by high hydrostatic pressure: an analysis of the first cleavage division in the eggs of Strongylocentrotus purpuratus. *Exp. Cell Res.* **38**, 592-603.

**Moreno, S., Klar, A. and Nurse, P.** (1991). Molecular genetic analysis of fission yeast Schizosaccharomyces pombe. *Meth. Enzymol.* **194**, 795-823.

**Otter, T. and Salmon, E. D.** (1979). Hydrostatic pressure reversibly blocks membrane control of ciliary motility in Paramecium. *Science* **206**, 358-361.

**Pearson, D. S., Swartz, D. R. and Geeves, M. A.** (2008). Fast pressure jumps can perturb calcium and magnesium binding to troponin C F29W. *Biochemistry* **47**, 12146-12158.

**Petrov, E., Rohde, P. R. and Martinac, B.** (2011). Flying-patch patch-clamp study of G22E-MscL mutant under high hydrostatic pressure. *Biophys. J.* **100**, 1635-1641.

**Roberts, T. M., Salmon, E. D. and Stewart, M.** (1998). Hydrostatic pressure shows that lamellipodial motility in Ascaris sperm requires membrane-associated major sperm protein filament nucleation and elongation. *J. Cell Biol.* **140**, 367-375.

**Russell, P. and Nurse, P.** (1987). Negative regulation of mitosis by wee1+, a gene encoding a protein kinase homolog. *Cell* **49**, 559-567.

**Salmon, E. D.** (1975a). Pressure-induced depolymerization of spindle microtubules. I. Changes in birefringence and spindle length. *J. Cell Biol.* **65**, 603-614.

**Salmon, E. D.** (1975b). Pressure-induced depolymerization of spindle microtubules. II. Thermodynamics of in vivo spindle assembly. *J. Cell Biol.* **66**, 114-127.

**Salmon, E. D., Goode, D., Maugel, T. K. and Bonar, D. B.** (1976). Pressure-induced depolymerization of spindle microtubules. III. Differential stability in HeLa cells. *J. Cell Biol.* **69**, 443-454.

**Shiozaki, K. and Russell, P.** (1995). Cell-cycle control linked to extracellular environment by MAP kinase pathway in fission yeast. *Nature* **378**, 739-743.

**Sudbery, P. E.** (2011). Growth of Candida albicans hyphae. *Nat. Rev. Micro.* **9**, 737-748.

**Swezey, R. R. and Somero, G. N.** (1985). Pressure effects on actin self-assembly: interspecific differences in the equilibrium and kinetics of the G to F transformation. *Biochemistry* **24**, 852-860.

**Tilney, L. G., Hiramoto, Y. and Marsland, D.** (1966). Studies on the microtubules in heliozoa. 3. A pressure analysis of the role of these structures in the formation and maintenance of the axopodia of Actinosphaerium nucleofilum (Barrett). *J. Cell Biol.* **29**, 77-95.

**Warbrick, E. and Fantes, P. A.** (1991). The Wis1 protein-kinase is a dosage-dependent regulator of mitosis in Schizosaccharomyces-Pombe. *EMBO J.* **10**, 4291-4299.

**Weast, R. C., Astle, M. J. and Beyer, W. H.** (1984). *CRC Handbook of Chemistry and Physics*. Boca Raton, CRC Press.

**Wilson, R. B., Davis, D. and Mitchell, A. P.** (1999). Rapid hypothesis testing with Candida albicans through gene disruption with short homology regions. *J. Bacteriol.* **181**, 1868-1874.

**Zuin, A., Vivancos, A. P., Sansó, M., Takatsume, Y., Ayté, J., Inoue, Y. and Hidalgo, E.** (2005). The glycolytic metabolite methylglyoxal activates Pap1 and Sty1 stress responses in Schizosaccharomyces pombe. *J. Biol. Chem.* **280**, 36708-36713.

## Appendix 3:

Johnson, C. A., Brooker, H. R., Gyamfi, I., O'Brien, J., Ashley, B., Brazier, J. E., Dean, A., Embling, J., Grimsey, E., Tomlinson, A. C., Wilson. E. G., Geeves, M., & Mulvihill, D. P. (2018). Temperature sensitive point mutations in fission yeast tropomyosin have long range effects on the stability and function of the actin-tropomyosin copolymer. *Biochemical and Biophysical Research Communications, 506*(2), 339-346. doi:10.1016/j.bbrc.2017.10.109

Time-lapses of cytokinesis in temperature sensitive *cdc8.27 rlc1-GFP* and *cdc8.110 rlc1-GFP* mutant *S. pombe* strains, were taken, to determine defects that substitutions E129K (*cdc8.27)*, A18T and E31K (*cdc8.110*) cause in the actin stabilising function of Cdc8 during cytokinesis. The strains were cultured at 25 $^{o}$C, 28 $^{o}$C, 30 $^{o}$C, 32 $^{o}$C, 34 $^{o}$C, 36 $^{o}$C over 48 hr, before imaging (Figure 1) (Johnson et al., 2018).

The severity of defects in CAR structure and constriction increased with increasing temperatures. Defects ranged from CAR displacement, aberrant CAR that eventually constricted, aberrant CAR that failed to constrict and the failure to form a CAR. The structural CAR defects and non-contractile rings observed in *cdc8.27 rlc1-GFP* and *cdc8.110 rlc1-GFP* cells were consistent with the actin stabilising role of Cdc8. The *cdc8.27* and *cdc8.110* alleles were therefore shown to hinder the attachment of the CAR to the cell cortex and the overall placement of the CAR. The two point mutations in the *cdc8.110* allele appeared to have an additive effect on Cdc8 function (Figure 1) (Johnson et al., 2018). This data is described in this thesis (Figure 3.2.1, Figure 3.2.2, Figure 3.2.3, Figure 3.2.4, Figure 3.2.5).

Biochemical and Biophysical Research Communications 506 (2018) 339–346

Contents lists available at ScienceDirect

Biochemical and Biophysical Research Communications

journal homepage: www.elsevier.com/locate/ybbrc

# Temperature sensitive point mutations in fission yeast tropomyosin have long range effects on the stability and function of the actin-tropomyosin copolymer

Chloe A. Johnson [1], Holly R. Brooker [1], Irene Gyamfi [1], Jennifer O'Brien, Brogan Ashley, Jodie E. Brazier, Annette Dean, James Embling, Elisabeth Grimsey, Alice C. Tomlinson, Elliot G. Wilson, Michael A. Geeves*, Daniel P. Mulvihill**

*School of Biosciences, University of Kent, Canterbury, Kent, CT2 7NJ, UK*

ARTICLE INFO

*Article history:*
Received 27 September 2017
Accepted 20 October 2017
Available online 1 November 2017

*Keywords:*
Acetylation
*Schizosaccharomyces pombe*
Fission yeast
Actin cytoskeleton
Cdc8
Thermal stability

ABSTRACT

The actin cytoskeleton is modulated by regulatory actin-binding proteins which fine-tune the dynamic properties of the actin polymer to regulate function. One such actin-binding protein is tropomyosin (Tpm), a highly-conserved alpha-helical dimer which stabilises actin and regulates interactions with other proteins. Temperature sensitive mutants of Tpm are invaluable tools in the study of actin filament dependent processes, critical to the viability of a cell. Here we investigated the molecular basis of the temperature sensitivity of fission yeast Tpm mutants which fail to undergo cytokinesis at the restrictive temperatures. Comparison of Contractile Actomyosin Ring (CAR) constriction as well as cell shape and size revealed the *cdc8.110* or *cdc8.27* mutant alleles displayed significant differences in their temperature sensitivity and impact upon actin dependent functions during the cell cycle. *In vitro* analysis revealed the mutant proteins displayed a different reduction in thermostability, and unexpectedly yield two discrete unfolding domains when acetylated on their amino-termini. Our findings demonstrate how subtle changes in structure (point mutations or acetylation) alter the stability not simply of discrete regions of this conserved cytoskeletal protein but of the whole molecule. This differentially impacts the stability and cellular organisation of this essential cytoskeletal protein.

## 1. Introduction

The ability to transiently perturb molecular interactions is invaluable in elucidating protein regulation and function in both a cellular and *in vitro* context. The yeasts provide excellent genetically tractable systems for exploring the cellular function of gene products. Their genomes can be rapidly modified to introduce labels or mutations of proteins using either directed or random genomic replacement approaches. These have been used to great effect and provided a unique insight into our understanding the molecular basis of cell cycle and cytoskeletal regulation [1,2]. Through the generation of conditional mutants, protein function can be specifically repressed within a culture of growing cells. In the case of temperature sensitive mutations normal function continues while cells are cultured at a lower permissive temperature (e.g. 25 °C), but shifting the culture to a higher temperature (e.g. 36 °C), specifically perturbs the functionality of the mutant protein and hence disrupts its individual role in cell proliferation. These mutants are invaluable in the study of dynamic processes critical to the viability of a cell. However, the molecular mechanisms that underlie the temperature sensitivity have yet to be defined for the majority of these mutants, despite being isolated more than 40 years ago.

Tropomyosin (Tpm) is a highly conserved alpha-helical, coiled-coil protein that forms two parallel polymers along the surface of the actin filament, stabilising the actin filament and regulating its interactions with other cytoskeleton components [3,4]. The Tpm helical coiled-coil structure is defined by a heptad repeat of residues within the polypeptide sequence. This promotes regular hydrophobic interactions along the coiled-coil to stabilise the dimer,

---

* Corresponding author.
** Corresponding author.
*E-mail addresses:* m.a.geeves@kent.ac.uk (M.A. Geeves), d.p.mulvihill@kent.ac.uk (D.P. Mulvihill).
[1] These authors contributed equally to this work.

https://doi.org/10.1016/j.bbrc.2017.10.109

and allows salt bridges to form between dimerising proteins. The propensity of Tpm to form end-to-end contacts and polymerise is significantly enhanced by N-terminal (Nt) acetylation, which changes the local charge, and stabilises the coiled-coil structure at the amino-terminus of Tpm [5–7].

Yeasts provide attractive model systems for studying diverse cellular processes. They contain the simplest mechanistic and regulatory systems to underpin cellular processes, which are often significantly more complex in metazoans. This simplification of cellular mechanisms is reflected in the yeast Tpm based regulatory system. Budding and fission yeasts each contain two functionally distinct Tpm isoforms compared to more than 40 in mammalian cells. *Saccharomyces cerevisiae* expresses two Tpm proteins, Tpm1 and Tpm2 [8], existing exclusively in Nt-acetylated forms in the cell, and each facilitate discrete cellular processes [9,10]. In contrast, the fission yeast, *Schizosaccharomyces pombe*, contains a single essential Tpm, Cdc8 (Tpm$^{Cdc8}$), which exists in both Nt-acetylated and non-acetylated forms within the cell, each of which associates with discrete sets of actin polymers to modulate their cellular function [11,12]. Cells lacking functional Tpm$^{Cdc8}$ fail to form a functional CAR and therefore fail to undergo cytokinesis. In addition they fail to deliver myosin V dependent cargoes to the normal sites of cell growth, and therefore lose polarity [13,14].

In this study we investigate the molecular basis of temperature sensitivity of two fission yeast temperature sensitive tropomyosin mutants, *cdc8.27* and *cdc8.110*, to provide an insight into the structure-function relationship of this conserved cytoskeletal protein. *In vivo* analysis revealed each mutant disrupts the ability of the fission yeast cell to grow and divide in discrete ways. Differences in functionality were seen to correlate with positions of amino-acid substitutions and thermal stability of the mutant proteins. These data show that subtle changes in the stability of specific regions of this conserved protein differentially impact the stability and function of this essential cytoskeletal component.

## 2. Materials and methods

*Cell culture*: The yeast strains used in the study were h$^-$ *cdc8*$^+$; h$^-$ *rlc1.gfp:kanMX6*; h$^-$ *cdc8.110 rlc1.gfp:kanMX6*; h$^-$ *cdc8.27 rlc1.gfp:kanMX6*. Cell culture and maintenance were carried out according to [15] using Yeast Extract supplement with amino acids (YES). All cells were maintained as early to mid-log phase cultures for 48 h (grown at 25 °C) before analyses were performed.

*Microscopy*: Imaging was undertaken as described previously [11]. Timelapse images of >20 cells of each strains undergoing cytokinesis were used to characterise AR formation and constriction at each temperature. Cell dimensions were calculated from images of >300 cells of each strain using a Matlab (Mathworks, Natick, USA) based automated image analysis programme, generated within this laboratory [16] with additional algorithms for measuring cell curvature (O'Brien et al., In preparation).

*Molecular Biology*: *cdc8* alleles were amplified from genomic DNA preparations of *cdc8.27* and *cdc8.110* cells, cloned into pGEM-T-Easy vector (Promega, Madison, USA) and sequenced. This procedure was repeated thrice from independent genomic preparations. pJC20*cdc8*$^+$ was described previously [11]. *cdc8.A18T, cdc8.E31K, cdc8.A18T E31K* and *cdc8.129K* were synthesised as *Nde1 – BamH1* fragments (ThermoFisher, Waltham, USA) and cloned into the pJC20 [17] bacterial expression vector. All constructs were sequenced prior to being used for recombinant protein expression.

*Protein Purification*: Tpm$^{Cdc8}$ proteins were expressed from pJC20 based plasmids in either BL21 DE3 or BL21 DE3 pNatB [15] cells to produce protein in non-acetylated and Nt-acetylated forms respectively. Mid-log phase cultures were grown for 3 h with 100 mg/l IPTG. Cells were harvested, resuspended in 30 ml lysis buffer (20 mM Tris pH 7.5, 100 mM NaCl, 2 mM EGTA and 5 mM MgCl$_2$), lysed by sonication and heated to either 85 °C (wild type) or 65 °C (mutant proteins) for 10 min. Debris and insoluble components were removed by centrifugation and nucleotides were removed from the resulting supernatant was incubated with 10 mg/l Bovine Pancreas purified DNase I (Sigma #69182) and RNase A (Sigma #R6513) at 4 °C for 1 h. After buffer exchange into FPLC loading buffer (5 mM Tris pH 7.0, 100 mM NaCl) the Tpm$^{Cdc8}$ was subjected to 3 rounds of FPLC purification using 2 × 5 ml Pharmacia HiTrap-Q columns in tandem, by elution with a 0.1-0.9 M NaCl gradient. After the final FPLC run the protein was resuspended in 5 mM Tris pH 7.0 and subjected to electrospray mass spectroscopy (Fig. S2), SDS-PAGE, and spectrophotometric analyses to determine mass, homogeneity, purity and protein concentration of each protein preparation (Tpm$^{Cdc8}$ extinction coefficient at 280 nm - 2980 M$^{-1}$ cm$^{-1}$). Rabbit actin was purified as described previously [18].

*Circular dichroism* (CD): Measurements were made in 1 mm quartz cuvettes using a Jasco 715 spectropolarimeter. Tpm$^{Cdc8}$ proteins were diluted in CD buffer (10 mM potassium phosphate, 5 mM MgCl$_2$ pH 7.0) to a concentration of 0.4 mg/ml. CD buffer was supplemented with 500 mM NaCl unless stated otherwise in the text to minimize end to end polymerization of Tpm$^{Cdc8}$. Thermal unfolding data were obtained by monitoring the CD signal at 222 nm with a heating rate of 1 °C.min$^{-1}$. At completion of the melting-curve the sample was cooled at a rate of 20 °C.min$^{-1}$. CD spectra are presented as differential absorption ($\Delta$A). Melting curves are reported as fraction of unfolded protein by normalizing the CD signal between 10 and 50 °C.

*Actin binding assay*: Co-sedimentation assays were performed at 25 °C by mixing 10 μM actin with increasing concentrations of Tpm and then assaying the proteins present in the pellet and supernatant using SDS-PAGE as described previously [19,20]. Briefly the gels are scanned to yield the relative density of the actin (loading control) and Tpm bands. The ratio of the densities of the Tpm band to the actin band provided an estimate of the fractional saturation of the actin by Tpm. Analysis of the binding isotherms using the Hill equation yields an estimate of free Tpm concentration required for half saturation of actin affinity (K$_{50\%}$). Values presented are an average of 3 indpendent experiments. This is not a true affinity measurement since Tpm is believed to polymerise on actin.

## 3. Results

The biophysical basis of the temperature sensitivity of two discrete alleles of the fission yeast tropomyosin, Tpm$^{Cdc8}$, *cdc8.27* and *cdc8.110* [1] were examined. Sequence analysis revealed these alleles encode for proteins with amino acid substitutions at opposite ends of the Tpm protein. The *cdc8.27* allele contains a single point mutation, resulting in an E129K amino acid substitution towards the carboxyl terminus of the resultant protein, as reported [21]. In contrast sequence analysis revealed the *cdc8.110* allele encodes for a protein with 2 discrete amino acid substitutions, A18T and E31K, both within the amino region of the protein.

CAR formation and constriction was examined at a range of temperatures (from 25 °C and 36 °C) in *cdc8*$^+$, *cdc8.27* and *cdc8.110* cells expressing fluorescent labelled myosin II regulatory light chain, *rlc1.gfp* [22]. This marker allele was chosen as, unlike the majority of other FP actin filament markers described to date, it has been reported to have no impact upon CAR formation or function [22,23]. In contrast to wild type *cdc8*$^+$ cells, which formed normal functional contractile CARs at each temperature examined (n > 80), cells containing the *cdc8.110* and *cdc8.27* demonstrated a variety of defects in the organisation and function of the contractile machinery (Fig. 1), which increased in severity as the temperature

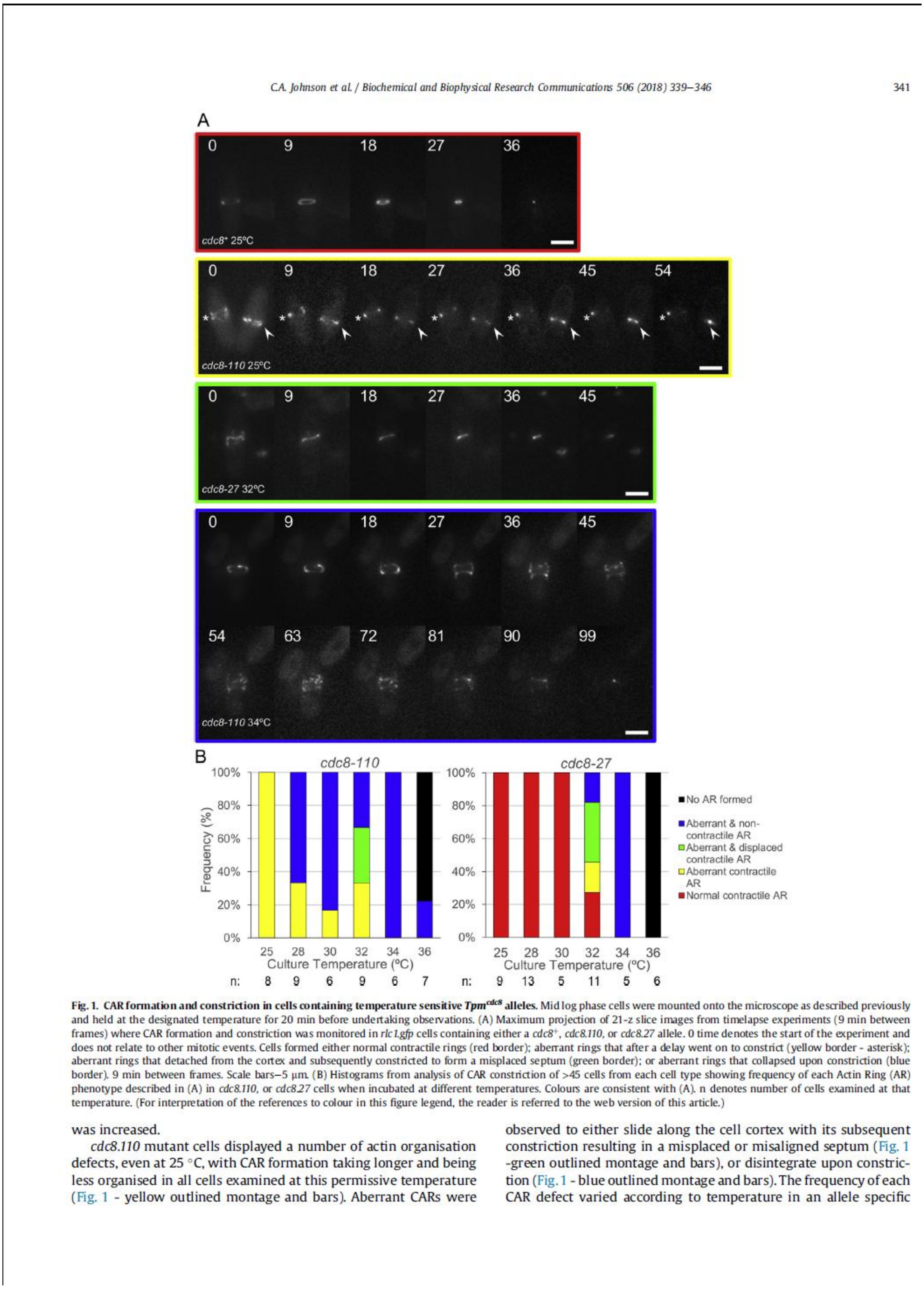

**Fig. 1. CAR formation and constriction in cells containing temperature sensitive *Tpm*$^{cdc8}$ alleles.** Mid log phase cells were mounted onto the microscope as described previously and held at the designated temperature for 20 min before undertaking observations. (A) Maximum projection of 21-z slice images from timelapse experiments (9 min between frames) where CAR formation and constriction was monitored in *rlc1.gfp* cells containing either a *cdc8*$^+$, *cdc8.110*, or *cdc8.27* allele. 0 time denotes the start of the experiment and does not relate to other mitotic events. Cells formed either normal contractile rings (red border); aberrant rings that after a delay went on to constrict (yellow border - asterisk); aberrant rings that detached from the cortex and subsequently constricted to form a misplaced septum (green border); or aberrant rings that collapsed upon constriction (blue border). 9 min between frames. Scale bars–5 μm. (B) Histograms from analysis of CAR constriction of >45 cells from each cell type showing frequency of each Actin Ring (AR) phenotype described in (A) in *cdc8.110*, or *cdc8.27* cells when incubated at different temperatures. Colours are consistent with (A). n denotes number of cells examined at that temperature. (For interpretation of the references to colour in this figure legend, the reader is referred to the web version of this article.)

was increased.

*cdc8.110* mutant cells displayed a number of actin organisation defects, even at 25 °C, with CAR formation taking longer and being less organised in all cells examined at this permissive temperature (Fig. 1 - yellow outlined montage and bars). Aberrant CARs were observed to either slide along the cell cortex with its subsequent constriction resulting in a misplaced or misaligned septum (Fig. 1 -green outlined montage and bars), or disintegrate upon constriction (Fig. 1 - blue outlined montage and bars). The frequency of each CAR defect varied according to temperature in an allele specific

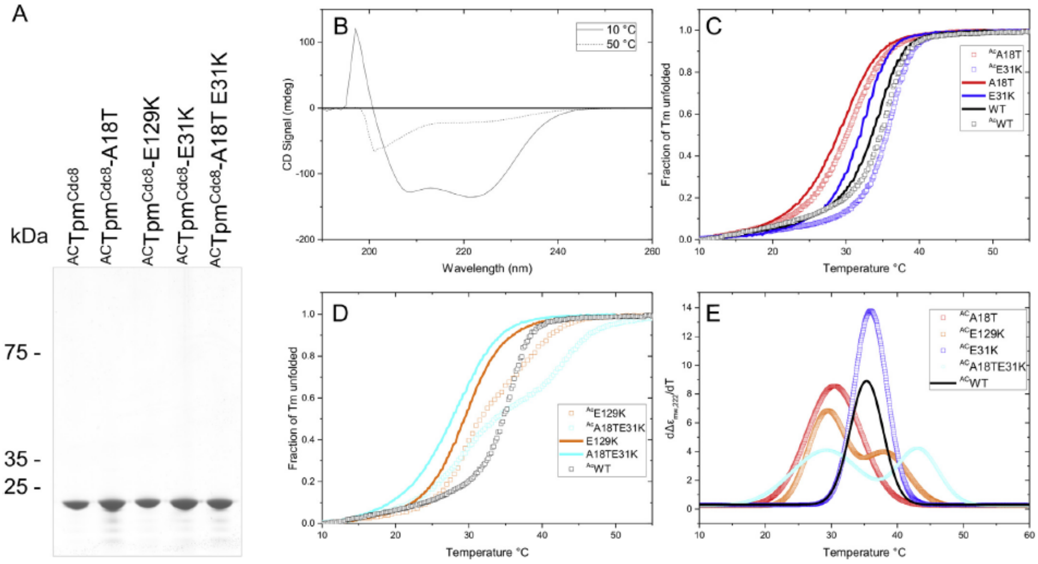

**Fig. 2. CD spectra and melting curves.** (A) Coomassie-Blue stained SDS-PAGE gel showing purified acetylated wild-type and mutant Tpm$^{cdc8}$ proteins. (B) CD spectra for unacetylated Tpm$^{Cdc8}$ at 10 and 50 °C. Normalised CD signal at 222 nm for $^{Ac}$Tpm and unacetylated Tpm as a function of temperature (C) WT-, A18T- and E31K-Tpm and (D) WT-, E129K- and A18TE31K-Tpm. (E) First derivative plots for the four $^{Ac}$Tpms melting curves.

manner. In contrast to *cdc8.110* cells which demonstrated a gradual increase in the frequency of defective CAR, *cdc8.27* cells grew normally and demonstrated normal CAR formation and function at temperatures up to 30 °C. Above this temperature, the majority of cells formed CARs that collapsed upon constriction. At 36 °C both mutant strains failed to form any discernible CAR structure and went on to form multinucleate dumb-bell shaped cells [1,24]. In contrast polarity defects were only observed in *cdc8.110* mutant cells at lower permissive temperatures of 25 °C and 28 °C. Automated image analysis [16] revealed that at these temperatures *cdc8.110* cells were ~10% shorter and 10% wider than both wild type and *cdc8.27* cells (*t*-test significance at >99% confidence), with a significant proportion (39%) displaying a bent cell morphology (Fig. S1). Both of these phenotypes are consistent with tropomyosin stabilised actin polymers having a direct impact upon either microtubule organisation and/or the regulation of polarised cell growth [25].

To determine how differences in the cooperative temperature effects related to the physical properties of the mutant Tpm$^{Cdc8}$ proteins, bacterial expression constructs were generated. These contained cDNA of the mutant *cdc8.27* and *cdc8.110* alleles (Tpm$^{Cdc8.}$E129K and Tpm$^{Cdc8.}$A18T-E31K respectively) as well as *Tpm$^{cdc8}$* containing individual mutations from the *cdc8.110* allele (Tpm$^{Cdc8.}$A18T and Tpm$^{Cdc8.}$E31K). Wild type and mutant Tpm$^{Cdc8}$ proteins were expressed and isolated from bacteria in both unmodified and Nt-acetylated forms [26]. The purity of each protein was confirmed by SDS-PAGE (Fig. 2A) and electrospray mass spectroscopy confirmed that the relative molecular mass of each protein was not only homogeneous but was also within 1 kDa of that predicted (Fig. S2).

In order to explore the impact each substitution has upon structure and thermal stability, each Tpm$^{Cdc8}$ protein was subjected to CD analysis. Tpm folds into α-helices along its entire length, which is consistent with the broad negative peaks at 208 and 222 nm and a positive peak at < 200 nm observed for both wild type and mutant Tpm$^{Cdc8}$ proteins (Fig. 2B). Spectra were collected between 190 and 260 nm before and after heating the proteins to 50 °C. Spectra obtained at 50 °C showed almost a complete removal of the positive peak at <200 nm, and a marked reduction in the signal intensity of the 2 broad negative peaks associated with all Tpm proteins, consistent with a shift from a folded to an unfolded state (Fig. 2B). The proteins were subsequently cooled to 10 °C and the CD spectra indicated a complete reversal of the unfolding as previously reported for Tpm$^{Cdc8}$ [27]. The samples were then

**Table 1**
Summary of thermal properties of Tpm$^{Cdc8}$ proteins.

| | $T_m$(°C) Tpm 0.5 M KCL | $T_m$(°C) Ace-Tpm 0.5 M KCL | $T_m$(°C) 0.1 M KCL | ΔH kJ·mol$^{-1}$ | ΔH Ace-Tpm kJ·mol$^{-1}$ |
|---|---|---|---|---|---|
| Tpm$^{Cdc8}$ | 34.1 | 35.4 | 30.3/33.9 | −455.8 | −555.7 |
| Tpm$^{Cdc8}$-A18T | 29.3 | 30.5 | | −315.4 | −342.3 |
| Tpm$^{Cdc8}$-E129K | 29.4 | 29.3, 38.1 | 24.5/26.2, 34.5 | −331.1 | −481.7, -403.6 |
| Tpm$^{Cdc8}$-E31K | 32.2 | 35.9 | | −447.2 | −571.3 |
| Tpm$^{Cdc8}$-A18TE31K | 27.9 | 29.2, 43.2 | | −276.0 | −256.8, -466.2 |

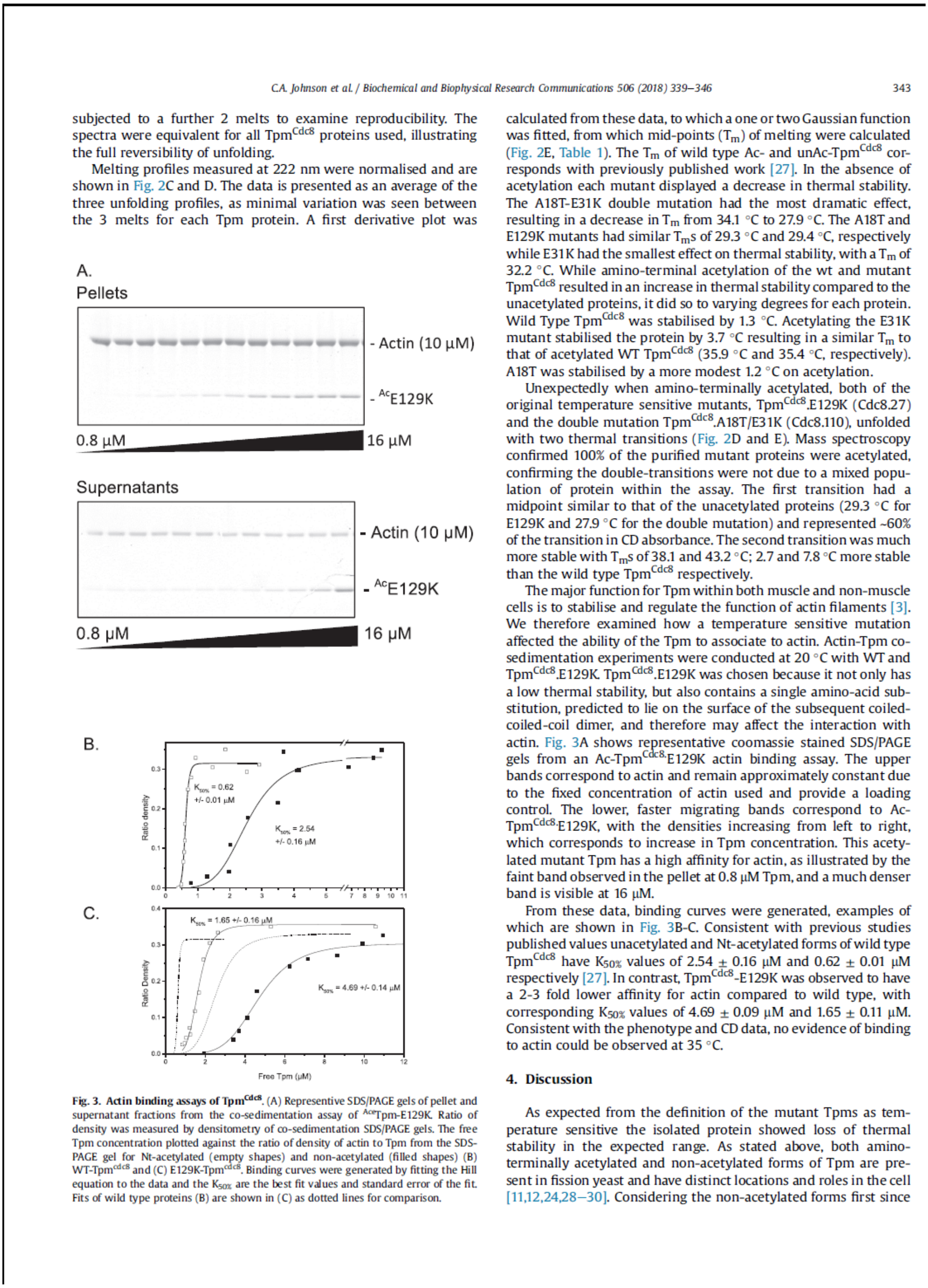

subjected to a further 2 melts to examine reproducibility. The spectra were equivalent for all Tpm$^{Cdc8}$ proteins used, illustrating the full reversibility of unfolding.

Melting profiles measured at 222 nm were normalised and are shown in Fig. 2C and D. The data is presented as an average of the three unfolding profiles, as minimal variation was seen between the 3 melts for each Tpm protein. A first derivative plot was calculated from these data, to which a one or two Gaussian function was fitted, from which mid-points ($T_m$) of melting were calculated (Fig. 2E, Table 1). The $T_m$ of wild type Ac- and unAc-Tpm$^{Cdc8}$ corresponds with previously published work [27]. In the absence of acetylation each mutant displayed a decrease in thermal stability. The A18T-E31K double mutation had the most dramatic effect, resulting in a decrease in $T_m$ from 34.1 °C to 27.9 °C. The A18T and E129K mutants had similar $T_m$s of 29.3 °C and 29.4 °C, respectively while E31K had the smallest effect on thermal stability, with a $T_m$ of 32.2 °C. While amino-terminal acetylation of the wt and mutant Tpm$^{Cdc8}$ resulted in an increase in thermal stability compared to the unacetylated proteins, it did so to varying degrees for each protein. Wild Type Tpm$^{Cdc8}$ was stabilised by 1.3 °C. Acetylating the E31K mutant stabilised the protein by 3.7 °C resulting in a similar $T_m$ to that of acetylated WT Tpm$^{Cdc8}$ (35.9 °C and 35.4 °C, respectively). A18T was stabilised by a more modest 1.2 °C on acetylation.

**Fig. 3. Actin binding assays of Tpm$^{Cdc8}$.** (A) Representive SDS/PAGE gels of pellet and supernatant fractions from the co-sedimentation assay of $^{Ace}$Tpm-E129K. Ratio of density was measured by densitometry of co-sedimentation SDS/PAGE gels. The free Tpm concentration plotted against the ratio of density of actin to Tpm from the SDS-PAGE gel for Nt-acetylated (empty shapes) and non-acetylated (filled shapes) (B) WT-Tpm$^{cdc8}$ and (C) E129K-Tpm$^{cdc8}$. Binding curves were generated by fitting the Hill equation to the data and the K$_{50\%}$ are the best fit values and standard error of the fit. Fits of wild type proteins (B) are shown in (C) as dotted lines for comparison.

Unexpectedly when amino-terminally acetylated, both of the original temperature sensitive mutants, Tpm$^{Cdc8}$.E129K (Cdc8.27) and the double mutation Tpm$^{Cdc8}$.A18T/E31K (Cdc8.110), unfolded with two thermal transitions (Fig. 2D and E). Mass spectroscopy confirmed 100% of the purified mutant proteins were acetylated, confirming the double-transitions were not due to a mixed population of protein within the assay. The first transition had a midpoint similar to that of the unacetylated proteins (29.3 °C for E129K and 27.9 °C for the double mutation) and represented ~60% of the transition in CD absorbance. The second transition was much more stable with $T_m$s of 38.1 and 43.2 °C; 2.7 and 7.8 °C more stable than the wild type Tpm$^{Cdc8}$ respectively.

The major function for Tpm within both muscle and non-muscle cells is to stabilise and regulate the function of actin filaments [3]. We therefore examined how a temperature sensitive mutation affected the ability of the Tpm to associate to actin. Actin-Tpm co-sedimentation experiments were conducted at 20 °C with WT and Tpm$^{Cdc8}$.E129K. Tpm$^{Cdc8}$.E129K was chosen because it not only has a low thermal stability, but also contains a single amino-acid substitution, predicted to lie on the surface of the subsequent coiled-coiled-coil dimer, and therefore may affect the interaction with actin. Fig. 3A shows representative coomassie stained SDS/PAGE gels from an Ac-Tpm$^{Cdc8}$.E129K actin binding assay. The upper bands correspond to actin and remain approximately constant due to the fixed concentration of actin used and provide a loading control. The lower, faster migrating bands correspond to Ac-Tpm$^{Cdc8}$.E129K, with the densities increasing from left to right, which corresponds to increase in Tpm concentration. This acetylated mutant Tpm has a high affinity for actin, as illustrated by the faint band observed in the pellet at 0.8 μM Tpm, and a much denser band is visible at 16 μM.

From these data, binding curves were generated, examples of which are shown in Fig. 3B-C. Consistent with previous studies published values unacetylated and Nt-acetylated forms of wild type Tpm$^{Cdc8}$ have K$_{50\%}$ values of 2.54 ± 0.16 μM and 0.62 ± 0.01 μM respectively [27]. In contrast, Tpm$^{Cdc8}$-E129K was observed to have a 2-3 fold lower affinity for actin compared to wild type, with corresponding K$_{50\%}$ values of 4.69 ± 0.09 μM and 1.65 ± 0.11 μM. Consistent with the phenotype and CD data, no evidence of binding to actin could be observed at 35 °C.

## 4. Discussion

As expected from the definition of the mutant Tpms as temperature sensitive the isolated protein showed loss of thermal stability in the expected range. As stated above, both amino-terminally acetylated and non-acetylated forms of Tpm are present in fission yeast and have distinct locations and roles in the cell [11,12,24,28–30]. Considering the non-acetylated forms first since the effect of mutations is more straight forward to interpret. The wild type protein unfolds with a single thermal transition with a $T_m$ of 34.1 °C. All three single point mutations resulted in a loss of stability; a 4.9 °C lower $T_m$ for A18T and E129K and a smaller 1.9 °C shift for E31K (summarised in Table 1). The double mutant A18T/E31K had the largest reduction in $T_m$ of 6.2° consistent with the effects of the two mutations being largely additive. These *in vitro* data are consistent with our phenotypic analysis of cell growth and AR dynamics in *cdc8+*, *cdc8.27* and *cdc8.110* cells (Fig. 1). While the *cdc8.27* cells displayed normal cell growth and cell division at temperatures up to 30 °C, *cdc8.110* cells displayed CAR formation and growth defects, even at the normal permissive temperature of 25 °C.

The almost >4.5 °C reduction in $T_m$ from 34.1 C for non-acetylated A18T, E129K and the double mutant A18T/E31K would be sufficient to render most of the protein unfolded at 36 °C. If the $T_m$ were similar in the cellular environment, much of the mutant protein would be unfolded at the permissive temperature for cell growth. For the single mutation E31K, which has not been shown to be a temperature sensitive mutation, the loss of stability is not as great and the cells are likely to remain viable at temperatures approaching 36 °C.

The CD studies described here were performed at 0.5 M KCl to prevent Tpm polymerizing end-to-end at the protein concentrations required for the CD measurements [27]. The end-to-end contact could provide additional stabilisation of the N & C-terminal regions in the Tpm polymer. However, little polymer is expected to form in the cell unless bound to actin. Reducing the KCl concentration to 0.1 M resulted in a 4.1 °C lower $T_m$ for the non-acetylated wt $\mathrm{Tpm}^{\mathrm{Cdc8}}$. This lower stability in 0.1 M KCl is consistent with hydrophobic interactions between the a & d positions in the heptad repeat being the primary driver for dimer formation. The loss of thermal stability was greater for the E129K mutant in 0.1 M KCl at between 4.9 °C. The environment of the cell is therefore likely to make the free Tpm even less stable than the values reported in Table 1.

Once acetylated the effects of the mutations are more complex. For wild type $\mathrm{Tpm}^{\mathrm{Cdc8}}$ acetylation results in a 1.3 °C stabilisation of the $T_m$ of the single unfolding transition of the protein. For A18T acetylation induces a similar 1.2 °C increase in $T_m$ meaning the $T_m$ remains 4.9 °C lower than the wild type. For E31K the stabilisation effect was larger at 3.7 °C, making the acetylated mutant marginally more stable than the wild type. This again suggests the single point mutation E31K on its own is unlikely to make the yeast cells temperature-sensitive.

For E129K and A18T/E31K acetylation results in a biphasic melting profile with ~60% of the CD change occurring during the lower temperature transition. For E129K the lower transition occurs at a Tm of 29.3 °C, indistinguishable from that of the single transition of the non-acetylated form. For the double mutation the lower transition occurs at 29.2 °C, 1.3 °C higher than for the non-acetylated form and 4.2 °C lower then wild type acetylated.

The upper, smaller unfolding transition is significantly more stable with $T_m$'s of 38.1 °C for E129K and 43.2 °C for the double

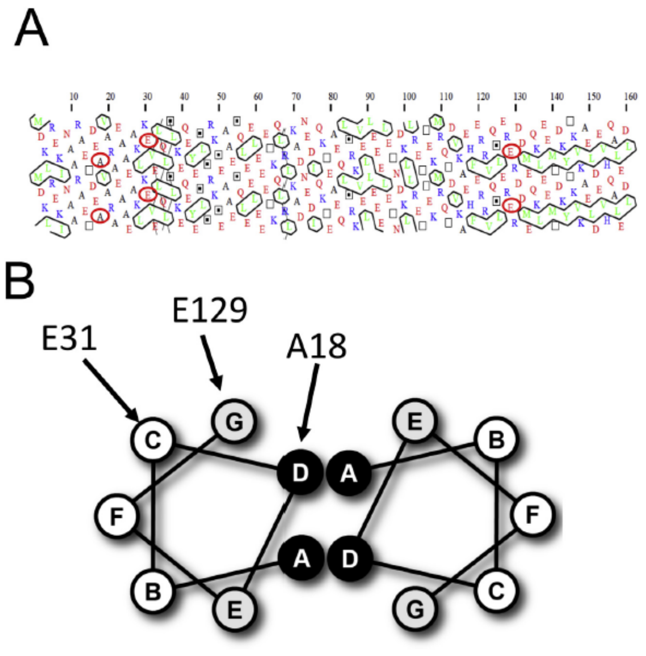

**Fig. 4. Positions of the subsitituted residues.** (A) Hydrophobicity Cluster Analysis showing residues of an α-helix of $\mathrm{Tpm}^{\mathrm{Cdc8}}$. The positions of mutations investigated in this study are shown circled in red. Red residues represent negatively charged amino acids, blue positively charged, and green hydrophobic amino acids. The black lines outlining hydrophobic patches indicate the hydrophobic core of the coiled coil. (B) Diagram illustrating a heptad repeat of 7 residues (A-G) between 2 α-helices. Residues in positions A and D are normally small compact hydrophobic residues involved in stabilising the coiled-coil interactions, and residues E and G are often charged and can form of a salt bridges between the two chains. (For interpretation of the references to colour in this figure legend, the reader is referred to the web version of this article.)

mutant. These are significantly higher than the single unfolding transition $T_m$ of the wild type protein (35.4 C). Since the major effect of N-terminal acetylation is a stabilisation of 40% of the Tpm it is likely this is the N-terminal 40% of the Tpm dimer. Since E129K and the double mutant disrupt the cell cycle at 36 °C this suggests this disruption occurs even though the more stable 40% of the protein will remain folded at this temperature. This could mean that the Tpm does not get rapidly cleared by the cell through proteolysis, but remains present in a semi-folded state allowing rapid refolding and reactivation if the temperature is lowered which permits refolding of the protein.

In the absence of a high-resolution Tpm structure it is difficult to give a precise interpretation of the destabilising effect of the mutations, but some features can be inferred from the position of the residue in the heptad repeat. Ala18 is in the core *d* position of the coiled-coil, normally occupied by small hydrophobic residues. An alanine in this position, with a single $CH_3$- side chain, is thought to introduce some flexibility into the structure by reducing the density of side-chain packing compared to that in the classic leucine zipper coiled coil [5,31]. In some vertebrate Tpms alanine appears in small clusters along the structure. The hydropathy plot of $Tpm^{Cdc8}$ (Fig. 1B) shows A18 is part of an alanine cluster (A11-T15-A18.A22-A25) between two strong hydrophobic clusters (MLI, LVL: ringed in green in Fig. 4A). Replacing Ala18 with Thr introduces a larger side chain and some hydrophilic character into the core and also places two Thr residues close together. This is the probable cause of some destabilistation of the coiled-coil.

Glu31 is at a *c* position of the heptad and therefore thought to play little role in stabilising the coiled-coil structure. It does however sit next to K28 which will be positioned one turn of the α helix below E31 allowing a charge-charge stabilisation of the singe turn of the α helix. The E31K mutation would change this to a charge - charge repulsion causing some loss of stability but the effect of this single mutation is quite modest.

Glu129 is in the *g* position, where salt bridges between position *g* on one chain and *e* on the second chain (Fig. 4B) can give additional stability to the coil-coil. The equivalent *e* position is also a Glu making such a salt bridge impossible and the change to K129 might be expected to stabilise the coiled-coil. A closer look indicates that the local sequence is R128 E129 R130 with R130 in the *a* position of the heptad so this local structure is unlikely to conform to the standard coiled coil structure.

It is currently unclear why amino-terminal acetylation brings about a localised stabilisation of both the Cdc8.110 and Cdc8.27 proteins and not the wild type or single amino-terminal region mutants. The mutations in these proteins are located at opposing ends of the alpha-helical protein, and is therefore consistent with previous studies that have shown acetylation status and amino-acid modifications can have long distance effects upon the tropomyosin structure [27,32,33]. Indeed, each single amino-acid substitution is predicted to have no significant effect on the local structure of the alpha-helix (https://ppopen.informatik.tu-muenchen.de) or coiled-coil [34]. This signifies the mutations and post-translational modification are likely to bring about changes to the overall structure of the polypeptide or coiled-coil dimer. This is consistent with observations and models suggest that the conformation of the protein (i.e. dimerization, coiled-coil and polymer status) can bring about a significant (up to 3-fold) change in CD signal at 222 nm [35].

Nt-acetylation causes increased stability of all Tpms examined and for the two well defined temperature sensitive mutations separates the unfolding into two distinct regions. Since Tpm does not have distinct structural domains it would be incorrect to refer to these two unfolding transitions as domain unfolding but it is clear that there are two distinct regions that unfold with about 60% of the CD change occurring in the first transition. However, it is wise to be cautious about assuming that the CD signal has a strictly linear response to the amount of α-helix present.

## Acknowledgments

We thank Sam Lynn for technical assistance and Ship Centurion for comments on the manuscript. This work was completed largely as an undergraduate final year project under the supervision of DM & MG. The work was supported by the University of Kent, and funding from the Biotechnology and Biological Sciences Research Council (BB/K012045/1 & BB/M015130/1) and a subcontract of an NIH grant (1549410) to Leslie Leinwand. Constructs generated during this study are available at Addgene (http://www.addgene.org/Dan_Mulvihill/).

## Transparency document

Transparency document related to this article can be found online at https://doi.org/10.1016/j.bbrc.2017.10.109.

## Appendix A. Supplementary data

Supplementary data related to this article can be found at https://doi.org/10.1016/j.bbrc.2017.10.109.

## References

[1] P. Nurse, P. Thuriaux, K. Nasmyth, Genetic control of the cell division cycle in the fission yeast *Schizosaccharomyces pombe*, Mol. Gen. Genet. 146 (1976) 167–178.

[2] L.H. Hartwell, R.K. Mortimer, J. Culotti, M. Culotti, Genetic control of the cell division cycle in yeast: V. Genetic analysis of cdc mutants, Genetics 74 (1973) 267–286.

[3] P.W. Gunning, E.C. Hardeman, P. Lappalainen, D.P. Mulvihill, Tropomyosin - master regulator of actin filament function in the cytoskeleton, J. Cell. Sci. 128 (2015) 2965–2974, https://doi.org/10.1242/jcs.172502.

[4] P.W. Gunning, E.C. Hardeman, Tropomyosins, Curr. Biol. 27 (2017) R8–R13, https://doi.org/10.1016/j.cub.2016.11.033.

[5] J.H. Brown, K.H. Kim, G. Jun, N.J. Greenfield, R. Dominguez, N. Volkmann, et al., Deciphering the design of the tropomyosin molecule, Proc. Natl. Acad. Sci. U.S.A. 98 (2001) 8496–8501, https://doi.org/10.1073/pnas.131219198.

[6] T. Palm, N.J. Greenfield, S.E. Hitchcock-DeGregori, Tropomyosin ends determine the stability and functionality of overlap and troponin T complexes, Biophysical J. 84 (2003) 3181–3189, https://doi.org/10.1016/S0006-3495(03)70042-3.

[7] J. Frye, V.A. Klenchin, I. Rayment, Structure of the Tropomyosin overlap complex from chicken smooth muscle: insight into the diversity of N-terminal recognition, Biochemistry 49 (2010) 4908–4920, https://doi.org/10.1021/bi100349a.

[8] B. Drees, C. Brown, B.G. Barrell, A. Bretscher, Tropomyosin is essential in yeast, yet the *TPM1* and *TPM2* products perform distinct functions, J. Cell Biol. 128 (1995) 383–392.

[9] T.M. Huckaba, T. Lipkin, L.A. Pon, Roles of type II myosin and a tropomyosin isoform in retrograde actin flow in budding yeast, J. Cell Biol. 175 (2006) 957–969, https://doi.org/10.1083/jcb.200609155.

[10] S.L. Alioto, M.V. Garabedian, D.R. Bellavance, B.L. Goode, Tropomyosin and profilin cooperate to promote formin-mediated actin nucleation and drive yeast actin cable assembly, Curr. Biol. 26 (2016) 3230–3237, https://doi.org/10.1016/j.cub.2016.09.053.

[11] M. Johnson, D.A. East, D.P. Mulvihill, Formins determine the functional properties of actin filaments in yeast, Curr. Biol. 24 (2014) 1525–1530, https://doi.org/10.1016/j.cub.2014.05.034.

[12] A.T. Coulton, D.A. East, A. Galinska-Rakoczy, W. Lehman, D.P. Mulvihill, The recruitment of acetylated and unacetylated tropomyosin to distinct actin polymers permits the discrete regulation of specific myosins in fission yeast, J. Cell. Sci. 123 (2010) 3235–3243, https://doi.org/10.1242/jcs.069971.

[13] T.Z. Win, Y. Gachet, D.P. Mulvihill, K.M. May, J.S. Hyams, Two type V myosins with non-overlapping functions in the fission yeast *Schizosaccharomyces pombe*: myo52 is concerned with growth polarity and cytokinesis, Myo51 is a component of the cytokinetic actin ring, J. Cell. Sci. 114 (2001) 69–79.

[14] F. Motegi, R. Arai, I. Mabuchi, Identification of two type V myosins in fission yeast, one of which functions in polarized cell growth and moves rapidly in the cell, Mol. Biol. Cell. 12 (2001) 1367–1380.

[15] S. Moreno, A. Klar, P. Nurse, Molecular genetic analysis of fission yeast Schizosaccharomyces pombe, Meth. Enzymol. 194 (1991) 795–823.

[16] J. O'Brien, S. Hoque, D. Mulvihill, K. Sirlantzis, Automated cell segmentation of fission yeast phase images-segmenting cells from light microscopy images, Bioimaging (2017), https://doi.org/10.5220/0006149100920099.

[17] J. Clos, S. Brandau, pJC20 and pJC40–two high-copy-number vectors for T7 RNA polymerase-dependent expression of recombinant genes in *Escherichia coli*, Protein Expr. Purif. 5 (1994) 133–137, https://doi.org/10.1006/prep.1994.1020.

[18] J.A. Spudich, S. Watt, The regulation of rabbit skeletal muscle contraction. I. Biochemical studies of the interaction of the tropomyosin-troponin complex with actin and the proteolytic fragments of myosin, J. Biol. Chem. 246 (1971) 4866–4871.

[19] A. Coulton, S.S. Lehrer, M.A. Geeves, Functional homodimers and heterodimers of recombinant smooth muscle tropomyosin, Biochemistry 45 (2006) 12853–12858, https://doi.org/10.1021/bi0613224.

[20] K. Skoumpla, A.T. Coulton, W. Lehman, M.A. Geeves, D.P. Mulvihill, Acetylation regulates tropomyosin function in the fission yeast *Schizosaccharomyces pombe*, J. Cell. Sci. 120 (2007) 1635–1645, https://doi.org/10.1242/jcs.001115.

[21] H. Kurahashi, Y. Imai, M. Yamamoto, Tropomyosin is required for the cell fusion process during conjugation in fission yeast, Genes cells. 7 (2002) 375–384.

[22] X. Le Goff, F. Motegi, E. Salimova, I. Mabuchi, V. Simanis, The S. pombe rlc1 gene encodes a putative myosin regulatory light chain that binds the type II myosins myo3p and myo2p, J. Cell. Sci. 113 (23) (2000) 4157–4163.

[23] N.I. Naqvi, K.C. Wong, X. Tang, M.K. Balasubramanian, Type II myosin regulatory light chain relieves auto-inhibition of myosin-heavy-chain function, Nat. Cell Biol. 2 (2000) 855–858, https://doi.org/10.1038/35041107.

[24] M.K. Balasubramanian, D.M. Helfman, S.M. Hemmingsen, A new tropomyosin essential for cytokinesis in the fission yeast *S. pombe*, Nature 360 (1992) 84–87, https://doi.org/10.1038/360084a0.

[25] J. Hayles, P. Nurse, A journey into space, Nat. Rev. Mol. Cell Biol. 2 (2001) 647–656, https://doi.org/10.1038/35089520.

[26] M. Johnson, A.T. Coulton, M.A. Geeves, D.P. Mulvihill, Targeted amino-terminal acetylation of recombinant proteins in E. coli, PLoS One 5 (2010) e15801, https://doi.org/10.1371/journal.pone.0015801.

[27] D.A. East, D. Sousa, S.R. Martin, T.A. Edwards, W. Lehman, D.P. Mulvihill, Altering the stability of the Cdc8 overlap region modulates the ability of this tropomyosin to bind co-operatively to actin and regulate myosin, Biochem. J. 438 (2011) 265–273, https://doi.org/10.1042/BJ20101316.

[28] B.C. Stark, T.E. Sladewski, L.W. Pollard, M. Lord, Tropomyosin and myosin-II cellular levels promote actomyosin ring assembly in fission yeast, Mol. Biol. Cell. 21 (2010) 989–1000, https://doi.org/10.1091/mbc.E09-10-0852.

[29] J.E. Clayton, M.R. Sammons, B.C. Stark, A.R. Hodges, M. Lord, Differential regulation of unconventional fission yeast myosins via the actin track, Curr. Biol. 20 (2010) 1423–1431, https://doi.org/10.1016/j.cub.2010.07.026.

[30] J.E. Clayton, L.W. Pollard, M. Sckolnick, C.S. Bookwalter, A.R. Hodges, K.M. Trybus, et al., Fission yeast tropomyosin specifies directed transport of myosin-V along actin cables, Mol. Biol. Cell. 25 (2013) 66–75, https://doi.org/10.1091/mbc.E13-04-0200.

[31] J.H. Brown, Z. Zhou, L. Reshetnikova, H. Robinson, R.D. Yammani, L.S. Tobacman, et al., Structure of the mid-region of tropomyosin: bending and binding sites for actin, Proc. Natl. Acad. Sci. U.S.A. 102 (2005) 18878–18883, https://doi.org/10.1073/pnas.0509269102.

[32] S. Ly, S.S. Lehrer, Long-range effects of familial hypertrophic cardiomyopathy mutations E180G and D175N on the properties of tropomyosin, Biochemistry 51 (2012) 6413–6420, https://doi.org/10.1021/bi3006835.

[33] M. Janco, A. Kalyva, B. Scellini, N. Piroddi, C. Tesi, C. Poggesi, et al., α-Tropomyosin with a D175N or E180G mutation in only one chain differs from tropomyosin with mutations in both chains, Biochemistry 51 (2012) 9880–9890, https://doi.org/10.1021/bi301323n.

[34] A. Lupas, M. Van Dyke, J. Stock, Predicting coiled coils from protein sequences, Science 252 (1991) 1162–1164, https://doi.org/10.1126/science.252.5009.1162.

[35] J.D. Hirst, C.L. Brooks, Helicity, circular dichroism and molecular dynamics of proteins, J. Mol. Biol. 243 (1994) 173–178, https://doi.org/10.1006/jmbi.1994.1644.